

Development of a sensor system for human breath acetone analysis based on photoacoustic spectroscopy



Dissertation

zur Erlangung des Doktorgrades der Naturwissenschaften
(Dr. rer. nat.)
der Fakultät für Chemie und Pharmazie
der Universität Regensburg

vorgelegt von
Stefan Weigl
aus Regensburg
im Jahr 2020

Die vorgelegte Dissertation entstand in der Zeit von Juli 2017 bis November 2020 in Kooperation des Instituts für Analytische Chemie, Chemo- und Biosensorik der naturwissenschaftlichen Fakultät IV - Chemie und Pharmazie - der Universität Regensburg (UR)

und

des Sensorik-Applikationszentrums (SappZ) der Ostbayerischen Technischen Hochschule (OTH) Regensburg.

Die Arbeit wurde angeleitet von: Prof. Dr. habil. Frank-Michael Matysik
Prof. Dr. rer. nat. Rudolf Bierl

Das Promotionsgesuch wurde eingereicht am: 18.11.2020
Termin des Kolloquiums: 01.02.2021

Vorsitz des Prüfungsausschusses übernimmt Prof. Dr. habil. Manfred Scheer. Erstgutachter ist Prof. Dr. habil. Frank-Michael Matysik, Zweitgutachter Prof. Dr. rer. nat. Rudolf Bierl und Drittprüfer ist Prof. Dr. habil. Alkwin Slenczka.

Ich möchte mich an dieser Stelle bei allen bedanken, die mich auf dem Wege der Promotion unterstützt und begleitet haben. Im Besonderen bedanke ich mich bei meiner Familie und meiner Freundin Luka für die ständige Unterstützung, Vertrauen und Motivation auch schon vor meiner Promotion. Spezieller Dank geht an Dr. Thomas Rück für die vielen Diskussionen, seine Zeit und sein Engagement. Ich bedanke mich bei Prof. Dr. Rudolf Bierl und Prof. Dr. Frank-Michael Matysik, für die Betreuung und Unterstützung während meiner Dissertationsarbeit. Schließlich bedanke ich mich auch bei Herrn Dr. Rudolf Jörres, der mich zu Beginn meiner Arbeit außerordentlich unterstützt hat.

I would like to take this opportunity to thank everyone who supported and accompanied me on my way to my doctorate. In particular, I would like to thank my family and my girlfriend Luka for their constant support, trust and motivation even before my graduation. Special thanks go to Dr. Thomas Rück for our discussions, his commitment and his engagement. I would also like to thank Prof. Dr. Rudolf Bierl and Prof. Dr. Frank-Michael Matysik for their supervision and support during my dissertation. Finally, I would like to thank Dr. Rudolf Jörres, who gave me extraordinary support at the beginning of my work, too.

*"Denn die einen sind im Dunkeln und die andern sind im Licht
und man [höret] die im Lichte die im Dunkeln [hört] man nicht"*
(Abgewandelt aus Berthold Brechts Dreigroschenoper, 1928, Berlin)

Contents

List of Figures	xi
List of Tables	xvii
List of Symbols	xxi
Curriculum Vitae	xxxvi
Oral and Poster Presentation	xxxvii
The Author's Original Publications	xxxviii
Declaration of Collaboration	xl
1 Introduction	1
2 Theory	7
2.1 Breath analysis	8
2.1.1 History	8
2.1.2 State of the art	9
2.1.3 Breathborne biomarkers: physiological pathways and applications	13
2.1.4 Acetone as a breathborne biomarker	18
2.1.5 Composition of breath	21
2.1.6 Challenges in modern breath analysis	27

2.1.7	Aerosols, particles and breath condensate . . .	30
2.1.8	References	31
2.2	Absorption spectroscopy (AS)	42
2.2.1	Absorption spectra	42
2.2.2	Lambert-Beer	54
2.2.3	Line intensity	56
2.2.4	Line shape	57
2.2.5	Laser spectroscopy	62
2.2.6	Wavelength modulation (WM)	64
2.2.7	References	70
2.3	Photoacoustic spectroscopy (PAS)	75
2.3.1	Heat production	76
2.3.2	Acoustic wave generation	80
2.3.3	References	84
2.4	Signal amplification	87
2.4.1	Acoustic resonance amplification	87
2.4.2	Lock-in amplification	93
2.4.3	References	97
2.5	Attenuation effects	101
2.5.1	The photoacoustic quality factor	101
2.5.2	Nonradiative relaxation	103
2.5.3	Collision rate	109
2.5.4	Acoustic attenuation	112
2.5.5	Frequency detuning	116
2.5.6	Photodissociation of acetone	118
2.5.7	References	127
3	Spectral interference analysis	135
3.1	Spectral databases	136

3.1.1	High-resolution transmission molecular absorption database (HITRAN)	136
3.1.2	Pacific Northwest National Laboratory (PNNL)	137
3.1.3	Spectral Atlas	138
3.1.4	<i>QuickSpec</i> software tool	139
3.1.5	References	140
3.2	Spectral interference analysis in the IR and UV region	142
3.2.1	The interfering species	142
3.2.2	Acetone spectra and wavelength modulation . .	144
3.2.3	Influence of temperature and pressure on the absorption bands of acetone	147
3.2.4	Simulation parameter	148
3.2.5	Results of the IR spectral interference analysis .	149
3.2.6	Summary and conclusion of the IR spectral interference analysis	157
3.2.7	Multicomponent analysis	159
3.2.8	Spectral interference analysis of the 278 nm absorption band of acetone	162
3.2.9	References	166
4	Experimental	171
4.1	Laboratory setup	172
4.1.1	Gas stream concept	172
4.1.2	Electronics	174
4.2	Light sources	178
4.3	Fourier Transform - Infrared (FT-IR) spectroscopy . .	185
4.4	References	186
5	Results and discussion	189
5.1	Photoacoustic detection of acetone in N ₂ and synthetic air using a high power UV LED	190

5.1.1	Experimental	192
5.1.2	LED collimation design	194
5.1.3	Deexcitation process of acetone and sensing mechanism	198
5.1.4	Acetone measurements	199
5.1.5	Comparison to other acetone gas sensing techniques	206
5.1.6	Conclusion	207
5.1.7	References	207
5.2	Effects of ambient parameters and cross-sensitivities from O_2 , CO_2 and H_2O on the photoacoustic detection of acetone in the UV region	213
5.2.1	Introduction	213
5.2.2	Experimental	214
5.2.3	Measurement settings	215
5.2.4	Calibration curves at small acetone concentrations	215
5.2.5	Influence of environmental parameters	216
5.2.6	Cross-sensitivities towards O_2 , CO_2 and H_2O	222
5.2.7	Analysis of the prepared dataset	228
5.2.8	Conclusion	232
5.2.9	References	234
5.3	Further UV LED measurements	238
5.3.1	Experimental	238
5.3.2	Results and discussion	240
5.3.3	Comparison of different photoacoustic cells and LEDs	240
5.4	IR measurements	244
5.4.1	Experimental	244
5.4.2	OPO measurements	244

5.4.3	QCL measurements	246
5.4.4	ICL measurements	248
5.4.5	References	250
5.5	Comparison of the photoacoustic systems	252
6	Summary	255
7	Zusammenfassung in deutscher Sprache	257
	Appendices	259
A	Miscellaneous	260
A.1	Acoustic modes and Bessel function	260
A.2	Relations between different types of viscosities .	261
A.3	Photodissociation quantum yield parameter . .	261
A.4	Simulation parameter	262
A.5	Equivalent noise bandwidth (ENBW)	263
B	Supplement to the datasets	264
C	Datasheets	270
C.1	LG Innotek UV LED	270
C.2	Bolb UV LED	273
C.3	nanoplus ICL	276
C.4	AdTech QCL	279

List of Figures

2.1	Generic overview for exhaled breath analysis.	10
2.2	Illustration of different exhale phases.	11
2.3	Visualisation of the pathways for certain potential markers.	13
2.4	Acetone structure formula and 3D structure.	19
2.5	Visualisation of the acetone pathway in the liver. . . .	20
2.6	Wavelength regions of electromagnetic waves important in molecular and atomic spectroscopy.	43
2.7	Energy diagram of the different rotational energy levels.	45
2.8	Morse potential visualising the anharmonic course of the parabolic curve at higher vibrational energies. . . .	47
2.9	Measured CO ₂ IR spectrum from the Pacific Northwest National Library.	48
2.10	Measured acetone IR spectrum from the Pacific Northwest National Library.	50
2.11	Jablonsky diagram visualising different energy states and quantum processes within a molecule.	52
2.12	Illustration of the carbonyl-group's molecule orbitals and the absorption spectra of acetone in the UV region.	53
2.13	Normalised peak shapes of a Gaussian, Lorentzian and Voigt peak profile.	61
2.14	Setup of a wavelength modulation absorption spectroscopy system.	64
2.15	Visualisation of the different parameters used in WMAS and resulting signal shapes after LIA demodulation. . .	66
2.16	Validation of the thin sample approximation for trace gas detection of acetone.	68

2.17	Schematic of the principle of photoacoustic signal generation within a measurement cell.	75
2.18	Time dependent relative state distribution for 10 ppmV of acetone.	79
2.19	Half cut drawing of one of the H-shaped PACs employed within this work.	88
2.20	Visualisation of the overlap integral and reciprocal coupling factor for two different laser beam diameters. . .	92
2.21	Sketch of the functional principle of a dual-phase lock-in amplifier.	94
2.22	Typical course of the phase during a frequency sweep. .	96
2.23	Illustration of the loss of energy due to exceeding the maximum modulation frequency.	106
2.24	Illustration of two different types of kinetic cooling. . .	108
2.25	Illustration of the Lennard-Jones potential, describing the process of molecular collision.	111
2.26	Illustration of a standing wave within an acoustic resonator showing the pressure amplitude and particle displacement.	114
2.27	Visualisation of the different acoustic dissipation phenomena.	115
2.28	Comparison of acoustic attenuation in air at 20 °C for varying relative humidity at different frequencies. . . .	116
2.29	Energy levels of the excited $n_S \rightarrow \pi_S^*$ state in acetone and corresponding energies necessary for photolysis. . .	119
2.30	Photodissociation quantum yields of acetone for different wavelengths at 295 K and 1000 mbar.	124
2.31	Photodissociation quantum yields of acetone at various temperature and pressure conditions.	125
2.32	Visualisation of the time needed to reach equilibrium between the number of excited states ρ' and total number of states ρ , neglecting dissociation.	127
2.33	Illustration of the relative loss for a 10 ppmV sample of acetone over time due to dissociation.	128

3.1	Snippet of the graphical user interface of the <i>QuickSpec</i> simulation tool.	139
3.2	Illustration of the broad acetone absorption bands at 1200 cm^{-1} and at 3000 cm^{-1}	145
3.3	Measured absorption cross section of the $n_S \rightarrow \pi_S^*$ transition in acetone at 298 K.	146
3.4	Demonstration of the influence of pressure and temperature on the IR acetone absorption cross section	147
3.5	General overview of spectral overlap introduced by exogenous species and water in the region from 1000 cm^{-1} to 4000 cm^{-1}	150
3.6	Comparison of simulated and measured water absorption coefficients.	151
3.7	Comparison of simulated and measured absorption coefficient of H_2O in a low absorbing region.	152
3.8	Spectral interference analysis including 50 000 ppmV of H_2O and 0.1 ppmV of acetone.	153
3.9	Comparison of simulated and measured carbon dioxide absorption cross sections between 1000 cm^{-1} and 4000 cm^{-1}	153
3.10	Spectral interference analysis including 50 000 ppmV of simulated CO_2 and 0.1 ppmV of acetone.	154
3.11	Spectral interference analysis of acetone in a mixture with endogenous species including CO , N_2O , and NH_3	155
3.12	Spectral interference analysis of acetone in a mixture with endogenous species including COS , isoprene, methane and methanol.	155
3.13	Spectral interference analysis of acetone in a mixture with exogenous species including formaldehyde, ethanol, 1-propanol and isopropanol.	156
3.14	Example of multicomponent analysis using multiple wavelengths.	160
3.15	Comparison of the absorption coefficient for 1.0 ppmV of acetone and 0.6 ppmV of formaldehyde in the UV.	165

4.1	Schematic of the gas stream concept used within this thesis.	173
4.2	Schematic of the employed electronic devices on measurement station 1.	175
4.3	Schematic of the used electronic devices on measurement station 2.	176
4.4	Schematic of the band profile and active region processes in LEDs, QCLs and ICLs.	179
4.5	Image of the cube ICL and HHL housed QCL and a schematic of the optical paths of the laser beams. . . .	180
4.6	Optical output power of the OPO laser for different wavelengths	182
4.7	Operation principle of an Nd:YAG pumped OPO system.	183
4.8	Schematic of the optical path of the OPO's laser beam.	184
4.9	Schematic of a Michelson interferometer, destructive, constructive and polychromatic interference and an interferogram.	186
5.1	Cross-section drawing of the employed PAC.	193
5.2	Simulation of a two-lens system in FRED.	195
5.3	Schematic drawing of the simulation verification setup.	197
5.4	Frequency sweep measurement of 50 ppmV of acetone using a high power UV LED.	199
5.5	Influence of the time constant τ_{LIA} on the noise and a histogram of a one-hour measurement.	201
5.6	Allan-Werle deviation over a one-hour measurement in synthetic air	202
5.7	Acetone drop measured by the FT-IR combined with the photoacoustic signal.	203
5.8	Frequency sweeps at different temperatures.	217
5.9	Illustration of several frequency sweeps at various pressures and shift of the resonance frequency at negative pressures.	219
5.10	Photoacoustic signal for different UV LED duty cycles.	221

5.11	UV absorption cross section including the different electronic transitions.	222
5.12	Influence of CO ₂ added to 30 ppmV of acetone diluted in synthetic air.	225
5.13	Influence of water onto the background signal for pure synthetic air and 30 ppmV of acetone in synthetic air. .	227
5.14	Varying H ₂ O and CO ₂ concentrations in typical breath mixtures and its influence on the photoacoustic signal.	228
5.15	Pearson correlation values of acetone and the measured magnitude to the other features.	229
5.16	Image of a half section of PAC2 and a three-quarter cut of PAC5.	239
5.17	Frequency sweep and calibration curve results, measured using LED2 and PAC2.	240
5.18	Characterisation of the QCL emission tuneability in cw-mode.	247
5.19	Characterisation of the ICL emission tuneability in cw-mode.	248
5.20	Photoacoustic spectrum of 10 ppmV of acetone and methane diluted in N ₂	250
A1	Schematic of the longitudinal, radial and azimuthal acoustic modes in a cylindrical acoustic resonator. . . .	260

List of Tables

2.1	Approved clinical tests by FDA and EMA.	14
2.2	List of the most abundant compounds of human breath exhale.	23
2.3	List of cleaning agents and disinfectants commonly used in clinical environment.	25
2.4	Complex compounds containing a carbonyl group, which are connected to a certain disease or metabolism. . . .	26
2.5	Confounding variables influencing the results of breath analysis in pulmonary diseases.	28
2.6	List of VT-relaxation times of species occurring in ex- haled breath and at atmospheric pressure.	105
2.7	List of VV energy transfer times of species occurring in exhaled breath.	107
2.8	List of the heats assigned to the different relaxation paths in excited acetone.	122
3.1	List of endogenous substances and their correspond- ing concentrations in human breath exhale employed within spectral interference analysis.	143
3.2	List of exogenous substances and their corresponding concentrations in human breath exhale, which are em- ployed within the spectral interference analysis.	144
3.3	Peak width and height of different prominent acetone peaks between 1000 cm^{-1} to 4000 cm^{-1}	146
3.4	Separation of the different interference species in differ- ent simulation groups.	149

3.5	Summary of the most promising absorption regions around the acetone absorption band at 3000 cm^{-1} and 1220 cm^{-1}	158
3.6	List of several chromophores, corresponding molecule classes, transitions, maximum wavelengths and maximum molar extinction coefficients.	162
3.7	High abundant endogenous molecules in human breath with low interference potential in the UV region.	163
4.1	PAC and light source combinations used within the results chapter of this thesis.	181
4.2	The lengths and diameters of the employed PACs	181
5.1	Simulated and measured results of the three beam guiding approaches.	196
5.2	Summary of the calibration measurements for acetone in nitrogen and synthetic air.	205
5.3	Summary of different approaches regarding acetone sensor techniques with their respective LODs.	206
5.4	All gas mixtures used during the experiments excluding pure N_2 and pure synthetic air.	215
5.5	Summary of the different calibration measurement series.	216
5.6	Seven most important features from Lasso ranking. . . .	231
5.7	Summary of the key parameters of the different UV LED measurement setups.	241
5.8	Summary of the OPO measurement results.	245
5.9	Summary of the QCL measurement results.	247
5.10	Summary of the ICL measurement results.	249
5.11	Comparison of the normalised noise equivalent absorption coefficients of the employed PAC systems.	253
A1	Values of $\pi\alpha_{\hat{u}\hat{v}}$ for some of the first radial and azimuthal modes of a cylindrical acoustic resonator.	260
A2	Simulation parameter for the <i>MolExplorer</i> and <i>HITRAN on the Web</i> simulations.	262

A3	Equivalent noise bandwidth for different time constants and filter slopes provided by the manufacturer of the lock-in amplifier.	263
----	--	-----

List of Symbols

Short cuts

3HB	3- β -hydroxybutyrate
A	absorption
AC	alternating current
AcAc	acetoacetate
ACS	absorption cross section
ADC	analog to digital converter
ADHF	acute decompensated heart failure
AM	amplitude modulation
AM-PAS	amplitude modulated photoacoustic spectroscopy
AS	absorption spectroscopy
AWD	Allan-Werle deviation
B.C.	before christ
BC	biconvex
BCFA	branched-chain fatty acids
Carbamoyl P	carbamoyl-phosphate
CF	cystic fibrosis
CIA	collision induced absorption
CoA	coenzym A
CRDS	cavity ringdown spectroscopy
CV	confounding variable
cw	continuous wave

dB	decibel
DC	direct current
DFB	distributed feedback
DSP	digital signal processing
EBA	exhaled breath aerosol
EBC	exhaled breath condensate
EC-QCL	external cavity quantum cascade laser
EMA	European Medicines Association
ENBW	equivalent noise bandwidth
F	fluorescence
F _E NO	fraction of exhaled NO
F1P	fructose 1-phosphate
FDA	Food and Drug Administration
FFT	fast Fourier transform
FG	function generator
FID	flame ionisation detector
FM	frequency modulation
FMAS	frequency modulated absorption spectroscopy
FST	fused silica tube
FT-IR	fourier transform infrared
FWHM	full width at half maximum
G1P	glucose 1-phosphate
GC	gas chromatography
GPIB	general purpose interface bus
HAPI	HITRAN Application Programming Interface
HHL	high heat load
HITEMP	high-temperature molecular spectroscopic database
HITRAN	high-resolution transmission molecular absorption database
HMG	hydroxy methyl glutaryl

HWHM	half width at half maximum
IC	internal conversion
ICL	interband cascade laser
IMS	ion mobility spectrometry
IPA	isopropyl alcohol
IR	infrared
ISC	intersystem crossing
ISO	International Organization for Standardization
LD	laser diode
LED	light emitting diode
LIA	lock-in amplifier
LIDAR	light detection and ranging
LiMAx	maximum liver function capacity
LOD	limit of detection
LPF	low-pass filter
MEMS	micro-electro-mechanical system
MEPS	microextraction by packed sorbent
MFC	mass flow controller
MI	Michelson interferometer
MOCAM	modulation cancellation method
MPI	Max-Planck Institute
MS	mass spectrometry
MST	measurement station
MVA	multivariate analysis
NDIR	nondispersive infrared
NIST	National Institute for Standards and Technology
NNEA	normalised noise equivalent absorbance
NTC	negative temperature coefficient
NTD	needle trap device

NWG	Nachweisgrenze
OA-ICOS	off-axis integrated cavity output spectroscopy
OBS	organic based sensor
OPO	optical parametric oscillator
PA	pseudomonas aeruginosa
PAC	photoacoustic measurement cell
PAS	photoacoustic spectroscopy
PCA	principal component analysis
PCB	printed circuit board
Ph	phosphorescence
pH	power of hydrogen
PLS	partial least-square
PNNL	Pacific Northwest National Library
POC	point of care
ppbV	parts per billion by volume
PPC	pre-pressure controller
ppmV	parts per million by volume
pptV	parts per trillion by volume
PRV	pressure relief valve
PSD	phase sensitive detection
PTR-MS	proton transfer reaction mass spectrometry
QCL	quantum cascade laser
QW	quantum well
RAM	residual amplitude modulation
RES	resonance
rH	relative humidity
SCFA	short chain fatty acids
SESI-MS	secondary electrospray ionisation mass spectrometry
SIBO	small intestinal bacterial overgrowth

SMD	surface mount device
SMO	semiconductor metal oxide
SMSD	statistical misconceptions in the study design
SNR	signal to noise ratio
SPM	single point measurement
SPME	solid phase microextraction
TAG	triacylglyceride
TD	thermal desorption
TDLAS	tunable diode laser absorption spectroscopy
TEC	thermoelectric cooler
TOF	time-of-flight
TpH	temperature-pressure-humidity
TSA	thin sample approximation
TTL	transistor-transistor logic
USB	universal serial bus
UV/VIS	ultra violet/ visible
VC	voodoo correlation
VECSEL	vertical external cavity surface emitting laser
VOC	volatile organic compound
VR	vibrational relaxation
WM	wavelength modulation
WM-PAS	wavelength modulated photoacoustic spectroscopy
WMAS	wavelength modulated absorption spectroscopy

Greek symbols**Unit**

$(\alpha_v \lambda_s)_m$	maximum absorption per wavelength associated with the vibrational relaxation	1
$\alpha(\tilde{\nu})$	molar extinction coefficient	cm^{-1}
α_a	acoustical absorption coefficient	m^{-1}

α_{cl}	acoustical absorption coefficient based on classical attenuation	m^{-1}
α_{HITRAN}	absorption coefficient in HITRAN units	cm^{-1}
α_{r}	strength of the repulsive forces	m^{-1}
α_{v}	acoustical absorption coefficient based on molecular attenuation	m^{-1}
β_{T}	coefficient of thermal expansion	K^{-1}
$\Delta\nu_{\text{dop}}$	Doppler line broadening frequency	s^{-1}
$\Delta\tilde{\nu}_{\text{V}}$	broadening line width of a Voigt profile	cm^{-1}
$\Delta\tilde{\nu}_{\text{col}}$	collisional line broadening	cm^{-1}
$\Delta\tilde{\nu}_{\text{dop}}$	Doppler line broadening	cm^{-1}
$\Delta\tilde{\nu}_{\text{nat}}$	natural line broadening	cm^{-1}
$\Delta\tilde{\nu}_{\text{tot}}$	total line broadening	cm^{-1}
δ_{as}	anti symmetrical deformation vibration	1
δ_{s}	symmetrical deformation vibration	1
$\Delta_{\text{WM}}\tilde{\nu}_{\text{ph}}$	scanning range	cm^{-1}
$\delta_{\text{WM}}\tilde{\nu}_{\text{ph}}$	modulation depth	cm^{-1}
δ_{ik}	Kronecker-Delta	1
η_{b}	bulk viscosity	$\frac{\text{kg}}{\text{m s}}$
η_{c}	light to sound conversion efficiency	1
η_{d}	dynamic viscosity	N s m^{-2}
η_{s}	shear viscosity	$\frac{\text{kg}}{\text{m s}}$
η_k	light-to-sound coupling factor	1
γ	heat capacity ratio	1
κ_{T}	isothermal compressibility	$\text{m}^2 \text{N}^{-1}$
λ_{s}	wavelength of an acoustic wave	m
$\lambda_{\text{b:air}}$	specific partition coefficient between blood and air	1
μ	transition dipole moment	A s m
μ_{k}	kinematic viscosity	$\text{m}^2 \text{s}^{-1}$

μ_{ii}	reduced mass of two molecules i	kg
ν	frequency	s^{-1}
ν_{as}	anti symmetrical stretching vibration	1
ν_{obs}	observed frequency of an observer	s^{-1}
ν_{o}	oscillation frequency of the vibrational mode	s^{-1}
ν_{s}	symmetrical stretching vibration	1
ν_{ph}	frequency of a photon	s^{-1}
ω	angular frequency	rad s^{-1}
ω_{r}	angular frequency of the reference signal	rad s^{-1}
ω_{st}	angular frequency of the slow sawtooth signal in WM	rad s^{-1}
ω_{s}	angular frequency of the acquired signal	rad s^{-1}
ω_{WM}	angular frequency of the fast sinusoidal signal in WM	rad s^{-1}
ω_k	angular resonance frequency of the k^{th} mode	rad s^{-1}
Φ_{d}	photodissociation quantum yield	1
Φ_{n}	nonradiative quantum yield	1
ϕ_{p}	phase lag between reference and measurement signal	rad
Φ_{r}	radiative quantum yield	1
ϕ_{r}	phase of the reference signal	rad
ϕ_{s}	phase of the measurement signal	rad
π	mathematical constant $\pi \approx 3.14159265359$	1
$\pi\alpha_{\hat{u}\hat{v}}$	the \hat{v}^{th} root of the derivative of the \hat{u}^{th} order Bessel function	1
π_{S}	π -bonding orbital	1
Ψ_0	offset photon flux without modulation of the light source	$\text{s}^{-1} \text{m}^{-2}$
Ψ_{ph}	photon flux	$\text{s}^{-1} \text{m}^{-2}$
ρ	particle density	cm^{-3}

$\rho'_u(t)$	excited molecules until time t	cm^{-3}
$\rho_d(t)$	dissociated molecules until time t	cm^{-3}
ρ_j	population density of the rotational state j	cm^{-3}
ρ_S	population density of the valence electron state S	cm^{-3}
ρ_v	population density of the vibrational state v	cm^{-3}
ρ_i	particle density of the molecule i	cm^{-3}
σ_0	separation at zero energy	m
$\sigma_{\text{A,HITRAN}}$	absorption cross section in HITRAN units	cm^2
σ_S	covalent bonding orbital	1
$\sigma_A(\tilde{\nu})$	absorption cross section	cm^2
σ_{TSA}	deviation of thin sample approximation	1
σ_{ii}	collision cross section of two molecules i	m^2
τ_d	lifetime of the photodissociation process	s
τ_e	total lifetime of the excited state	s
τ_{LIA}	time constant of a lock-in amplifier	s
τ_n	nonradiative lifetime	s
τ_{RT}	rotational-translational relaxation lifetime	s
τ_r	radiative lifetime	s
τ_{VT}	vibrational-translational relaxation lifetime	s
τ_{col}	collisional lifetime of a state	s
τ_{sp}	spontaneous lifetime of a state	s
θ	phase difference between photon flux and population density of the excited state	rad
Θ_{WM}	phase shift between AM and WM	rad
$\tilde{\nu}$	wavenumber	cm^{-1}
$\tilde{\nu}_c$	wavenumber at the center of a peak	cm^{-1}
$\tilde{\nu}_{\text{ph,c}}$	peak center wavenumber of emitted photon in WM	cm^{-1}

$\tilde{\rho}$	volume density	kg m^{-3}
$\tilde{\rho}_a$	volume density amplitude induced by light absorption	kg m^{-3}
$\tilde{\rho}_e$	volume density at equilibrium	kg m^{-3}
$\varepsilon(\tilde{\nu})$	molar extinction coefficient	$\frac{\text{L}}{\text{mol cm}}$
ε_0	vacuum permittivity constant	A s m
φ	phase lag between local heat input and modulated laser beam	rad
ξ_{wu}	acoustic mode dependent factor	1
$\zeta_p(\vec{r}, t)$	particle displacement	m
$v_p(\vec{r}, t)$	particle velocity	m s^{-1}

Latin symbols**Unit**

$\bar{v}_{\text{rel},ii}$	average relative velocity of two molecules i	m s^{-1}
ΔL_{dif}	optical path difference	m
$\dot{H}(t)$	time dependent heat production rate	W m^{-3}
\dot{H}_0	power density at equilibrium	W m^{-3}
\dot{Q}_C	cardiac output	L min^{-1}
\dot{V}_A	alveolar ventilation	L min^{-1}
\hat{A}_{01}	probability of absorption	s^{-1}
\hat{A}_{10}	probability of spontaneous emission	s^{-1}
\hat{B}_{10}	probability of stimulated emission	s^{-1}
\hat{C}_{01}	probability of collision induced excitation	s^{-1}
\hat{C}_{10}	probability of collision induced relaxation	s^{-1}
\hat{S}_n	photoacoustic signal	V
\hat{u}	index representing the radial mode	1
\hat{U}_i	low-pass filtered and reference corrected in-phase signal	V
\hat{U}_q	low-pass filtered and reference corrected quadrature signal	V

\hat{u}_r	amplitude of the reference signal	V
\hat{u}_s	amplitude of the signal	V
\hat{v}	index representing the azimuthal mode	1
\hat{v}_i	most probable velocity of a molecule i	m s^{-1}
\hat{w}	longitudinal wave mode	1
\hbar	reduced Planck's quantum of action	J s
\mathcal{J}	total angular momentum quantum number	$\frac{\text{kg m}^2}{\text{s}}$
j	imaginary number	1
c_0	speed of light in vacuum = 299 792 458	m s^{-1}
h	Planck's quantum of action	J s
k	Boltzmann constant = $1.380\,649 \times 10^{-23}$	J K^{-1}
M	multiplicity	1
N_A	Avogadro constant = $6.022\,140\,76 \times 10^{23}$	mol^{-1}
n_s	unbound electron orbital	1
Pr	Prandtl number	1
R	universal gas constant = 8.314 472 462 618 153 24	$\frac{\text{J}}{\text{mol K}}$
$\tilde{A}(\tilde{\nu})$	absorbance at $\tilde{\nu}$	1
\tilde{A}_{PNNL}	absorbance in PNNL units	$\text{ppmV}^{-1} \text{m}^{-1}$
\tilde{B}	rotation constant	cm^{-1}
\tilde{D}_e	depth of the potential well	cm^{-1}
$\tilde{F}(j)$	rotational term of j	cm^{-1}
\tilde{g}	degeneracy of the lower state within a transition	1
$\tilde{G}(v)$	vibrational term of v	cm^{-1}
$\tilde{k}_{r,d}$	rate coefficient for photodissociation	s^{-1}
$\tilde{T}(\tilde{\nu})$	transmittance at $\tilde{\nu}$	1
\vec{v}	velocity vector	m s^{-1}
\vec{v}_l	longitudinal component of the velocity vector	m s^{-1}

a_M	displacement factor	m^{-1}
A_{10}	Einstein coefficient for spontaneous emission	s^{-1}
A_P	the line shape's peak area	cm^2
A_k	amplitude of an acoustic mode k	Pa
B_{01}	Einstein coefficient for absorption	$\frac{\text{m}^3}{\text{J s}^2}$
B_{10}	Einstein coefficient for stimulated emission	$\frac{\text{m}^3}{\text{J s}^2}$
C_A	alveolar concentration	mol L^{-1}
C_a	arterial blood concentration	mol L^{-1}
C_p	specific isobar heat capacity	$\frac{\text{J}}{\text{mol K}}$
c_s	speed of sound	m s^{-1}
C_V	specific isochoric heat capacity	$\frac{\text{J}}{\text{mol K}}$
c_i	concentration of the molecule i	mol L^{-1}
$C_{\bar{V}}$	mixed venous blood concentration	mol L^{-1}
d	sample thickness	cm
d_b	beam diameter	m
$d_{F,\text{eff}}$	effective degrees of freedom participating in wave propagation	1
d_F	available degrees of freedom	1
$d_{k,T}$	thermal boundary layer thickness	m
$d_{k,V}$	viscous boundary layer thickness	m
E	energy	J
E_{av}	available energy of a molecule	J
E_{imp}	energy of the impulsive reservoir	J
E_{int}	internal energy of a molecule	J
E_{st}	energy of the statistical reservoir	J
E_{tr}	translational energy of a molecule	J
E_j	rotation energy	J
E_S	energy of the electronic state	J

E_v	vibration energy	J
E_{ph}	energy of a photon	J
f_c	cut-off frequency of a filter	Hz
f_{LS}	line shape function	cm
f_{mod}	modulation frequency	Hz
f_s	frequency of sound	Hz
$f_{\hat{w}}$	frequency of the longitudinal wave mode	Hz
$f_G(\tilde{\nu})$	Gaussian line shape function	cm
$f_L(\tilde{\nu})$	Lorentzian line shape function	cm
F_{st}	frequency of the slow sawtooth signal in WM	Hz
$f_V(\tilde{\nu})$	Voigt line shape function	cm
f_{WM}	frequency of the fast sinusoidal signal in WM	Hz
f_{res}	resonance frequency	Hz
$G_{\text{dB,f}}$	gain in dB of a field quantity	1
$G_{\text{dB,p}}$	gain in dB of a power quantity	1
G_{I_0}	Gaussian shaped beam profile	m^{-2}
H_u	Fourier coefficient indexed by integer u	cm^{-1}
h_{peak}	height of an absorption cross section peak	cm^2
I	moment of inertia	kg m^2
I_0	incident light intensity	W m^{-2}
I_1	transmitted light intensity	W m^{-2}
$I_{\text{c,c}}$	peak center DC injection current	A
I_c	DC injection current	A
i_c	modulation depth inducing current	A
I_k	coupling integral	1
J	angular momentum	$\frac{\text{kg m}^2}{\text{s}}$
j	angular momentum quantum number	1
$J_{\hat{u}}$	Bessel function of the \hat{u}^{th} order	1

k_T	thermal conductivity	$\frac{W}{m K}$
k_v	spring force	$N m^{-1}$
L_{eff}	effective resonator length	m
L_e	end correction length for two-side open tube resonator	m
L_f	optical path of fixed mirror beam	m
L_m	optical path of movable mirror beam	m
L_{res}	length of the acoustic resonator	m
l_{opt}	optical pathlength	m
m_{mod}	modulation index	1
M_i	molar mass of the molecule i	$kg mol^{-1}$
m_i	mass of the molecule i	kg
m_{eff}	effective mass	kg
N_{Atoms}	number of atoms in a molecule	1
n_m	number of moles	mol
n_r	refractive index	1
n_T	temperature coefficient of collisional broadening	1
N_i	volume fraction of the molecule i	1
p	pressure	Pa
P_0	optical power	W
p_0	initial pressure at the distance $x = 0$	Pa
p_a	pressure amplitude induced by light absorption	Pa
p_e	pressure at equilibrium	Pa
p_k	spatial distribution of the k^{th} mode	1
p_x	pressure at the distance x	Pa
Q_{int}	total internal partition function	1
q_i	released heat during process i	J
$Q_{k,s}$	surface quality factor of an acoustic mode k	1

$Q_{k,V}$	volumetric quality factor of an acoustic mode k	1
Q_k	quality factor of an acoustic mode k	1
r_{res}	radius of the acoustic resonator	m
R_i	radical of the type i	1
r_i	radius of the molecule i	m
R_n	the response of the photoacoustic system at the wavelength n	V W^{-1}
$R_{\text{h-w}}$	height-to-width ratio of an absorption peak	cm^3
S	total spin quantum number	1
s	line strength	cm
S_n	n^{th} -singlet state	1
$S_{2f}(\tilde{\nu}_{\text{ph}})$	signal representation of the 2 nd harmonic in WM	A cm^{-1}
T	absolute temperature	K
t	time	s
T_a	absolute temperature amplitude induced by light absorption	K
T_e	absolute temperature at equilibrium	K
T_n	n^{th} -triplet state	1
t_{90}	time until 90 % of a system's response to a stimulus are reached	m
u_i	in-phase signal	V^2
u_r	reference signal	V
u_s	measured signal	V
V	potential energy	J
v	vibrational quantum number	1
V_{il}	illuminated volume	m^3
V_m	molar volume	L mol^{-1}
V_{res}	volume of the acoustic resonator	m^3

v_i	velocity of a molecule i	m s^{-1}
$w_{\text{G}}(\tilde{\nu})$	line width of the Gaussian function	cm
$w_{\text{L}}(\tilde{\nu})$	line width of the Lorentzian function	cm
x_{e}	anharmonic constant	1
x_{r}	displacement of the molecular bond length from equilibrium	m
x_{ij}	distance between two molecules i and j	m
z	z -coordinate within the acoustic resonator	m
Z_{ij}	collision rate between two molecules i and j	s^{-1}

Miscellaneous symbols

Δ	Laplace operator: second partial derivative in space	m^{-2}
∇	Nabla operator: first partial derivative in space	m^{-1}

Person

Full name Stefan Weigl
E-Mail stefan.weigl@oth-regensburg.de
Date and place of birth 29th October 1990 in Regensburg

Education

07/2017–10/2020 Doctorate at the University of Regensburg
 Faculty of Chemistry and Pharmacy, Institute of Analytical
 Chemistry, Chemosensors and Biosensors
03/2014–04/2016 Completion of the master study "Electrical and Microsystems
 Engineering", M.Eng.
10/2010–03/2014 Completion of the bachelor study "Sensor Technology and Ana-
 lytics ", B.Sc.

Positions and Employment

12/2018 Company foundation, Futuro Farming GmbH
since 05/2016 Research associate at the Ostbayerische Technische Hochschule
 (OTH) Regensburg and coordinator of the "BreathSens" project
04/2015–04/2016 Student assistant at the Sensorik-Applikationszentrum, OTH
 Regensburg
 FPGA programming with LabVIEW
04/2013–03/2014 Student assistant at the Sensorik-Applikationszentrum, OTH
 Regensburg
 Evaluation of distance sensors for quadrocopters
10/2012–02/2013 Internship at Infineon, Kulim, Malaysia
 Chemical analysis in the area of electrochemical wafer deposition

Poster presentations

"Portable photoakustische Messeinheit zur NO₂ Detektion im Spurenbereich"

Peter Gaida, Stefan Weigl, Thomas Rück, Rudolf Bierl

Presented at the *Mikrosystemtechnikkongress* in 2017 (München, Germany), ISBN 978-3-8007-4491-6

"Development of a sensor system for analysis of human breath exhale",
Stefan Weigl, Rudolf Bierl, Frank-Michael Matysik

Presented at the *BayWISS Herbstakademie* in 2018 (Plankstetten, Germany)

"Evaluation of acetone absorption bands for breath analysis in the UV and IR region with optical sensors",

Stefan Weigl, Elisabeth Wittmann, Rudolf Bierl, Frank-Michael Matysik

Presented at the *BreathSummit* in 2019 (Loughborough, UK)

Oral presentation

"Portable Measurement Unit for NO₂ Trace Gas Detection",

Stefan Weigl, Peter Gaida, Thomas Rück, Rudolf Bierl

Presented at the *Open Communication Section at the PHOTOPTICS* in 2018 (Madeira, Portugal)

The authors' original publications

Parts that were adapted from the author's publications form the basis of chapter 5. The adapted text parts are indicated by [P1] and [P2]. This section lists the abstracts of the original publications.

[P1]

Photoacoustic detection of acetone in N₂ and synthetic air using a high power UV LED

S. Weigl, F. Feldmeier, R. Bierl and F.-M. Matysik
in *Sensors Actuators, B Chem.*, vol. 316, no. August 2020, p.
128109, Aug. 2020, doi:10.1016/j.snb.2020.128109.

Abstract

The performance of a photoacoustic trace gas sensor for the detection of acetone in N₂ and synthetic air is reported. The sensor system utilises an amplitude modulated UV LED. The light source has an emission maximum at 278 nm and a maximum CW output power of 300 mW according to the datasheet. Three different collimating and focusing approaches have been investigated to guide the highly divergent LED light into the acoustic resonator of the photoacoustic measurement cell. A 3D printed aluminium cell was designed to optimise light coupling by simultaneously minimizing the photoacoustic background signal generation. Hence, the diameter of the resonator was set to a comparable large diameter of 10 mm and the inner walls of the resonator were mirror polished. The additive manufacturing procedure allowed for integration of a spirally formed gas channel, enabling gas heating prior to detection. The sensor performance was investigated by measuring acetone in N₂ and synthetic air at different concentrations. The UV LED current was set to 86 % of the maximum value according to the datasheet of the light source in order to increase the lifetime and thermal stability. An Allan-Werle deviation analysis validates a stable sensor performance. The limit of detection was determined at a 3σ noise level with a 10 s lock-in amplifier time constant by sampling data points over 20 s with a data acquisition rate

of 5 Hz. LODs of 80.9 ppbV and 19.6 ppbV were obtained for acetone in N₂ and synthetic air, respectively.

[P2]

Effects of ambient parameters and cross-sensitivities from O₂, CO₂ and H₂O on the photoacoustic detection of acetone in the UV region

S. Weigl, E. Wittmann, T. Rück, R. Bierl and F.-M. Matysik
in *Sensors Actuators, B Chem.*, vol. 328, no. February 2021, p.
129001, Feb. 2021, doi:10.1016/j.snb.2020.129001.

Abstract

We present a sensitive UV LED photoacoustic setup for the detection of gaseous acetone and discuss its applicability towards breath analysis. We investigated the performance of the sensor for low acetone concentrations down to 0.1 parts per million (ppmV). The influences of temperature, flow, pressure, optical power and LED duty cycle on the measured signal have been examined. To gain a better understanding of the different effects on the photoacoustic signal, correlation analysis was applied and feature importance was determined using a large measured dataset. Furthermore, the cross-sensitivities towards O₂, CO₂ and H₂O have been studied extensively. Finally, the sensor's performance to detect acetone between 0.1 – 1 ppmV within gas mixtures simulating breath exhale conditions has been investigated, too. With a limit of detection of 12.5 parts per billion (ppbV) (3σ) measured under typical breath exhale gas mixture conditions, the sensor demonstrated a high potential for the application of acetone detection in human breath analysis.

Declaration of Collaboration

Most of the theoretical and experimental scientific work that is presented within this thesis was done independently by the author. In some cases, however, the practical implementation of concepts and the performance of measurements was carried out in collaboration with other researchers and individuals. In any case, assistance was guided and supervised by the author. In accordance with § 7 Abs. 3 Satz 3 of *Ordnung zum Erwerb des akademischen Grades eines Doktors der Naturwissenschaften (Dr. rer. nat.) an der Universität Regensburg vom 18. Juni 2009 (Änderungssatzung vom 6. Februar 2014)*, this section gives a detailed declaration of those collaborations.

Gas stream

(section 4.1.1, p.172)

The concept of the gas mixing unit was created by Thomas Rück and the author. The implementation was carried out by the company INTEGA GmbH (Kirchheim, Germany).

Optical parametric oscillator (OPO) setup

(section 4.2, p.178)

The optical parametric oscillator setup including the optical parts and the laser beam alignment have been carried out by Thomas Rück. The neutral density filter array, which was designed to attenuate OPO laser radiation in order to facilitate optical alignment, was designed by Thomas Rück and implemented by Ignaz Läßle. The author has implemented the optical fibre alignment for continuous wavelength tracking of the OPO.

Collimation optics for the UV LED

(section 5.1.2, p.194 and section 5.3.1, p.238)

The ray trace analysis simulations and the design of the two-lens system as well as the design of the elliptic and parabolic shaped reflectors have been performed by Florian Feldmeier in close consultation with the author. The same applies for the collimation concept for the Bolb UV LED.

Integration into the measurement station has been mainly performed

by Florian Feldmeier. The measurements with the different optics have been performed by the author.

***Photoacoustic cells (PAC) in IR measurements
(section 5.4, p.244)***

The concept and dimensioning of the PAC used within the OPO measurements was conceived by the Thomas Rück. The transfer from concept studies to design drawing was done in collaboration with Ignaz Läßle. The other two cells used for the ICL and QCL measurements base on the PAC designed by Peter Gaida.

***Photoacoustic cells in UV measurements
(section 5.1.1, p.192 and section 5.3.1, p.238)***

The PACs used for the UV measurements are based on the PAC designed by Peter Gaida, but have been adapted in several aspects in close consultation with or directly by the author.

***Interband cascade laser (ICL) and quantum cascade laser (QCL) setup and wavelength characterisation
(section 4.2, p.178 and section 5.4, p.244)***

The integration into the measurement station and the optical alignment of the ICL and QCL have been performed by Viktor Weingardt and Florian Feldmeier, respectively. In both cases, the conceptualisation of the optical design and the supervision of the optical alignment was carried out by the author. The cooling system of the QCL was designed and implemented by Florian Feldmeier in close consultation with the author.

The wavelength characterisations for the ICL and QCL were conducted by Viktor Weingardt and Florian Feldmeier, respectively. However, the measurement series design for the characterisation and the interpretation of the results were done by the author.

***Simulation of suitable wavelengths for multicomponent analysis
(section 3.2.7, p.159)***

The preparation and execution of the simulation was conducted by Elisabeth Wittmann in close consultation with the author.

Dataset preparation and analysis***(section 5.2.7, p.228)***

The preparation and analysis of the dataset was performed by Elisabeth Wittmann in close consultation with the author. All data used based on the measurements of the author. The interpretation of the results was mainly performed by the author in consultation with Elisabeth Wittmann.

Aluminium coating***(section 5.3.1, p.238)***

The aluminium coating of the fused silica tube was performed by Sebastian Peller in close consultation with the author.

Funding

Financial support was received within the scope of the *BreathSens* research project by the Federal Ministry of Education and Research (BMBF) - Grant number: 13GW0325C.

The author received a Ph.D. scholarship from the Hanns-Seidel-Foundation from July 2018 until December 2020. Furthermore, the author received financial support within the scope of the BayWISS - Health initiative from November 2017 until November 2020.

Chapter 1

Introduction

Pandemics like COVID-19 demonstrate the importance of modern and fast diagnosis tools as well as testing equipment to quickly identify infected people, break infection chains and contain the virus' spread. However, not only in pandemic situations but in everyday life such diagnosis tools can be useful. Especially in wealthier countries the life expectancy increases continuously, while birthrates decrease causing a demographic change in the society [1]. Due to that demographic change, the number of people suffering from old-age illnesses like cancer is rising in Germany. According to the Robert-Koch Institute, the cancer case numbers have been rising more than 2 % between 2016 and the end of 2020 causing more than half a million cases of cancer [2]. In addition, the number of adipositas cases has risen perceptibly in the industrialised countries over the last years. Between 2000 and 2015, the number of people suffering from obesity in Germany has risen from 12 % to 23.6 % resulting in a doubling of the adipositas prevalence [3]. The direct and indirect costs of adipositas patients in Germany for the year 2015 were estimated to €23.39 billion and €33.65 billion, respectively [4, pp. 155]. Furthermore, the numbers of diabetes patients are growing significantly world wide and it is estimated, that 10 % (\$670 billion) of the global health expenditure is spent on diabetes each year [5]. Therefore, the need for innovative medical technology will be ubiquitous in the future.

Breath analysis has a high potential to fulfill the requirements of a fast and non-invasive point of care (POC) device. The idea behind exhaled breath gas analysis is based on the fact that all volatile substances dissolved in the blood can reach the exhaled air via the lungs. Hence, changes in the composition of the breath can be used to draw conclusions about the volatile components within the bloodstream and thus about systemic processes [6]. However, although modern breath analysis started in 1971 with Linus Pauling's studies [7], only few breath analysis devices are used in the clinical routine today [8]. There are several reasons for this situation. On the one hand, it is very difficult to identify reliable biomarkers of certain diseases in the vast amount of volatile substances being exhaled and, on the other hand, the concentration ranges are usually in the ppmV (parts per million, 10^{-6}), ppbV (parts per billion, 10^{-9}) or even in the pptV (parts per trillion, 10^{-12}) region and hence, very difficult to measure [9]. With the development of highly selective, sensitive and, in some cases, fast separating techniques like gas chromatography mass spectrometry (GC-MS), ion mobility spectrometry (IMS) or proton transfer reaction spectrometry (PTR-MS) it is possible to detect trace amounts of most of the volatile compounds being present in the exhaled breath. However, these devices are too bulky, expensive and too difficult to use to be employed as a POC device in clinical routine [8], though they are very useful in studies to identify potential biomarkers like acetone. Therefore, there is a need for a small, affordable and easy-to-use POC, which can be employed in human breath gas analysis.

In terms of small targeted sensor devices, semiconductor metal oxide (SOM) sensors are well established in the field of trace gas sensor technology in general [10] and also in breath analysis [11]. However, optical sensor techniques, which claim a high sensitivity and selectivity, might be more suitable for trace gas analysis in complex gas matrixes like breath exhale [8]. Hodgkinson and Tatam [12] as well as Patimisco

et al. [13] supply comprehensive overviews, in which most common optical sensor techniques have been compared in terms of their suitability for trace gas analysis. In their studies, they used the normalised noise equivalent absorbance (NNEA) coefficient and the optical path length for comparison of the different sensor principles. The NNEA coefficient on one hand is a good measure to compare the sensitivity of an optical system, since it considers the employed optical power, the strength of the analyte's absorption cross section (ACS) and the integration time used in the measurements [13]. The optical path length on the other hand is a measure for the sensor's compactness and alignment complexity. The results demonstrate that photoacoustic spectroscopy (PAS) can compete with other optical approaches like off-axis integrated cavity output spectroscopy (OA-ICOS) or cavity ringdown spectroscopy (CRDS) regarding the NNEA coefficient. While PAS sensors have dimensions of approximately 2 to 10 cm, both, OA-ICOS or CRDS, exhibit complex alignment approaches to obtain pathlengths of up to several km, necessary to achieve comparable NNEA coefficients like PAS does. The reason for the high compactness of PAS systems is the fact that the photoacoustic signal does not depend on the optical pathlength. Hence, PAS applications have been reported reaching limits of detection (LOD) in the pptV region employing tube lengths below 1 cm [14]. The combination of a comparable high selectivity, sensitivity and compactness therefore make photoacoustic spectroscopy a promising sensor principle for the detection of gaseous acetone in human breath exhale.

Acetone is a well known constituent of exhaled breath. With a relatively high abundance usually ranging from approximately 200 ppbV up to 1000 ppbV in healthy humans [15, 16] breath acetone has been subject of many breath analysis studies including topics like diabetes [17], epileptic seizure prevention [18] as well as fat burning rate during physical excitation [19] to name a few. Compared to breath components like isoprene the exhaled acetone breath level is rather stable and fluctuates less with different sampling procedures [20, 21]. Furthermore, the systemic source of acetone, which is the metabolism of fat to gain energy and the dehydrogenation of isopropanol [17], is well understood and significant changes in the exhaled acetone concentration can provide valuable information for attending physicians. These properties make acetone an ideal biomarker for first evaluations of the applicability of photoacoustic spectroscopy in human breath analysis. So far, only few photoacoustic studies have been published with acetone being the target analyte. Holthoff et al. [22] used a continuously tunable quantum cascade laser (QCL) and reached an LOD of 550 ppbV (3σ). Viola et al. [23] and Dunayevskiy et al. [24], both employed an external cavity-QCL (EC-QCL) achieving an LOD of 110 ppbV (1σ) and 3 ppbV (1σ). The studies demonstrate, that PAS is a highly sensitive measurement principle, however, especially the systems employing an EC-QCL are too expensive to be used as a POC device. Besides, the measurement matrix was totally different compared to breath, hence, providing insufficient information regarding the selectivity of the system for breath analysis. An exception is the recently published study from Mitrayana et al. [25] employing a CO₂ laser for the detection of ammonia, ethylene and acetone in the breath of humans with lung cancer. Their study demonstrates the applicability of PAS for breath analysis. However, their approach

might still need improvements regarding costs and bulkiness of the system to be deployed in the clinical routine except for extensive care units. Hence, compact and cost-effective solutions are in demand to overcome this issue to provide breath analysis POC devices to a wide range of users.

This thesis is meant to provide information on the current status, pitfalls and the potential of modern breath analysis. To define the measurement matrix of human breath, the results of comprehensive breath analysis studies are reviewed and the challenges of finding relevant biomarkers or fingerprints as target analytes for POC devices are addressed. The role of acetone, which is the biomarker of choice within this work, as well as its possible applications in clinical breath analysis are considered in detail. Furthermore, the challenging steps towards a photoacoustic sensor for the detection of trace amounts of acetone in the complex measurement matrix human breath will be pointed out. Finally, the results of acetone measurements employing different photoacoustic sensor approaches in varying gas mixtures are presented and discussed regarding their applicability for breath acetone detection.

References

- [1] U. Nations. *World Population Prospects 2019: Highlights (ST/ESA/SER.A/423)*. Department of Economic and Social Affairs, Population Division (2019), 2019. ISBN: 9789211483161 (cit. on p. 2).
- [2] R. Koch-Institut and G. d. e. K. i. D. E.V. *Krebs in Deutschland für 2015/2016*. 12. Ausg. Berlin, 2019. ISBN: 978-3-89606-298-7. DOI: 10.25646/5977 (cit. on p. 2).
- [3] OECD. *Health at a Glance 2017*. Health at a Glance. OECD, Nov. 2017. ISBN: 9789264280397. DOI: 10.1787/health_glance-2017-en (cit. on p. 2).
- [4] S. Klein et al. *Weißbuch Adipositas*. Medizinisch Wissenschaftliche Verlagsgesellschaft, 2016. ISBN: 978-3-95466-274-6 (cit. on p. 2).
- [5] R. Williams et al. *IDF Atlas 9th Edition 2019*. 2019. ISBN: 978-2-930229-87-4 (cit. on p. 2).
- [6] D. Smith and P. Španěl. “The challenge of breath analysis for clinical diagnosis and therapeutic monitoring”. In: *The Analyst* 132.5 (2007), pp. 390–396. ISSN: 0003-2654. DOI: 10.1039/B700542N (cit. on p. 2).
- [7] L. Pauling et al. “Quantitative Analysis of Urine Vapor and Breath by Gas-Liquid Partition Chromatography”. In: *Proceedings of the National Academy of Sciences* 68.10 (Oct. 1971), pp. 2374–2376. ISSN: 0027-8424. DOI: 10.1073/pnas.68.10.2374 (cit. on p. 2).
- [8] P. R. Fortes et al. *Optical Gas Sensors for Exhaled Breath Analysis*. SPIE PRESS, 2017. ISBN: 9781510613782. DOI: 10.1117/3.2284712 (cit. on p. 2).

- [9] P. Mochalski et al. “Blood and breath levels of selected volatile organic compounds in healthy volunteers”. In: *The Analyst* 138.7 (2013), p. 2134. ISSN: 0003-2654. DOI: 10.1039/c3an36756h (cit. on p. 2).
- [10] X. Liu et al. “A Survey on Gas Sensing Technology”. In: *Sensors* 12.7 (July 2012), pp. 9635–9665. ISSN: 1424-8220. DOI: 10.3390/s120709635 (cit. on p. 2).
- [11] M. Masikini et al. “Review—Metal Oxides: Application in Exhaled Breath Acetone Chemiresistive Sensors”. In: *Journal of The Electrochemical Society* 167.3 (2020), p. 037537. ISSN: 1945-7111. DOI: 10.1149/1945-7111/ab64bc (cit. on p. 2).
- [12] J. Hodgkinson and R. P. Tatam. “Optical gas sensing: a review”. In: *Measurement Science and Technology* 24.1 (Jan. 2013), pp. 1–95. ISSN: 0957-0233. DOI: 10.1088/0957-0233/24/1/012004 (cit. on p. 2).
- [13] P. Patimisco et al. “Quartz-Enhanced Photoacoustic Spectroscopy: A Review”. In: *Sensors* 14.4 (Mar. 2014), pp. 6165–6206. ISSN: 1424-8220. DOI: 10.3390/s140406165 (cit. on p. 3).
- [14] Y. Ma et al. “Sensitive Detection of CO and N₂O using a High Power CW 4.61 μ m DFB-QCL Based QEPAS Sensor”. In: *Optics Express* 21.1 (2013), pp. 1008–19. DOI: 10.1364/CLEO_AT.2013.JW2A.80 (cit. on p. 3).
- [15] M. Righettoni et al. “Breath acetone monitoring by portable Si:WO₃ gas sensors”. In: *Analytica Chimica Acta* 738 (Aug. 2012), pp. 69–75. ISSN: 00032670. DOI: 10.1016/j.aca.2012.06.002 (cit. on p. 3).
- [16] T. Bruderer et al. “On-Line Analysis of Exhaled Breath”. In: *Chemical Reviews* 119.19 (Oct. 2019), pp. 10803–10828. ISSN: 0009-2665. DOI: 10.1021/acs.chemrev.9b00005 (cit. on p. 3).
- [17] Z. Wang and C. Wang. “Is breath acetone a biomarker of diabetes? A historical review on breath acetone measurements”. In: *Journal of Breath Research* 7.3 (2013), p. 037109. ISSN: 17527155. DOI: 10.1088/1752-7155/7/3/037109 (cit. on p. 3).
- [18] K. Musa-Veloso et al. “Breath acetone is a reliable indicator of ketosis in adults consuming ketogenic meals”. In: *The American Journal of Clinical Nutrition* 76.1 (July 2002), pp. 65–70. ISSN: 0002-9165. DOI: 10.1093/ajcn/76.1.65 (cit. on p. 3).
- [19] D. Samudrala et al. “Breath acetone to monitor life style interventions in field conditions: An exploratory study”. In: *Obesity* 22.4 (Apr. 2014), pp. 980–983. ISSN: 19307381. DOI: 10.1002/oby.20696 (cit. on p. 3).
- [20] P. Sukul et al. “Instant effects of changing body positions on compositions of exhaled breath”. In: *Journal of breath research* 9.4 (2015), p. 047105. ISSN: 17527163. DOI: 10.1088/1752-7155/9/4/047105 (cit. on p. 3).
- [21] P. Sukul et al. “Immediate effects of breath holding maneuvers onto composition of exhaled breath”. In: *Journal of Breath Research* 8.3 (2014), p. 037102. ISSN: 17527163. DOI: 10.1088/1752-7155/8/3/037102 (cit. on p. 3).

- [22] E. Holthoff et al. “Quantum cascade laser-based photoacoustic spectroscopy for trace vapor detection and molecular discrimination”. In: *Sensors* 10.3 (2010), pp. 1986–2002. ISSN: 14248220. DOI: 10.3390/s100301986 (cit. on p. 3).
- [23] R. Viola et al. “Quartz Enhanced Photoacoustic Spectroscopy for Detection of Improvised Explosive Devices and Precursors”. In: *Advances in Optical Technologies* 2016 (2016). ISSN: 16876407. DOI: 10.1155/2016/5757361 (cit. on p. 3).
- [24] L. Dunayevskiy et al. “High-sensitivity detection of triacetone triperoxide (TATP) and its precursor acetone”. In: *Applied Optics* 46.25 (2007), pp. 6397–6404. ISSN: 15394522. DOI: 10.1364/AO.46.006397 (cit. on p. 3).
- [25] Mitrayana et al. “CO₂ Laser photoacoustic spectrometer for measuring acetone in the breath of lung cancer patients”. In: *Biosensors* 10.6 (2020). ISSN: 20796374. DOI: 10.3390/BIOS10060055 (cit. on p. 3).

Chapter 2

Theory

2.1 Breath analysis

Breath is not only a symbol for life but as a part of the human volatilome it provides valuable information about processes taking place in the human body. Besides saliva, sweat, urine and stool as well as blood, which are also part of the human volatilome, exhaled breath is a very useful biological matrix. It consists of aerosols, particles and gases, which can originate from endogenous* or exogenous† sources. Mainly endogenous breathborne molecules can offer insights into the physiology and state of health of an individual and are called biomarkers. They are of great interest since they can be accessed easily and noninvasively to name only a few advantages [1].

In the following sections, this thesis will focus on the composition and complexity of the medium breath gas and its applicability in various fields. The challenges in finding reliable biomarker or sets of biomarkers correlating with certain disease or providing valuable information for the attending doctor will be addressed. Besides, the current state of the art and approaches to improve the probability of breath analysis implementation into clinical routine will be discussed. Since this thesis primarily deals with the gaseous part of the human exhale, breath particles and aerosols will be considered only briefly at the end of this chapter.

2.1.1 History

Breath analysis has a long history reaching back to ancient times. It might have been the Chinese being the first using different breath smells as medical diagnosis [2]. However, during the period of Hippocrates (460 – 370 B.C.), human breath was used for diagnosis, too. At this time, bad breath odor like halitosis was a sign for periodontal diseases. The sweet, fruity scent of acetone was an indication for diabetic ketoacidosis, a fishy smell for a liver disease, kidney failure was diagnosed due to urine like smell and a lung abscess was indicated by a rotten odor [3].

It was then Antoine Laurent Lavoisier (1743 – 1794) who, accompanied by Pierre Simon de Laplace (1749 – 1827) and Armand Séguin (1767 – 1835), achieved significant progress in the field of breath analysis. Building on the calorimetric experiments of Adair Crawford and Joseph Priestly, Lavoisier and Laplace were able to describe the metabolism of a guinea pig in 1780. They found out, that in a closed system, oxygen was metabolised to carbon dioxide in the body under the emission of warmth. It was demonstrated with breath analysis, that oxidative processes were influenced by physical exercise, ambient temperature and food intake [3–5].

Basing on the results of Lavoisier and his contemporaries, Justus von Liebig (1803 – 1873) and his protégé Wilhelm Henneberg (1825 – 1890) devoted their studies to the field "animal chemistry" as well as the animal nutrition. By means of metabolic

*Endogenous substances arise from the human body.

†Exogenous substances do not arise from the human body.

studies, including breath analysis, they were able to establish standards for the feeding and calculated the proper energy yield achieved by metabolic processes [6].

It was A. Nebelthau who established one of the first colorimetric test for breath analysis with humans around 1800 at the Marburger Polyklinik. With his technique, he was able to detect acetone in the breath of people serving as evidence for Diabetes Mellitus. By means of an alkaline iodine trap, he could measure strongly enhanced acetone concentrations in human breath, which are typical for diabetic metabolism changes. The cornerstone for other colorimetric measurements, like the ethanol breath test, which is used by the police, was set in 1874 by Francis Edmund Anstie (1833 – 1874). He was a British doctor and used an acidic chrome solution, which altered its colour from red-brown to green in the presence of ethanol [3, 7].

It was Linus Pauling (1901 – 1994) with his studies in 1971, who introduced modern breath analysis. His focus was on the analytes, which are under regular conditions present in the exhaled breath. Besides, he studied disturbing matrix effects through ambient air as well as metabolic products caused by food intake. To minimize these effects he kept his study subjects on a certain chemical diet. Following these instructions caused the generation of only low molecular compounds leading to a strong reduction of the intestinal flora. The standard deviation of a studied sample could therefore be reduced to 10 %. During his measurements, the breath condensed inside a cooling trap, was chromatographically separated and detected by means of a flame ionisation analyser. 250 different analytes were measured with this technique, though an identification of the analytes was not possible at this time, due to the low concentrations, the partly bad separation and the insensitive detectors [8].

2.1.2 State of the art

Nowadays, breath analysis has gone a step further and several hundreds of volatile organic compounds (VOC) have been detected in breath so far [9, 10]. Today GC-MS is still considered the gold standard in breath analysis, since it convinces with high reproducibility, robustness and the provided fingerprint in the resulting spectrum [11]. In some cases, the gas chromatograph is combined with hyphenated features by means of thermal desorption (TD), time-of-flight (TOF) or flame ionisation detectors (FID) replacing the MS, to name a few [12, 13]. However, GC-MS is considered an off-line measurement technique, which is performed in a laboratory due to its lack of mobility. In modern breath analysis new online measurement techniques have been used widely in the past two decades including PTR-MS, SIFT-MS or ion mobility spectrometry (IMS) and more recently secondary electrospray ionisation mass spectrometry (SESI-MS) [12, 14]. Together with GC-MS and sometimes LC-MS [1] these technologies form the group of comprehensive analysis methods in human breath analysis. Employing high resolution mass spectrometers, modern devices have opened up new opportunities due to their capability of unknown identification and detection features [14]. With their high sensitivity and selectivity, comprehensive devices are inevitable in human breath research. However, all have

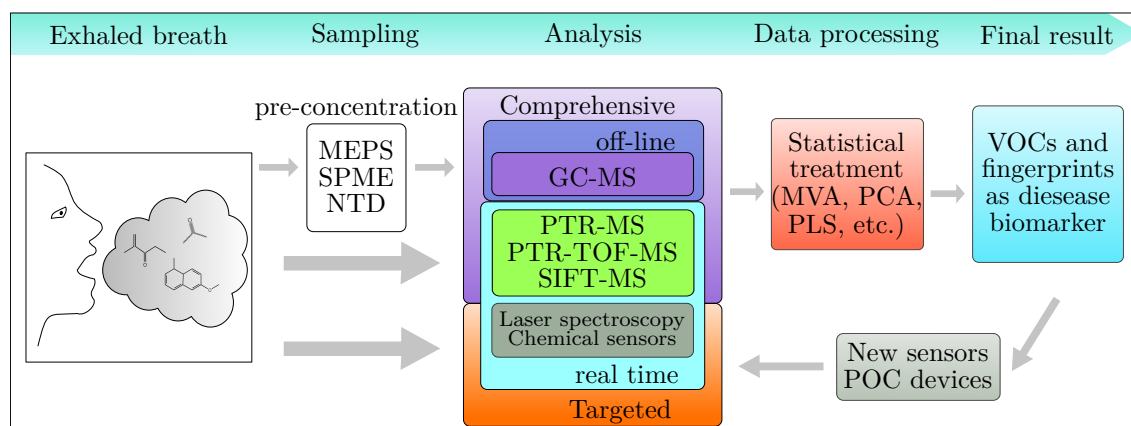


Fig. 2.1. Generic overview for exhaled breath analysis after [12]. **MEPS** - microextraction by packed sorbent, **SPME** - solid phase microextraction, **NTD** - needle trap device, **GC** - gas chromatography, **MS** - mass spectrometry, **PTR** - proton transfer reaction, **TOF** - time of flight, **SIFT** - selected ion flow tube, **MVA** - multivariate analysis, **PCA** - principal component analysis, **PLS** - partial least-square, **VOC** - volatile organic compound, **POC** - point of care.

in common, that they are rather bulky, expensive and need trained personal for operation [12].

Figure 2.1 provides a generic overview of modern breath analysis. It visualises the different steps from comprehensive analysis towards the development of small and cheap POC devices, which measure single or few target analytes only. Most studies trying to find a single or set of biomarkers correlating with a certain pathological state can be simplified to three sequential steps. (i) The breath is sampled and if necessary pre-concentrated. This step is followed by (ii) the detection of the compounds, which is usually performed by means of GC-MS, SIFT-MS or PTR-MS and finally (iii) processing and analysis of the measured data [12]. When a biomarker or fingerprint has been found and verified in follow up studies, the development of a POC by means of targeted online sensor technique is initiated. However, the past has proven, that the path from "bench to bed" is more difficult than expected and will be addressed in section 2.1.6.

To sample breath, different approaches can be pursued. First it has to be decided, which part of the exhaled breath should be collected. One breath exhale cycle can be separated into three phases as indicated in figure 2.2. Therefore, sampling of late expiratory, end-tidal or mixed expiratory air is possible. To distinguish these phases and to have a better sampling reproducibility, parameters like the partial pressure of exhaled CO_2 , flow, temperature etc. can be used. Important for reliable phase recognition, the time resolution of the acquired parameter should not be greater than 200 ms [15]. Late expiratory sampling means, that the dead-space volume, which is the initial part of exhaled breath, is discarded and the rest of the exhaled volume of one breath cycle is sampled. The advantage of dead-space volume minimisation during sampling is the greater share of endogenous substances within the sample.

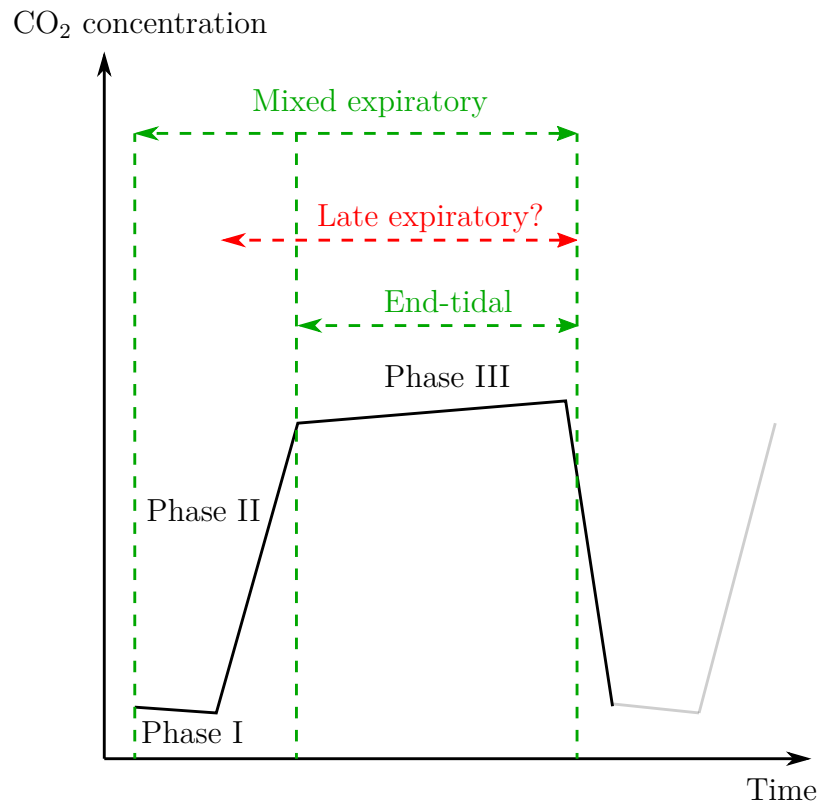


Fig. 2.2. Illustration of different exhale phases after [17]. The late expiratory sampling range is undefined due to lack of standardisation.

However, if a biomarker like H_2S , which is a marker for halitosis and is formed in the mouth [16], is of interest, this volume can obviously not be discarded. Using end-tidal breath ensures to have a high contribution of endogenous substances and only a few exogenous. To verify sampling only from phase III a CO_2 sensor can be used as mentioned before [18–20]. At the beginning of the exhale cycle the CO_2 level is low, quickly rising within phase II until a plateau is reached indicating the start of phase III. However, applying end-tidal sampling causes endogenous VOCs, which have no systemic origin, to be missed. Hence, marker originating from the airways are not sampled making this method unattractive for airways disease research. Since phase III can be detected more easily than phase II, the end-tidal sampling approach helps standardizing [15] the sampling process and is thus more suitable for the application in clinics [21]. Utilizing the whole exhaled volume as sample is called mixed expiratory sampling method. It is obviously the simplest breath collection approach, which makes it appealing, however, the share of exogenous, mouth and nose contaminants is great [22].

The ideal breath sampling method would be simple and easily reproducible. It should be well applicable to ventilated patients as well as during sports activities and it should be possible to distinguish between different VOC origins e.g. by targeted selection of compounds from alveolar or airway volume. Finally, the elimination of dead space and exogenous contaminants is important to avoid mismatching of

exogenous constituents with certain pathology states. However, such a method is not available today and the currently applied sampling procedures always require a compromise in at least one of the mentioned requirements, being one of the reasons why breath analysis is not more common in clinical practice today [21].

Additionally, it can be distinguished between single breath and multiple breath cycles being sampled. The former one has to be preferred in rapidly changing situations like different physical activities, which have a short-term influence on some breath constituents. However, since the composition of a single breath can vary significantly from each other, in studies with a high interest in reproducible breath composition and quantitative marker analysis, multiple breath sampling has to be preferred [22].

The analysis of the breath sample can be performed directly, which is the same as real-time or online, or indirectly (off-line), which is usually off-site in a laboratory. Hence, the sample has to be stored prior to analysis when the sample has to be acquired outside the laboratory in indirect analysis scenarios. Storage techniques will be addressed in the next paragraph. Direct or online measurements are analysed onsite and not in a laboratory and the measurement result is provided within seconds or minutes. Real-time spectrometry like PTR-MS, IMS, SIFT-MS or SESI as well as optical sensing methods like classical absorption spectroscopy or photoacoustic spectroscopy are used for online measurements. For off-line analysis usually a GC-MS or a similar approach is utilised. Obviously, other direct measurement techniques can be used for laboratory-based off-line measurements as well [15].

Since concentrations of certain volatiles in breath are often quite low, pre-concentration steps are performed prior to analysis. Therefore, techniques like microextraction by packed sorbent (MEPS), solid phase microextraction (SPME), needle trap device (NTD) or thermal desorption tubes as well as cryogenic trapping are applied [12, 21]. Usually, a breath sample is stored prior to pre-concentration, although Basanta et al. [23] performed direct breath sampling onto an adsorbent trap demonstrating the applicability of such an approach as well [21]. The most prominent breath collection container utilised are polymer bags, especially Tedlar bags. Besides, canister or glass combined with gas-tight vials with syringes are used among several other special breath collection apparatus [21]. Although storing and pre-concentrating of breath samples can be useful, contamination and altering of the original breath composition is possible and will be discussed in section 2.1.6.

More detailed information regarding the current workflow concept in breath analysis, sampling methods and the operating principle of the mentioned comprehensive analysis methods as well as data interpretation and approaches for compound identification can be found elsewhere [12, 14, 21].

2.1.3 Breathborne biomarkers: physiological pathways and applications

In the plethora of expired VOCs, researcher have tried to find biomarkers over the last decades, which can be assigned to certain pathological states. Consisting of mainly nitrogen, oxygen, water, carbon dioxide and argon, the low abundant substances of interest make up only about 100 ppmV of the total exhaled volume and are thus well hidden in the measurement matrix of human breath exhale. Well-known species of low abundance are acetone, isoprene, methane or carbon monoxide, to name only a few [24, 25]. The use of exhaled species as breathborne biomarkers in different applications will be discussed within this section. Besides, pathways of endogenous biomarkers and the potential of biomarker profiles compared to single biomarkers will be addressed, too.

As mentioned above, only a few tests have found their way into clinical practice so far and some are considered to have a high potential but are still under investigation. In order to become an accepted biomarker, knowing the corresponding pathways and origins in the human body is inevitable. However, the biochemical

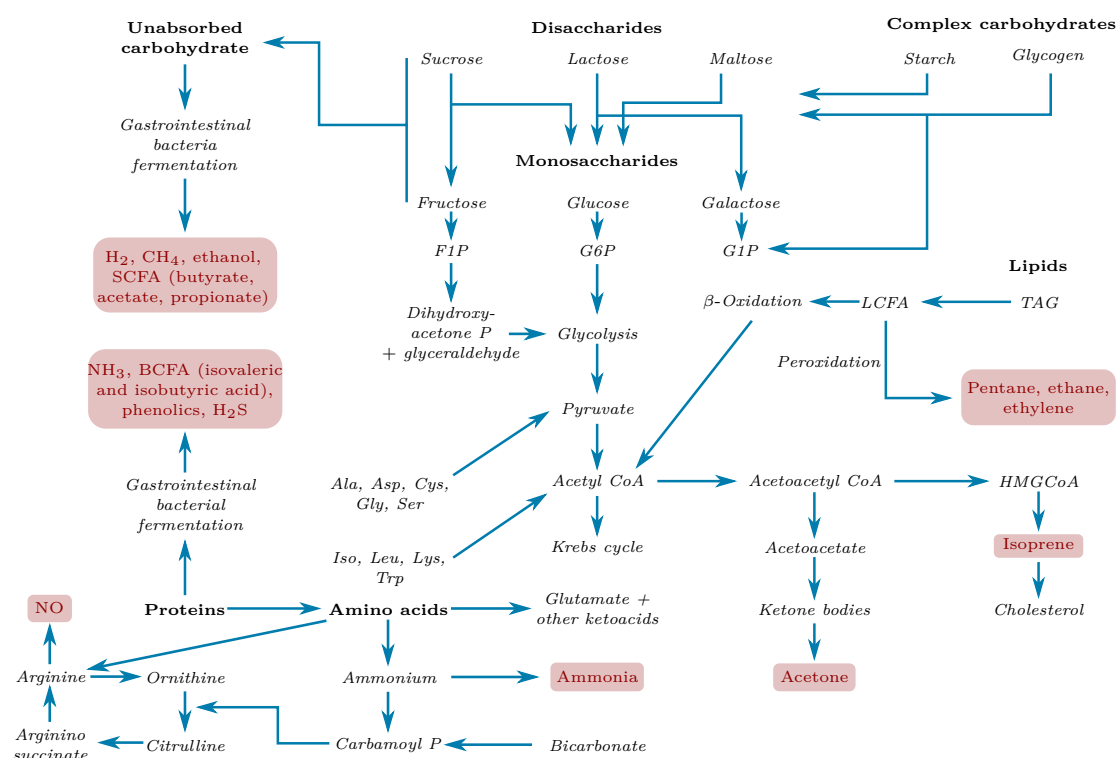


Fig. 2.3. Visualisation of the pathways for certain potential markers (red boxes) after [26]. **SCFA** – Short Chain Fatty Acids; **BCFA** – Branched-Chain Fatty Acids; **LCFA** – Long-Chain Fatty Acids; **TAG** – Triacylglyceride; **F1P** – Fructose 1-Phosphate; **G1P** – Glucose 1-Phosphate; **G6P** – Glucose 6-Phosphate; **Carbamoyl P** – Carbamoyl-Phosphate; **HMG** - Hydroxy Methyl Glutaryl; **CoA** – Coenzym A.

processes occurring inside the body are quite complex as indicated in the overview provided by figure 2.3. Nevertheless, when the pathway of a certain biomarker is well understood, the probability of an application targeting this marker in medical diagnosis increases [27]. Examples are the F_{ENO} and *heartsbreath* test as well as the ^{13}C isotope labeled breath tests listed in table 2.1. Furthermore, for an endogenous marker originating from the systemic part of the human body, the relationship between its blood levels compared to exhaled concentrations are of interest, especially for modeling dynamics of marker concentrations in breath, too. This is often necessary to validate the robustness and reliability of marker monitoring regarding clinical application suitability. For this purpose the well-established Farhi equation [28] can be consulted. With C_A being the alveolar and hence the measured concentration, $\lambda_{b:air}$ the substance specific partition coefficient between blood and air (describes the diffusion equilibrium at the alveolar-capillary interface according to Henry's law), C_a and $C_{\bar{v}}$ being the arterial and mixed venous blood concentration, respectively. \dot{V}_A being the alveolar ventilation and \dot{Q}_C being the cardiac output.

$$C_A = \lambda_{b:air} C_a = \frac{C_{\bar{v}}}{\lambda_{b:air} + \frac{\dot{V}_A}{\dot{Q}_C}} \quad (2.1)$$

Although this equation is not adequate for usage in non-steady-state situations it can be used for a fundamental understanding of how to monitor systemic processes using breathborne biomarkers. Further information regarding more sophisticated modeling concepts can be found elsewhere [29].

Tab. 2.1. Summary of breath tests approved by the Food and Drug Administration (FDA) of the United States or the European Medicines Association (EMA) of the European Union or are used as diagnostic aids in clinical practice after [1].

Biomarker	Test	Target/Disease	Comment
Breathalyzer	Ethanol	Alcohol intake (law enforcement)	Ethanol concentration in breath is linearly correlated to blood ethanol levels and can hence be used to ascertain alcohol abuse in traffic.
Capnography	CO ₂	Ventilation/ breathing	Is used to verify stable breathing of a patient e.g. in the intensive care unit.

Carbon monoxide	CO	Neonatal jaundice	An increase of CO can be an indicator for jaundice. The accumulation of CO in the blood is due to an impaired conjugation of bilirubin in the liver of the newborn.
Heartsbreath	Alkanes	Heart transplant rejection	Transplant recipients who suffer from grade 3 organ rejections can be detected by monitoring the alkanes level in the exhaled breath. The origin for the increase of these alkanes is oxidative stress.
Hydrogen breath test	H ₂	Lactase deficiency	After ingestion of lactose the hydrogen level rises significantly if lactose intolerance is present.
F _E NO	NO	Asthma	The fraction of exhaled NO (F _E NO) can be used as a marker of type 2 inflammation in asthma.
Maximum liver function capacity (LiMAx)	¹³ CO ₂ *	Liver function	LiMAx detects a malfunction or nonexistence of cytochrome P450 1A2 enzyme in the liver. The ability of metabolising ¹³ C-methacetin is monitored via detection of ¹³ CO ₂ concentration changes in exhaled breath. In general, ¹³ C labeled substances can be used to identify metabolism processes in the human body.

Some other species of interest with a great amount of studies conducted in the past years are ammonia, HCN, isoprene and acetone.

*There are also the Gastric emptying breath test using labeled spirulina to determine delayed gastric emptying and the urea breath test to detect a helicobacter pylori infection employing labeled urea.

Ammonia as breathing gas biomarker has been of great interest especially in the field of nephrology in the last decades. It is one of the markers which should be sampled from nasal and not oral-exhaled breath, since studies demonstrated that it is formed by enzymes on salivary urea in the oral cavity [30]. Therefore, mouth-exhaled NH_3 can be expected to show elevated levels compared to ammonia levels from equilibrated blood ammonia concentrations. Besides, ambient NH_3 abundance in testing rooms should be considered as well [31]. Regarding possible applications of ammonia as a biomarker, Spanel et al. [30] conclude, that mouth-exhaled NH_3 could represent high blood urea or a high pH^* of the mucosa from saliva, mouth or airways, poor oral hygiene or a mix of these. Furthermore, Davies et al. [32] consider breath NH_3 concentrations to help estimating the severity of uremia.

In an in vitro study from 2004, hydrogen cyanide was identified to be a metabolisation product of *pseudomonas aeruginosa* (PA) and that the bacterial infection can be associated with cystic fibrosis (CF) [33]. To study the clinical value of HCN detection in PA infection, 233 children with CF but without PA infection were followed in a longitudinal study over two years. The results demonstrated mostly a high disease detection sensitivity using HCN as biomarker, however, due to genetic variability of PA strains, further biomarkers should be used complementarily to avoid false negatives in some cases [34].

A correlation between exhaled isoprene and blood cholesterol was suggested for patients treated with lovastatins, which are used for cholesterol reduction [35]. Besides, King et al. [19] demonstrated that breath isoprene increases quickly during physical exercise, however, this was not the case for muscle dystrophy patients [36]. Furthermore, isoprene has a potential for metabolic monitoring, too, however, its systemic pathway and clinical relevance have to be clarified first [37].

Breath acetone has been studied excessively in the last decades due to the proposed association with blood glucose and diabetes. However, no evidence for a reliable correlation has been found, yet [38]. In Walton et al. [39] it was demonstrated, that breath acetone correlated linearly with blood glucose in a group of type 1 diabetes patients, however, the acetone concentrations varied greatly among the patients with a similar blood glucose level indicating that it is unlikely that breath analysis can completely replace common blood glucose testing. Nevertheless, there are several application areas of breath acetone demonstrating its potential usefulness not only in clinical applications.

In Boshier et al. [40] the role of exhaled ketones, including acetone, as noninvasive markers of nutritional status in patients undergoing bariatric surgery in obesity treatments was investigated. It was demonstrated, that especially acetone can provide clinical useful information.

To fight obesity, correct dieting can be very useful to achieve a negative energy balance and a higher fat burn rate. Breath acetone demonstrated its usefulness in reflecting the elevated fat metabolism rate during ketogenic diet [41] and can thus be

* pH = power or potential of hydrogen

used to support weight reduction. Musa-Veloso et al. [42, 43] investigated the use of breath acetone for ketogenic diet monitoring in children with epileptic seizures. In two longitudinal studies significantly increased breath acetone levels were detected for children following a ketogenic diet compared to the control group. Hence, breath acetone can be used to support children following a ketogenic diet due to epileptic seizure reduction.

Combined with dieting, physical exercise is a common approach to loose weight in order to fight obesity. However, the efficiency of fat metabolisation can vary between graded [44] and nongraded [45] exercise. Further, breath acetone optima can be used to noninvasively detect the anaerobic threshold [46]. Hence, breath acetone detection could also be deployed in the professional sport field to replace invasive blood tests to determine the anaerobic threshold of athletes.

In 2013, Samara et al. [47] studied patients being admitted to the hospital with acute decompensated heart failure (ADHF) using SIFT-MS. Significantly increased acetone and pentane levels were detected compared to the control groups, emphasizing the clinical relevance of breath acetone detection once more.

Until now mainly single breath biomarker have been discussed. However, there have been several studies indicating that for certain disease detection and monitoring or similar applications, analysis of biomarker profiles are more suitable. Except for the examples mentioned before like NO, which can be regarded as a single-breath biomarker for asthma screening and monitoring, unique biomarkers have mostly failed so far to be a useful tool in the detection of complex conditions like certain metabolic disorders or cancer. Examples, where the analysis of a breathprint was superior to that of single-breath biomarker is the detection of ADHF [47], patients suffering from alcoholic hepatitis [48], hypertension [49], inflammatory bowel disease [50] and renal failure [51] to name a few. To detect breathprints, usually either electronic noses also called sensor arrays or MS techniques are used. The former has the advantage of being easier to use, however, it lacks the possibility of identifying the VOCs causing a unique pattern and thus no connection to the underlying pathobiology of the disease is possible [31].

Further scenarios where breath analysis is currently used as an aiding tool in different research areas and medical diagnosis are summarised briefly.

- Besides alcohol abuse, breath tests can be applied to detect therapeutic drugs [52] or in doping controls [53].
- Having not been deployed in the field so far, research is conducted towards urban search and rescue by means of the detection of emitted volatiles including breath components [54].
- Breath analysis can be used to detect exposures of human to harmful substances either by directly measuring the component of interest in the exhale or by measuring a so called marker of effect. For example, healthy volunteers were exposed to O₃ and a variation in the F_ENO could be detected [55].

Describing all (potential) markers of exhaled breath, the areas of breath research in general and its potential applications would go far beyond the scope of this work, however, a very detailed summary of breath analysis research and its progress over the last decades can be found in *Breathborne Biomarkers and the Human Volatilome* [56].

2.1.4 Acetone as a breathborne biomarker

In the previous subsection many different breathborne biomarkers have been presented and discussed. Since it is beyond the scope of this work to focus on all or several markers, a choice had to be made. The following criteria have been applied to decide, which marker is suitable to be used as a target analyte for the development of a photoacoustic sensor system:

1. The marker should have relatively high abundance.
2. The relation between inhaled and exhaled concentration is understood and controllable and the endogenous origin is known.
3. There should be a manageable spectrum of diseases correlated with the biomarker change.
4. The biomarker provides clinical relevant information (e.g. metabolism).

Since these points are all applicable for acetone it was decided to focus on the development of a sensor for acetone detection within this thesis. Table 2.2 indicates the high abundance of acetone, the ambient concentration is very low, which will be discussed later in this section, the endogenous origin is well understood and acetone has a manageable spectrum of diseases correlated with varying concentration (e.g. heart failure, ketogenic diet, etc.). Moreover, breath acetone provides clinical relevant information, which was already discussed in section 2.1.3 and in [27] Solga et al. describes acetone as a useful biomarker.

Other highly promising breath constituents are NO as well as the $^{13}\text{CO}_2/^{12}\text{CO}_2$ isotope ratio detection. Since for both of them plenty of clinical approved devices are already available, a reliable and precise acetone POC device would have a higher impact on further breath research.

The potential applications of breath acetone detection have been discussed in the previous section, hence, this section addresses further properties and information of acetone. Acetone, or propan-2-one after *IUPAC*, is a colourless liquid at room temperature. It has the chemical formula $\text{C}_3\text{H}_6\text{O}$ and hence a molecular weight of 58.08 g mol^{-1} . Acetone smells sweet and fruity having an odour threshold of 9.5 mg m^{-3} , which is equal to 3.94 ppmV . It has a low vapor pressure at ambient temperatures and its boiling point is at 56.2°C at 1 atm [57, 58].

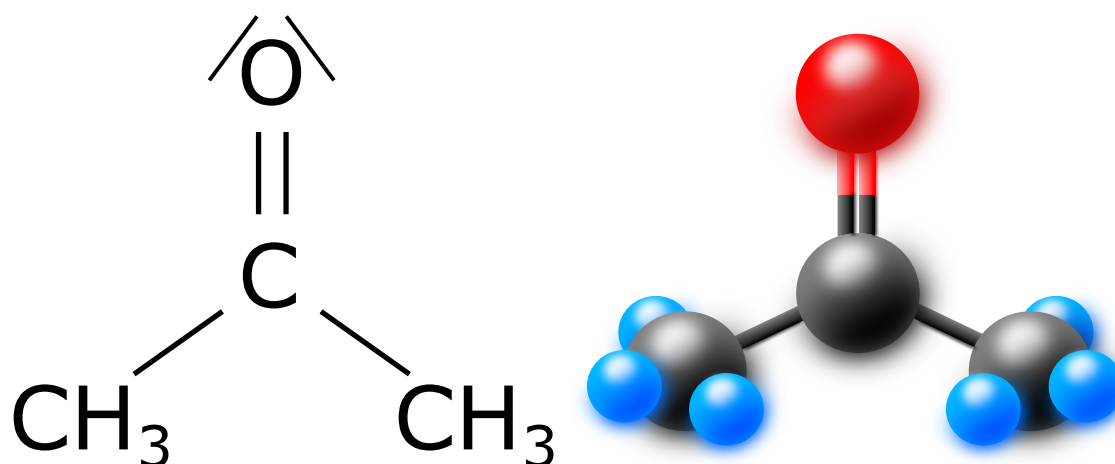


Fig. 2.4. Acetone structure formula (left) and 3D structure of the molecule acetone (right). Red ball represents an oxygen atom, black balls are carbon atoms and blue balls represent hydrogen atoms.

In the troposphere, acetone is omnipresent with a concentration between 0.35 – 2.31 ppbV [59]. Due to photolysis reactions in the upper troposphere, acetone is a main source for hydrogen oxide radicals, having important implications for atmospheric chemistry [60]. Sources are listed including anthropogenic emission, biomass burning, terrestrial vegetation and plant decay, though the overall dynamics of sinks and sources are still poorly understood [61, 62]. This paragraph demonstrates, that precise acetone measurements are not only important medical applications, but can be useful in environmental monitoring, too.

According to a study from the *US Department of Health and Human Services* in 1994 [63], acetone has a concentration of less than 1 ppbV in remote areas, 3 ppbV and 6.9 ppbV in rural areas and in urban air, respectively, as well as 8 ppbV in indoor air due to the use of household consumer products. In a more recent study about the acetone concentration in Hongkong from Guo et al. [64] in 2013, mean acetone levels measured at two locations were about 3.8 ppbV and 3.3 ppbV. Since acetone has a relatively high abundance in exhaled air, the references demonstrate, that the acetone concentration in the ambient air can be neglected and does not alter the measured exhaled concentration significantly. Besides breath acetone and atmospheric acetone, its role as a precursor in the synthesis of explosives [65] makes acetone an interesting target analyte as well, but will not be discussed further in this work.

In the human body, acetone is one of three ketone bodies, which are produced in the liver. Besides acetone, acetoacetate (AcAc) and 3- β -hydroxybutyrate (3HB) are the other ketone bodies. Acetone is created either by the dehydrogenation of isopropanol or by the decarboxylation of acetoacetate. The latter one is illustrated in figure 2.5 and accounts for approximately 52 % in diabetic patients in moderate to severe ketoacidosis [66] and for 37 % of the AcAc metabolised in fasting patients [67]. Considering the location of the diffusion of acetone into the exhaled breath,

the solubility of acetone in blood given by the blood-air partition coefficient has to be regarded. Low soluble gases, e.g. oxygen or carbon dioxide having a coefficient $\lambda_{b:air} = 0.7$ and $\lambda_{b:air} = 3$, respectively, exchange in the alveoli, while high blood-soluble gases like ethanol $\lambda_{b:air} = 1756$ diffuse via the airways [66]. This could be the reason, that there is a short-term variability in breath acetone values, whereas the blood concentration stays constant, because acetone has a high $\lambda_{b:air}$ around 340, too. This is one of the reasons, why acetone perfusion into the lungs cannot simply be modeled using the Farhi equation, which was already mentioned briefly in section 2.1.4. Furthermore, the type of exhalation maneuver can influence the acetone concentration, although it is more stable than others [68]. According to the models of Anderson et al., during a tidal, where the patient exhales 500 mL passively, 96 % of the acetone exchange takes place in the airways [69]. During a prolonged exhalation maneuver, which includes inspiring to total lung capacity and slow constant exhale rate, only 81 % to 73 % occurred in the airways, depending on the simulated epithelium and mucosal tissue thickness [70]. Following the conclusion that the airways participate in the exchange of acetone, no anatomic dead space is existing for acetone in an expirogram [71]. At this point, it has to be stressed out again, that for acetone measurements in human exhaled breath, a breathing protocol will be mandatory for better comparability and reproducible measurements. However, since acetone is a source of the breakdown of fatty acids for the energy support of the human body, it is comprehensible that diseases, life style interventions

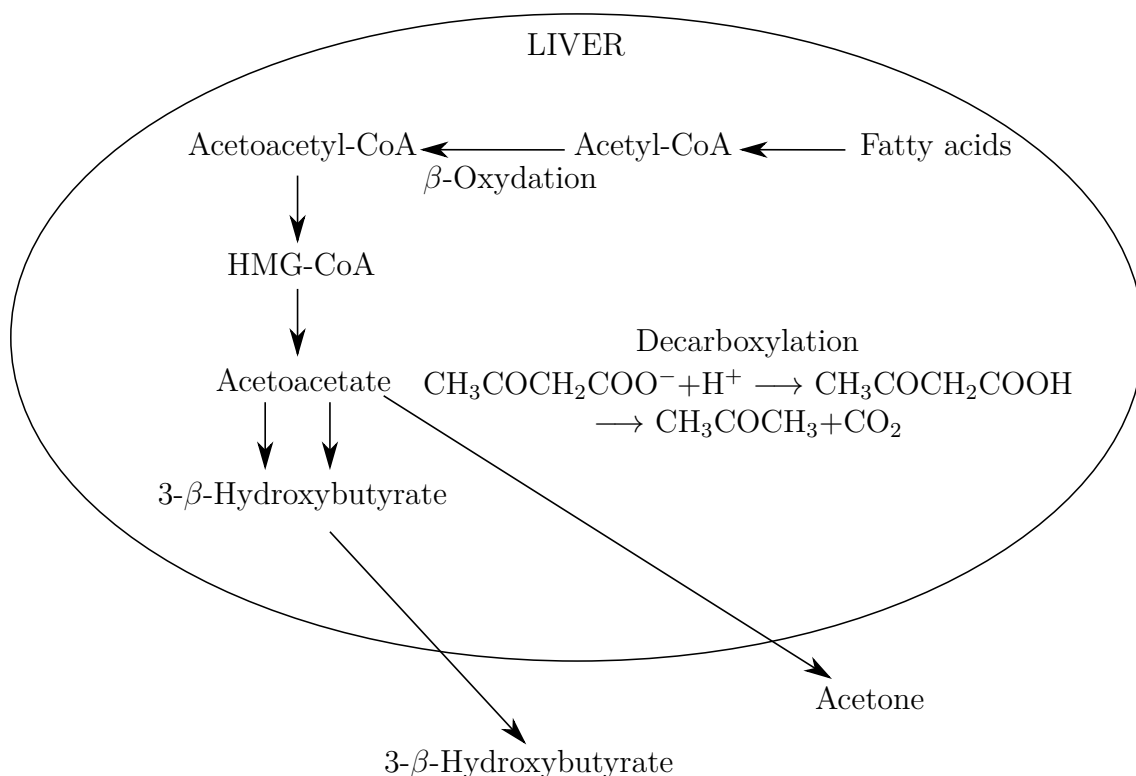


Fig. 2.5. Visualisation of the acetone pathway in the liver after [72].

or physical activity can be monitored by human breath acetone measurements and provide useful information.

Concluding, acetone is an interesting and useful biomarker. Regarding a later application, taking multiple breath samples should be preferred, since it increases reproducibility (refer to section 2.1.2). Besides, since photoacoustic spectroscopy is probably too slow in order to distinguish between the different exhale phases, it should be combined with a CO₂ sensor and either the late or the end-tidal exhale phase should be sampled. Since the exhaled concentration of acetone is comparably high, no pre-concentration step is necessary, facilitating a later application.

2.1.5 Composition of breath

Modern breath analysis has demonstrated, that human exhale is a very complex measurement matrix consisting of hundreds of VOCs [8, 73]. Hence, this section's main purpose is to provide a detailed overview over the composition of breath in general and to identify substances having a potential for cross-sensitivities towards photoacoustic detection of breath acetone.

Inspired air consists of approximately 78 %V of N₂, 21 %V of O₂, about 1.2 %V (at 20 °C and 50 % relative humidity (rH)) of gaseous water and about 1 %V of argon [74]. Two main processes cause the expired air to change significantly. (i) Oxygen concentration is diluted since it diffuses into the blood and is replaced by carbon dioxide, which was metabolised in the human body using oxygen. (ii) The expired air is enriched with water vapor diluting the other components of inspired air during respiration. The average exhaled water concentration within expired air ranges from 2.9 %V to 5.0 %V according to Mansour et al. [75]. Approximately 4 %V to 5 %V CO₂ is exhaled [74, 76]. Hence, the other inspired components' concentrations change to about 74 %V for N₂, O₂ is decreased to approximately 14 %V to 16 %V and argon is quite stable at around 1 %V. Note that these concentrations can obviously vary depending on the situation, e.g. physical activity. The rest of the exhaled gas is comprised of some inorganic species and some hundred VOCs. The VOC profile can differ from person to person, since it depends on factors like age, physiology, diet, health status, medication and environmental exposure [1].

Those VOCs having a low abundance in breath ranging from the ppmV to the pptV are of high interest, since some of them could be breathborne biomarkers or are already accepted ones like described in section 2.1.3. In order to get a good overview of the main components and the relatively high abundant VOCs in breath, which is necessary for the later spectral interference analysis, a list was compiled. Table 2.2 summarises all species with (i) a concentration above 50 ppbV in a healthy condition and (ii) which have been cited regularly in literature. For example low abundance compounds like H₂S having a concentration of about 26 ppbV [77] or formaldehyde with ca. 3 ppbV [78] are not listed, because of their low concentration ranges. This requirement is useful for a later interference analysis in chapter 3, where only com-

pounds with a certain concentration can cause spectral cross-sensitivities. The second requirement verifies that this component is actually present in breath and is not an artefact or measurement error of one single study. Therefore, longitudinal studies are often preferred as reference [79–83]. If a breath constituent’s concentration alters due to a diseased state or food intake it is noted in the column **Altered concentration in disease state** in ppmV. Note that all species listed in table 2.2 below 1 %V (except for argon) are regarded as endogenous substances. Moreover, note that the list does not claim comprehensiveness due to the sheer amount of published studies but provides a representative overview. Care was taken to use the values of healthy people or of the control group from the cited studies for the column **Concentration (healthy)** in ppmV.

Additionally to this summary of the most abundant (mostly) endogenous breath constituents exogenous contaminants can occur in breath as well. They can be introduced by food, drinks, medication or simply by a high ambient concentration, which is inspired and either directly expired again or accumulated in the body and exhaled again after some time [1]. Basically, such compounds can be of interest as well, which is discussed in section 2.1.3, however, now they will be considered due to their cross-sensitivity potential.

Depending on the area of application of a later breath analysis sensor, the concentration and the type of substances of these exogenous contaminants vary significantly. Since a newly developed device is usually employed first in either a controlled environment like a laboratory or as a next step in a clinical trial, exogenous substances from a clinical environment and their expected concentrations in breath have been evaluated, too.

In clinics or in doctor’s practice cleaning agents or disinfectants may be the primary exogenous source of contaminants since they are present in elevated concentrations and hence, have interference potential regarding the measurement of exhaled breath components. Despite of that, breath research literature has not treated cleaning agent concentrations directly, but copes with ambient air measurements additionally to exhaled breath measurements. These are mandatory for reliable interpretation of breath measurement data and include the detection of cleaning agents in the ambient air.

One example is isopropyl alcohol (IPA), which can be an ingredient of cleaning agents. In the experiments of Ghimenti et al. [84], a subject of an experiment showed a concentration of 1500 ± 70 ppbV in her breath, whereas other nurses had a mean value of 20 ± 20 ppbV. Apparently, the nurse was too close to the basket, where the used IPA soaked cotton balls were disposed. Furthermore, in approximately half an hour, this value dropped to a seventh of the original value. In the studies of Kischkel et al. [85], the detected concentration range for IPA in exhaled breath is $2.87 - 212.69 \text{ nmol L}^{-1}$, which equals $0.073 - 5.38 \text{ ppmV}^*$ and the concentration of IPA within the synthetic air used was $1.42 - 58.8 \text{ nmol L}^{-1}$ ($= 0.036$

*Note that the concentrations have been converted from nmol L^{-1} in ppmV using $V_M = 25.28 \text{ L mol}^{-1}$ and $T = 308 \text{ K}$.

Tab. 2.2. List of the most abundant compounds of human breath exhale. **SIBO** - small intestinal bacterial overgrowth.

Molecule	Concentration (healthy) in ppmV*	Altered concentration (non-healthy) in ppmV	Reference
Nitrogen	740,000	-	<i>derived in text</i>
Oxygen	140,000 – 160,000	-	<i>derived in text</i>
Water	29,000 – 50,000	-	[75]
Carbon dioxide	40,000 – 50,000	-	[74, 76]
Argon	10,000	-	[74]
Carbon monoxide	0.4 – 0.8 [†]	-	[24]
	1.14 – 1.37	13.6 – 19.3 (recent exposure to CO, smoking)	[87]
Methane	3 – 8 [‡]	Rise of 10 from baseline (SIBO)	[24, 88]
Hydrogen	ppmV range	Rise of 20 from baseline (SIBO)	[88, 89]
Ammonia	0.425 – 1.800	Up to 14.7 unhealthy (end-stage renal failure)	[90]
	0.050 – 0.150 [§]	-	[24]
	0.628	-	[25]
Dinitrogen monoxide	0.080 ± 0.017 (male) 0.177 ± 0.055 (female)	0.246 ± 0.087 (elevated NO ₂ ⁻ in gastric juice, linked to gastric cancer risk)	[91]
Isoprene	0.118 ± 0.068	< 0.014 as cut-off value for fibrosis	[80, 92]
	0.037	-	[25]
	0.022 – 0.234	-	[79]

*The values provided from the references represent different statistical quantities like median, mean etc. for further details refer to the corresponding reference.

[†]Additional to the ambient CO concentration.

[‡]Additional to the ambient methane concentration.

[§]Additional to the ambient ammonia concentration.

Methanol	0.461	Change due to food intake	[82, 93]
	0.261	-	[25]
	0.238	-	[94]
Ethanol	0.196 ± 0.244	Change due to food intake	[83, 95]
	0.261	-	[25]
	0.238	-	[79]
Carbonyl sulfide*	0.096 ± 0.193	0.637 ± 0.377 (after lung transplant rejection)	[96, 97]
Acetone	0.3 – 0.9	128 ± 23.6 (children on ketogenic diet)	[79], [43]
	0.297	-	[25]
	0.280 – 1.269	-	[98]

– 1.49 ppmV). Additionally, the air passing a double-lumen endotracheal tube was studied and the IPA concentration ($\approx 75 \text{ nmol L}^{-1}$) was significantly higher than the patients exhaled IPA value ($< 10 \text{ nmol L}^{-1}$). In another study of Kischkel et al. [86], the inhaled air had an IPA concentration of $0.72 - 117.62 \text{ nmol L}^{-1}$ compared to an exhaled concentration of $0.72 - 103.02 \text{ nmol L}^{-1}$. These three studies indicate, that the endogenously produced IPA in human exhale breath is in the low ppbV range, though can be highly influenced by exogenous IPA sources.

In the same study [86] the abundance of ethanol, which is also often used in disinfectants or cleaning agents, in the room air was $5.10 - 124.67 \text{ nmol L}^{-1}$, whereas expired samples had $5.10 - 99.22 \text{ nmol L}^{-1}$. Similar results were found for 1-propanol, which is also known as cleaning agent/disinfectant, having an abundance of $0.09 - 125.61 \text{ nmol L}^{-1}$ and $0.13 - 65.78 \text{ nmol L}^{-1}$ for inhaled and exhaled samples, respectively.

Finally, formaldehyde will be included in this list, too, because it is known to be in several cleaning agents or air fresheners. Solga et al. [99] provide a table of such products together with the measured formaldehyde concentration. In most of the products the value was around $10 \mu\text{g m}^{-3}$ or lower. For one floor wipe it was even about $1249 \mu\text{g m}^{-3}$, which is approximately 1.1 ppmV. However, for the *worst-case* scenario, the defined short-term exposition limit for Germany, which is 600 ppbV [100], will be applied in the later spectral cross-sensitivity investigations (refer to chapter 3).

These studies demonstrate that ambient air measurements are mandatory prior to any breath measurements, since exogenous substances can have significant influence

*The concentrations have been converted from nmol L^{-1} in ppmV using $V_M = 25.28 \text{ L mol}^{-1}$ and $T = 308 \text{ K}$.

on the result. Table 2.3 summarises the cleaning agents and disinfectants, which will be included into the interference analysis. There might be more disinfectants and cleaning agents having high potential to distort breath measurements, however, based on the results of the sources [84–86, 100] only these four substances will be considered.

In view of spectral interference potential all molecules present in breath having a carbonyl group are considered, too, even if their abundance is below 50 ppbV since they likely interfere spectroscopically and hence may alter the measurement significantly. Therefore, the abundance in breath of potential interference species aldehydes, ketone bodies, organic acids and esters will be discussed.

Tab. 2.3. List of cleaning agents and disinfectants commonly used in clinical environment.

Molecule	Expected <i>worst-case</i> concentration in ppmV*	Reference
Ethanol	2.5 (= 99.22 nmol L ⁻¹)	[86]
1-propanol	1.7 (= 65.78 nmol L ⁻¹)	[86]
Isopropyl alcohol	5.4 (= 212.69 nmol L ⁻¹)	[84–86]
Formaldehyde	0.6 [†]	[99]

In the study of De Lacy Costello et al. [73] the VOCs of breath, skin secretions, saliva, urine, faeces, blood and milk emanating from the human body have been analysed. Altogether 1840 VOCs have been assigned, 872 from breath, although only 199 have been identified by spectral library match and retention time allowing them to be regarded as identified with high certainty. The subjects of these studies have been healthy humans and their breath constitutes of several aldehydes, ketones, organic acids and esters. Though listed clearly in tables, no quantitative information is given. In the study of Mochalski et al. [101], 67 VOCs from healthy volunteers were analysed by means of GC-MS and compared to the ambient air and blood levels of the patients. Only three compounds had mean concentrations above 10 ppbV, namely acetone (950 ppbV), isoprene (131 ppbV) and 2,3-butanedione (29 ppbV), whereas the values in brackets represent the mean values. 2,3-butanedione, however, was not present in blood but in room air and hence is regarded as an exogenous substance. This example indicates again, that taking room air samples before measurements should be performed if high accuracy is necessary. However, 29 ppbV of 2,3-butanedione might not be noteworthy in breath acetone measurements in applications like ketogenic diet monitoring with breath acetone concentrations > 1 ppmV.

*The concentrations have been converted from nmol L⁻¹ in ppmV using $V_M = 25.28 \text{ L mol}^{-1}$ and $T = 308 \text{ K}$.

[†]Defined short-term exposition limit for Germany [100, p. 31].

Table 2.4 shows that diseased states like inflammatory processes and bacterial infections can add various long-chain compounds with a carbonyl group to the exhaled breath, however, they are usually determined in exhaled breath condensate [102] and not in the gas phase and hence are not further considered. They will be discussed in more detail in section 2.1.7. Acetaldehyde can be detected in the gas phase but has only a mean abundance of 24 ppbV in healthy patients and hence is not included in table 2.2 [83]. Nevertheless, if an application is required with high breath acetone accuracy at the lower breath acetone concentration limit around 200 ppbV, acetaldehyde should be considered as potential interferent in optical sensing. Besides, if acetaldehyde is an issue, care should be taken if breath containers or NDTs are used during sampling, because they could emit acetaldehyde [101]. Furthermore, in the studies of Erhart et al. [103] and King et al. [104] ketones like 3-heptanone, 2-pentanone and methyl acetate are discussed. Patients with epilepsy had elevated 3-heptanone concentrations with a mean of 14.7 ppbV and a median of 13.8 ppbV, whereas the values of the control group lay in the sub-ppbV region. For 2-pentanone and methyl acetate, the highest detected values of seven healthy patients were 0.44 ppbV and 9.27 ppbV, respectively, demonstrating, that these ketone bodies do not interfere significantly.

The studies referenced in this paragraph demonstrate that there are various different more or less volatile compounds in healthy or ill human's breath including aldehydes, ketones, organic acids and esters. However, their concentrations range usually in the single to low double-digit ppbV region or below. Besides, some of them are not volatile and are detected in breath condensate. Hence, their influence on the measured breath acetone level can be considered neglectable in most application scenarios. Therefore, only the components of table 2.2 and table 2.3 will be used for further optical interference analysis, which is discussed later in chapter 3.

Tab. 2.4. Complex compounds containing a carbonyl group, which are connected to a certain disease or metabolism after [95].

Molecule	Abundance	Pyhsiological basis
Acetaldehyde (Ethanal)	ppbV	Ethanol digestion
2-aminoacetophenone	ppbV	Bacterial infections
Leukotriene	ppbV	Inflammatory process
Isoprostanes	ppbV	Inflammatory process
Methylnicotinate	ppbV	Bacterial infections
Prostanoids	ppbV	Pulmonary inflammation

2.1.6 Challenges in modern breath analysis

It has been discussed before, that only a few breath tests have found their way into clinical practice, yet. This section is dedicated to address some of the reasons for this situation and what has to be changed to overcome it.

Already during the biomarker search phase of this work, difficulties occurred like the discrimination between the exogenous and endogenous origins of the measured substances in human breath in some studies. Besides, analysis results, not only during biomarker research but also in later clinical applications, can be influenced by the subject itself, too. Due to individual diet, origin, age, sex and physical state the composition of the exhaled breath varies greatly [1]. Table 2.5 summarises various error sources and factors influencing the breath analysis results in pulmonary disease detection studied by Van de Kant et al. [105]. These factors are termed confounding variables (CV).

Regarding the analytical aspects, further issues have to be addressed, including standardisation. A lack of standardisation of the experimental procedures causes broad variations in the results. This includes the poor storage solutions and the deficient reliability of the available prototypes for exhaled breath real-time analysis [12].

The time resolution of a measurement, for instance, determines, if different breathing phases can be distinguished or not. This is important since some VOCs get into the exhaled breath from the oral cavity, the upper airways, the bronchial tubes (e.g. NO) or the alveoli. Thus, it has to be considered, that intermediate storage and analysis of the complete exhale of one breath can lead to the dilution of the analyte, compared to the direct measurement of the composition of the different breathing phases. Furthermore, Miekisch et al. [106] analysed a breath sample by means of SPME and GC-MS prior to storage in a Tedlar bag. After 48 hours, the concentration of substances like acetone or propanal dropped to 72 % and even 60 % respectively, demonstrating the susceptibility of storage devices to analytical errors. Besides breath sampling methods like Tedlar bags or pre-concentration methods, the type of air sampled is important. Approaches using alveolar air from the end-tidal breath phase or mixed air originating additionally from the upper airway paths have to be distinguished. Moreover, the analysed sample can contain a single breath or multiple breaths and it can be sampled from mouth or nose. All these aspects can change the concentration of a marker, hence, providing another example that standards are crucial for breath analysis to become a standard diagnosis tool. Furthermore, since exhaled breath has a high water content, which can lead to cross-sensitivities, dehumidifier can be applied in the gas line as well, improving the sensor performance [107], though it is mandatory to validate, that these techniques are not altering the marker of interest concentration significantly.

Besides the error source CV, voodoo correlations (VC) and statistical misconceptions in the study design (SMSD) have to be addressed as well. Especially for the correct interpretation of a whole breath spectrum with several analytes sound data

Tab. 2.5. Confounding variables influencing the results of breath analysis in pulmonary diseases after [105].

Error source	Factor
<i>Analysis</i>	Pre-concentration procedure
	Storage time and storage procedure
	Breath collection: alveolar air or mixed air, exhaled through nose or mouth
	Collection method: e.g. metal containers or tedlar bags
	Analytical method: e.g. eNose, MS-technique
<i>Environment</i>	Ambient VOC composition (e.g. air pollution)
	Ambient temperature
	Humidity of exhaled and inhaled air
	Season
<i>Subject</i>	Individual characteristics: e.g. age, gender, weight
	Tobacco smoking
	Medication
	Nutrition
	Circadian rhythm
	Breathing pattern: e.g. exhaled flow, minute ventilation, breath hold
	Further diseases: e.g. diabetes, bacterial infection
	Lifestyle and physical state

processing is necessary to avoid artificial significance, since this can easily lead to a false assignment of a biomarker to a certain disease [106]. Although this work is not coping with such an assignment, an example for VC and a solution for avoiding such misinterpretation will be demonstrated briefly due to its importance in many fields of scientific research. Voodoo correlations can be seen as coincidentally appearing statistically true correlations, commonly provoked by a vast number of measured variables [108]. The term VC originates from Ed Vul et al. [108] and was first mentioned in their work *Puzzlingly High Correlations in fMRI Studies of Emotion, Personality, and Social Cognition*. From then on, the topic is still discussed animatedly. Since VCs occur due to a high number of measured variables, the analysis of exhaled breath, containing hundreds of different molecules, is very vulnerable for this kind of misinterpretation. Miekisch et al. [106] used the vivid example of a coin being flipped. The task of the coin was to detect cancer in a study with $n = 8$ study members, including four patients and four control subjects. When the number of coins (number of coins = m) is increased to 128, it has a high probability, that one of the coins is the *magic coin* with a 100 % prediction reliability. This is obviously possible, due to the disproportion of 128 variables and only 8 study members. If

the prediction factor is set to 87.5 %, only 16 coins (on average) are necessary to find a variable, which can be applied as an excellent cancer detector. This clearly demonstrates, that the *m-to-n ratio* determines the susceptibility for VCs, hence, either the number of measured variables, in human breath analysis, this means the number of VOCs used for data interpretation, is decreased or the amount of independent samples (study members) has to be increased. It has been proven, that *m* should be five to ten times lower than *n* to avoid VCs [109, 110]. This issue can also be obviated, when the discovered predictor of a primary study is tested again with an independent set of data, e.g. new group of subjects, in a secondary study to validate the predictor performance. Unfortunately, this procedure is still not a standard practice in modern breath analysis [106]. Besides, understanding the biochemical pathways of molecules being considered as potential biomarkers is crucial and cannot only help identifying voodoo correlations in some cases, but also provides some physiological basis. This is an important requirement, since clinicians need to gain trust in the new diagnosis tool in order to employ the breath test in clinical routine [27].

In medical studies, observatory or retrospective are not as valuable as prospective, randomised and blinded experiments [111]. Hence, the latter properties should be applied in clinical but also in pre-clinical trials. Further SMSD include neglecting prevalence rates of 100 %. Significant correlations between diseases and biomarkers frequently occur only as long as the disease prevalence is high. This can lead to false positives and false negatives in clinical applications (e.g. screening), when the subjects do not show a high prevalence. Besides, studies with low numbers of subjects or even results from single observations cannot be consulted in practice, since they do not have a high significance [106].

Concluding, the discussed error sources clearly demonstrate the need for

- standardisation regarding analysis techniques and procedure,
- consideration of environmental influence in the study design,
- proper choice of subjects,
- and an adequate design of the study as well as self-reflection considering the validation of study results and the concomitant proclamation of new biomarkers.

Without large-scaled studies, using standardised procedures allowing comparable results, breath analysis will have great difficulties to find its place in clinical or home care applications as a modern and reliable diagnosis tool. Therefore, the breath analysis community has recently launched the *Peppermint Experiment* initiative to tackle these issues and improve standardisation [112]. The interested reader is encouraged to read [27, 105, 106] to receive a more holistic overview of confounding variables, voodoo correlation and SMSD in context of breath analysis as well as of further obstacles regarding breath tests in clinical routine.

2.1.7 Aerosols, particles and breath condensate

This section provides a short overview of the usability of aerosols, particles and breath condensate in terms of medical diagnosing. Exhaled breath condensate (EBC) is a biofluid comparable to urine, saliva or serum. Besides water vapor, which is the main part of EBC, EBC contains aerosolised particle fractions [113].

Several systems have been introduced in the past to classify fractions of EBC [114], including

- volatile and nonvolatile,
- pH- or redox-relevant and nonreactive,
- nonproteinaceous and proteinaceous,
- or organic and inorganic.

Exhaled breath aerosols (EBA) containing particles can be acquired separately from EBC and both contain different substances. The concept of EBC sampling is quite simple since only a cool surface like a window or a mirror is necessary. To separate EBC from the aerosolised particles usually filters are used. The condensation step is controlled by three variables [113], namely:

1. The available volume of exhaled breath.
2. The condenser's surface area.
3. The temperature gradient between condenser and sampled breath.

Again, a lack of standardisation aggravates progress in research and towards applications. Therefore, commercially available devices are to be preferred compared to self-made sampling systems since the former ones allow more standardisation between different operators [113].

Few tests have been clinically approved including a pH test, which can be used in the diagnosis of reflux-induced cough [115]. Ionic substances like lactic, acetic and formic acid are determined within this pH test [116]. Besides, hydrogen peroxide detection for the measurement of airway inflammation and oxidant stress [117] as well as *tuberculosis bacilli* detection [113]. Other potential biomarkers, most of them being associated with airways diseases [115], are still in the research stage and have to be validated first, including glutathione [118], cytokines [118] or 8-isoprostane [119], to name a few.

EBA accounts for approximately 0.1 % of EBC [120] and its exact generation mechanisms in the airways have not been clarified yet [113]. The diameter of the particles found in breath is usually in the range of 0.3 to 0.4 μm . So far, no clinical approved

test for EBA has been developed. One reason for that is the extremely low concentration of aerosolised particles and new analytic equipment is needed to advance EBA research. However, molecules like cytokines and chemokines have been detected in EBA and are of great interest for researchers and clinicians since the same substances have been identified in blood or bronchoalveolar lavage fluid [121] and thus could replace invasive tests [113]. In a recent study from Carpaij et al. [122] the size and mass of the particles from EBC were measured and could be used to distinguish between degrees of asthma remission.

Concluding, not only breath gas but also EBC and EBA with its particles can be used to detect diseases and abnormal pathological states. In general, every source of emission, which can be sampled noninvasively should be considered for further research towards new diagnosing tools. It cannot be excluded, that in the future, breath analysis might offer the possibility of noninvasive and fast detection of virus infections ore similar.

References

- [1] J. D. Pleil et al. “Breath biomarkers and the exposome”. In: *Breathborne Biomarkers and the Human Volatilome*. Ed. by J. Beauchamp et al. 2nd ed. Elsevier, 2020, pp. 4–20. ISBN: 9780128199671 (cit. on pp. 8, 9, 14, 21, 22, 27).
- [2] G. Maciocia. *Grundlagen der Chinesischen Medizin*. Urban & Fischer/ Elsevier, 2016 (cit. on p. 8).
- [3] M. Phillips. “Breath tests in medicine”. In: *Scientific American* 267.1 (1992), pp. 74–79. ISSN: 00368733. DOI: 10.1038/scientificamerican0792-74 (cit. on pp. 8, 9).
- [4] I. Lamprecht. “Calorimetry and thermodynamics of living systems”. In: *Thermochimica Acta* 405.1 (2003), pp. 1–13. ISSN: 00406031. DOI: 10.1016/S0040-6031(03)00123-0 (cit. on p. 8).
- [5] M. Karamanou and G. Androutsos. “Antoine-Laurent de Lavoisier (1743–1794) and the birth of respiratory physiology”. In: *Thorax* 68.10 (Oct. 2013), pp. 978–979. ISSN: 0040-6376. DOI: 10.1136/thoraxjnl-2013-203840 (cit. on p. 8).
- [6] Gesellschaft Deutscher Chemiker. *Justus von Liebig*. 2003 (cit. on p. 9).
- [7] A. D. Baldwin. “Anstie’s Alcohol Limit”. In: *Public Health Then and Now* 67.7 (1977), pp. 679–681. ISSN: 0090-0036. DOI: 10.2105/AJPH.67.7.679 (cit. on p. 9).
- [8] L. Pauling et al. “Quantitative Analysis of Urine Vapor and Breath by Gas-Liquid Partition Chromatography”. In: *Proceedings of the National Academy of Sciences* 68.10 (Oct. 1971), pp. 2374–2376. ISSN: 0027-8424. DOI: 10.1073/pnas.68.10.2374 (cit. on pp. 9, 21).

- [9] T. Risby and S. Solga. “Current status of clinical breath analysis”. In: *Applied Physics B* 85.2-3 (Nov. 2006), pp. 421–426. ISSN: 0946-2171. DOI: 10.1007/s00340-006-2280-4 (cit. on p. 9).
- [10] M. Hakim et al. “Volatile Organic Compounds of Lung Cancer and Possible Biochemical Pathways”. In: *Chemical Reviews* 112.11 (Nov. 2012), pp. 5949–5966. ISSN: 0009-2665. DOI: 10.1021/cr300174a (cit. on p. 9).
- [11] P. R. Fortes et al. *Optical Gas Sensors for Exhaled Breath Analysis*. SPIE PRESS, 2017. ISBN: 9781510613782. DOI: 10.1117/3.2284712 (cit. on p. 9).
- [12] J. Pereira et al. “Breath Analysis as a Potential and Non-Invasive Frontier in Disease Diagnosis: An Overview”. In: *Metabolites* 5.1 (Jan. 2015), pp. 3–55. ISSN: 2218-1989. DOI: 10.3390/metabo5010003 (cit. on pp. 9, 10, 12, 27).
- [13] A. Catino et al. “Breath Analysis: A Systematic Review of Volatile Organic Compounds (VOCs) in Diagnostic and Therapeutic Management of Pleural Mesothelioma”. In: *Cancers* 11.6 (June 2019), p. 831. ISSN: 2072-6694. DOI: 10.3390/cancers11060831 (cit. on p. 9).
- [14] T. Bruderer et al. “On-Line Analysis of Exhaled Breath”. In: *Chemical Reviews* 119.19 (Oct. 2019), pp. 10803–10828. ISSN: 0009-2665. DOI: 10.1021/acs.chemrev.9b00005 (cit. on pp. 9, 12).
- [15] A. Amann et al. “The human volatilome: volatile organic compounds (VOCs) in exhaled breath, skin emanations, urine, feces and saliva”. In: *Journal of Breath Research* 8.3 (June 2014), p. 034001. ISSN: 1752-7155. DOI: 10.1088/1752-7155/8/3/034001 (cit. on pp. 10–12).
- [16] N. Sterer and M. Rosenberg. *Breath Odors*. 1st ed. Berlin, Heidelberg: Springer Berlin Heidelberg, 2011. ISBN: 978-3-642-19311-8. DOI: 10.1007/978-3-642-19312-5 (cit. on p. 11).
- [17] W. Miekisch et al. “Impact of sampling procedures on the results of breath analysis”. In: *Journal of Breath Research* 2.2 (June 2008), p. 026007. ISSN: 1752-7155. DOI: 10.1088/1752-7155/2/2/026007 (cit. on p. 11).
- [18] T. Birken et al. “A novel visually CO₂ controlled alveolar breath sampling technique”. In: *Technology and Health Care* 14.6 (Nov. 2006), pp. 499–506. ISSN: 09287329. DOI: 10.3233/THC-2006-14605 (cit. on p. 11).
- [19] J. King et al. “Isoprene and acetone concentration profiles during exercise on an ergometer”. In: *Journal of Breath Research* 3.2 (June 2009), p. 027006. ISSN: 1752-7155. DOI: 10.1088/1752-7155/3/2/027006 (cit. on pp. 11, 16).
- [20] W. Miekisch et al. “Construction and Evaluation of a Versatile CO₂ Controlled Breath Collection Device”. In: *IEEE Sensors Journal* 10.1 (Jan. 2010), pp. 211–215. ISSN: 1530-437X. DOI: 10.1109/JSEN.2009.2035757 (cit. on p. 11).
- [21] O. Lawal et al. “Exhaled breath analysis: a review of ‘breath-taking’ methods for off-line analysis”. In: *Metabolomics* 13.10 (Oct. 2017), p. 110. ISSN: 1573-3882. DOI: 10.1007/s11306-017-1241-8 (cit. on pp. 11, 12).

- [22] A. Amann et al. “Methodological issues of sample collection and analysis of exhaled breath”. In: *Exhaled Biomarkers*. European Respiratory Society, Sept. 2010, pp. 96–114. DOI: 10.1183/1025448x.00018509 (cit. on pp. 11, 12).
- [23] M. Basanta et al. “Non-invasive metabolomic analysis of breath using differential mobility spectrometry in patients with chronic obstructive pulmonary disease and healthy smokers”. In: *The Analyst* 135.2 (2010), p. 315. ISSN: 0003-2654. DOI: 10.1039/b916374c (cit. on p. 12).
- [24] K. L. Moskalenko et al. “Human breath trace gas content study by tunable diode laser spectroscopy technique”. In: *Infrared Physics & Technology* 37.1 (1996), pp. 181–192. ISSN: 13504495. DOI: 10.1016/1350-4495(95)00097-6 (cit. on pp. 13, 23).
- [25] B. Enderby et al. “Concentrations of some metabolites in the breath of healthy children aged 7 – 18 years measured using selected ion flow tube mass spectrometry (SIFT-MS)”. In: (2009). DOI: 10.1088/1752-7155/3/3/036001 (cit. on pp. 13, 23, 24).
- [26] O. A. Ajibola et al. “Effects of dietary nutrients on volatile breath metabolites”. In: *Journal of Nutritional Science* 2.October (2013), pp. 1–15. ISSN: 20486790. DOI: 10.1017/jns.2013.26 (cit. on p. 13).
- [27] S. F. Solga et al. “Challenges in clinical breath research development”. In: *Breathborne Biomarkers and the Human Volatilome*. Ed. by J. Beauchamp et al. 2nd ed. Elsevier, 2020. Chap. 36, pp. 601–612. ISBN: 9780128199671 (cit. on pp. 14, 18, 29).
- [28] L. Farhi. “Elimination of inert gas by the lung”. In: *Respiration Physiology* 3.1 (Aug. 1967), pp. 1–11. ISSN: 00345687. DOI: 10.1016/0034-5687(67)90018-7 (cit. on p. 14).
- [29] J. King et al. “Physiological modeling of exhaled compounds”. In: *Breathborne Biomarkers and the Human Volatilome*. Ed. by J. Beauchamp et al. 2nd ed. Elsevier, 2020. Chap. 3, pp. 44–60. ISBN: 9780128199671 (cit. on p. 14).
- [30] P. Španěl and D. Smith. “What is the real utility of breath ammonia concentration measurements in medicine and physiology?” In: *Journal of Breath Research* 12.2 (Jan. 2018), p. 027102. ISSN: 1752-7163. DOI: 10.1088/1752-7163/aa907f (cit. on p. 16).
- [31] D. Smith et al. “Selected ion flow tube mass spectrometry”. In: *Breathborne Biomarkers and the Human Volatilome*. Ed. by J. Beauchamp et al. 2nd ed. Elsevier, 2020. Chap. 9, pp. 137–150. ISBN: 9780128199671 (cit. on pp. 16, 17).
- [32] S. J. Davies et al. “Breath analysis of ammonia, volatile organic compounds and deuterated water vapor in chronic kidney disease and during dialysis”. In: *Bioanalysis* 6.6 (Mar. 2014), pp. 843–857. ISSN: 1757-6180. DOI: 10.4155/bio.14.26 (cit. on p. 16).

- [33] D. Smith et al. “Hydrogen cyanide, a volatile biomarker of *Pseudomonas aeruginosa* infection”. In: *Journal of Breath Research* 7.4 (Nov. 2013), p. 044001. ISSN: 1752-7155. DOI: 10.1088/1752-7155/7/4/044001 (cit. on p. 16).
- [34] F. J. Gilchrist et al. “Exhaled breath hydrogen cyanide as a marker of early *Pseudomonas aeruginosa* infection in children with cystic fibrosis”. In: *ERJ Open Research* 1.2 (Oct. 2015), pp. 00044–2015. ISSN: 2312-0541. DOI: 10.1183/23120541.00044-2015 (cit. on p. 16).
- [35] B. G. Stone et al. “Effect of regulating cholesterol biosynthesis on breath isoprene excretion in men”. In: *Lipids* 28.8 (Aug. 1993), pp. 705–708. ISSN: 0024-4201. DOI: 10.1007/BF02535990 (cit. on p. 16).
- [36] J. King et al. “Breath isoprene: Muscle dystrophy patients support the concept of a pool of isoprene in the periphery of the human body”. In: *Biochemical and Biophysical Research Communications* 423.3 (July 2012), pp. 526–530. ISSN: 0006291X. DOI: 10.1016/j.bbrc.2012.05.159 (cit. on p. 16).
- [37] S. Abegg and A. T. Güntner. “Lifestyle applications”. In: *Breathborne Biomarkers and the Human Volatilome*. Ed. by J. Beauchamp et al. 2nd ed. Elsevier, 2020. Chap. 23, pp. 363–373. ISBN: 9780128199671 (cit. on p. 16).
- [38] D. Smith et al. “Can volatile compounds in exhaled breath be used to monitor control in diabetes mellitus?” In: *Journal of Breath Research* 5.2 (June 2011), p. 022001. ISSN: 1752-7155. DOI: 10.1088/1752-7155/5/2/022001 (cit. on p. 16).
- [39] C. Walton et al. “The use of a portable breath analysis device in monitoring type 1 diabetes patients in a hypoglycaemic clamp: validation with SIFT-MS data”. In: *Journal of Breath Research* 8.3 (Sept. 2014), p. 037108. ISSN: 1752-7155. DOI: 10.1088/1752-7155/8/3/037108 (cit. on p. 16).
- [40] P. R. Boshier et al. “Variation in Exhaled Acetone and Other Ketones in Patients Undergoing Bariatric Surgery: a Prospective Cross-sectional Study”. In: *Obesity Surgery* 28.8 (Aug. 2018), pp. 2439–2446. ISSN: 0960-8923. DOI: 10.1007/s11695-018-3180-5 (cit. on p. 16).
- [41] A. Prabhakar et al. “Acetone as biomarker for ketosis buildup capability - a study in healthy individuals under combined high fat and starvation diets”. In: *Nutrition Journal* 14.1 (Dec. 2015), p. 41. ISSN: 1475-2891. DOI: 10.1186/s12937-015-0028-x (cit. on p. 16).
- [42] K. Musa-Veloso et al. “Breath acetone is a reliable indicator of ketosis in adults consuming ketogenic meals”. In: *The American Journal of Clinical Nutrition* 76.1 (July 2002), pp. 65–70. ISSN: 0002-9165. DOI: 10.1093/ajcn/76.1.65 (cit. on p. 17).
- [43] K. Musa-Veloso et al. “Breath acetone predicts plasma ketone bodies in children with epilepsy on a ketogenic diet”. In: *Nutrition* 22.1 (2006), pp. 1–8. ISSN: 08999007. DOI: 10.1016/j.nut.2005.04.008 (cit. on pp. 17, 24).
- [44] K. Yamai et al. “Influence of cycle exercise on acetone in expired air and skin gas”. In: *Redox Report* 14.6 (Dec. 2009), pp. 285–289. ISSN: 1351-0002. DOI: 10.1179/135100009X12525712409850 (cit. on p. 17).

- [45] A. T. Güntner et al. “Noninvasive Body Fat Burn Monitoring from Exhaled Acetone with Si-doped WO₃ -sensing Nanoparticles”. In: *Analytical Chemistry* 89.19 (Oct. 2017), pp. 10578–10584. ISSN: 0003-2700. DOI: 10.1021/acs.analchem.7b02843 (cit. on p. 17).
- [46] R. Schubert et al. “Metabolic monitoring and assessment of anaerobic threshold by means of breath biomarkers”. In: *Metabolomics* 8.6 (Dec. 2012), pp. 1069–1080. ISSN: 1573-3882. DOI: 10.1007/s11306-012-0408-6 (cit. on p. 17).
- [47] M. A. Samara et al. “Single Exhaled Breath Metabolomic Analysis Identifies Unique Breathprint in Patients With Acute Decompensated Heart Failure”. In: *Journal of the American College of Cardiology* 61.13 (Apr. 2013), pp. 1463–1464. ISSN: 07351097. DOI: 10.1016/j.jacc.2012.12.033 (cit. on p. 17).
- [48] I. A. Hanouneh et al. “The Breathprints in Patients With Liver Disease Identify Novel Breath Biomarkers in Alcoholic Hepatitis”. In: *Clinical Gastroenterology and Hepatology* 12.3 (Mar. 2014), pp. 516–523. ISSN: 15423565. DOI: 10.1016/j.cgh.2013.08.048 (cit. on p. 17).
- [49] F. S. Cikach et al. “Breath Analysis in Pulmonary Arterial Hypertension”. In: *Chest* 145.3 (Mar. 2014), pp. 551–558. ISSN: 00123692. DOI: 10.1378/chest.13-1363 (cit. on p. 17).
- [50] F. Rieder et al. “A Distinct Colon-Derived Breath Metabolome is Associated with Inflammatory Bowel Disease, but not its Complications”. In: *Clinical and Translational Gastroenterology* 7.11 (Nov. 2016), e201. ISSN: 2155-384X. DOI: 10.1038/ctg.2016.57 (cit. on p. 17).
- [51] S. Demirjian et al. “Molecular breath analysis identifies the breathprint of renal failure”. In: *Journal of Breath Research* 11.2 (June 2017), p. 026009. ISSN: 1752-7163. DOI: 10.1088/1752-7163/aa7143 (cit. on p. 17).
- [52] P. Kintz et al. “Testing for Drugs in Exhaled Breath Collected With ExaBreath in a Drug Dependence Population”. In: *Therapeutic Drug Monitoring* 38.1 (Feb. 2016), pp. 135–139. DOI: 10.1097/FTD.0000000000000228 (cit. on p. 17).
- [53] M. Thevis et al. “Sports drug testing using complementary matrices: Advantages and limitations”. In: *Journal of Pharmaceutical and Biomedical Analysis* 130 (Oct. 2016), pp. 220–230. ISSN: 07317085. DOI: 10.1016/j.jpba.2016.03.055 (cit. on p. 17).
- [54] V. Ruzsanyi et al. “Urban search and rescue”. In: *Breathborne Biomarkers and the Human Volatilome*. Ed. by J. Beauchamp et al. 2nd ed. Elsevier, 2020. Chap. 31, pp. 509–520. ISBN: 9780128199671 (cit. on p. 17).
- [55] F. Hoffmeyer et al. “Different Patterns in Changes of Exhaled Breath Condensate pH and Exhaled Nitric Oxide After Ozone Exposure”. In: 2014, pp. 39–47. DOI: 10.1007/5584_2014_63 (cit. on p. 17).
- [56] J. Beauchamp et al. *Breathborne Biomarkers and the Human Volatilome*. Ed. by J. Beauchamp et al. Elsevier, 2020, p. 722. ISBN: 9780128199671 (cit. on p. 18).

- [57] International Programme on Chemical Safety. *Environmental Health Criteria 207. Acetone*. Tech. rep. Genf: Published under joint sponsorship of the United Nations Environment Program (UNEP), the International Labour Organisation (ILO), and the World Health Organisation (WHO)., 1998 (cit. on p. 18).
- [58] K. Verschueren. *Handbook of environmental data on organic chemicals*. 4th. New York: Wiley, 2001. ISBN: 0471374903 (cit. on p. 18).
- [59] H. B. Singh et al. “Acetone in the atmosphere : Distribution , sources , and sinks”. In: *Journal of geophysical Research* 99.93 (1994), pp. 1805–1819 (cit. on p. 19).
- [60] J.-F. Müller and G. Brasseur. “Sources of upper tropospheric HOX : A three-dimensional study”. In: *Journal of Geophysical Research: Atmospheres* 104.D1 (Jan. 1999), pp. 1705–1715. ISSN: 01480227. DOI: 10.1029/1998JD100005 (cit. on p. 19).
- [61] D. J. Jacob et al. “Atmospheric budget of acetone”. In: *Journal of Geophysical Research: Atmospheres* 107.D10 (May 2002), ACH 5–1–ACH 5–17. ISSN: 01480227. DOI: 10.1029/2001JD000694 (cit. on p. 19).
- [62] E. V. Fischer et al. “The role of the ocean in the global atmospheric budget of acetone”. In: *Geophysical Research Letters* 39.1 (2012), pp. 3–7. ISSN: 00948276. DOI: 10.1029/2011GL050086 (cit. on p. 19).
- [63] Agency for Toxic Substances and Disease Registry (US Department of Health and Human Services). *Toxicological profile for acetone*. Tech. rep. Atlanta: Agency for Toxic Substances and Disease Registry, 1994 (cit. on p. 19).
- [64] H. Guo et al. “Acetone in the atmosphere of Hong Kong: Abundance, sources and photochemical precursors”. In: *Atmospheric Environment* 65 (Feb. 2013), pp. 80–88. ISSN: 13522310. DOI: 10.1016/j.atmosenv.2012.10.027 (cit. on p. 19).
- [65] L. Dunayevskiy et al. “High-sensitivity detection of triacetone triperoxide (TATP) and its precursor acetone”. In: *Applied Optics* 46.25 (2007), pp. 6397–6404. ISSN: 15394522. DOI: 10.1364/AO.46.006397 (cit. on p. 19).
- [66] G. A. Reichard et al. “Acetone metabolism in humans during diabetic ketoacidosis”. In: *Diabetes* 35.6 (1986), pp. 668–674. ISSN: 00121797. DOI: 10.2337/diab.35.6.668 (cit. on pp. 19, 20).
- [67] G. A. Reichard et al. “Plasma Acetone Metabolism in the Fasting Human”. In: *Journal of Clinical Investigation* 63.4 (Apr. 1979), pp. 619–626. ISSN: 0021-9738. DOI: 10.1172/JCI109344 (cit. on p. 19).
- [68] P. Sukul et al. “Immediate effects of breath holding maneuvers onto composition of exhaled breath”. In: *Journal of Breath Research* 8.3 (2014), p. 037102. ISSN: 17527163. DOI: 10.1088/1752-7155/8/3/037102 (cit. on p. 20).
- [69] J. C. Anderson et al. “Modeling Soluble Gas Exchange in the Airways and Alveoli”. In: *Annals of Biomedical Engineering* 31.11 (Dec. 2003), pp. 1402–1422. ISSN: 0090-6964. DOI: 10.1114/1.1630600 (cit. on p. 20).

- [70] J. C. Anderson. “Measuring airway exchange of endogenous acetone using a single-exhalation breathing maneuver”. In: *Journal of Applied Physiology* 100.3 (2005), pp. 880–889. ISSN: 8750-7587. DOI: 10.1152/jappphysiol.00868.2005 (cit. on p. 20).
- [71] J. C. Anderson and M. P. Hlastala. “Breath tests and airway gas exchange”. In: *Pulmonary Pharmacology and Therapeutics* 20.2 (2007), pp. 112–117. ISSN: 10945539. DOI: 10.1016/j.pupt.2005.12.002 (cit. on p. 20).
- [72] Z. Wang and C. Wang. “Is breath acetone a biomarker of diabetes? A historical review on breath acetone measurements”. In: *Journal of Breath Research* 7.3 (2013), p. 037109. ISSN: 17527155. DOI: 10.1088/1752-7155/7/3/037109 (cit. on p. 20).
- [73] B. de Lacy Costello et al. “A review of the volatiles from the healthy human body”. In: *Journal of Breath Research* 8.1 (Jan. 2014), p. 014001. ISSN: 1752-7155. DOI: 10.1088/1752-7155/8/1/014001 (cit. on pp. 21, 25).
- [74] J. Wojtas et al. “Ultrasensitive laser spectroscopy for breath analysis”. In: *Opto-Electronics Review* 20.1 (Jan. 2012), pp. 121–136. ISSN: 1896-3757. DOI: 10.2478/s11772-012-0011-4 (cit. on pp. 21, 23).
- [75] E. Mansour et al. “Measurement of temperature and relative humidity in exhaled breath”. In: *Sensors and Actuators B: Chemical* 304 (Feb. 2020), p. 127371. ISSN: 09254005. DOI: 10.1016/j.snb.2019.127371 (cit. on pp. 21, 23).
- [76] D. Zhao et al. “A novel real-time carbon dioxide analyzer for health and environmental applications”. In: *Sensors and Actuators B: Chemical* 195 (May 2014), pp. 171–176. ISSN: 09254005. DOI: 10.1016/j.snb.2013.12.110 (cit. on pp. 21, 23).
- [77] C. F. Toombs et al. “Detection of exhaled hydrogen sulphide gas in healthy human volunteers during intravenous administration of sodium sulphide”. In: *British Journal of Clinical Pharmacology* 69.6 (2010), pp. 626–636. ISSN: 03065251. DOI: 10.1111/j.1365-2125.2010.03636.x (cit. on p. 21).
- [78] A. Wehinger et al. “Lung cancer detection by proton transfer reaction mass-spectrometric analysis of human breath gas”. In: *International Journal of Mass Spectrometry* 265.1 (Aug. 2007), pp. 49–59. ISSN: 13873806. DOI: 10.1016/j.ijms.2007.05.012 (cit. on p. 21).
- [79] A. M. Diskin et al. “Time variation of ammonia, acetone, isoprene and ethanol in breath: A quantitative SIFT-MS study over 30 days”. In: *Physiological Measurement* 24.1 (2003), pp. 107–119. ISSN: 09673334. DOI: 10.1088/0967-3334/24/1/308 (cit. on pp. 22–24).
- [80] C. Turner et al. “A longitudinal study of breath isoprene in healthy volunteers using selected ion flow tube mass spectrometry (SIFT-MS)”. In: *Physiological Measurement* 27.1 (2006), pp. 13–22. ISSN: 09673334. DOI: 10.1088/0967-3334/27/1/002 (cit. on pp. 22, 23).

- [81] C. Turner et al. “A longitudinal study of methanol in the exhaled breath of 30 healthy volunteers using selected ion flow tube mass spectrometry, SIFT-MS”. In: *Physiological Measurement* 27.7 (2006), pp. 637–648. ISSN: 09673334. DOI: 10.1088/0967-3334/27/7/007 (cit. on p. 22).
- [82] C. Turner et al. “A longitudinal study of methanol in the exhaled breath of 30 healthy volunteers using selected ion flow tube mass spectrometry, SIFT-MS”. In: *Physiological Measurement* 27.7 (2006), pp. 637–648. ISSN: 09673334. DOI: 10.1088/0967-3334/27/7/007 (cit. on pp. 22, 24).
- [83] C. Turner et al. “A longitudinal study of ethanol and acetaldehyde in the exhaled breath of healthy volunteers using selected-ion flow-tube mass spectrometry”. In: *Rapid Communications in Mass Spectrometry* 20.1 (2006), pp. 61–68. ISSN: 09514198. DOI: 10.1002/rcm.2275 (cit. on pp. 22, 24, 26).
- [84] S. Ghimenti et al. “Determination of sevoflurane and isopropyl alcohol in exhaled breath by thermal desorption gas chromatography-mass spectrometry for exposure assessment of hospital staff”. In: *Journal of Pharmaceutical and Biomedical Analysis* 106 (Mar. 2014), pp. 218–223. ISSN: 0731-7085. DOI: <https://doi.org/10.1016/j.jpba.2014.11.052> (cit. on pp. 22, 25).
- [85] S. Kischkel et al. “Breath analysis during one-lung ventilation in cancer patients”. In: *European Respiratory Journal* 40.3 (2012), pp. 706–713. ISSN: 09031936. DOI: 10.1183/09031936.00125411 (cit. on pp. 22, 25).
- [86] S. Kischkel et al. “Breath biomarkers for lung cancer detection and assessment of smoking related effects - confounding variables, influence of normalization and statistical algorithms”. In: *Clinica Chimica Acta* 411.21-22 (2010), pp. 1637–1644. ISSN: 00098981. DOI: 10.1016/j.cca.2010.06.005 (cit. on pp. 24, 25).
- [87] A. J. Cunningham and P. Hormbrey. “Breath analysis to detect recent exposure to carbon monoxide”. In: *Postgraduate medical journal* 78.918 (2002), pp. 233–237. ISSN: 00325473. DOI: 10.1136/pmj.78.918.233 (cit. on p. 23).
- [88] A. Rezaie et al. “Hydrogen and Methane-Based Breath Testing in Gastrointestinal Disorders: The North American Consensus”. In: *American Journal of Gastroenterology* 112.5 (2017), pp. 775–784. ISSN: 15720241. DOI: 10.1038/ajg.2017.46 (cit. on p. 23).
- [89] F. K. Tittel. “Current status of midinfrared quantum and interband cascade lasers for clinical breath analysis”. In: *Optical Engineering* 49.11 (2010), p. 111123. ISSN: 0091-3286. DOI: 10.1117/1.3498768 (cit. on p. 23).
- [90] S. Davies et al. “Quantitative analysis of ammonia on the breath of patients in end-stage renal failure”. In: *Kidney International* 52.1 (July 1997), pp. 223–228. ISSN: 00852538. DOI: 10.1038/ki.1997.324 (cit. on p. 23).
- [91] T. Kondo et al. “Association of Fasting Breath Nitrous Oxide Concentration with Gastric Juice Nitrate and Nitrite Concentrations and Helicobacter pylori Infection”. In: 45.10 (2000), pp. 2054–2057 (cit. on p. 23).

- [92] N. Alkhoury et al. “Isoprene in the exhaled breath is a novel biomarker for advanced fibrosis in patients with chronic liver disease: A pilot study”. In: *Clinical and Translational Gastroenterology* 6.9 (2015), e112–7. ISSN: 2155384X. DOI: 10.1038/ctg.2015.40 (cit. on p. 23).
- [93] C. Lourenço and C. Turner. “Breath Analysis in Disease Diagnosis: Methodological Considerations and Applications”. In: *Metabolites* 4.2 (2014), pp. 465–498. ISSN: 2218-1989. DOI: 10.3390/metabo4020465 (cit. on p. 24).
- [94] P. Španěl et al. “The concentration distributions of some metabolites in the exhaled breath of young adults”. In: *Journal of Breath Research* 1 (2007). DOI: 10.1088/1752-7155/1/2/026001 (cit. on p. 24).
- [95] A. Mazzatenta et al. “Pathologies currently identified by exhaled biomarkers”. In: *Respiratory Physiology and Neurobiology* 187.1 (2013), pp. 128–134. ISSN: 15699048. DOI: 10.1016/j.resp.2013.02.016 (cit. on p. 24, 26).
- [96] S. Studer et al. “Patterns and significance of exhaled-breath biomarkers in lung transplant recipients with acute allograft rejection”. In: *The Journal of Heart and Lung Transplantation* 20.11 (Nov. 2001), pp. 1158–1166. ISSN: 10532498. DOI: 10.1016/S1053-2498(01)00343-6 (cit. on p. 24).
- [97] S. S. Sehnert et al. “Breath biomarkers for detection of human liver diseases: preliminary study”. In: *Biomarkers : biochemical indicators of exposure, response, and susceptibility to chemicals* 7.2 (2002), pp. 174–187. ISSN: 1354750X. DOI: 10.1080/135475001101 (cit. on p. 24).
- [98] K. Schwarz et al. “Breath acetone - Aspects of normal physiology related to age and gender as determined in a PTR-MS study”. In: *Journal of Breath Research* 3.2 (2009), p. 027003. ISSN: 17527155. DOI: 10.1088/1752-7155/3/2/027003 (cit. on p. 24).
- [99] C. Solal et al. “VOCs and formaldehyde emissions from cleaning products and air fresheners”. In: *11. International Conference on Indoor Air Quality and Climate (Indoor Air 2008)*. 2008, Paper ID : 183 (cit. on pp. 24, 25).
- [100] B. f. A. und Soziales. *Arbeitsplatzgrenzwerte (Fassung vom 29.03.2019) / TRGS 900*. Tech. rep. 2006, pp. 1–69 (cit. on pp. 24, 25).
- [101] P. Mochalski et al. “Blood and breath levels of selected volatile organic compounds in healthy volunteers”. In: *The Analyst* 138.7 (2013), p. 2134. ISSN: 0003-2654. DOI: 10.1039/c3an36756h (cit. on pp. 25, 26).
- [102] P. Montuschi. “Indirect monitoring of lung inflammation”. In: *Nature Reviews Drug Discovery* 1.3 (Mar. 2002), pp. 238–242. ISSN: 1474-1776. DOI: 10.1038/nrd751 (cit. on p. 26).
- [103] S. Erhart et al. “3-Heptanone as a potential new marker for valproic acid therapy”. In: *Journal of Breath Research* 3.1 (2009). ISSN: 17527155. DOI: 10.1088/1752-7155/3/1/016004 (cit. on p. 26).

- [104] J. King et al. “Dynamic profiles of volatile organic compounds in exhaled breath as determined by a coupled PTR-MS/GC-MS study”. In: *Physiological Measurement* 31.9 (2010), pp. 1169–1184. ISSN: 09673334. DOI: 10.1088/0967-3334/31/9/008 (cit. on p. 26).
- [105] K. D. G. van de Kant et al. “Clinical use of exhaled volatile organic compounds in pulmonary diseases: A systematic review”. In: *Respiratory Research* 13 (2012). ISSN: 14659921. DOI: 10.1186/1465-9921-13-117 (cit. on pp. 27–29).
- [106] W. Miekisch et al. “Data interpretation in breath biomarker research: Pitfalls and directions”. In: *Journal of Breath Research* 6.3 (2012), p. 036007. ISSN: 17527155. DOI: 10.1088/1752-7155/6/3/036007 (cit. on pp. 27–29).
- [107] J.-W. Yoon and J.-H. Lee. “Toward breath analysis on a chip for disease diagnosis using semiconductor-based chemiresistors: Recent progress and future perspectives”. In: *Lab Chip* (2017). ISSN: 1473-0197. DOI: 10.1039/C7LC00810D (cit. on p. 27).
- [108] E. Vul et al. “Puzzlingly High Correlations in fMRI Studies of Emotion, Personality, and Social Cognition”. In: 4.3 (2011), pp. 274–290. ISSN: 17456916. DOI: 10.1111/j.1745-6924.2009.01132.x (cit. on p. 28).
- [109] J. D. Pleil et al. “Breath biomarkers in environmental health science: Exploring patterns in the human exposome”. In: *Journal of Breath Research* 5.4 (2011). ISSN: 17527155. DOI: 10.1088/1752-7155/5/4/046005 (cit. on p. 29).
- [110] J. D. Pleil and M. N. Lorber. “Relative congener scaling of polychlorinated dibenzo-p-dioxins and dibenzofurans to estimate building fire contributions in air, surface wipes, and dust samples”. In: *Environmental Science and Technology* 41.21 (2007), pp. 7286–7293. ISSN: 0013936X. DOI: 10.1021/es070714a (cit. on p. 29).
- [111] J. P. Higgins et al. “The Cochrane Collaboration’s tool for assessing risk of bias in randomised trials”. In: *BMJ (Online)* 343.7829 (2011), pp. 1–9. ISSN: 09598146. DOI: 10.1136/bmj.d5928. arXiv: sdfasdff (cit. on p. 29).
- [112] B. Henderson et al. “A benchmarking protocol for breath analysis: the peppermint experiment”. In: *Journal of Breath Research* 14.4 (Aug. 2020), p. 046008. ISSN: 1752-7163. DOI: 10.1088/1752-7163/aba130 (cit. on p. 29).
- [113] M. D. Davis. “Exhaled breath condensate and aerosol”. In: *Breathborne Biomarkers and the Human Volatilome*. Ed. by J. Beauchamp et al. 2nd ed. Elsevier, 2020. Chap. 7, pp. 109–118. ISBN: 9780128199671 (cit. on pp. 30, 31).
- [114] I. Horváth et al. “Exhaled breath condensate: methodological recommendations and unresolved questions”. In: *European Respiratory Journal* 26.3 (Sept. 2005), pp. 523–548. ISSN: 0903-1936. DOI: 10.1183/09031936.05.00029705 (cit. on p. 30).

- [115] E. M. Konstantinidi et al. “Exhaled Breath Condensate: Technical and Diagnostic Aspects”. In: *The Scientific World Journal* 2015 (2015), pp. 1–25. ISSN: 2356-6140. DOI: 10.1155/2015/435160 (cit. on p. 30).
- [116] R. Greenwald et al. “Ionic determinants of exhaled breath condensate pH before and after exercise in adolescent athletes”. In: *Pediatric Pulmonology* 44.8 (Aug. 2009), pp. 768–777. ISSN: 87556863. DOI: 10.1002/ppul.21055 (cit. on p. 30).
- [117] D. M. Neville et al. “Using the Inflammacheck Device to Measure the Level of Exhaled Breath Condensate Hydrogen Peroxide in Patients With Asthma and Chronic Obstructive Pulmonary Disease (The EXHALE Pilot Study): Protocol for a Cross-Sectional Feasibility Study”. In: *JMIR Research Protocols* 7.1 (Jan. 2018), e25. ISSN: 1929-0748. DOI: 10.2196/resprot.8768 (cit. on p. 30).
- [118] L. Scheideler et al. “Detection of Nonvolatile Macromolecules in Breath: A Possible Diagnostic Tool?” In: *American Review of Respiratory Disease* 148.3 (Sept. 1993), pp. 778–784. ISSN: 0003-0805. DOI: 10.1164/ajrccm/148.3.778 (cit. on p. 30).
- [119] C. Mondino et al. “Effects of inhaled corticosteroids on exhaled leukotrienes and prostanoids in asthmatic children”. In: *Journal of Allergy and Clinical Immunology* 114.4 (Oct. 2004), pp. 761–767. ISSN: 00916749. DOI: 10.1016/j.jaci.2004.06.054 (cit. on p. 30).
- [120] R. S. PAPINENI and F. S. ROSENTHAL. “The Size Distribution of Droplets in the Exhaled Breath of Healthy Human Subjects”. In: *Journal of Aerosol Medicine* 10.2 (Jan. 1997), pp. 105–116. ISSN: 0894-2684. DOI: 10.1089/jam.1997.10.105 (cit. on p. 30).
- [121] M. A. Stiegel et al. “Analysis of inflammatory cytokines in human blood, breath condensate, and urine using a multiplex immunoassay platform”. In: *Biomarkers* 20.1 (Jan. 2015), pp. 35–46. ISSN: 1354-750X. DOI: 10.3109/1354750X.2014.988646 (cit. on p. 31).
- [122] O. A. Carpaij et al. “Assessing small airways dysfunction in asthma, asthma remission and healthy controls using particles in exhaled air”. In: *ERJ Open Research* 5.4 (Oct. 2019), pp. 00202–2019. ISSN: 2312-0541. DOI: 10.1183/23120541.00202-2019 (cit. on p. 31).

2.2 Absorption spectroscopy (AS)

When it comes to any kind of optical spectroscopy, interaction between light and matter has to be considered. Possible physical observations include scattering, reflection, transmission or absorption of the light. Regarding trace gas detection and quantification three types of interactions have to be addressed. These are inelastic scattering processes, where the energy of a light quantum (photon) is transferred onto a molecule, like Raman* scattering [1] as well as absorption processes [2] (e.g. infrared (IR) spectroscopy, UV/VIS spectroscopy) and fluorescence processes [3]. A figure of merit that makes sense in order to compare the applicability of these three basic processes in terms of gaseous analyte quantification, is the available cross section. Cross sections specify the probability of a certain process to occur after interaction of a photon with another particle. Absorption cross sections are significantly stronger than Raman scattering or laser induced fluorescence cross sections [4, 5]. Therefore, absorption spectroscopy can be considered superior in terms of trace gas analysis. Both other techniques obviously have their *raison d'être* but will not be further discussed within this work.

The following sections will provide the physical fundamentals of molecular absorption and excitation. The position, shape and intensity of absorption bands will be addressed as well as the different types of relaxation processes. Furthermore, the various absorption spectroscopy techniques and their advantages and drawbacks will be discussed. Since this work copes only with the detection of gaseous analytes, effects present in liquid and solid spectroscopy will not be discussed.

2.2.1 Absorption spectra

The energy of a photon is given by

$$E_{\text{ph}} = h \cdot \nu_{\text{ph}} \quad (2.2)$$

with h being Planck's[†] quantum of action and ν_{ph} being the frequency of a photon. The relation between the frequency of a photon ν_{ph} , its wavelength λ_{ph} and its wavenumber $\tilde{\nu}_{\text{ph}}$ is

$$\nu_{\text{ph}} = \tilde{\nu}_{\text{ph}} c_0 = \frac{c_0}{\lambda_{\text{ph}}} \quad (2.3)$$

with c_0 being the speed of light in vacuum. When the energy of the photon is equal to the energy difference of two different energy states of a molecule, a certain probability exists that the energy of the photon is transferred onto the molecule promoting it to the higher energy state. Electronic, vibrational and rotational transitions or a combination of these can occur. For example, exciting a molecule's ro-vibronic state refers to electronic, vibrational and rotational energy state interaction, whereas a ro-vibrational state describes rotational and vibrational degrees of freedom interacting

*Sir Chandrasekhara Venkata Raman (1888 – 1970)

[†]Max Karl Ernst Ludwig Planck (1858 – 1947)

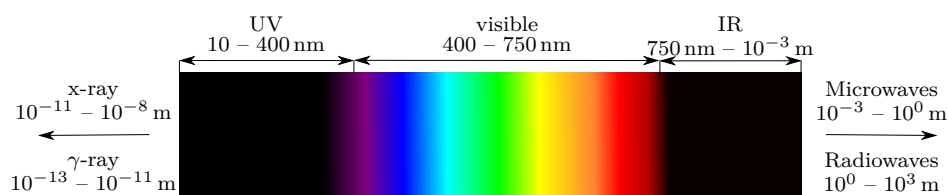


Fig. 2.6. Wavelength regions of electromagnetic waves important in molecular and atomic spectroscopy.

with each other. The necessary energy for transition from a ground state to the first excited state can be described as follows

$$E_{01} = E_{\text{ph}} \quad (2.4)$$

The advantage of using the wavenumber is the fact, that it is an energy quantity. Since $\nu_{\text{ph}} = \tilde{\nu}_{\text{ph}}c_0$ and with $\tilde{\nu}_1$ and $\tilde{\nu}_0$ being the wavenumber of the first excited and the ground state, respectively, the energy gap can be expressed as

$$\tilde{\nu}_{\text{ph}} = \tilde{\nu}_{01} = \tilde{\nu}_1 - \tilde{\nu}_0 \quad (2.5)$$

Therefore, equation 2.4 can now be rewritten to

$$E_{01} = hc_0(\tilde{\nu}_1 - \tilde{\nu}_0) \quad (2.6)$$

In general, the conversion factor from the wavenumber $[\tilde{\nu}] = \text{cm}^{-1}$ into energy $[E] = \text{J}$ is given by

$$E = hc_0\tilde{\nu} \quad (2.7)$$

with $[hc_0] = 1.986\,445\,44 \times 10^{-25} \text{ kg m}^3 \text{ s}^{-2}$. Although the wavenumber in units of cm^{-1} is frequently used in IR spectroscopy [6, p. 40], the wavelength in units of nm is usually employed in UV/VIS spectroscopy. In figure 2.6 the classification of wavelength regions of light is visualised covering the regions of interest for molecular and atomic spectroscopy.

The UV region can be divided into UVC reaching from 10 – 280 nm, UVB 280 – 320 nm and UVA covering 320 – 400 nm [6]. In atmospheric chemistry, UVC photons, having the highest energy in the UV region, are completely absorbed by ozone, whereas UVA and UVB partially penetrate the atmosphere and reach the earth's surface [7]. The infrared region can be subdivided as well. According to the ISO 20473:2007 [8] the near-IR includes the wavelengths from 0.78 – 3 μm ($= 12\,820.5 - 3333.3 \text{ cm}^{-1}$), the mid-IR reaches from 3 – 50 μm ($= 3333.3 - 200 \text{ cm}^{-1}$) and the far-IR from 50 – 1000 μm ($= 200 - 10 \text{ cm}^{-1}$).

2.2.1.1 Rotational spectra

In infrared spectroscopy only ro-vibrational states and no electronic states are excited. In microwave spectroscopy, however, solely rotational excitation is exploited

for chemical analysis, e.g. determination of binding lengths [9, pp. 478]. The energy differences for rotational states are not equidistant and the energy increment between two rotational states is usually expressed with the rotation constant \tilde{B} [9, p. 475] being

$$\tilde{B} = \frac{h}{8\pi^2 c_0 I} \quad (2.8)$$

with the moment of inertia I . In classical physics, the energy of a simple linear rotor like CO₂ rotating around the x-axis is presented by

$$E = \frac{1}{2} I_x \omega^2 \quad (2.9)$$

with ω being the angular frequency in rad s⁻¹. If the body is rotating freely in three dimensional space*, then the energy is given by

$$E = \frac{J_x^2}{2I_x} + \frac{J_y^2}{2I_y} + \frac{J_z^2}{2I_z} \quad \text{with} \quad J = I\omega \quad (2.10)$$

with J_x , J_y and J_z representing the angular momentum around the axes x, y and z, respectively. Beside linear tops, there are also spherical tops, symmetric tops and asymmetric tops [9, p. 480]. Methane for example can be considered a spherical top where all moments of inertia have the same value and thus equation 2.10 can be simplified to

$$E = \frac{J_x^2 + J_y^2 + J_z^2}{2I} = \frac{\mathcal{J}^2}{2I} \quad (2.11)$$

whereby $\mathcal{J}^2 = J_x^2 + J_y^2 + J_z^2$ is the total angular momentum. Substituting $\mathcal{J}^2 \rightarrow j(j+1)\frac{h^2}{4\pi^2}$ with $j = 0, 1, 2, \dots$ being the total angular momentum quantum number leads to the discrete rotational energy levels of a spherical top [9, p. 475]

$$E_j = j(j+1) \frac{h^2}{8\pi^2 I} \quad \text{with} \quad j = 0, 1, 2, \dots \quad (2.12)$$

Applying 2.8, the energy can finally be rewritten to

$$E_j = j(j+1) \tilde{B} h c_0 \quad \text{with} \quad j = 0, 1, 2, \dots \quad (2.13)$$

To express the energy in wavenumbers, 2.13 has to be divided by $h c_0$ providing the term of rotation $\tilde{F}(j)$:

$$\tilde{F}(j) = j(j+1) \tilde{B} \quad \text{with} \quad j = 0, 1, 2, \dots \quad (2.14)$$

Equation 2.13 demonstrates, that the energy gap between two rotational states increases towards higher j . An energy diagram visualising the energy gaps between the rotational states is provided in figure 2.7. Although the solution of the rotational energy states provides discrete energy levels, there is always a finite broadness present. The reason for that are different broadening effects, which will be discussed in section 2.2.4.

*This is actually only the case in the gas phase.

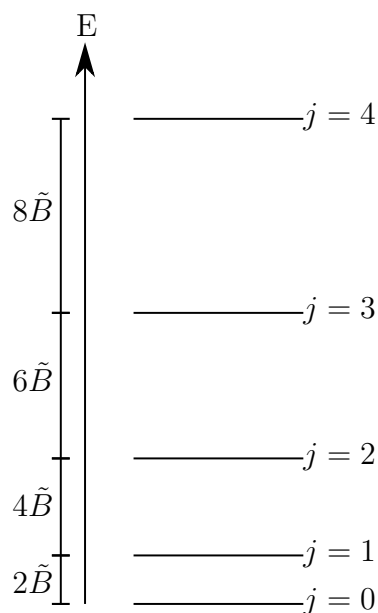


Fig. 2.7. Energy diagram of the different rotational energy levels.

For a molecule to possess a pure rotation spectrum it has to be a polar molecule exhibiting a permanent dipole moment. Besides, the selection rule $\Delta j = \pm 1$ is valid for all types of tops. This means that during absorption ($\Delta j = +1$) the rotational energy level can only be excited to the next higher level. The same applies for deexcitation ($\Delta j = -1$).

The intensity of an absorption line represents the probability of an absorption process once a photon interacts with a molecule. The probability increases with a high population density of the initial state participating in the absorption process, e.g. the rotational ground state $j = 0$. In order to calculate the occupation ratio between two states the Boltzmann* distribution can be applied [6, p. 9]

$$\frac{\rho_{j+1}}{\rho_j} = \exp\left(-\frac{\Delta\tilde{F}(j)}{kT}\right) \quad (2.15)$$

where ρ_{j+1} and ρ_j are the population densities of the first excited state and the ground state, respectively, k is the Boltzmann constant $= 1.380\,649 \times 10^{-23} \text{ J K}^{-1}$ and T is the temperature in Kelvin. At room temperature, $kT \approx 200 \text{ cm}^{-1}$ and with a rotational energy $\Delta\tilde{F}_{01} \approx 50 \text{ cm}^{-1}$ [6, p. 9], the distribution is calculated to

$$\frac{\rho_{j+1}}{\rho_j} = \exp\left(-\frac{50}{200}\right) = 0.78 \quad (2.16)$$

demonstrating the higher population density of the lower state. Using equation 2.15 the intensity distribution of the rotational spectrum (wings) of figure 2.9 can be explained, though the degeneration[†] of the states has been neglected.

*Ludwig Boltzmann (1844 – 1906)

[†]Two different states have the same energy.

For more information regarding degeneration of rotational energy levels and a more detailed discussion on selection rules and rotational energy levels for different types of tops, the interested reader may refer to [9, pp. 471].

2.2.1.2 Vibrational spectra

In order to understand the vibrational behavior of molecules, the connections of the atoms within a molecule can be regarded as springs. Considering the potential curve $V(x)$ of a diatomic molecule as a harmonic oscillator

$$V(x) = \frac{1}{2}k_v x_r^2 \quad (2.17)$$

with k_v being the spring force constant and x_r being the displacement of the atoms' bond lengths at equilibrium, the vibrational energy levels are given by

$$E_v = \left(v + \frac{1}{2}\right) \frac{h}{2\pi} \omega \quad \text{with} \quad \omega = \left(\frac{k_v}{m_{\text{eff}}}\right)^{\frac{1}{2}} \quad \text{and} \quad v = 0, 1, 2, \dots \quad (2.18)$$

with m_{eff} being the effective mass of the molecule and v being the vibrational quantum number. In order to express the vibrational energy levels of a molecule in wavenumbers, the equation 2.18 can be rewritten to

$$\tilde{G}(v) = \left(v + \frac{1}{2}\right) \tilde{\nu} \quad \text{with} \quad \tilde{\nu} = \frac{1}{2\pi c_0} \left(\frac{k_v}{m_{\text{eff}}}\right)^{\frac{1}{2}} \quad \text{and} \quad v = 0, 1, 2, \dots \quad (2.19)$$

However, these equations are based on a pure parabolic approximation of the potential. Since this would disallow a dissociation of a molecule, this approximation is not valid anymore at higher energy states. At these energy states the movements of the molecule are then considered anharmonic. This means, that at large distances between the nuclei the restoring force is not proportional to its displacement from the resting position anymore. The potential curve opens faster than in a parabolic shaped curve causing the energy gap between two consecutive vibrational states to get smaller. The Morse* potential [10] accounts for this anharmonicity [9, p. 488] having the form

$$V(x) = hc_0 \tilde{D}_e \left[1 - e^{-a_M x_r}\right]^2 \quad \text{with} \quad a_M = \left(\frac{m_{\text{eff}} \omega^2}{2hc_0 \tilde{D}_e}\right)^{\frac{1}{2}} \quad (2.20)$$

with a_M being a displacement factor and \tilde{D}_e being the depth of the potential well. Figure 2.8 visualises the discrete distribution of the vibrational energy states, the shape of the Morse potential and the dissociation energy of the molecule as well as the depth of the potential well. Applying the Morse potential, equation 2.19 becomes

$$\tilde{G}(v) = \left(v + \frac{1}{2}\right) \tilde{\nu} - \left(v + \frac{1}{2}\right)^2 \tilde{\nu} x_e \quad \text{with} \quad v = 0, 1, 2, \dots \quad (2.21)$$

*Philip McCord Morse (1903 – 1985)

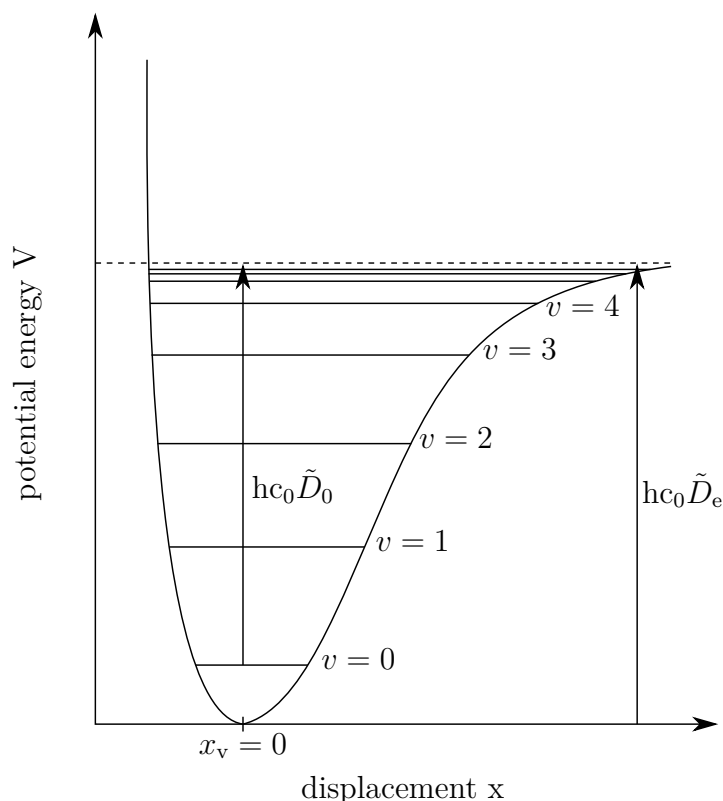


Fig. 2.8. Morse potential (refer to 2.20) visualising the anharmonicity of molecular vibrations at higher energies after [9, p. 488]. The dashed line displays the energy necessary for molecular dissociation, $hc_0\tilde{D}_0$ is the dissociation energy and $hc_0\tilde{D}_e$ is the depth of the potential well.

with x_e being the anharmonic constant

$$x_e = \frac{a^2\hbar}{4\pi m_{\text{eff}}\omega} = \frac{\tilde{\nu}}{4\tilde{D}_e} \quad (2.22)$$

Figure 2.9 presents a measured spectrum of the triatomic molecule CO_2 . The general selection rule for vibrational energy transitions demands a change of the molecule's dipole moment during vibration* and in addition, the selection rule $\Delta v \pm 1$ applies. Besides, during a transition, the angular momentum quantum number j has to change by ± 1 . The spectrum of CO_2 shows three energy regions of interest also called branches. The P-branch represents all transitions with $\Delta j = -1$ and the R-branch describes the transitions with the selection rule $\Delta j = +1$. In both cases, the absolute value of the energetic increment of the peaks within the R- or P-branch is $2\tilde{B}$. This is also visualised in the small energy states diagram of figure 2.9. The Q-branch consists of all transitions with $\Delta j = 0$, which is an actually forbidden transition. Thus, not every vibrational spectrum features a Q-branch. However, the selection rules for the Q-branch will be discussed later. Since these transitions are energetically close to each other, the spectrum displays a broader peak with high

*Otherwise the transition is only Raman active but not IR active.

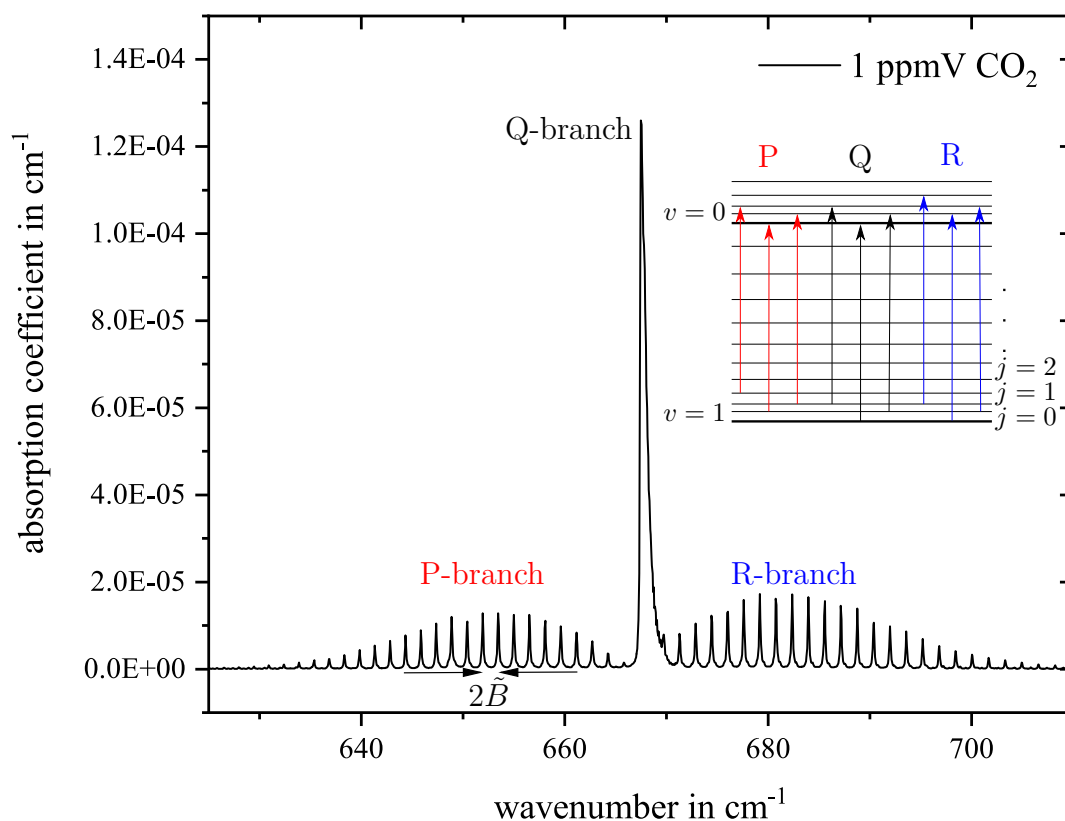


Fig. 2.9. Measured 1 ppmV CO₂ IR spectrum from the Pacific Northwest National Library (PNNL)[11] and the differences between R, P and Q-branch. v are vibrational energy levels and j are rotational energy states. The ordinate is specified in base-e.

intensity. A Q-branch is also an example, where the transition is pure vibrational and not ro-vibrational [9, pp. 490].

Figure 2.9 shows some ro-vibrational transitions of CO₂. The absorption coefficient has been converted into base-e format, since the PNNL (Pacific Northwest National Laboratory) database only provides spectra in base-10 format. The difference will be addressed in section 2.2.2 and 3.1. However, compared to a biatomic molecule, molecules consisting of more atoms, obviously might get excited to different types of vibrations. For non-linear molecules consisting of N_{Atoms} atoms the amount of possible degrees of vibrational freedom is $3N_{\text{Atoms}} - 6$ and for linear molecules there are $3N_{\text{Atoms}} - 5$ possibilities [9, p. 493].

The vibrations can be categorised into [6, pp. 47]

- stretching vibrations, which change the bond lengths within the molecule and
- deformation vibrations, which alter mainly the bond angles.

Besides, vibrations are classified regarding their symmetry into

- symmetrical vibrations, which preserve the symmetry of a group or the molecule,
- anti symmetrical vibrations, which do not preserve symmetry and
- twice or multiple degenerated vibrations, which distort the molecule keeping the symmetry and express identical frequencies.

Symmetrical and anti symmetrical stretching vibrations are labeled ν_s and ν_{as} , whereas symmetrical and anti symmetrical deformation vibrations are labeled with δ_s and δ_{as} , respectively [6, p. 48]. Note that literature often denotes vibration types simply with ν_n , where $n = 1, 2, 3, \dots$

In case of acetone, which consists of 10 atoms, it becomes clear that there are several vibrational degrees of freedom, namely 24. However, on the one hand, due to selection rules like the change of a dipole moment during vibration, not all of them are infrared active. On the other hand, additional absorption bands might occur due to overtones (harmonics of a fundamental vibration) or combination tones and differential tones. Nevertheless, since the coupling of molecular groups, e.g. methyl-group or carbonyl-group in acetone, with the rest of the molecule is often quite weak, those groups exhibit unique spectral features allowing an interpretation of the IR spectrum [6, p. 48].

Figure 2.10 shows an IR spectrum of acetone, which has been measured by the PNNL. The absorption cross section has been converted into base-e format. In the higher energy region at around 3000 cm^{-1} the absorption features result from stretching vibrations usually containing an H-atom. Deformation vibrations are present in the lower energy region. Peaks or similar features occurring below 1500 cm^{-1} are usually called "fingerprint" regions and are unique for every molecule but often quite chaotic and the assignment of peaks to certain vibrations is quite difficult. Some of these mechanisms, which can lead to misinterpretation are discussed briefly hereinafter [6, p. 48].

- **Coupling** can occur between two spatially adjacent groups. The coupling is amplified when the vibrational frequencies of the involved groups are similar. The higher participating frequencies are then blue-shifted and the lower involved frequencies are red-shifted.
- **Overtones** occur if $\Delta v = +2$ or even higher. There is one overtone present in figure 2.10 at around 3400 cm^{-1} . The intensity is quite weak, because the selection rule $\Delta v = \pm 1$ applies. Due to the overstretching of the molecule the overtones' wavenumbers are always slightly below the multiple of the fundamental vibration.
- **Fermi resonance** appears i.a. by coupling of a fundamental vibration with an overtone. The energies of the coupling vibrations are very close to each other. This can cause a stronger intensity and shift of the wavenumber of both participating vibrations and hence, can lead to misinterpretation.

- **Combination bands and difference bands** occur if for example an absorbed photon excites two different vibrations at once (combination band) or an already excited vibration is transformed to a higher energy level (difference band). Hence, the wavenumber of a combination band is the sum of both fundamental vibration wavenumbers and the difference band's wavenumber is at the difference between the two involved states.

Comparing the spectra from figure 2.9 and figure 2.10 it can be seen, that the acetone bands, especially the R- and P-branches are broad and do not show a fine structure. The reason for that are the great number of rotational and vibrational transitions, which are energetically very close to each other and overlap due to line broadening. The effect of line broadening will be addressed in section 2.2.4.

Before moving to the description of electronic transitions, the intensity of vibrational transitions and the existence of Q-branches must be addressed in more detail. Starting with the latter, the condition of $\Delta j = \pm 1$ has already been mentioned causing the R- and P-branch structures. Although the Q-branch is actually forbidden, there are a few exceptions. E.g. the paramagnetic molecule NO has a Q-branch due to its electronic orbital angular momentum [12, p. 512]. The deformation vibration

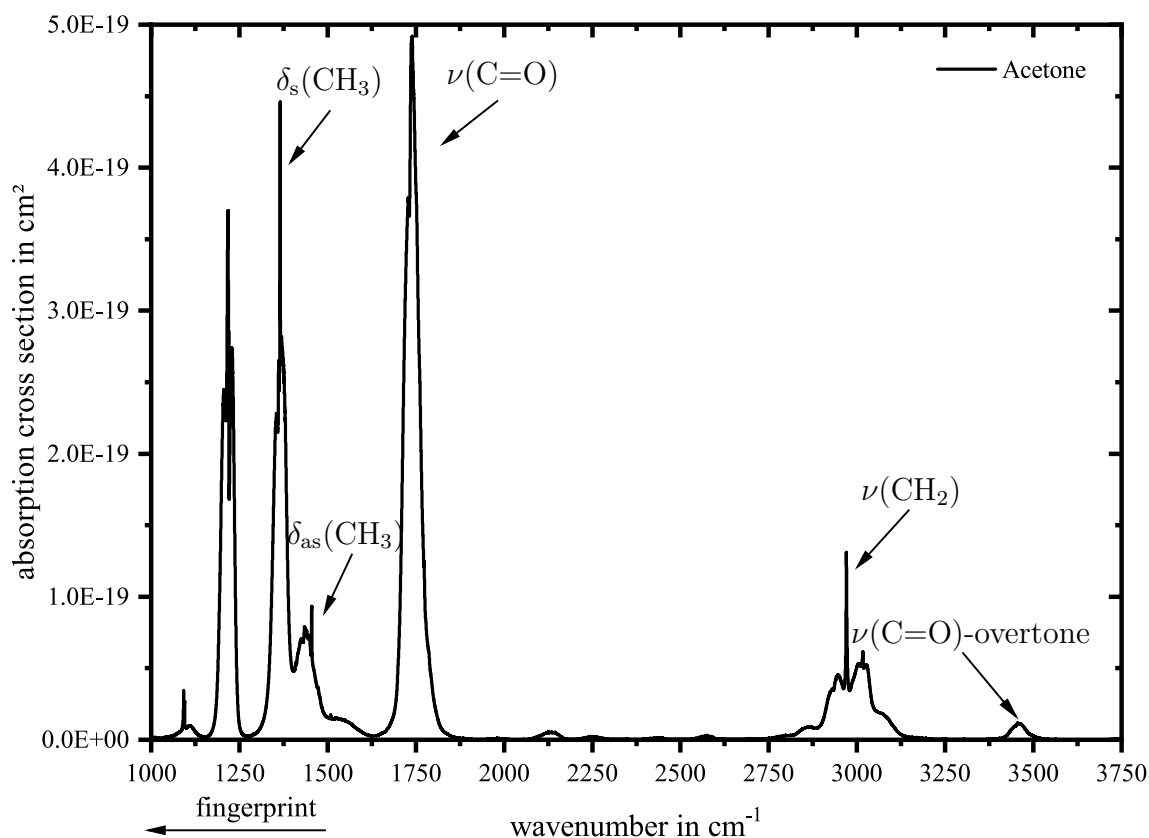


Fig. 2.10. Measured acetone IR spectrum from the Pacific Northwest National Library (PNNL)[11] normalised to 1 ppmV including the assignment of different vibration bands [6, p. 49]. The ordinate is specified in base-e.

of CO₂ in figure 2.9 also shows a Q-branch, because the linearity of the molecule is suspended during the vibration. The dipole moment is altered perpendicular to the molecular axis. The resulting absorption band is also called *perpendicular band*. The anti symmetric stretching vibration of the linear molecule CO₂ alters the dipole moment parallel to the molecular axis and is thus called *parallel band*. However, since the *parallel band* transition at around 2350 cm⁻¹ does not suspend the linearity of the molecule it does not have a Q-branch transition. Besides, the symmetric stretching vibration at 1390 cm⁻¹ does not change the dipole moment, and hence, is not IR active but Raman active [12, p. 517].

Regarding the intensity of a peak, which represents the probability of a transition, the population density of the initial state has to be considered. To calculate the population density of the vibrational states equation 2.15 can be written as

$$\frac{\rho_{v+1}}{\rho_v} = \exp\left(-\frac{\Delta\tilde{G}(v)}{kT}\right) \quad (2.23)$$

With a typical vibrational energy of $\tilde{G}(v) \approx 1000 \text{ cm}^{-1}$, the distribution of the vibrational state population density is about 0.0067 at room temperature [6, p. 9]. Therefore, only 0.7 % of the energetically higher state is occupied. Hence, the transition from $v = 0$ to $v = 1$ is the main contributor to the Q-branch intensity. Another reason for a low intensity of an absorption line is the selection rule $\Delta v = \pm 1$, which is the reason for the low probability of overtones. Only due to the anharmonicity of the potential curve, these transitions are partially permitted [12, p. 511].

2.2.1.3 Electronic transitions

Contrary to liquid analysis, gaseous UV/VIS spectra can show a fine structure including rotational and vibrational transitions [12, p. 539]. However, the energy gap between two electronic states of a molecule is much larger compared to the one between vibrational or rotational states [6, p. 7].

$$E_S > E_v > E_j \quad (2.24)$$

Therefore, excitation of electronic states, e.g. from the singlet states S_0 to S_1 , usually occur when UV or visible light is absorbed by a molecule. The total energy necessary for a ro-vibronic excitation from S_0 to S_1 is the sum of all promoted types of states. Note that in this section, both, the *enumerative* description of the electronic energy states (e.g. S_n and T_n) and the description after *Kasha** [13] (σ_S , π_S and n_S) will be used. The index S within the Kasha description is unusual, but serves the clarity of the script.

Figure 2.11 shows a Jabonski[†] [14] diagram illustrating the different types of excitation and relaxation including radiative emission processes, which mostly occur in

*Michael Kasha (1920 – 2013)

†Aleksander Jabłoński (1898 – 1980)

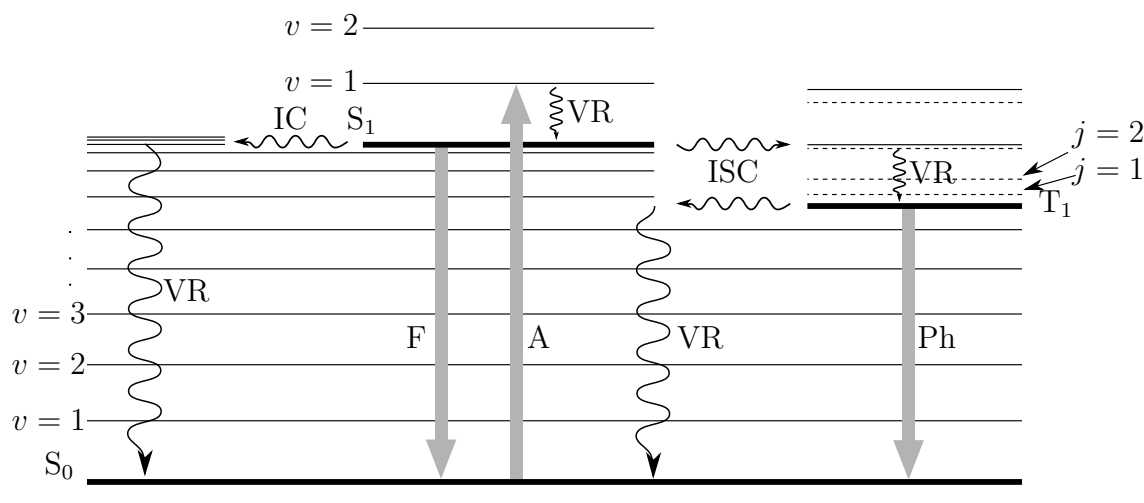


Fig. 2.11. Jablonsky diagram [14] visualising the different energy states and quantum processes within a molecule after [6, pp. 9]. **nonradiative** processes: **IC** - internal conversion, **ISC** - intersystem crossing, **VR** - vibrational relaxation; **radiative** processes: **A** - absorption, **F** - fluorescence, **Ph** - phosphorescence.

the UV and visible region. Beside the displayed unimolecular processes bimolecular processes like quenching or Charge-Transfer-Processes [6, pp. 4] can occur, too, but go beyond the scope of this work and will therefore not be discussed.

The diagram visualises*, that the electronic ground state can have different vibrational ($v = 0, v = 1, v = 2, \dots$) and rotational states ($j = 0, j = 1, j = 2, \dots$). Those energy levels are superimposed on triplet or doublet states, too. An atom or a molecule is in a singlet state when its multiplicity M , given by $M = 2S + 1$ equals 1. With S being the total spin quantum number, which should not be mixed up with the electronic states like S_0 . For a molecule, S is the sum of all electron spins [9, p. 516]. A doublet state has one unpaired electron and the triplet state has two unpaired electrons, hence, S is $\frac{1}{2}$ and 1, respectively. Therefore, the multiplicity of the doublet state is 2 and for the triplet state 3.

Like in rotational and vibrational transitions, there are also selection rules in electronic transitions. They can lead to so called forbidden transition. The Pauli exclusion principle [15] states, that multiplicity must not change during the transition, no matter if the transition refers to an absorption or emission. An example for a changing multiplicity during relaxation is phosphorescence. The fact that this transition is forbidden explains the long lifetime of the excited molecules trapped on the T_1 surface compared to fluorescence. Besides, there is the rule of Laporte [16] stating, that electronic transitions are only allowed between orbitals of different parity. This rule only applies to centrosymmetric molecules like benzene. Moreover, there is the so called overlap prohibition. This is valid for electronic transitions where the participating orbitals do not or only slightly overlap. An intramolecular example is

*To avoid an unclear illustration, the vibrational and rotational ground states on the different excited electronic states have been omitted.

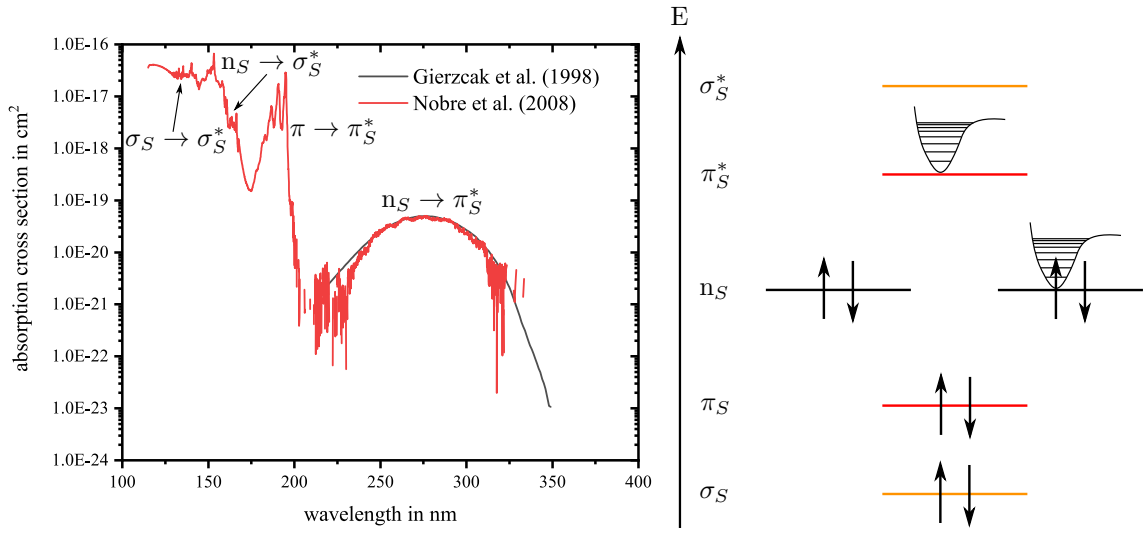


Fig. 2.12. Illustration of the carbonyl-group's molecule orbitals including the Morse potential displaying the vibrational energy states after [17] (right) and the absorption spectra of acetone in the UV region measured by Gierczak et al. [18] and Nobre et al. [19] (left). The $n_S \rightarrow \sigma_S^*$ transition assignment to 166 nm is proposed by Barnes and Simpson [20].

the $n_S \rightarrow \pi_S^*$ transition of a carbonyl-group. Note that these forbidden transitions often still occur, though their intensity is significantly lower compared to permitted transitions [6, pp. 3]. The right side of figure 2.12 visualises the different molecule orbitals of a carbonyl-group and their electronic ground state population. The left side shows the UV spectrum of acetone, resulting from the different ro-vibronic transitions. As mentioned before, when a forbidden $n_S \rightarrow \pi_S^*$ transition occurs, one of the electrons from the unbound orbital n_S is excited into the π_S^* orbital. Besides, vibrational and rotational transitions occur as well. The spectra demonstrates, that the probability of this forbidden transition is some orders of magnitude lower than that one of the allowed transitions $\sigma_S \rightarrow \sigma_S^*$ and $\pi_S \rightarrow \pi_S^*$. Note that the $\sigma_S \rightarrow \sigma_S^*$ transition actually originates from the C-H bond. A group like the carbonyl group or a certain bond are also called chromophor, since they have specific transition energies, which can also be in the visible region and are causing the molecule's characteristic color. A list of such chromophors can be found in table 3.6.

Besides the different transition regions, figure 2.12 also visualises the lack of a fine structure for the $n_S \rightarrow \pi_S^*$ transition. Again, this is due to the overlap of the rotational and vibrational transition lines. Regarding the population density of the different states S_0 and S_1 , the Boltzmann-distribution can be applied.

$$\frac{\rho_{S+1}}{\rho_S} = \exp\left(-\frac{\Delta E_S}{kT}\right) \quad (2.25)$$

At room temperature $kT \approx 200 \text{ cm}^{-1}$ and choosing the $n_S \rightarrow \pi_S^*$ at 35.971 cm^{-1} , which equals 278 nm, the population ratio of $\frac{\rho_{S+1}}{\rho_S} \approx 0$. Hence, S_1 or higher electronic states can be considered completely depleted at room temperature.

The excitation of a molecular state is of finite lifetime before it relaxes back to the ground state again. As indicated in figure 2.11 different processes can occur, which are separated into radiative and nonradiative relaxation processes. Fluorescence and phosphorescence are both radiative processes. Fluorescence usually decays quite fast after excitation, meaning its lifetime is very short compared to phosphorescence [12, p. 551]. During fluorescence the energy state of an electron decays towards a lower energy level (e.g. from S_1 to S_0) by releasing the energy in form of a photon. The energy of the photon released, however, is usually lower than the energy of the absorbed photon. This phenomenon is called red-shift. The reason for this shift are vibrational and rotational relaxations to their corresponding ground states $v = 0$ or $j = 0$ on a higher electronic state like S_1 . During this nonradiative relaxation, the energy of the molecule is transferred to its environment by means of collisions with surrounding molecules [12, pp. 551].

Phosphorescence relaxation rates are relatively small compared to fluorescence since the electron lifetime on T_1 is high. The first steps to the S_1 ground state are the same as in the fluorescence process. For the molecule to transit to a triplet state an intersystem crossing (ISC) step has to be performed. A high spin-orbital coupling is necessary to cause decoupling of the initial electron spin leading to an ISC transition. The reason for the long retention time is the radiative relaxation origin on the triplet state T_1 . As discussed before, the multiplicity must not change between an absorption or emission process, hence, this transition is forbidden, lowering the transition's probability. Like in fluorescence, a red-shift occurs for phosphorescent emission, due to the mentioned intermediate nonradiative vibrational and rotational relaxation processes [12, pp. 551].

Another nonradiative process is the internal conversion (IC). Compared to ISC, the molecule's multiplicity stays the same. During an IC the molecule transits from a higher electronically state like S_1 with $v = 0$ to S_0 by exciting vibrational states. Such a conversion can also lead to dissociation of a molecule, if the vibrational energy of the lower S state exceeds the dissociation limit from figure 2.8. This process is called *pre-dissociation* and usually occurs close to the intersection of two potential wells of different electronic states. A direct photon induced dissociation without IC is called photolysis. During dissociation, the atomic bond within a molecule breaks leading to radical fragments having an unquantised translational movement. In a spectrum, the dissociation limit is indicated by a sudden end of the fine structure of the vibrational absorption lines transiting into a continuum [12, pp. 551].

Further discussions regarding nonradiative relaxation processes and their influence on the photoacoustic signal will be discussed in section 2.3. A comprehensive table including further important photo physical processes are provided in [9, p. 867].

2.2.2 Lambert-Beer

In terms of quantitative spectroscopy in the IR or UV/VIS region, classic absorption spectroscopy relies on the quantities transmittance $\tilde{T}(\tilde{\nu})$ and absorbance $\tilde{A}(\tilde{\nu})$ of a

sample at a certain wavenumber. The relation between absorbance and transmittance is give by

$$\tilde{T}(\tilde{\nu}) = \frac{I_1(\tilde{\nu})}{I_0(\tilde{\nu})} \quad \text{and} \quad \tilde{A}(\tilde{\nu}) = -\ln \tilde{T}(\tilde{\nu}) \quad (2.26)$$

with $I_1(\tilde{\nu})$ and $I_0(\tilde{\nu})$ being the transmitted and the incident light intensity, respectively. Rewriting equation 2.26 constitutes the well-known equation from Lambert* [2] and Beer† [21]

$$I_1(\tilde{\nu}) = I_0(\tilde{\nu})e^{-\tilde{A}(\tilde{\nu})} \quad (2.27)$$

The absorbance can be replaced by

$$\tilde{A}(\tilde{\nu}) = \varepsilon(\tilde{\nu})c_i l_{\text{opt}} \quad (2.28)$$

where $\varepsilon(\tilde{\nu})$ is the molar extinction coefficient, c_i is the concentration of the analyte and l_{opt} the thickness of the illuminated sample, often also referred to as optical path-length. This form of the Lambert-Beer equation is usually applied in spectroscopy with liquid samples. $\varepsilon(\tilde{\nu})$ ranges from $\approx 10 \frac{\text{L}}{\text{mol cm}}$ for forbidden transitions up to $\approx 100\,000 \frac{\text{L}}{\text{mol cm}}$ for extremely probable transitions.

For gaseous samples, the absorption coefficient $\alpha(\tilde{\nu})$ is used instead, replacing the term $\varepsilon(\tilde{\nu})c_i$. Hence, equation 2.27 can be rewritten to

$$I_1(\tilde{\nu}) = I_0(\tilde{\nu})e^{-\alpha(\tilde{\nu})l_{\text{opt}}} \quad (2.29)$$

Besides, the absorbance can be expressed in Naperian (base-e) or logarithmic base (base-10). If logarithmic base is used, equation 2.29 is changed to

$$I_1(\tilde{\nu}) = I_0(\tilde{\nu})10^{-\alpha(\tilde{\nu})l_{\text{opt}}} \quad (2.30)$$

This has to be kept in mind when comparing spectra from different databases or different papers (refer to section 3.1). Furthermore, the absorption coefficient is the product of the absorption cross section $\sigma_A(\tilde{\nu})$ and the particle density ρ .

$$\alpha(\tilde{\nu}) = \sigma_A(\tilde{\nu})\rho_i \quad \text{with} \quad \rho_i = N_i \frac{N_A}{V_m} \quad (2.31)$$

where N_i is the volume ratio of the analyte i in the sample, ρ_i the particle density of the analyte, N_A is the Avogadro constant and V_m is the molar volume. The ACS $\sigma_A(\tilde{\nu})$ is a measure for the probability of a transition at $\tilde{\nu}$ for a single molecule and has the unit cm^2 . The analyte's volume ratio can now be derived by combining equation 2.29 and 2.31.

$$N_i = -\frac{V_m}{\sigma_A(\tilde{\nu})l_{\text{opt}}N_A} \ln \frac{I_1(\tilde{\nu})}{I_0(\tilde{\nu})} \quad (2.32)$$

*Johann Heinrich Lambert (1728 – 1777)

†August Beer (1825 – 1863)

2.2.3 Line intensity

In previous sections the intensity of an absorption line has been discussed qualitatively. This section addresses the quantitative intensity of an absorption line, i.e. the line strength s . In general, the intensity of an absorption line is characterised by its ACS. The line strength is linked to $\sigma_A(\tilde{\nu})$ by

$$\sigma_A(\tilde{\nu}) = s \cdot f_{LS}(\tilde{\nu}) \quad (2.33)$$

where f_{LS} is a normalised function representing the line shape. The shape will be discussed in the next subsection. The line strength s_{01}^* of a transition, e.g. ground and first excited state, is determined by considering the different population densities of the two participating states ρ_0 and ρ_1 , with the energy levels E_0 and E_1 as well as the Einstein[†] coefficient for absorption B_{01} , providing the probability of the transition:

$$s_{01} = \frac{h\tilde{\nu}_{01}}{\rho c_0} B_{01}(\rho_0 - \rho_1) \quad (2.34)$$

The Einstein coefficient B_{01} and thus the transition probability is proportional to the square of the transition dipole moment μ . The coefficient is given by [12, pp. 468]

$$B_{01} = \frac{2\pi^2}{3\varepsilon_0 h^2} |\mu|^2 \quad (2.35)$$

where ε_0 is the vacuum permittivity constant. The difference between the two states' population density can be calculated after

$$\rho_0 - \rho_1 = \rho_0 \left[1 - \exp\left(-\frac{hc_0\tilde{\nu}_{01}}{kT}\right) \right] \quad (2.36)$$

The population density of the lower state is given by

$$\rho_0 = \rho \frac{\tilde{g}_m}{Q_{\text{int}}} \exp\left(-\frac{E_m}{kT}\right) \quad (2.37)$$

with \tilde{g}_m being the degree of degeneracy of the lower state and Q_{int} being the total internal partition function, i.e. the sum of all internal energy states weighted by their degeneracy, which is defined as:

$$Q_{\text{int}} = \sum_m \tilde{g}_m \exp\left(-\frac{E_m}{kT}\right) \quad (2.38)$$

The equations 2.36 and 2.37 can be merged into equation 2.34 leading to

$$s_{01} = \frac{h\tilde{g}_m\tilde{\nu}_{01}}{c_0 Q_{\text{int}}} B_{01} \exp\left(-\frac{E_m}{kT}\right) \left[1 - \exp\left(-\frac{hc_0\tilde{\nu}_{01}}{kT}\right) \right] \quad (2.39)$$

*For the following paragraphs, the example of a transition from the ground state 0 to first excited state 1 or the other way round, will be considered in the calculations.

[†]Albert Einstein (1879 – 1955)

Equation 2.39 demonstrates that the intensity of an absorption line depends on the temperature. The next chapter will show, that absorption bands are also quite sensitive to pressure. The HITRAN (High-resolution TRANsmision molecular absorption database) database provides simulated and empirical line strengths for different temperatures [22]. Databases will be discussed later in more detail in section 3.1.

2.2.4 Line shape

In the previous sections, several terms have been derived to determine the discrete energy levels of certain states and the corresponding transition intensity. However, in real applications, these calculated energies only represent the position of an absorption line in a spectrum but provide no information regarding the finite width and shape every line possesses. The shape of the line is described by the already introduced normalised function $f_{LS}(\tilde{\nu})$.

$$1 = \int_0^{\infty} f_{LS} \cdot d\tilde{\nu} \quad (2.40)$$

Several factors influence the broadness of spectral lines depending on the type of broadening effect. There are mainly three different effects, namely Doppler broadening, natural broadening and collisional broadening, which will be discussed in the following paragraphs.

2.2.4.1 Doppler broadening

The Doppler effect in spectroscopy is similar to the acoustic Doppler effect where an ambulance with a howling siren has a higher frequency if the car is moving towards the observer or lower if the car moves away due to compression and stretching of the acoustic wave, respectively. In a gaseous volume, the molecules move with high velocities in all directions since they show Brownian* motion [23, 24]. The distribution of the velocities is a Maxwell†-Boltzmann distribution $p_{MW}(v)$ given by [25, 26]

$$p_{MW}(v) = 4\pi \left(\frac{M_i}{2\pi RT} \right)^{\frac{3}{2}} v^2 \cdot \exp \left(-\frac{M_i v^2}{2RT} \right) \quad (2.41)$$

with R being the ideal gas constant and M_i being the molar mass of the analyte i . The most probable velocity \hat{v}_i of an analyte molecule is hence

$$\hat{v}_i = \sqrt{\frac{2RT}{M_i}} = \sqrt{\frac{2kT}{m_i}} \quad (2.42)$$

*Robert Brown (1773 – 1858)

†James Clerk Maxwell (1831 – 1879)

with m_i being the mass of the analyte molecule i . The relative velocity shifts the observed frequency ν_{obs} to

$$\nu_{\text{obs}} = \nu \left(\frac{1}{1 \pm \frac{v_i}{c_0}} \right) \quad (2.43)$$

The Doppler broadening is described by a Gaussian* distribution, therefore the full width at half maximum (FWHM) is given by [9, p. 370]

$$\Delta\nu_{\text{dop}} = \frac{2\nu_{01}}{c_0} \sqrt{\frac{2kT \ln 2}{m_i}} \quad \text{or} \quad \Delta\tilde{\nu}_{\text{dop}} = \frac{2\tilde{\nu}_{01}}{c_0} \sqrt{\frac{2RT \ln 2}{M_i}} \quad (2.44)$$

For mid-IR, typical $\Delta\nu_{\text{dop}}$ values of Doppler broadening are around 1000 cm^{-1} and for near-IR transitions the broadening is $\sim 30 \text{ MHz}$ and $\sim 200 \text{ MHz}$ [27].

2.2.4.2 Natural broadening

Even if the Doppler broadening in gaseous samples would be removed by applying very low temperatures the spectral line would not be infinitely sharp. The remaining broadness is based on a fundamental quantum mechanic phenomenon called natural line broadening $\Delta\tilde{\nu}_{\text{nat}}$. The uncertainty ΔE of a state with the characteristic lifetime τ_{sp} of a certain excited state (i.e. E_1) is linked via the Heisenberg's† uncertainty principle [12]:

$$\tau_{\text{sp}} \hbar c_0 \Delta\tilde{\nu}_{\text{nat}} = \tau_{\text{sp}} \Delta E \geq \hbar \quad \text{with} \quad \hbar := \frac{h}{2\pi} \quad (2.45)$$

where \hbar is the reduced Planck constant. The lifetime expresses the time needed for the population density of an excited state to decay to $1/e$ of its initial value, besides the lifetime is related directly to the Einstein coefficient for spontaneous emission A_{10} by

$$\tau_{\text{sp}} = \frac{1}{A_{10}} \quad (2.46)$$

Neglecting degeneration of the participating states, the Einstein coefficients for spontaneous absorption B_{01} and spontaneous emission A_{10} are coupled by

$$A_{10} = \frac{8\pi h \nu_{01}^3}{c_0^3} B_{01} = 8\pi h \tilde{\nu}_{01}^3 B_{01} = \frac{16\pi^3 \tilde{\nu}_{01}^3}{3\varepsilon_0 h} |\mu|^2 \quad (2.47)$$

Note that if degeneration is neglected, the Einstein coefficient for stimulated emission B_{10} is equal to B_{01} . Merging 2.45 and 2.47 the expression for the natural broadening is obtained

$$\Delta\tilde{\nu}_{\text{nat}} \geq \frac{16\pi^2 \tilde{\nu}_{01}^3}{6\varepsilon_0 c_0 h} |\mu|^2 \quad (2.48)$$

A more simplified solution, which is useful if the lifetime is known can be derived from equation 2.45 and gives [12, p. 491]

$$\Delta\tilde{\nu}_{\text{nat}} \geq \frac{1}{2\pi c_0 \tau_{\text{sp}}} \approx \frac{5.3 \text{ cm}^{-1}}{\tau_{\text{sp}} \text{ ps}} \quad (2.49)$$

*Johann Carl Friedrich Gauß (1777 – 1855)

†Werner Karl Heisenberg (1901 – 1976)

Since no excited state exists with an infinite lifetime, all transitions are subject to natural broadening. Due to $\Delta\tilde{\nu}_{\text{nat}} \propto \tilde{\nu}_{01}^3$, natural line broadening is significantly higher for electronic transitions ($\sim 10^{-3} \text{ cm}^{-1} \approx 30 \text{ MHz}$) than for vibrational ($\sim 10^{-7} \text{ cm}^{-1}$, few kilohertz) or rotational ($\sim 10^{-14} \text{ cm}^{-1}$, less than a millihertz) transitions. Compared to Doppler broadening, natural broadening results in a Lorentzian profile [27].

2.2.4.3 Collisional broadening

Collisional broadening sometimes also referred to as pressure broadening results from collision of two molecules. Since collision is more likely if more molecules are present in a volume, this effect is strongly dependent on pressure. Broadening is related to the mean time between collisions τ_{col} and can be linked with the Heisenberg principle like in equation 2.45 leading to [9, p. 371]

$$\Delta\tilde{\nu}_{\text{col}} \approx \frac{1}{2\pi c_0 \tau_{\text{col}}} \quad (2.50)$$

For simplicity, the considered gaseous volume for the following derivations consists only of analyte molecules of the species i , hence $N_i = 1$. The reciprocal mean time between collisions can then be described by

$$\tau_{\text{col}}^{-1} = \rho_i \bar{v}_{\text{rel},ii} \sigma_{ii} \quad (2.51)$$

With $\bar{v}_{\text{rel},ii}$ being the relative mean velocity of two molecules of the species i and σ_{ii} being the collision cross section of the colliding molecules. According to the ideal gas law, the molar volume is

$$V_{\text{m}} = \frac{RT}{p} \quad (2.52)$$

with p being the pressure within the volume. Recalling 2.41 the average velocity is given by

$$\bar{v}_i = \sqrt{\frac{8RT}{\pi M_i}} \quad (2.53)$$

However, the relative mean velocity \bar{v}_{rel} of two different molecules is [12]

$$\bar{v}_{\text{rel},ij} = \sqrt{\frac{8kT}{\pi \mu_{ij}}} \quad \text{with} \quad \mu_{ij} = \frac{m_i m_j}{m_i + m_j} \quad (2.54)$$

Since $m_i = m_j$ the reduced mass becomes $\mu_{ii} = \frac{m_i}{2}$. Therefore, equation 2.54 can be rewritten to

$$\bar{v}_{\text{rel},ii} = \sqrt{\frac{16kT}{\pi m_i}} = \sqrt{\frac{16RT}{\pi M_i}} \quad (2.55)$$

The collision cross section can be calculated after [28]

$$\sigma_{ij} = \pi(r_i + r_j)^2 \quad (2.56)$$

Again, since only molecules of the type i are assumed, the cross section becomes $4\pi r_i^2$. Merging equations 2.55 and 2.56 with 2.51 and recalling that $\rho_i = N_i \frac{N_A}{V_m}$ leads to

$$\tau_{\text{col}}^{-1} = 16 \cdot r_i^2 \cdot p \sqrt{\frac{\pi}{kTm_i}} \quad (2.57)$$

Like in natural broadening, the shape can be approximated by a Lorentzian curve and the typical values for collision broadening at standard conditions are about 2 GHz [27]. Besides the shape, collisional broadening can also alter the peak's transition energy due to an alteration of the averaged potential distortion. This effect is quite complex since it depends on the molecules distance influencing the shape of the potential curves of ro-vibrational states. The phenomenon can cause a negative or positive shift of the peak's transition energy.

Besides the pressure dependency of collisional broadening, temperature has an influence as well, although the peak shifting effect is the reason why there are different dependencies provided in literature. According to [27] the temperature dependency is

$$\Delta\tilde{\nu}_{\text{col}} \propto T^{-n_T} \quad (2.58)$$

with n_T being in the range of 0.5 to 0.8 [22] compared to

$$\Delta\tilde{\nu}_{\text{col}} \propto \frac{1}{\sqrt{T}} \quad (2.59)$$

from equation 2.57.

Concluding the influences of the different broadening effects on the spectral line width, natural broadening cannot be extinguished due to its dependency on the spontaneous emission lifetime every excited state is subject to. However, compared to the other effects, it can be neglected since under normal conditions its broadening effect is a few orders of magnitude smaller compared to collisional broadening even for vibronic transitions. Doppler broadening is less pronounced for large molecules like acetone compared to H_2O or CH_4 . However, it is also dependent on temperature and the transition energy and its broadening effect can exceed the one from collisional broadening for high temperatures and with increasing peak transition energy. Since acetone has a large radius, its collisional cross section and hence the broadening effect of collisional broadening is quite strong especially at normal pressure conditions and is therefore likely to have the strongest influence on the line broadening, at least in the IR region. As can be seen in the acetone spectra in figure 2.10 and 2.12 there is no visible fine structure at normal conditions. The reason for that is the great number of different ro-vibrational transitions combined with broadening effects causing the spectral lines to overlap resulting in broad absorption features. Regarding the line shape functions representing the different broadening effects, a Gaussian profile can be applied for Doppler broadening and a Lorentzian profile

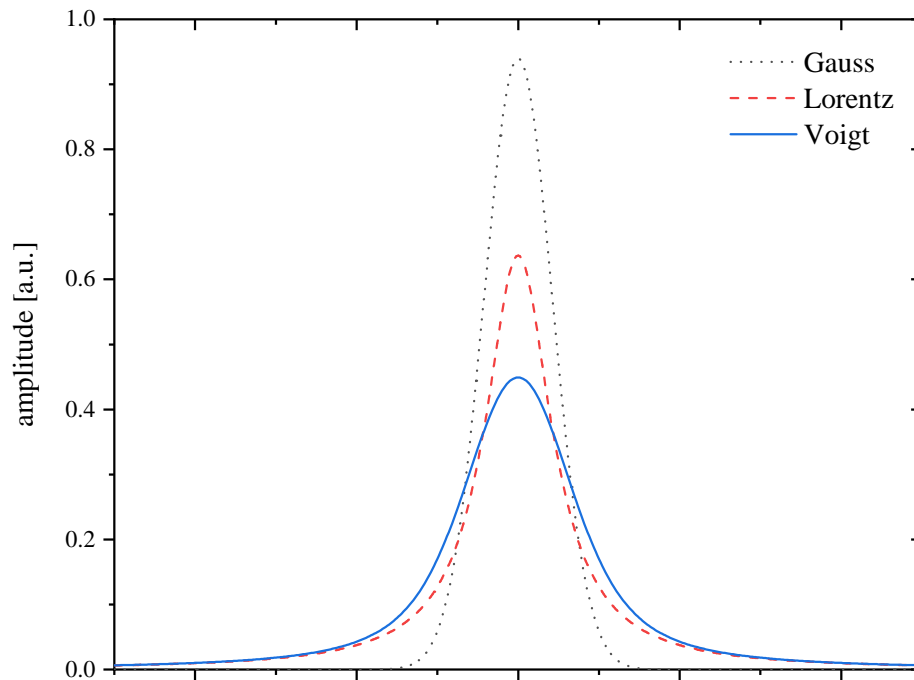


Fig. 2.13. Normalised peak shapes of a Gaussian (black dotted), Lorentzian (red dashed) and Voigt (blue solid) peak profile.

for natural and collisional broadening. Equation 2.60 and 2.61 represent the corresponding offset free ($y_0 = 0$) line shape functions $f_G(\tilde{\nu})$ and $f_L(\tilde{\nu})$ *

$$f_G(\tilde{\nu}) = \frac{A_P \cdot \exp - \frac{4 \ln 2 (\tilde{\nu} - \tilde{\nu}_c)^2}{w_G^2}}{w_G \sqrt{\frac{\pi}{4 \ln 2}}} \quad (2.60)$$

$$f_L(\tilde{\nu}) = \frac{2A_P}{\pi} \cdot \frac{w_L}{4(\tilde{\nu} - \tilde{\nu}_c)^2 + w_L^2} \quad (2.61)$$

w_G and w_L represent the Gaussian and Lorentzian absorption bands' FWHM, A_P is the peak area and $\tilde{\nu}_c$ is the wavenumber of the peak center.

In practical applications, Doppler and collisional broadening coexist and therefore both shapes have to be considered to correctly determine the line shape. The solu-

*These peak functions are adapted from the internal peak shape functions from *OriginPro 2019*. The names of the functions are *nlf_Gaussian* and *nlf_lorentz* for the Gaussian and Lorentzian line shape functions, respectively.

tion is a Voigt function, which is the convolution of both functions and is obtained by [27]

$$f_V(\tilde{\nu}) = (f_L * f_G)(\tilde{\nu}) = \int_0^{\infty} f_L(\tilde{\nu}') f_G(\tilde{\nu} - \tilde{\nu}') d\tilde{\nu}' \quad (2.62)$$

Basing on a Voigt profile, Olivero and Longbothum [29] provided an approximation for the half width at half maximum (HWHM) $\Delta\tilde{\nu}_V$ with a maximal inaccuracy of $\approx 0.02\%$:

$$\Delta\tilde{\nu}_V = \frac{1}{2}(1.0692\Delta\tilde{\nu}_{\text{col}} + \sqrt{0.86639\Delta\tilde{\nu}_{\text{col}}^2 + 4\Delta\tilde{\nu}_{\text{dop}}^2}) \quad (2.63)$$

Figure 2.13 visualises a normalised Gaussian, Lorentzian and Voigt distribution.

2.2.5 Laser spectroscopy

Today, there are a variety of applications for optical gas sensors, e.g. environmental and atmospheric monitoring, food production, process control and optimisation, combustion emission monitoring, indoor air quality detection as well as medical diagnosing. Although not comprehensive, this list demonstrates the importance of gas sensing. Depending on the application, optical devices can be quite small like the *SCD40* sensor from *Sensirion AG* having the size of $\approx 1 \text{ cm}^3$ measuring temperature, humidity and CO_2 , although only the latter one is based on an optical sensing method, namely PAS. In contrast, modern differential absorption light detection and ranging (LIDAR) systems can measure environmental pollution or atmospheric compositions remotely over several kilometers but some of these devices have to be placed in lorries due to their sheer size [30]. Regarding compact trace gas detection, however, mainly three techniques are available today. Namely tunable diode laser absorption spectroscopy (TDLAS), nondispersive infrared (NDIR)- and UV/VIS spectroscopy [31].

NDIR technology usually employs a broadband emitter followed by two filters. One filter removes the light equally to the absorption band of the target gas (active channel) while the other filter covers another wavelength region (reference channel). It is important, that no interfering gas species is present with an absorption feature in one of the two filters. The transmission monitored in the active channel is comprised by absorption, whereas the reference channel detects alterations in the light source's emission. The setup has high potential towards miniaturisation and the employed components can be quite cheap including unsophisticated broad band emitters and detectors working at room temperature [32]. NDIR devices are used in breath analysis as well, monitoring the $^{13}\text{CO}_2/^{12}\text{CO}_2$ ratio in $^{13}\text{CO}_2$ -breath tests [33]. However, the technology lacks selectivity (e.g. towards H_2O) if suitable filter or high intensity absorption bands are not available.

NDIR and TDLAS usually exploit ro-vibrational transitions in the IR region. However, TDLAS systems do not apply broad band emitters like NDIR does, but monochromatic laser sources with a narrow emission line width and a tuneable

emission wavelength. If applied in a simple direct absorption spectroscopy (DAS) setup, which was discussed in 2.2.2, both approaches suffer from certain drawbacks:

- i In order to obtain the analyte concentration, $I_1(\tilde{\nu})$ and $I_0(\tilde{\nu})$ have to be determined. The concentration is then derived from their ratio. Hence, DAS can be considered an indirect method. By detecting trace amounts of the analyte gas, the difference between these two quantities is very small since almost no light is absorbed within the sample. Therefore, the detector must be able to adequately measure a high incident light intensity and a small variation on top, introduced by a changing analyte concentration. This is very challenging for the detector's analog to digital converter (ADC) since dynamic range and resolution are contrary. Hence, the variation introduced by the analyte gets easily covered by the detectors intrinsic noise. In order to overcome this issue in devices like FT-IR (Fourier* transform infrared) spectrometer, the detector is cooled by means of liquid N₂.
- ii Since the absorbance linearly depends on the optical path length (see 2.29), measurement cells are designed preferably long contradicting miniaturisation. In direct TDLAS setups typical pathlengths vary from 0.5 – 100 m [32]. In order to achieve long pathways, multipass cells like Herriott cells are employed. Within such a cell the light is reflected between two mirrors, passing the sample several times. McManus et al. [34] used a Herriott cell in a direct TDLAS setup with an optical path length of 76 m detecting N₂O in the sub ppbV region. Compared to that, Sonnenfroh et al. [35] used a single pass cell with an optical path length of 0.5 m achieving a minimal detectable gas concentration of N₂O in the two-digit ppmV region, demonstrating the need for high optical path lengths in direct TDLAS for trace gas analysis.
- iii Equation 2.29 demonstrates the non-linear but exponential dependency between the analyte concentration and measured intensities.
- iv Low frequency laser intensity noise, often referred to as $1/f$ -noise, limits the sensitivity of a direct TDLAS systems [36].
- v Trace gas DAS is prone to scattering effects like Rayleigh[†] scattering. Such loss effects altering the measured intensity are difficult to separate from absorption losses and can cause misinterpretation [37].
- vi DAS often suffers from spectral cross-sensitivities due to overlapping absorption bands of different molecules at atmospheric conditions. Since this spectral interference is one of the main obstacles in breath analysis due to its extremely complex measurement matrix, chapter 3 will provide a detailed discussion.

To overcome the disadvantages addressed in iv, v and vi literature provides several modulation approaches forming specialisations of the basic TDLAS technique. The

*Joseph Fourier (1768 – 1830)

[†]John William Strutt 3rd Baron Rayleigh (1842 – 1919)

most common is the wavelength modulation absorption spectroscopy (WMAS). This technique can also be applied in photoacoustic spectroscopy and is called wavelength modulated PAS (WM-PAS). Although this work mainly deals with amplitude modulated PAS (AM-PAS) the fundamentals of WMAS will be addressed in the next section, since they provide a basis for later discussions.

2.2.6 Wavelength modulation (WM)

Today wavelength modulation is a powerful analysis tool in trace gas detection. Especially in environmental monitoring and remote sensing WMAS is commonly used encompassing the detection of small molecules like CO [38], NO₂ [39] or formaldehyde [40] to name a few. WMAS is sometimes used as a synonym for TDLAS, which is not correct, since it is only one among other modulation techniques like frequency modulation absorption spectroscopy (FMAS). Both techniques are quite similar since both consider the frequency of light as carrier frequency. Additionally, both methods attempt to optimise sensitivity by increasing the detection band's frequency to avoid $1/f$ laser noise [41]. However, the frequency modulation (FM) technique usually applies high modulation frequencies of 100 MHz or above, but only small modulation depths are employed [42]. WMAS on the other hand uses large modulation depths but frequencies in the kHz range or up to a few MHz [41, 43]. In terms of signal to noise ratio (SNR), FM outperforms WM since it may even be shot- or quantum-noise limited [44]. However, to achieve such a performance ex-

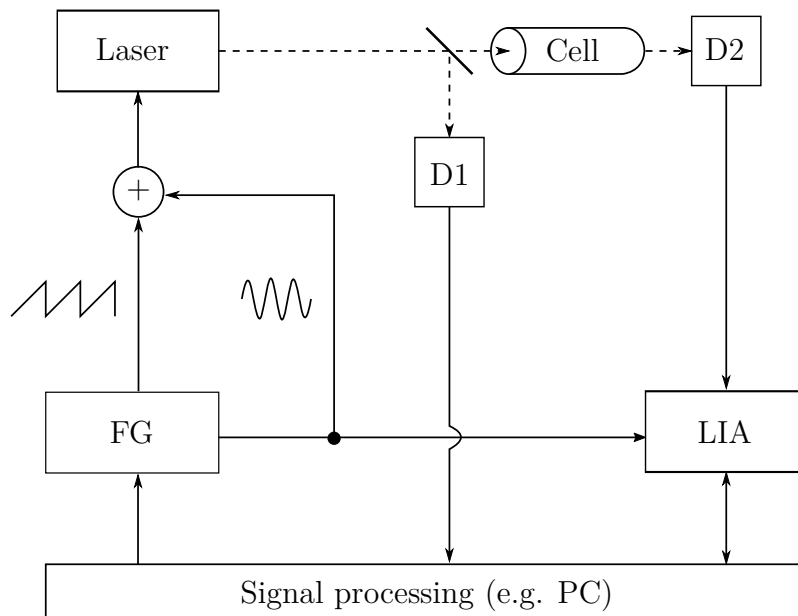


Fig. 2.14. Setup of a wavelength modulation absorption spectroscopy system. The laser beam is indicated by dashed line, while connections are illustrated by solid lines after [31]. **FG** - (dual channel) function generator, **LIA** - lock-in amplifier, **D1** and **D2** - detectors 1 and 2.

tremely high modulation frequencies would be necessary and FM in general is more complex, expensive and less common compared to WM [45]. Since only WMAS will be considered in this thesis, FMAS will not be further discussed.

Figure 2.14 visualises a basic WMAS setup. A function generator (FG) controls a laser by providing a sawtooth modulated injection signal, which is superimposed by means of a sine wave. A fraction of the laser light is directed into a reference detector (D1) by means of a semi transparent mirror while the rest of laser beam illuminates a measurement cell with the length l_{opt} filled with a gas sample. Since the injection current is modulated by means of a slow sawtooth signal superimposed by a fast sinusoidal modulation, a wavelength scan over an absorption peak is possible. The transmitted light impinges onto an optical detector (D2). The measured signal from D2 is transferred to a lock-in amplifier (LIA), which post-processes the signal. Since the FG provides the LIA with the same frequency as the laser is modulated, the LIA can demodulate the acquired signal from the detector at the laser's modulation frequency or a multiple of that. Finally, the signal from D1 and the LIA are transferred to a further signal processing unit (e.g. a PC) for further signal interpretation and processing. A simple direct TDLAS setup, however, does not add a sinusoidal signal on top of the sawtooth signal and hence does not need a lock-in amplifier for demodulation but directly transfers the acquired intensity signal from the optical detectors to the signal processing unit since it is not based on WM.

Regarding WMAS, the modulation frequency f_{WM} is usually in the kHz range. If

$$f_{\text{WM}} \gg F_{\text{st}} = \frac{\omega_{\text{st}}}{2\pi} \quad (2.64)$$

is valid, where F_{st} is the sawtooth modulation frequency with a superimposed sinusoidal peak-to-peak amplitude of the frequency f_{WM} the modulation depth of $\delta_{\text{WM}}\tilde{\nu}_{\text{ph}}$ is given. This depth is smaller than the total broadness of the absorption line $\Delta\tilde{\nu}_{\text{tot}}$. With a scanning range of $\Delta_{\text{WM}}\tilde{\nu}_{\text{ph}}$ the relation of these three parameters is given by

$$\Delta_{\text{WM}}\tilde{\nu}_{\text{ph}} > \Delta\tilde{\nu}_{\text{tot}} > \delta_{\text{WM}}\tilde{\nu}_{\text{ph}} \quad (2.65)$$

In WMAS literature, the applied modulation depth is usually provided by the modulation index m_{mod} , which relates to the HWHM of the absorption band $\frac{\Delta\tilde{\nu}_{\text{tot}}}{2}$ leading to [42]

$$m_{\text{mod}} = \frac{2\delta_{\text{WM}}\tilde{\nu}_{\text{ph}}}{\Delta\tilde{\nu}_{\text{tot}}} \quad (2.66)$$

Figure 2.15 shows the superimposed modulation of the sawtooth peak scanning frequency $\Delta_{\text{WM}}\tilde{\nu}_{\text{ph}}$ (black) with the sinusoidal modulation $\delta_{\text{WM}}\tilde{\nu}_{\text{ph}}$ (blue) on top. The figure indicates, the relation of the different WMAS parameters from 2.65. The FWHM of the Gaussian shaped absorption peak is indicated by $\Delta\tilde{\nu}_{\text{tot}}$ (green). The resulting signal $S_{\text{WM},\tilde{\nu}_{01}}$ (red) is a snapshot representing the fast modulation of the emission wavelength solely around the peak center with f_{WM} . By the modulation only around the peak, the resulting signal is characterised by a frequency twice of f_{WM} . The demodulation of $S_{\text{WM},\tilde{\nu}_{01}}$ for a complete scan by means of a LIA results in

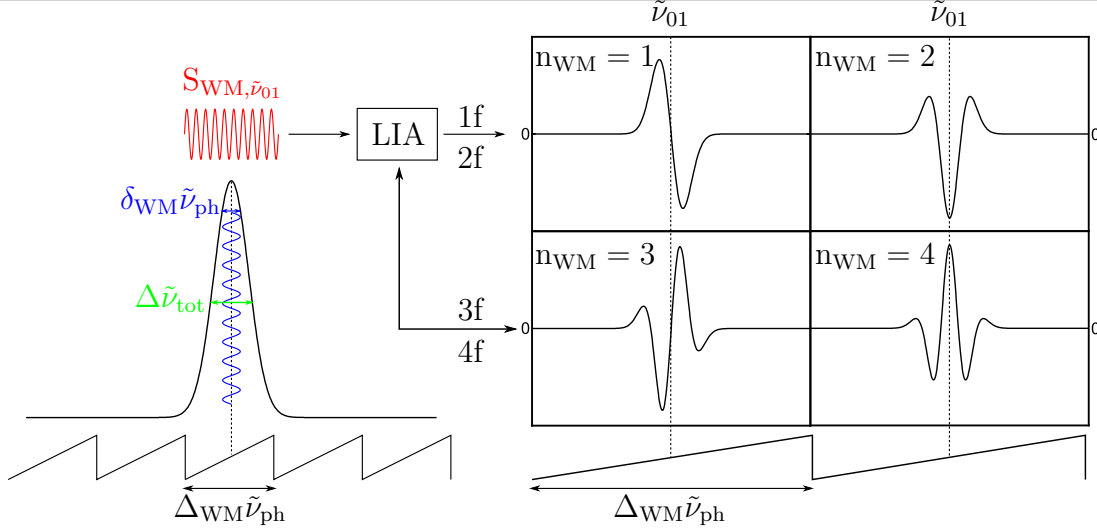


Fig. 2.15. Visualisation of the different parameters used in WMA and resulting signal shapes after LIA demodulation for the first four harmonics. $\Delta_{\text{WM}}\tilde{\nu}_{\text{ph}}$: sawtooth modulation depth (black), $\delta_{\text{WM}}\tilde{\nu}_{\text{ph}}$: sinusoidal modulation depth (blue), $\tilde{\nu}_{01}$: emission wavenumber at peak center, $S_{\text{WM},\tilde{\nu}_{01}}$: resulting $2f_{\text{WM}}$ at peak center modulation (red), $\Delta\tilde{\nu}_{\text{tot}}$: FWHM (green).

one of the four symmetrical shaped curves depending on the demodulation frequency $n \cdot f_{\text{WM}}$ with $n = 1, 2, 3, \dots$. Note that for the rest of this section $f_{\text{WM}} = f$. Since the shapes of these curves are the derivatives of the absorption peaks line shape, this type of spectroscopy is often referred to as derivative spectroscopy. The basics of the LIA's principle of operation will be discussed in section 2.4.2. In terms of $2f$ modulation for $n = 2$, the demodulated signal has a negative maximum at a modulation around the peak at $\tilde{\nu}_{01}$ where the $1f$ signal has a zero crossing. This behavior is valid for all even and odd harmonics of f , respectively, although the maxima for the even harmonics can either be positive or negative.

Demodulation at higher harmonics can have several advantages. For example, demodulating at $2f$ or higher harmonics instead of $1f$, causes the signal to be free from background drifts. However, $2f$ modulation still suffers from unwanted residual amplitude modulation (RAM) causing an offset shift. RAM is a consequence of the laser current modulation accompanying wavelength modulation [46–48]. Higher harmonics are even less susceptible to external distortions like RAM, however, they have smaller amplitudes and they require lock-in amplifier, being able to demodulate the signal at very high frequencies. Furthermore, the offset shift from the $2f$ signal intensifies with the modulation depth and thus has to be compensated by self referencing the $2f$ amplitude peak value to the $2f$ background beyond its foothills [32]. Additionally, $2f$ signals might be subject to distortions as well, due to non-linearities in the response of amplitude modulation to laser current changes [48].

Another feature of demodulating the acquired signal at odd harmonics is wavelength tracking. Since it is often important to detect or remain at the center of an absorption line, continuously tracking of the zero crossing of an odd harmonic demodulated

signal can be performed. Although $3f$ demodulation offers some benefits regarding wavelength tracking [32], it is only applicable if the LIA device is capable of demodulation at three times the modulation frequency.

Besides wavelength tracking, signal normalisation sometimes also referred to as $2f/1f$ normalisation is another approach regarding signal enhancement. This normalisation offers the following benefits [49]:

- Scattering losses can be avoided.
- Compensation of RAM induced offset.
- Less susceptibility to beam steering and window fouling.
- Less sensitivity towards beam attenuations and mechanical vibrations.

Further RAM suppression methods are double-beam-double-resonator schemes [50], electrical nulling method [51] and a three-section QCL setup allowing pure WM or AM [52]. The next paragraphs provide some mathematical expressions regarding wavelength modulation and RAM, while non-linearities in RAM responses will be neglected [47]. WM can be expressed as

$$\tilde{\nu}_{\text{ph}}(t) = \tilde{\nu}_{\text{ph},c} + \frac{\delta_{\text{WM}}\tilde{\nu}_{\text{ph}}}{2} \cdot \cos(\omega_{\text{WM}}t) \quad (2.67)$$

and RAM is given by

$$I_c(t) = I_{c,c} + \frac{i_c}{2} \cdot \cos(\omega_{\text{WM}}t + \Theta_{\text{WM}}) \quad (2.68)$$

with $\tilde{\nu}_{\text{ph},c}$ being the center emission wavenumber for a DC injection current $I_{c,c}$ and $\delta_{\text{WM}}\tilde{\nu}_{\text{ph}}$ being the modulation depth adjusted by i_c . Furthermore, ω_{WM} is the angular frequency of the fast sinusoidal signal and Θ_{WM} is the phase shift between AM and WM. For the following derivations, this shift is assumed to be zero.

To further simplify matters regarding mathematical description of WM signals optical thin sample approximation (TSA) is assumed in most literature references, which alters equation 2.27 from an exponential to a linear dependency [48]

$$e^{-\tilde{A}(\tilde{\nu})} \approx 1 - \tilde{A}(\tilde{\nu}) \quad (2.69)$$

Since this TSA is not only valid in WM, a short simulation was performed, to verify this approximation for trace gas detection of acetone. The deviation of approximation σ_{TSA} is given by

$$\sigma_{\text{TSA}} = \left(1 - \frac{e^{-\tilde{A}(\tilde{\nu})}}{1 - \tilde{A}(\tilde{\nu})}\right) \cdot 100\% \quad \text{with} \quad \tilde{A}(\tilde{\nu}) = \sigma_{\text{A}}(\tilde{\nu})N_i \frac{N_{\text{A}}}{V_{\text{m}}}l_{\text{opt}} \quad (2.70)$$

Note that the absorbance $\tilde{A}(\tilde{\nu})$ was already discussed in section 2.2.2. The maximum ACS exploited within this thesis is about $2.4 \times 10^{-23} \text{ m}^2 \text{ molecule}^{-1}$ at around

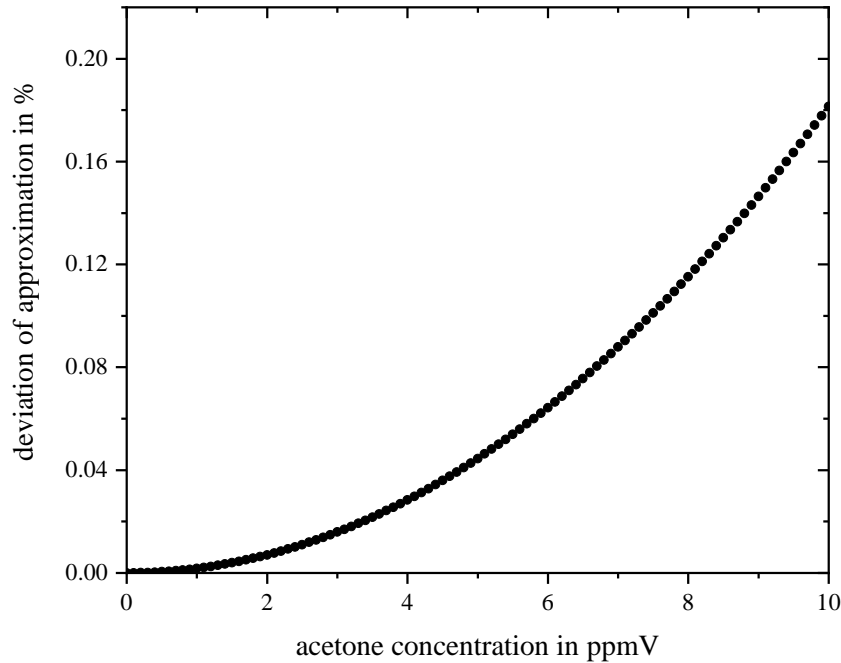


Fig. 2.16. Validation of the thin sample approximation for trace gas detection of acetone at 1205 cm^{-1} , a pathlength of 10 m and a molar volume $V_m = 0.02447\text{ m}^3\text{ mol}^{-1}$.

1205 cm^{-1} , a theoretical optical pathlength of 10 m, a maximum concentration of 10 ppmV and molar volume of $0.02447\text{ m}^3\text{ mol}^{-1}$ are further assumed. The resulting deviation for different concentrations is provided in figure 2.16. The curve indicates, that for concentrations up to 10 ppmV the deviation induced by the TSA is below 0.2 %. Therefore, the TSA can be applied for trace gas analysis of acetone. Combining 2.67 with 2.69 leads to the wavenumber and time dependent absorbance $\tilde{A}(\tilde{\nu}_{\text{ph}}, t)$, which is given by

$$\tilde{A}(\tilde{\nu}_{\text{ph}}, t) = \tilde{A} \left[\tilde{\nu}_{\text{ph},c} + \frac{\delta_{\text{WM}} \tilde{\nu}_{\text{ph}}}{2} \cos(\omega_{\text{WM}} t) \right] \quad (2.71)$$

This is an even periodic function in $\omega_{\text{WM}} t$, which can be expanded in a Fourier cosine series [48]

$$-\tilde{A} \left[\tilde{\nu}_{\text{ph},c} + \frac{\delta_{\text{WM}} \tilde{\nu}_{\text{ph}}}{2} \cos(\omega_{\text{WM}} t) \right] = \sum_{u=0}^{\infty} H_u(\tilde{\nu}_{\text{ph}}, \delta_{\text{WM}} \tilde{\nu}_{\text{ph}}) \cos(u \omega_{\text{WM}} t) \quad (2.72)$$

Combining $\tilde{A}(\tilde{\nu}) = \alpha(\tilde{\nu})l_{\text{opt}}$ with 2.31 and 2.72 the Fourier coefficients of the modulated signal are given by [53]

$$H_u(u > 0) = -\frac{\rho_i l_{\text{opt}}}{\pi} \int_{-\pi}^{\pi} \sigma_A(\tilde{\nu}) \left[\tilde{\nu}_{\text{ph},c} + \frac{\delta_{\text{WM}} \tilde{\nu}_{\text{ph}}}{2} \cos(\omega_{\text{WM}} t) \right] \cos(u \cdot \omega_{\text{WM}} t) d(\omega_{\text{WM}} t) \quad (2.73)$$

$$H_0 = -\frac{\rho_i l_{\text{opt}}}{\pi} \int_{-\pi}^{\pi} \sigma_A(\tilde{\nu}) \left[\tilde{\nu}_{\text{ph},c} + \frac{\delta_{\text{WM}} \tilde{\nu}_{\text{ph}}}{2} \cos(\omega_{\text{WM}} t) \right] d(\omega_{\text{WM}} t) \quad (2.74)$$

Based on the derived Fourier coefficients, the $2f$ signal can be calculated after [47]

$$S_{2f}(\tilde{\nu}_{\text{ph}}) = \frac{i_{0,c}}{2} H_3(\tilde{\nu}_{\text{ph}}, \delta_{\text{WM}} \tilde{\nu}_{\text{ph}}) + I_{0,c} H_2(\tilde{\nu}_{\text{ph}}, \delta_{\text{WM}} \tilde{\nu}_{\text{ph}}) + \frac{i_{0,c}}{2} H_1(\tilde{\nu}_{\text{ph}}, \delta_{\text{WM}} \tilde{\nu}_{\text{ph}}) \quad (2.75)$$

For the quantification of the peak intensity considering only the 2nd term is valid. From 2.33 it follows that

$$H_2(\tilde{\nu}_{\text{ph}}) = -\frac{s \rho_i l_{\text{opt}}}{\pi} \int_{-\pi}^{\pi} f_{\text{LS}} \left[\tilde{\nu}_{\text{ph},c} + \frac{\delta_{\text{WM}} \tilde{\nu}_{\text{ph}}}{2} \cos(\omega_{\text{WM}} t) \right] \cos(2\omega_{\text{WM}} t) d(\omega_{\text{WM}} t) \quad (2.76)$$

where the peak height depends on the line shape function f_{LS} . Line shape functions have already been addressed in 2.2.4.

Recalling the drawbacks of direct TDLAS discussed on page 63, WMAS offers some advantages, namely [49]

- improved SNR due to noise suppression by means of lock-in amplification,
- less spectral cross-sensitivity and
- lower susceptibility towards light scattering.

However, there are some requirements that must be met to allow WM. On the one hand, there must be a tunable and preferably mod-hop free light source available in the wavelength region of interest and on the other hand, the absorption peak should be sharp. The latter one means, that the height-to-width ratio $R_{\text{h-w}} = \frac{h_{\text{peak}}}{FWHM}$ has to be a large value*. This is important, since the tuning range of most semiconductor lasers is limited and high $R_{\text{h-w}}$ values lead to a smaller tuning range compared to broad peaks considering the same modulation index for both absorption lines. In [31, p. 27] a table is provided summarizing a variety of light sources and their intrinsic potential regarding WM gas sensing.

As mentioned before, WM is also applicable in PAS leading to similar improvements compared to AM-PAS.

Additionally to the advantages of WMAS, PAS (including AM-PAS) can be

*Assuming that $[FWHM] = \text{cm}^{-1}$ and $[h_{\text{peak}}] = \text{cm}^2$, $[R_{\text{h-w}}] = \text{cm}^3$ applies.

- i regarded a direct measurement method,
- ii the relation between the acquired pressure signal from the acoustic transducer and the analyte concentration is linear and
- iii it has a high potential for miniaturised trace gas sensing since PAS is not depending on the pathlength.

In chapter 3 the applicability of WM-PAS for acetone detection will be addressed in detail. In the following sections, however, the fundamentals of photoacoustic spectroscopy as well as amplification and attenuation effects will be discussed.

References

- [1] C. V. Raman. “A new radiation”. In: *Indian Journal of Physics* 2 (Mar. 1928), pp. 387–398. ISSN: 0370-0089. DOI: 10.1007/BF03052651 (cit. on p. 42).
- [2] J. H. Lambert. *Photometria, sive de mensura et gradibus luminis, colorum et umbrae*. Sumptibus Vidae Eberhardi Klett, Augsburg, 1760 (cit. on pp. 42, 55).
- [3] G. G. Stokes. “On the change of refrangibility of light”. In: *Philosophical Transactions of the Royal Society of London* 142 (1852), pp. 463–562. DOI: 10.1098/rstl.1852.0022 (cit. on p. 42).
- [4] H. Inaba. “Detection of atoms and molecules by Raman scattering and resonance fluorescence”. In: *Laser Monitoring of the Atmosphere*. Springer Berlin Heidelberg, 1976, pp. 153–236. ISBN: 978-3-540-38239-3. DOI: 10.1007/3-540-07743-X_19 (cit. on p. 42).
- [5] P. L. Meyer and M. W. Sigrist. “Atmospheric pollution monitoring using CO₂-laser photoacoustic spectroscopy and other techniques”. In: *Review of Scientific Instruments* 61.7 (1990), pp. 1779–1807. ISSN: 00346748. DOI: 10.1063/1.1141097 (cit. on p. 42).
- [6] M. Hesse et al. *Spektroskopische Methoden in der organischen Chemie*. Ed. by M. Hesse et al. 8th ed. Stuttgart: Georg Thieme Verlag, 2012. ISBN: 9783135761084. DOI: 10.1055/b-002-46984 (cit. on pp. 43, 45, 48–53).
- [7] P. E. Hockberger. “A History of Ultraviolet Photobiology for Humans, Animals and Microorganisms”. In: *Photochemistry and Photobiology* 76.6 (2002), p. 561. ISSN: 0031-8655. DOI: 10.1562/0031-8655(2002)076<0561:AHOUF>2.0.CO;2 (cit. on p. 43).
- [8] International Organization for Standardization. *ISO 20473:2007 Optics and photonics - Spectral bands*. Tech. rep. 2007 (cit. on p. 43).

- [9] P. W. Atkins and J. de Paula. *Physikalische Chemie*. 5th ed. Weinheim: WILEY-VCH, 2013. ISBN: 978-3-527-33247-2 (cit. on pp. 44, 46–48, 52, 54, 58, 59).
- [10] P. M. Morse. “Diatomic Molecules According to the Wave Mechanics. II. Vibrational Levels”. In: *Physical Review* 34.1 (July 1929), pp. 57–64. ISSN: 0031-899X. DOI: 10.1103/PhysRev.34.57 (cit. on p. 46).
- [11] S. Sharpe et al. “The PNNL quantitative IR database for infrared remote sensing and hyperspectral imaging”. In: *Applied Imagery Pattern Recognition Workshop, 2002. Proceedings*. IEEE Comput. Soc, 2002, pp. 45–48. ISBN: 0-7695-1863-X. DOI: 10.1109/AIPR.2002.1182253 (cit. on pp. 48, 50).
- [12] P. W. Atkins and J. de Paula. *Physikalische Chemie*. 4th ed. Weinheim: WILEY-VCH, 2006. ISBN: 9783527315468 (cit. on pp. 50, 51, 54, 56, 58, 59).
- [13] M. Kasha. “Characterization of electronic transitions in complex molecules”. In: *Discussions of the Faraday Society* 9 (1950), p. 14. ISSN: 0366-9033. DOI: 10.1039/df9500900014 (cit. on p. 51).
- [14] A. Jablonski. “Efficiency of Anti-Stokes Fluorescence in Dyes”. In: *Nature* 131.3319 (June 1933), pp. 839–840. ISSN: 0028-0836. DOI: 10.1038/131839b0 (cit. on pp. 51, 52).
- [15] W. Pauli. “Über den Zusammenhang des Abschlusses der Elektronengruppen im Atom mit der Komplexstruktur der Spektren”. In: *Zeitschrift für Physik* 31.1 (Feb. 1925), pp. 765–783. ISSN: 0044-3328. DOI: 10.1007/BF02980631 (cit. on p. 52).
- [16] O. Laporte and W. F. Meggers. “Some Rules of Spectral Structure*”. In: *Journal of the Optical Society of America* 11.5 (Nov. 1925), p. 459. ISSN: 0030-3941. DOI: 10.1364/JOSA.11.000459 (cit. on p. 52).
- [17] T. Preukschat et al. “Comparison of the Photoacoustic Effect in the IR and the UV Regions”. In: *International Journal of Thermophysics* 36.9 (2015), pp. 2318–2327. ISSN: 0195928X. DOI: 10.1007/s10765-015-1885-4 (cit. on p. 53).
- [18] T. Gierczak et al. “Photochemistry of acetone under tropospheric conditions”. In: *Chemical Physics* 231.2-3 (June 1998), pp. 229–244. ISSN: 03010104. DOI: 10.1016/S0301-0104(98)00006-8 (cit. on p. 53).
- [19] M. Nobre et al. “The VUV electronic spectroscopy of acetone studied by synchrotron radiation”. In: *Phys. Chem. Chem. Phys.* 10.4 (2008), pp. 550–560. ISSN: 1463-9076. DOI: 10.1039/B708580J (cit. on p. 53).
- [20] E. E. Barnes and W. T. Simpson. “Correlations among Electronic Transitions for Carbonyl and for Carboxyl in the Vacuum Ultraviolet”. In: *The Journal of Chemical Physics* 39.3 (Aug. 1963), pp. 670–675. ISSN: 0021-9606. DOI: 10.1063/1.1734305 (cit. on p. 53).
- [21] A. Beer. “Bestimmung der Absorption des rothen Lichts in farbigen Flüssigkeiten”. In: *Annalen der Physik und Chemie* 162.5 (1852), pp. 78–88. ISSN: 00033804. DOI: 10.1002/andp.18521620505 (cit. on p. 55).

- [22] I. Gordon et al. “The HITRAN2016 molecular spectroscopic database”. In: *Journal of Quantitative Spectroscopy and Radiative Transfer* 203 (Dec. 2017), pp. 3–69. ISSN: 00224073. DOI: 10.1016/j.jqsrt.2017.06.038 (cit. on pp. 57, 60).
- [23] R. Brown. “XXVII. A brief account of microscopical observations made in the months of June, July and August 1827, on the particles contained in the pollen of plants; and on the general existence of active molecules in organic and inorganic bodies”. In: *The Philosophical Magazine* 4.21 (Sept. 1828), pp. 161–173. ISSN: 1941-5850. DOI: 10.1080/14786442808674769 (cit. on p. 57).
- [24] A. Einstein. “Über die von der molekularkinetischen Theorie der Wärme geforderte Bewegung von in ruhenden Flüssigkeiten suspendierten Teilchen”. In: *Annalen der Physik* 322.8 (1905), pp. 549–560. ISSN: 00033804. DOI: 10.1002/andp.19053220806 (cit. on p. 57).
- [25] J. C. Maxwell. “Illustrations of the dynamical theory of gases. Part I. On the motions and collisions of perfectly elastic spheres”. In: *The London, Edinburgh, and Dublin Philosophical Magazine and Journal of Science* 19.124 (Jan. 1860), pp. 19–32. ISSN: 1941-5982. DOI: 10.1080/14786446008642818 (cit. on p. 57).
- [26] J. C. Maxwell. “Illustrations of the dynamical theory of gases. Part II. On the process of diffusion of two or more kinds of moving particles among one another”. In: *The London, Edinburgh, and Dublin Philosophical Magazine and Journal of Science* 20.130 (July 1860), pp. 21–37. ISSN: 1941-5982. DOI: 10.1080/14786446008642902 (cit. on p. 57).
- [27] J.-P. Besson. “Photoacoustic spectroscopy for multi-gas sensing using near infrared lasers”. Ph. D. thesis. University of Lausanne, 2006 (cit. on pp. 58–60, 62).
- [28] H. A. Beck. “Anwendung der Photoakustischen Spektroskopie in der Prozess- und Umweltanalytik”. Ph. D. thesis. Technical University of Munich, 2003 (cit. on p. 59).
- [29] J. Olivero and R. Longbothum. “Empirical fits to the Voigt line width: A brief review”. In: *Journal of Quantitative Spectroscopy and Radiative Transfer* 17.2 (Feb. 1977), pp. 233–236. ISSN: 00224073. DOI: 10.1016/0022-4073(77)90161-3 (cit. on p. 62).
- [30] R. Bogue. “Detecting gases with light: a review of optical gas sensor technologies”. In: *Sensor Review* 35.2 (Mar. 2015), pp. 133–140. ISSN: 0260-2288. DOI: 10.1108/SR-09-2014-696 (cit. on p. 62).
- [31] T. Rück. “Development, characterization and miniaturization of a trace gas detection system for NO₂ in air based on photoacoustic spectroscopy”. Ph. D. thesis. University of Regensburg, 2017 (cit. on pp. 62, 64, 69).
- [32] J. Hodgkinson and R. P. Tatam. “Optical gas sensing: a review”. In: *Measurement Science and Technology* 24.1 (Jan. 2013), pp. 1–95. ISSN: 0957-0233. DOI: 10.1088/0957-0233/24/1/012004 (cit. on pp. 62, 63, 66, 67).

- [33] J. A. Vogt et al. “Adaptation of the NDIR technology to 13 CO₂ breath tests under increased inspiratory O₂ concentrations”. In: *Journal of Applied Physiology* 107.1 (July 2009), pp. 302–307. ISSN: 8750-7587. DOI: 10.1152/japplphysiol.90913.2008 (cit. on p. 62).
- [34] J. McManus et al. “Pulsed quantum cascade laser instrument with compact design for rapid, high sensitivity measurements of trace gases in air”. In: *Applied Physics B* 92.3 (Sept. 2008), pp. 387–392. ISSN: 0946-2171. DOI: 10.1007/s00340-008-3129-9 (cit. on p. 63).
- [35] D. M. Sonnenfroh et al. “Application of balanced detection to absorption measurements of trace gases with room-temperature, quasi-cw quantum-cascade lasers”. In: *Applied Optics* 40.6 (Feb. 2001), p. 812. ISSN: 0003-6935. DOI: 10.1364/AO.40.000812 (cit. on p. 63).
- [36] P. Werle et al. “The limits of signal averaging in atmospheric trace-gas monitoring by tunable diode-laser absorption spectroscopy (TDLAS)”. In: *Applied Physics B Photophysics and Laser Chemistry* 57.2 (Aug. 1993), pp. 131–139. ISSN: 0721-7269. DOI: 10.1007/BF00425997 (cit. on p. 63).
- [37] D. Ityaksov et al. “Deep-UV absorption and Rayleigh scattering of carbon dioxide”. In: *Chemical Physics Letters* 462.1-3 (Sept. 2008), pp. 31–34. ISSN: 00092614. DOI: 10.1016/j.cplett.2008.07.049 (cit. on p. 63).
- [38] T. Schilling et al. “TDLAS Trace Gas Measurements within Mountain Waves Over Northern Scandinavia during the POLSTAR Campaign in Early 1997”. In: *Geophysical Research Letters* 26.3 (Feb. 1999), pp. 303–306. ISSN: 00948276. DOI: 10.1029/1998GL900314 (cit. on p. 64).
- [39] J. Reid et al. “Sensitivity limits of a tunable diode laser spectrometer, with application to the detection of NO₂ at the 100-ppt level”. In: *Applied Optics* 19.19 (Oct. 1980), p. 3349. ISSN: 0003-6935. DOI: 10.1364/AO.19.003349 (cit. on p. 64).
- [40] T. Gilpin et al. “Intercomparison of six ambient [CH₂O] measurement techniques”. In: *Journal of Geophysical Research: Atmospheres* 102.D17 (Sept. 1997), pp. 21161–21188. ISSN: 01480227. DOI: 10.1029/97JD01314 (cit. on p. 64).
- [41] D. S. Bomse et al. “Frequency modulation and wavelength modulation spectroscopies: comparison of experimental methods using a lead-salt diode laser”. In: *Applied Optics* 31.6 (Feb. 1992), p. 718. ISSN: 0003-6935. DOI: 10.1364/AO.31.000718 (cit. on p. 64).
- [42] S. Schilt et al. “Wavelength Modulation Spectroscopy: Combined Frequency and Intensity Laser Modulation”. In: *Applied Optics* 42.33 (2003), p. 6728. ISSN: 0003-6935. DOI: 10.1364/AO.42.006728 (cit. on pp. 64, 65).
- [43] I. D. Lindsay et al. “Mid-infrared wavelength- and frequency-modulation spectroscopy with a pump-modulated singly-resonant optical parametric oscillator”. In: *Optics Express* 14.25 (2006), p. 12341. ISSN: 1094-4087. DOI: 10.1364/OE.14.012341 (cit. on p. 64).

- [44] H. I. Schiff et al. “The use of tunable diode laser absorption spectroscopy for atmospheric measurements”. In: *Research on Chemical Intermediates* 20.3-5 (Jan. 1994), pp. 525–556. ISSN: 0922-6168. DOI: 10.1163/156856794X00441 (cit. on p. 64).
- [45] P. Kluczynski et al. “Wavelength modulation absorption spectrometry — an extensive scrutiny of the generation of signals”. In: *Spectrochimica Acta Part B: Atomic Spectroscopy* 56.8 (Aug. 2001), pp. 1277–1354. ISSN: 05848547. DOI: 10.1016/S0584-8547(01)00248-8 (cit. on p. 65).
- [46] F. S. Pavone and M. Inguscio. “Frequency- and wavelength-modulation spectroscopies: Comparison of experimental methods using an AlGaAs diode laser”. In: *Applied Physics B Photophysics and Laser Chemistry* 56.2 (Feb. 1993), pp. 118–122. ISSN: 0721-7269. DOI: 10.1007/BF00325250 (cit. on p. 66).
- [47] J. Liu et al. “Wavelength Modulation Absorption Spectroscopy with 2f Detection for Combustion Temperature Measurements Using Multiplexed Near-Infrared Diode Lasers”. In: *42nd AIAA Aerospace Sciences Meeting and Exhibit*. Reston, Virigina: American Institute of Aeronautics and Astronautics, Jan. 2004. ISBN: 978-1-62410-078-9. DOI: 10.2514/6.2004-647 (cit. on pp. 66, 67, 69).
- [48] H. Li et al. “Extension of wavelength-modulation spectroscopy to large modulation depth for diode laser absorption measurements in high-pressure gases”. In: *Applied Optics* 45.5 (Feb. 2006), p. 1052. ISSN: 0003-6935. DOI: 10.1364/AO.45.001052 (cit. on pp. 66–68).
- [49] G. B. Rieker. “WAVELENGTH-MODULATION SPECTROSCOPY FOR MEASUREMENTS OF GAS TEMPERATURE AND CONCENTRATION IN HARSH ENVIRONMENTS”. Ph. D. thesis. University of Stanford, 2009 (cit. on pp. 67, 69).
- [50] K. Ruxton et al. “Tunable diode laser spectroscopy with wavelength modulation: Elimination of residual amplitude modulation in a phasor decomposition approach”. In: *Sensors and Actuators B: Chemical* 150.1 (Sept. 2010), pp. 367–375. ISSN: 09254005. DOI: 10.1016/j.snb.2010.06.058 (cit. on p. 67).
- [51] K. Duffin et al. “Tunable Diode-Laser Spectroscopy With Wavelength Modulation: A Calibration-Free Approach to the Recovery of Absolute Gas Absorption Line Shapes”. In: *Journal of Lightwave Technology* 25.10 (Oct. 2007), pp. 3114–3125. ISSN: 0733-8724. DOI: 10.1109/JLT.2007.904937 (cit. on p. 67).
- [52] P. Patimisco et al. “Purely wavelength- and amplitude-modulated quartz-enhanced photoacoustic spectroscopy”. In: *Optics Express* 24.23 (Nov. 2016), p. 25943. ISSN: 1094-4087. DOI: 10.1364/OE.24.025943 (cit. on p. 67).
- [53] M. M. Jozdani et al. “Modulation index optimization for wavelength modulation spectroscopy”. In: *Optica Applicata* 46.4 (2016), pp. 639–650. DOI: 10.5277/oa160411 (cit. on p. 69).

2.3 Photoacoustic spectroscopy (PAS)

Photoacoustic spectroscopy, like classical absorption spectroscopy, bases on the absorption of light. However, PAS differs significantly from AS in terms of signal detection. As described before, AS can be considered an indirect measurement method, since it compares the transmitted light intensity with the incident intensity. In contrast, PAS uses an acoustic transducer to detect the pressure caused by the absorption of light followed by relaxation. Actually, PAS quantifies an absorption induced periodical heat input into the volume, which leads to a periodical increase in pressure. Hence, PAS can not only be considered a direct measurement method, but also a calorimetric one [1].

It was Alexander Graham Bell* who discovered the photoacoustic effect in 1880 [2]. He investigated the interactions between chopped sun light and solids. However, since at his time no suitable light sources and acoustic transducers were available, it took several decades until Viegerov [3] employed this technique in gas analysis for the first time. It was then in the 1970s that Dewey et al. [4] and Kamm [5] demonstrated the first approach using resonance amplification combined with laser modulation. Today, this type of PAS setup is commonly used in trace gas analysis.

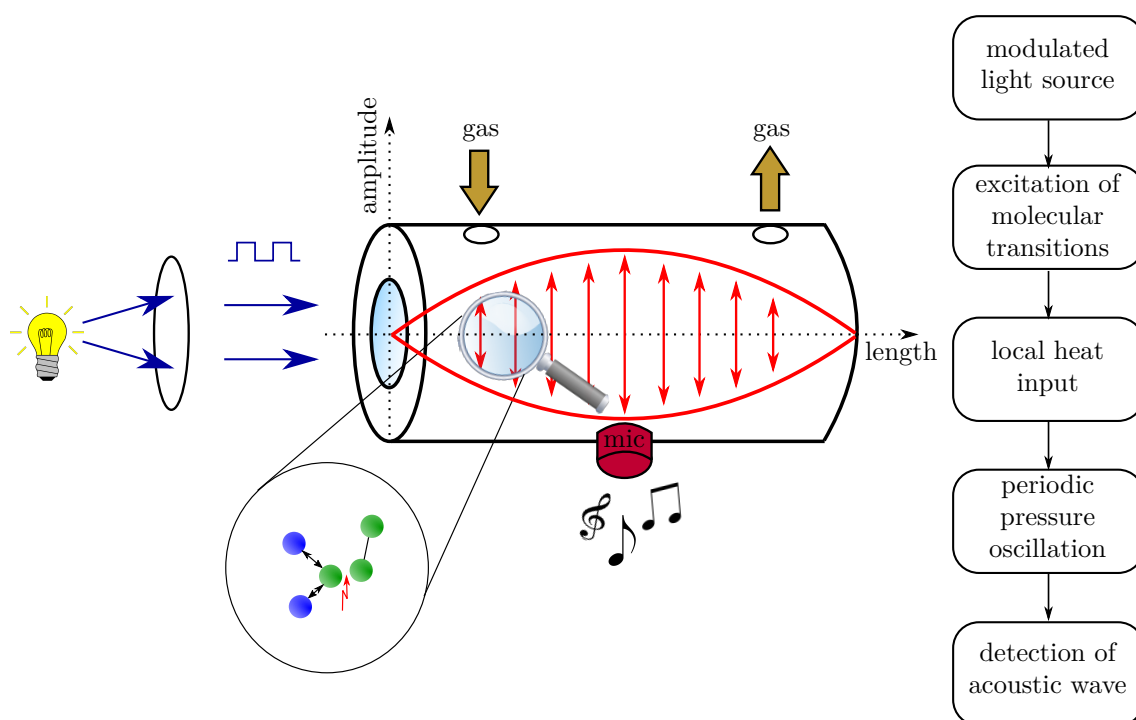


Fig. 2.17. Schematic of the principle of photoacoustic signal generation within a measurement cell.

*Alexander Graham Bell (1847 – 1922)

Figure 2.17 visualises the functional principle of photoacoustic signal generation within a tube shaped photoacoustic measurement cell (PAC). In terms of PAS, either the amplitude (AM) or the wavelength (WM) of an illumination source is modulated. The former one can be performed electrically or by means of a chopper, whereas WM-PAS modulation is usually achieved by current tuning above the threshold. In both scenarios, however, the amplitude of the resulting acoustic wave depends on the periodic delta of the amount of absorbed light. I.e., in electrically AM-PAS the current is square wave modulated from below threshold current to operating current causing a photon flux oscillation of the light source leading to a periodic delta of the amount of absorbed light. In WM-PAS the periodic fluctuation of the amount of absorbed light is achieved by varying the intensity of the absorption cross section dynamically by means of wavelength tuning of the light source.

After excitation of the molecules, there are three main relaxation paths including photolysis, radiative relaxation or nonradiative deexcitation*. Considering PA signal generation, only nonradiative relaxation processes contribute†. Furthermore, the lifetime of the excited state has to be short enough. The relation between the total lifetime of the excited state τ_e and modulation frequency f_{mod} is given by [6]

$$f_{\text{mod}} \leq \frac{1}{10\tau_e} \quad (2.77)$$

Deactivation is mainly achieved by collision, since especially for excited vibrational and rotational states the spontaneous emission lifetime is quite long $\tau_{\text{sp}} \propto \tilde{\nu}^{-3}$ (refer to section 2.2.4.2) compared to the collision induced relaxation time at normal temperature and pressure conditions. During collision, the absorbed energy is transferred into translational energy (i.e. kinetic energy) of the collision partner‡. This increase in kinetic energy causes a local heat input into the volume. Since this process is periodic, a pressure oscillation is generated, which is a synonym for an acoustic wave. The resulting wave is then detected by means of an acoustic transducer, e.g. a microphone, a quartz tuning fork or a cantilever. Techniques exploiting quartz tuning forks or cantilever for signal detection are called quartz enhanced photoacoustic spectroscopy (QEPAS) and cantilever enhanced photoacoustic spectroscopy (CEPAS). No matter which approach is employed, the detected pressure signal is always directly proportional to the analyte concentration present in the sample.

2.3.1 Heat production

To describe the distribution of the population densities§ of the ground state ρ_0 ¶ and the excited state ρ' with the corresponding energy levels E_0 and E_1 , respectively,

*Relaxation processes have been already addressed briefly and will be discussed in more detail in section 2.5.2.

†Actually, photolysis contributes as well, but is neglected at this point and will be discussed later in section 2.5.6

‡Note that the partners can be different molecules, e.g. analyte and N_2 .

§Only the population densities within the illuminated sample are considered.

¶Which can be considered equivalent to the particle density.

during photoacoustic signal generation, a rate equation of a simplified two-level system is employed [7]. It is assumed that ρ only represents the particle number density of molecules having an absorption cross section at $\tilde{\nu}_{\text{ph}}$. The total population density within the illuminated volume is

$$\rho = \rho_0 + \rho' \quad (2.78)$$

and since

$$\rho' \ll \rho_0 \quad (2.79)$$

can be considered for vibrational and electronic energy population densities (refer to equations 2.23 and 2.25), ρ_0 can be replaced by ρ .

Neglecting photolysis*, a universal rate equation considering the excitation rates by collision \hat{C}_{01} and absorption \hat{A}_{01} , as well as spontaneous emission \hat{A}_{10} , stimulated emission \hat{B}_{10} and collision induced \hat{C}_{10} relaxation is given by [7]

$$\frac{\partial \rho'}{\partial t} = (\hat{A}_{01} + \hat{C}_{01}) \cdot (\rho - \rho') - (\hat{C}_{10} + \hat{A}_{10} + \hat{B}_{10}) \cdot \rho' \quad (2.80)$$

The collision induced relaxation and absorption rates show a Boltzmann distribution and have the following relation [7]

$$\hat{C}_{01} = \hat{C}_{10} \cdot \exp \left(-\frac{E_{01}}{kT} \right) \quad (2.81)$$

Recalling the results from equation 2.25 for an excitation at 278 nm and from equation 2.23 for IR photon absorption at 1000 cm^{-1} , collision induced excitation is below 1 % compared to collision induced relaxation and can therefore be neglected.

The absorption rate \hat{A}_{01} can be derived from the photon flux Ψ_{ph} and the ACS after

$$\hat{A}_{01} = \sigma_A(\tilde{\nu}) \cdot \Psi_{\text{ph}} \quad (2.82)$$

The photon flux depends on the optical power P_0 of the light source and the geometrical area of the beam profile. For a collimated circular beam profile d_b the photon flux can be calculated after

$$\Psi_{\text{ph}} = \frac{I_0}{h\nu_{\text{ph}}} = \frac{P_0}{hc_0 \tilde{\nu}_{\text{ph}} \cdot \pi \left(\frac{d_b}{2} \right)^2} \quad (2.83)$$

The total lifetime of an excited state τ_e represents the time until $1/e$ of the corresponding state has decayed and relates to the nonradiative lifetime τ_n and radiative lifetime τ_r after

$$\tau_e^{-1} = \tau_r^{-1} + \tau_n^{-1} \quad (2.84)$$

The radiative lifetimes for excited vibrational levels are relatively long (0.01 – 1 s) and radiative lifetimes of rotational states are even longer [8]. Collision induced,

*A two-level rate equation including photolysis is presented in 2.5.6.

nonradiative relaxation processes are thus dominating in the IR region at normal pressure conditions. Therefore, in case of IR spectroscopy, \hat{A}_{10} and \hat{B}_{10} can be neglected. However, this is not the general case for excited electronic states. But according to Lee et al. [9] radiative relaxation in acetone is very low for 296 nm and is expected to be even lower for smaller wavelengths. At 296 nm for example, the reported fluorescence and phosphorescence quantum yields (refer to section 2.5.6) are 0.00096 and 0.007, respectively [10]. Hence, for both wavelength regions UV and IR, spontaneous and stimulated emission processes can be neglected and $\tau_e = \tau_n$ is valid.

Considering the approximations from equations 2.78, 2.79 and 2.81 as well as the low spontaneous and stimulated emission quantum yields, equation 2.80 simplifies to

$$\frac{d\rho'}{dt} = \hat{A}_{01} \cdot \rho - \hat{C}_{10} \cdot \rho' \quad (2.85)$$

For a sinusoidal laser modulation with angular frequency ω , the photon flux is given by*

$$\Psi_{ph} = \Psi_0 (1 + e^{-j\omega t}) \quad (2.86)$$

where Ψ_0 is the photon flux without modulation. At the beginning of this section it has been mentioned, that the signal depends on the periodic delta of the amount of absorbed light. Thus, only the time dependent term is relevant for the photoacoustic signal generation. Merging 2.82 with 2.86 a solution of the partial differential equation 2.85 is [11]

$$\rho'(t) = \frac{\rho\sigma_A(\tilde{\nu})\Psi_0\tau_n}{\sqrt{1 + (\omega\tau_n)^2}} \cdot e^{j(\omega t - \theta)} \quad \text{with} \quad \theta = \arctan(\omega\tau_n) \quad (2.87)$$

where θ is the phase difference between photon flux and population density of the excited state. This equation can be further simplified if a Heaviside step function for light modulation is assumed [7]

$$\rho'(t) = \rho\sigma_A(\tilde{\nu})\Psi_0\tau_n \left(1 - e^{-\frac{t}{\tau_n}} \right) \quad (2.88)$$

The approximation from 2.88 is only valid for moderate excitation rates [12]. Since literature does not provide exact relaxation rates of acetone neither for the IR nor the UV region a simulation in the IR region is performed to estimate the applicable square wave modulation frequency. The IR region is chosen since the product of $\sigma_A(\tilde{\nu})\Psi_0$ at 1200 cm^{-1} is the highest one that was employed in terms of this work. For an optical power of about 300 mW^\dagger , an ACS of approximately $2.4 \times 10^{-23} \text{ m}^2$ at around 1205 cm^{-1} , a concentration of 10 ppmV, a beam diameter of ca. 4 mm and standard pressure of 1 atm, the relation between ρ'/ρ can be simulated for different τ_n . From 2.83, the photon flux can be calculated to $\Psi_0 = 9.97 \times 10^{23} \text{ s}^{-1} \text{ m}^{-2}$.

*Note that j is the imaginary unit and should not be mixed up with the angular momentum quantum number j .

[†]This is the optical output power in cw (continuous wave) mode at 25°C stated in the data sheet of the HHL-19-26 distributed feedback (DFB) QCL from AdTech.

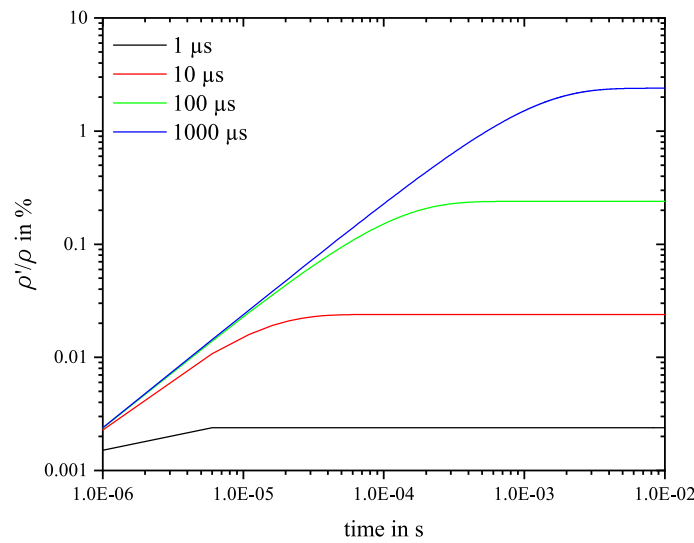


Fig. 2.18. Time dependent relative state distribution for 10 ppmV of acetone illuminated with 300 mW at 1200 cm^{-1} for different estimated τ_n .

Figure 2.18 visualises the time dependent relative state distribution for 10 ppmV of acetone illuminated with 300 mW at 1200 cm^{-1} for different estimated nonradiative relaxation times τ_n . For all relaxation rates, the steady state is reached after $t \approx 6\tau_n$ and is significantly below 1 % for relaxation times of about 100 μs or less. The simulation demonstrates, that equation 2.79 is valid for acetone detection for relaxation times below 100 μs .

As mentioned before, no specification for relaxation rates was found for acetone in the IR region. For the UV region around 278 nm, no exact relaxation time was found, too, but it was estimated to be below 20 μs according to Oka. et al. [13], if oxygen is present in the measurement matrix. In section 2.5.3 the probability for collision induced relaxation will be discussed, demonstrating, that the probability for VT relaxation is indirectly proportional to the energy of the vibrationally excited state. Since the nonradiative relaxation pathway to S_0 from acetone in the UV region via T_1 obviously contains the collision induced relaxation of higher excited vibrational states, the nonradiative relaxation of acetone in the IR at normal conditions is likely to be even faster than the mentioned 20 μs . For $\tau_n = 20\text{ }\mu\text{s}$ the applied modulation frequency of about 5000 Hz for the employed photoacoustic cell fulfils equation 2.77. However, since the nonradiative relaxation time may also depend on the collision partners and collision induced VV energy transfers*, experiments will be necessary to finally verify the applicability of the modulation frequency of about 5000 Hz.

So far, only absorption and relaxation processes without photodissociation have been discussed. In most cases, this may be valid for the IR region, however, it is usually not for the UVC region. Disassociation rates of acetone excited in the UVC region and its influence on the photoacoustic signal will therefore be discussed in detail in section 2.5.6.

*Collision induced vibrational-vibrational energy transfer will be discussed in section 2.5.2.

As a consequence of nonradiative relaxation, a certain heat input into the volume can be observed. Based on 2.87 the time dependent heat production rate $\dot{H}(t)^*$ per volume for a 100 % efficiency is given by

$$\dot{H}(t) = \rho'(t) \cdot \frac{hc_0 \tilde{\nu}_{ph}}{\tau_n} = \dot{H}_0 \cdot e^{j(\omega t - \varphi)} \quad \text{with} \quad \dot{H}_0 = \frac{\rho \sigma_A(\tilde{\nu}) I_0}{\sqrt{1 + (\omega \tau_n)^2}} \quad (2.89)$$

\dot{H}_0 is the amplitude of power density at equilibrium, φ is the phase lag between modulated laser beam and local heat input and $I_0 = \Psi_0 hc_0 \tilde{\nu}_{ph}$.

If $\omega \tau_n \ll 1$ is valid, i.e. a small modulation frequency of 5 kHz and fast relaxation time $< 20 \mu s$, the denominator can be neglected causing an error of $\sim 0.5 \%$ and φ approaches zero. Thus equation 2.89 can be simplified to

$$\dot{H}(t) = \dot{H}_0 \cdot e^{j\omega t} \quad \text{with} \quad \dot{H}_0 = \rho \sigma_A(\tilde{\nu}) I_0 \quad (2.90)$$

2.3.2 Acoustic wave generation

Sound and thermal waves can be described by different classical disciplines of physics including thermodynamics and fluid mechanics. Therefore, literature provides different approaches considering photoacoustic signal generation such as thermodynamically/kinetically [1, 7, 14–17], electrodynamically [18, 19] and acoustically [1, 7, 11, 15, 18, 20–22]. This section, however, will describe the signal generation acoustically. In order to characterise the generation of photoacoustic and photothermal signals, the six physical quantities of pressure, density, temperature and the three dimensional velocity vector of the involved particles have to be considered. The physical laws governing the system are [22]

1. momentum conservation law (Navier[†]-Stokes[‡]),
2. mass conservation law (continuity),
3. energy conservation law (heat diffusion),
4. classical fluid-mechanics,
5. classical thermodynamics and
6. thermodynamic equation of state.

Compared to the equilibrium values (indicated with an index e), the amplitude variations (indicated with an index a) of pressure, density and temperature are usually quite small [22]:

$$p(\vec{r}, t) = p_e + p_a(\vec{r}, t) \quad (2.91)$$

*From now on, the heat production rate will be referred to as power density.

[†]Claude-Louis Navier (1785 – 1836)

[‡]Sir George Stokes, 1st Baronet (1819 – 1903)

$$\tilde{\rho}(\vec{r}, t) = \tilde{\rho}_e + \tilde{\rho}_a(\vec{r}, t) \quad (2.92)$$

$$T(\vec{r}, t) = T_e + T_a(\vec{r}, t) \quad (2.93)$$

Therefore, by introducing the deviating amplitudes of the equilibrium values as new variables, the equilibrium values as constant and by neglecting the small products of the variables the equations can be linearised. In order to link pressure and density with molecular motion, the linearised Navier-Stokes equation is applied [23, p. 279]:

$$\frac{\partial \vec{v}}{\partial t} = -\frac{1}{\tilde{\rho}_e} \nabla \cdot p_a(\vec{r}, t) + \mu_k \nabla (\nabla \cdot \vec{v}_l) \quad (2.94)$$

\vec{v} is the velocity vector and μ_k the kinematic viscosity*. The velocity vector can always be separated into a longitudinal component $\text{rot } \vec{v}_l = 0$ and a transversal component $\text{div } \vec{v}_t = 0$. Since continuity equations and heat diffusion are coupled to the Navier-Stokes equation only by the nonrotational component, the transversal component can be omitted [22]. Hence, $\vec{v} = \vec{v}_l$ is valid.

The equation of mass-density continuity is satisfied by [23, p. 279]

$$\frac{\partial p_a(\vec{r}, t)}{\partial t} = -\tilde{\rho}_e \nabla \cdot \vec{v}_l \quad (2.95)$$

and can be rearranged to

$$\nabla \cdot \vec{v}_l = -\frac{1}{\tilde{\rho}_e} \frac{\partial p_a(\vec{r}, t)}{\partial t} \quad (2.96)$$

By calculating the divergence of the pressure vector field†, replacing \vec{v} with \vec{v}_l and substituting $\nabla \cdot \vec{v}_l$ in 2.94 leads to‡

$$\Delta p_a(\vec{r}, t) = \frac{\partial^2}{\partial t^2} \tilde{\rho}_a(\vec{r}, t) - \mu_k \Delta \left(\frac{\partial}{\partial t} p_a(\vec{r}, t) \right) \quad (2.97)$$

The acoustic pressure contribution to the vector fields of temperature and density is linked by thermodynamics equation of state [23, p. 281].

$$\tilde{\rho}_a(\vec{r}, t) = \left(\frac{\partial \tilde{\rho}}{\partial p} \right)_{T_e} p_a(\vec{r}, t) + \left(\frac{\partial \tilde{\rho}}{\partial T} \right)_{p_e} T_a(\vec{r}, t) = \frac{\gamma}{c_s^2} \left(p_a(\vec{r}, t) - \frac{\beta_T}{\kappa_T} T_a(\vec{r}, t) \right) \quad (2.98)$$

with $\gamma = \frac{C_p}{C_v}$ being the heat capacity ratio of specific isobar C_p and specific isochoric C_v heat capacities. c_s is the speed of sound, β_T is the coefficient of thermal expansion and κ_T is the isothermal compressibility. The speed of sound is defined after

$$c_s = \sqrt{\frac{\gamma R T}{M}} \quad (2.99)$$

* $\mu_k = \frac{4\eta_s}{3\tilde{\rho}_e} + \frac{\eta_b}{\tilde{\rho}_e}$, where η_s is the sheer and η_b the bulk viscosity.

† Multiplying equation 2.94 with ∇ (Nabla-operator).

‡ Note that no Greek Δ is applied within in section but only Laplace [Pierre-Simon Marquis de Laplace (1749 – 1827)] operators.

Inserting 2.98 in 2.97 eliminates the volumetric mass density dependency and therefore the resulting wave equation only depends on the temperature vector field.

$$\Delta p_a(\vec{r}, t) = \frac{\gamma}{c_s^2} \left[\frac{\partial^2}{\partial t^2} - \mu_k \Delta \frac{\partial}{\partial t} \right] \left(p_a(\vec{r}, t) - \frac{\beta_T}{\kappa_T} T_a(\vec{r}, t) \right) \quad (2.100)$$

In addition, pressure fluctuations are always coupled with temperature variations, which can be described by the heat diffusion equation [23, p. 282],

$$\frac{k_T}{\tilde{\rho}_e C_p} \Delta T_a(\vec{r}, t) = \frac{\partial}{\partial t} \left(T_a(\vec{r}, t) - \frac{\gamma - 1}{\gamma \beta_T} \kappa_T p_a(\vec{r}, t) \right) - \frac{\dot{H}(\vec{r}, t)}{\tilde{\rho}_e C_p} \quad (2.101)$$

with k_T as the thermal conductivity and $\dot{H}(\vec{r}, t)$ being the local power density described in equation 2.89. Solving the linked equations 2.100 and 2.101 results in two independent solutions of a plane wave equation [22].

The 1st solution is a strongly dampened wave with a length in the sub-millimeter range, which can be regarded as an isobaric thermal expansion, since the amplitudes of the temperature and density fluctuations are significantly larger than the pressure oscillation amplitude. Besides, due to the large damping factor, this wave is not propagating far from its origin, e.g. the laser beam. Hence, the second spatial derivation of $T_a(\vec{r}, t)$ can be neglected [22]. This solution is used to describe photothermal phenomena [24].

The 2nd solution is a slightly dampened sound wave having a wavelength in the range of centimeter or meter. Within this sound wave, a quasi-adiabatic state is propagating with c_s and the oscillation amplitudes of pressure, temperature and density are similar [22]. This solution will be applied in further derivations considering the photoacoustic signal generation.

However, in order to obtain the solutions of 2.100 and 2.101, the dimensions of the photoacoustic measurement cell are assumed large compared to the propagation range of the thermal wave. Since this is usually the case in PAS* for the strongly dampened wave, the second spatial derivation of $T_a(\vec{r}, t)$ will be neglected and the equations 2.100 and 2.101 can be rewritten to

$$\Delta p_a(\vec{r}, t) = \frac{\gamma}{c_s^2} \left(\frac{\partial^2}{\partial t^2} p_a(\vec{r}, t) - \mu_k \frac{\partial}{\partial t} \Delta p_a(\vec{r}, t) - \frac{\beta_T}{\kappa_T} \frac{\partial^2}{\partial t^2} T_a(\vec{r}, t) \right) \quad (2.102)$$

and

$$0 = \frac{\partial}{\partial t} T_a(\vec{r}, t) - \frac{\gamma - 1}{\gamma \beta_T} \kappa_T \frac{\partial}{\partial t} p_a(\vec{r}, t) - \frac{\dot{H}(\vec{r}, t)}{\tilde{\rho}_e C_p} \quad (2.103)$$

*The tube shaped resonator used within the PACs of this thesis are all in the range of a few cm, thus exceeding the sub-millimeter propagation range of the strongly dampened thermal wave.

In order to substitute the term $\frac{\partial^2}{\partial t^2}T_a(\vec{r}, t)$ in 2.102 with the equation 2.103, the time derivative of the latter equation has to be build on both sides first and solved after $\frac{\partial^2}{\partial t^2}T_a(\vec{r}, t)$. Equation 2.103 is therefore rewritten to

$$\frac{\partial^2}{\partial t^2}T_a(\vec{r}, t) = \frac{\gamma - 1}{\gamma\beta_T}\kappa_T\frac{\partial^2}{\partial t^2}p_a(\vec{r}, t) + \frac{1}{\tilde{\rho}_e C_p}\frac{\partial}{\partial t}\dot{H}(\vec{r}, t) \quad (2.104)$$

Finally merging equation 2.104 with equation 2.102 and performing a few adjustments leads to

$$\Delta p_a(\vec{r}, t) - \frac{1}{c_s^2} \left[\frac{\partial^2}{\partial t^2}p_a(\vec{r}, t) - \gamma\mu_k\Delta\frac{\partial}{\partial t}p_a(\vec{r}, t) \right] = -\frac{\gamma\beta_T}{c_s^2\kappa_T\tilde{\rho}_e C_p}\frac{\partial}{\partial t}\dot{H}(\vec{r}, t) \quad (2.105)$$

According to Morse and Ingard [23, pp. 280] the following thermodynamic relation is valid:

$$\frac{\beta_T}{C_p} = (\gamma - 1)\frac{\kappa_T\tilde{\rho}_e}{\gamma T\beta_T} \quad (2.106)$$

Additionally, thermodynamics provide a further description of β_T , where

$$\beta_T = \frac{1}{V} \left(\frac{\partial V}{\partial T} \right)_p \quad (2.107)$$

With the ideal gas law

$$V = \frac{n_m RT}{p} \quad (2.108)$$

where p is the pressure, V the volume and n_m the number of moles and according to 2.107, β_T can be rewritten to

$$\beta_T \equiv \frac{1}{V} \left(\frac{\partial}{\partial T} \frac{n_m RT}{p} \right)_p \equiv \frac{n_m R}{pV} \equiv \frac{1}{T} \quad (2.109)$$

Hence, the right hand side term can be adapted, leading to the second solution, which is presented by

$$\Delta p_a(\vec{r}, t) - \frac{1}{c_s^2} \left[\frac{\partial^2}{\partial t^2}p_a(\vec{r}, t) - \underbrace{\gamma\mu_k\Delta\frac{\partial}{\partial t}p_a(\vec{r}, t)}_{\text{loss term}} \right] = -\underbrace{\frac{\gamma - 1}{c_s^2}\frac{\partial}{\partial t}\dot{H}(\vec{r}, t)}_{\text{source term}} \quad (2.110)$$

Several dissertations [6, 11, 20] provide a similar solution, however, the red labeled $-\gamma$ of the loss term is missing. Since a detailed derivation led to this result, this thesis will proceed with 2.110.

The damping of the wave is related to the loss term, which results from the viscosity of the medium. Since this loss term prevents an analytical solution it will be neglected within further derivations and will be added again later in form of an excess

term [1, 20]. The result is a non-dampened inhomogeneous wave equation, which can be solved by Fourier transformation [15, p. 6], leading to

$$\left(\Delta + \frac{\omega^2}{c_s^2}\right) p_a(\vec{r}, \omega) = \left(\frac{\gamma - 1}{c_s^2}\right) j\omega \dot{H}(\vec{r}, \omega) \quad (2.111)$$

with

$$p_a(\vec{r}, t) = \int_{-\infty}^{\infty} p_a(\vec{r}, \omega) e^{-j\omega t} d\omega \quad (2.112)$$

$$\dot{H}(\vec{r}, t) = \int_{-\infty}^{\infty} \dot{H}(\vec{r}, \omega) e^{-j\omega t} d\omega \quad (2.113)$$

The frequency dependent heat production rate resulting from light absorption, which was discussed in 2.3.1 can now be linked to the generation of an acoustic wave by the inhomogeneous wave equation 2.111. The boundary conditions of the PAC have to be chosen appropriate, in order to obtain the correct oscillation modes of this acoustic wave [22]. Since in this work tube shaped resonant PACs have been employed, further derivations of the resonance amplified acoustical signal will be discussed in the next section.

References

- [1] A. Rosencwaig. “Photoacoustic Spectroscopy”. In: *Annual Review of Biophysics and Bioengineering* 9.1 (1980), pp. 31–54. ISSN: 0084-6589. DOI: 10.1146/annurev.bb.09.060180.000335 (cit. on pp. 75, 80, 84).
- [2] A. G. Bell. “On the production and reproduction of sound by light”. In: *American Journal of Science* s3-20.118 (1880), pp. 305–324. ISSN: 0002-9599. DOI: 10.2475/ajs.s3-20.118.305 (cit. on p. 75).
- [3] M. L. Viegrov. “Eine Methode der Gasanalyse, beruhend auf der optisch-akustischen Tyndall-röntgenerscheinung”. In: *Doklady Akademii Nauk SSSR* 19 (1938), pp. 687–688 (cit. on p. 75).
- [4] C. F. Dewey et al. “Acoustic amplifier for detection of atmospheric pollutants”. In: *Applied Physics Letters* 23.11 (Dec. 1973), pp. 633–635. ISSN: 0003-6951. DOI: 10.1063/1.1654774 (cit. on p. 75).
- [5] R. D. Kamm. “Detection of weakly absorbing gases using a resonant optoacoustic method”. In: *Journal of Applied Physics* 47.8 (Aug. 1976), pp. 3550–3558. ISSN: 0021-8979. DOI: 10.1063/1.323153 (cit. on p. 75).
- [6] T. Rück. “Development, characterization and miniaturization of a trace gas detection system for NO₂ in air based on photoacoustic spectroscopy”. Ph. D. thesis. University of Regensburg, 2017 (cit. on pp. 76, 83).

- [7] O. Schulz. “Bestimmung physikalischer und technischer Randbedingungen zur Umsetzung eines photoakustischen Gassensors in der Mikrosystemtechnik”. Ph. D. thesis. University of Ilmenau, 2008 (cit. on pp. 77, 78, 80).
- [8] P. Hess. “Resonant photoacoustic spectroscopy”. In: 1983, pp. 1–32. DOI: 10.1007/3-540-12065-3_1 (cit. on p. 77).
- [9] K. L. K. Lee et al. “Photodissociation of acetone from 266 to 312 nm: Dynamics of CH₃ + CH₃CO channels on the S₀ and T₁ states”. In: *Journal of Chemical Physics* 146.4 (2017), pp. 0–12. ISSN: 00219606. DOI: 10.1063/1.4974035 (cit. on p. 78).
- [10] I. Szilágyi et al. “Photochemical and photophysical study on the kinetics of the atmospheric photodissociation of acetone”. In: *Reaction Kinetics and Catalysis Letters* 96.2 (Apr. 2009), pp. 437–446. ISSN: 0133-1736. DOI: 10.1007/s11144-009-5538-0 (cit. on p. 78).
- [11] M. Mattiello. “Gas Traces Measurement by Photoacoustic Spectroscopy Using Helmholtz Resonator-Based Sensors”. Ph. D. thesis. University of Lausanne, 2008 (cit. on pp. 78, 80, 83).
- [12] H. A. Beck. “Anwendung der Photoakustischen Spektroskopie in der Prozess- und Umweltanalytik”. Ph. D. thesis. Technical University of Munich, 2003 (cit. on p. 78).
- [13] T. Oka et al. “Photoacoustic Study of 280 nm Band of Acetone Vapor”. In: *Bulletin of the Chemical Society of Japan* 61.1 (1988), p. 199. DOI: <https://doi.org/10.1246/bcsj.61.199> (cit. on p. 79).
- [14] P. L. Meyer and M. W. Sigrist. “Atmospheric pollution monitoring using CO₂-laser photoacoustic spectroscopy and other techniques”. In: *Review of Scientific Instruments* 61.7 (1990), pp. 1779–1807. ISSN: 00346748. DOI: 10.1063/1.1141097 (cit. on p. 80).
- [15] L. Kreuzer. “The Physics of Signal Generation and Detection”. In: *Optoacoustic spectroscopy and detection*. New York: Academic Press, 1977, pp. 1–25. ISBN: 9780323158817 (cit. on pp. 80, 84).
- [16] G. Wysocki et al. “Influence of molecular relaxation dynamics on quartz-enhanced photoacoustic detection of CO₂ at $\lambda = 2 \mu\text{m}$ ”. In: *Applied Physics B* 85.2-3 (Nov. 2006), pp. 301–306. ISSN: 0946-2171. DOI: 10.1007/s00340-006-2369-9 (cit. on p. 80).
- [17] N. Barreiro et al. “Quenching effects on pulsed photoacoustic signals in NO₂-air samples”. In: *Applied Physics B* 99.3 (May 2010), pp. 591–597. ISSN: 0946-2171. DOI: 10.1007/s00340-010-3936-7 (cit. on p. 80).
- [18] A. Miklós et al. “Application of acoustic resonators in photoacoustic trace gas analysis and metrology”. In: *Review of Scientific Instruments* 72.4 (Apr. 2001), pp. 1937–1955. ISSN: 0034-6748. DOI: 10.1063/1.1353198 (cit. on p. 80).

- [19] M. Tavakoli et al. “Design, simulation and structural optimization of a longitudinal acoustic resonator for trace gas detection using laser photoacoustic spectroscopy (LPAS)”. In: *Optics & Laser Technology* 42.5 (July 2010), pp. 828–838. ISSN: 00303992. DOI: 10.1016/j.optlastec.2009.12.012 (cit. on p. 80).
- [20] J.-P. Besson. “Photoacoustic spectroscopy for multi-gas sensing using near infrared lasers”. Ph. D. thesis. University of Lausanne, 2006 (cit. on pp. 80, 83, 84).
- [21] A. V. Masurkar. “Extensions of quartz-enhanced photoacoustic spectroscopy”. Ph. D. thesis. Massachusetts Institute of Technology, 2009 (cit. on p. 80).
- [22] A. Miklós et al. “Photoacoustic Spectroscopy, Theory”. In: *Encyclopedia of Spectroscopy and Spectrometry*. Elsevier, 1999, pp. 1815–1822. DOI: 10.1006/rwsp.2000.0234 (cit. on pp. 80–82, 84).
- [23] P. M. Morse and K. U. Ingard. *Theoretical Acoustics*. McGraw Hill Book Company, 1968. ISBN: 9780691024011 (cit. on pp. 81–83).
- [24] W. B. Jackson et al. “Photothermal deflection spectroscopy and detection”. In: *Applied Optics* 20.8 (Apr. 1981), p. 1333. ISSN: 0003-6935. DOI: 10.1364/AO.20.001333 (cit. on p. 82).

2.4 Signal amplification

Today most PACs are driven in an acoustically resonant mode to exploit resonance amplification of the generated acoustic wave. However, there are also PAS systems using nonresonant cells [1, 2]. For resonant systems, it can be distinguished between photoacoustic sensors employing simple microphones as an acoustic transducer or systems using mechanical amplification by means of quartz tuning forks (QTF) [3–8] or cantilever [9–11] to detect the photoacoustic signal. Besides, amplification can also be achieved by application of an optical cavity [12, 13]. A simple form of such an optical cavity enhanced photoacoustic system is the Herriott cell, which has already been mentioned in section 2.2.5, or a White cell setup [14]. By increasing the light intensity within the illuminated sample the introduced heat and thus the detected pressure increases, as has been derived elaborately in the last sections.

Since the work bases on tube shaped PACs, this section will discuss resonance amplification based on the H-shaped geometry visualised in figure 2.19. Besides, phase sensitive detection of the amplified signal by means of lock-in amplification and the information provided by the phase will be addressed, too.

2.4.1 Acoustic resonance amplification

The PAC from figure 2.19 can be regarded as a one-dimensional two-side opened resonator tube. Literature provides a theoretical description of the applied cell design [15–18]. The following derivations are based on them and will be used to finally derive a term of the photoacoustic signal, i.e. the generated photoacoustic pressure $p_a(\vec{r}, \omega)$.

Figure 2.19 visualises a half cut sketch of one of the measurement cells applied within this thesis. It shows a tube-shape resonator enclosed by two buffer volumes.

The resonator can be considered one-dimensional, since its cross section is significantly smaller than the acoustic wavelength. As a consequence, the generated sound field develops a spatial variation in z-direction only [16]. A one-dimensional H-shaped resonator applied in PAS is characterised by two openings, where the length of the resonator L_{res} exceeds the diameter of the resonator $2r_{\text{res}}$. To compute the normal mode solutions $p_k(\vec{r})$ of the homogeneous wave equation, appropriate boundary conditions are required [15]. Thus, the walls of the resonator will be considered rigid

$$\nabla_{\perp} p(\vec{r})|_{r=r_{\text{res}}} = 0 \quad (2.114)$$

and the openings are considered to present zero acoustic impedance [17].

$$p(\vec{r})|_{z=0, L_{\text{res}}} = 0 \quad (2.115)$$

The resulting homogeneous wave equation is given by

$$\left[\Delta + \left(\frac{\omega_k^2}{c_s^2} \right) \right] p_k(\vec{r}) = 0 \quad (2.116)$$

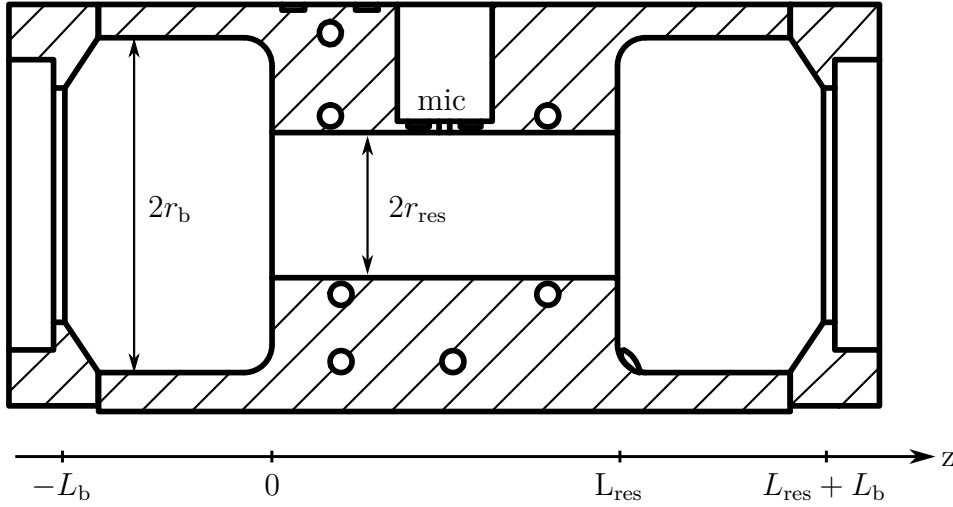


Fig. 2.19. Half cut drawing of one of the H-shaped PACs employed within this work. **mic** being the microphone positioned at $L_{\text{res}}/2$, r_b and L_b being the buffer radius and length, respectively. r_{res} and L_{res} being the resonator radius and length, respectively. The holes are the cross sections of the spiral gas stream within the PAC used for tempering the gas.

with ω_k being the angular frequency of the normal modes. A description of these modes can be found below. Neglecting losses, the normal mode solutions of equation 2.116 are orthonormal and thus can be normalised to the cell volume V_{res} by the normalisation condition given by [19]

$$\int p_i^*(\vec{r}) p_k(\vec{r}) = \delta_{ik} V_{\text{res}} \quad (2.117)$$

Using cylindrical coordinates and taking the orthogonality into account, different expressions can be derived for $p_k(\vec{r})$ using the Bessel* functions [20]. The results contain three different kinds of acoustic modes, which appear within tube-shaped cavities, namely radial (index \hat{u}), azimuthal (index \hat{v}) and longitudinal (index \hat{w}) [16]. The eigenfrequencies of these pressure modes are represented by

$$f_{\hat{u}\hat{v}\hat{w}} = \frac{c_s}{2} \sqrt{\left(\frac{\alpha_{\hat{u}\hat{v}}}{r_{\text{res}}}\right)^2 + \left(\frac{\hat{w}}{L_{\text{res}}}\right)^2} \quad (2.118)$$

with $\alpha_{\hat{u}\hat{v}}$ being the roots of derivatives of the Bessel functions divided by π . Tables for $\alpha_{\hat{u}\hat{v}}$ and a graphical visualisation of the radial and azimuthal modes are provided in the appendix A.1[†]. However, since the PACs within this work are all tube shaped, only the longitudinal resonance mode is considered, because both other modes are excited at significantly higher frequencies. Even for the PAC presented in figure 2.19 with the largest resonator diameter[‡], the frequencies $f_{100} \approx 41\,860$ Hz and $f_{010} \approx$

*Friedrich Wilhelm Bessel (1784 – 1846)

[†]Table A1 has been adopted from [21] and figure A1 has been adopted from [16].

[‡]The diameter $2r_{\text{res}} = 10$ mm and tube length $L_{\text{res}} = 31$ mm. $c_s = 343.2$ m s⁻¹ for dry air at 25 °C.

20 112 Hz are significantly higher than the longitudinal mode having its resonance frequency at $f_{001} \approx 5535$ Hz. Setting $\hat{u} = \hat{v} = 0$ simplifies equation 2.118 to

$$f_{\hat{w}} = \frac{\hat{w}c_s}{2L_{\text{res}}} \quad (2.119)$$

Applying $\lambda_s = c_s/f_{\hat{w}}$ results in the well-known longitudinal resonance criteria within a tube open on both ends

$$L_{\text{res}} = \hat{w} \frac{\lambda_s}{2} \quad (2.120)$$

However, empirical analysis has shown, that equation 2.119 has to be extended by means of an excess term called "end correction" term L_e [16].

$$f_{\hat{w}} = \frac{\hat{w}c_s}{2(L_{\text{res}} + L_e)} = \frac{\hat{w}c_s}{2(L_{\text{eff}})} \quad (2.121)$$

This effect is well-known by manufacturers of flutes and organ pipes. The reason is an effect called node shifting, which has been investigated in [16, 22] and [23, p. 80]. However, no universal valid excess term could be derived, hence the end correction had to be performed empirically for each cell design, which is demonstrated in section 5.1.4.1. The complexity of this phenomenon arises from different effects including [22]:

- The nodes of the standing pressure wave shift into the buffer volume.
- Furthermore, the buffer volumes of the H-shaped cell are considered infinite compared to V_{res} and decreasing the volumes counteracts longitudinal mode lengthening.
- Decreasing the pressure within the PAC results in lower longitudinal resonance frequencies, which was attributed to a mode lengthening due to less node shift resistance within the buffer volume (refer to section 5.1.4.1).
- The out-coupling hole in the middle of the resonator, connecting resonator with the microphone, has a compensating effect on the lengthening as well.
- Real gases do not show inherent pressure since they do not exhibit perfectly adiabatic behavior, hence, higher pressures result in an increase of c_s , at least at some extend, causing mode lengthening.
- Thermal and viscous boundary layer formation (refer to section 2.5.1) lead to a decreasing sound velocity resulting in less mode lengthening [24].

However, in order to proceed with the derivation of the resonance amplified photoacoustic signal, the effect of pressure node shifting will be disregarded. The acoustic

pressure $p_a(\vec{r}, \omega)$ can be represented by an expansion over all modes from $p_k(\vec{r})$ with the respective amplitude $A_k(\omega)$ [19]*:

$$p_a(\vec{r}, \omega) = \sum_k A_k(\omega) p_k(\vec{r}) \quad (2.122)$$

Considering $p_k(\vec{r})$, merging the equations 2.122 and 2.116 and substituting this result in equation 2.111 leads to a solution of the homogeneous wave equation [19]

$$A_k(\omega) = \underbrace{\frac{j}{\omega - \frac{\omega_k^2}{\omega}}}_{\text{resonance criterion}} \underbrace{\frac{\gamma - 1}{V_{\text{res}}} \int p_k^*(\vec{r}) \dot{H}(\vec{r}) dV}_{\text{overlap integral}} \quad (2.123)$$

The first term contains the resonance criterion and the last term the overlap integral, computing the coupling between the pressure mode $p_k^*(\vec{r})$ and the spatial part of the heat rate $\dot{H}(\vec{r})$. Since the first term of 2.123 and thus, the amplitude $A_k(\omega)$, becomes infinite for ω approaching ω_k the so far disregarded loss term has to be introduced. This is achieved by introducing a mode damping described by the quality factor Q_k of the k^{th} normal mode.

$$A_k(\omega) = \frac{j}{\omega - \frac{\omega_k^2}{\omega} + \underbrace{\frac{j\omega_k}{Q_k}}_{\text{loss term}}} \frac{\gamma - 1}{V_{\text{res}}} \int p_k^*(\vec{r}) \dot{H}(\vec{r}) dV \quad (2.124)$$

The physical interpretation of the quality factor Q_k is the ratio of accumulated and dissipated energy within one period of the acoustic oscillation [16].

$$Q_k = \frac{2\pi \text{ accumulated energy}}{\text{energy lost over one period}} \quad (2.125)$$

Another, rather simple representation of Q_k is[†]

$$Q_k = \frac{f_k}{\Delta f_{\text{FWHM}}} \quad (2.126)$$

with f_k being the resonance frequency of the mode k . A description of different loss effects can be found in section 2.5.

In order to derive the relation between photoacoustic signal and optical power, the heat rate presented in 2.124 has to be replaced by the light intensity term from equation 2.90 yielding to [19]

$$A_k(\omega) = \frac{j}{\omega - \frac{\omega_k^2}{\omega} + \frac{j\omega_k}{Q_k}} \frac{(\gamma - 1)\rho\sigma_A(\tilde{\nu})}{V_{\text{res}}} \int p_k^*(\vec{r}) I_0(\vec{r}) dV \quad (2.127)$$

*Note that the index k is used to represent all possible modes including radial, azimuthal and longitudinal modes.

[†]The Δ is actually a Greek Delta and not a Laplace operator.

Since the light intensity $I_0(\vec{r})$ is the product of the optical power P_0 and the normalised spatial distribution of the light beam intensity $G_{I_0}(\vec{r})$ [17], equation 2.127 can be rewritten to

$$A_k(\omega) = \frac{j}{\omega - \frac{\omega_k^2}{\omega} + \frac{j\omega_k}{Q_k}} \frac{(\gamma - 1)\rho\sigma_A(\tilde{\nu})P_0}{V_{\text{res}}} \int p_k^*(\vec{r})G_{I_0}(\vec{r})dV \quad (2.128)$$

Assuming a Gaussian intensity distribution (refer to 2.60), which does not change while the beam propagates through the PAC, the integral term can be rewritten to [17]

$$\int p_k^*(\vec{r})G_{I_0}(\vec{r})dV = L_{\text{res}}I_k = L_{\text{res}}p_k e^{-\eta_k} \quad (2.129)$$

where p_k is a normalisation coefficient, which is represented by

$$p_k = \sqrt{\frac{\xi_{\hat{u}\hat{w}}}{1 - \left(\frac{\hat{u}}{\pi\alpha_{\hat{u}\hat{v}}}\right)^2}} \frac{1}{J_{\hat{u}}(\pi\alpha_{\hat{u}\hat{v}})} \quad (2.130)$$

with $\xi_{00} = 1$, $\xi_{01} = \xi_{10} = 2$ and $\xi_{\hat{u}\hat{w}} = 4$ for $\hat{u} + \hat{w} > 1$ with $k \in [\hat{u}, \hat{v}, \hat{w}]^*$. $J_{\hat{u}}(\pi\alpha_{\hat{u}\hat{v}})$ is the Bessel function of the \hat{u}^{th} order at the position $\pi\alpha_{\hat{u}\hat{v}}$. Since $\pi\alpha_{\hat{u}\hat{v}}$ is the \hat{v}^{th} root of the derivative of the \hat{u}^{th} Bessel function, it represents the maximum or minimum of the respective Bessel function. Values for $\pi\alpha_{\hat{u}\hat{v}}$ can be found in the appendix A.1. Hence, $\hat{w} = 1$ and $\hat{u} = \hat{v} = 0$ results in $p_{001} = \sqrt{2}$ and for all higher longitudinal modes $p_{00\hat{w}} = 2$ with $\hat{w} = 2, 3, 4, \dots$ applies. The solutions of the first radial and first azimuthal modes yield to $J_1(\pi\alpha_{10}) \approx 0.581$ and $J_0(\pi\alpha_{01}) \approx -0.4026$ [25, p. 895], respectively. This results in $p_{100} = 2.89$ and $p_{010} = -2.48$.

η_k is the reciprocal coupling factor specifying the strength of light-to-sound[†] coupling. Figure 2.20 visualises the resulting overlap integral (red hatch) with the first longitudinal pressure mode for two different laser beam diameters d_b . The blue hatch represents η_k , where $\eta_k = 0$ is the optimum coupling. Perfect coupling is achieved, when all laser light is illuminating only the pressure mode inside the resonator and no further volume. The addition of L_{res} is due to the fact that $G_{I_0}(\vec{r})$ only depends on dy and dx , since it describes the cross sectional intensity profile of the laser beam. This means the profile does not change, while the beam propagates in z -direction, at least for $0 \leq z \leq L_{\text{res}}$ [22]. I_k can be referred to as the coupling integral describing the normalised efficiency of the sound-to-light energy transfer. Inserting 2.129 into 2.128 results in

$$A_k(\omega) = \frac{j}{\omega - \frac{\omega_k^2}{\omega} + \frac{j\omega_k}{Q_k}} \frac{(\gamma - 1)\rho\sigma_A(\tilde{\nu})P_0 L_{\text{res}}}{V_{\text{res}}} p_k e^{-\eta_k} \quad (2.131)$$

*Where \hat{w} is the longitudinal, \hat{u} is the radial and \hat{v} the azimuthal mode.

[†]Note that "light-to-sound coupling" can be somehow misleading as it could be interpreted as a factor solely describing the ratio of light energy being transferred into sound energy, which is not the case.

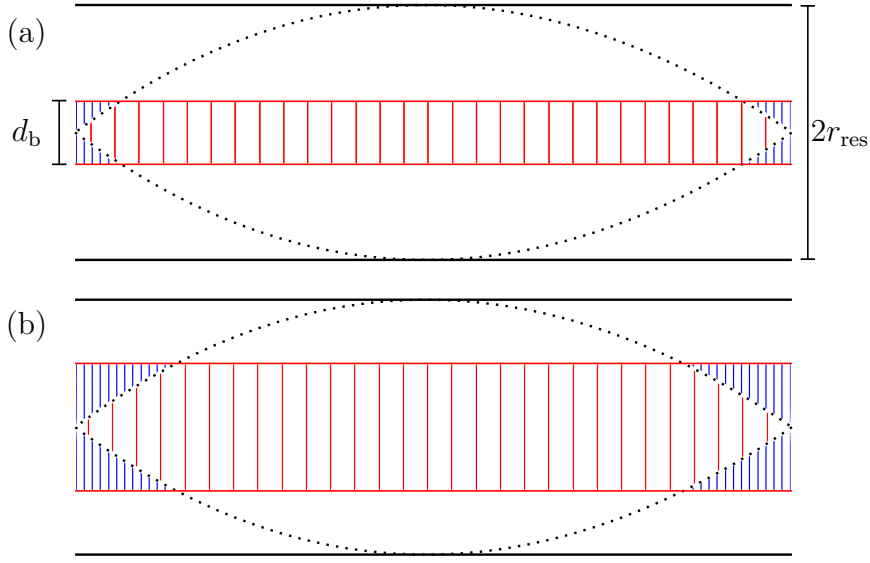


Fig. 2.20. Visualisation of the overlap integral and reciprocal coupling factor η_k for two different laser beam diameters d_b . Red stripes visualise the overlap of the laser light (red) with the first longitudinal pressure mode (dotted lines). η_k represents the volume indicated by the blue hatch. $\eta_k = 0$ represents the optimum case, where the blue hatched volume is zero.

For the resonant case with $\omega = \omega_k$ 2.128 can be rewritten to

$$A_k(\omega) = \frac{Q_k}{\omega_k} (\gamma - 1) \frac{L_{\text{res}}}{V_{\text{res}}} \rho \sigma_A(\tilde{\nu}) P_0 p_k e^{-\eta_k} \quad \text{with} \quad p_k e^{-\eta_k} = I_k \quad (2.132)$$

An optimum in light-to-sound coupling is obtained, when the reciprocal coupling factor η_k can be considered $\eta_k \ll 1$, since this yields to $e^{-\eta_k} = 1$. Besides, the spatial distribution of the pressure modes $p_k(\vec{r})$ is dependent on the z -position within the tube shaped resonator. In case of the first longitudinal* mode excitation, $p_k(\vec{r})$ can be represented by a sinusoidal half-wave ranging from 0 to 1

$$p_k(\vec{r}) = p_1(z) = \sin\left(z \frac{\pi}{L_{\text{res}}}\right) \quad z \in [0, L_{\text{res}}] \quad (2.133)$$

Thus, for $z = \frac{L_{\text{res}}}{2} = z_{\text{mic}}^\dagger$, the spatial distribution $p_k(\vec{r}) = 1$. In order to obtain a final expression for the photoacoustic signal, the aforementioned conditions (e.g. $\eta_k \ll 1$ and $p_1 = \sqrt{2}$) are applied and equation 2.132 is merged with equation 2.122 yielding to

$$p_a(z_{\text{mic}}, \omega_1) = (\gamma - 1) \underbrace{\frac{Q_1 L_{\text{res}}}{\omega_1 V_{\text{res}}}}_{\text{cell constant}} \sqrt{2} \rho \sigma_A(\tilde{\nu}) P_0 \quad (2.134)$$

From equation 2.134, improvements regarding trace gas analysis by means of PAS can be derived. It is suggested to [22]

*Since only longitudinal modes will be considered in the rest of this thesis, it will be represented by a single index, e.g. 1 instead of 001.

†This is the z -position where the outcoupling hole, guiding the sound to the microphone, is placed.

- exploit molecular transitions with strong ACS $\sigma_A(\tilde{\nu})$ and minimize spectral overlapping to avoid cross sensitivities.
- Use light sources with high output power*,
- employ cells with high quality factors† and
- use PACs with small resonator cross sections‡.
- A compromise between a small cell volume§, a long resonator length, miniaturisation and low resonance frequency has to be found.
- Effective sound-to-light coupling has to be considered by illuminating the pressure waves' anti nodes.

Regarding application of non-resonant photoacoustic spectroscopy, where $\omega_0 = 0$ and the pressure variation can be considered uniform, the amplitude of the acoustic wave is represented by

$$A_0(\omega) = \frac{j}{\omega}(\gamma - 1) \frac{L_{\text{res}}}{V_{\text{res}}} \rho \sigma_A(\tilde{\nu}) P_0 \quad (2.135)$$

In this case, the sound wavelength is larger compared to the cell dimension, since the modulation frequency is significantly smaller than the lowest resonance frequency. Thus, no standing wave is formed. The advantage of a non-resonant system is the low susceptibility towards resonance frequency detuning. However, compared to the resonant system described with 2.132, the sensitivity can be significantly lower. The ratio is given by¶

$$\left| \frac{A_1(\omega_1)}{A_0(\omega)} \right| = \frac{\omega}{\omega_1} p_1 Q_1 \quad (2.136)$$

Therefore, resonant systems can be driven at higher frequencies and the quality factor mainly influences the gain of a resonant system.

2.4.2 Lock-in amplification

Lock-in amplification is based on phase sensitive demodulation (PSD) of an acquired measurement signal and a reference signal, whereby both signals must have the same frequency. Therefore, phase sensitive detection is only possible, if the frequency of the signal of interest is known.

*But the limits from 2.79 still have to be respected.

†Avoid frequency detuning, which will be discussed in section 2.5.5.

‡The finite laser beam diameter has to be considered, too, since light interacting with the cell walls can cause unwanted background signal.

§Assuming a completely illuminated resonator volume, a small volume has also the drawback of less total analyte molecules present, which could absorb light and contribute to the PAS signal.

¶Note that $|j| = 1$ applies.

In PAS, the detected acoustic signal can be orders of magnitude smaller compared to the noise superimposing it, no matter whether AM-PAS or WM-PAS is performed. Thus, lock-in amplification or similar signal processing is employed in virtual every PAS application. Since the modulation frequency of the laser specifies the resulting frequency of the acoustic wave, the frequency of interest within the acquired photoacoustic signal is known and therefore, can be used as reference signal for the LIA.

A lock-in amplifier, sometimes also referred to as lock-in filter, can be considered a very small bandpass filter with a high quality factor (refer to 2.126). In addition, a lock-in amplifier provides the phase difference between both, the reference and measured signal, where this phase can contain useful information. The fundamentals of lock-in amplification will be discussed hereinafter, however, detailed theoretical considerations can be found elsewhere [26, 27].

Figure 2.21 visualises the functional principle of dual-phase lock-in amplification. This type of LIA is referred to as dual-phase, since the signal is multiplied with the sine and cosine of a frequency equal to the measured signal frequency, respectively. The resulting signals are called quadrature and in-phase signal. Considering the in-phase signal processing first, the result of the phase sensitive demodulation is given by the product of reference $u_{r,i}(t)$ signal and photoacoustic signal $u_s(t)$

$$u_i(t) = u_s(t) \cdot \hat{u}_r \cos(\omega_r t + \phi_r) \quad \text{with} \quad u_s(t) = \hat{u}_s \cos(\omega_s t + \phi_s) \quad (2.137)$$

This yields to

$$u_i(t) = \hat{u}_s \hat{u}_r \frac{1}{2} [\cos((\omega_r - \omega_s)t + (\phi_r - \phi_s)) + \cos((\omega_r + \omega_s)t + (\phi_r + \phi_s))] \quad (2.138)$$

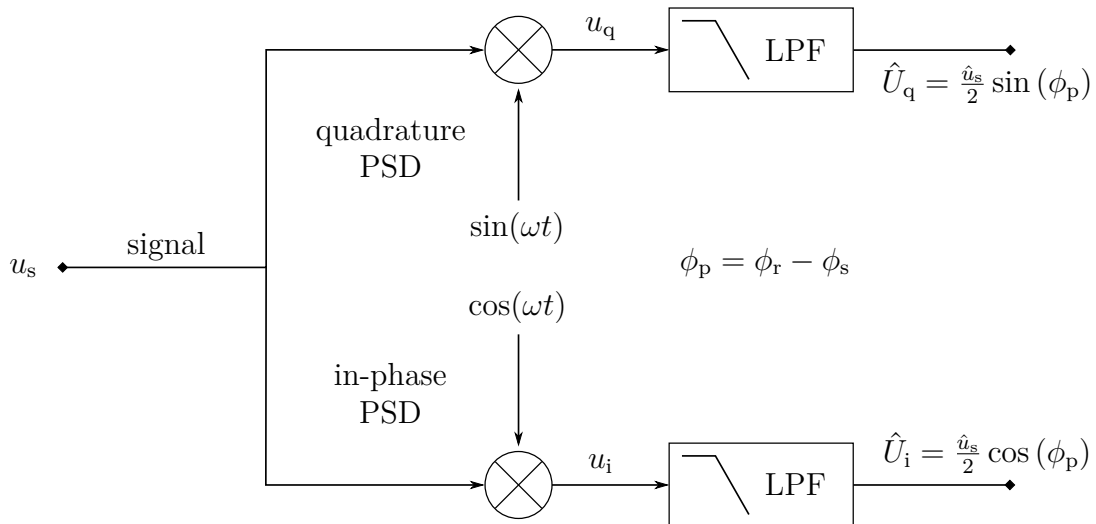


Fig. 2.21. Sketch of the functional principle of a dual-phase lock-in amplifier after [22]. u_s is the noise covered AC signal, u_i is the in-phase signal, u_q is the quadrature signal, \hat{U}_i is the filtered DC in-phase signal and \hat{U}_q is the filtered DC quadrature signal. **PSD** - phase sensitive detection, **LPF** - low-pass filter.

and with $\omega_r = \omega_s = \omega_{\text{mod}}$ equation 2.138 can be rewritten to

$$u_i(t) = \underbrace{\frac{\hat{u}_s \hat{u}_r}{2} \cos(\phi_r - \phi_s)}_{\text{DC term}} + \underbrace{\frac{\hat{u}_s \hat{u}_r}{2} \cos(2\omega_{\text{mod}}t + \phi_r + \phi_s)}_{\text{AC term}} \quad (2.139)$$

The phase sensitive modulation has split the energy stored within the periodic photoacoustic signal into two parts. A DC and an AC component, where the latter one can be simply removed by means of a low-pass filter. Eliminating the known amplitude of the reference signal \hat{u}_r , the resulting amplitude of the in-phase signal is

$$\hat{U}_i = \frac{\hat{u}_s}{2} \cos \phi_p \quad \text{with} \quad \phi_p = \phi_r - \phi_s \quad (2.140)$$

The quadrature channel signal processing is equal to that of the in-phase channel, but the reference signal is shifted by 90° . Thus, $u_{r,q}(t) = \hat{u}_r \sin(\omega_r t + \phi_r)$. The low-pass filtered quadrature signal is presented by

$$\hat{U}_q = \frac{\hat{u}_s}{2} \sin \phi_p \quad (2.141)$$

The photoacoustic amplitude has to be reconstructed from the in-phase and quadrature signal as follows

$$\hat{u}_s = 2\sqrt{\hat{U}_q^2 + \hat{U}_i^2} = \frac{2\hat{u}_s}{2} \underbrace{\sqrt{\sin^2 \phi_p + \cos^2 \phi_p}}_{=1} \quad (2.142)$$

As mentioned before, the LIA also provides the phase difference between reference and signal. It can be obtained by

$$\frac{\hat{U}_q}{\hat{U}_i} = \frac{\sin \phi_p}{\cos \phi_p} = \tan \phi_p \quad \Rightarrow \quad \phi_p = \arctan \left(\frac{\hat{U}_q}{\hat{U}_i} \right) \quad (2.143)$$

The noise suppression performance of the LIA and the resulting response time of the measurement system is determined by the roll-off in dB/decade and the lock-in time constant τ_{LIA} of the low-pass filter. For a field quantity like voltage or pressure, the gain in *quasi*-unit dB (decibel) is defined as

$$G_{\text{dB},f} = 20 \cdot \log \frac{\hat{F}_1}{\hat{F}_0} \quad (2.144)$$

with \hat{F}_1 being the amplitude before amplification (or attenuation) and \hat{F}_0 being the initial amplitude of a field quantity. For power quantities the gain $G_{\text{dB},p}$ is defined after

$$G_{\text{dB},p} = 10 \cdot \log \frac{\hat{P}_1}{\hat{P}_0} \quad (2.145)$$

For a filter, the cut-off frequency f_c defines, where half of the power (or $\frac{1}{\sqrt{2}}$ of a field quantity) of a signal is still remaining. According to 2.145 this refers to -3 dB.

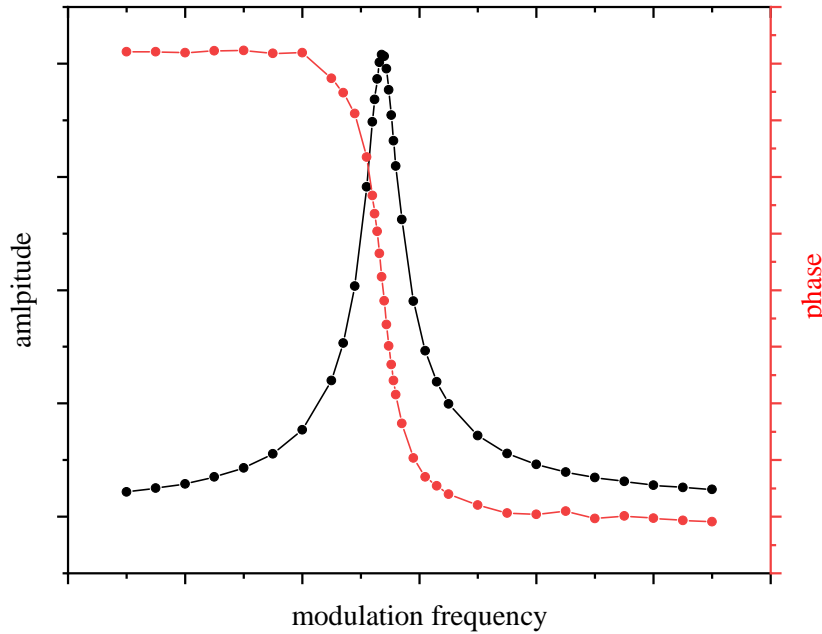


Fig. 2.22. Typical course of the phase during a frequency sweep.

Therefore this frequency is also referred to as -3 dB cut-off frequency. The cut-off frequency is linked to the time constant τ_{LIA} by

$$f_c = \frac{1}{2\pi\tau_{LIA}} \quad (2.146)$$

The roll-off of a filter determines the slope of the filter curve usually within a logarithmic scale, commencing after the cut-off frequency. In general, the slope depends on the order of the applied filter. A first order low-pass filter has 20 dB/decade, whereas a filter of the second order has 40 dB/decade. Sometimes the slope is specified in units of dB/octave, as well, where 20 dB/decade equals 6 dB/octave. Since the noise level is direct proportional to the bandwidth of the acquired signal, reducing the bandwidth is crucial considering noise reduction. Thus, in order to increase the SNR, high time constants and a high roll-off are preferable. However, by increasing the time constant τ_{LIA} the response time t_{90}^* of the system increases after the following relation

$$t_{90} \approx 2.3\tau_{LIA} \quad (2.147)$$

Hence, a trade-off has to be made between repsonsitivity of the system and noise suppression.

* t_{90} is the time, a system in the equilibrium state needs to reach 90 % of the final value induced by a stimulus.

Besides the amplitude, the phase provided by the lock-in amplifier can be of interest as well. It is defined by 2.143 and describes the phase shift between the reference and photoacoustic signal. In other words, it characterises the time between the quasi-instant excitation due to absorption and the impingement of the resulting acoustic pressure on the microphone membrane. Figure 2.22 visualises the course of the phase signal during a frequency sweep measurement. At the resonance frequency, the condition $\left| \frac{\partial \phi_p}{\partial \omega_{\text{mod}}} \right| = \max$ is valid. Besides, for a specific photoacoustic cell, the phase of the signal is stable as long as the modulation frequency equals the resonance frequency. This remains valid, even if the resonance frequency itself changes, e.g. due to changing c_s . By implication, this means that the phase is very sensitive when $f_{\text{mod}} = f_{\text{res}}$ and even minor resonance detuning (see section 2.5.5) can be detected easily.

Furthermore, the phase can be used to investigate relaxation times or to detect changes of the relaxation time during a measurement, induced by changes of the main gas mixture components [28–30].

In addition, the phase can be used for vector based offset correction, too. However, since this work does not apply this type of offset correction it is not further discussed, but has been explained in detail elsewhere [22].

References

- [1] Z. Shen-long et al. “Application of Photoacoustic Spectroscopy in Multi-component Gas Concentration Detection”. In: *ACTA PHOTONICA SINICA* 46.6 (2017), p. 612002. ISSN: 1004-4213. DOI: 10.3788/gzxb20174606.0612002 (cit. on p. 87).
- [2] J. J. Zhao et al. “Macro Machined Photoacoustic Non-Resonant Cell”. In: *Key Engineering Materials* 483 (June 2011), pp. 411–416. ISSN: 1662-9795. DOI: 10.4028/www.scientific.net/KEM.483.411 (cit. on p. 87).
- [3] Y. Ma et al. “QEPAS based ppb-level detection of CO and N₂O using a high power CW DFB-QCL”. In: *Optics Express* 21.1 (2013), p. 1008. ISSN: 1094-4087. DOI: 10.1364/OE.21.001008 (cit. on p. 87).
- [4] L. Dong et al. “QEPAS spectrophones: Design, optimization, and performance”. In: *Applied Physics B: Lasers and Optics* 100.3 (2010), pp. 627–635. ISSN: 09462171. DOI: 10.1007/s00340-010-4072-0 (cit. on p. 87).
- [5] R. Lewicki et al. “A Compact CW Quantum Cascade Laser based QEPAS Sensor for Sensitive Detection of Nitric Oxide”. In: *Conference on Lasers and Electro-Optics 2012* 1 (2012). DOI: 10.1364/CLEO_SI.2012.CW3B.4 (cit. on p. 87).

- [6] L. Dong et al. “Compact portable QEPAS multi-gas sensor”. In: *Proc. SPIE* 2011 7945 (2011), 79450R. ISSN: 0277786X. DOI: 10.1117/12.875108 (cit. on p. 87).
- [7] L. Dong et al. “Compact QEPAS sensor for trace methane and ammonia detection in impure hydrogen”. In: *Applied Physics B: Lasers and Optics* 107.2 (2012), pp. 459–467. ISSN: 09462171. DOI: 10.1007/s00340-012-4908-x (cit. on p. 87).
- [8] S. Schilt et al. “Performance evaluation of a near infrared QEPAS based ethylene sensor”. In: *Applied Physics B: Lasers and Optics* 95.4 (2009), pp. 813–824. ISSN: 09462171. DOI: 10.1007/s00340-008-3306-x (cit. on p. 87).
- [9] J. Peltola et al. “High sensitivity trace gas detection by cantilever-enhanced photoacoustic spectroscopy using a mid-infrared continuous-wave optical parametric oscillator”. In: *Optics Express* 21.8 (2013), p. 10240. ISSN: 1094-4087. DOI: 10.1364/OE.21.010240 (cit. on p. 87).
- [10] J. Peltola et al. “Parts-per-trillion-level detection of nitrogen dioxide by cantilever-enhanced photo-acoustic spectroscopy”. In: *Optics Letters* 40.13 (2015), p. 2933. ISSN: 0146-9592. DOI: 10.1364/OL.40.002933 (cit. on p. 87).
- [11] C. B. Hirschmann et al. “Trace gas detection of benzene, toluene, p-, m- and o-xylene with a compact measurement system using cantilever enhanced photoacoustic spectroscopy and optical parametric oscillator”. In: *Vibrational Spectroscopy* 68 (2013), pp. 170–176. ISSN: 09242031. DOI: 10.1016/j.vibspec.2013.07.004 (cit. on p. 87).
- [12] M. Hippler et al. “Cavity-enhanced resonant photoacoustic spectroscopy with optical feedback cw diode lasers: A novel technique for ultratrace gas analysis and high-resolution spectroscopy”. In: *The Journal of Chemical Physics* 133.4 (July 2010), p. 044308. ISSN: 0021-9606. DOI: 10.1063/1.3461061 (cit. on p. 87).
- [13] T. Tomberg et al. “Cavity-enhanced cantilever-enhanced photo-acoustic spectroscopy”. In: *The Analyst* 144.7 (2019), pp. 2291–2296. ISSN: 0003-2654. DOI: 10.1039/C9AN00058E (cit. on p. 87).
- [14] K. Krzempek et al. “Multi-pass cell-assisted photoacoustic/photothermal spectroscopy of gases using quantum cascade laser excitation and heterodyne interferometric signal detection”. In: *Applied Physics B* 124.5 (May 2018), p. 74. ISSN: 0946-2171. DOI: 10.1007/s00340-018-6941-x (cit. on p. 87).
- [15] A. Miklós et al. “Photoacoustic Spectroscopy, Theory”. In: *Encyclopedia of Spectroscopy and Spectrometry*. Elsevier, 1999, pp. 1815–1822. DOI: 10.1006/rwsp.2000.0234 (cit. on p. 87).
- [16] A. Miklós et al. “Application of acoustic resonators in photoacoustic trace gas analysis and metrology”. In: *Review of Scientific Instruments* 72.4 (Apr. 2001), pp. 1937–1955. ISSN: 0034-6748. DOI: 10.1063/1.1353198 (cit. on pp. 87–90).

- [17] J.-P. Besson. “Photoacoustic spectroscopy for multi-gas sensing using near infrared lasers”. Ph. D. thesis. University of Lausanne, 2006 (cit. on pp. 87, 91).
- [18] M. Mattiello. “Gas Traces Measurement by Photoacoustic Spectroscopy Using Helmholtz Resonator-Based Sensors”. Ph. D. thesis. University of Lausanne, 2008 (cit. on p. 87).
- [19] L. Kreuzer. “The Physics of Signal Generation and Detection”. In: *Optoacoustic spectroscopy and detection*. New York: Academic Press, 1977, pp. 1–25. ISBN: 9780323158817 (cit. on pp. 88, 90).
- [20] A. V. Masurkar. “Extensions of quartz-enhanced photoacoustic spectroscopy”. Ph. D. thesis. Massachusetts Institute of Technology, 2009 (cit. on p. 88).
- [21] J. P. Besson. “Photoacoustic spectroscopy for multi-gas sensing using near infrared lasers”. PhD thesis. Lausanne: EPF Lausanne, 2006, pp. 1–189. DOI: 10.5075/epfl-thesis-3670 (cit. on p. 88).
- [22] T. Rück. “Development, characterization and miniaturization of a trace gas detection system for NO₂ in air based on photoacoustic spectroscopy”. Ph. D. thesis. University of Regensburg, 2017 (cit. on pp. 89, 91, 92, 94, 97).
- [23] S. W. Rienstra and A. Hirschberg. *An Introduction to Acoustics*. Eindhoven, 2004 (cit. on p. 89).
- [24] R. H. Johnson et al. “Loss mechanisms in resonant spectrophones”. In: *Applied Optics* 21.1 (Jan. 1982), p. 81. ISSN: 0003-6935. DOI: 10.1364/AO.21.000081 (cit. on p. 89).
- [25] P. M. Morse and K. U. Ingard. *Theoretical Acoustics*. McGraw Hill Book Company, 1968. ISBN: 9780691024011 (cit. on p. 91).
- [26] L. A. Barragán et al. “A modular, low-cost, digital signal processor-based lock-in card for measuring optical attenuation”. In: *Review of Scientific Instruments* 72.1 (Jan. 2001), pp. 247–251. ISSN: 0034-6748. DOI: 10.1063/1.1333046 (cit. on p. 94).
- [27] M. Sonnaillon et al. “Implementation of a high-frequency digital lock-in amplifier”. In: *Canadian Conference on Electrical and Computer Engineering*. IEEE, 2005, pp. 1229–1232. ISBN: 0-7803-8885-2. DOI: 10.1109/CCECE.2005.1557199 (cit. on p. 94).
- [28] T. L. Cottrell et al. “Measurement of vibrational relaxation times by the spectrophone. Application to CH₄, CO₂, N₂O, COS, NH₃ and HCN”. In: *Transactions of the Faraday Society* 62 (1966), p. 2655. ISSN: 0014-7672. DOI: 10.1039/tf9666202655 (cit. on p. 97).
- [29] M. Huetz-Aubert et al. “Phase-Lag Equation for CO₂ in a Spectrophone and Its Application to Deducing the Predominant Vibration–Vibration Transitions”. In: *The Journal of Chemical Physics* 54.5 (Mar. 1971), pp. 2289–2291. ISSN: 0021-9606. DOI: 10.1063/1.1675175 (cit. on p. 97).

- [30] B. Lang et al. “Molecular relaxation effects on vibrational water vapor photoacoustic spectroscopy in air”. In: *Applied Physics B* 126.4 (Apr. 2020), p. 64. ISSN: 0946-2171. DOI: 10.1007/s00340-020-7409-3 (cit. on p. 97).

2.5 Attenuation effects

In section 2.2.5, the advantages of photoacoustic spectroscopy compared to other absorption spectroscopy techniques have been highlighted. This section, however, will deal with the drawbacks of PAS evoked by effects introduced by certain buffer gas components. In addition, the quality factor will be addressed and different relaxation processes and pathways as well as their influence on the resulting photoacoustic signal will be summarised, too.

2.5.1 The photoacoustic quality factor

The Q-factor is a measure for the amount of acoustic energy loss per heat generation cycle in a photoacoustic system (refer to equation 2.125). In photoacoustics, there are several effects resulting in energy dissipation due to non-ideal conditions. In general, they can be separated into volumetric losses and boundary losses [1, 2][3, pp. 13]. Volumetric losses can be separated into [2]

- relaxation losses of excited states*
- effects from radiation,
- diffusion effects,
- free-space viscous dissipation
- and thermal dissipation in free-space.

Friction induced by compression motion yields viscous losses. Besides, the volumetric thermal losses are due to the transfer of organised energy into dispersed heat resulting from the temperature gradients within the gas volume. These phenomena are called the Stokes-Kirchhoff[†] losses and account for an insignificant amount of energy dissipation. Contrary to that, relaxation processes can have a perceptible influence on the dissipation of energy [2].

Losses due to the interactions between the standing acoustic wave and the internal chamber surfaces account for a large part of the dissipated energy, too. These loss mechanism can be categorised after [2]:

- dissipation at the microphone,
- wave reflection losses resulting from the compliance of the chamber walls,

*This includes only relaxation losses causing the acoustic energy to dissipate, i.e. molecular attenuation (refer to 2.5.4).

[†]Gustav Kirchhoff (1824 – 1887)

- losses due to wave scattering at surface obstructions like gas inlet and optical components as well as
- thermal and viscous dissipation inside the boundary layers at the smooth inner surfaces.

As a consequence of the surface losses, a PAC with low energy dissipation has to be designed carefully. As an example, the material should be rigid to avoid reflection losses and have a low thermal conductivity. Besides, increasing the acoustic impedance at the openings can decrease radiation losses. This can be achieved by acoustic bandstop filters terminating the cavity resonator [4].

Viscous and thermal losses can be expressed in terms of temperature and velocity gradients close to the walls of the PAC. Within the volume, the periodic expansion and contraction of the gas occurs nearly adiabatically. However, at the boundaries, the process is isothermal due to the thermal conductivity of the PAC material. The layer, where the expansion of the gas can occur isothermally or adiabatically is called the thermal boundary layer [1]. The thickness of this layer can be calculated via [5, p. 286]

$$d_{k,T} = \sqrt{\frac{2k_T}{\tilde{\rho}\omega_k C_p}} \quad (2.148)$$

with $\tilde{\rho}$ being the volume density of the gas.

The tangential vector of the acoustic velocity is zero at the surface due to the viscosity η_s [1]. Within the volume, however, the vector is proportional to the gradient of the acoustic pressure (refer to 2.95). The losses occur in the so called viscous boundary layer, whose thickness is given by [5, p. 286]

$$d_{k,V} = \sqrt{\frac{2\eta_s}{\tilde{\rho}\omega_k}} \quad (2.149)$$

From the equations 2.148 and 2.149 it can be derived, that the losses decrease with higher frequencies. At standard conditions in air, the thickness of both layers is similar [5, p. 286]. Besides, radial modes do not suffer from viscosity losses since they do not have a tangential velocity but only a radial one. Therefore, carefully designing spherical resonators can result in extremely high quality factors of 2000 – 10000 [6]. However, section 2.5.5 demonstrates, that high quality factors are not always preferable.

The final quality factor of a PAC is given by

$$\frac{1}{Q_k} = \frac{1}{Q_{k,s}} + \frac{1}{Q_{k,V}} \quad (2.150)$$

with $Q_{k,s}$ and $Q_{k,v}$ being the surface quality factor and the volumetric quality factor of the normal modes k , respectively.* The latter one can be computed after [7]

$$\frac{1}{Q_{k,v}} = \frac{\omega_k}{2c_s^2} \left[\frac{4}{3} \frac{\eta_s}{\tilde{\rho}} + (\gamma - 1) \frac{k_T}{\tilde{\rho} C_p} + \frac{\eta_b}{\tilde{\rho}} \right] \quad (2.151)$$

The surface losses for the first longitudinal acoustic mode are given by[†] [8]

$$\frac{1}{Q_{k,s}} = \frac{1}{r_{\text{res}}} \left[d_{k,v} + (\gamma - 1) d_{k,T} \left(1 + \frac{2r_{\text{res}}}{L_{\text{res}}} \right) \right] \quad (2.152)$$

Since the quality factor is also represented by $\frac{f_k}{f_{\text{FWHM}}}$ literature sometimes assigns losses of a PAS system to the FWHM or HWHM of a photoacoustic frequency sweep curve. A typical frequency sweep curve is visualised in figure 2.22. An overview of the different losses and their share of the half-width of a PAS system is visualised for a system detecting different relaxation processes in SF₆ [9].

2.5.2 Nonradiative relaxation

The periodic heat influx, introduced into the system by modulated light, is the fundamental requirement for the generation of a photoacoustic signal. Chemical reaction or radiative relaxation as a consequence of absorption are counterproductive effects regarding optimal conversion from light energy into pressure. Thus, nonradiative relaxation with a transfer from ro-vibronic or ro-vibrational energy into translational (kinetic) energy is necessary for the excited state to contribute to the photoacoustic signal. However, the lifetime of the excited state is an important quantity as well. If the relaxation time is too long (refer to equation 2.77) regarding a specific modulation frequency ω_{mod} the stored energy will not be released in time and thus cannot completely contribute to the photoacoustic signal.

Therefore, it is important to understand what kind of relaxation processes exist[‡] and how long the corresponding lifetimes are. Radiative relaxation by means of phosphorescence or fluorescence usually occur after excitation of valence electrons in the UV or visible wavelength region. The lifetime of a radiative decay in the visible region is about 100 ns[§]. Since the quantum yields of these two effects are very low for acetone excitation in the 278 nm region [10], they can be neglected in terms of photoacoustic acetone detection. However, these effects should be kept in mind for analysis of other species in this wavelength region. Radiative decay can

*A short description of the relations between different viscosities is provided in appendix A.2.

[†]In order to reproduce the derivation provided in [8] equation 2.119 has to be applied. Note that the index k representing all modes is kept as index in equation 2.152, although the surface losses of the first longitudinal mode are discussed.

[‡]Note that ISC and IC processes will not be discussed again. For information refer to the end of section 2.2.1.

[§]Lifetime of phosphorescence processes is usually significantly longer.

also occur in the infrared region for excited rotational or vibrational states. Since the lifetime for spontaneous emission is indirect proportional to third power of the excited states energy $\tau_{\text{sp}} \propto \tilde{\nu}^{-3}$ (see 2.47), this time is quite long (0.01 – 1 s) [7]. Hence, considering the IR region the relaxation of excited ro-vibrational states of acetone will be dominated by collision induced relaxation at ambient conditions. For the UV region, chemical reactions by means of photolysis have to be considered as well. Photolysis of acetone will be addressed in 2.5.6.

Nonradiative relaxation by means of collision can lead to the following energy transfers:

- rotational-rotational relaxation
- rotational-translational (RT) relaxation
- vibrational-rotational relaxation
- vibrational-vibrational relaxation
- vibrational-translational relaxation

Since the energy stored in rotational excited states is small compared to excited vibrational energy levels, the first two listed relaxation processes can usually be neglected, if ro-vibrational or ro-vibronic excitation is considered. Especially, RR-relaxations are unimportant, since they are very inefficient [11]. In the case of vibrational-rotational relaxation where the vibrational energy of a state v from one collision partner is transferred to a high rotational level j^* of the other partner, with $E_{j^*} \approx E_v$ being valid, the energy stored in rotational states can get significant. In order to contribute to the photoacoustic signal, these states have to decay in a cascading collision processes. Although RT-transitions at higher rotational levels become progressively less efficient, the RT-relaxation times still tend to be significantly faster than VT-relaxation processes, and therefore, the RT heat release is efficient enough in order to contribute to the acoustic signal [11]. Note that absorption induced high rotational excited energy levels, where $E_{j^*} \approx E_v$ is valid, are very unlikely since the selection rule of $\Delta j = \pm 1$ applies and such high rotational levels like $j^* - 1$ are depleted at normal temperature conditions (see 2.15). As an example, Lei and Bartolo [9] investigated the RT-relaxation time in pure SF₆, the pressure dependent RT-relaxation time was $(p\tau_{RT}) = 0.09 \pm 0.06 \text{ ns atm}$ compared to $(p\tau_{VT}) = 0.21 \pm 0.01 \text{ } \mu\text{s atm}$ for the VT-relaxation. Based on these facts, RT-relaxations are usually not the dominant factor when the total lifetime of an excited state τ_e is considered.

2.5.2.1 VT-relaxation

Most important for photoacoustic signal generation are the VT relaxations, where the vibrational energy is transferred into kinetic energy. If the relaxation time of the

VT transfer process is too long, the corresponding energy exchange processes cannot respond fast enough anymore to contribute to the photoacoustic signal. This results in a loss of kinetic energy and thus diminishes the photoacoustic signal. Figure 2.23 (lower part) visualises the consequence of a modulation frequency exceeding the limit provided by the estimation from equation 2.77. The upper part demonstrates the case, when $f_{\text{mod},1} < f_{\text{max}}$ applies and all absorbed light energy is transferred into the volume as heat before the light is switched on again*.

Tab. 2.6. List of VT-relaxation times of species occurring in exhaled breath and at atmospheric pressure. The excited molecule is highlighted with an *. The indicated vibration types ν_2 for CO_2 and H_2O are the vibrations at energies of 2001 cm^{-1} and 1595 cm^{-1} , respectively [12].

Collision species	τ_{VT}	Ref.	Collision species	τ_{VT}	Ref.
$\text{N}_2^* + \text{N}_2$	1 s 1 ms 300 μs	[13] [14] [15]	$\text{CO}_2^*(\nu_2) + \text{CO}_2$	4.6 μs^\dagger 5.6 μs	[16] [13]
$\text{N}_2^* + \text{H}_2\text{O}$	9.1 μs	[13]	$\text{CO}_2^*(\nu_2) + \text{N}_2$	7 μs , 11 μs 29.4 μs	[17] [13]
$\text{N}_2^* + \text{O}_2$	1 s	[13]	$\text{CO}_2^*(\nu_2) + \text{H}_2\text{O}$	2 ns	[13]
$\text{N}_2^* + \text{CO}_2$	1 s	[13]	$\text{CO}_2^*(\nu_2) + \text{O}_2$	33.3 μs	[13]
$\text{O}_2^* + \text{O}_2$	15.9 ms 2 ms	[13] [15]	$\text{H}_2\text{O}^*(\nu_2) + \text{H}_2\text{O}$	37 ns 1 ns	[18] [13]
$\text{O}_2^* + \text{N}_2$	25 ms	[13]	$\text{H}_2\text{O}^*(\nu_2) + \text{N}_2$	714 ns	[13]
$\text{O}_2^* + \text{H}_2\text{O}$	910 ns	[13]	$\text{H}_2\text{O}^*(\nu_2) + \text{O}_2$	16.7 μs	[13]

VT-relaxation occur due to collision with surrounding molecules, thus, the relaxation times of the buffer matrix has to be considered regarding trace gas analysis. Table 2.6 lists the VT-relaxation time of species occurring in the measurement matrix of breath.

Striking are the long relaxation times due to quenching of N_2 and O_2 , hence collision induced vibrational excitation of these two species by means of VV energy transfer can alter the systems relaxation time significantly. However, the VT-relaxation times of $\text{H}_2\text{O}^*(\nu_2)$ and $\text{CO}_2^*(\nu_2)$ are sufficiently fast enough to cause none or only minor losses at a modulation frequency of 5000 Hz. These considerations demonstrate the effects of buffer molecules, which have to be taken into account regarding signal generation.

*This is the case for AM-PAS. For WM-PAS, the shape of both curves would be rather sinusoidal.

† At 21 °C and 600 Torr

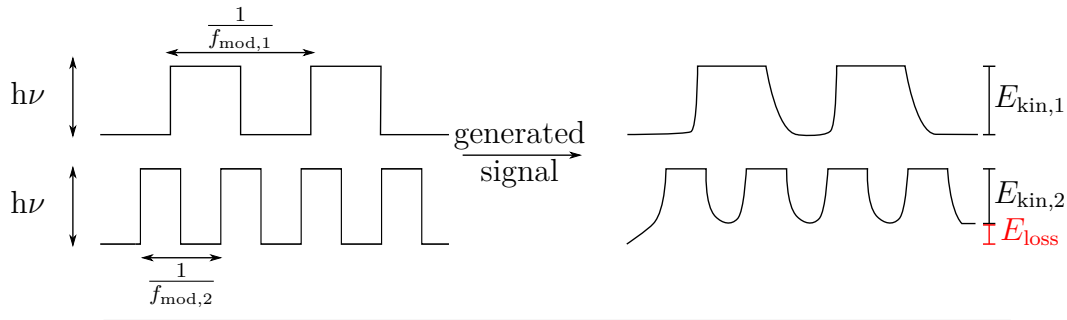


Fig. 2.23. Illustration of the loss of energy E_{loss} due to exceeding the maximum modulation frequency after [19]. $h\nu$ is the initial photon energy introduced into the system, E_{kin} is the resulting kinetic energy and f_{mod} is the applied modulation frequency.

When the particle number density of the major components and their corresponding relaxation times are known, the total relaxation time for a species i can be calculated after [19]

$$\frac{1}{\tau_i} = \rho_i \frac{1}{\tau_{ii}} + \rho_m \frac{1}{\tau_{im}} + \rho_j \frac{1}{\tau_{ij}} \quad (2.153)$$

within a gas matrix containing the species i , j and m . This can be useful to estimate the maximum modulation frequency, which is an important parameter in cell design. In order to quantify the energy loss E_{loss} from figure 2.23 due to slow relaxation processes, a new quantity called conversion efficiency η_c is introduced and is given by

$$\eta_c = \frac{1}{\sqrt{1 + (\omega_{\text{mod}}\tau_e)^2}} \quad (2.154)$$

For small $\omega_{\text{mod}}\tau_e$, i.e. fast relaxation time and small modulation frequency, the conversion efficiency equals 1. For a system with $\eta_c < 1$, additives can be added to the gas mixture in order to fasten the relaxation time. A successful promotion of relaxation processes is not only indicated by the amplitude, but also the by phase of the signal, since

$$\phi_p = \arctan(\omega_{\text{mod}}\tau_e) \quad (2.155)$$

applies* [20]. In order to use this formula to experimentally measure the relaxation times, Cottrell et al. [20] point out two important aspects. First, the PAC has to be non-resonant over the applied frequency range in order to avoid interference with the $\pi/2$ phase lag at the resonance frequency. Second, the relaxation time measured may not correspond to a single relaxation time, since several relaxation processes might occur serial or even parallel, if different relaxation paths exist. Especially in terms of decay processes in the visible and UV region, the relaxation paths can be quite complex. Hence, all possible relaxation processes have to be investigated before conclusions may be drawn. An example of different relaxation and heat releasing paths in acetone being excited in the UV region, will be discussed in section 2.5.6. Further information regarding the application of phase lags and the combination of

*If an additive is added to the matrix, care has to be taken, to readjust the modulation frequency back to the resonance frequency, since detuning can occur!

in-of-phase and out-of-phase photoacoustic spectra to determine relaxation times or distinguish between fast and slow relaxation process can be found elsewhere [21, 22].

There are some species known for their promotion and retardation of relaxation times. For example, H_2O is well-known to support relaxation processes, which is not surprising according to the VT-relaxation times of H_2O listed in table 2.6. Dong et al. [23] could increase their signal in CO detection by a factor of 10 when 2.2 %V of water vapor were added. Besides, signal amplification was also achieved for NO [24] and CO_2 [25] detection, respectively, although for the latter one, adding more than 0.2 %V of H_2O had no further supportive effect. Further references concerning the promotion of relaxation times by means of water can be found elsewhere [26–29]. Further species enhancing relaxation processes are SF_6 [30–32], NH_3 [33], C_2H_2 [34] or CH_4 [11].

However, as mentioned before, there are also species causing a retardation of the total relaxation time by means of VV transfer mechanism. This type of process as well as the phenomenon kinetic cooling, will be considered in the following section.

2.5.2.2 Kinetic cooling and vibrational-vibrational (VV) transfer mechanism

Tab. 2.7. List of VV energy transfer times of species occurring in exhaled breath from Bass et al. [13]. Intramolecular transitions are in bold. Molecules in their first excited state are labeled with an *, higher excited states are labeled with the equivalent number of *. ν_1 represents the symmetrical vibration, ν_3 the anti symmetrical vibration and ν_2 the deformation vibration of CO_2 .

Collision species			τ_{VV}
$\text{N}_2^* + \text{O}_2$	\rightarrow	$\text{N}_2 + \text{O}_2^*$	6.7 ms
$\text{O}_2^* + \text{CO}_2$	\rightarrow	$\text{O}_2 + \text{CO}_2^*(\nu_2)$	3.3 μs
$\text{H}_2\text{O}^*(\nu_2) + \text{O}_2$	\rightarrow	$\text{H}_2\text{O} + \text{O}_2^*$	22 ns
$\text{CO}_2^*(\nu_3) + \text{O}_2$	\rightarrow	$\text{CO}_2^{***}(\nu_2) + \text{O}_2$	17 μs
$\text{CO}_2^*(\nu_1) + \text{O}_2$	\rightarrow	$\text{CO}_2^{**}(\nu_2) + \text{O}_2$	2.2 ns
$\text{CO}_2^*(\nu_3) + \text{N}_2$	\rightarrow	$\text{CO}_2 + \text{N}_2^*$	56 ns
$\text{CO}_2^*(\nu_3) + \text{N}_2$	\rightarrow	$\text{CO}_2^{***}(\nu_2) + \text{N}_2$	17 μs
$\text{CO}_2^*(\nu_3) + \text{N}_2$	\rightarrow	$\text{CO}_2^{**}(\nu_2) + \text{N}_2$	22 ns
$\text{CO}_2^*(\nu_3) + \text{CO}_2$	\rightarrow	$\text{CO}_2^{***}(\nu_2) + \text{CO}_2$	6.7 μs
$\text{CO}_2^*(\nu_1) + \text{CO}_2$	\rightarrow	$\text{CO}_2^{**}(\nu_2) + \text{CO}_2$	2.2 ns

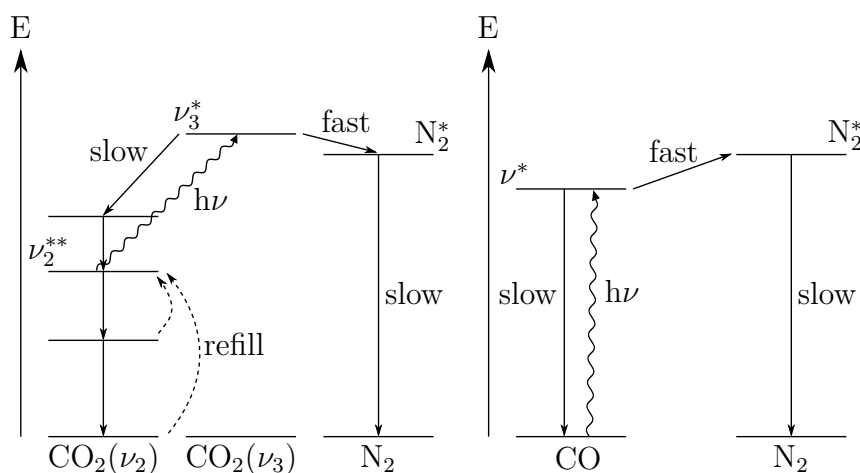


Fig. 2.24. Illustration of two different types of kinetic cooling. The left side visualises kinetic cooling of CO₂ in N₂ including hot band transitions after [35] and the right side shows kinetic cooling of CO diluted in N₂ after [36]. Dotted arrows represent refill processes.

The previous paragraphs demonstrated the influence of relaxation times onto the performance of a photoacoustic sensor. Since oxygen and nitrogen have slow relaxation times, they can influence the generated photoacoustic signal significantly. The excitation of vibrational states of N₂ or O₂ can result from collisions with vibrationally excited molecules, once these excited states of the collision partners are of similar energy. Such phenomena are called VV energy transfer processes. For a better estimation of possible VV transfer mechanism in breath, a few VV lifetimes τ_{VV} are presented in table 2.7.

The table also indicates, that the most studied molecule in terms of VV transfer mechanisms is CO₂. The reason is an interesting phenomenon called kinetic cooling, which is strongly expressed by carbon dioxide. This effect is described in detail by Wood et al. [12] and was later investigated by means of photoacoustic spectroscopy by Hammerich et al. [35]. An excitation from the already excited anti symmetric stretching mode ν_2^{**} to ν_3^* occurs, where ν_3^* refers to an excited anti symmetric stretching mode. Due to laser excitation, the state ν_2^{**} gets depleted. In order to refill this state, energy redistribution of the other vibrational states occurs causing kinetic cooling. The left side of figure 2.24 visualises the refilling process from lower vibrational energy states of the ν_2 vibration leading to kinetic cooling, since the necessary energy for redistribution is taken from the translational energy of the participating molecules. The excitation of CO₂^{*}(ν_3) is followed by a fast VV energy transfer with N₂. According to table 2.7 the VV energy transfer with N₂ is significantly faster than the intramolecular decay of excited CO₂^{*}(ν_3). The stored energy in excited N₂^{*} consists not only of the energy from the absorbed photon but also the translational energy drawn from the system. Since VT-relaxations (refer to table 2.6) of excited N₂^{*} are quite long, the signal detected by means of photoacoustic spectroscopy is only a consequence of kinetic cooling of the gas sample and not due to heat influx induced by light. Furthermore, a phase shift of 180° can be observed

since the cooling causes a periodic compression followed by an expansion and not vice versa [35].

Adding water, however, can cause this effect to be reduced or even to vanish, depending on the applied modulation frequency, since the VT-relaxation time of $N_2^* + H_2O$ is only about 9 μs . Adding water, the signal drops first, since only the amount of energy causing the kinetic cooling is returned to the system until kinetic cooling is completely suspended. After passing this point by adding further H_2O , the signal starts to rise again, since part of the introduced energy by means of light, is converted sufficiently fast to contribute to the photoacoustic signal. The phase shift is obviously reversible, too.

In addition to CO_2 , there are further species suffering from similar cooling effects, which do not base on hot band transition*, namely CO and N_2O [36, 37] as well as CH_4 [38]. The right side of figure 2.24 visualises the cooling process without hot band transitions. In the depicted scenario, CO is excited into its first excited vibrational state. If N_2 is present, a fast, endothermic VV energy transfer process ($N_2 + CO^* \rightarrow CO + N_2^*$) is observed. Since an energy gap of about 180 cm^{-1} exists between the CO^* and N_2^* states, energy is drawn from the rotational and translational energy pool of the participating CO^* molecules [37]. Like in the kinetic cooling mechanism of CO_2 , the energy is stored within the N_2^* molecule, resulting in kinetic cooling of the CO/N_2 mixture if the modulation frequency of the laser inhibits complete VT-relaxation of the N_2^* molecule.

Considering isolated VV energy transfer processes, without kinetic cooling, can cause decreasing PA signals as well. Oxygen, is a well-known candidate, when it comes to VV transfer induced signal loss. Table 2.6 indicates the VT-relaxation time of O_2 , thus a collision induced excitation of O_2 has to be considered as a potential loss effect in photoacoustic signal. Rück et al. [29] identified a loss of 15 % to originate from VV energy transfer between NO_2^* and O_2 , where the buffer gas was synthetic air. This loss was in good agreement with the results from Kalkmann and Kestern [39], who observed a drop of 20 % when 50 V% of oxygen were added. Besides, Schilt et al. [26] have published results, where the PA signal diminished by two orders of magnitude when nitrogen was replaced by oxygen as buffer in CH_4 detection.

Since relaxation times are strongly dependent on the collision rate, the following section will address this physical quantity in detail.

2.5.3 Collision rate

Previous sections have demonstrated, that collision is an important process in photoacoustic signal generation. Kinetic gas theory provides an approach in calculating

*A hot band transition is a transition, where two excited states are involved.

physical quantities like the relative mean velocity (see equation 2.54) and the collision rate Z_{ij} of two molecules of type i and j . The collision rate is given by

$$Z_{ij} = \frac{1}{\tau_{ij}} = \rho_j(r_i + r_j)^2 \sqrt{\frac{8\pi kT}{\mu_{ij}}} \quad (2.156)$$

where τ_{ij} represents the collisional lifetime defined in 2.51 and with ρ_j being the volume number density of the buffer gas. Regarding acetone with an diameter of 0.616 nm [40] diluted in the buffer gas N₂ with a diameter of 0.364 nm [41], the relative mean velocity and the collision rate can be calculated to 330 m s⁻¹ and 18.3 GHz, respectively, at 298 K and 1 atm. Assuming a relaxation time of 20 μs for the excitation at around 278 nm, this results in 36 683 collisions necessary for complete deexcitation of acetone. However, kinetic gas theory lacks important considerations and is based on assumptions like [11]

- particles being considered rigid spheres,
- molecules traveling in a straight line through space,
- interaction of the electron clouds are neglected and
- the collision process is regarded binary, where only hit and miss are considered and nothing in-between.

For a better understanding of the collision process, a new potential has to be introduced, describing the energies and forces appearing during this process. Therefore, a Lennard-Jones* potential [42] can be assumed, which is given by

$$V_{\text{LJ}}(x_{ij}) = 4hc_0\tilde{D}_e \left[\left(\frac{\sigma_0}{x_{ij}} \right)^{12} - \left(\frac{\sigma_0}{x_{ij}} \right)^6 \right] \quad (2.157)$$

Where x_{ij} is the distance between a vibrationally excited molecule i with $v = 1$ and a vibrationally non-excited molecule j with $v = 0$. \tilde{D}_e is the depth of the potential well and σ_0 is the separation at zero energy ($V(x_{ij}) = 0$). The first term in the Lennard-Jones potential describes the long-range attractive London forces and the second term represents the short-range repulsive forces due to overlapping electron orbitals [11].

Figure 2.25 visualises the potential curve of the Lennard-Jones approximation.

Molecule j approaches molecule i having a certain relative mean velocity and thus a kinetic energy $E_{\text{kin},j}$. This energy reaches a maximum at point A, due to attractive London forces. Passing point B, this energy has returned to its initial value due to repulsive forces. At the distance of point C, $E_{\text{kin},j} = 0$. This describes the point of return and can be considered the actual collision point.

*Sir John Edward Lennard-Jones (1894 – 1954)

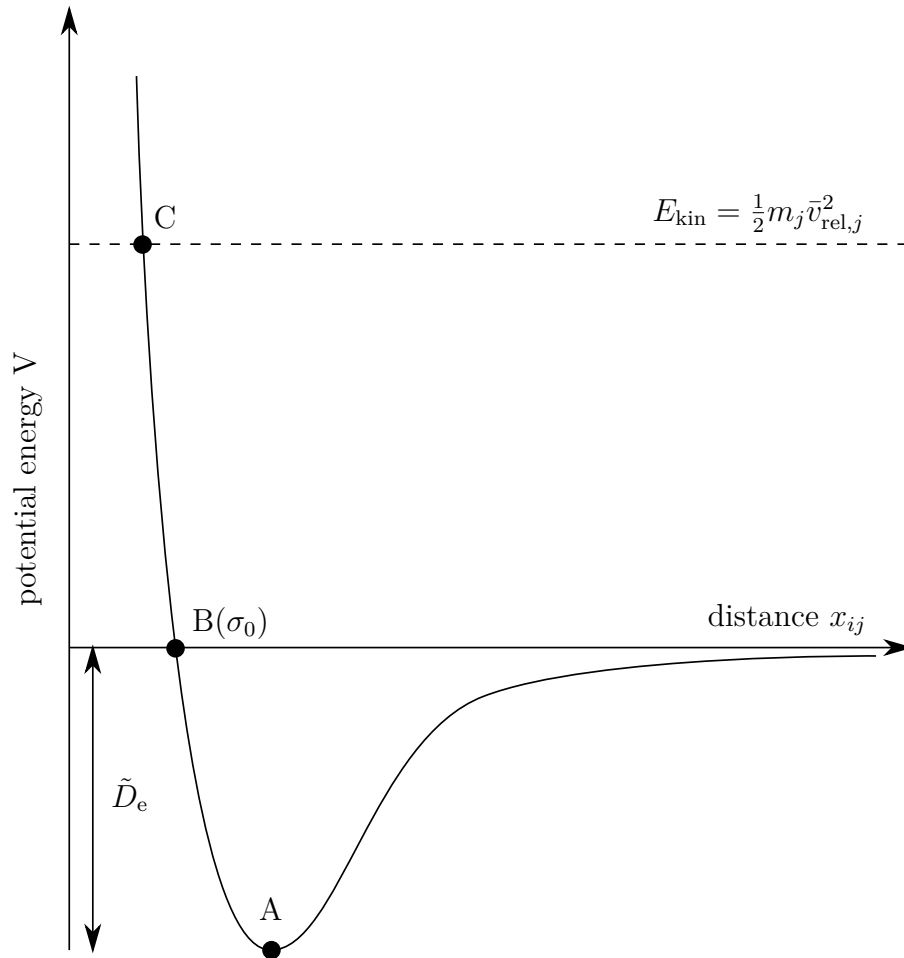


Fig. 2.25. Illustration of the Lennard-Jones potential [42] describing the process of molecular collision. With A being the point of maximum kinetic energy of molecule j , point B represents the point of initial kinetic energy and point C represents the point of zero kinetic energy (point of return).

Regarding inelastic collisions including the transfer of vibrational energy, Landau and Teller [43] developed the first theoretical approach. Neglecting attractive forces, they assumed a potential shape of the form

$$V_{\text{LT}}(x_{ij}) = V_0 e^{\alpha_r x_{ij}} \quad (2.158)$$

with α_r representing the strength of the repulsive forces. From this potential, the probability of a VT-relaxation from $v = 1$ to $v = 0$ can be computed using classical time-dependent perturbation theory. Further approximations can be found in [11], leading to

$$P_{10} = \exp \left[-3 \left(\frac{2\pi^4 \mu_{ij} \nu_o^2}{\alpha_r^2 kT} \right)^{\frac{1}{3}} \right] \quad (2.159)$$

where ν_o is the oscillating frequency of the vibrational mode. From this equation, it can be derived, that the probability of a VT-relaxation decreases with higher

vibrational energy levels within a mode. An observation, which applies for higher excited rotational states, too [11]. Due to that, it can be assumed that the relaxation time of fundamental vibrational modes at 3000 cm^{-1} and 1200 cm^{-1} is shorter than the nonradiative relaxation time of an excited electronic state of acetone. Results of experiments presented in section 5.4 do not postulate a quantified relaxation time, however, they demonstrate that the relaxation time τ_e is at least fast enough that equation 2.77 is not violated using a modulation frequency of 5000 Hz.

Returning to the Landau-Teller model, several improvements have been made in the past decades to achieve better consistency between simulated and empirical data. The still most commonly applied method bases on the model developed by Schwartz, Slawsky and Herzfeld (SSH) [44, 45] having been improved by Tanczos [46]. However, these enhancements have also increased the complexity of the applied models significantly. But despite of all improvements, the methods are still unable to cope with strong population of rotational modes, distinct polarities and the fact that polyatomic molecules change their effective shape during vibration as well as collision [11].

2.5.4 Acoustic attenuation

The previous sections described certain loss mechanism and collision induced relaxation effects and provided a physical background for those processes. They will be useful for the description of the main acoustic attenuation classes, namely classical attenuation, losses due to gas diffusion and molecular acoustic absorption.

Similar to light being attenuated while travelling through a medium, the acoustic pressure diminishes, too. The pressure p_x after travelling a certain distance x is given by [47]

$$p_x = p_0 e^{-\alpha_a(\omega_s)x} \quad (2.160)$$

where p_0 is the initial pressure and $\alpha_a(\omega_s)$ describes the acoustical absorption coefficient, which is frequency dependent. In literature, the acoustical absorption coefficient is often presented as $\alpha_a(\omega_s)\lambda_s$, with λ_s being the wavelength of the sound wave. This results in two benefits. The unit of the product is dimensionless and the baseline drift of the product, resulting from the linear increase of attenuation with frequency, vanishes [19]. The unit is called nepers. The difference between dB (see page 95) and neper is the use of the natural logarithm instead of the decadic one.

The Q-factor, which has been discussed in section 2.5.1, considers several effects causing acoustic attenuation, including thermal conductivity, viscosity, gas diffusion and losses due to relaxation times. Attenuation caused by gas diffusion is large for gas mixtures containing molecules with different masses (e.g. hydrogen/nitrogen mixture) [47]. Since this is not the case in a breath mixtures, containing mainly nitrogen, oxygen, carbon dioxide and water, acoustic attenuation due to diffusion can be neglected. Further information regarding acoustic attenuation caused by diffusion can be found elsewhere [48].

Neglecting gas diffusion, $\alpha_a(\omega_s)$ can be calculated as the sum of classical absorption $\alpha_{cl}(\omega_s)$ and all contributing molecular relaxation processes $\alpha_v(\omega_s)$ [49, p. 640]

$$\alpha_a(\omega_s) = \alpha_{cl}(\omega_s) + \sum_v \alpha_v(\omega_s) \quad (2.161)$$

The classical acoustic attenuation is given by [49, pp. 636]

$$\alpha_{cl}(\omega_s) = \frac{\omega_s^2 \eta_d}{2\tilde{\rho}_e c_s^3} \left(\frac{4}{3} + \frac{\eta_b}{\eta_d} + \frac{\gamma - 1}{\text{Pr}} \right) \quad \text{with} \quad \text{Pr} = \frac{C_p \eta_d}{k_T} \quad (2.162)$$

where η_d is the dynamic or absolute viscosity, and Pr the Prandtl*-number. Equation 2.162 is only valid for frequencies below rotational and translational relaxation frequencies. As a rule of thumb, this applies for $f_s < 100$ kHz [50].

The molecular or vibrational absorption coefficient $\alpha_v(\omega_s)$ is represented by [49, pp. 639]

$$\alpha_v(\omega_s) = \frac{\omega_s}{2\pi c_s} (\alpha_v \lambda_s)_m \frac{2\omega_s \tau_{VT}}{1 + (\omega_s \tau_{VT})^2} \quad (2.163)$$

with $(\alpha_v \lambda_s)_m$ being the dimensionless maximum absorption per wavelength associated with the corresponding vibrational relaxation process. Typical values in air are 0.0011 and 0.0002 for O₂ and N₂ in air at 20 °C, respectively [49, p. 641].

In order to describe acoustic dispersion propagation of a sound wave on a molecular level has to be addressed. In equilibrium, the molecules follow Brownian motion, during sound propagation, however, the movement is superimposed by a certain displacement $\zeta_p(\vec{r}, t)$ of the particles involved, which represents the amplitude of the wave. The displacement of the particles has a certain velocity $v_p(\vec{r}, t)$ and is introduced by a periodic pressure oscillation including compression followed by dilatation. Figure 2.26 visualises the curve of the acoustic wave amplitude and the pressure amplitude for the case of the first longitudinal mode of an acoustic wave within a tube shaped resonator. At the open ends, the amplitude, e.g. the displacement $|\zeta_p(\vec{r}, t)|$ in z -direction, has its maximum, where this is the position of the pressure amplitude nodes of the standing wave. When the pressure wave reaches its maximum at $L_{\text{res}}/2$, where the microphone should be located, the density of the particles is at its maximum causing the displacement in z -direction to approach zero. It is worth mentioning, that the product of the pressure and particle velocity provides the intensity $I_s(\vec{r}, t)$ of the sound wave [51, pp. 9].

$$I_s(\vec{r}, t) = v_p(\vec{r}, t) p_a(\vec{r}, t) = \zeta_p^2(\vec{r}, t) \omega_s^2 c_s \tilde{\rho} \quad (2.164)$$

Equation 2.164 provides a simple explanation, why the sound intensity in vacuum is zero. Returning to the spreading wave, in order to propagate, the energy stored in the moving particle is transferred onto another particle by collision. As previously discussed, different degrees of freedom, including rotational, vibrational and translational degrees, of the collision partner can get excited during the process of collision.

*Ludwig Prandtl (1875 – 1953)

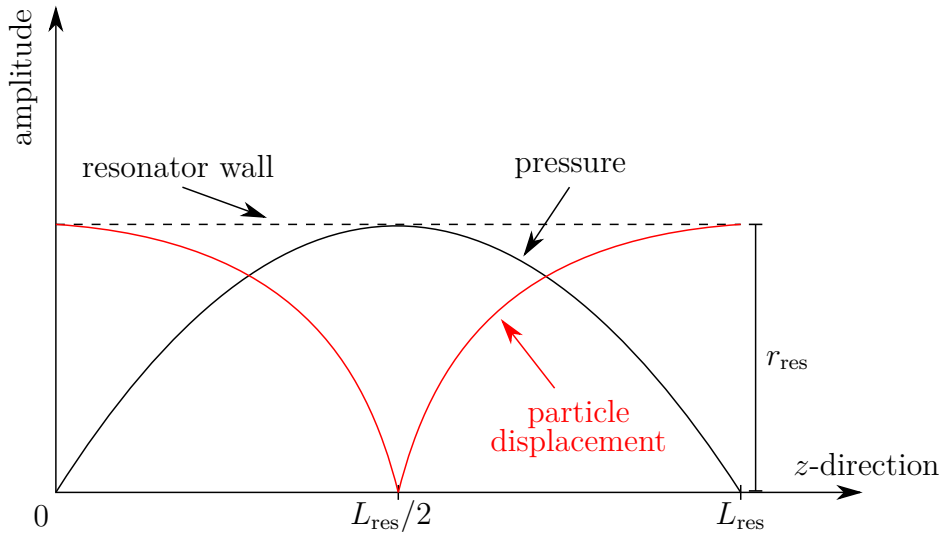


Fig. 2.26. Illustration of a standing wave within an acoustic resonator indicating maximum pressure amplitude (black) at the microphone position at $L_{\text{res}}/2$, whereas the particle displacement amplitude $|\zeta_p(\vec{r}, t)|$ (red) demonstrates the high displacement at the open ends and now displacement at $L_{\text{res}}/2$, where the particle density is high.

The dependency of the heat capacity γ and the effective degrees of freedom $d_{\text{F,eff}}^*$ of a molecule is given by [53]

$$\gamma = \frac{d_{\text{F,eff}} + 2}{d_{\text{F,eff}}} \quad (2.165)$$

In general, a molecule has $3N_{\text{Atoms}}$ degrees of freedom d_{F} , which are distributed on translational, rotational and vibrational degrees of freedom. The translational degrees of freedom are always three. A molecule with two atoms (e.g. N_2) has thus, three translational, two rotational and one vibrational degree of freedom. A non-linear three-atomic molecule has three translational, three rotational and three vibrational ($d_{\text{F}} = 3N_{\text{Atoms}} - 6$) degrees of freedom, whereas a linear one like CO_2 has again three translational, two rotational and four vibrational ($d_{\text{F}} = 3N_{\text{Atoms}} - 5$) degrees of freedom.

If τ_{VT} is too long for the applied frequency ω_s to allow relaxation, than the corresponding vibrational degree of freedom is no longer involved in the sound propagation process. As a consequence, $d_{\text{F,eff}}$ diminishes, which in turn, decreases γ . Since equation 2.99, $c_s \propto \sqrt{\gamma}$ applies, this effect enhances the speed of sound of the propagating wave. The phenomenon of a changing phase velocity due to a changing frequency of the propagating wave is called acoustic dispersion. Figure 2.27 visualises the influence of acoustic energy dissipation (black) and acoustic dispersion (red). For lower frequencies, the molecular attenuation monotonically ascends having a peak at $\omega_s \tau_{\text{VT}} = 1$ [49, p. 640] and decreases afterwards. When molecular attenuation takes place, less degrees of freedom are involved in the sound propagation

* $d_{\text{F,eff}}$ represents the degrees of freedom participating in sound propagation [52].

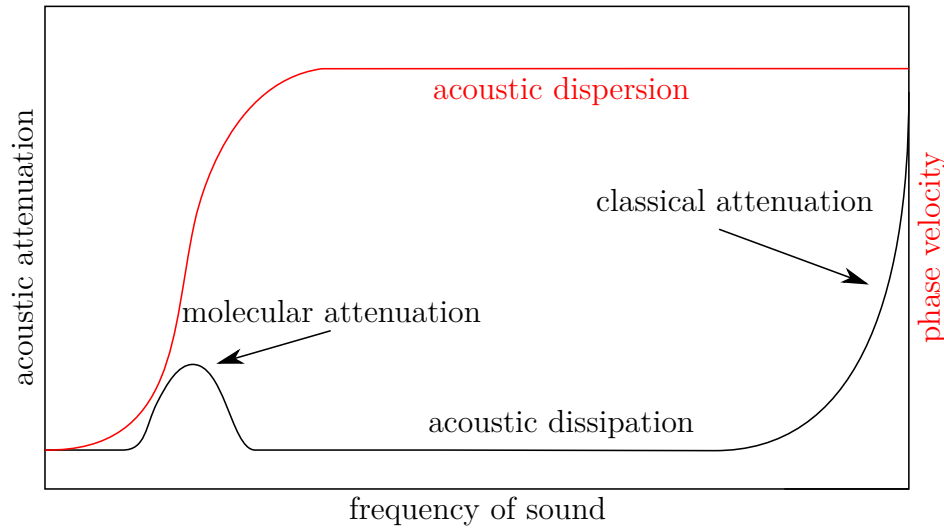


Fig. 2.27. Visualisation of the different acoustic dissipation phenomena and their region of effect (black) as well as the change of phase velocity with rising sound frequency due to acoustic dispersion (red) after [19].

and hence, the phase velocity of the wave increases. At the frequency representing $(\alpha_v \lambda_s)_m$, the slope of the phase velocity has a maximum. The speed of sound reaches its maximum, when the molecular attenuation is zero again. At higher frequencies, classical attenuation starts and causes significant energy dissipation. However, classical attenuation does not cause a further change in the speed of sound.

Since sound attenuation is amplified by the acoustic resonator, classic attenuation cannot be neglected even at low frequencies like 5 kHz [29]. In addition, molecular attenuation can cause perceptible changes within the photoacoustic system, too, including a variation in the speed of sound. The consequences of a changing speed of sound will be discussed in section 2.5.5. Ejakov et al. [47] demonstrated, that in air no notable acoustical attenuation exists until 100 kHz and then mainly arises from classic attenuation. For pure CO₂, however, the acoustic attenuation has a maximum of $\alpha_a \approx 5.3 \times 10^{-3} \text{ m}^{-1}$ at about $\sim 40 \text{ kHz}$ [55]. Besides, for different CO₂ concentrations diluted in N₂, the maximum attenuation was estimated to be at around 28 kHz, which was reproducible for different CO₂ concentrations between 20 %V and 80 %V [47]. Unfortunately, no data was found in literature for CO₂ being diluted in air at comparable levels occurring in breath. Besides, since the acoustic attenuation (see 2.162 and 2.163) is indirectly dependent on temperature and pressure, theoretical estimations are difficult and the need for empirical data is great, though quite scarce.

Furthermore, considering exhaled breath with H₂O being a main component, the catalytic property of water regarding fast relaxation has to be considered as well. This has been demonstrated by Knudsen and Fricke [56], where small impurities of water have been added to CO₂ causing a strong blue-shift of the frequency of maximum sound attenuation for CO₂. In addition, Harris [54] investigated the influence of

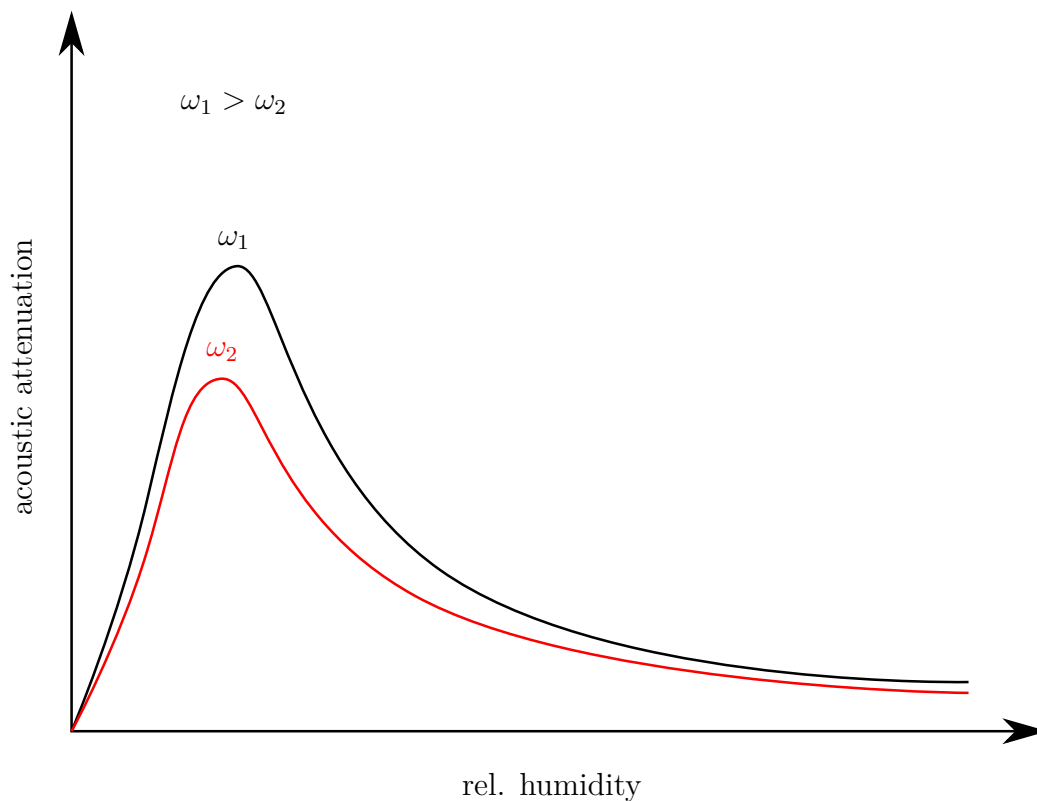


Fig. 2.28. Comparison of acoustic attenuation in air at 20 °C for varying rH at different frequencies after [54].

humidity and different temperatures in air. He demonstrated, that with increasing frequency, the maximum attenuation coefficient increased and its position shifted towards higher water vapor concentrations. E.g. at 5 kHz the maximum attenuation value was about 0.032 m^{-1} and located at about 12 %rH at 20 °C. Figure 2.28 demonstrates the shape of the attenuation curve with increasing relative humidity in air at 20 °C for two frequencies, qualitatively. Comparing the results from Ejakov [47], Knudsen and Fricke [56] as well as from Harris [54], shows the complexity of acoustic attenuation in multicomponent gas mixtures. Water on the one hand increases the acoustic attenuation compared to dry air at a certain extent, but causes molecular absorption induced by CO_2 to be blue-shifted to higher frequencies, reducing the amplification of the attenuation value due to CO_2 . Hence, studies on the acoustic attenuation of complex gas matrices at different temperatures, pressures, CO_2 and H_2O content would be very useful.

2.5.5 Frequency detuning

For PAS applications employing resonant PACs, frequency detuning can be a serious issue, especially when double resonant systems are used. For the case of excitation of the first longitudinal mode of the two-sided open tube resonator, equation 2.121

applies, demonstrating that f_{res} is proportional to c_s/L_{eff} . Recalling equation 2.99, c_s is relating to $\gamma^{\frac{1}{2}}$, $T^{\frac{1}{2}}$ and $M^{-\frac{1}{2}}$. Hence, changing the temperature or the main composition of the gas causes the speed of sound and thus the resonance frequency to shift leading to a variation in the photoacoustic amplitude and phase. An increase of 1 °C caused the frequency to blue-shift 7.8 Hz (compare to section 5.1.4.1), which is in agreement with theory (7.9 Hz). Due to that, the temperature of the gas should be kept constant. For breath analysis, detuning is a major issue, since the CO₂ and H₂O content varies causing the other main constituents N₂ and O₂ to alter as well. The theoretical change of c_s due to different mixture composition was calculated after

$$c_s = \sqrt{RT \frac{\sum_i N_i \gamma_i}{\sum_i N_i M_i}} \quad (2.166)$$

with N_i representing the volume ratio of the component i . There are two options to handle this situation, on the one hand logging the CO₂ and H₂O by means of secondary sensors and computing the composition and the corresponding speed of sound or on the other hand directly measuring the sound velocity, e.g. by means of ultrasonic run-time measurements. However, since sound dispersion is a further effect causing the speed of sound to alter, care must be taken that for the run-time measurements an appropriate frequency is applied. The best choice would be a measurement frequency for the run-time measurements, which equals the modulation frequency applied in the photoacoustic measurement, since this would eliminate any possible dispersion effects. As an example for detuning, adding 1 %V of H₂O vapor to a mix of synthetic air caused the frequency to blue-shift of approximately 8.0 Hz, where the resonance frequency of pure synthetic air was located at 4938 Hz. Adding 1 %V of CO₂ caused an even more pronounced red-shift of approximately 14.9 Hz. The deviation from the theoretical values calculated after 2.166, where 0.74 % and 1.3 %, respectively. A further promising approach for fast resonance frequency adjustment was published by Sherstov et al. [57]. They placed a small sound radiator into the PAC and produced a short train of square wave pulses. The resulting time response of the resonator was detected by means of a microphone and by applying an FFT on the time response, the frequency response and hence the resonance frequency of the system could be derived. This method is not only quite fast (> 0.1 s) but also quite accurate with an error of 60 ppm at ~ 1700 Hz.

For the assumption of an ideal gas, 2.99 can be rewritten to

$$c_s = \sqrt{\frac{\gamma p}{\tilde{\rho}}} \quad \text{with} \quad p = \frac{m}{V} \frac{RT}{M} = \tilde{\rho} \frac{RT}{M} \quad (2.167)$$

with m being the mass of the gas volume, demonstrating that changes in p and $\tilde{\rho}$ cancel each other out. In the case of non-ideal conditions, considering the molar volume of the molecules and intermolecular interactions, the speed of sound slightly depends on the pressure. This non-ideal behavior is described by the van der Waals*

*Johannes Diderik van der Waals 1837 – 1923

equations [58]. However, perfect adiabatic conditions and thus an ideal behavior can be assumed.

Although the geometrical length of the resonator can be assumed constant for a wide temperature range, the node-shifting effect can cause alterations of the effective resonator length L_{eff} . By decreasing the pressure within the cell a mode lengthening was observed, which has been attributed to enhanced node-shifting into the buffer volumes of the PAC. In order to cause a shift of more than 2 Hz, the pressure had to be lowered by approximately 200 mbar. However, this is not planned in terms of breath analysis. Nevertheless, node shifting has to be kept in mind regarding other photoacoustic applications, where ambient pressure fluctuations can occur.

Concluding, there are several effects causing detuning, demonstrating that a low Q-factor is advantageous, since it is less prone to signal loss induced by detuning. Besides, temperature should be controlled at all times. If detuning, induced by a changing gas composition, is detected either by an alteration of the phase or by means of secondary sensors, the frequency can be readjusted using equation 2.166 and 2.121. The readjustment of f_{mod} to f_{res} can be performed by temperature adaption of the PAC or by adaption of the modulation frequency of the light source. In PAS applications using double resonant systems, detuning can be even more serious. In the case of QEPAS using a micro resonator, the resonance of this tube shaped resonator is affected differently compared to the tuning fork. For example, an increase in temperature shifts the resonance frequency of the tube, but not the resonance frequency of the tuning fork. In addition, such systems often have very high Q-factors making this issue even more problematic. Details can be found elsewhere [19]. Therefore, QEPAS and CEPAS systems might not be an adequate approach for photoacoustic breath analysis.

2.5.6 Photodissociation of acetone

After absorbing a highly energetic photon, e.g. in the UV or visible wavelength regime, different decay mechanisms exist. Luminescence, including fluorescence and phosphorescence, nonradiative relaxation mechanism and photodecomposition of the molecule are possible. The probability of each mechanism is often represented as a quantum yield, where the sum of the different quantum yields is always one.

$$\Phi_{\text{total}} = \Phi_{\text{r}} + \Phi_{\text{n}} + \Phi_{\text{d}} \quad (2.168)$$

where Φ_{r} is the radiative quantum yield, Φ_{n} is the nonradiative relaxation quantum yield and Φ_{d} is the photodissociation quantum yield. A further relation between quantum yield and lifetime of a state is given by the rate coefficient \tilde{k}_{r} , which is often specified in literature in terms of reaction kinetics.

$$\Phi_{\text{d}} = \tau_{\text{d}} \tilde{k}_{\text{r,d}} \quad (2.169)$$

with $\tilde{k}_{\text{r,d}}$ being a specific photolysis rate coefficient and τ_{d} is the lifetime of the state prior to photodecomposition. In general, there are two different scenarios causing

decomposition of a light absorbing molecule. The energy of the photon can either be high enough to cause immediate ruption of the covalent bindings or the molecule is first excited to a higher electronic state (e.g. S_1) and after crossing onto a lower energy state by means of intersystem crossing (e.g. $S_1 \rightarrow T_1$) or internal conversion (e.g. $S_1 \rightarrow S_0$), higher vibrational modes get excited exceeding the dissociation energy causing the molecule to decompose [59, p. 554]. In the following section, the different quantum yields and the proposed relaxation pathways as well as their dependency on temperature, pressure, wavelength and buffer composition will be discussed.

Figure 2.29 illustrates the electronic energy levels of the $n_S \rightarrow \pi_S^*$ transition and dissociation barriers as well as the corresponding energies in the unit kJ mol^{-1} . Moreover, it visualises the distribution of the injected photon energy $h\nu_{\text{ph}}$ on the available and dissociation energy. The conversion from the wavelength in nm into the corresponding energy in kJ mol^{-1} can be calculated as follows:

$$1 \text{ kJ mol}^{-1} = \frac{hc_0 N_A}{1000 \cdot \lambda_{\text{ph}}} \quad (2.170)$$

Where λ_{ph} is the wavelength of the photon in meter. The energy levels of the barriers and the $T_{1,\text{min}}$ energy have been determined using molecular beams being crossed with the laser light preventing collision induced relaxation, allowing an almost direct measurement [61, 63] of the dissociation mechanism.

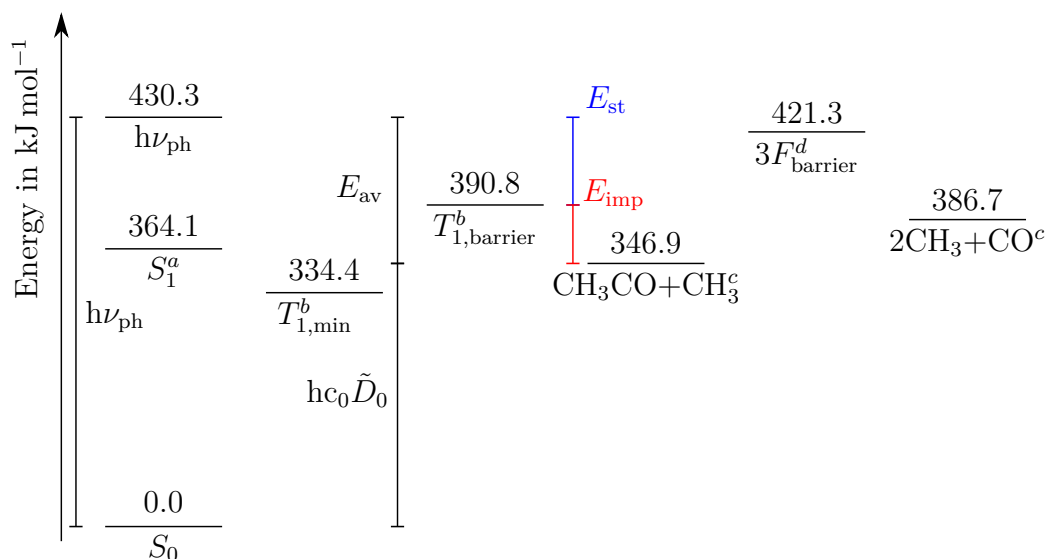
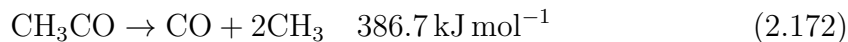


Fig. 2.29. Energy levels of the excited $n_S \rightarrow \pi_S^*$ state in acetone and corresponding energies necessary for photolysis. (a) [60], (b) [61], (c) calculated by [10] using data from [62] and the three fragment barrier ($3F_{\text{barrier}}^d$) (d) [63]. Energy distribution after excitation of a photon with a wavelength of 278 nm ($= 430.3 \text{ kJ mol}^{-1}$). E_{av} is the available energy after dissociation, which can be split into the impulsive reservoir E_{imp} and the statistical reservoir E_{st} . $hc_0\tilde{D}_0$ is the dissociation energy.

The corresponding chemical equations for both decomposition steps are [10]



where the energy values at the end of the reaction represent the threshold bond dissociation energies. A wavelength equally to the energy of the $T_{1,\text{barrier}}$ is necessary to cause decomposition on the T_1 surface. Thus a wavelength of approximately 306 nm can cause dissociation of acetone following equation 2.171. The available energy E_{av} of the products after decomposition is given by [10]

$$E_{\text{av}} = h\nu_{\text{ph}} + E_{\text{int,pa}} - hc_0\tilde{D}_0 = E_{\text{imp}} + E_{\text{st}} \quad (2.173)$$

with $E_{\text{int,pa}}$ being the internal energy of the parent molecule prior to excitation, which can be assumed zero at normal conditions compared to the other terms. $hc_0\tilde{D}_0$ is the dissociation energy and E_{imp} and E_{st} are the energy of the impulse and statistical reservoir, respectively. Since energy conservation has to be respected, the remaining available energy E_{av} is distributed on the generated radicals on the product side of the equations 2.171 and 2.172. Thus, increasing their translational, vibrational and rotational degrees of freedom. The partitioning of the available energy can be written as [10]

$$E_{\text{av}} = E_{\text{tr}} + E_{\text{int,CH}_3\text{CO}} + E_{\text{int,CH}_3} \quad (2.174)$$

where E_{tr} is the translational energy and E_{int} the corresponding internal energy of the respective fragment. In order to estimate the distribution of the energy on the different degrees of freedom, a framework called statistical adiabatic impulse (SAI) model, proposed by Mordaunt, Osborn and Neumark [64], is commonly used. It divides the available energy into a statistical and an impulsive energy reservoir (refer to figure 2.29). The latter one only depends on the energy height of the exit channel and is hence fixed for all photolysis energies. If the excited state of the molecule contains an excess energy above the dissociation barrier, this energy will be partitioned statistically into fragment internal and translational energy states.

Measurements by Lee et al. [10] demonstrated, that for excitation at about 280 nm ($= 35\,714 \text{ cm}^{-1}$) the average internal energy of the CH_3 fragment was about 3200 cm^{-1} after decomposition, which was approximately 2/3 of the available energy. Besides, their data demonstrated that the ratio between translational energy and available energy of the CH_3 fragment further increased towards longer wavelengths. In a further experiment, they determined the average translational energy of the acetyl radical to be 71 % and the internal energy states to solely account for the other 29 % for an excitation at 280 nm. At 301 nm the average translational energy of the acetyl radical even represented 91 % of the available energy.

At quite high photon energies, the second dissociation step was observed. North et al. [63] performed measurements at 193 nm and 248 nm. They observed, that at excitation with 248 nm, approximately 30 % of the nascent acetyl radicals decomposed a second time and for 193 nm the stepwise formation of two methyl and one CO

radical was the only dissociation pathway observed. In general, the second photodecomposition step occurs, if still enough internal energy* is available after the first decomposition step.

However, since at normal pressure and temperature conditions, collision induced relaxation paths will compete with the discussed photolysis pathways, relaxation mechanism in excited acetone will be addressed in view of photoacoustic spectroscopy in the following paragraphs.

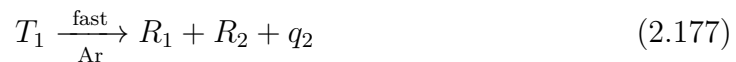
Oka et al. [22] demonstrated, that there are two different heat producing relaxation pathways for acetone after excitation into the S_1 state. They are presented in the following equations with the corresponding released heats q_i . In their experiments, they used either Argon (Ar) or synthetic air as buffer gases. The Ar or O_2 beneath the reaction arrow indicates the buffer gas present. For wavelengths $\lambda_{ph} > 310$ nm only one fast ($\tau_1 \approx 2.63$ ns[†]) heat release path was determined as follows



where the heat q_1 was released due to VT-relaxation onto the T_1 vibrational ground state[‡]. This process was followed by a slow ($\tau_3 = 0.2$ ms) heat release assigned to



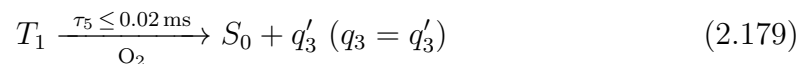
Below 310 nm, a second path, including decomposition of acetone on the T_1 surface was proposed, causing acetone to disassociate into the radicals R_1 and R_2 following



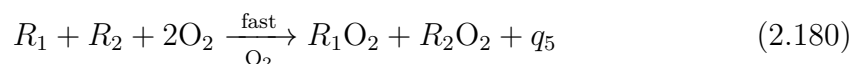
The heat released by q_2 is quite fast as well, whereas the heat release due to recombination in the buffer gas Argon was quite slow.



However, Oka et al. also showed, that adding O_2 to the buffer gas decreased the relaxation time by at least one order



In addition, the recombination of the radical fragments due to the reaction with oxygen, were enhanced, too. The two paths via the radicals R_i are



*The remaining internal energy of the acetyl radical has to be $421.3 \text{ kJ mol}^{-1} - 346.9 \text{ kJ mol}^{-1} = 74.4 \text{ kJ mol}^{-1}$ (refer to figure 2.29).

[†][65].

[‡]Which refers to $T_{1,\min}$ of figure 2.29.

and

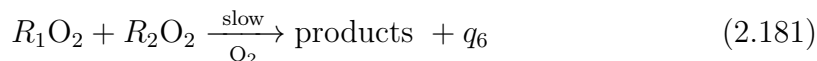


Table 2.8 lists the assignment of the released heat observed. According to the results, O_2 can be assumed a strong promoter of the nonradiative relaxation mechanism of excited acetone in the UV region. The measurements presented in section 5.1, demonstrate, that using N_2 as buffer has the same effect as using Ar and the results using synthetic air are superior in terms of sensitivity.

According to table 2.8, Oka et al. estimated an energy q_2 of 94 kJ mol^{-1} to be released quickly, for a wavelength of 280 nm. This is a quite good approximation compared to the results of Lee et al., who measured 96 kJ mol^{-1} of average translational energy distributed on the recoiling methyl and acetyl radical fragments.

Tab. 2.8. List of the heats assigned to the different relaxation paths in excited acetone after [22]. $\alpha_q = \frac{1.2 \times 10^{-4}}{\lambda_{\text{ph}}} - 385 \text{ kJ mol}^{-1}$ and the numbers in parentheses are estimates of the released heat.

Buffer	Path via T_1		Path via R_i	
	Slow	Fast	Slow	Fast
Ar	q_3 (335)	q_1 (50 + α_q)	q_4 (335)	q_2 (50 + α_q)
air	-	$q_1 + q'_3$ (385 + α_q)	q_6	$q_2 + q_5$ (385 + α_q)

The results of Oka et al. show, that photoacoustic detection of acetone in the UV region is quite promising, especially when oxygen is present in the measurement matrix. Besides, different heat producing pathways via T_1 and decomposition were observed contributing to the photoacoustic signal. Regarding the relaxation time, only the relaxation path via T_1 could be assigned with a semi-quantitative relaxation time, which is specified to less than $20 \mu\text{s}$ when oxygen is present.

Preukschat et al. [66] detected acetone photoacoustically at a modulation frequency of 7 kHz^* in a setup with continuous flow rate of 100 mL/min . According to them, no performance loss or non-linear behavior regarding photodissociation could be observed within a simple calibration measurement, where acetone diluted in synthetic air was increased in 50 ppmV steps. However, measuring 2 ppmV propofol in the same setup with continuous flow, they observed an asymptotic course of the photoacoustic signal, which stabilised after few hours. They assigned the drop to photodissociation but also to adsorption of propofol to the walls and windows of the

*The modulation frequency was communicated via personal correspondence.

cell. In the case of acetone detection, however, Preukschat et al. claim that nearly all energy introduced into the gas by means of laser light is released as heat. This coincides with the results of Oka et al. [22], where only the energy amount q_6 was attributed to be slow in the case of oxygen being present.

Regarding sensor design, one further aspect has to be discussed considering photodissociation. Namely, the photodissociation rate and the recombination products at typical breath conditions. This is important, since in a closed photoacoustic sensor setup, where the sample is trapped within the cell, a high dissociation rate could lead to a rapid decrease of acetone concentration. This would cause the sensor signal to diminish over time, as the fragments cannot be excited a second time, if they do not recombine to acetone. First, the formula of Blitz et al. [67] will be used to compute the disassociation rate for typical breath conditions. Second, the recombination products will be discussed and based on both results, a mathematical expression will be presented to calculate the number of disassociated molecules after a certain time.

According to Blitz et al. [67], the total photodissociation quantum yield Φ_d can be calculated after

$$\Phi_d(\lambda_{ph}, \rho, T) = \Phi_{CH_3CO}(\lambda_{ph}, \rho, T) + \Phi_{CO}(\lambda_{ph}, T) \quad (2.182)$$

with

$$\Phi_{CO}(\lambda_{ph}, T) = \frac{1}{1 + \tilde{A}_0} \quad \text{for } 279 \text{ nm} < \lambda_{ph} < 327.5 \text{ nm} \quad (2.183)$$

$$\Phi_{CH_3CO,1}(\lambda_{ph}, \rho, T) = \frac{1 - \Phi_{CO}(\lambda_{ph}, T)}{1 + \tilde{A}_1 \rho} \quad \text{for } 279 \text{ nm} < \lambda_{ph} < 302 \text{ nm} \quad (2.184)$$

$$\Phi_{CH_3CO,2}(\lambda_{ph}, \rho, T) = (1 - \Phi_{CO}(\lambda_{ph}, T)) \frac{1 + \tilde{A}_3 + \tilde{A}_4 \rho}{(1 + \tilde{A}_2 \rho + \tilde{A}_3)(1 + \tilde{A}_4 \rho)} \quad (2.185)$$

$$\text{for } 302 \text{ nm} < \lambda_{ph} < 327.5 \text{ nm}$$

A description of the variables $\tilde{A}_0 - \tilde{A}_4$ can be found in the appendix A.3.

The equations are valid* in the temperature region from 218 K – 295 K, the wavelength region 279 nm – 327.5 nm and within the pressure range of 0 mbar – 1000 mbar. This is still close enough to the emission wavelength of the light emitting diode (LED) with 278 nm and ambient pressure conditions being expected in exhaled breath. The upper temperature limit, however, is only 295 K instead of the applied PAC temperature of 318 K within the measurements shown in chapter 5. Nevertheless, solving the above equations using 295 K should provide a good estimate of the photodecomposition quantum yield.

According to equation 2.183, at 279 nm and 295 K, $\Phi_{CO} = 0.18$. Assuming 1000 mbar for the pressure dependence of equation 2.184 yields to $\Phi_{CH_3CO,1} = 0.45$, which sums

*The equations actually allow for certain extrapolation, however, the error beyond the limits is not specified.

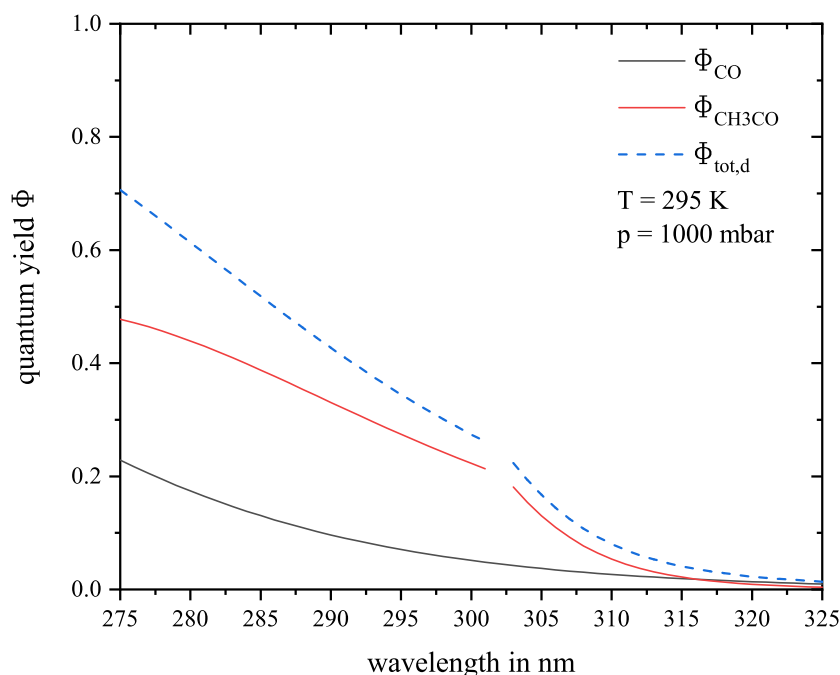


Fig. 2.30. Photodissociation quantum yields of acetone for different wavelengths at 295 K and 1000 mbar. Caution is required regarding the accuracy of data visualised exceeding the wavelength limits of equations 2.183, 2.184 and 2.185.

up to $\Phi_d = 0.63^*$. Figure 2.30 visualises the photolysis quantum yield of acetone for different wavelengths. The interruption in the graph of $\Phi_{\text{CH}_3\text{CO}}$ and Φ_d is due to the finite wavelength interval in which the equations 2.184 and 2.185 are valid. In figure 2.31 the photodecomposition quantum yields at a fixed temperature and varying pressure (top) as well as vice versa (bottom), are simulated for a wavelength of 279 nm. It is striking, that there is only a slight variation in Φ_d between 280 K and 320 K. Although the equations are only valid until 295 K, no significant influence on Φ_d is to be expected within this temperature range. The variations in Φ_{CO} and $\Phi_{\text{CH}_3\text{CO}}$, however, are quite strong. For different pressures, the situation is different, since between 900 mbar and 1000 mbar, Φ_d is constant and increases towards lower pressures. This seems valid, since with lower pressures, no collision induced deactivation of excited acetone molecules occurs anymore. Moreover, equation 2.183 demonstrates, that Φ_{CO} is pressure independent according to Blitz et al. [67]. This has been disproved by Somnitz et al. [68], Khamaganov et al. [69] and Rajakumar et al. [70]. All of them measured a certain pressure dependency of the formation of the CO radical due to secondary decomposition. However, they provide quite different dependencies and the exact relation between CO production and pressure remains unclear. Due to that and the recommendation by the NASA Panel for Data evaluation [71], the results of the equations from Blitz et al. [67] will be used for further calculations.

*For 278 nm, which actually exceeds the wavelength limit of the applied equations, a total photodissociation quantum yield of 0.65 is expected.

The influence of oxygen being present in the sample has been already discussed and its effect on the radical recombination products will be addressed in the next paragraph. Considering H_2O , Aloisio et al. [72] claim a loss in the total photolysis yield when H_2O (up to 9 Torr) was added to a mixture of acetone diluted in N_2 and O_2 . These results, however, were not confirmed by Nádasdi et al. [73]. The influence of water vapor on the photodissociation rate of acetone in the UVC region remains therefore unclear, too.

Besides dissociation, the recombination products are of interest as well. A comprehensive list of reactions expected to occur as a consequence of photolysis of acetone diluted in air, is provided by Meyrahn et al. [74]. The results indicate, that there are several possible reactions, though none is leading to a reformation of acetone. Hence, a decomposed acetone molecule is considered to be lost irreversible. For the derivation of an equation to calculate the lost percentage of illuminated acetone

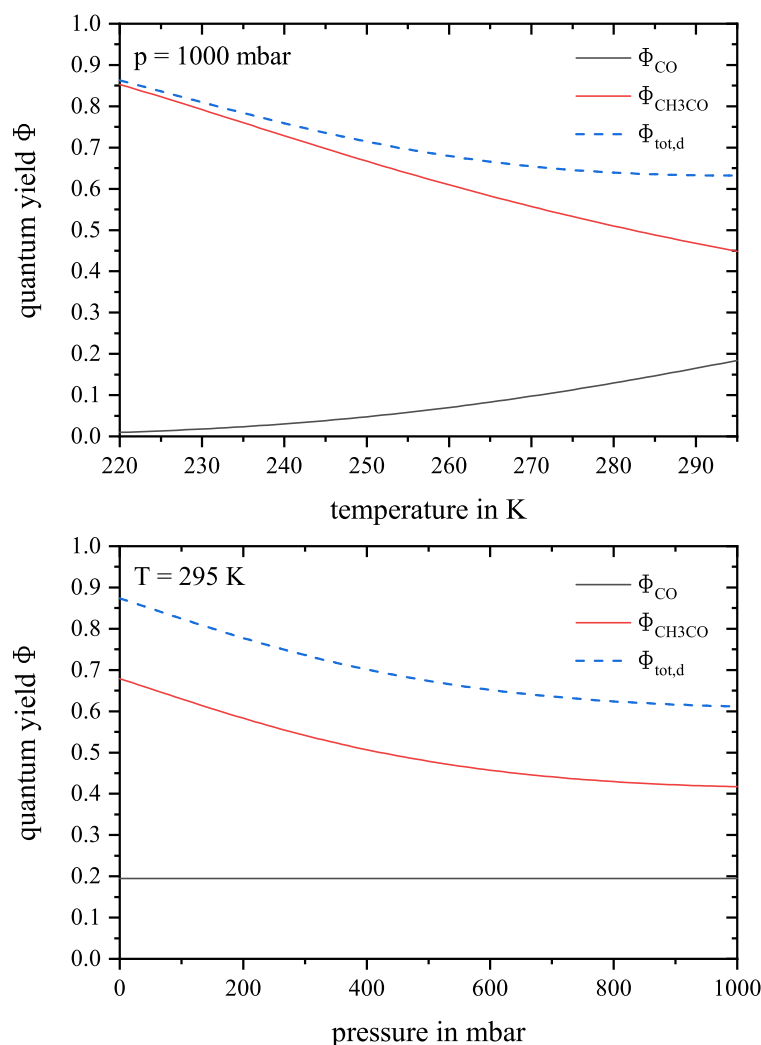


Fig. 2.31. Photodissociation quantum yields of acetone at 279 nm for different temperatures with varying pressure (top) and vice versa (bottom) based on the calculations from Blitz et al. [67].

molecules after a certain time, a two-level rate equation is used (refer to section 2.3.1).

To simplify calculations, a few assumptions have to be made at the beginning.

1. The considered volume V is completely illuminated, thus $V = V_{il}$.
2. A static case is considered, where no gas exchange occurs over time.
3. A decomposed acetone molecule is irreversibly lost.
4. $\rho'(t)$ for $t = 0$ is zero.
5. The molecular density describing the number of temporarily excited molecules at a certain time $\rho'(t)$ is negligible.

Assumption 4 has already been discussed in section 2.3.1. At room temperature, the Boltzmann distribution of the electronic states (refer to equation 2.25) demonstrates that only the ground state is occupied at the time $t = 0$. Therefore, $\rho_0 \gg \rho'$ and thus $\rho = \rho_0 + \rho' = \rho_0$ for $t = 0$ applies.

Without assumption 5, the rate equation would have the following form:

$$\frac{\partial \rho'_u}{\partial t} = \hat{A}_{01}(\rho - \Phi_d \rho'_u(t) - \rho'(t)) \quad (2.186)$$

where $\rho'_u(t)$ is the number of excited molecules **until** the time t and $\rho'(t)$ is the amount of excited molecules **at** the time t . However, assumption 5 can be verified by applying equation 2.88, inserting the corresponding values for excitation at 278 nm with an average optical power of $\approx 88 \text{ mW}^*$ and a concentration of 10 ppmV at 25 °C and 1 atm. Figure 2.32 demonstrates, that the equilibrium is reached after approximately 150 μs even when 100 % relaxation and no photodissociation is assumed. The figure also visualises the low ratio ρ'/ρ even at equilibrium, verifying assumption 5. Therefore, the term $\rho'(t)$ can be neglected. Equation 2.186 can therefore be simplified to

$$\frac{\partial \rho'_u}{\partial t} = \hat{A}_{01}(\rho - \Phi_d \rho'_u(t)) \quad (2.187)$$

Inserting equation 2.82 in 2.187 and solving this equation, while applying assumption 4 as boundary condition, leads to

$$\rho'_u(t) = \frac{\rho}{\Phi_d} [1 - \exp(-\Psi_0 \sigma_A(\tilde{\nu}) t \Phi_d)] \quad (2.188)$$

The number of decomposed molecules $\rho_d(t)$ until time t is then given by

$$\rho_d(t) = \rho'_u(t) \Phi_d = \rho [1 - \exp(-\Psi_0 \sigma_A(\tilde{\nu}) t \Phi_d)] \quad (2.189)$$

*In section 5.1.4.3, the optical power at 50 % duty cycle before the PAC was measured to be $\approx 88 \text{ mW}$. This value is used for the presented calculation.

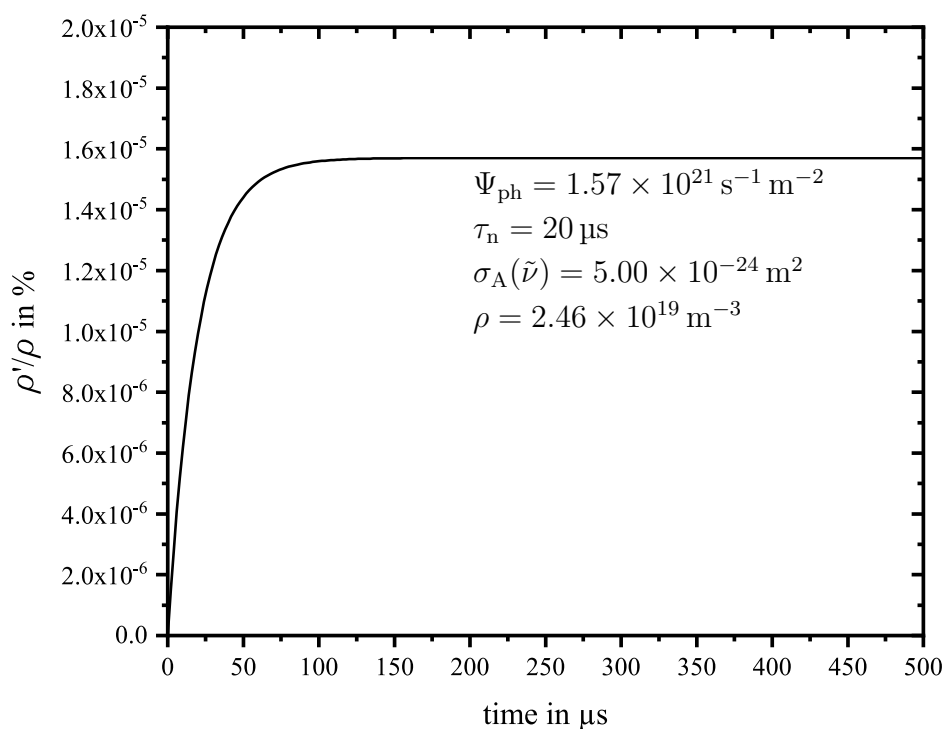


Fig. 2.32. Visualisation of the time needed to reach equilibrium between the number of excited states ρ' and total number of states ρ , neglecting dissociation. Values used for the simulation are presented within the figure.

Note, that these derivations have also been used within section 5.1.4.3 to be able to describe the signal loss detected within the FT-IR being connected in series with the PAC, where a non-static case* was considered, which resulted in a good agreement between calculation and measurement. Figure 2.33 visualises the relative loss of acetone over time for a gas sample containing 10 ppmV.

These results can be used for development to optimise the design of a UV based photoacoustic sensor employed in breath acetone detection.

Concluding this section, photolysis may cause a significant contribution to the photoacoustic signal, since a great share of the photon energy is directly converted into translational energy. However, the photon energy being distributed onto internal degrees of freedom has to be released via collision induced VT-relaxations or recombination (refer to 2.8). For acetone, several relaxation pathways have been discussed and oxygen was identified to have a strong promotional effect on the relaxation time and fast heat release of electronically excited acetone.

*The gas within the PAC was exchanged with a certain flow rate.

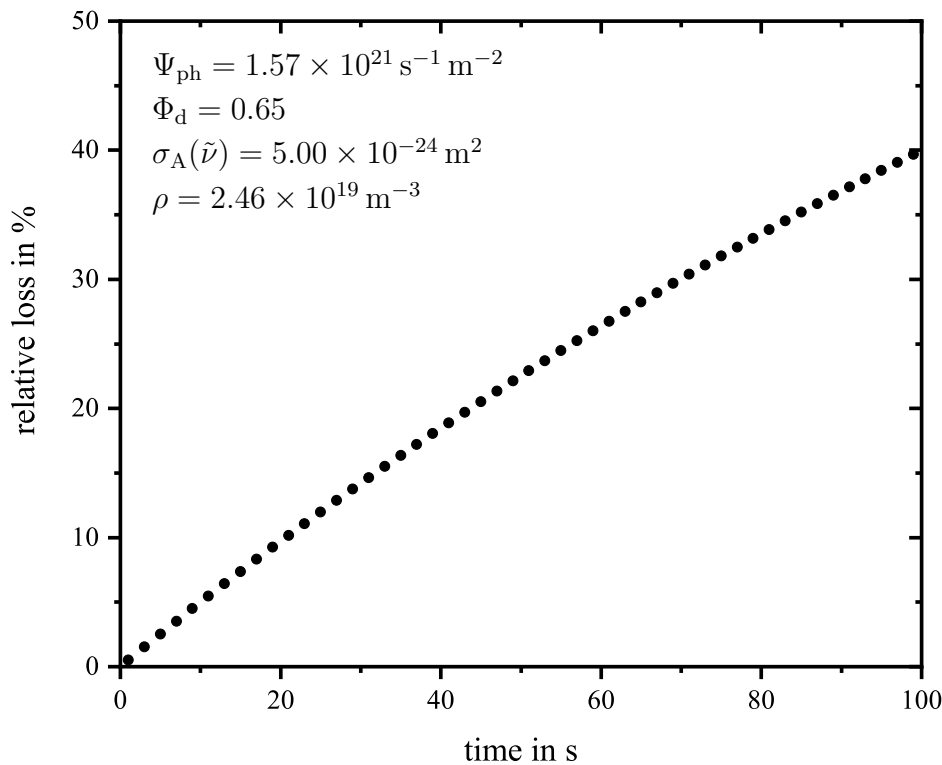


Fig. 2.33. Illustration of the relative loss for a 10 ppmV sample of acetone over time due to dissociation. Values used for the simulation are presented within the figure.

References

- [1] L. Kreuzer. “The Physics of Signal Generation and Detection”. In: *Optoacoustic spectroscopy and detection*. New York: Academic Press, 1977, pp. 1–25. ISBN: 9780323158817 (cit. on pp. 101, 102).
- [2] R. D. Kamm. “Detection of weakly absorbing gases using a resonant optoacoustic method”. In: *Journal of Applied Physics* 47.8 (Aug. 1976), pp. 3550–3558. ISSN: 0021-8979. DOI: 10.1063/1.323153 (cit. on p. 101).
- [3] P. M. Morse and K. U. Ingard. “Linear Acoustic Theory”. In: ed. by S. Flügge. *Acoustics*. Springer-Verlag OHG, 1961, pp. 1–128. DOI: 10.1007/978-3-642-45956-6_1 (cit. on p. 101).
- [4] A. Miklós and A. Lörincz. “Windowless resonant acoustic chamber for laser-photoacoustic applications”. In: *Applied Physics B Photophysics and Laser Chemistry* 48.3 (Mar. 1989), pp. 213–218. ISSN: 0721-7269. DOI: 10.1007/BF00694347 (cit. on p. 102).
- [5] P. M. Morse and K. U. Ingard. *Theoretical Acoustics*. McGraw Hill Book Company, 1968. ISBN: 9780691024011 (cit. on p. 102).

- [6] J. B. Mehl and M. R. Moldover. “Precision acoustic measurements with a spherical resonator: Ar and C₂H₄”. In: *The Journal of Chemical Physics* 74.7 (Apr. 1981), pp. 4062–4077. ISSN: 0021-9606. DOI: 10.1063/1.441587 (cit. on p. 102).
- [7] P. Hess. “Resonant photoacoustic spectroscopy”. In: 1983, pp. 1–32. DOI: 10.1007/3-540-12065-3_1 (cit. on pp. 103, 104).
- [8] A. Karbach and P. Hess. “High precision acoustic spectroscopy by laser excitation of resonator modes”. In: *The Journal of Chemical Physics* 83.3 (Aug. 1985), pp. 1075–1084. ISSN: 0021-9606. DOI: 10.1063/1.449470 (cit. on p. 103).
- [9] G. Lei and B. Di Bartolo. “Measurement of rotational and vibrational relaxation in gases by photoacoustic resonance: Application to SF₆”. In: *Journal of Applied Physics* 79.6 (Mar. 1996), pp. 2890–2895. ISSN: 0021-8979. DOI: 10.1063/1.361284 (cit. on pp. 103, 104).
- [10] K. L. K. Lee et al. “Photodissociation of acetone from 266 to 312 nm: Dynamics of CH₃ + CH₃CO channels on the S₀ and T₁ states”. In: *Journal of Chemical Physics* 146.4 (2017), pp. 0–12. ISSN: 00219606. DOI: 10.1063/1.4974035 (cit. on pp. 103, 119, 120).
- [11] J.-P. Besson. “Photoacoustic spectroscopy for multi-gas sensing using near infrared lasers”. Ph. D. thesis. University of Lausanne, 2006 (cit. on pp. 104, 107, 110–112).
- [12] A. D. Wood et al. “Effects of 106- μ Laser Induced Air Chemistry on the Atmospheric Refractive Index”. In: *Applied Optics* 10.8 (Aug. 1971), p. 1877. ISSN: 0003-6935. DOI: 10.1364/A0.10.001877 (cit. on pp. 105, 108).
- [13] H. E. Bass and H.-J. Bauer. “Kinetic Model for Thermal Blooming in the Atmosphere”. In: *Applied Optics* 12.7 (July 1973), p. 1506. ISSN: 0003-6935. DOI: 10.1364/A0.12.001506 (cit. on pp. 105, 107).
- [14] F. J. Harren et al. “Photoacoustic Spectroscopy in Trace Gas Monitoring”. In: *Encyclopedia of Analytical Chemistry*. Chichester, UK: John Wiley & Sons, Ltd, Mar. 2012. DOI: 10.1002/9780470027318.a0718.pub2 (cit. on p. 105).
- [15] R. H. Johnson et al. “Loss mechanisms in resonant spectrophones”. In: *Applied Optics* 21.1 (Jan. 1982), p. 81. ISSN: 0003-6935. DOI: 10.1364/A0.21.000081 (cit. on p. 105).
- [16] M.-H. Wallmann. “Die Einstelldauer der Schwingungswärme in CO₂ in Abhängigkeit von Fremdgaszusätzen und vom Druck”. In: *Annalen der Physik* 413.7 (1935), pp. 671–681. ISSN: 00033804. DOI: 10.1002/andp.19354130704 (cit. on p. 105).
- [17] A. Glière et al. “Challenges in the Design and Fabrication of a Lab-on-a-Chip Photoacoustic Gas Sensor”. In: *Sensors* 14.1 (Jan. 2014), pp. 957–974. ISSN: 1424-8220. DOI: 10.3390/s140100957 (cit. on p. 105).

- [18] T. L. Cottrell and J. McCoubrey. *Molecular Energy Transfer in Gases*. Butterworth, 1961 (cit. on p. 105).
- [19] T. Rück. “Development, characterization and miniaturization of a trace gas detection system for NO₂ in air based on photoacoustic spectroscopy”. Ph. D. thesis. University of Regensburg, 2017 (cit. on pp. 106, 112, 115, 118).
- [20] T. L. Cottrell et al. “Measurement of vibrational relaxation times by the spectrophone. Application to CH₄, CO₂, N₂O, COS, NH₃ and HCN”. In: *Transactions of the Faraday Society* 62 (1966), p. 2655. ISSN: 0014-7672. DOI: 10.1039/tf9666202655 (cit. on p. 106).
- [21] M. B. Robin. “Photoacoustic Spectroscopy of Gases in the Visible and Ultra-violet Spectral Region”. In: *Optoacoustic spectroscopy and detection1*. New York: Academic Press, 1977, pp. 167–191. ISBN: 0125441509 (cit. on p. 107).
- [22] T. Oka et al. “Photoacoustic Study of 280 nm Band of Acetone Vapor”. In: *Bulletin of the Chemical Society of Japan* 61.1 (1988), p. 199. DOI: <https://doi.org/10.1246/bcsj.61.199> (cit. on pp. 107, 121–123).
- [23] L. Dong et al. “Ultra-sensitive carbon monoxide detection by using EC-QCL based quartz-enhanced photoacoustic spectroscopy”. In: *Applied Physics B* 107.2 (May 2012), pp. 275–283. ISSN: 0946-2171. DOI: 10.1007/s00340-012-4949-1 (cit. on p. 107).
- [24] L. Dong et al. “Ppb-level detection of nitric oxide using an external cavity quantum cascade laser based QEPAS sensor”. In: *Optics Express* 19.24 (Nov. 2011), p. 24037. ISSN: 1094-4087. DOI: 10.1364/OE.19.024037 (cit. on p. 107).
- [25] L. Dong et al. “Compact portable QEPAS multi-gas sensor”. In: *Proc. SPIE* 2011 7945 (2011), 79450R. ISSN: 0277786X. DOI: 10.1117/12.875108 (cit. on p. 107).
- [26] S. Schilt et al. “Near-infrared laser photoacoustic detection of methane: The impact of molecular relaxation”. In: *Applied Physics B: Lasers and Optics* 82.2 SPEC. ISS. (2006), pp. 319–329. ISSN: 09462171. DOI: 10.1007/s00340-005-2076-y (cit. on pp. 107, 109).
- [27] R. Lewicki et al. “Carbon dioxide and ammonia detection using 2 μ m diode laser based quartz-enhanced photoacoustic spectroscopy”. In: *Applied Physics B* 87.1 (Mar. 2007), pp. 157–162. ISSN: 0946-2171. DOI: 10.1007/s00340-006-2474-9 (cit. on p. 107).
- [28] A. Kosterev et al. “QEPAS methane sensor performance for humidified gases”. In: *Applied Physics B* 92.1 (July 2008), pp. 103–109. ISSN: 0946-2171. DOI: 10.1007/s00340-008-3056-9 (cit. on p. 107).
- [29] T. Rück et al. “NO₂ trace gas monitoring in air using off-beam quartz enhanced photoacoustic spectroscopy (QEPAS) and interference studies towards CO₂, H₂O and acoustic noise”. In: *Sensors and Actuators B: Chemical* 255 (Feb. 2017), pp. 2462–2471. ISSN: 09254005. DOI: 10.1016/j.snb.2017.09.039 (cit. on pp. 107, 109, 115).

- [30] S. Gray et al. “Detection of nitric oxide in air with a 5.2 μm distributed-feedback quantum cascade laser using quartz-enhanced photoacoustic spectroscopy”. In: *Optics Express* 18.22 (Oct. 2010), p. 23353. ISSN: 1094-4087. DOI: 10.1364/OE.18.023353 (cit. on p. 107).
- [31] A. A. Kosterev et al. “Applications of quartz tuning forks in spectroscopic gas sensing”. In: *Review of Scientific Instruments* 76.4 (Apr. 2005), p. 043105. ISSN: 0034-6748. DOI: 10.1063/1.1884196 (cit. on p. 107).
- [32] M. van Herpen et al. “Optical parametric oscillator-based photoacoustic detection of CO₂ at 4.23 μm allows real-time monitoring of the respiration of small insects”. In: *Applied Physics B* 82.4 (Feb. 2006), pp. 665–669. ISSN: 0946-2171. DOI: 10.1007/s00340-005-2119-4 (cit. on p. 107).
- [33] R. A. Rooth et al. “Photoacoustic measurement of ammonia in the atmosphere: influence of water vapor and carbon dioxide”. In: *Applied Optics* 29.25 (Sept. 1990), p. 3643. ISSN: 0003-6935. DOI: 10.1364/AO.29.003643 (cit. on p. 107).
- [34] J. H. Doty et al. “Recent advances in resonant optothermalacoustic detection”. In: ed. by M. Razeghi et al. Jan. 2011, 79450Q. DOI: 10.1117/12.875105 (cit. on p. 107).
- [35] M. Hammerich et al. “Photoacoustic study of kinetic cooling”. In: *Chemical Physics* 163.2 (June 1992), pp. 173–178. ISSN: 03010104. DOI: 10.1016/0301-0104(92)87101-E (cit. on pp. 108, 109).
- [36] N. Truong et al. “Detecting Carbon Monoxide (CO) With Photoacoustic Spectroscopy: The Role of Molecular Collision Dynamics”. In: *AIP Conference Proceedings*. AIP, 2009, pp. 3–8. DOI: 10.1063/1.3250106 (cit. on pp. 108, 109).
- [37] A. Kosterev et al. “Ultrasensitive gas detection by quartz-enhanced photoacoustic spectroscopy in the fundamental molecular absorption bands region”. In: *Applied Physics B* 80.1 (Jan. 2005), pp. 133–138. ISSN: 0946-2171. DOI: 10.1007/s00340-004-1619-y (cit. on p. 109).
- [38] F. G. C. Bijnen et al. “Intracavity CO laser photoacoustic trace gas detection: cyclic CH₄, H₂O and CO₂ emission by cockroaches and scarab beetles”. In: *Applied Optics* 35.27 (Sept. 1996), p. 5357. ISSN: 0003-6935. DOI: 10.1364/AO.35.005357 (cit. on p. 109).
- [39] J. Kalkman and H. van Kesteren. “Relaxation effects and high sensitivity photoacoustic detection of NO₂ with a blue laser diode”. In: *Applied Physics B* 90.2 (Feb. 2008), pp. 197–200. ISSN: 0946-2171. DOI: 10.1007/s00340-007-2895-0 (cit. on p. 109).
- [40] A. B. Nadykto. “Uptake of neutral polar vapor molecules by charged clusters/particles: Enhancement due to dipole-charge interaction”. In: *Journal of Geophysical Research* 108.D23 (2003), p. 4717. ISSN: 0148-0227. DOI: 10.1029/2003JD003664 (cit. on p. 110).

- [41] N. Mehio et al. “Quantum Mechanical Basis for Kinetic Diameters of Small Gaseous Molecules”. In: *The Journal of Physical Chemistry A* 118.6 (Feb. 2014), pp. 1150–1154. ISSN: 1089-5639. DOI: 10.1021/jp412588f (cit. on p. 110).
- [42] J. E. Lennard-Jones. “On the determination of molecular fields. —II. From the equation of state of a gas”. In: *Proceedings of the Royal Society of London. Series A, Containing Papers of a Mathematical and Physical Character* 106.738 (Oct. 1924), pp. 463–477. ISSN: 0950-1207. DOI: 10.1098/rspa.1924.0082 (cit. on pp. 110, 111).
- [43] L. Landau and E. Teller. “Theory of sound dispersion”. In: *Physik Zeitschrift der Sowjetunion* 10 (1936), pp. 34–38 (cit. on p. 111).
- [44] R. N. Schwartz et al. “Calculation of Vibrational Relaxation Times in Gases”. In: *The Journal of Chemical Physics* 20.10 (Oct. 1952), pp. 1591–1599. ISSN: 0021-9606. DOI: 10.1063/1.1700221 (cit. on p. 112).
- [45] J. T. Vanderslice and S. Weissman. “On the Theory of Vibrational Energy Exchange”. In: *The Journal of Chemical Physics* 37.10 (Nov. 1962), pp. 2247–2249. ISSN: 0021-9606. DOI: 10.1063/1.1732993 (cit. on p. 112).
- [46] F. I. Tanczos. “Calculation of Vibrational Relaxation Times of the Chloromethanes”. In: *The Journal of Chemical Physics* 25.3 (Sept. 1956), pp. 439–447. ISSN: 0021-9606. DOI: 10.1063/1.1742943 (cit. on p. 112).
- [47] S. G. Ejakov et al. “Acoustic attenuation in gas mixtures with nitrogen: Experimental data and calculations”. In: *The Journal of the Acoustical Society of America* 113.4 (Apr. 2003), pp. 1871–1879. ISSN: 0001-4966. DOI: 10.1121/1.1559177 (cit. on pp. 112, 115, 116).
- [48] A. Bhatia. *Ultrasonic Absorption*. New York: Dover Publications Inc., 1984. ISBN: 9780486649177 (cit. on p. 112).
- [49] A. D. Pierce. “Effects of Viscosity and Other Dissipative Processes”. In: *Acoustics*. Springer International Publishing, 2019, pp. 583–648. DOI: 10.1007/978-3-030-11214-1_10 (cit. on pp. 113, 114).
- [50] A. Cottet et al. “Acoustic absorption measurements for characterization of gas mixing”. In: *The Journal of the Acoustical Society of America* 116.4 (Oct. 2004), pp. 2081–2088. ISSN: 0001-4966. DOI: 10.1121/1.1785631 (cit. on p. 113).
- [51] S. W. Rienstra and A. Hirschberg. *An Introduction to Acoustics*. Eindhoven, 2004 (cit. on p. 113).
- [52] M. Müller. “Hard- und Softwareentwicklung eines Moduls zur Schallgeschwindigkeitsmessung in komplexen Gasgemischen bei 32 kHz”. M. Eng. thesis. OTH Regensburg, 2020 (cit. on p. 114).
- [53] D. A. Bohn. “Environmental effects on the speed of sound”. In: *Journal of the Audio Engineering Society* 36.4 (1988), pp. 223–231 (cit. on p. 114).

- [54] C. M. Harris. “Absorption of Sound in Air versus Humidity and Temperature”. In: *The Journal of the Acoustical Society of America* 40.1 (July 1966), pp. 148–159. ISSN: 0001-4966. DOI: 10.1121/1.1910031 (cit. on pp. 115, 116).
- [55] B. V. D. Weerd. “Entwicklung und Charakterisierung von CO₂ -Sensoren für die Bestimmung der CO₂ -Eliminierung während extrakorporaler Membranoxygenierung”. Ph.D. thesis. University of Regensburg, 2016 (cit. on p. 115).
- [56] V. O. Knudsen and E. Fricke. “The Absorption of Sound in Impurities , Containing Added The Absorption of Sound in CO₂, N₂O, COS , and in CS₂, Containing Added Impurities”. In: *The Journal of the Acoustical Society of America* 12 (1940), pp. 255–259 (cit. on pp. 115, 116).
- [57] I. V. Sherstov et al. “Method for measuring the resonant frequency of photoacoustic detector in the real-time mode”. In: *Instruments and Experimental Techniques* 59.5 (Sept. 2016), pp. 749–753. ISSN: 0020-4412. DOI: 10.1134/S0020441216050079 (cit. on p. 117).
- [58] J. D. van der Waals. “The equation of state for gases and liquids”. Nobel lecture. 1910 (cit. on p. 118).
- [59] P. W. Atkins and J. de Paula. *Physikalische Chemie*. 4th ed. Weinheim: WILEY-VCH, 2006. ISBN: 9783527315468 (cit. on p. 119).
- [60] M. Baba et al. “The S 1 (n , π^*) states of acetaldehyde and acetone in supersonic nozzle beam: Methyl internal rotation and C=O out-of-plane wagging”. In: *The Journal of Chemical Physics* 82.9 (May 1985), pp. 3938–3947. ISSN: 0021-9606. DOI: 10.1063/1.448886 (cit. on p. 119).
- [61] H. Zuckermann et al. “Dissociation energy of an isolated triplet acetone molecule”. In: *The Journal of Physical Chemistry* 92.17 (Aug. 1988), pp. 4835–4837. ISSN: 0022-3654. DOI: 10.1021/j100328a007 (cit. on p. 119).
- [62] B. Ruscic et al. “IUPAC Critical Evaluation of Thermochemical Properties of Selected Radicals. Part I”. In: *Journal of Physical and Chemical Reference Data* 34.2 (June 2005), pp. 573–656. ISSN: 0047-2689. DOI: 10.1063/1.1724828 (cit. on p. 119).
- [63] S. W. North et al. “Evidence for stepwise dissociation dynamics in acetone at 248 and 193 nm”. In: *The Journal of Chemical Physics* 102.11 (Mar. 1995), pp. 4447–4460. ISSN: 0021-9606. DOI: 10.1063/1.469493 (cit. on pp. 119, 120).
- [64] D. H. Mordaunt et al. “Nonstatistical unimolecular dissociation over a barrier”. In: *The Journal of Chemical Physics* 108.6 (Feb. 1998), pp. 2448–2457. ISSN: 0021-9606. DOI: 10.1063/1.475627 (cit. on p. 120).
- [65] D. A. Hansen. “Radiative and nonradiative transitions in the first excited singlet state of symmetrical methyl-substituted acetones”. In: *The Journal of Chemical Physics* 62.1 (1975), p. 183. ISSN: 00219606. DOI: 10.1063/1.430259 (cit. on p. 121).

- [66] T. Preukschat et al. “Comparison of the Photoacoustic Effect in the IR and the UV Regions”. In: *International Journal of Thermophysics* 36.9 (Sept. 2015), pp. 2318–2327. ISSN: 0195-928X. DOI: 10.1007/s10765-015-1885-4 (cit. on p. 122).
- [67] M. A. Blitz et al. “Pressure and temperature-dependent quantum yields for the photodissociation of acetone between 279 and 327.5 nm”. In: *Geophysical Research Letters* 31.6 (Mar. 2004), n/a–n/a. ISSN: 00948276. DOI: 10.1029/2003GL018793 (cit. on pp. 123–125).
- [68] H. Somnitz et al. “Acetone photolysis at 248 nm revisited: pressure dependence of the CO and CO₂ quantum yields”. In: *Physical Chemistry Chemical Physics* 11.38 (2009), p. 8522. ISSN: 1463-9076. DOI: 10.1039/b906751e (cit. on p. 124).
- [69] V. Khamaganov et al. “Photolysis of CH₃C(O)CH₃ (248 nm, 266 nm), CH₃C(O)C₂H₅ (248 nm) and CH₃C(O)Br (248 nm): pressure dependent quantum yields of CH₃ formation”. In: *Physical Chemistry Chemical Physics* 9.31 (2007), p. 4098. ISSN: 1463-9076. DOI: 10.1039/b701382e (cit. on p. 124).
- [70] B. Rajakumar et al. “The CH₃CO quantum yield in the 248nm photolysis of acetone, methyl ethyl ketone, and biacetyl”. In: *Journal of Photochemistry and Photobiology A: Chemistry* 199.2-3 (Sept. 2008), pp. 336–344. ISSN: 10106030. DOI: 10.1016/j.jphotochem.2008.06.015 (cit. on p. 124).
- [71] J. B. Burkholder et al. “Chemical Kinetics and Photochemical Data for Use in Atmospheric Studies”. In: *JPL Publication 15-10* 18 (2015). DOI: 10.13140/RG.2.1.2504.2806 (cit. on p. 124).
- [72] S. Aloisio and J. S. Francisco. “The photochemistry of acetone in the presence of water”. In: *Chemical Physics Letters* 329.3-4 (Oct. 2000), pp. 179–184. ISSN: 00092614. DOI: 10.1016/S0009-2614(00)01001-0 (cit. on p. 125).
- [73] R. Nádasdi et al. “Exciplex laser photolysis study of acetone with relevance to tropospheric chemistry”. In: *Chemical Physics Letters* 440.1-3 (May 2007), pp. 31–35. ISSN: 00092614. DOI: 10.1016/j.cplett.2007.04.014 (cit. on p. 125).
- [74] H. Meyrahn et al. “Quantum yields for the photodissociation of acetone in air and an estimate for the life time of acetone in the lower troposphere”. In: *Journal of Atmospheric Chemistry* 4.2 (June 1986), pp. 277–291. ISSN: 0167-7764. DOI: 10.1007/BF00052006 (cit. on p. 125).

Chapter 3

Spectral interference analysis

3.1 Spectral databases

For any kind of absorption spectra analysis, access to a spectral library, is mandatory in order to simulate absorption bands of the gas matrix of interest for different mixtures or ambient conditions. Spectral databases offer either mathematically derived or experimentally acquired information regarding absorption profiles of analytes and interference species of interest. In some cases, this data is provided for different temperatures, pressures and even broadener*, e.g. air, N₂, He, Ar etc. Some prominent spectral databases are provided by NIST (National Institute for Standards and Technology), HITRAN (high-resolution transmission molecular absorption database), PNNL (Pacific Northwest National Laboratory) and the MPI-Mainz UV/VIS Spectral Atlas (from now on referred to as Spectral Atlas) to name only a few. The following subsections will discuss the Spectral Atlas, the PNNL and HITRAN database, as well as *MolExplorer* and *HITRAN on the Web*, which exploit the “line-by-line” HITRAN database, more detailed since these sources have been used for the spectral interference analysis discussed within this chapter.

3.1.1 High-resolution transmission molecular absorption database (HITRAN)

HITRAN stands for high-resolution transmission molecular absorption database and its online database, *HITRANonline*, currently includes the following features:

- Line-by-line
- Absorption cross sections
- Collision induced absorption (CIA)
- Aerosol properties
- High-temperature molecular spectroscopic database (HITEMP)
- HITRAN Application Programming Interface (HAPI) [1]

The database offers a compilation of spectroscopic parameters exploited by software (e.g. HAPI, *Hitran on the Web*) in order to help understanding and to simulate the emission, absorption and transmission of light in the atmosphere. The Air Force Cambridge Research Laboratories founded the database in the late 1960s when information regarding the infrared properties of the atmosphere was scarce and needed [2].

*Broadener refers to buffer molecules causing a certain collisional broadening (refer to section 2.2.4).

The most prominent part is the line-by-line spectrum. It includes experimental and calculated information regarding spectral line intensities usually representing ro-vibrational energy transitions at certain wavelengths. Furthermore, various parameters like the Einstein coefficients for a certain transition are provided, too, allowing to simulate the line intensities and the broadening profile for various conditions including temperature, pressure and different types of broadener. Most of the parameters have already been addressed in the sections 2.2.3 and 2.2.4, however, the interested reader can receive more information elsewhere [3, 4].

Nowadays, offline and online tools like, *MolExplorer*, *Hitran on the Web* or HITRAN's own python based HAPI software, allow easy exploitation and simulations based on the HITRAN database. With *MolExplorer* for example, the user can either simulate spectral profiles of one analyte of interest or even investigate the absorption profiles of customised gas mixtures at different ambient conditions. HITRAN also offers the user to download the line-by-line data of the molecules and isotopes directly from *HITRANonline* in common formats allowing customised applications with the data sets. These approaches are useful in most of the cases, however, these line-by-line data is only available for a limited number of molecules, mostly small atmospheric molecules like H₂O, CO₂ or CO. For larger molecules like acetone, experimentally measured absorption cross sections are available. In most cases, the data sets are available at different temperatures and pressures. The data sets of one molecule can then be plotted online or downloaded to be used externally. The features CIA, aerosol properties and HITEMP have not been used within this thesis and further information is provided elsewhere [3, 5].

Hitran on the Web exploits the HITRAN2012 database [6] and allows easy and fast simulations of the line-by-line spectrum of selected analytes. The tool allows modeling high-resolution spectra by selecting e.g. the molecule and the desired isotopes of interest or a user defined gas mixture. The user can then set the wavelength range, the line shape (e.g. Voigt profile) and the pressure as well as many more options. Although this web tool has further application scenarios and options, they will not be discussed in this thesis since they were not used. The publication by Mikhailenko et al. [7] describes the underlying functions of the *Hitran on the Web* online tool. Note, that during the thesis *MolExplorer* and *Hitran on the Web* have been used rather rarely and mainly in order to distinguish between noise or small absorption features in empirically acquired data sets. For the spectral interference analysis in the IR region, however, mainly measured PNNL data was used.

3.1.2 Pacific Northwest National Laboratory (PNNL)

The data sets provided by the PNNL database were all experimentally collected and contain nearly 500 gas-phase species [8]. The employed PNNL FT-IR for measurements offered a resolutions of approximately 0.1 cm⁻¹. The sample temperature is usually 25 °C, though, for some gases measurements have been performed at 5 °C and 50 °C as well. The analyte gas is diluted in ultra high purity N₂ and the sample is

kept at 760 Torr. For each spectrum, different analyte concentrations are measured at least ten times and re-normalised to 1 ppmV per 1 meter of optical pathlength at 296 K. The normalised spectrum plots the absorbance in $\text{ppmV}^{-1} \text{m}^{-1}$ against the wavenumber. One spectrum ranges usually from 600 cm^{-1} to 6500 cm^{-1} , allowing sophisticated analysis regarding interference in the IR. Since the PNNL absorbance \tilde{A}_{PNNL} is specified in $1 \text{ ppmV}^{-1} \text{m}^{-1}$ in base-10 format and not in base-e format, care has been taken to convert all data into base-e HITRAN absorption cross sections $\sigma_{\text{A,HITRAN}}$ or base-e HITRAN absorption coefficients α_{HITRAN} , before comparing the PNNL data to the HITRAN data. The conversion factor between \tilde{A}_{PNNL} and α_{HITRAN} is

$$\alpha_{\text{HITRAN}} = \tilde{A}_{\text{PNNL}} \ln(10) \cdot 0.01 \quad (3.1)$$

where the factor $\ln(10)$ describes the conversion from base-10 to base-e and the factor 0.01 is necessary to convert the unit m^{-1} into cm^{-1} . Since \tilde{A}_{PNNL} is normalised to 1 ppmV, the computed HITRAN absorption coefficient α_{HITRAN} from equation 3.1 still refers to a concentration of 1 ppmV. Referring to equation 2.31, $\sigma_{\text{A,HITRAN}} = \alpha_{\text{HITRAN}}/\rho_i$. Therefore, the HITRAN base-e absorption cross section in m^2 is thus

$$\sigma_{\text{A,HITRAN}} = \tilde{A}_{\text{PNNL}} \ln(10) \cdot \frac{V_{\text{m}}}{N_i N_{\text{A}}} \quad (3.2)$$

Since $V_{\text{m}} = \frac{RT}{p} = \frac{N_{\text{A}} kT}{p}$ applies* and converting $\sigma_{\text{A,HITRAN}}$ into the unit cm^2 , equation 3.2 can be rewritten to

$$\sigma_{\text{A,HITRAN}} = \tilde{A}_{\text{PNNL}} \ln(10) \cdot \frac{kT}{p_i} 10^4 \quad \text{with} \quad p_i = N_i p \quad (3.3)$$

where p_i is the partial pressure of the molecule i . As \tilde{A}_{PNNL} always refers to 1 ppmV, N_i can be replaced by 10^{-6} . This leads to the final conversion specified by

$$\sigma_{\text{A,HITRAN}} = \tilde{A}_{\text{PNNL}} \ln(10) \cdot 4.03 \times 10^{-16} \quad (3.4)$$

with $[\sigma_{\text{A,HITRAN}}] = \text{cm}^2$. Further information regarding the comparability between PNNL and NIST, as well as a comment on the comparability between PNNL and HITRAN line-by-line data can be found elsewhere [9, 10]. It has to be noted, that from 2019 on, the PNNL IR database has unfortunately been shut down due to funding issues†.

3.1.3 Spectral Atlas

The Max Planck Institute (MPI) of Mainz presents the "MPI-Mainz UV/VIS Spectral Atlas of Gaseous Molecules". In 2013, it was the largest online collection of quantum yields and absorption cross sections in the UV and visible wavelength region including gaseous molecules and radicals. The data files consist of individual

*101.325 kPa and 296 K are assumed for pressure and temperature, respectively.

†The information was provided via personal correspondence with Timothy Johnson.

measurements of almost a complete century and can be accessed via Spectral Atlas - Link* [11]. The data sets have been collected from publications, PhD theses, books, conference proceedings, from other research centers and even unpublished results were the authors directly contacted the MPI. The Spectral Atlas does neither endorse the data sets nor claim high quality and recommends comparing experimental results within the atlas for one species. All absorption cross section data presented in the Spectral Atlas has been converted into cm^2 in base-e, allowing a better comparability. Furthermore, the web page of the MPI Spectral Atlas offers a quantum yield tab, allowing the user to search for specific photolytic reactions and the corresponding rate coefficients, though this data is rather limited. More detailed information regarding quantum yields is usually dealt with in the papers discussing the absorption cross section of the analyte of interest [11].

Another useful source for absorption cross sections and quantum yields of atmospheric gases is the “Chemical Kinetics and Photochemical Data for Use in Atmospheric Studies” report, which is carried out by the Jet Propulsion Laboratory and updated frequently [12].

3.1.4 *QuickSpec* software tool

Since it is often necessary to compare data from different databases, a LabVIEW based software tool, called *QuickSpec*, has been developed. Currently, the tool can load and compare data sets from PNNL and the absorption cross section of HITRAN without further ado. Data from other data bases can be used, too, if the data containing file is set up properly. The software allows to display the absorption

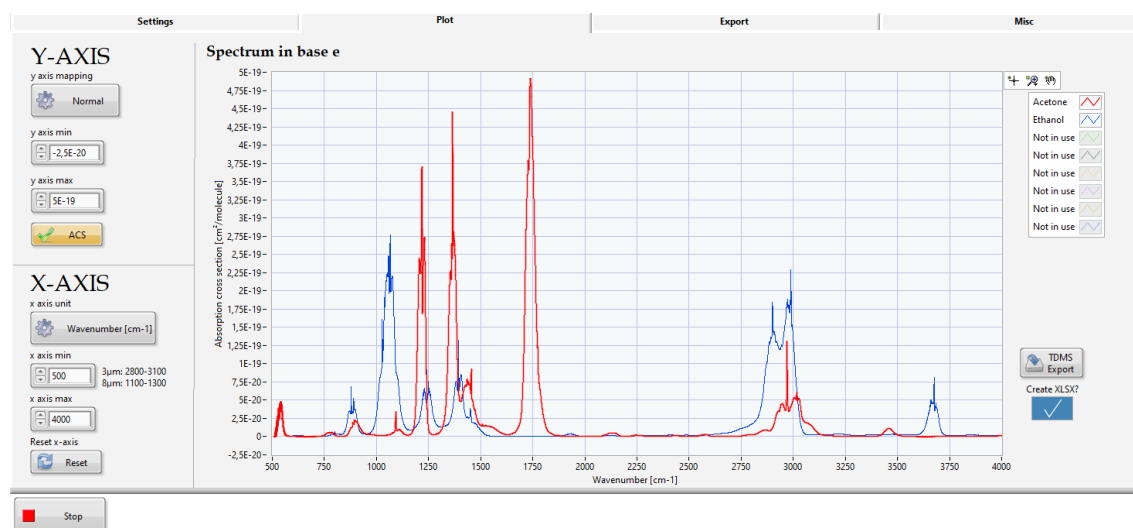


Fig. 3.1. Snippet of the graphical user interface of the *QuickSpec* simulation tool visualising the absorption cross sections of acetone (red) and ethanol (blue).

*http://satellite.mpic.de/spectral_atlas/

cross section or the absorption coefficient for a user defined concentration for up to eight substances simultaneously. Figure 3.1 shows a snippet of the graphical user interface of the software tool visualising the graph containing the results of a simulation of acetone and ethanol from 500 cm^{-1} to 4000 cm^{-1} . The tool can display either the absorption cross section or the absorption coefficient on the ordinate and the abscissa can be set to units of cm^{-1} or μm .

Using this tool, multiple data bases can be exploited easily, allowing simulation of several species with different concentrations simultaneously. When a region with low spectral overlap has been identified, this excerpt of the simulation can be exported in different file formats and further processed by means of a more suitable tool for data visualisation like *OriginPro 2019*.

References

- [1] R. Kochanov et al. “HITRAN Application Programming Interface (HAPI): A comprehensive approach to working with spectroscopic data”. In: *Journal of Quantitative Spectroscopy and Radiative Transfer* 177 (July 2016), pp. 15–30. ISSN: 00224073. DOI: 10.1016/j.jqsrt.2016.03.005 (cit. on p. 136).
- [2] L. S. Rothman. *The HITRAN Database*. URL: <https://hitran.org/about/> (cit. on p. 136).
- [3] I. Gordon et al. “The HITRAN2016 molecular spectroscopic database”. In: *Journal of Quantitative Spectroscopy and Radiative Transfer* 203 (Dec. 2017), pp. 3–69. ISSN: 00224073. DOI: 10.1016/j.jqsrt.2017.06.038 (cit. on p. 137).
- [4] M. Šimečková et al. “Einstein A-coefficients and statistical weights for molecular absorption transitions in the HITRAN database”. In: *Journal of Quantitative Spectroscopy and Radiative Transfer* 98.1 (Mar. 2006), pp. 130–155. ISSN: 00224073. DOI: 10.1016/j.jqsrt.2005.07.003 (cit. on p. 137).
- [5] L. Rothman et al. “HITEMP, the high-temperature molecular spectroscopic database”. In: *Journal of Quantitative Spectroscopy and Radiative Transfer* 111.15 (Oct. 2010), pp. 2139–2150. ISSN: 00224073. DOI: 10.1016/j.jqsrt.2010.05.001 (cit. on p. 137).
- [6] L. Rothman et al. “The HITRAN2012 molecular spectroscopic database”. In: *Journal of Quantitative Spectroscopy and Radiative Transfer* 130 (Nov. 2013), pp. 4–50. ISSN: 00224073. DOI: 10.1016/j.jqsrt.2013.07.002 (cit. on p. 137).
- [7] C. N. Mikhailenko et al. “Information-calculating system Spectroscopy of Atmospheric Gases. The structure and main functions.” In: *Atmospheric and Oceanic Optics* 18.9 (2005), pp. 685–695 (cit. on p. 137).

- [8] S. Sharpe et al. “The PNNL quantitative IR database for infrared remote sensing and hyperspectral imaging”. In: *Applied Imagery Pattern Recognition Workshop, 2002. Proceedings.* IEEE Comput. Soc, 2002, pp. 45–48. ISBN: 0-7695-1863-X. DOI: 10.1109/AIPR.2002.1182253 (cit. on p. 137).
- [9] S. W. Sharpe et al. “Gas-phase databases for quantitative infrared spectroscopy”. In: *Applied Spectroscopy* 58.12 (2004), pp. 1452–1461. DOI: 10.1366/0003702042641281. arXiv: arXiv:1011.1669v3 (cit. on p. 138).
- [10] R. V. Kochanov et al. “Comment on ”Radiative forcings for 28 potential Archean greenhouse gases” by Byrne and Goldblatt (2014)”. In: *Climate of the Past* 11.8 (Aug. 2015), pp. 1097–1105. ISSN: 1814-9332. DOI: 10.5194/cp-11-1097-2015 (cit. on p. 138).
- [11] H. Keller-Rudek et al. “The MPI-Mainz UV/VIS Spectral Atlas of Gaseous Molecules of Atmospheric Interest”. In: *Earth System Science Data* 5.2 (Dec. 2013), pp. 365–373. ISSN: 1866-3516. DOI: 10.5194/essd-5-365-2013 (cit. on p. 139).
- [12] J. B. Burkholder et al. “Chemical Kinetics and Photochemical Data for Use in Atmospheric Studies”. In: *JPL Publication 15-10* 18 (2015). DOI: 10.13140/RG.2.1.2504.2806 (cit. on p. 139).

3.2 Spectral interference analysis in the IR and UV region

Spectral cross-sensitivities can be a major issue in absorption based sensing techniques. Especially in a complex measurement matrix like human breath exhale. Therefore, the species and their corresponding concentrations used within the simulations will be addressed in the following sections. Besides, the analysis will be divided into subsections discussing the IR and the UV region, respectively. The considered absorption regions of acetone within this interference study include the $n_s \rightarrow \pi_s^*$ absorption band, which ranges from ~ 266 nm to 315 nm* and a wavelength region in the IR between 1000 cm^{-1} to 4000 cm^{-1} . There is no significant absorption feature of acetone present in the visible wavelength region.

If not mentioned otherwise, all data sets used within the simulation were supplied by the databases mentioned in section 3.1, simulated using the *QuickSpec* tool and visualised by means of *OriginPro 2019*. Note that solely cross-sensitivities arising from spectral overlap will be addressed within this chapter. Frequency detuning (refer to section 2.5.5), acoustic attenuation (refer to section 2.5.4) or effects on the relaxation behavior (refer to section 2.5.2) will not be discussed.

3.2.1 The interfering species

Lists of high abundant, endogenous and exogenous breath components have been presented in section 2.1.5. Though these tables might not be comprehensive for all applications, they provide a good estimate of the concentrations of most of the species present in breath under normal circumstances and in the clinical environment.

In order to cause cross-sensitivities in terms of photoacoustic spectroscopy, two conditions have to be met by the interfering species. On the one hand, the spectral overlap, in terms of the absorption coefficient, has to be significant and on the other hand, the excited interferent has to generate a heat influx during deexcitation, distorting the photoacoustic signal generated by the target analyte. The latter one is usually the case in the IR region except for situations when the VT-relaxation time is too long to allow contribution to the detected photoacoustic signal. In the UV region, however, the excited interference species might decay radiatively leading to no perceptible distortion of the photoacoustic signal. The acceptable spectral overlap depends on two conditions as well. First, if a non-tuneable light source is applied and simple AM-PAS at one wavelength has to be performed and second, if secondary sensors are available to allow for compensation for certain molecules. This

*On the one hand, this region corresponds to an absorption cross section above $1.00 \times 10^{-20}\text{ cm}^2$ and on the other hand UV LEDs emitting in this wavelength region were applied within this thesis.

topic will be addressed more closely in the respective result part of the following sections.

3.2.1.1 Endogenous species

Some of the molecules listed in table 2.2 can be excluded from spectral interference analysis in the IR region. This includes N_2 , O_2 , Ar and H_2 since they are not IR active due to their immutable dipole moment. Besides, there is no significant absorption band in the UV region between 266 nm and 315 nm expected, since there is no data available in the Spectral Atlas at this wavelength region.

An exception, however, is oxygen. For O_2 Bogumil et al. [1] measured an ACS of below $1.0 \times 10^{-24} \text{ cm}^2$ from 260 nm to 300 nm, however, this was doubted by Fally et al. [2], who measured an ACS with only about $1.0 \times 10^{-26} \text{ cm}^2$. Due to the results of Oka et al. [3] and Preukschat et al. [4] a promoting effect caused by O_2 is expected, however, none of them investigated the photoacoustic signal at different O_2 concentrations. Nevertheless, for the following spectral interference analysis, O_2 was neglected. Results regarding different O_2 concentrations will be presented in section 5.2.6.1.

Tab. 3.1. List of endogenous substances and their corresponding concentrations in human breath exhale employed within spectral interference analysis.

Molecule	Concentration in ppmV
H_2O	50 000
CO_2	50 000
CO	1.5
NH_3	2.0
N_2O	0.35
CH_4	8.0
COS	0.70
Isoprene	0.30
Methanol	1.0

Neglecting the above discussed species, endogenous substances and their corresponding concentrations used within the spectral interference analysis are listed in table 3.1. Note that the concentrations of ethanol and methanol can exceed endogenously produced quantities due to exogenous influences, thus they are listed in table 3.2.

The concentration of acetone within the simulation was either 1.0 ppmV, 0.5 ppmV or 0.1 ppmV to provide a better impression of the strength of spectral overlap in the different simulations.

3.2.1.2 Exogenous species

Discussing every possible exogenous source within this thesis would certainly go beyond the scope and intention of this work. However, breath research is likely to take place in a hospital. In order to fulfill high hygienic requirements, cleaning agents and disinfectants are omnipresent in clinics.

Tab. 3.2. List of exogenous substances and their corresponding concentrations in human breath exhale, which are employed within the spectral interference analysis.

Molecule	Concentration in ppmV
Ethanol	2.5
Formaldehyde	0.60
1-propanol	1.7
Isopropyl alcohol	5.4

Table 3.2 bases on table 2.3 provided in section 2.1.5 and presents some prominent disinfectants and cleaning agents used in clinical environment as well as their concentrations having been detected in related exhaled breath studies. Their concentrations in the ambient air might be even higher in some cases, hence, ambient air measurements in environments, which can distort the exhaled breath composition due to exogenous influences, are mandatory in a later application.

3.2.2 Acetone spectra and wavelength modulation

This section discusses the UV and IR absorption spectra of acetone in detail. Furthermore, the influence of temperature and pressure on the shape of the absorption bands is analysed. Finally, a table is provided, indicating where WM-PAS would be possible theoretically, based on the light sources employed within this thesis.

Figure 2.10 visualises the complete spectrum of acetone from 1000 cm^{-1} to 4000 cm^{-1} and is provided in section 2.2.1. In order to find absorption features suitable for WM-PAS, a detailed analysis of the absorption peaks of acetone has been performed. Figure 3.2 visualises two sections of the acetone absorption bands located at approximately 1200 cm^{-1} (left) and 3000 cm^{-1} (right). Since the R- and P-branches often merge with the Q-branch of a vibrational absorption band, a virtual baseline has

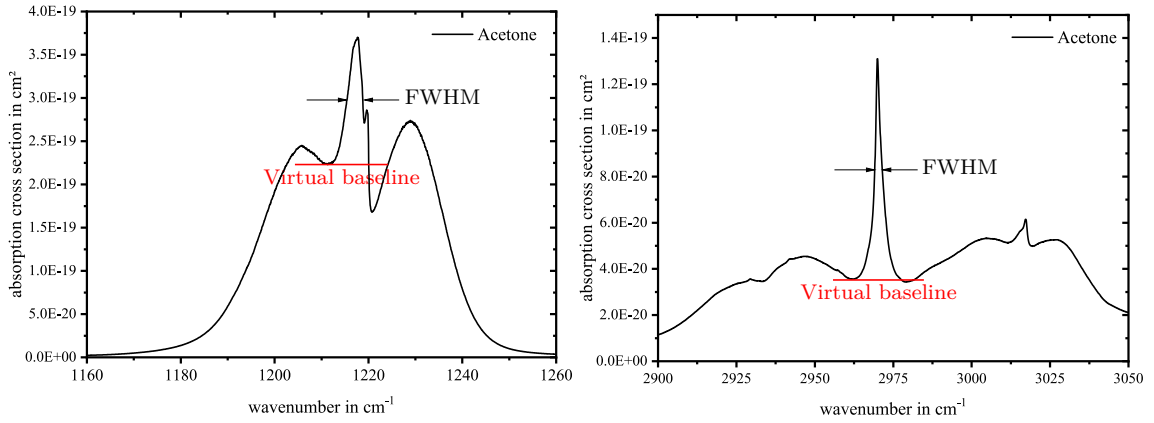


Fig. 3.2. Illustration of the broad acetone absorption bands at 1200 cm^{-1} (left) and at 3000 cm^{-1} (right) visualising the merge of Q-branch with P- and R-branch as well as the virtual baseline (red).

been set at the merge-intersection in order to derive the modulation depth relevant FWHM of the peak.

Table 3.3 provides the FWHM in cm^{-1} and in nm as well as the peak height in cm^2 for the most prominent acetone peaks in the IR region between 1000 cm^{-1} and 4000 cm^{-1} . Note that the peak height of the absorption bands is calculated as the difference between peak maximum and virtual baseline.

In terms of tuneability of the light sources employed within this thesis, it has to be distinguished between fast and slow tuneability. Regarding semiconductor laser sources like interband cascade lasers (ICL) and quantum cascade lasers (QCL), the emission wavelength can be tuned by means of current or temperature variation*. However, the latter one is usually too slow to be used for WM, which requires modulation frequencies $f_{\text{mod}} = f_{\text{res}}/n$, with n being the n^{th} harmonic used as demodulation frequency in the lock-in amplifier. Besides, most optical parametric oscillators (OPO) cannot be used at all for fast wavelength tuning, since adjustment of the optical components and stability is too slow. Further information regarding the light sources applied within this thesis is provided in section 4.2.

Since the tuning ranges, by means of current tuning, of available ICL and QCL are less than 15 nm^\dagger the peaks at 1217.5 cm^{-1} and 1739.0 cm^{-1} can be neglected regarding WM-PAS, as they are too broad. The results of the spectral interference analysis will provide further information, if WM-PAS might be applicable for the other peaks in the IR region.

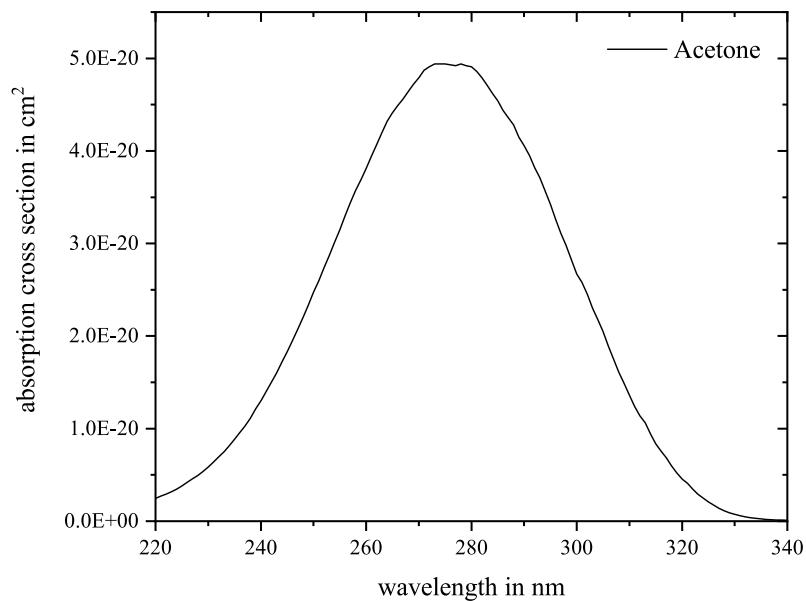
*Actually, the emission wavelength depends only on the temperature of the component, but increasing the current increases the temperature of the laser as well.

[†]No ICL or QCL was found at relevant shops having a higher tuneability. However, there might certainly be exceptions.

Tab. 3.3. Peak width and height of different prominent acetone peaks between 1000 cm^{-1} to 4000 cm^{-1} .

Center in cm^{-1}	FWHM in cm^{-1}	Center in nm	FWHM in nm	Peak height in cm^2
1091.7	0.7	9160	5.5	2.2×10^{-20}
1217.5	3.4	8214	22.3	1.8×10^{-19}
1365.5	0.7	7323	3.9	1.5×10^{-19}
1554.9	0.7	6431	3.0	3.5×10^{-20}
1739.0	11.9	5750	39.4	1.3×10^{-19}
2970.0	2.4	3367	2.7	9.5×10^{-20}

Considering the UV region, WM-PAS is not an option, since the peak is very broad. According to figure 3.3, the FWHM is approximately 51 nm. Besides, there are no easily and fast tuneable light sources in the UV available like for the IR. In most of the cases, broad band or multiline emitter like Xe- or Hg-Arc lamps are employed. Combining the light source with a monochromator yields in a single wavelength emission spectrum. This results usually in quite low optical output power below 1 mW, which makes them impractical for trace gas PAS applications. There are

**Fig. 3.3.** Absorption cross section of the $n_S \rightarrow \pi_S^*$ transition in acetone at 298 K measured by [5].

several types of laser sources for the UV region as well, but they are usually quite complex and bulky. The interested reader can find more information regarding the current status of UV lasers in a review from Kaneda [6] from 2018.

Due to the broad absorption feature, the lack of suitable light sources in the UV and the fact that a non-tuneable UV LED was employed within this thesis, only AM-PAS will be considered for the spectral interference analysis in the UV region.

3.2.3 Influence of temperature and pressure on the absorption bands of acetone

The general effect of temperature and pressure on the shape and intensity of an absorption line has been discussed in section 2.2.4 and 2.2.3, respectively. Figure 3.4 visualises the absorption band for different pressures and at a fixed temperature (top) and vice versa (bottom) at the absorption band around 2790 cm^{-1} . In order to compare the absorption band at different pressures. Harrison et al. [7] kept the partial pressure of acetone constant and added air to the gas sample steadily. The result indicates, that pressure has only a small effect on the absorption cross section. Between 601 Torr and 204 Torr the intensity of the peak dropped only 3 %. There is a different situation when the temperature is varied. Since pressure has a quite small

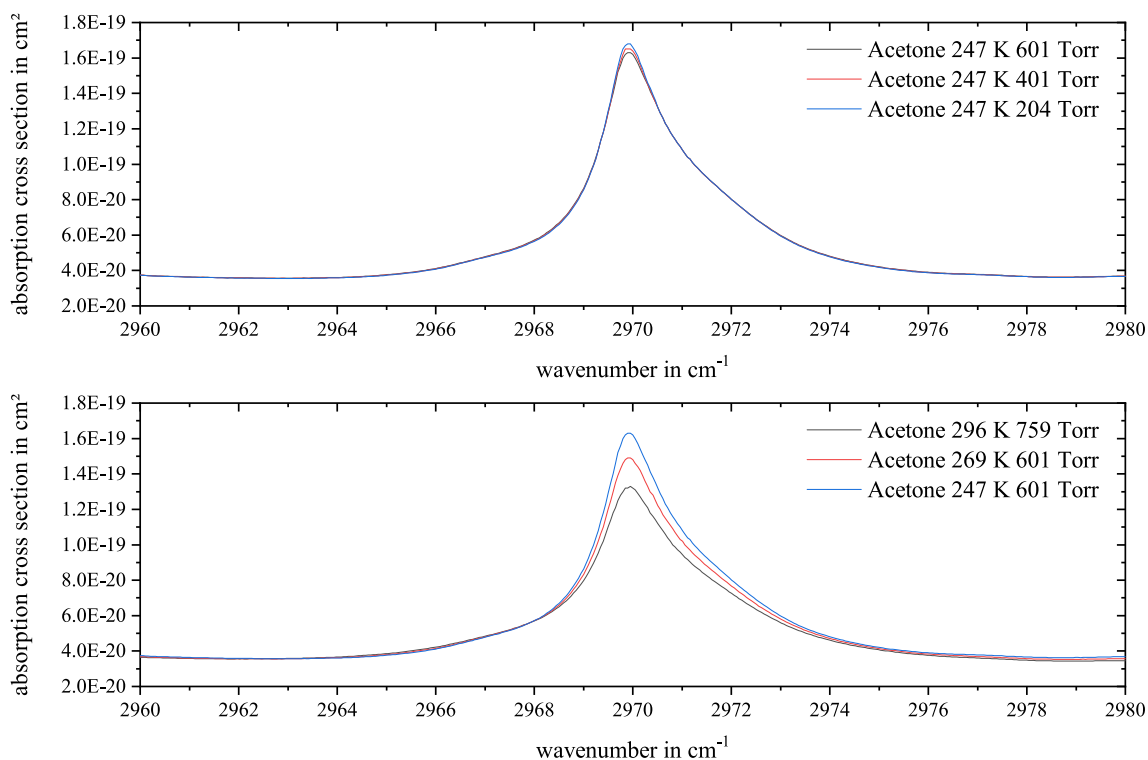


Fig. 3.4. Demonstration of the influence of pressure (top) and temperature (bottom) on the IR acetone ACS at 2790 cm^{-1} measured by Harrison et al. [7].

influence, a third measurement with different temperature and pressure (759 Torr instead of 601 Torr) was included in the comparison visualised in the bottom graph. Within approximately 50 °C, the intensity increased by 23 % towards lower temperatures. Besides, it could be noticed, that only the Q-branch, but not the broad wing features are influenced neither by pressure nor by temperature. Harrison et al. [8] also investigated the absorption band structure of acetone in the region between 1950 cm⁻¹ and 830 cm⁻¹. The pressure and temperature dependency of the absorption cross section was similar to the one observed in the 3000 cm⁻¹ region.

In the ultraviolet region, Gierczak et al. [5] provided an analytical solution to calculate the change in intensity for the acetone transition $n_S \rightarrow \pi_S^*$ depending on the temperature given by

$$\sigma_A(\lambda_{ph}, T) = \sigma_A(\lambda_{ph}, 298)(1 + c_1(\lambda_{ph})T + c_2(\lambda_{ph})T^2) \quad (3.5)$$

with c_1 and c_2 being temperature coefficients. This equation has been superseded by Burkholder using the expression

$$\sigma_A(\lambda_{ph}, T) = \sigma_A(\lambda_{ph}, 298)(1 + \bar{A}(\lambda_{ph})T + \bar{B}(\lambda_{ph})T^2 + \bar{C}(\lambda_{ph})T^3) \quad (3.6)$$

with \bar{A} , \bar{B} and \bar{C} being new temperature coefficients provided by Burkholder [9, pp. 610]. Only a modest temperature dependency at wavelengths above 300 nm was detected, causing the cross section to increase with a rising temperature. At shorter wavelengths, however, no significant relation between temperature and absorption cross section was detected.

Concluding this section, neither small temperature variations within a few degree Celsius nor pressure fluctuations in general affect the absorption cross sections of acetone significantly in the UV or IR region.

3.2.4 Simulation parameter

Since most of the bigger molecules included in the spectral interference analysis are not available in common line-by-line databases like HITRAN, e.g. acetone, isopropanol or ethanol, the measured spectra from the PNNL database are used for the interference simulation and analysis, where not mentioned otherwise. Exhaled breath usually has a temperature around 308 K [10] and the pressure is assumed to be close to the ambient pressure. Since for most of the spectra only data for 296 K is available, this temperature will be used in the simulations although this might cause some error if the PAC is heated to a different temperature. Furthermore, measured data is often more accurate, when performed correctly and, if available, should be used for spectral interference analysis [11]. However, simulated absorption spectra have some advantages compared to measured spectra, too. First, the simulated absorption spectra can be calculated easily for different mixtures, pressures and temperatures providing a rather comprehensive set of data. Second, they are not limited by measurement artefacts, noise or measurement errors. Hence, for CO₂

and H₂O, simulated absorption spectra from *HITRAN on the Web* and *MolExplorer* have been considered, respectively, to allow better interpretation of the measured data in regions with low or close to zero absorption. At these regions, actual small absorption features cannot be distinguished from noise. Since the PNNL spectra from H₂O and CO₂ have to be multiplied by 50 000* the noise is amplified as well making an interpretation of the spectrum in these low absorbance regions quite difficult. The simulation parameters applied in *MolExplorer* and *HITRAN on the Web* for the simulation of H₂O and CO₂ are summarised in the appendix A.4. The simulated data was exported from *MolExplorer* and *HITRAN on the Web* and was loaded into *QuickSpec* in order to compare it to the PNNL data for further analysis.

3.2.5 Results of the IR spectral interference analysis

The simulation and analysis were subdivided into several parts for the sake of more clear graphs. The groups are listed in table 3.4. For water and carbon dioxide, a separate analysis was performed. The other endogenous breath gases have been divided into group 3, including carbon monoxide, ammonia and dinitrogen monoxide and the 4th group including carbonyl sulfide, isoprene, methanol[†] and methane. The exogenous molecules include ethanol, formaldehyde, isopropanol and 1-propanol.

Tab. 3.4. Separation of the different interference species in different simulation groups.

Group 1	Group 2	Group 3	Group 4	Group 5
H ₂ O	CO ₂	CO	Methanol	Ethanol
		NH ₃	Methane	Formaldehyde
		N ₂ O	Isoprene	Isopropanol
			COS	1-propanol

3.2.5.1 Overview between 1000 cm⁻¹ and 4000 cm⁻¹

To narrow down the region of interests from the complete range from 1000 cm⁻¹ to 4000 cm⁻¹ first, simulations of water and the exogenous substances with acetone have been performed first, since these are expected to have the highest interference potential. The upper graph of figure 3.5, visualises the strong absorption features of water at a concentration of 50 000 ppmV. For better visualisation, the y-axis is

*This is necessary since PNNL spectra are normalised to 1 ppmV and both species are simulated with a concentration of 50 000 ppmV.

[†]Methanol can be considered as both, exogenous and endogenous species.

set to a logarithmic scaling, though this has the drawback, that negative values* are not displayed, which distorts the evaluation in the noisy baseline regions. In order to analyse these noisy regions, the y-axis scaling was set to normal scaling when zoomed in for further evaluation. However, it is still clearly visible, that only the acetone bands at 1090 cm^{-1} , 1220 cm^{-1} and at 3000 cm^{-1} show relatively low spectral overlap and thus will be focused on regarding a more elaborate spectral interference analysis. The other absorption features of acetone are completely covered by water absorption bands. In addition, considering the bottom graph of figure 3.5, only the R-branch from 3010 cm^{-1} to 3050 cm^{-1} and the Q- and P- branches from 1200 cm^{-1} to 1220 cm^{-1} , of the respective acetone absorption bands, will be considered in the spectral interference analysis, since otherwise the spectral overlap from the exogenous substances, especially isopropanol, are too strong. The absorption band intensity plays an important role in terms of sensitivity, too, thus 3050 cm^{-1} was chosen to be the lowest acceptable absorption cross section with a value of about $2.1 \times 10^{-20}\text{ cm}^2$. Therefore, the wavenumber region between 3010 cm^{-1} and 3050 cm^{-1} , having absorption cross section values varying from $5.2 \times 10^{-20} - 2.1 \times 10^{-20}\text{ cm}^2$, will be

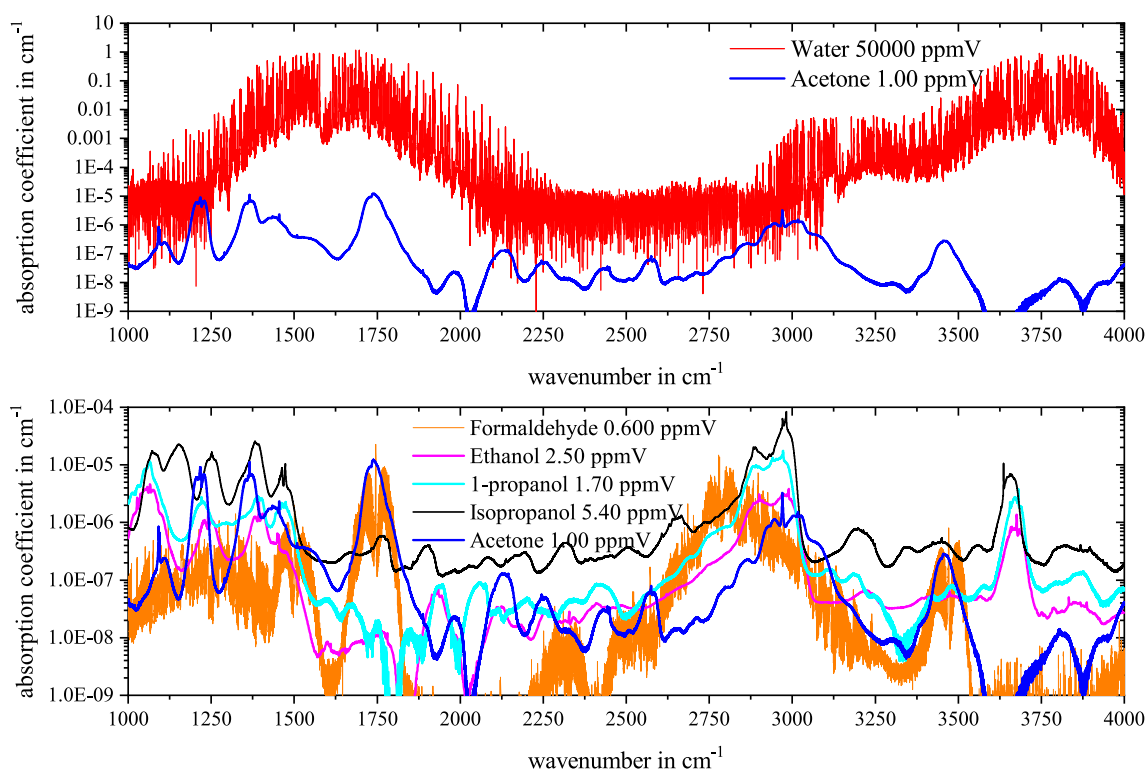


Fig. 3.5. General overview of spectral overlap introduced by exogenous species and water in the region from 1000 cm^{-1} to 4000 cm^{-1} . (Top) presenting the absorption coefficient from 50 000 ppmV water and 1 ppmV acetone in the wavenumber region from 1000 cm^{-1} to 4000 cm^{-1} and (bottom) demonstrating the strong interference of exogenous substances from cleaning agents and disinfectants in the same wavenumber range.

*Negative values only occur in the measured data close to the baseline due to noise.

evaluated more closely. Besides, in the lower wavenumber region around 1215 cm^{-1} , the absorbance of acetone is generally stronger and thus the lowest acceptable ACS limit could be set to approximately $2.0 \times 10^{-19}\text{ cm}^2$ at 1200 cm^{-1} . Towards higher wavenumbers, spectral congestion due to interferences is the limiting factor resulting in an investigated region between $1200 - 1220\text{ cm}^{-1}$.

3.2.5.2 Results of group 1 & 2

In order to verify if the simulated data of CO_2 and H_2O is more appropriate than the PNNL data for further interference simulation, both simulated data sets have been compared to the measured data.

Figure 3.6 visualises the simulated and measured data set for 50 000 ppmV of H_2O at the previously identified regions with high potential towards low spectral cross-sensitivities. Besides, figure 3.7 demonstrates that most of the fluctuations within the measured data can be assigned to noise.

The results of the comparison of simulated and measured H_2O data can be summarised as follows:

1. The maximum peak strength of a line is slightly lower if measured.

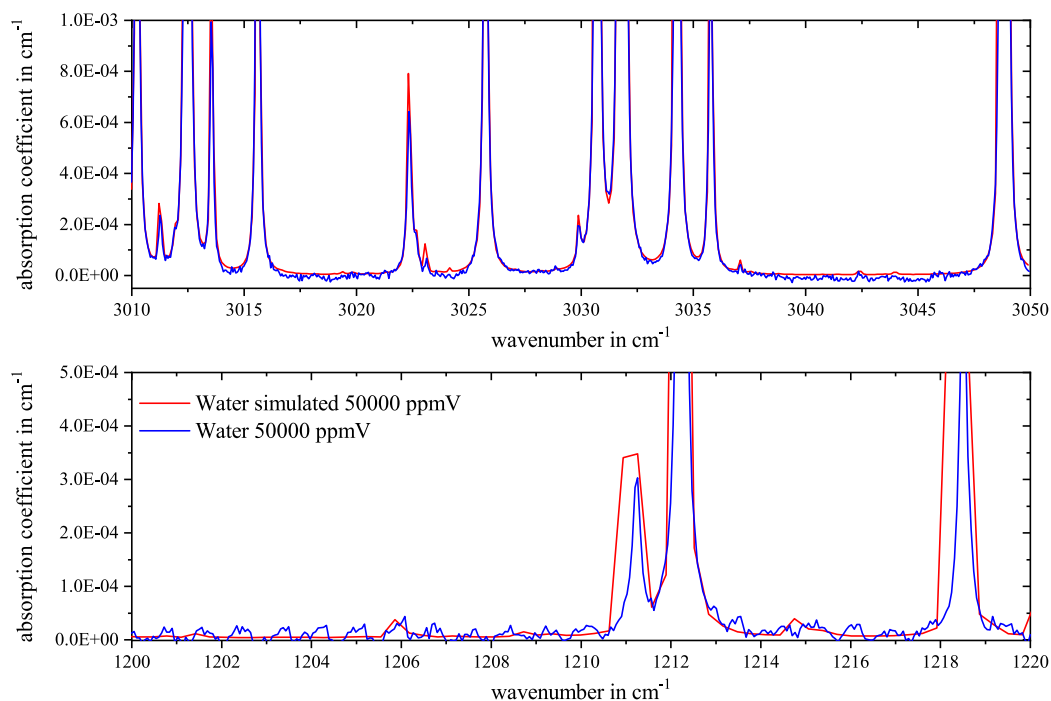


Fig. 3.6. (Top) simulated and measured absorption coefficients of 50 000 ppmV water in the region from 3010 cm^{-1} to 3050 cm^{-1} and (bottom) in the region between $1200 - 1220\text{ cm}^{-1}$, visualising the differences between measured and simulated data.

2. A smooth baseline is provided in the simulated data, whereas a lot of noise is present in the measured data in wavenumber regions with lower absorption.
3. The baseline lift due to two merging peaks is often significantly (up to five times around the valley at 3020 cm^{-1}) higher in simulated data than in measured data.

The simulated data is quite useful to distinguish between noise and small absorption peaks, however, since the baseline level often deviates significantly from measured data, the experimentally acquired data from H_2O will be used for further spectral analysis.

Regarding water interference, the most promising regions have been defined to be at $3017.5 - 3019\text{ cm}^{-1}$, $3023.7 - 3024.5\text{ cm}^{-1}$ and $3038.5 - 3045.5\text{ cm}^{-1}$ within the 3000 cm^{-1} wavenumber regime (refer to figure 3.8). Since the bottom of figure 3.6 indicates that most of the H_2O peaks within the water spectrum around 1200 cm^{-1} can be assigned to noise, comparably low spectral congestion due to water is expected between $1200 - 1205.5\text{ cm}^{-1}$ and from 1207 cm^{-1} to 1208 cm^{-1} . However, it is obvious, that at both wavenumber regions water will cause a certain distortion regarding the photoacoustic signal due to spectral interference. The results and consequences will be discussed in the results part of this section. Like water, carbon dioxide has a high abundance in exhaled breath. Its volume concentration is quite similar around $50\,000\text{ ppmV}$, as well. A simulated line-by-line spectrum exported from *HITRAN on the Web* was considered, too, in order to allow better interpretation of the measured data from PNNL. The graphs in figure 3.9 demonstrate, that the peaks are in a good agreement between the measured and simulated data. The

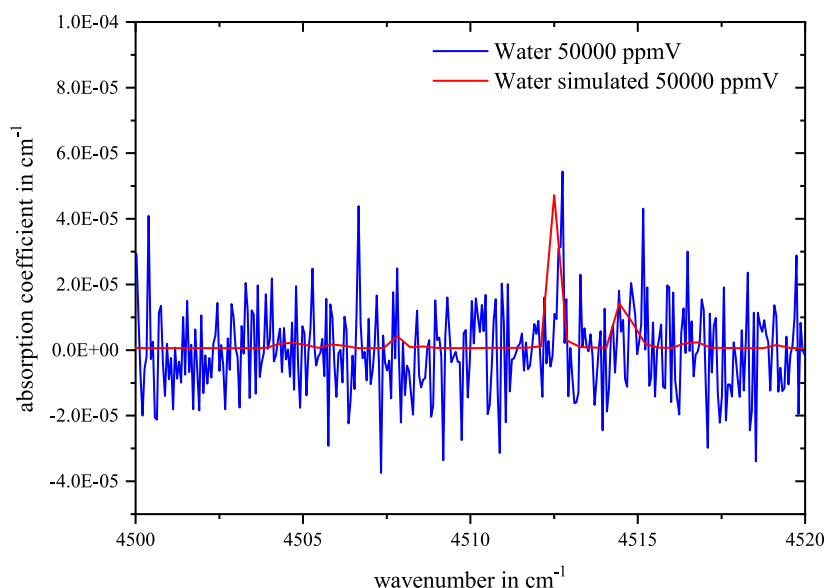


Fig. 3.7. Comparison of simulated and measured absorption coefficient for $50\,000\text{ ppmV}$ of H_2O in a low absorption region.

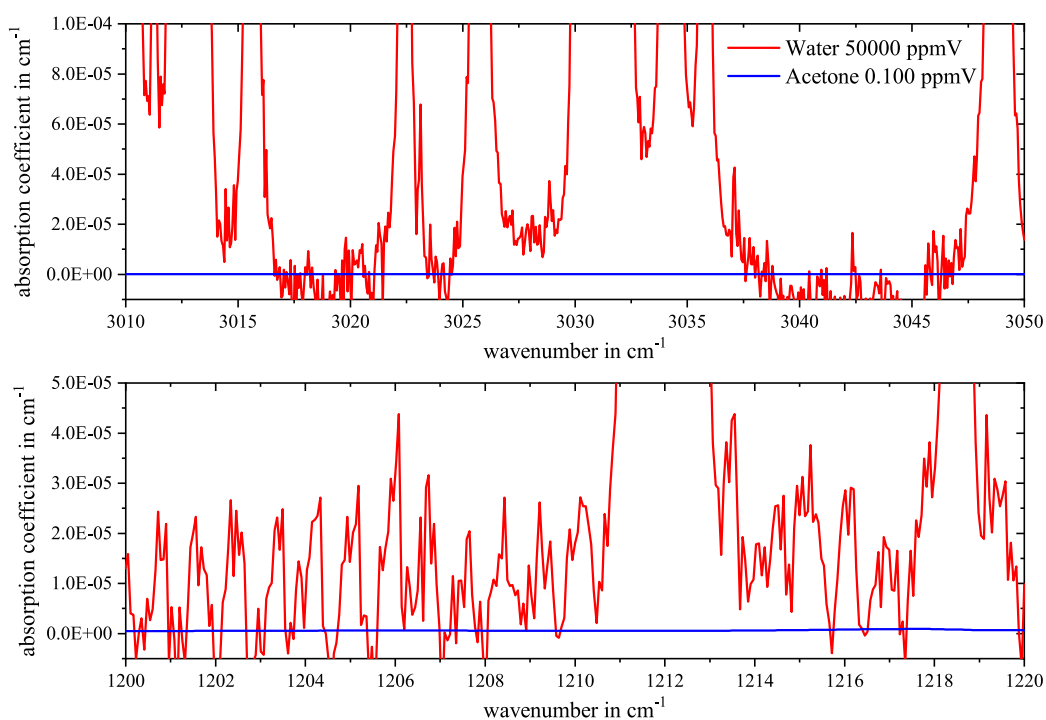


Fig. 3.8. Spectral interference analysis including 50 000 ppmV of H_2O and 0.1 ppmV of acetone. (Top) spectral analysis within the region from 3010 cm^{-1} to 3050 cm^{-1} and (bottom) between $1200 - 1220\text{ cm}^{-1}$.

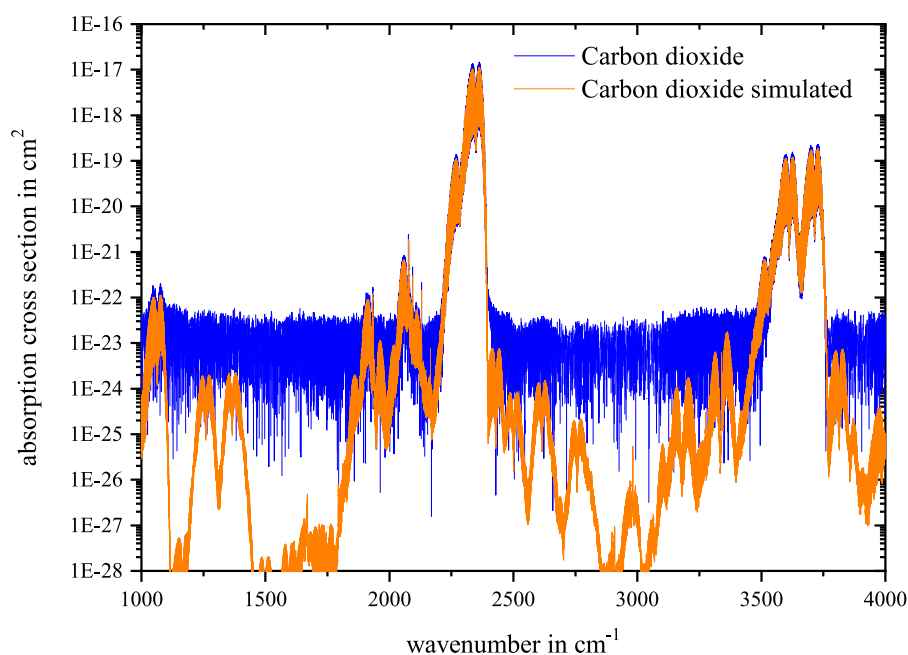


Fig. 3.9. Comparison of simulated and measured carbon dioxide absorption cross sections between 1000 cm^{-1} and 4000 cm^{-1} .

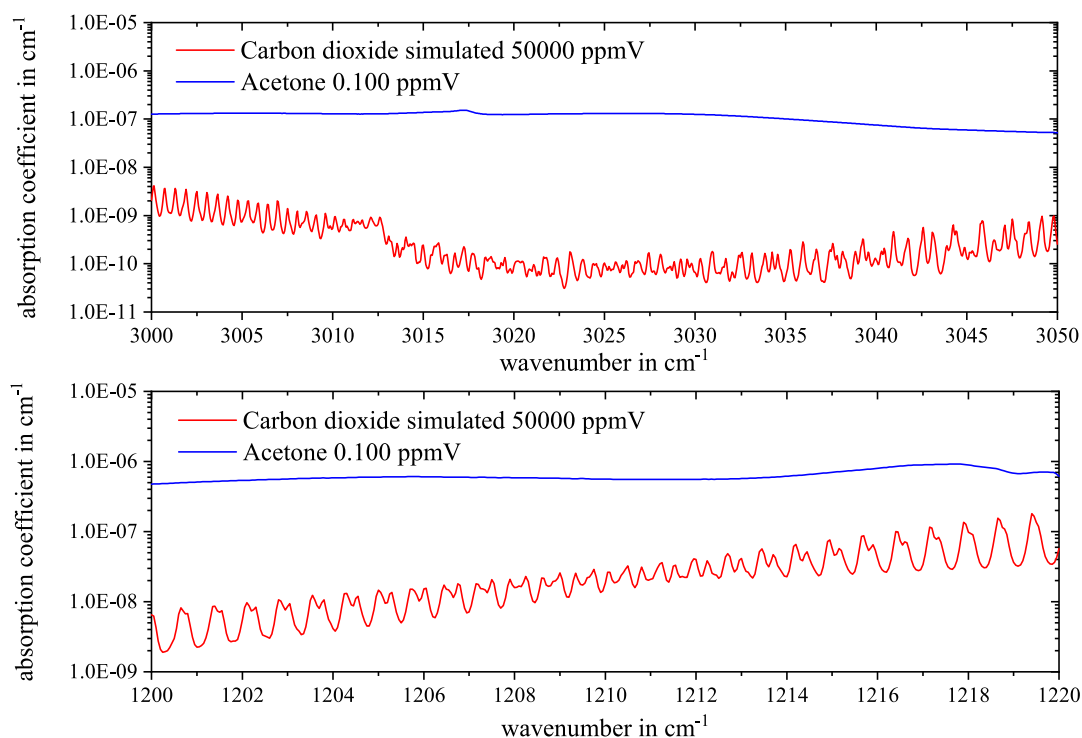


Fig. 3.10. Spectral interference analysis including 50 000 ppmV of simulated CO₂ and 0.1 ppmV of acetone. (Top) spectral analysis within the region from 3000 cm⁻¹ to 3050 cm⁻¹ and (bottom) between 1200 – 1220 cm⁻¹ indicating no spectral interference from CO₂.

baseline around 3000 cm⁻¹ and 1200 cm⁻¹, however, is several orders of magnitude lower in the simulated data compared to the measured data.

Based on the simulated data, the spectral interference of 50 000 ppmV of CO₂ and 0.100 ppmV of acetone for both regions of interest are presented in figure 3.10. They indicate low spectral interference in both regions, thus no cross-sensitivities by CO₂ due to spectral overlap are expected.

3.2.5.3 Results of group 3 & 4

Considering figure 3.11, the interference potential of group 3, including carbon monoxide, dinitrogen monoxide and ammonia, is obviously low, especially in the 3000 cm⁻¹ region. In the region from 1200 – 1220 cm⁻¹, the peaks of ammonia located at 1204.5 cm⁻¹, 1206 cm⁻¹, 1210.5 cm⁻¹ and 1213 cm⁻¹ should be avoided. According to the top part of figure 3.12, the species of group 4 including isoprene, methane and methanol do have a high interference potential, whereas carbonyl sulfide can be neglected in the wavenumber regime around 3000 cm⁻¹. Even at 1 ppmV of acetone the absorption band of methanol is similarly strong compared to the acetone band and methane, with a pronounced fine structure, exceeds the absorption band of acetone at some points with its sharp absorption features. Due to that,

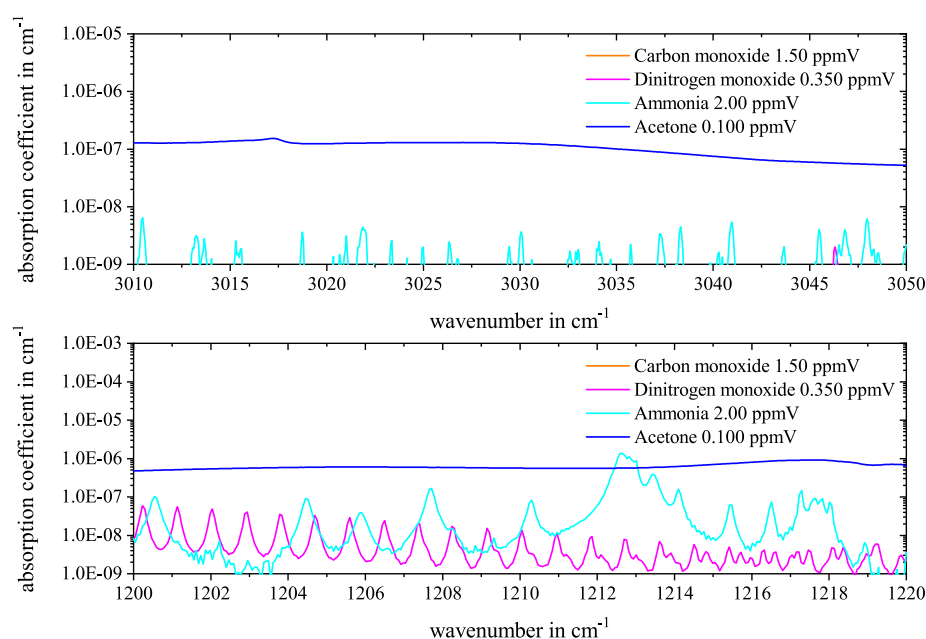


Fig. 3.11. Spectral interference analysis of acetone in a mixture with endogenous species including CO, N₂O, and NH₃. (Top) spectral analysis in the region from 3010 cm⁻¹ to 3050 cm⁻¹ with 0.1 ppmV of acetone and (bottom) between 1200 cm⁻¹ and 1220 cm⁻¹, again, with 0.1 ppmV of acetone.

sub ppmV concentrations of acetone are only reliably measurable in the 3000 cm⁻¹

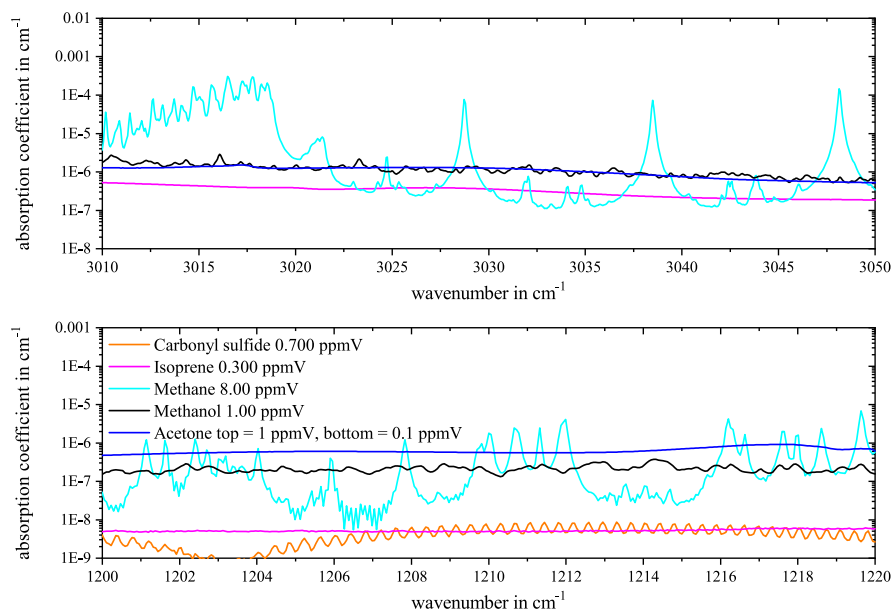


Fig. 3.12. Spectral interference analysis of acetone in a mixture with endogenous species including COS, isoprene, methane and methanol. (Top) spectral analysis in the region from 3010 cm⁻¹ to 3050 cm⁻¹ with 1 ppmV of acetone and (bottom) between 1200 cm⁻¹ and 1220 cm⁻¹ with 0.1 ppmV of acetone.

regime, if evaluation methods based on chemometrics are performed. This will be discussed in more detail in section 3.2.6.

In the region of 1220 cm^{-1} (refer to bottom part of figure 3.12), the situation is significantly better. For 0.1 ppmV of acetone, the absorption band is a few times higher than the rest between 1200 cm^{-1} and 1220 cm^{-1} . However, the absorption band of methane with its sharp features succeeds the absorption band of acetone at some points and methanol's absorption coefficient is only a few times lower than the absorption coefficient of 0.1 ppmV of acetone. The wavenumber spots demonstrating minimal spectral overlap are from $1204.5 - 1209.5\text{ cm}^{-1}$ with an interruption from $1207.5 - 1208\text{ cm}^{-1}$.

3.2.5.4 Results of group 5

The simulation results for group 5 are visualised in figure 3.13. For the region around 3000 cm^{-1} , the absorption bands of the exogenous molecules are stronger than the acetone absorption bands even for a concentration of 1 ppmV of acetone. Only beyond 3041 cm^{-1} , the ethanol absorption band at 2.5 ppmV is smaller as the one of acetone, which is also the case for the other substances. At 3022 cm^{-1} , the absorption coefficient of acetone is only covered by the one of ethanol, the latter one

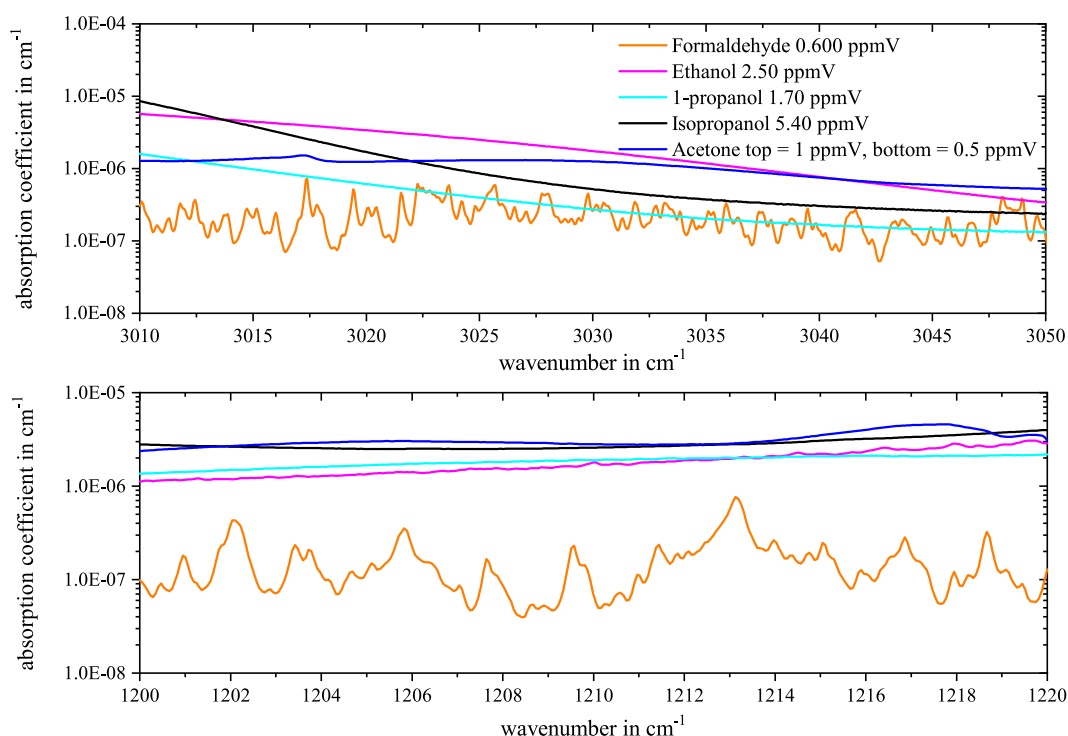


Fig. 3.13. Spectral interference analysis of acetone in a mixture with exogenous species including formaldehyde, ethanol, 1-propanol and isopropanol. (Top) spectral analysis in the region from 3010 cm^{-1} to 3050 cm^{-1} with 1 ppmV of acetone and (bottom) between 1200 cm^{-1} and 1220 cm^{-1} with 0.5 ppmV of acetone.

being 3 times stronger at this point and approaching towards the absorption band of acetone until they intersect at 3041 cm^{-1} . Moving closer towards 3000 cm^{-1} the absorption bands of ethanol, isopropanol and 1-propanol are becoming significantly stronger, whereas the absorption band of acetone is rather constant. Again, sub ppmV concentrations of acetone are only reliably measurable in the 3000 cm^{-1} region, with high ambient concentrations of disinfectants and cleaning agents, if further post-processing methods are performed. Nevertheless, the region from $3022 - 3050\text{ cm}^{-1}$ is the most promising within this setting.

At the region around 1220 cm^{-1} , however, the absorption coefficient for acetone at 0.5 ppmV is significantly stronger and hence, is not covered completely by the absorption bands of the exogenous molecules. The wavenumber range from $1203 - 1212\text{ cm}^{-1}$ of the P-branch of the absorption band of acetone for 0.5 ppmV is higher than the others, though only slightly. Except for formaldehyde, interference will certainly distort the photoacoustic acetone detection if solely AM-PAS is applied, if the abundance of the exogenous substances in the exhaled breath is as high as simulated within this thesis for an acetone abundance of 0.5 ppmV.

3.2.6 Summary and conclusion of the IR spectral interference analysis

This section discusses the results of the spectral interference analysis for the IR region. It has to be noted, that this analysis simulates the worst case scenario regarding the concentration of the interfering species.

Water and carbon dioxide having both an abundance of about 50 000 ppmV were investigated closely. The PNNL data is quite noisy in the regions of interest at 3000 cm^{-1} and 1200 cm^{-1} , and the interference simulation in *QuickSpec* magnifies this close to baseline noise in absorption coefficient simulations, due to the high abundance of both species. Therefore, a simulated line-by-line spectrum of carbon dioxide and water have been considered, too. For CO_2 , figure 3.10 demonstrates low interference potential in both wavenumber regions of interest. Water, however, has some peaks within the 3000 cm^{-1} wavenumber regime. Low spectral interference region are $3017.5 - 3019\text{ cm}^{-1}$, $3023.7 - 3024.5\text{ cm}^{-1}$ and $3038.5 - 3045.5\text{ cm}^{-1}$ as well as between $1200 - 1205.5\text{ cm}^{-1}$ and from 1207 cm^{-1} to 1208 cm^{-1} . Although measurements would be necessary for a precise quantitative statement, a certain spectral cross-sensitivity from water can be expected for both regions due to a high absorption baseline of water.

The endogenous molecules, carbonyl sulfide, carbon monoxide, dinitrogen monoxide and ammonia, do not show a significant interference potential for 0.1 ppmV acetone in both regions of interest. Only ammonia must be considered due to a few peaks between 1204 cm^{-1} to 1213 cm^{-1} . Regarding the endogenous molecules, isoprene, methane and methanol, set to their worst-case scenario concentrations, the absorp-

tion coefficients of these species bury the absorption band of acetone for 0.1 and 0.5 ppmV.

Tab. 3.5. Summary of the most promising absorption regions around the acetone absorption band at 3000 cm^{-1} and 1220 cm^{-1} . All significantly interfering molecules are listed, except for the exogenous substances.

Molecule	wavelength region in cm^{-1}	
	3010 – 3050	1200 – 1220
Water	3017.5 – 3019.5	1200 – 1205.5
	3023.7 – 3024.5	1207 – 1208
	3038.5 – 3045.5	
Methanol Methane Isoprene	3022 – 3024.5	1204.5 – 1207.5
	3025 – 3028	1208 – 1209.5
	3029.5 – 3037	
	3040 – 3045	
	3023.7 – 3024.5	1204.5 – 1205.5
Agreement	3040 – 3045	1208

At 1 ppmV acetone concentration in the region from $3020 - 3050\text{ cm}^{-1}$, the absorption coefficient of methanol is the same as the absorption coefficient of acetone and some peaks of methane pierce through acetone's absorption band, as well. Nevertheless, the regions with the comparably lowest spectral overlap are from 3022 cm^{-1} to 3045 cm^{-1} with interruptions at 3024.8 cm^{-1} , from $3028 - 3029.5\text{ cm}^{-1}$ and from $3037 - 3040\text{ cm}^{-1}$. At the region around 1022 cm^{-1} , though, even at 0.1 ppmV of acetone, some areas are promising regarding low spectral interferences. Especially from $1204.5 - 1209.5\text{ cm}^{-1}$, interrupted only from $1207.5 - 1208\text{ cm}^{-1}$ by one of the very sharp methane peaks penetrating the acetone absorption band.

The exogenous molecules, formaldehyde, ethanol, 1-propanol and isopropanol, set to high concentrations simulating a worst-case scenario, present strong absorption bands in the 3000 cm^{-1} region. Thus, even at 1 ppmV of acetone, the absorption band of acetone is covered with ethanol and isopropanol in the most promising regions from $3022 - 3045\text{ cm}^{-1}$, where acetone still expresses a considerably strong absorption coefficient. In the area around 1200 cm^{-1} , however, even at an acetone concentration of 0.5 ppmV the absorption coefficient of acetone is slightly higher than the others from $1203 - 1212\text{ cm}^{-1}$.

In table 3.5, an overview of the absorption regions with low spectral interferences of acetone regarding the endogenous species is provided. Only molecules, which showed an interference potential in the simulation before are listed. The exogenous molecules are considered in the conclusion.

Concluding, the exogenous molecules have the highest spectral interference potential. Even for 1 ppmV the acetone absorption spectrum is buried at least under the ethanol absorption band up to 3041 cm^{-1} . In the region around 1200 cm^{-1} , acetone must have a concentration of 0.5 ppmV or higher in order to express an absorption band stronger than the interfering molecules do. For methanol, methane and isoprene acetone has to be abundant at around 1 ppmV to express a similar strong absorption band in between $3022 - 3045\text{ cm}^{-1}$, though sharp peaks of methane eventually penetrate the flat absorption curve of acetone in this area. However, in the 1200 cm^{-1} region, even 0.1 ppmV of acetone is only slightly affected by the absorption bands of these three species. Finally, water limits the useful wavenumbers at the regions of 3000 cm^{-1} and 1200 cm^{-1} significantly as well, though even at 0.1 ppmV the valley between the water peaks seem promising and low spectral interference from water is likely to be compensable with a simple humidity sensor. Hence, at both regions, small acetone concentrations will only be determined reliably, if a cross-sensitivity suppression method like a chemometrics based technique is applied, which is discussed in section 3.2.7. Besides, small and cheap secondary sensors can be used in order to determine H_2O or CO_2 , which can assist in cross-sensitivity compensation methods.

To sum it up, for further experiments in the region around 3000 cm^{-1} , the wavenumbers from **$3023.7 - 3024.5\text{ cm}^{-1}$** and from **$3040 - 3042\text{ cm}^{-1}$** should be used. Around 1200 cm^{-1} the wavenumbers around **1205 cm^{-1}** and **1208 cm^{-1}** provide less congested areas. In addition, the results of figure 3.5 demonstrate, that the acetone absorption peaks accessibly with WM-PAS (refer to table 3.3) are all located in regions strongly congested with water absorption lines and absorption bands originating from the exogenous species. Hence, classical WM-PAS is no option for detecting breath acetone.

3.2.7 Multicomponent analysis

In the previous section, it has been deduced, that low acetone concentrations around 0.1 ppmV are not reliably detectable in a complex gas mixture like human breath within the IR region using simple AM-PAS. In order to distinguish the photoacoustic signals resulting from the different components i present in the gas mixture, the photoacoustic signal has to be measured at different wavelengths n chosen on the basis of the corresponding absorption spectra of the individual gas mixture components. In a simplified consideration, the resulting photoacoustic signal \hat{S}_n is given by [12, p. 68]

$$\hat{S}_n = P_n N_i R_n \quad (3.7)$$

where N_i is the volume ratio of the molecule i , P_n is the optical power at λ_n and R_n is the response of the PAS system at λ_n^* . For a gas sample containing several components, equation 3.7 extends to

$$\hat{S}_n = P_n \sum_{i=1}^K N_i R_{in} \quad (3.8)$$

where R_{in} is the response due to component i at wavelength n and K is the number of components present in the mixture. Solving equation 3.8 after N_i leads to

$$N_i = \sum_{n=1}^K R_{ni}^{-1} \frac{\hat{S}_n}{P_n} \quad (3.9)$$

with R_{ni}^{-1} being the inverse of the matrix R_{in} . As an example, in order to deduce the concentration of five different components within a mixture consisting only of those five species, at least measurements at five different wavelengths are necessary to obtain an unambiguous solution of the linear system of equations[†]. Figure 3.14 demonstrates a simple example scenario consisting of two components A and B. The two overlapping absorption features from both components add up to the resulting absorption band C. Measuring the concentration only at one wavelength would lead

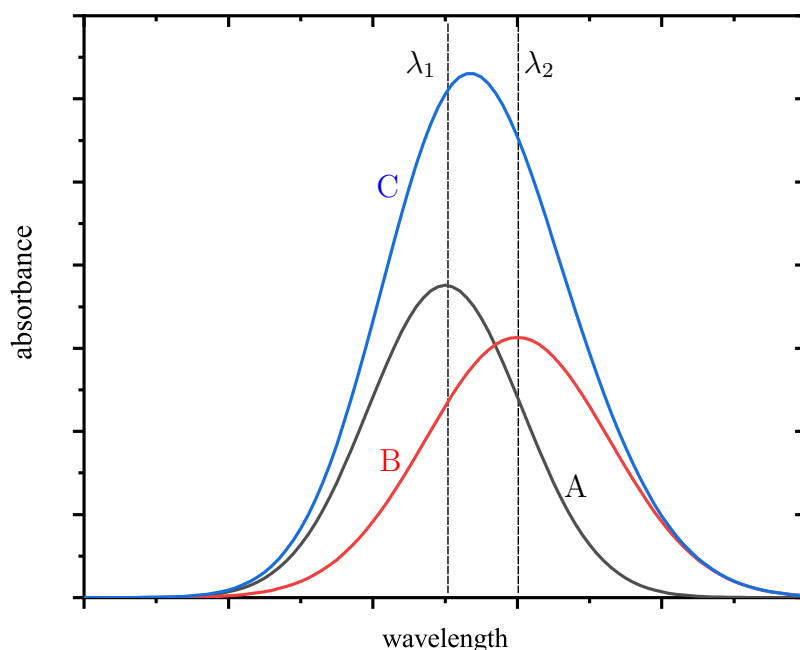


Fig. 3.14. Example of multicomponent analysis using multiple wavelengths. C is the cumulative absorption band resulting from the absorption bands from species A and B. λ_1 and λ_2 are the wavelengths, which are used for deducing the concentrations of the components A and B.

*Note that the response of a PAS system for each component needs to be calibrated.

[†]If only the concentration of one analyte needs to be derived, less measurement points could be sufficient, depending on the absorption spectrum of the mixture.

to an incorrect result for component A or B, since the response resulting from component A **and** B cannot be distinguished. Measuring at the indicated wavelengths λ_1 and λ_2 and solving equation 3.9, though, provides the concentration of both components.

However, this approach cannot be applied if the absorption features have identical shapes. Imagining two very broad absorption features, which resemble two parallel horizontal lines, this approach is obviously not applicable. Thus choosing appropriate wavelengths based on the individual and complementary absorption spectrum is important. Regions with small absorption coefficient slopes, i.e. absorption peaks or flat absorption bands are preferable*, since the absorption coefficient is less prone to pressure or temperature induced changes. Elisabeth Wittmann performed an analysis of the IR region between 3020 cm^{-1} and 3044 cm^{-1} including the same species and concentrations used within the spectral interference analysis described in the previous sections†, in order to determine an optimisation of the following parameters:

- The number of wavelengths to perform a measurement at,
- wavelength increment between two measurement points and
- the initial wavelength for the measurement series.

Note that the simulation neglected noise and possible calibration errors and was purely based on the absorption spectra provided by the databases. Obviously, an infinite number of measurements, each at a different wavelength, would result in a maximum accuracy. However, since this is not feasible in terms of a fast photoacoustic measurement, a compromise between speed and accuracy has to be found. The results, using linear regression methods, predict a sufficient accuracy using eleven data points in order to deduce the concentration of acetone, with an increment of 1 cm^{-1} . The wavelength regions from 3024 cm^{-1} to 3034 cm^{-1} and from 3031 cm^{-1} to 3041 cm^{-1} demonstrated the least mean percentage error of 0.32 % and 0.16 %, respectively.

These results provide a good approach for further research towards multicomponent analysis in breath. However, calibration data is necessary to improve such simulations in order to develop reliable evaluation schemes allowing proper handling of complex gas matrixes like breath exhale. An example of such a calibration measurement is provided in section 5.4.4.

There have been recent studies using such methods in breath analysis. Tuzson et al. [13] used a vertical external cavity surface emitting laser (VECSEL) and measured acetone in the presence of a few volume percent of H_2O as well as isoprene levels and ethanol. They demonstrated a good interference suppression, though most of the measurements were performed at concentration ranges above 1 ppmV of acetone.

*As long as the other components do not feature similar shapes at the same wavelength.

†The acetone level was set to 0.1 ppmV.

Besides, Mitrayana et al. [14] detected acetone, ammonia and ethylene in breath by means of photoacoustic spectroscopy, measuring at several emission lines of their CO₂ laser in the wavenumber regime below 1000 cm⁻¹ using the method described within this section.

3.2.8 Spectral interference analysis of the 278 nm absorption band of acetone

The number of interfering species in terms of photoacoustic spectroscopy in the UV is expected to be smaller than in the IR region. For example, methanol and ethanol are well known solvents in UV/VIS spectroscopy. They can be used down to approximately 210 nm [15, p. 11]. Below, these substances distort UV/VIS measurements, since they perceptibly absorb the light by themselves. Besides, saturated hydrocarbons or polar solvents like acetonitril and water can be used at least down to 195 nm. The following subsections consider the same species and corresponding concentrations discussed in the IR spectral interference analysis (refer to 3.2.1). A final conclusion will be provided explaining the further focus of this thesis.

3.2.8.1 Low interfering molecules

The location of an absorption feature in the UV and visible region depends mainly on the chromophores present in a species.

Tab. 3.6. List of several chromophores, corresponding molecule classes, transitions, maximum wavelengths and maximum molar extinction coefficients after [15, p. 13].

Chromophor	Molecule class/group	Transition	λ_{\max} in nm	ϵ_{\max}
C–C	Alkane	$\sigma_S \rightarrow \sigma_S^*$	135	Strong
C=C	Alkene	$\pi_S \rightarrow \pi_S^*$	162.5	15 000
C–H	Methane	$\sigma_S \rightarrow \sigma_S^*$	122	Strong
C–O	Alcohol	$n_S \rightarrow \sigma_S^*$	177	200
N–H	Ammonia	$n_S \rightarrow \sigma_S^*$	194	5700
C=O	Acetone	$n_S \rightarrow \sigma_S^*$	166*	-
C=O	Acetone	$\pi_S \rightarrow \pi_S^*$	189	900
C=O	Acetone	$n_S \rightarrow \pi_S^*$	279	15

*Refer to [16].

Table 3.6 lists several chromophores, corresponding molecule classes or groups, the associated transition type, the maximum wavelength and the approximately maximum molar extinction coefficient of the absorption band.

Although table 3.6 cannot be considered comprehensive, it demonstrates that alcohol species, as well as alkanes like methane and isoprene will quite certainly cause no spectral interference around 278 nm. Based on further literature research, table 3.7 summarises all species with an expected low interfering potential and the corresponding references. For most of the species, no spectral data was found between 240 – 310 nm, which provides further evidence for the non-existence of absorption features in this wavelength region. The molecules with absorption bands close to the absorption feature of acetone are isoprene and COS having a λ_{max} at 222 nm and 220 nm, respectively. For carbonyl sulfide it is remarkable, that for 295 K, no interference can be expected in the region of interest, however, at elevated temperatures like 773 K the absorption band experiences a strong red shift and the maximum absorption cross section increases significantly [17]. However, since this can be certainly not expected in breath analysis and as the absorption profiles of COS and isoprene only slightly overlap with the acetone absorption profile at the edges at normal conditions, no interference is expected.

Though water is used as solvent even below 200 nm, too, and has an absorption maximum at 167 nm ([15, p. 13], [18]) published studies discuss its influence on the UV/VIS spectra measured from 290 nm to 340 nm. Du et al. [19] measured a fine structure with peaks at 330 nm and 315 nm and a rising absorption coefficient at 290 nm, all in the range of 2.0×10^{-24} to $3.0 \times 10^{-24} \text{ cm}^2$.

Tab. 3.7. High abundant endogenous molecules in human breath with low interference potential in the UV region between 240 – 310 nm.

Molecule	References
Water	[15, p.11][18–21]
Methane	[22–24]
Ammonia	[25]
Isoprene	[26]
Methanol	[27, 28]
Ethanol	[29, 30]
Carbon dioxide	[22, 31]
Carbon monoxide	[32, 33]
Dinitrogen monoxide	[34, 35]
Carbonyl sulfide	[17, 36]

However, in 2016 Wilson et al. [20] and later Pei et al. [37] contradict these values, publishing a spectrum with another profile and absorption cross sections more than an order of magnitude lower. Furthermore, Lampel et al. [21] used calculated data simulating absorption cross sections in the order of 10^{-27} cm^2 between 330 nm and 370 nm. Due to these contradicting statements and lack of data in the region of interest around 278 nm, water is excluded from the theoretical interference simulation and analysis. More information regarding contradictory water vapour absorption data is summarised elsewhere [38]. Note, that water might still have an influence on the measured photoacoustic signal due to relaxation time alterations (refer to section 2.5.2) and acoustic detuning (refer to section 2.5.5). The measurement result of Shemansky et al. [31] demonstrate the tail of an absorption profile for CO_2 to be around 196 nm with an absorption cross section of about $1.0 \times 10^{-23} \text{ cm}^2$. It is stated, that extinction in the region above 203.5 nm is completely caused by Rayleigh scattering. This could be the reason for the relatively high measured absorption cross section of $2.1 \times 10^{-23} \text{ cm}^2$. However, since the origin is assigned to Rayleigh scattering, no photoacoustical cross-sensitivity is expected from CO_2 . Nevertheless, CO_2 , may still influence the photoacoustic signal, like water, due to acoustic detuning and relaxation time variations. Besides, CO_2 is also a known species to increase acoustic attenuation at low frequencies (refer to section 2.5.4).

3.2.8.2 Strong interfering molecules

Since the acetone absorption band around 278 nm originates from the $n_{\text{S}} \rightarrow \pi_{\text{S}}^*$ transition, molecules containing a carbonyl group have a high interference potential. The only species containing a carbonyl group within this interference study, besides acetone, is formaldehyde*. Rogers [39] measured the absorption cross section of formaldehyde at 296 K and atmospheric pressure. Figure 3.15 depicts the spectral overlapping of acetone and formaldehyde due to the $n_{\text{S}} \rightarrow \pi_{\text{S}}^*$ transition.

Although formaldehyde and acetone have overlapping absorption features, the question regarding cross-sensitivities in terms of photoacoustic signal remains. Unfortunately, no quantitative results for radiative decay quantum yields have been found in literature for formaldehyde. Smith and Meyer [40] measured fluorescence between 250 nm and 350 nm with a maximum of emission around 295 nm, though no quantification was provided. Photodissociation quantum yields have been calculated by [41] and resulted in approximately 0.8 between 250 nm and 280 nm. Finally, Boutonnat et al. [42] used photoacoustic spectroscopy, in order to detect formaldehyde in the UV region from 300 nm to 310 nm. Using a pulsed laser source with 15 Hz repetition rate, they were able to determine the photoacoustic signal to occur 70 μs after laser excitation. This gives rise to the assumption, that the relaxation time is quite slow compared to acetone, but is sufficiently fast to distort the photoacoustic signal acquired at a modulation frequency of 5 kHz.

*Actually, COS and CO_2 do have carbonyl groups as well, however, they do not have a strong absorption band around 278 nm.

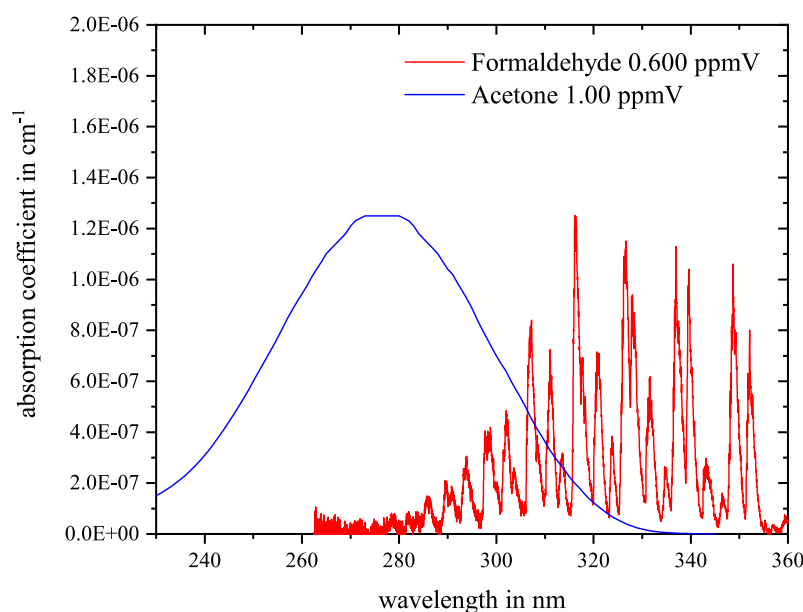


Fig. 3.15. Comparison of the absorption coefficient for 1.0 ppmV of acetone and 0.6 ppmV of formaldehyde around 278 nm. Spectral data from acetone and formaldehyde was provided by [5] and [39], respectively.

According to the results from literature research, perceptible spectral interference has to be expected from formaldehyde, if its concentration is in the range of acetone or above. Fortunately, under normal circumstances, the endogenously produced amount of formaldehyde in human breath exhale is considerably low and lies within the single digit ppbV range [43]. Thus, only if high ambient concentrations of formaldehyde are present or if the sample has been taken from a person shortly after an elevated exposition has occurred, the breath measurement can be distorted due to cross-sensitives. The risk of such an interference can be decreased significantly, if an ambient air sample is surveyed prior to the actual breath acetone measurement.

3.2.8.3 Summary and conclusion

In terms of spectral interference, molecules with a carbonyl group like aldehydes, ketones and organic acids could have a high interfering potential, but since acetone has a significantly higher abundance in exhaled human breath they can be neglected. The high abundant molecules, which have been identified in section 2.1.5, have been investigated regarding their absorption profiles in the UV region. Except for formaldehyde, none of them is absorbing in the same region as acetone and hence, do not have an interference potential in the UV. Precautions like performing an ambient air measurement prior to breath gas measurements can avoid misleading high measurement values caused by exogenous formaldehyde. Besides, the spectral interfering potential of water remains unclear so far. A further discussion regarding this topic is provided in section 5.2.

Concluding, with an available and cheap UV LED* emitting at the peak of the carbonyl's group $n_s \rightarrow \pi_s^*$ transition and due to significantly less spectral interference, the UV region is a very promising wavelength region for photoacoustic detection of breath acetone. Due to that, the experimental part of this thesis presented in chapter 5, mainly focuses on the photoacoustic detection of acetone in the UV region.

References

- [1] K. Bogumil et al. "Measurements of molecular absorption spectra with the SCIAMACHY pre-flight model: instrument characterization and reference data for atmospheric remote-sensing in the 230–2380 nm region". In: *Journal of Photochemistry and Photobiology A: Chemistry* 157.2-3 (May 2003), pp. 167–184. ISSN: 10106030. DOI: 10.1016/S1010-6030(03)00062-5 (cit. on p. 143).
- [2] S. Fally et al. "Fourier Transform Spectroscopy of the O₂ Herzberg Bands. III. Absorption Cross Sections of the Collision-Induced Bands and of the Herzberg Continuum". In: *Journal of Molecular Spectroscopy* 204.1 (Nov. 2000), pp. 10–20. ISSN: 00222852. DOI: 10.1006/jmsp.2000.8204 (cit. on p. 143).
- [3] T. Oka et al. "Photoacoustic Study of 280 nm Band of Acetone Vapor". In: *Bulletin of the Chemical Society of Japan* 61.1 (1988), p. 199. DOI: <https://doi.org/10.1246/bcsj.61.199> (cit. on p. 143).
- [4] T. Preukschat et al. "Comparison of the Photoacoustic Effect in the IR and the UV Regions". In: *International Journal of Thermophysics* 36.9 (2015), pp. 2318–2327. ISSN: 0195928X. DOI: 10.1007/s10765-015-1885-4 (cit. on p. 143).
- [5] T. Gierczak et al. "Photochemistry of acetone under tropospheric conditions". In: *Chemical Physics* 231.2-3 (June 1998), pp. 229–244. ISSN: 03010104. DOI: 10.1016/S0301-0104(98)00006-8 (cit. on pp. 146, 148, 165).
- [6] Y. Kaneda. "UV Lasers". In: *Encyclopedia of Modern Optics*. Elsevier, 2018, pp. 446–450. DOI: 10.1016/B978-0-12-803581-8.09370-X (cit. on p. 147).
- [7] J. J. Harrison et al. "Infrared absorption cross sections for acetone (propanone) in the 3 μ m region". In: *Journal of Quantitative Spectroscopy and Radiative Transfer* 112.1 (2011), pp. 53–58. ISSN: 00224073. DOI: 10.1016/j.jqsrt.2010.08.011 (cit. on p. 147).
- [8] J. J. Harrison et al. "Mid-infrared absorption cross sections for acetone (propanone)". In: *Journal of Quantitative Spectroscopy and Radiative Transfer* 112.3 (Feb. 2011), pp. 457–464. ISSN: 00224073. DOI: 10.1016/j.jqsrt.2010.09.002 (cit. on p. 148).

*The applied light source for the UV region will be addressed in detail later in section 4.2.

- [9] J. B. Burkholder et al. “Chemical Kinetics and Photochemical Data for Use in Atmospheric Studies”. In: *JPL Publication 15-10* 18 (2015). DOI: 10.13140/RG.2.1.2504.2806 (cit. on p. 148).
- [10] E. Mansour et al. “Measurement of temperature and relative humidity in exhaled breath”. In: *Sensors and Actuators B: Chemical* 304 (Feb. 2020), p. 127371. ISSN: 09254005. DOI: 10.1016/j.snb.2019.127371 (cit. on p. 148).
- [11] L. S. Rothman. *The HITRAN Database*. URL: <https://hitran.org/about/> (cit. on p. 148).
- [12] A. Rosencwaig. “Photoacoustic Spectroscopy”. In: *Annual Review of Biophysics and Bioengineering* 9.1 (1980), pp. 31–54. ISSN: 0084-6589. DOI: 10.1146/annurev.bb.09.060180.000335 (cit. on p. 159).
- [13] B. Tuzson et al. “Highly Selective Volatile Organic Compounds Breath Analysis Using a Broadly-Tunable Vertical-External-Cavity Surface-Emitting Laser”. In: *Analytical Chemistry* 89.12 (June 2017), pp. 6377–6383. ISSN: 0003-2700. DOI: 10.1021/acs.analchem.6b04511 (cit. on p. 161).
- [14] Mitrayana et al. “CO₂ Laser photoacoustic spectrometer for measuring acetone in the breath of lung cancer patients”. In: *Biosensors* 10.6 (2020). ISSN: 20796374. DOI: 10.3390/BIOS10060055 (cit. on p. 162).
- [15] M. Hesse et al. *Spektroskopische Methoden in der organischen Chemie*. Ed. by M. Hesse et al. 8th ed. Stuttgart: Georg Thieme Verlag, 2012. ISBN: 9783135761084. DOI: 10.1055/b-002-46984 (cit. on pp. 162, 163).
- [16] E. E. Barnes and W. T. Simpson. “Correlations among Electronic Transitions for Carbonyl and for Carboxyl in the Vacuum Ultraviolet”. In: *The Journal of Chemical Physics* 39.3 (Aug. 1963), pp. 670–675. ISSN: 0021-9606. DOI: 10.1063/1.1734305 (cit. on p. 162).
- [17] H. Grosch et al. “UV absorption cross-sections of selected sulfur-containing compounds at temperatures up to 500°C”. In: *Journal of Quantitative Spectroscopy and Radiative Transfer* 154 (Mar. 2015), pp. 28–34. ISSN: 00224073. DOI: 10.1016/j.jqsrt.2014.11.020 (cit. on p. 163).
- [18] M. Schürgers and K. H. Welge. “Absorptionskoeffizient von H₂O₂ und N₂H₄ zwischen 1200 und 2000 Å”. In: *Zeitschrift für Naturforschung A* 23.10 (Oct. 1968), pp. 1508–1510. ISSN: 1865-7109. DOI: 10.1515/zna-1968-1011 (cit. on p. 163).
- [19] J. Du et al. “The influence of water vapor absorption in the 290-350 nm region on solar radiance: Laboratory studies and model simulation”. In: *Geophysical Research Letters* 40.17 (Sept. 2013), pp. 4788–4792. ISSN: 00948276. DOI: 10.1002/grl.50935 (cit. on p. 163).
- [20] E. M. Wilson et al. “Upper limits for absorption by water vapor in the near-UV”. In: *Journal of Quantitative Spectroscopy and Radiative Transfer* 170 (Feb. 2016), pp. 194–199. ISSN: 00224073. DOI: 10.1016/j.jqsrt.2015.11.015 (cit. on pp. 163, 164).

- [21] J. Lampel et al. “On the relative absorption strengths of water vapour in the blue wavelength range”. In: *Atmospheric Measurement Techniques* 8.10 (Oct. 2015), pp. 4329–4346. ISSN: 1867-8548. DOI: 10.5194/amt-8-4329-2015 (cit. on pp. 163, 164).
- [22] P. G. Wilkinson and H. L. Johnston. “The Absorption Spectra of Methane, Carbon Dioxide, Water Vapor, and Ethylene in the Vacuum Ultraviolet”. In: *The Journal of Chemical Physics* 18.2 (Feb. 1950), pp. 190–193. ISSN: 0021-9606. DOI: 10.1063/1.1747586 (cit. on p. 163).
- [23] U. Fink et al. “Band model analysis of laboratory methane absorption spectra from 4500 to 10500 Å”. In: *Journal of Quantitative Spectroscopy and Radiative Transfer* 18.4 (Oct. 1977), pp. 447–457. ISSN: 00224073. DOI: 10.1016/0022-4073(77)90077-2 (cit. on p. 163).
- [24] J. W. Au et al. “The valence shell photoabsorption of the linear alkanes, C_nH_{2n+2} ($n=1-8$): absolute oscillator strengths (7–220 eV)”. In: *Chemical Physics* 173.2 (June 1993), pp. 209–239. ISSN: 03010104. DOI: 10.1016/0301-0104(93)80142-V (cit. on p. 163).
- [25] B.-M. Cheng et al. “Absorption Cross Sections of NH_3 , NH_2D , NHD_2 , and ND_3 in the Spectral Range 140–220 nm and Implications for Planetary Isotopic Fractionation”. In: *The Astrophysical Journal* 647.2 (Aug. 2006), pp. 1535–1542. ISSN: 0004-637X. DOI: 10.1086/505615 (cit. on p. 163).
- [26] P. Sahay et al. “Measurements of the Weak UV Absorptions of Isoprene and Acetone at 261–275 nm Using Cavity Ringdown Spectroscopy for Evaluation of a Potential Portable Ringdown Breath Analyzer”. In: *Sensors* 13.7 (June 2013), pp. 8170–8187. ISSN: 1424-8220. DOI: 10.3390/s130708170 (cit. on p. 163).
- [27] J. Nee et al. “Photoexcitation processes of CH_3OH : Rydberg states and photofragment fluorescence”. In: *Chemical Physics* 98.1 (Aug. 1985), pp. 147–155. ISSN: 03010104. DOI: 10.1016/0301-0104(85)80102-6 (cit. on p. 163).
- [28] G. R. Burton et al. “Absolute oscillator strengths for photoabsorption (6–360 eV) and ionic photofragmentation (10–80 eV) of methanol”. In: *Chemical Physics* 167.3 (Nov. 1992), pp. 349–367. ISSN: 03010104. DOI: 10.1016/0301-0104(92)80208-D (cit. on p. 163).
- [29] J. Han et al. “Fluorescence from photoexcitation of C_2H_5OH by Vacuum ultraviolet radiation”. In: *Journal of Quantitative Spectroscopy and Radiative Transfer* 42.6 (Dec. 1989), pp. 557–562. ISSN: 00224073. DOI: 10.1016/0022-4073(89)90046-0 (cit. on p. 163).
- [30] D. Salahub and C. Sandorfy. “The far-ultraviolet spectra of some simple alcohols and fluoroalcohols”. In: *Chemical Physics Letters* 8.1 (Jan. 1971), pp. 71–74. ISSN: 00092614. DOI: 10.1016/0009-2614(71)80578-X (cit. on p. 163).
- [31] D. E. Shemansky. “ CO_2 Extinction Coefficient 1700–3000 Å”. In: *The Journal of Chemical Physics* 56.4 (Feb. 1972), pp. 1582–1587. ISSN: 0021-9606. DOI: 10.1063/1.1677408 (cit. on pp. 163, 164).

- [32] H. P. White et al. “The ultraviolet absorption spectrum of CO: Applications to planetary atmospheres”. In: *Journal of Geophysical Research: Planets* 98.E3 (Mar. 1993), pp. 5491–5497. ISSN: 01480227. DOI: 10.1029/92JE02809 (cit. on p. 163).
- [33] W. Chan et al. “Absolute optical oscillator strengths for discrete and continuum photoabsorption of carbon monoxide (7–200 eV) and transition moments for the $X\ 1\Sigma^+ \rightarrow A\ 1\Pi$ system”. In: *Chemical Physics* 170.1 (Feb. 1993), pp. 123–138. ISSN: 03010104. DOI: 10.1016/0301-0104(93)80098-T (cit. on p. 163).
- [34] G. Selwyn et al. “Nitrous oxide ultraviolet absorption spectrum at stratospheric temperatures”. In: *Geophysical Research Letters* 4.10 (Oct. 1977), pp. 427–430. ISSN: 00948276. DOI: 10.1029/GL004i010p00427 (cit. on p. 163).
- [35] H. S. Johnston and G. S. Selwyn. “New cross sections for the absorption of near ultraviolet radiation by nitrous oxide (N_2O)”. In: *Geophysical Research Letters* 2.12 (Dec. 1975), pp. 549–551. ISSN: 00948276. DOI: 10.1029/GL002i012p00549 (cit. on p. 163).
- [36] S. Hattori et al. “Ultraviolet absorption cross sections of carbonyl sulfide isotopologues $OC^{32}S$, $OC^{33}S$, $OC^{34}S$ and $O^{13}S$,” in: *Atmospheric Chemistry and Physics* 11.19 (Oct. 2011), pp. 10293–10303. ISSN: 1680-7324. DOI: 10.5194/acp-11-10293-2011 (cit. on p. 163).
- [37] L. Pei et al. “Water Vapor Near-UV Absorption: Laboratory Spectrum, Field Evidence, and Atmospheric Impacts”. In: *Journal of Geophysical Research: Atmospheres* 124.24 (Dec. 2019), pp. 14310–14324. ISSN: 2169-897X. DOI: 10.1029/2019JD030724 (cit. on p. 164).
- [38] M. M. Makogon et al. “The problem of water vapor absorption in the UV spectral range”. In: *Atmospheric and Oceanic Optics* 26.1 (Feb. 2013), pp. 45–49. ISSN: 1024-8560. DOI: 10.1134/S1024856013010119 (cit. on p. 164).
- [39] J. D. Rogers. “Ultraviolet absorption cross sections and atmospheric photodissociation rate constants of formaldehyde”. In: *The Journal of Physical Chemistry* 94.10 (May 1990), pp. 4011–4015. ISSN: 0022-3654. DOI: 10.1021/j100373a025 (cit. on pp. 164, 165).
- [40] J. J. Smith and B. Meyer. “Fluorescence and Induced Phosphorescence of Formaldehyde in Solid Low-Temperature Solutions”. In: *The Journal of Chemical Physics* 50.1 (Jan. 1969), pp. 456–459. ISSN: 0021-9606. DOI: 10.1063/1.1670819 (cit. on p. 164).
- [41] E.-P. Röth and D. H. Ehhalt. “A simple formulation of the CH_2O photolysis quantum yields”. In: *Atmospheric Chemistry and Physics* 15.13 (July 2015), pp. 7195–7202. ISSN: 1680-7324. DOI: 10.5194/acp-15-7195-2015 (cit. on p. 164).

- [42] M. Boutonnat et al. “Photoacoustic Detection of Formaldehyde as a Minority Component in Gas Mixtures”. In: 1988, pp. 137–138. DOI: 10.1007/978-3-540-48181-2_34 (cit. on p. 164).
- [43] A. Wehinger et al. “Lung cancer detection by proton transfer reaction mass-spectrometric analysis of human breath gas”. In: *International Journal of Mass Spectrometry* 265.1 (Aug. 2007), pp. 49–59. ISSN: 13873806. DOI: 10.1016/j.ijms.2007.05.012 (cit. on p. 165).

Chapter 4

Experimental

4.1 Laboratory setup

This chapter describes the laboratory setup and the devices used within this thesis. It is separated into several parts describing the gas stream concept including the gas mixing unit and the software controlling it (subsection 4.1.1), the interconnection of electronic devices used for controlling and for photoacoustic signal processing (subsection 4.1.2) and finally, the light sources (subsection 4.2) applied within this thesis and the FT-IR (subsection 4.3) used for reference measurements.

4.1.1 Gas stream concept

The gas stream concept visualised in figure 4.1 can be separated into two gas cabinets holding up to eight and seven gas bottles, respectively, a gas distribution panel supplying measurement station 1 and 2 (MST1 and MST2) with the gas mixtures, a humidity generator, a vacuum pump and an FT-IR.

Each bottle in the cabinets is connected to a mass flow controller (MFC) node (Bronkhorst, Karmen, Germany) of the type F-201CV-500-XXX. The gases used within this thesis are different analytes, diluted in either pure nitrogen (6.0) or synthetic air* with less than 0.1 ppmV of contamination by carbohydrates and have been supplied by Westfalen AG (Münster, Germany). Further dilution of the analyte-containing bottles can be achieved by mixing the gas with pure synthetic air or N₂. The final MFC before the gas leaves cabinet 1, is the cut-off MFC setting the final mass flow rate. Two gas bottles (in the left cabinet of figure 4.1) can be fed to the humidity generator. Caution is required that only gases like synthetic air or N₂ are used for humidifying since corrosive gases can harm the humidity generator. The gas hoses containing humidified gas are all wrapped with silicon rubber heat bands and isolated with a further, thick layer of isolating foam, in order to avoid condensation in the gas pipes. In figure 4.1, these hoses are all labeled red.

For measurements containing humidified samples, each PAC was equipped with a temperature, humidity and pressure (TpH) sensor (BME280) from Bosch (Robert Bosch GmbH, Gerlingen, Germany). However, the dashed red TpH box indicates, that a second TpH sensor, based on the MPL3115A2 (Adafruit Industries, New York, US) and a SHT25 (Sensirion AG, Staefa, Switzerland), can be integrated into the gas stream on request, e.g. if verification of the TpH values from the BME is necessary. After passing the PAC, the temperature controlled hose ends in a TC-Standard 6111 peltier cooler (Bühler Technologies GmbH, Ratingen, Germany). The gas distribution panel has six in series interconnected ports, whereas a closed port is simply bypassed. This setup allows for reference measurements with an FT-IR of the type MKS MultiGas™ 2030-HS (MKS Instruments Inc., Andover, US), since the gas first passes one of the PACs and enters the FT-IR afterwards. Finally, in order to achieve vacuum, a pre-pressure controller (PPC) of the type P-

*Sometimes also referred to as zero air.

720CV-6K0A-RAD-33-Z (Bronkhorst) was placed behind the gas distribution panel in downstream direction, but before a rotary vane vacuum pump of the type TRIVAC D 2.5 E pump (Leybold GmbH, Aschheim, Germany). If no vacuum is needed, the gas exiting the distribution panel can be fed directly to the exhaust, as well. This setup enabled measurements with pressures down to 200 mbar within a PAC.

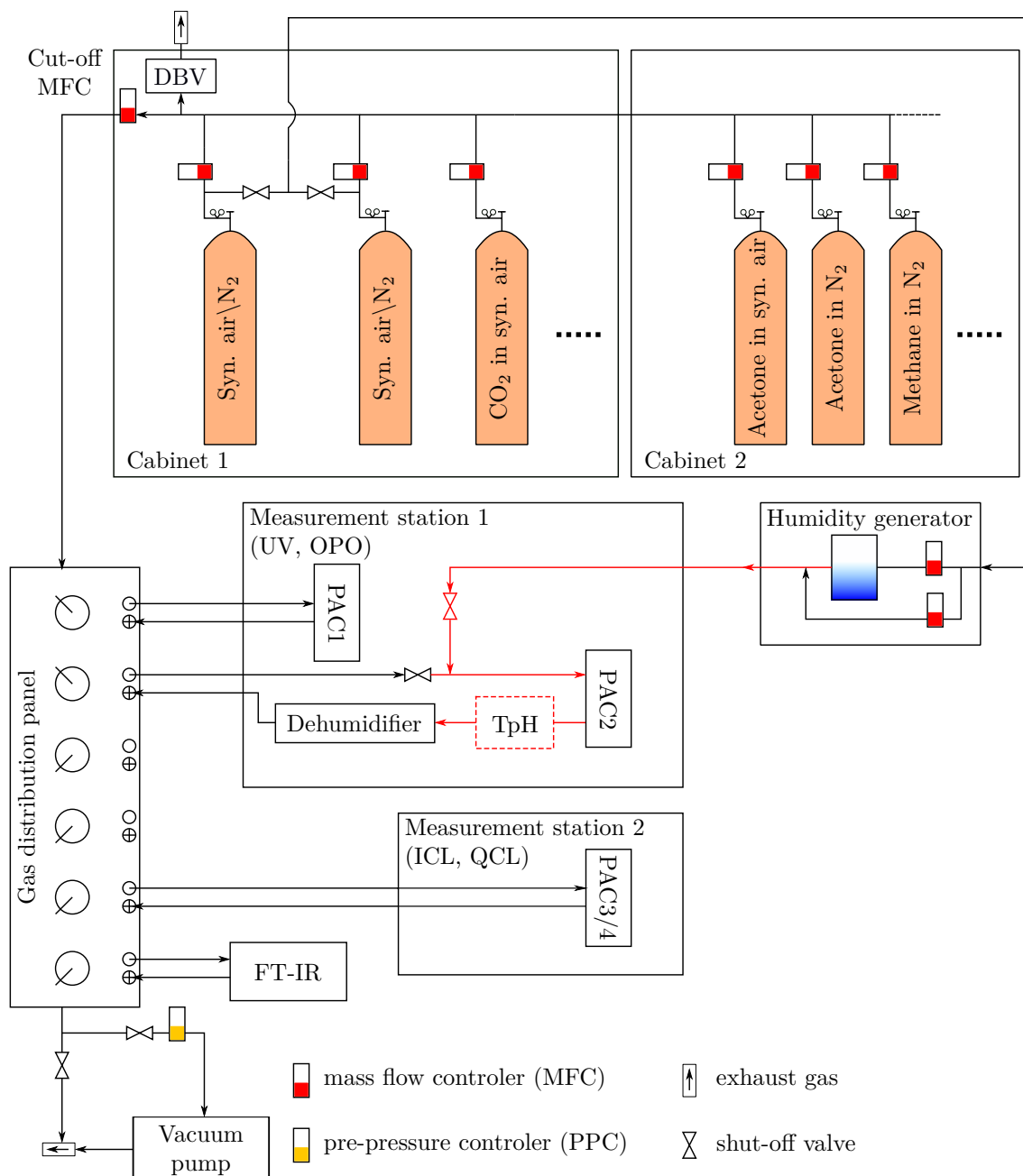


Fig. 4.1. Schematic of the gas stream concept used within this thesis. **PRV** - pressure relief valve. Further explanation can be found in the text.

A LabVIEW (National Instruments, Austin, Texas, US) based software tool was developed allowing the user to mix the contents of up to 15 different gas bottles*. From the graphical user interface, the user has a real-time graph displaying the flow rates of all active MFCs. Moreover, all user set concentrations and the actual concentrations within the gas mixture, based on the MFC flow rates, are monitored continuously as well. This prevents measurements under incorrect flow conditions, since any irregularities can be detected quickly. The tool further provides control over the humidity generator and the pressure settings of the measurement stations. In addition, all humidity generator parameters (e.g. actual flow rate, temperature, relative humidity etc.) as well as the pressure, temperature and humidity within the PAC (or gas stream) are displayed and updated in real-time, too. Furthermore, all data acquired by the program is provided to other LabVIEW programs over the local network using shared variables. This allows further programs, like the *photoacoustic measurement tool* (discussed in the next section), to access this data and save it together with the acquired photoacoustic measurement data.

4.1.2 Electronics

This subsection addresses the electronic devices used within this thesis. Since the space on the optical mounting plate on MST1 was not sufficient anymore, a second MST was created within the same laboratory. For this purpose, another optical mounting plate was equipped with the necessary electronic devices and a separate PC for data acquisition and control. Due to that, two separate figures 4.2 and 4.3 illustrate the employed electronic devices within the respective measurement stations.

The core part of each MST is a data acquisition and control unit (PC). This unit collects the data from all sensor devices and controls the other units via digital interfaces, e.g. universal serial bus (USB), Ethernet, RS-232 serial ports and general purpose interface bus (GPIB). In the following paragraphs, the electronic devices employed in the respective MST will be addressed separately.

The powermeter PM100D combined with either an S302C or an S120VC (Thorlabs GmbH, Munich, Germany) sensor head, monitors the optical power of the used light sources. In order to characterise the emitting wavelength and peak width of the IR laser sources, a spectrum analyzer of the type BRI-771B-MIR from Bristol Instruments, Inc. (Victor, US) was employed. In order to use the spectrum analyser with several light sources from both measurement stations without repositioning the lasers each time, a hollow core silica optical fiber (HSW-Assembly, JTHWEH 500 μm , Laser Components, Olching, Germany) with a length of 3 m was coupled with the spectrum analyzer and placed in front of the respective light source under test.

*Actually, the number is not limited by the software but the number of MFC nodes available and can be easily scaled.

The microphone signal is post-processed by means of a lock-in amplifier and from there forwarded to the PC on request. The microphone used in all PACs is an ultra-low noise MEMS microphone of the type ICS-40720* (InvenSense Inc., California, US). The supply voltage of the microphone is provided by means of a PL601-P power supply (AimTTi, Cambridgeshire, UK). The PC can set several LIA parameters, e.g. time constant or roll-off and controls the function generator (33522B, Keysight Technologies, Santa Rosa, US), which supplies the reference signal to the LIA for demodulation of the microphone signal. The lock-in amplifier used within MST1 is a 7225 DSP LIA (Signal Recovery, Tennessee, US).

In addition, the PC controls the humidifier as well as the MFCs and the PPC and in return stores the sensor feedback from these devices and from the TpH sensor. For temperature control of up to two PACs, a dual-channel TEC-1122-SV from Meerstetter Engineering (Rubigen, Switzerland) is employed.

MST1 is only equipped with light sources performing AM-PAS. In order to amplitude modulate the UV LED, the function generator provides a transistor-transistor logical (TTL) signal to the 4 channel LED-Pulse-Controller. The LED was either an LEUVA77M00HU00 4in1 flat LED by LG Innotek (Seoul, Korea) with 300 mW or a 275-6060-125 by Bolb, Inc. (Livermore, US) with 125 mW. The rising edge of the TTL signal triggers the current output of the driver, setting the modulation frequency. Providing a pulse length in μs to the driver as well, allows the user to alter the duty cycle of the square wave modulation signal. Since the LED driver can only provide a finite time resolution for the pulse length, the duty cycle cannot be set to exactly 50 % for every applied frequency. Besides, the finite slew rate of the driver has to be accounted for. This is discussed in more detail in section 5.2.5.4.

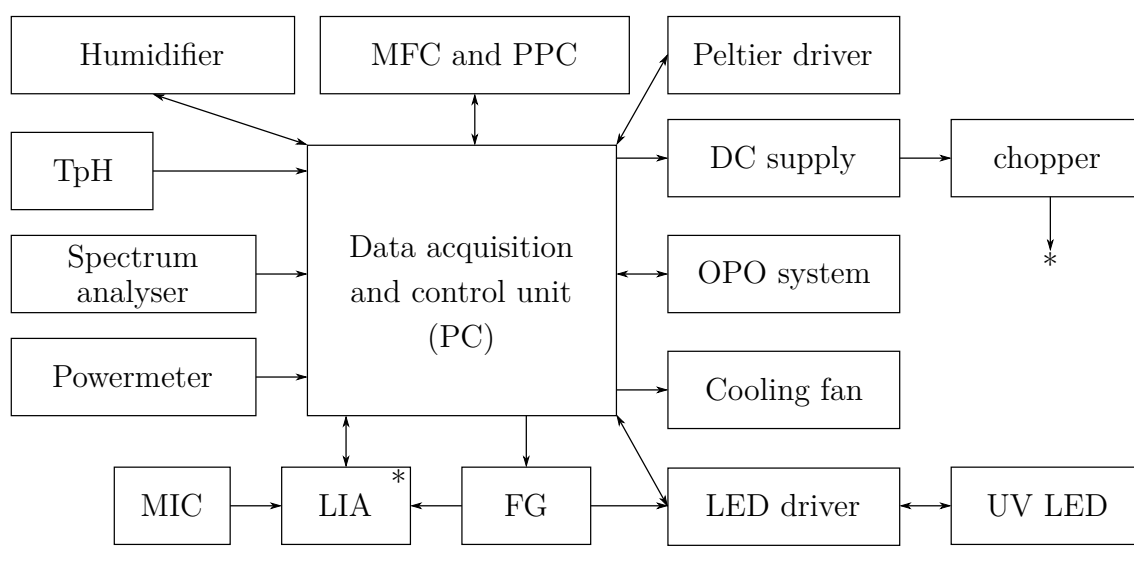


Fig. 4.2. Schematic of the employed electronic devices on measurement station 1. The * represents an interdevice connection. **DC** - direct current.

*Except for the PACs combined with the ICL and QCL.

In order to cool the LED, which is mounted on a metal printed circuit board (PCB) attached to a heat sink, a simple 80 mm USB fan (Eluteng, ShenZhen, China) was employed. For the 4in1 LED with a 6868 package, an AMPYR LED33PCB-6868 PCB was used. Besides, for the Bolb LED an AMPYR LED33UV PCB was employed. Both PCBs are attached to a small heatsink AMPYR LED33HS. The LED driver, PCBs and heatsinks have been provided by Leistungselektronik Jena GmbH (Jena, Germany).

Amplitude modulation of the OPO system requires a mechanical chopper unit of the type SCT-Model-310CD, which was equipped with a 300D30 30 slot chopping disc (Scitec Instruments Ltd, Trowbridge, UK). The chopper is controlled by means of an E3631A triple output power DC supply (Agilent Technologies, Santa Clara, California, US).

The software used to control all the devices and for storing all measurement values as well as the measurement parameters, another LabVIEW based tool was developed, called the *photoacoustic measurement tool*. It mainly bases on the tool described in the bachelor thesis of Maximilian Ade [1] and was expanded in order to integrate all new devices including peltier driver and LED driver. Furthermore, the save routine of the code was improved in order to be able to store the data provided by the shared variables from the gas mixing LabVIEW tool addressed in subsection 4.1.1.

In figure 4.3, the schematic of MST2 is illustrated. At MST2, the tunable semiconductor light sources, e.g. QCL and ICL, are installed. Both lasers need a laser diode driver and a TEC driver for operation. The QCL HHL-19-26 from AdTech Optics (Cortney Court, US) is controlled by an LDC-3736. The ICL 3159-22-16* from

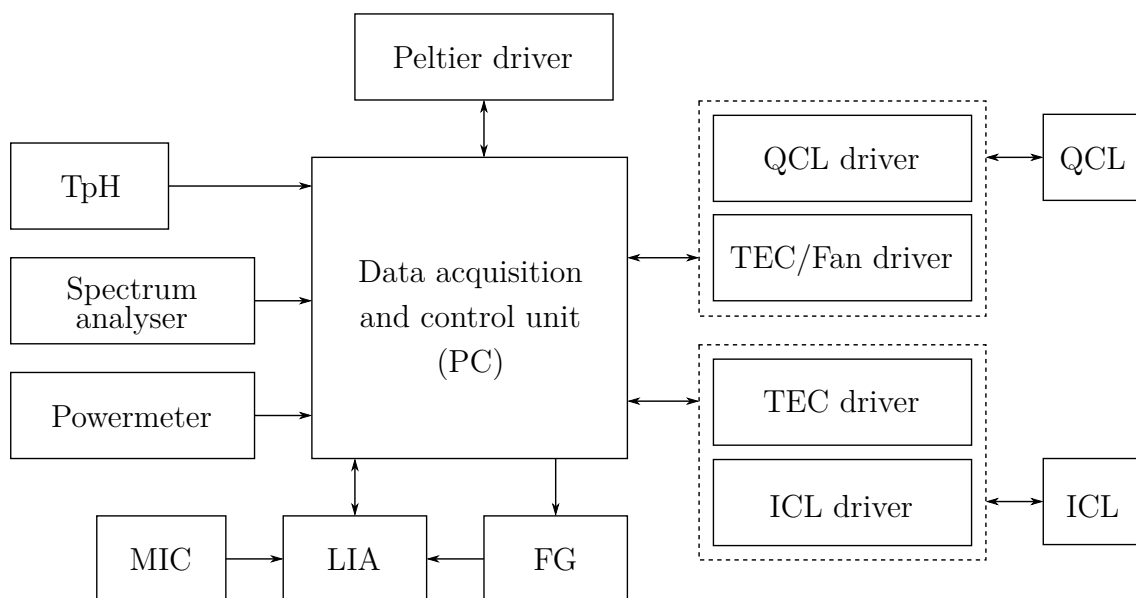


Fig. 4.3. Schematic of the used electronic devices on measurement station 2.

*This laser has been developed within the research project BreathSens: 13GW0325C.

nanoplus (Nanosystems and Technologies GmbH, Gerbrunn, Germany) is regulated by means of an ILX Lightwave LDC 3726. Both drivers are provided by the Newport Corporation (Irving, US). The peltier driver, the function generator, the spectrum analyser and the TpH sensor are the same as applied at MST1. The powermeter is a PM400 equipped with an S401C sensor head, both supplied by Thorlabs. The lock-in amplifier is a 7270 DSP LIA from Ametek, Inc. (Berwyn, US), which is able to demodulate the photoacoustic signal at two different harmonics simultaneously. The microphones employed within the PACs of this measurement station are ICS-40730, which are provided by InvenSense as well, having a better SNR compared to the ICS-40720*. Finally, the microphones have been powered by means of an Agilent E3631A power supply.

The software tool for pure WM-PAS was developed from scratch by the author of this thesis. The functionality concepts of the software tools for the pure AM-PAS and the photoacoustic spectrum acquisition modes for both, the ICL and QCL, have been developed by the author of this thesis, however, the implementation was performed by Elisabeth Wittmann. The AM-PAS content of the software is similar to the code of the software used at MST1, whereas the photoacoustic spectrum measurement mode allows for tuning of the light source to a certain wavelength, followed by an AM-PAS measurement. The result of such a current sweep measurement is presented in section 5.4.4.

*70 dBA versus 74 dBA.

4.2 Light sources

This subsection discusses the light sources and optical parts used within this thesis briefly. In addition, the working principles of the employed light sources are addressed. The collimation concept of the UV LEDs, however, will be discussed in detail in the respective results sections. The section is concluded by the description of the OPO system.

The 4in1 flat LED by LG Innotek had the highest optical output power for a single LED 6060 surface mount device (SMD) chip on the market* with about 350 mW at a driving current of 350 mA and 34 V supply voltage according to the datasheet†. The specified emitter center wavelength is 278 nm and the FWHM of the emission peak is about 10 nm with a full divergence angle of about 125°. However, LG Innotek has abandoned its UV LED division in 2019 and the LED is not available anymore. As a replacement, two UV LEDs 275-6060-125 from Bolb have been used for further experiments. The Bolb LED has only one instead of four active zones within one chip. Their first generation has about 100 mW power at 350 mA and 6.5 V and their second generation has about 100 mW power at 250 mA and 6.5 V. Their center emission wavelength is 275 nm and the FWHM is about 10 nm. The full divergence angle is approximately 150°. An excerpt of the datasheet of the second generation UV LED is attached to the appendix C.2. The high divergence angle of the UV LEDs demonstrates the need for collimation in order to guide as much light as possible into the acoustic resonator and to achieve minimal interaction with the resonator walls. From now on, the LED from LG Innotek and the first and second generation LEDs from Bolb will be referred to as LED1, LED2 and LED2*, respectively.

Avoiding a too detailed description, figure 4.4 illustrates the different heteroband structures and photon generation types of an LED, an ICL and a QCL. One of the main differences between a semiconductor laserdiode (LD) and a UV LED is the fact, that the emission of the LD is based on an electron population inversion resulting in stimulated emission. The emission of an LED, however, is based on spontaneous emission. This leads to higher output power and narrower emission line widths in LDs but is less energy efficient. The band structure of an LED is visualised in figure 4.4. Electrons are injected into the conductive band by means of a forward bias. If correctly designed, quantum wells (QW) occur within the conductive band and the energetically lower valence band. The electrons can get confined within the QWs and eventually recombine with a hole in the valence band by emission of a photon. The energy of the photon is specified by the energy difference of the band gap.

In a QCL, the electrons are distributed within a single band consisting of several QWs. The population density of the electrons on different energy states within a QW depends mainly on the thickness and also on the material of the layers the heterostructure consists of. When a forward bias is applied, the electrons from the ground state of one quantum well can tunnel to a neighbouring QW, occupying a

*To the best of the author's knowledge.

†The important pages from the datasheet have been attached to the appendix C.1

higher electronic state. By deexcitation of the electron from the higher state within a QW into its ground state, a photon is emitted. Depending on the design, one electron can cause the emission of several photons by decaying within a cascade of relaxation and intraband tunneling steps, like illustrated in the top right corner of figure 4.4.

ICLs, like LEDs, contain a valence band and an energetically higher conductive band. Like QCLs, they consist of a complex layer system of different semiconductor materials forming a heterostructure. In a typical ICL, electrons are injected into the conductive band and get eventually trapped in a QW. The confined electron recombines with a hole of the valence band of another material layer causing a photon to be emitted. Due to the design of the heterostructure, the electron can tunnel from a valence band QW into another conductive band QW, performing an interband tunneling step. This process can be repeated in a cascading manner, which is illustrated on the bottom of figure 4.4. Therefore, like in QCLs, one electron can recombine more than once leading to a quantum efficiency above one in terms of photon generation. Since a detailed description of the working principles and structure designs of the employed light sources would go beyond the scope of this work, the interested reader shall refer to [2, 3].

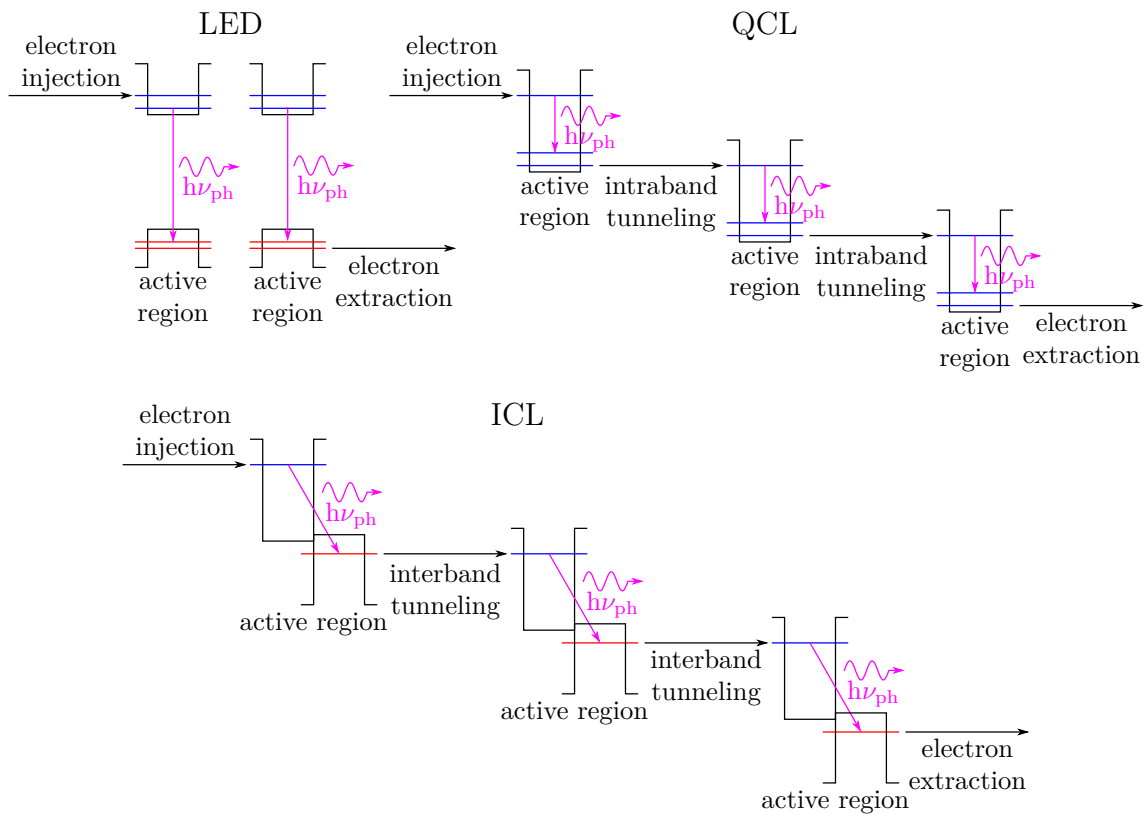


Fig. 4.4. Schematic of the band profile and active region processes in LEDs (top-left), QCLs (top-right) and ICLs (bottom) after [2]. Blue and red lines visualise energy levels of electrons in the conductive band and valence band, respectively.

The distributed feedback (DFB) ICL provided by nanoplus is housed within a cube containing a peltier cooling element and a collimation lens. The device operates at 6 V, has a threshold current of about 31 mA and a maximum current of 120 mA. The slope efficiency is about 0.69 mW mA^{-1} and the operation temperature is between $10 - 45^\circ\text{C}$. The center wavelength is about 3307.2 nm and the optical output power for the cw mode has a maximum of 40 mW at 120 mA, 6 V and 25°C . Further details are discussed in section 5.4. Some pages from the datasheet have been attached to the appendix C.3.

The DFB QCL from AdTech Optics is placed into a high heat load (HHL) package, which contains a peltier element and a collimation lens as well. The laser can be operated between $15 - 45^\circ\text{C}$ and has a temperature dependent maximum current of 530 – 525 mA, respectively. At 25°C , the threshold current is about 300 mA and the center wavelength is 8270 nm at 420 mA. The output power at 25°C , 420 mA and 10.5 V is 144 mW in cw mode. Again, pages from the datasheet have been attached to the appendix C.4.

Figure 4.5 provides an image of the ICL and QCL (top) and a schematic (bottom) visualising the optical path of the laser beams. The collimated beam of the QCL is directly focused in PAC3, which has two wedged ZnSe windows (WW80530-E3) from Thorlabs.

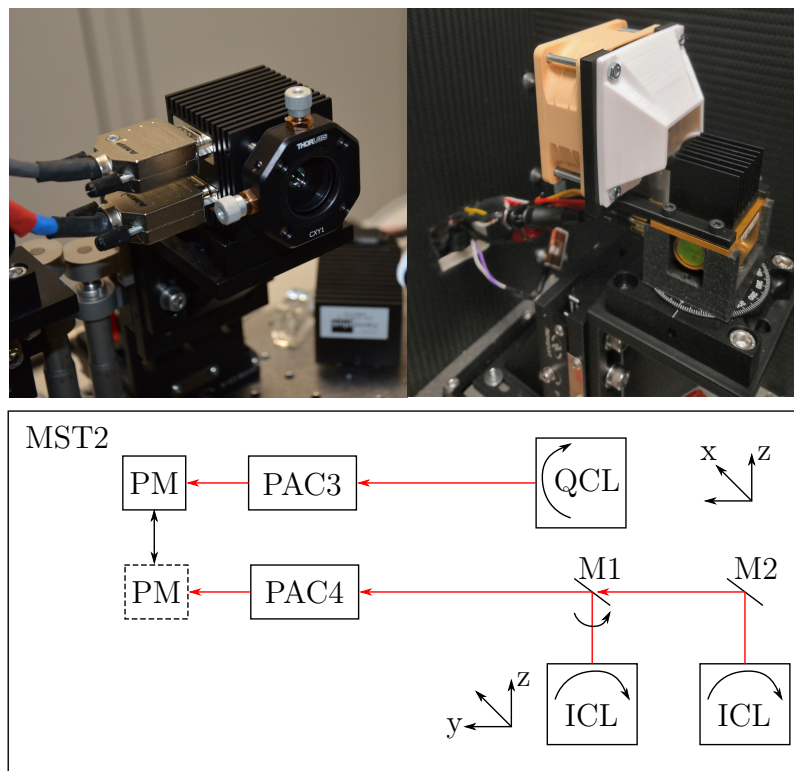


Fig. 4.5. Image of the cube ICL (top-left) and HHL housed QCL (top-right) and a schematic of the optical paths of the laser beams (bottom). Red arrows indicate laser beams.

Tab. 4.1. PAC and light source combinations used within the results chapter of this thesis. The corresponding sections, where the systems are presented, are provided in the respective cells.

Light source	PAC						
	1	2	2*	3	4	5	6
LED1	5.1/5.2	-	5.3.3	-	-	-	-
LED2	-	5.3.3	5.3.3	-	-	-	-
LED2*	-	-	5.3.3	-	-	5.3.3	-
QCL	-	-	-	5.4.3	-	-	-
ICL	-	-	-	-	5.4.4	-	-
OPO	-	-	-	-	-	-	5.4.2

The sensor head of the powermeter can be positioned behind PAC3 or PAC4.

The ICL and QCL are both placed on an RP01-M rotation stage from Thorlabs, which allows rotation around the z-axis. Besides, the lasers can be moved along the z-axis and the y- or x-axis by means of linear stages of the type 433 by Newport, in order to correctly guide the light into the PAC minimizing the interaction between beam and resonator walls. The collimated light of the ICL, however, is not directly guided into the PAC, but reflected by means of a gold coated mirror first. The mirror M1 can be tilted by 180° enabling the setup to switch easily between two aligned light sources without any realignment.

Table 4.1 provides an overview of the employed PACs and LEDs as well as their combinations. The notation used to describe a setup follows the PAC/LED notation, i.e. 2/2 describes a photoacoustic setup employing PAC2 and LED2.

Tab. 4.2. The lengths L_{res} and diameters d_{res} of the employed PACs. Dimensions of PAC6 are provided elsewhere [4].

Part	PAC						
	1	2	2*	3	4	5	6
L_{res} in mm	31	31	33	31	31	33	[4]
d_{res} in mm	10	13	10	4	4	4	[4]

A second table (table 4.2) summarises the different resonator geometries, since the rest of the cells are quite similar, except for PAC5 and PAC6. PAC1 to PAC5 have all been 3D printed out of an aluminum alloy (AlSi10Mg) and post-processed. Post-processing steps included the insertion of threads or milling of surfaces to allow gas tight sealing to name a few. More details and visualisations of the PACs are presented in the corresponding sections.

Concluding this subsection, the OPO system and its optical path will be described. The optical parametric oscillator (cwOPO-GIGA, Qioptiq Photonics GmbH, Munich) allows for tunable cw emission of IR light between 1.4 to 2.0 and 2.3 to 4.3 μm . The output power depends strongly on the emitted wavelength and can be as high as 2.4 W at around 1.6 μm and between 2.9 μm to 3.3 μm (refer to figure 4.6). The spectral bandwidth $\Delta\nu_{\text{ph}}$ of the OPO laser emission is specified to be below 2 GHz. For a wavelength of 3.0 μm , this results in an FWHM of about 60 pm.

Since this section is not meant to describe the operation principle of the OPO system in detail, it will be solely addressed briefly. As indicated in figure 4.7, a Nd:YAG pump laser emitting a wavelength of 1064 nm with an output power up to 20 W is connected to the OPO laser by means of a fiber. The core element of the OPO is a non-linear optical LiNbO_3 crystal, positioned in the center of the cavity. The crystal has a polarisation pattern, which is indicated by the rake-shaped lines in figure 4.7. As a consequence of the non-linear optical properties of the crystal, the pump laser wavelength is divided into an Idler and a Signal laser beam following the laws of energy conservation. The Signal beam, indicated as a blue arrow, has a

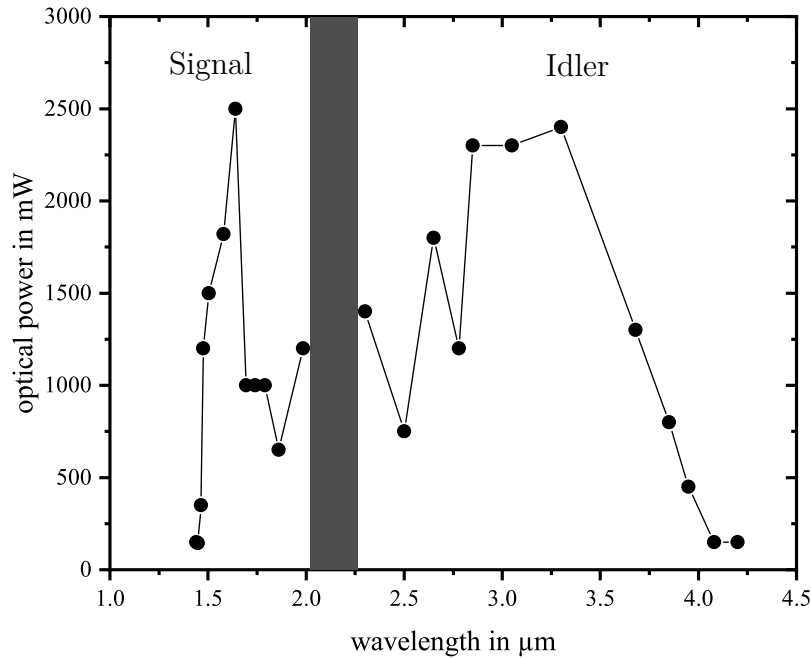


Fig. 4.6. Optical output power of the OPO laser for different wavelengths. Idler and Signal are separated by the dark grey band, which is not available from OPO radiation.

shorter wavelength as the Idler beam, which is labeled with a red arrow. In addition, a small amount of visible light between 580 nm to 700 nm is emitted by the OPO as well, which is useful considering beam alignment. The Fabry-Pérot etalon employed in the OPO laser system, suppresses other modes and therefore counteracts mode hopping, which can result from temperature drifts. In order to tune the emission wavelength of the OPO, several parameters can be adjusted including

- the z-position of the optical crystal,
- the temperature of the LiNbO_3 crystal,
- the temperature of the etalon,
- the wavelength of the pump laser* or
- the resonator length of the cavity.

The list is ordered ascendingly regarding their tuning resolution and in descending order considering their applicable tuning range.

The beam alignment of the OPO laser is visualised in the schematic provided by figure 4.8. Either the shutter of the Signal or Idler beam is opened at the front of the OPO and guided into a neutral density filter array (i). The array consists of thin Si plates each attenuating the IR light to a certain extend. The attenuation can be controlled by the number of silicon plates placed in the filter holder, which allows

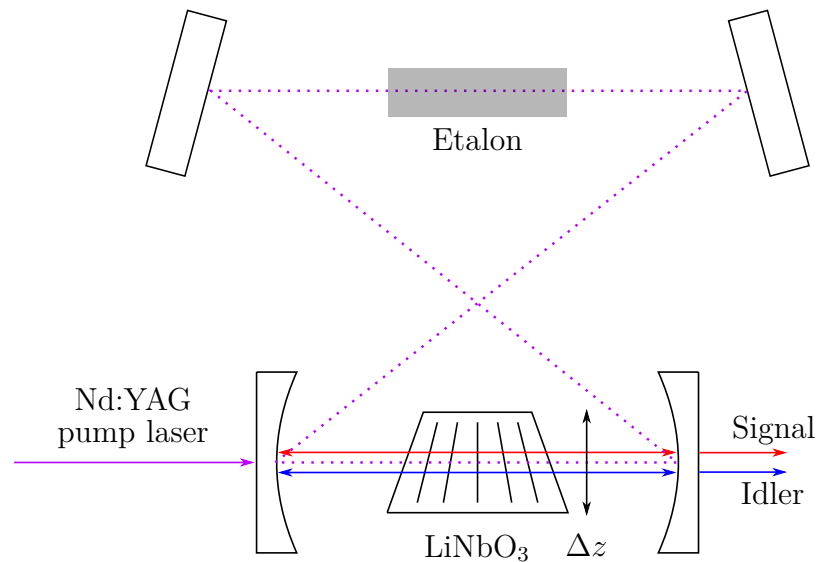


Fig. 4.7. Operation principle of an Nd:YAG pumped OPO system. Blue arrows and red arrows represent Idler and Signal beams, respectively. Visualisation after [5].

*This affects the Idler emission only.

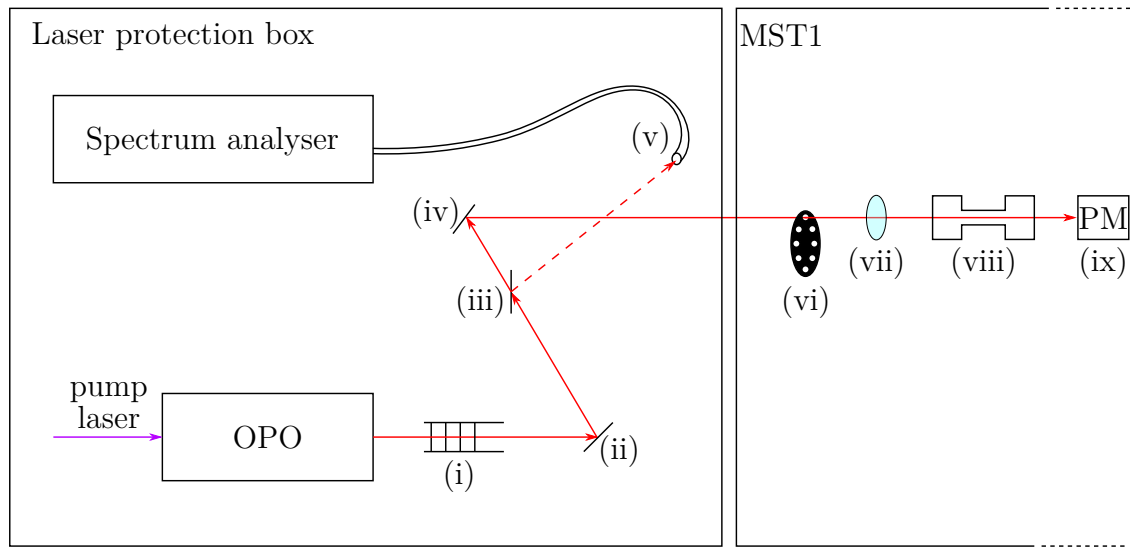


Fig. 4.8. Schematic of the optical path of the OPO's laser beam. Further descriptions can be found in the text.

stacking of up to 10 plates in a row. After reflection by means of a mirror (ii), the light passes a beam splitter (iii). A small portion of the light is reflected into the optical fibre (v), guiding the light into the spectrum analyzer. The rest of the light passes another mirror (iv) and is then directed towards the optical chopper (vi) and the PAC (viii) placed behind the chopper. In front of the PAC a collecting lens (vii) is positioned, to focus the beam before the light enters the PAC to minimize the interaction between light and resonator walls. After the PAC, the light is guided into the powermeter's sensor head (ix), which monitors the optical power of the OPO and in addition, serves as a beam dump.

4.3 Fourier Transform - Infrared (FT-IR) spectroscopy

Concluding this chapter, the employed FT-IR and its operating principle are described briefly. The light source of the FT-IR is a silicon carbide broad band emitter heated to 1200 °C. The optical detector of the FT-IR has to be cooled with liquid N₂ in order to improve the SNR. It can perform one complete scan within 0.2 s and has a spectral resolution of up to 0.5 cm⁻¹. One scan provides a spectrum ranging from 500 to 8000 cm⁻¹. For species like ammonia, carbon dioxide or carbon monoxide, the device has a lowest detectable limit between 0.2 ppmV to 1 ppmV. The manufacturer does not provide an official detection limit for acetone. However, measurements below 5 ppmV demonstrated strong deviations from the photoacoustic measurements and were considered unreliable.

Comparing an FT-IR spectrometer to a dispersive measurement system, like a grating monochromator, the FT-IR is able to measure the spectrum for all wavelengths simultaneously. This is achieved by collecting an interferogram using an interferometer. In order to obtain the corresponding transmission spectrum, the interferogram is post-processed by means of a Fourier transformation.

Figure 4.9 (top-left) visualises a Michelson interferometer (MI), which is typically used to collect the interferogram. It consists of a beam splitter, a fixed mirror and a movable mirror, which can be shifted back and forth. At the beam splitter, one part of the light is transmitted to a movable mirror and the other is reflected towards a fixed mirror. The light is reflected once more by the mirrors causing the light to meet at the beam splitter again and either interfere constructive or destructive, depending on the wavelength of the light and the current position of the movable mirror. In order to interfere constructively, the following condition has to be met

$$\Delta L_{\text{dif}} = n\lambda_{\text{ph}} \quad \text{with} \quad n = 1, 2, 3, \dots \quad (4.1)$$

where ΔL_{dif} is the path difference between the light wave being reflected by the movable mirror and the light wave being reflected at the fixed mirror (refer to figure 4.9 (top-left)). The difference can be calculated by $\Delta L_{\text{dif}} = 2(L_{\text{m}} - L_{\text{f}})$ with L_{m} and L_{f} being the distance between beam splitter and movable mirror as well as the distance between beam splitter and fixed mirror, respectively. Destructive interference occurs if the following condition applies

$$\Delta L_{\text{dif}} = \left(n + \frac{1}{2}\right) \lambda_{\text{ph}} \quad \text{with} \quad n = 1, 2, 3, \dots \quad (4.2)$$

Both interference scenarios are depicted in figure 4.9 (top-right). For the constructive case, the amplitudes of both waves are summed up and in the destructive case, the waves cancel each other out completely, due to their 180° phase shift. So far, only monochromatic light has been considered. The result of two interfering waves with different wavelengths is depicted in figure 4.9 (bottom-left). The interferogram of an FT-IR, however, results from the interference of all wavelengths emitted by

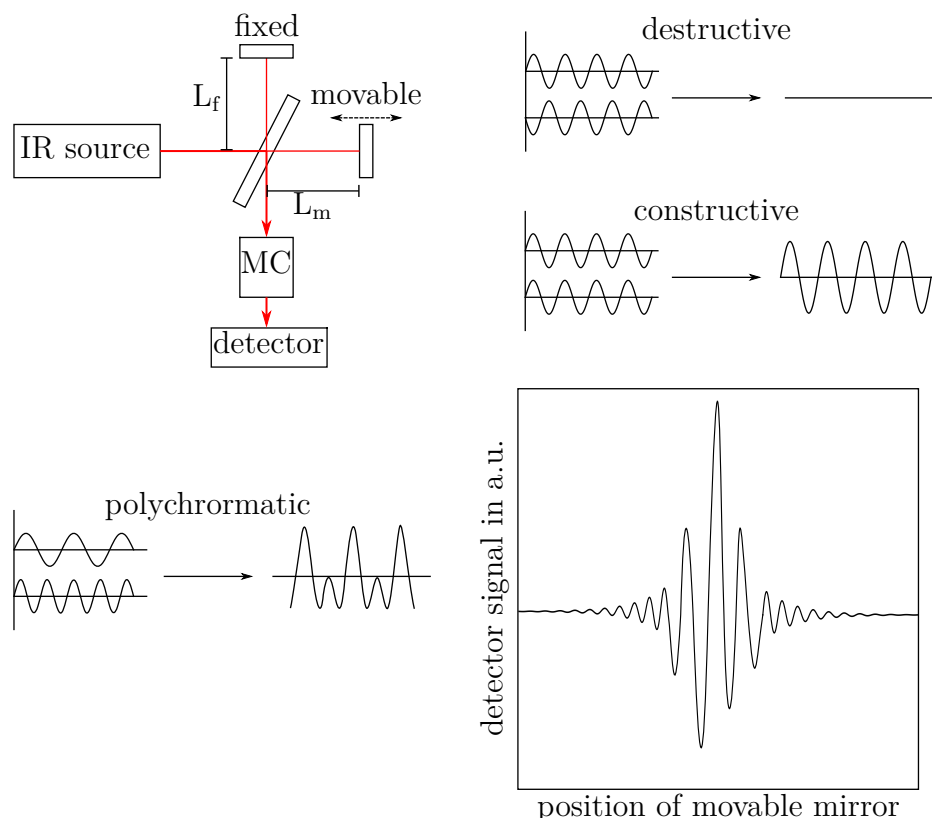


Fig. 4.9. Schematic of a Michelson interferometer, destructive, constructive and polychromatic interference and an interferogram. Further description can be found in the text.

the broad band emitter and is summed up by the detector over the time of a complete scan of the movable mirror. Such an interferogram is visualised in figure 4.9 (bottom-right). The strong peak located at the center of the interferogram is called center burst and refers to the position of the movable mirror at which no optical path difference exists, i.e. where $L_m = L_f$ applies. By performing an FFT, the interferogram is converted into a transmission spectrum. Since the light passes the measurement cell before it impinges onto the detector, certain wavelengths of the incident light can get absorbed by analyte molecules. This results in an alteration of the calculated spectrum compared to an acquired spectrum with the measurement cell being completely flushed with N_2 . The latter spectrum is also called background or reference spectrum. In order to quantify the concentration of a certain analyte being present in the measurement cell of the FT-IR, the software of the FT-IR compares the reference spectrum with the measured spectrum and calculates the analyte concentration based on calibration data.

References

- [1] M. Ade. “Konzeptionierung und Entwicklung einer intuitiv bedienbaren Messsoftware eines photoakustischen Labormessplatzes mittels LabVIEW”. B. Sc. thesis. OTH Regensburg, 2016 (cit. on p. 176).
- [2] A. Bauer et al. “Mid-infrared semiconductor heterostructure lasers for gas sensing applications”. In: *Semiconductor Science and Technology* 26.1 (Jan. 2011), p. 014032. ISSN: 0268-1242. DOI: 10.1088/0268-1242/26/1/014032 (cit. on p. 179).
- [3] J. Chen et al. “LED revolution: fundamentals and prospects for UV disinfection applications”. In: *Environmental Science: Water Research & Technology* 3.2 (2017), pp. 188–202. ISSN: 2053-1400. DOI: 10.1039/C6EW00241B (cit. on p. 179).
- [4] T. Rück et al. “Low-cost photoacoustic NO₂ trace gas monitoring at the pptV-level”. In: *Sensors and Actuators A: Physical* 263.2 (2017), pp. 501–509. ISSN: 09244247. DOI: 10.1016/j.sna.2017.06.036 (cit. on p. 181).
- [5] T. Rück. “Development, characterization and miniaturization of a trace gas detection system for NO₂ in air based on photoacoustic spectroscopy”. Ph. D. thesis. University of Regensburg, 2017 (cit. on p. 183).

Chapter 5

Results and discussion

Synopsis

Chapter 5 is subdivided into four sections. The first section describes a detailed characterisation of a UV LED based photoacoustic sensor for the detection of acetone in N_2 and synthetic air. The second part presents the investigations regarding effects of ambient parameters and cross-sensitivities introduced by high humidity or CO_2 . The penultimate section describes the results of the characterisation of further photoacoustic cells comparing the performance of both types of UV LEDs. Finally, the results of acetone detection in the IR using an OPO, an ICL and a QCL as light sources as well as one photoacoustic spectrum measurement are presented outlining the potential of IR breath acetone detection.

5.1 Photoacoustic detection of acetone in N_2 and synthetic air using a high power UV LED

The detection of trace gas species is of great interest for a wide range of applications. Optical sensor principles, especially photoacoustic spectroscopy, allow highly sensitive and selective measurements, which are mandatory in trace gas analysis of samples consisting of multiple gas species. Application areas of PAS are exhaust gas emissions, ambient air quality, safety and stack gas emission analysis as well as medical diagnosis, plant physiology and entomology to name a few [1].

PAS has proven to detect analytes down to the pptV range. Reported systems reached limits of detection (LOD) of 25 pptV (3σ) [2] and 110 pptV (3σ) [3] for ethane as well as 65 pptV (1σ) for methane and 190 pptV (1σ) [4] for hydrogen cyanide using a continuous wave optical parametric oscillator laser system. In 2018, Tyas et al. [5] used a CO_2 laser in an intracavity setup with up to 50 W optical power to detect acetone in breath, reaching an LOD of 30 ppbV. In 2007 Dunayevskiy [6] et al. employed an EC-QCL with > 200 mW* obtaining an excellent LOD of 3 ppbV (1σ) for the detection of acetone. Besides, Viola et al. [7] used an EC-QCL, too, emitting between 7 to 8.5 μm and Holthoff et al. [8] used a pulsed QCL being tuneable from 1015 cm^{-1} to 1240 cm^{-1} achieving LODs of 110 ppbV (1σ) and 550 ppbV (3σ) for acetone detection, respectively. Recently, Yin et al. [9] published a photoacoustic sensor for SO_2 detection using an EC-QCL at 7.41 μm reaching an LOD of 2.45 ppbV (1σ). Furthermore, interband cascade lasers [10–13] and near-IR DFB lasers [14, 15] have been used for PAS in the IR wavelength region in order to excite multiple harmonics of fundamental molecular vibration.

Another photoacoustically well-investigated species is NO_2 , using mainly blue laser diodes for its detection. At around 450 nm photoacoustic systems have reached LODs at the ppbV and pptV range. Kalkman and van Kesteren [16] used a GaN based diode laser for NO_2 detection at 444 nm achieving an LOD of 200 pptV (1σ). Exploiting electronic excitation, too, applying a 450 nm diode laser, Yi et al. [17]

*The output power of a single wavelength was about 100 mW.

reported an LOD of 18 ppbV (1σ). Yin et al. [18] used a 3.5 W multimode diode laser at 447 nm reaching an LOD of 54 pptV (1σ). In 2017 and 2018 Rück et al. reported an LOD of 2.0 ppbV (3σ) with a stainless-steel cell [19], 1.8 ppbV (3σ) in air employing a QEPAS setup [20] and an LOD of 33 pptV (1σ), using a low-cost 3D printed measurement cell [21].

In the past, mainly lasers were used for photoacoustic analysis in the ultraviolet region. In 1978, Koch and Lahmann [22] reached an LOD of 120 pptV (SNR= 1) for SO₂. In their study, a frequency doubled and argon pumped dye laser with an output power of approximately 1 mW and an emitting wavelength between 290 nm and 310 nm was applied. In 1988, it was Boutonnat et al. [23] using a Nd:YAG pumped dye laser emitting between 300 – 310 nm with a typical pulse energy of 5 mJ per pulse (15 Hz repetition rate) to detect formaldehyde. Their minimum detectable concentration was at the 50 ppbV level. In 2017, it was Yin et al. [24] who used a diode pumped solid-state laser measuring SO₂ at 303 nm reaching an LOD of 74 ppbV (1σ) with 5 mW of power. To the best of our knowledge, it was Oka et al. who reported the first UV-PAS study detecting acetone in 1988 by exploiting the broad acetone absorption feature around 278 nm [25]. This absorption band originates from an oxygen n_S-orbital electron being promoted into the excited π^*_S -orbital ($n_S \rightarrow \pi^*_S$). The group used a 500 W xenon arc lamp emitting light between 230 – 340 nm. In 2015, Preukschat et al. [26] compared the LODs for acetone detection using an OPO for excitation of vibrational states in the IR and a 266 nm UV laser. At 3367 nm the LOD was 200 ppbV and at the second harmonic of a 1064 nm YAG laser, the LOD was 100 ppbV. Böttger et al. [27] employed a 285 nm UV-LED with an output power of 0.8 mW to detect ozone using the Hartley band. They reached an LOD of 1.27 ppmV (1σ). Finally, El-Safoury et al. [28] demonstrated the capability of a UV LED emitting at 285 nm to photoacoustically detect acetone in 2018. However, El-Safoury et al. did not focus on acetone during their study, since it was only employed as a nontoxic substituent for SO₂.

Summarizing the aforementioned, no matter if applied in the IR, visible or UV range, PAS has been proven a useful tool when it comes to trace gas detection. Due to that, this study investigates the performance of a UV LED photoacoustic sensor for the detection of acetone mainly for the later application in human breath analysis. The novelty of this work results from the use of an LED instead of a laser as light source in the UV region emitting at the peak of the acetone absorption band around 278 nm. Besides, different collimation approaches for highly diverging UV light were investigated. The photoacoustic measurement cell was designed and manufactured using cutting-edge 3D printing technology combined with precise post-processing with the ambition to create a high performing compact sensor, facilitating a future integration in a compact device. Additionally to the innovative measurement system design, the paper addresses the influence of acetone photodissociation on the photoacoustic signal at 278 nm.

Acetone is a metabolic product of the human body, which is produced in the liver. Two pathways are reported for the systemic generation of acetone in humans. The first pathway is the decarboxylation of acetoacetate and the second is the dehy-

drogenation of isopropanol [29]. Studies have demonstrated that acetone is an interesting biomarker since it correlates with some metabolic anomalies and diseases. Measuring breath acetone can help to monitor the effectiveness of a ketogenic diet, which can help children with epilepsy [30, 31] or simply helps burning more fat. Furthermore, F. G. Marcondes-Braga et al. suggest, that breath acetone levels can deliver important information for patients suffering from chronic and acute heart failure [32]. Still intensively debated is the question if acetone can also provide useful information in the case of diabetic patients. Besides, it is difficult to determine a range of acetone abundance for healthy humans due to different measurement and study approaches, however, an acetone sensor for breath analysis should have a detection range down to at least 100 ppbV [29]. Atmospheric acetone [33] and acetone as a precursor in synthesis of explosives [6] is of interest, too, but not further discussed within this work. Further information regarding toxicology of ambient acetone can be found elsewhere [34].

Especially the medical applications point out the usefulness of a simple and non-expensive acetone detector. Such a device could be used to conduct more comprehensive medical studies contributing to a better understanding of the correlations between diseases and exhaled breath acetone.

5.1.1 Experimental

The concept of the laboratory setup has been described in the subsections of section 4.1. Therefore, the main focus of this subsection is on the cell design.

Figure 5.1 depicts a cross section drawing of the photoacoustic measuring cell. The cell is 3D printed using an aluminium alloy powder AlSi10Mg (EOS GmbH, Munich, Germany). Describing the different parts from outside to the inside, starting with a “pressure plate” (a) used to press the window (b) against a sealing (c). Both, the sealing and the window are integrated in a window holder (d). The window is from Edmund Optics (Edmund Optics Ltd, Nether Poppleton, UK) part number #65875, has a diameter of 25 mm, a thickness of 3 mm, is made of fused silica and has an anti-reflective coating for the UV region. The pressure plate is a laser-cut acrylic glass with a thickness of 5 mm and the sealing is laser-cut from a 3 mm thick silicon rubber mat (IR Dichtungstechnik, Konstanz, Germany). The sealing is pressed against the window holder (which is not shown in figure 5.1). The PAC* can be heated using a peltier element ET-161-12-08-E (European Thermodynamics LTD, Leicestershire, UK) and a TEC driver TEC-1122-SV (Meerstetter Engineering, Rubigen, Switzerland) in order to ensure homogeneous temperature distribution within the resonator and buffer volumes next to it. A graphite sealing (e) of 1 mm thickness is employed between the body of the PAC and the pressure holder (a) to ensure optimal thermal conductivity. The feedback for temperature controlling the PAC is provided by a 10 kOhm NTC resistor B57861S0103F040 (TDK, Tokio,

*The PAC referred to within this section always refers to PAC1.

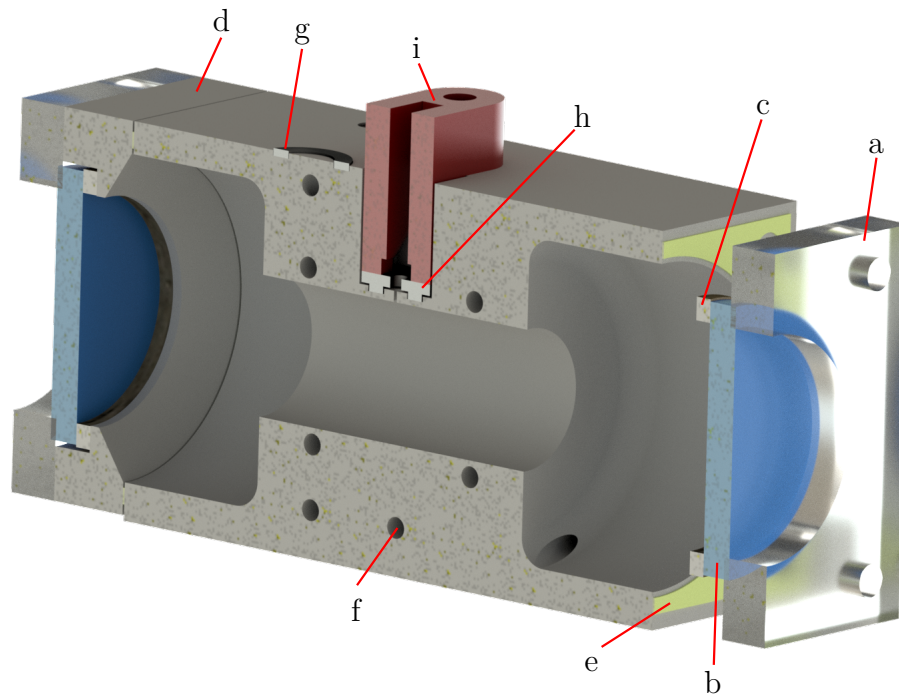


Fig. 5.1. Cross-section drawing of the employed PAC. Acrylic glass plate (a), optical window (b) and a ring shaped sealing (c). The window holder (d) and a thermally conductive graphite sealing (e). (f) points on one of six holes originating from the gas heating channel. Ring shaped sealing for the TpH sensor opening (g), ring shaped sealing (h) between resonator and microphone and the microphone holder (i).

Japan). The NTC is placed in a 10 mm deep hole located centrally on the side of the measurement cell and fixed using thermal conductive glue.

The buffer volumes of the PAC have a length of approximately 15.5 mm and a diameter of 30 mm. The length of the resonator is 31 mm and its diameter is 10 mm. The aspect ratio between resonator and buffer volume diameter has been set to $d_b \geq 3d_{res}$, which is suggested by [35]. The relatively large diameter of the resonator is necessary, since the divergence angle of the used LED is approximately 125° . This issue will be discussed more closely in section 5.1.2. On top is a square opening surrounded by a ring shaped cavity filled with a laser-cut 2 mm thick EPDM (IR Dichtungstechnik, Konstanz, Germany) sealing (g). During this study, the opening was closed pressing an acrylic glass plate onto the sealing, however, in future a temperature, pressure and humidity sensor is planned to be placed into the hole. The six holes around the resonator indicate a spirally shaped gas stream channel within the aluminium body of the cell allowing the gas to heat up before entering the buffer and resonator. A small opening in the middle of the resonator ensures sound coupling to a microphone. The microphone is placed on top of the hole, while another ring shaped 2 mm silicon gas sealing (h) is placed underneath the microphone for better gas tightness of the system. The microphone on its PCB is

pressed onto the sealing using a 3D printed microphone holder (i), which is fixed using two screws.

The 3D printed cell has to undergo post-processing including smoothing of the resonator, threading and milling the ring shaped cavities for the seals. The window holders are not 3D printed but directly milled and lathed out of an aluminium block.

5.1.2 LED collimation design

The PAC is designed as an acoustic resonator for signal amplification, hence, employing the mathematical representation of a first longitudinal mode* of the acoustic resonator, the photoacoustic signal can be written as [36–39][†]

$$p_a(\vec{r}, t) = (\gamma - 1)\rho\sigma_A(\tilde{\nu})P_0\frac{Q}{\omega}I_1p_1(\vec{r})\frac{L_{\text{res}}}{V_{\text{res}}} \quad (5.1)$$

where ρ is the analyte particle density, $\sigma_A(\tilde{\nu})$ is the absorption cross section at the wavenumber $\tilde{\nu}$ and P_0 is the optical power of the light source. γ represent the heat capacity ratio, i.e. the ratio of specific isobar and isochore heat capacities. Q is the quality factor of the acoustic resonator, ω the angular modulation frequency of the light, I_1 is the normalised overlap integral describing the normalised efficiency of energy transfer from light to heat, the distribution function of the resonant acoustic oscillation is $p_1(\vec{r})$, L_{res} is the length and V_{res} the volume of the acoustic resonator. One main task to allow using the highly divergent LED as an excitation source was to find a way guiding as much light as possible into the resonator by keeping the resonator diameter small. This is important, since according to equation 5.1 the photoacoustic amplitude is indirectly proportional to the square of the resonator's radius $p_a(\vec{r}, t) \propto \frac{1}{r_{\text{res}}^2}$. To find an optimum solution with a maximum of two additional optical parts, the simulation software FRED (Photon Engineering, Tucson, US) was used. Three different approaches of optical constellations were simulated and the results were compared. A system made of two lenses consisting of an aspheric (#33955, Edmund Optics) and a biconvex (BC) lens (#48304, Edmund Optics), one using a parabolic shaped aluminium reflector combined with the same BC lens from the two-lens approach and a system consisting only of an elliptic shaped aluminium reflector. The BC lens was chosen since it has a high numerical aperture of 0.5 with a large diameter of 25 mm, on the one hand collecting much light and on the other hand keeping the system comparable small with a short focal length. Figure 5.2 provides the “Ray Summary Analysis” simulation, where the resonator was simply a hollow cylinder with a diameter of 10 mm.

The aperture in front of the resonator is an imaginary aperture necessary to provide an end wall for rays, which would hit the outer resonator wall. This would count as a photon having entered the resonator and has to be avoided. The optical output

*Note that the index 1 in equation 5.1 represents the first longitudinal mode.

[†]A detailed derivation of this equation is provided in section 2.4.1.

power of the LED was set to 300 mW and the number of rays to be simulated was 3000. Every ray is allocated to the last surface it hits. Note that the different rays are assigned with different optical power depending on their divergence angle. The aim of the simulation was set to optimise the maximum number of rays guided into the resonator. Hence, all counts of the resonator wall and the backplane of the resonator contributed to that result. The simulation results suggested the parabolic reflector approach to be the most promising one with 22 mW, followed by the two-lens system and the elliptic reflector system having 200 mW and 198 mW, respectively. The reflectivity of the reflector was set to 100 % for the simulation. This assumption

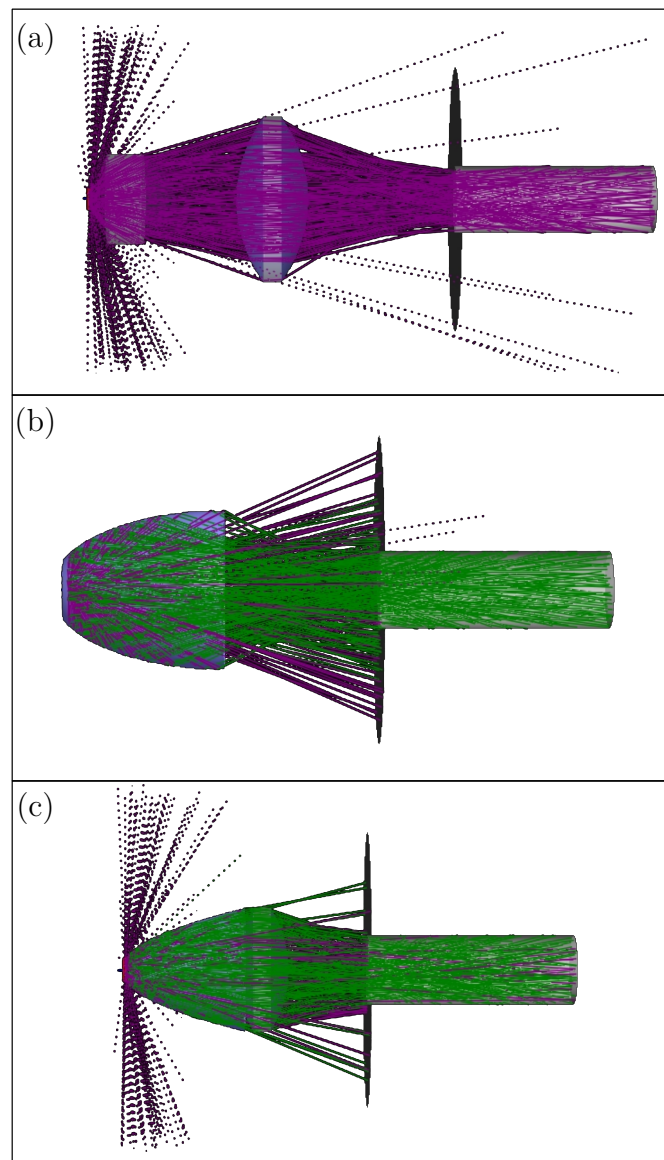


Fig. 5.2. Simulation of a two-lens system in FRED. Two-lens system (a), elliptic reflector (b) and parabolic reflector (c). Green rays represent reflected, purple not reflected rays and the spotted lines are rays not hitting any wall. The circle in front of the resonator is an imaginary aperture.

can be made since for large incident angles, the reflectivity for aluminum at the employed wavelength of 278 nm is close to 1 [40].

Figure 5.3 visualises the simulation verification setup (a), as well as the test setup for the evaluation of the final measurement setup (b) and (c). For the measurement of the optical power, the LED was driven at a constant current of 344 mA and cooled using a fan combined with a 3D printed conically shaped attachment to guide the airflow directly into the heat sink of the LED. Using 3D printed adapters (j), the aspheric lens and the reflectors were positioned approximately 1 mm in front of the LED, respectively. Besides, the adapter allowed the integration of the LED and the first optical part into a cage system. The cage system was fixed onto an x,y-translation plate (d) using a post (k). The BC lens (l) was positioned beyond the post. Since the lens needed a special lens holder to be integrated into the cage system, the lens holder could point the lens either towards the post or towards the detector. The cage system was necessary to enable an easy fine adjustment of the optical parts and made the setup flexible. The S302C powermeter detector (f) was used to measure the optical output power since the detector head's entrance has a diameter of about 10 mm and is thus comparable to the resonator. The detector element (e) is placed 15 mm behind the entrance and has a diameter of 12 mm. However, note that the light hitting the sidewalls between sensor element and entrance will not reach the sensor element.

Demonstrated in table 5.1, the two-lens system achieved the best results. After switching on the light source, the value rose up to 238 mW and then dropped slowly to 228 mW within four minutes due to the settling time of the thermal equilibrium of the LED. The distances (g), (h) and (i) from figure 5.3 of this setup are 0 mm, 13.8 mm and 23.8 mm, respectively. The main reason for the higher measured optical power value compared to the simulated one is most likely due to a higher total optical output power of the LED than it is specified in the datasheet. The document for a single LED package states, that one of the four LEDs is rated with 100 mW whereas the datasheet for the 4in1 system rates the package only with 300 mW. The performances of the reflectors were significantly lower as simulated. This is mainly due to the fact, that the surface quality of the manufactured parts was not as good as expected. The surface was flawed with dents and small scratches causing the light rays to be scattered instead of being guided correctly into the resonator.

Tab. 5.1. Simulated and measured results of the three beam guiding approaches.

		Two-lenses	Parabolic reflector	Elliptic reflector
Simulated	optical power	200 mW	222 mW	198 mW
Measured	optical power	228 mW	92 mW	117 mW

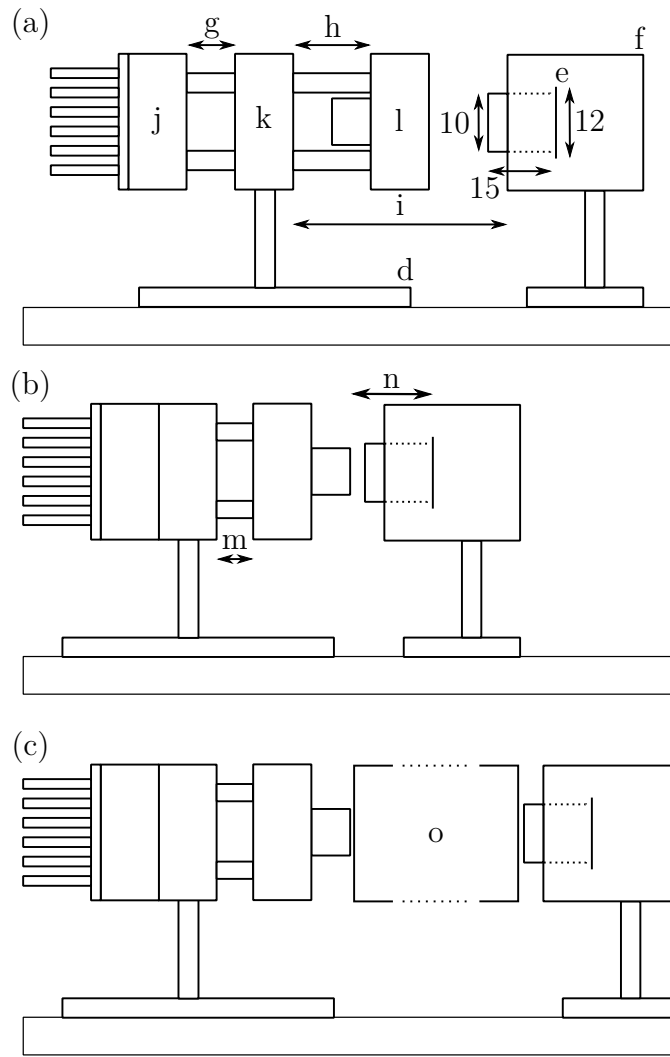


Fig. 5.3. Schematic drawing of the simulation verification setup (a), and measurement setups (b) and (c). An x,y-translation plate (d) and the active sensor element (e) of the powermeter (f). (g), (h) and (i) are the distances between the optical parts. Aspheric lens or reflector holder (j), the post-cage adapter (k) and the BC lens holder (l). Distance between post adapter and BC lens holder (m) in the final setup, distance between sensor area lens (n) and the measurement cell (o). All numbers in mm.

Further post-processing of the parts would have been necessary but was difficult to realize.

In view of a final application, it had to be tested, if good performance can be obtained using this two-lens setup combined with the measurement cell (o). Since the performance factor of interest was the amount of photons guided into the resonator, the powermeter was positioned as close as possible to the opposite end of the measurement cell beyond the second optical window for monitoring the optical power (figure 5.3 setup (c)). The highest optical power was detected, when the lens holder

of the BC lens was turned around and the lens was positioned as close as possible in front of the measurement window. The optimum distance (m) between lens holder and post was determined to be 2.5 mm, all other distances were set to zero. To compare optical power in front (figure 5.3 setup (b)) and behind the measurement cell with the final setup (figure 5.3 setup (c)), a 50 % duty cycle and 298 mA were applied to the LED. The settling time decreased significantly and was in the range of 1 min. The optical power declined to 88 mW and 15 mW measured in front (figure 5.3 setup (b)) and behind (figure 5.3 setup (c)) the measurement cell, respectively. The high loss from 88 mW to 15 mW can be explained by the absorption and reflection at both windows, by not entering the resonator, by absorption of the light by the resonator walls and of course by light being reflected from the resonator into the second buffer volume and thus not reaching into the optical detector. It can be assumed that the amount of light illuminating the resonator is significantly lower than the measured 88 mW since the distance (n) \approx 25 mm is shorter than the distance from lens to the resonator entrance, which is approximately 35 mm. Hence, some light entering the PAC was not illuminating the resonator but hit the walls of the first buffer volume.

Although there is some space for improvements to guide even more light into the resonator, this setup was employed for the photoacoustic measurements since the results of the collimation tests indicate a sufficient performance of the system.

5.1.3 Deexcitation process of acetone and sensing mechanism

This chapter provides a quick overview of relaxation processes and the photoacoustic sensing mechanism in general. To generate a photoacoustic signal, it is inevitable for the excited analyte molecules to deexcite nonradiatively. The energy of the excited molecules can be released either by collision induced VT relaxation or by a collision induced VV transfer mechanism with another molecule, e.g. N₂ or O₂, followed by a VT relaxation of the previous collision partner. Both processes have an influence on the overall relaxation time and thus influence the sensitivity of the signal.

The absorption band around 278 nm used for acetone detection within this work originates from the $n_S \rightarrow \pi_S^*$ transition from the carbonyl group of acetone. There are two important laws, the energy gap law [41] and Rayleigh-Jeans law [42], describing, that the nonradiative relaxation rate of a molecule decreases significantly with an increasing energy gap between ground and excited state. Hence, it is rather unexpected to achieve a strong photoacoustic signal using absorption bands in the UV region. However, the nonradiative relaxation path of acetone is rather complex [25] and can be promoted by O₂ causing a relatively fast relaxation time of $< 20 \mu s$ making acetone attractive for photoacoustic detection.

5.1.4 Acetone measurements

This study focused on the first measurements of acetone in nitrogen and in synthetic air using a UV LED combined with the described PAC and optical setup. If not mentioned otherwise, the measurements have been performed at 300 mL/min flow rate, $\tau_{LIA} = 2$ s with a filter slope of 12 dB/octave, 298 mA of LED current and a data acquisition rate of 5 Hz. Every measurement point plotted within this work was recorded with 20 s averaging time, i.e. 100 measurement points. The temperature of the PAC was set to 45 °C. This temperature was chosen, since in a later application like breath analysis the same temperature has to be applied to avoid condensation.

5.1.4.1 Acoustic resonance analysis

In order to characterise the resonance profile of the measurement cell, the modulation frequency was continuously tuned from 2500 – 7500 Hz. The gas mixture used for the measurement was 50 ppmV acetone in synthetic air or pure nitrogen.

Figure 5.4(b) shows the zoomed resonance profile with a peak frequency for acetone in synthetic air of 4938 Hz. Figure 5.4(a) visualises the complete resonance profile demonstrating a high quality factor. The quality factor of the PAC can be calculated by

$$Q = \frac{f_{\text{res}}}{\Delta f_{\text{FWHM}}} \quad (5.2)$$

where f_{res} is the resonance frequency of the fundamental longitudinal oscillation of a both-sided opened resonator tube and Δf_{FWHM} is the full width of the resonance peak at half maximum. The factor was determined to $Q = 51.4$. This is a high quality factor compared to other similar designed PACs reported in [19, 21] with Q factors of 7.9 and 21.9, respectively. For acetone diluted in nitrogen, the resonance

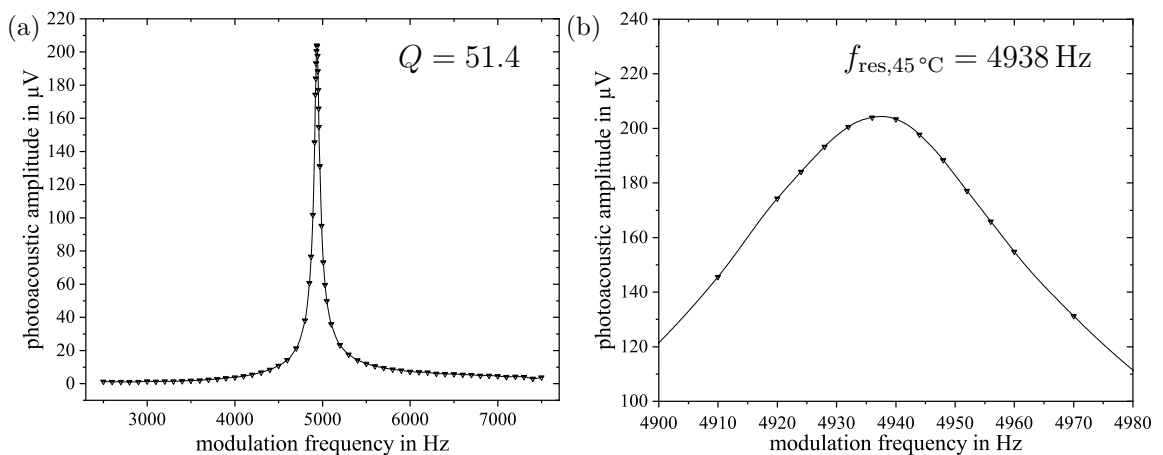


Fig. 5.4. (a) Frequency sweep from 2.5 kHz to 7.5 kHz with 50 ppmV acetone in synthetic air at 45 °C and (b) zoomed detail of the resonance peak at 4938 Hz. Data points are connected using an Akima-Spline.

frequency was 5010 Hz at a temperature of 45 °C. The shift of 72 Hz corresponds to a relative increase of 1.43 % and can be explained by a lower speed of sound in synthetic air compared to nitrogen. The speed of sound in dry air at 45 °C is 358.28 m s⁻¹ and in nitrogen 363.59 m s⁻¹, which equals a ratio of 1.46 %. The speed of sound was calculated using equation 5.3, where R is the universal gas constant, T the absolute temperature and M the molar mass of the gas.

$$c_s = \sqrt{\frac{\gamma RT}{M}} \quad (5.3)$$

Additionally, the photoacoustic amplitudes for the measurements in nitrogen were significantly lower than for the measurements in synthetic air. The temperature dependency of the resonance frequency was measured from 25 °C to 50 °C in 5 °C steps. Both, for acetone in synthetic air and nitrogen the shift was 7.8 Hz/°C.

However, according to

$$f_{\text{res}} = \frac{c_s}{2L_{\text{res}}} \quad (5.4)$$

with the theoretical resonance frequency f_{res} of the fundamental longitudinal oscillation in a two side opened resonator tube with the length L_{res} and the speed of sound c_s , the resonance frequency for synthetic air is 5771 Hz and for nitrogen 5864 Hz. Both theoretical frequencies show a relative shift of 14.4 % to the measured resonance frequencies. The shift between theoretical and measured resonance frequency can be explained by node shifting of the standing acoustic wave. The nodes shift into the buffer volumes and by this increase of the acoustic wavelength λ_s the frequency decreases according to

$$c_s = \lambda_s f_{\text{res}} \quad (5.5)$$

Due to the node shifting, L_{res} has to be replaced by the effective length L_{eff} . There have been different approaches to find a universally valid expression for L_{eff} , all failing to address the different geometries of measurement cells sufficiently [19, 21]. For the PAC of this study L_{eff} has to be 36.28 mm to explain a resonance frequency of 4938 Hz in synthetic air at 45 °C. Hence, describing L_{eff} as

$$L_{\text{eff}} = L_{\text{real}} + r_{\text{res}} \quad (5.6)$$

results in an L_{eff} of 36 mm, which corresponds to a resonance frequency of 4976 Hz that deviates only 0.8 % from the measured value. Combined with the manufacturing tolerances, this provides a useful approximation for the node shifting occurring within this PAC. According to equation 5.1 this comparably high resonance frequency causes a lower photoacoustic signal due to $p_a(\vec{r}, t) \propto \frac{1}{f}$. However, to facilitate the integration of this sensor in a compact device, a smaller PAC is preferred. Besides, since printing space of 3D printers is finite, smaller cells are easier to manufacture.

Finally, it has to be noted that for all further measurements the actual resonance frequency was determined manually at the beginning of each measurement. This was necessary, because only the feedback from the NTC in the wall of the isolated PAC was used as temperature reference point and since the room was not at a constant temperature, the resonance frequency deviation was ± 1 Hz.

5.1.4.2 Background signal analysis

The background signal of a photoacoustic system originates from an acoustic signal generation due to light absorption by the optical windows of the PAC, the interaction of the light with the walls of the resonator and of course photons interacting with the acoustic transducer, i.e. the membrane of the detector microphone. Due to that, care has to be taken during the alignment of the LED and its corresponding optics. Furthermore, the optical parts of the system should remain unchanged to avoid changes in the background signal and increase the repeatability. Lowering the background signal has the advantages of increasing the dynamic range as well as the reproducibility of the system. Since the light beam is not completely collimated, a great amount of light hits the walls of the resonator, thus a high background signal was expected. However, with a background signal at around $64 \mu\text{V}$ for measurements in pure synthetic air and pure nitrogen, the results are better than expected. This leads to the assumption, that light rays with a large angle of incidence towards the resonator wall do not have a strong influence on the background signal. Besides, minimizing the roughness of the resonator walls by means of post-processing seems to positively affect the background amplitude, too.

Further measurements implicated, that the amplitude of the background signal depends on environmental parameters, e.g. temperature. Measuring this background signal at different temperatures between 25°C and 50°C identified its amplitude to linearly decrease by approximately $0.43 \mu\text{V}/^\circ\text{C}$. Although various authors assess this drop to solely result from a temperature dependency of the microphone sensitivity [43, 44], the integration of further secondary sensors into the PAC is intended, in order to quantify and further investigate the different effects on the background signal in a holistic manner. This issue will be tackled in the future, but exceeds the scope of this work.

The noise is a very important factor since it directly influences the LOD of the system, which is defined as the noise level of the background signal divided by the

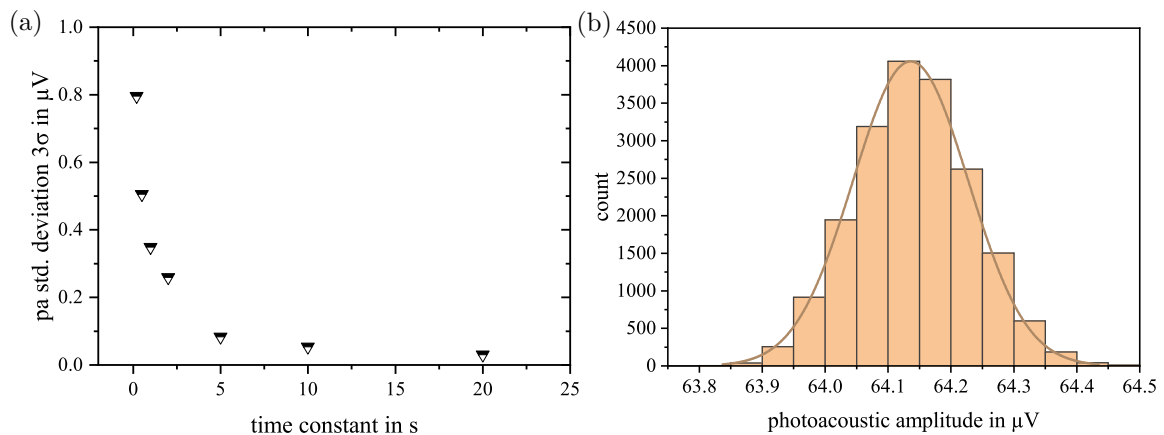


Fig. 5.5. (a) Influence of the time constant τ_{LIA} on the noise and (b) histogram of a one-hour measurement. Both performed in synthetic air.

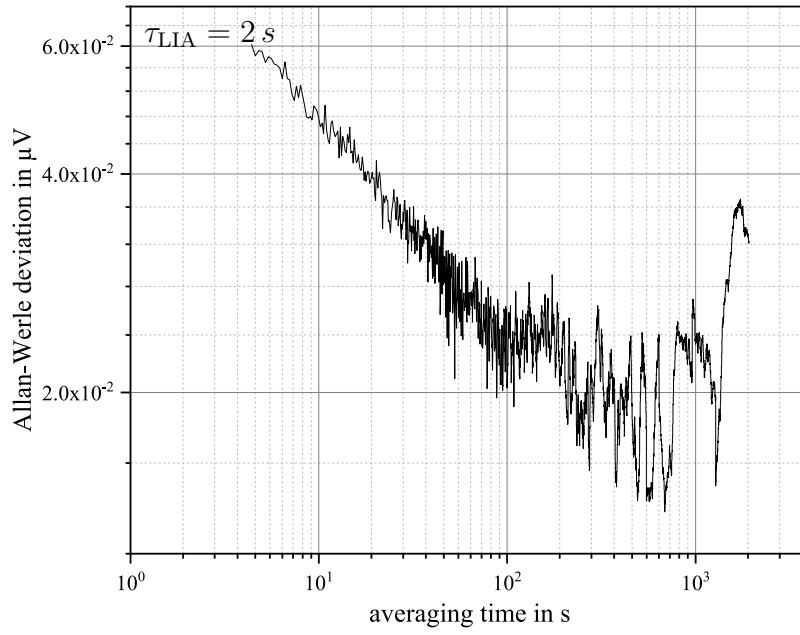


Fig. 5.6. Allan-Werle deviation over a one-hour measurement in synthetic air, with a τ_{LIA} of 2 s and 5 Hz data acquisition rate.

sensitivity of the system. The slope of the linear photoacoustic calibration curve gives the sensitivity. This study always uses 3σ for the noise level if not mentioned otherwise. Noise levels of $0.076 \mu\text{V}$ and $0.053 \mu\text{V}$ have been detected in pure nitrogen and synthetic air, respectively. These values are the averages of three measurement points acquired consecutively with a $\tau_{LIA} = 10 \text{ s}$. Changing the time constant has two effects. On the one hand the higher the time constant, the lower the noise, but on the other hand, the response time of the system increases. A time constant of 10 s was chosen since it offers a good agreement between measurement speed and noise suppression. The responsivity provided for $\tau_{0-90\%}$ was measured to be $\approx 4.2 \text{ s}$ and $\approx 20 \text{ s}$ for $\tau_{LIA} = 2 \text{ s}$ and $\tau_{LIA} = 10 \text{ s}$, respectively.

Figure 5.5(b) shows a histogram of the background data measured over approximately one hour showing a Gauss distribution, which indicates that mainly white noise and no drift is present. Additionally, (a) demonstrates the enhancement of noise suppression by increasing the lock-in time constant.

To investigate the stability of the system, an Allan-Werle deviation (AWD) was performed. Therefore, the same data points used for the histogram were applied to calculate the AWD. Note that no further averaging besides the lock-in amplifier filtering was performed to acquire the measurement points for the histogram or AWD. The results are presented in figure 5.6. As mentioned at the beginning of section 5.1.4, the averaging time for one measurement point plotted within this work was usually set to 20 s. The AWD plot indicates that an averaging time of up to 800 s can be applied improving the signal stability, afterwards no further benefit can be expected due to drift.

5.1.4.3 Influence of the optical power

According to equation 5.1, the photoacoustic signal is directly proportional to the optical power. This behaviour was confirmed by performing a measurement series where the LED current was constantly increased from 0 to 344 mA in approximately 50 mA steps. The photoacoustic signal for 50 ppmV of acetone in synthetic air increased linearly. The linear fit has an $R^2 = 0.9999$ and thus can be considered linear. Besides, the slope was $14.2 \mu\text{V mW}^{-1}$ and the curve's origin is located at approximately $0 \mu\text{V}$. Hence, with a switched off light source the measured signal is approximately $0 \mu\text{V}$, since no photoacoustic signal is generated. As the increase of the optical power does not affect the noise level* but improves the sensitivity and thus the LOD, more optical power is a common approach to boost the performance of a PAS system.

Note that the actual output power of the LED is significantly higher than indicated in the graph. However, as shown in figure 5.3 setup (c), the optical detector is positioned behind the measurement cell and thus approximately 83 % of the light gets lost passing the PAC. Similar to Preukschat et al. no effects regarding photolysis have been observed during the photoacoustic measurements [26]. However, there was a drop of acetone concentration visible in the results of the FT-IR measurements when the gas stream first entered the illuminated PAC and then the FT-IR cell. This rapid decline is illustrated in figure 5.7. The delay of the acetone drop is

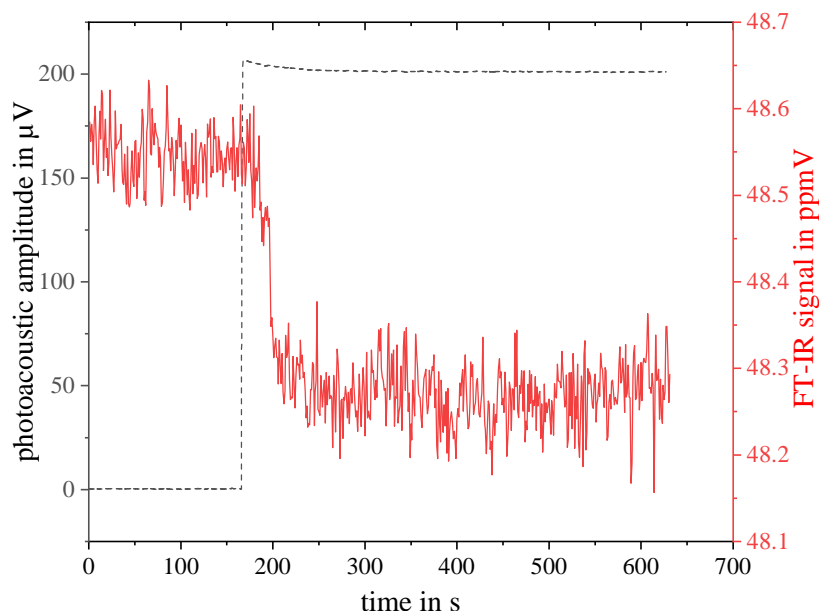


Fig. 5.7. Acetone drop measured by the FT-IR (red, solid) combined with the photoacoustic signal (black, dashed). The latter one indicating the time when the LED was switched on at approximately 166 s.

*As long as the light output is stable.

due to the long gas transfer time from the PAC to the FT-IR. It is very likely, that photolysis contributes to the photoacoustic signal, however, decomposed acetone was quickly exchanged due to the gas flow rate of 300 mL/min and thus no significant signal drop was detected. This flow rate causes a complete gas exchange within the illuminated volume inside the measurement cell within approximately 0.98 s. The above mentioned drop in acetone concentration was approximately 0.6 % for 50 ppmV of acetone in synthetic air. Blitz et al. provide a formula for the calculation of the photolysis quantum yield Φ_d for acetone at different pressures, temperatures and wavelengths [45].

$$\Phi_d(\lambda_{ph}, \rho, T) = \Phi_{CH_3CO}(\lambda_{ph}, \rho, T) + \Phi_{CO}(\lambda_{ph}, T) \quad (5.7)$$

Further details regarding the calculations of the respective quantum yields of the carbonyl and acetaldehyde radicals can be found in [45]. Equation 5.7 is suggested by the NASA, too, and provides an overall dissociation quantum yield of about 65 % at 278 nm, 295 K and 1 atm [46]. With a constant flow of 300 mL/min and approximately 88 mW of optical power with a 10 mm collimated beam illuminating the PAC the theoretical drop was calculated to be 0.5 % after equation 2.189. A description of the applied formula for the drop calculation is provided in section 2.5.6. The difference between calculated and real value is likely due to wrong assumptions, including a perfectly collimated beam and idealised residence duration of the gas within the PAC. However, further investigations regarding photodissociation of acetone are not within the scope of this work.

5.1.4.4 Recovery and repeatability

To investigate the recovery and repeatability behavior of the sensor, a measurement at different concentrations of acetone diluted in synthetic air was performed. This time the flow rate was set to 500 mL/min to enable a faster gas exchange within the long pipelines of the gas mixing unit. The measurement started with pure synthetic air. Different concentrations were set and rerun in order to investigate the repeatability of the photoacoustic signal. The concentration sequence was set as follows: pure synthetic air, 10 ppmV, 50 ppmV, 90 ppmV, 50 ppmV, 60 ppmV, 20 ppmV and 10 ppmV of acetone diluted in synthetic air, respectively. At the end of the measurement the system was flushed with pure synthetic air again in order to investigate proper recovering of the photoacoustic background signal. The repeatability was calculated by comparing the photoacoustic signal resulting from the different acetone concentrations. Note that the signal amplitudes were averaged over 60 s (= 100 values) for comparison. The deviation in repeatability was 0.13 % for the background signal, 0.63 % at 10 ppmV and 0.26 % in case of 50 ppmV acetone in synthetic air. The recovery time $\tau_{0-99\%}$ of the sensor in terms of changing the acetone concentration from 90 ppmV to 50 ppmV was only 30 s. The recovering of the background signal by purging the PAC with pure synthetic air after the measurement took several minutes, which is most likely due to acetone molecules remaining at the inner walls of the pipelines as well as the measurement cell itself.

5.1.4.5 Calibration curves in nitrogen and synthetic air

This chapter deals with the calibration curve of measurements of different acetone concentrations in nitrogen or synthetic air ranging from 10 ppmV to 100 ppmV. The results of the measurements are summarised in table 5.1. The coefficients of determination R^2 of 0.9999 and 0.9984 validate the linearity of both calibration curves, respectively. The photoacoustic amplitude and, thus, the sensitivity is significantly lower for the measurement with acetone in nitrogen. This phenomenon is attributed to oxygen acting as a promoter and causing excited acetone molecules to deexcite faster and thus to contribute to the photoacoustic signal even for modulation frequencies in the kHz range. This effect has also been observed by Oka et al. [25] in 1988. Oka and his team investigated the relaxation and photoacoustic signal behaviour by comparing air and argon as carrier gas. They demonstrated that oxygen is a strong promoter for a fast heat-producing deexcitation process from the T_1 to the S_0 state generating a photoacoustic signal. Besides, also the fast recombination of radicals and the accompanying heat release was promoted by O_2 .

The sensitivities for acetone diluted in synthetic air were $2.7 \mu\text{V/ppmV}$ and for nitrogen $0.94 \mu\text{V/ppmV}$. Thus, the LODs were 19.6 ppbV and 80.9 ppbV, respectively. For a better comparability, the NNEA coefficient was calculated. The manufacturer of the lock-in amplifier provides a table with a list of the equivalent noise bandwidth (ENBW) for different combinations of time constants and filter slopes (refer to the appendix A.5). For 10 s and a slope of 6 dB/octave the ENBW is 0.025 Hz. The mean optical power used for the calculations are the 15 mW detected after the PAC.

Tab. 5.2. Summary of the calibration measurements for acetone in nitrogen and synthetic air including the applied resonance frequency f_{res} , the background noise (3σ) with $\tau_{\text{LIA}} = 10\text{s}$, the sensitivity, the limit of detection, the coefficient of determination for the linear fit and the NNEA coefficient.

Buffer gas	f_{res} in Hz	Noise (3σ) in μV	Sensitivity in $\mu\text{V/ppmV}$	LOD (3σ) in ppbV	R^2	NNEA in $\frac{\text{W}}{\text{cm}\sqrt{\text{Hz}}}$
N_2	5010	0.076	0.94	80.9	0.9984	1.87×10^{-8}
Syn. air	4938	0.053	0.27	19.6	0.9999	4.53×10^{-9}

The LED emits light with a spectral width $\Delta\lambda$ of 10 nm. From 273 nm to 283 nm the absorption cross section can be considered constant since the deviation from the peak is only approximately 0.2 % and 4.1 %, respectively.

The NNEA coefficient can be calculated after

$$\text{NNEA} = \frac{\text{LOD } N_A \sigma_A(\lambda) P_0}{\text{SNR } V_{\text{mol}} \sqrt{\Delta f}} \quad (5.8)$$

with N_A being the Avogadro constant, $\sigma_A(\lambda)$ the absorption cross section at λ , e.g. 278 nm, Δf being the ENBW and V_{mol} the molecular volume. The LOD is given

as the minimum detectable volume ratio. For this setup, this leads to an NNEA coefficient of $4.53 \times 10^{-9} \frac{\text{W}}{\text{cm}\sqrt{\text{Hz}}}$ for acetone in synthetic air and $1.87 \times 10^{-8} \frac{\text{W}}{\text{cm}\sqrt{\text{Hz}}}$ for acetone in nitrogen. Considering the achieved NNEAs and LODs of this work and recalling the LODs of other studies for acetone from the introduction, this study presents one of the best results for the photoacoustic detection of acetone so far.

5.1.5 Comparison to other acetone gas sensing techniques

Tab. 5.3. Summary of different approaches regarding acetone sensor techniques with their respective LODs. **n.a.** = not available, **ZnO/S, N:GQDs/PANI** - Metal-organic frameworks-derived zinc oxide nanopolyhedra/S, N:graphene quantum dots/polyaniline, **OBS** - organic based sensor, **TFB** - poly[(9,9-dioctylfluorenyl-2,7-diyl)-co-(4,4'-(N-(4-sec-butylphenyl)diphenylamine)]

Reference	Method	Material/ Lightsource	LOD in ppbV
This work	PAS	UV LED at 278 nm	19.3 (3σ)
Preukschat et al. [26]	PAS	UV Laser at 266 nm	100 (n.a.)
Dunayevskiy et al. [6]	PAS	EC-QCL at 7.150 – 7.500 nm	3 (1σ)
Viola et al. [7]	PAS	EC-QCL at 7.100 – 8.500 nm	110 (1σ)
Holthoff et al. [8]	PAS	EC-QCL at 8.064 – 9.852 nm	550 (3σ)
Whang and Mbi [47]	CRDS	UV Laser at 266 nm	490 (1σ)
Moon et al. [48]	SMO	Pt functionalised SnO ₂ at 300 °C	3.6 (2σ)
Guan et al. [49]	SMO	N-SnO ₂ at 300 °C	7 (n.a.)
Liu et al. [50]	SMO	CdMoO ₄ at 625 °C	500 (n.a.)
Liu et al. [51]	SMO	Pt-loaded α -Fe ₂ O ₃ at 220 °C	900 (n.a.)
Zhang et al. [52]	SMO	ZnO/S, N:GQDs/PANI at RT	100 (n.a.)
Chuang et al. [53]	OBS	TFB at RT	300 (n.a.)

According to a review paper from Masikini et al. in 2020 [54], semiconductor metal oxide sensors have by far the highest share in publication numbers in the field of breath acetone sensors, followed by optical approaches.

SMOs have the advantage of being cheap and small, however, they often still lack selectivity and stability [54]. In some cases optical approaches can be superior by overcoming these disadvantages. The following table summarises the LODs from photoacoustic methods, recent SMO gas sensing techniques and further acetone gas sensing approaches to highlight the performance of the current work.

The SMO sensor results have been taken from Masikini et al. [54] who published a list with SMO acetone sensor publications between 2017 and 2019 with LODs ranging from the ppmV down to the single digit ppbV region. Besides that, an approach with an organic based sensor being driven at room temperature [53] and a comparable good LOD was added, too. The table indicates that our first measurements can not only compete with previous photoacoustic publications but also other gas sensing approaches. However, based on the data provided and the different types of study concepts, a detailed comparison with the other methods within this work is not always possible. Note that this table provides a representative selection of different acetone gas sensing approaches but does not claim completeness (refer to table 5.3).

5.1.6 Conclusion

We developed a new photoacoustic measurement cell for the use of a high power UV LED for the detection of acetone. The presented two-lens system provides an elegant approach to guide a sufficient amount of light into the resonator and thus provides an inexpensive alternative compared to CO₂, Nd:YAG, QCL or IC lasers. The PAC consists of a 3D printed aluminium cell and a low-cost analog microphone detecting the photoacoustic signal.

With a flow rate of 300 mL/min, a lock-in amplifier time constant of $\tau_{LIA} = 10$ s and an averaging over 100 points, our first characterisation measurements identified an LOD of 19.6 ppbV (3σ) for acetone in synthetic air and 80.9 ppbV (3σ) for acetone in nitrogen. Besides, the stability of the system allows an averaging time of approximately 800 s before drift effects deteriorate the performance.

The photoacoustic detection of acetone diluted in synthetic air showed a 2.9 times higher sensitivity than acetone diluted in nitrogen. This effect is attributed to the property of oxygen causing the acetone molecule to deexcite fast enough to contribute to the photoacoustic signal. This has to be kept in mind if planning an application without oxygen being present.

There is still space for optimisation of the system regarding the collimation and PAC design increasing the amount of light illuminating the acoustic resonator and decreasing the diameter of the resonator. Besides, increasing the optical power of the LED by applying more current or exchanging it with a more powerful light source could easily increase the systems performance.

In view of a later application for human breath analysis, the LOD is sufficient to detect trace gas concentrations of acetone, as they exist in breath exhale. However, at this stage of development it is not possible to make a final statement if the system can be used for human breath exhale measurements. Such a final evaluation requires further comprehensive investigations in view of background signal fluctuations. Besides, the influence of other main breath components, e.g. water and CO₂, on the systems performance has to be investigated in detail, too, since those may affect the relaxation mechanism of photoacoustic signal generation as well.

References

- [1] F. J. Harren et al. “Photoacoustic Spectroscopy in Trace Gas Monitoring”. In: *Encyclopedia of Analytical Chemistry*. Wiley, Oct. 2000, pp. 2203–2226. ISBN: 0471976709. DOI: 10.1002/9780470027318.a0718 (cit. on p. 190).
- [2] F. Müller et al. “Cw-OPO-based photoacoustic spectrometer for highly sensitive detection of ethane and other volatile organic compounds”. In: *Photons Plus Ultrasound: Imaging and Sensing*. Ed. by A. A. Oraevsky and L. V. Wang. Vol. 5320. 0. July 2004, p. 138. DOI: 10.1117/12.532706 (cit. on p. 190).
- [3] F. Müller et al. “Transportable, highly sensitive photoacoustic spectrometer based on a continuous-wave dualcavity optical parametric oscillator”. In: *Optics Express* 11.22 (Nov. 2003), p. 2820. ISSN: 1094-4087. DOI: 10.1364/OE.11.002820 (cit. on p. 190).
- [4] J. Peltola et al. “High sensitivity trace gas detection by cantilever-enhanced photoacoustic spectroscopy using a mid-infrared continuous-wave optical parametric oscillator”. In: *Optics Express* 21.8 (2013), p. 10240. ISSN: 1094-4087. DOI: 10.1364/OE.21.010240 (cit. on p. 190).
- [5] F. H. Tyas et al. “The Performance of CO₂ Laser Photoacoustic Spectrometer In Concentration Acetone Detection As Biomarker For Diabetes Mellitus Type 2”. In: *Journal of Physics: Conference Series* 1011.1 (Apr. 2018), p. 012056. ISSN: 1742-6588. DOI: 10.1088/1742-6596/1011/1/012056 (cit. on p. 190).
- [6] L. Dunayevskiy et al. “High-sensitivity detection of triacetone triperoxide (TATP) and its precursor acetone”. In: *Applied Optics* 46.25 (2007), pp. 6397–6404. ISSN: 15394522. DOI: 10.1364/AO.46.006397 (cit. on pp. 190, 192, 206).
- [7] R. Viola et al. “Quartz Enhanced Photoacoustic Spectroscopy for Detection of Improvised Explosive Devices and Precursors”. In: *Advances in Optical Technologies* 2016 (2016). ISSN: 16876407. DOI: 10.1155/2016/5757361 (cit. on pp. 190, 206).
- [8] E. Holthoff et al. “Quantum Cascade Laser-Based Photoacoustic Spectroscopy for Trace Vapor Detection and Molecular Discrimination”. In: *Sensors* 10.3 (Mar. 2010), pp. 1986–2002. ISSN: 1424-8220. DOI: 10.3390/s100301986 (cit. on pp. 190, 206).
- [9] X. Yin et al. “ppb-Level SO₂ Photoacoustic Sensors with a Suppressed Absorption–Desorption Effect by Using a 7.41 μm External-Cavity Quantum Cascade Laser”. In: *ACS Sensors* 5.2 (Jan. 2020), pp. 549–556. ISSN: 2379-3694. DOI: 10.1021/acssensors.9b02448 (cit. on p. 190).
- [10] M. Horstjann et al. “Formaldehyde sensor using interband cascade laser based quartz-enhanced photoacoustic spectroscopy”. In: *Applied Physics B: Lasers and Optics* 79.7 (2004), pp. 799–803. ISSN: 09462171. DOI: 10.1007/s00340-004-1659-3 (cit. on p. 190).

- [11] C. Li et al. "Ppbv-level ethane detection using quartz-enhanced photoacoustic spectroscopy with a continuous-wave, room temperature interband cascade laser". In: *Sensors (Switzerland)* 18.3 (2018). ISSN: 14248220. DOI: 10.3390/s18030723 (cit. on p. 190).
- [12] H. Wu et al. "Ppb-level nitric oxide photoacoustic sensor based on a mid-IR quantum cascade laser operating at 52 °C". In: *Sensors and Actuators, B: Chemical* 290.January (2019), pp. 426–433. ISSN: 09254005. DOI: 10.1016/j.snb.2019.04.007 (cit. on p. 190).
- [13] H. Wu et al. "Atmospheric CH₄ measurement near a landfill using an ICL-based QEPAS sensor with V-T relaxation self-calibration". In: *Sensors and Actuators B: Chemical* 297 (Oct. 2019), p. 126753. ISSN: 09254005. DOI: 10.1016/j.snb.2019.126753 (cit. on p. 190).
- [14] H. Wu et al. "Enhanced near-infrared QEPAS sensor for sub-ppm level H₂S detection by means of a fiber amplified 1582 nm DFB laser". In: *Sensors and Actuators, B: Chemical* 221 (2015), pp. 666–672. ISSN: 09254005. DOI: 10.1016/j.snb.2015.06.049 (cit. on p. 190).
- [15] H. Wu et al. "Quartz enhanced photoacoustic H₂S gas sensor based on a fiber-amplifier source and a custom tuning fork with large prong spacing". In: *Applied Physics Letters* 107.11 (2015), pp. 2–6. ISSN: 00036951. DOI: 10.1063/1.4930995 (cit. on p. 190).
- [16] J. Kalkman and H. van Kesteren. "Relaxation effects and high sensitivity photoacoustic detection of NO₂ with a blue laser diode". In: *Applied Physics B* 90.2 (Feb. 2008), pp. 197–200. ISSN: 0946-2171. DOI: 10.1007/s00340-007-2895-0 (cit. on p. 190).
- [17] H. Yi et al. "Application of a broadband blue laser diode to trace NO₂ detection using off-beam quartz-enhanced photoacoustic spectroscopy". In: *Optics Letters* 36.4 (Feb. 2011), p. 481. ISSN: 0146-9592. DOI: 10.1364/OL.36.000481 (cit. on p. 190).
- [18] X. Yin et al. "Sub-ppb nitrogen dioxide detection with a large linear dynamic range by use of a differential photoacoustic cell and a 3.5 W blue multimode diode laser". In: *Sensors and Actuators B: Chemical* 247 (Aug. 2017), pp. 329–335. ISSN: 09254005. DOI: 10.1016/j.snb.2017.03.058 (cit. on p. 191).
- [19] T. Rück et al. "Development and characterization of a laboratory setup for photoacoustic NO₂ determination based on the excitation of electronic 2B₂ and 2B₁ states using a low-cost semiconductor laser". In: *Sensors and Actuators, A: Physical* 258.2 (2017), pp. 193–200. ISSN: 09244247. DOI: 10.1016/j.sna.2017.03.024 (cit. on p. 191, 199, 200).
- [20] T. Rück et al. "NO₂ trace gas monitoring in air using off-beam quartz enhanced photoacoustic spectroscopy (QEPAS) and interference studies towards CO₂, H₂O and acoustic noise". In: *Sensors and Actuators, B: Chemical* 255.2 (2018), pp. 2462–2471. ISSN: 09254005. DOI: 10.1016/j.snb.2017.09.039 (cit. on p. 191).

- [21] T. Rück et al. “Low-cost photoacoustic NO₂ trace gas monitoring at the pptV-level”. In: *Sensors and Actuators A: Physical* 263.2 (2017), pp. 501–509. ISSN: 09244247. DOI: 10.1016/j.sna.2017.06.036 (cit. on pp. 191, 199, 200).
- [22] K. P. Koch and W. Lahmann. “Optoacoustic detection of sulphur dioxide below the parts per billion level”. In: *Applied Physics Letters* 32.5 (1978), pp. 289–291. ISSN: 00036951. DOI: 10.1063/1.90023 (cit. on p. 191).
- [23] M. Boutonnat et al. “Photoacoustic Detection of Formaldehyde as a Minority Component in Gas Mixtures”. In: *Applied Spectroscopy* 42.8 (1988), pp. 1520–1524 (cit. on p. 191).
- [24] X. Yin et al. “Highly sensitive SO₂ photoacoustic sensor for SF₆ decomposition detection using a compact mW-level diode-pumped solid-state laser emitting at 303 nm”. In: *Optics Express* 25.26 (Dec. 2017), p. 32581. ISSN: 1094-4087. DOI: 10.1364/OE.25.032581 (cit. on p. 191).
- [25] T. Oka et al. “Photoacoustic Study of 280 nm Band of Acetone Vapor”. In: *Bulletin of the Chemical Society of Japan* 61.1 (1988), p. 199. DOI: <https://doi.org/10.1246/bcsj.61.199> (cit. on pp. 191, 198, 205).
- [26] T. Preukschat et al. “Comparison of the Photoacoustic Effect in the IR and the UV Regions”. In: *International Journal of Thermophysics* 36.9 (2015), pp. 2318–2327. ISSN: 0195928X. DOI: 10.1007/s10765-015-1885-4 (cit. on pp. 191, 203, 206).
- [27] S. Böttger et al. “Off-beam quartz-enhanced photoacoustic spectroscopy with LEDs”. In: *Applied Physics B: Lasers and Optics* 113.2 (2013), pp. 227–232. ISSN: 09462171. DOI: 10.1007/s00340-013-5462-x (cit. on p. 191).
- [28] M. El-Safoury et al. “Photoacoustic gas detector for the monitoring of sulfur dioxide content in ship emissions”. In: *ITG-Fb. 281: Sensoren und Messsysteme*. 2018, pp. 450–452 (cit. on p. 191).
- [29] Z. Wang and C. Wang. “Is breath acetone a biomarker of diabetes? A historical review on breath acetone measurements”. In: *Journal of Breath Research* 7.3 (2013), p. 037109. ISSN: 17527155. DOI: 10.1088/1752-7155/7/3/037109 (cit. on p. 192).
- [30] K. Musa-Veloso et al. “Breath acetone predicts plasma ketone bodies in children with epilepsy on a ketogenic diet”. In: *Nutrition* 22.1 (2006), pp. 1–8. ISSN: 08999007. DOI: 10.1016/j.nut.2005.04.008 (cit. on p. 192).
- [31] K. Musa-Veloso et al. “Breath acetone is a reliable indicator of ketosis in adults consuming ketogenic meals”. In: *The American Journal of Clinical Nutrition* 76.1 (July 2002), pp. 65–70. ISSN: 0002-9165. DOI: 10.1093/ajcn/76.1.65 (cit. on p. 192).
- [32] F. G. Marcondes-Braga et al. “Impact of Exhaled Breath Acetone in the Prognosis of Patients with Heart Failure with Reduced Ejection Fraction (HFrEF). One Year of Clinical Follow-up”. In: *Plos One* 11.12 (2016), e0168790. ISSN: 1932-6203. DOI: 10.1371/journal.pone.0168790 (cit. on p. 192).

- [33] D. J. Jacob et al. "Atmospheric budget of acetone". In: *Journal of Geophysical Research: Atmospheres* 107.D10 (May 2002), ACH 5–1–ACH 5–17. ISSN: 01480227. DOI: 10.1029/2001JD000694 (cit. on p. 192).
- [34] Toxico-Logic Consulting Inc. *Assessment report on acetone for developing ambient air quality objectives*. Tech. rep. Edmonton, 2004 (cit. on p. 192).
- [35] Y. Cai et al. "Buffer structure optimization of the photoacoustic cell for trace gas detection". In: *Optoelectronics Letters* 9.3 (May 2013), pp. 233–237. ISSN: 1673-1905. DOI: 10.1007/s11801-013-3017-3 (cit. on p. 193).
- [36] P. Claspy et al. *Optoacoustic spectroscopy and detection*. Academic Press, 1977. ISBN: 0-12-544150-9 (cit. on p. 194).
- [37] A. Rosencwaig. *Photoacoustics and Photoacoustic Spectroscopy*. John Wiley & Sons, 1980, pp. 17–30. ISBN: 0471044954 (cit. on p. 194).
- [38] T. Rück. "Development, characterization and miniaturization of a trace gas detection system for NO₂ in air based on photoacoustic spectroscopy". Ph. D. thesis. University of Regensburg, 2017 (cit. on p. 194).
- [39] A. Miklós et al. "Application of acoustic resonators in photoacoustic trace gas analysis and metrology". In: *Review of Scientific Instruments* 72.4 (2001), pp. 1937–1955. ISSN: 00346748. DOI: 10.1063/1.1353198 (cit. on p. 194).
- [40] M. N. Polyanskiy. *Refractive index database*. URL: <https://refractiveindex.info> (visited on 11/25/2019) (cit. on p. 196).
- [41] N. Turro et al. *Principles of Molecular Photochemistry: An Introduction*. University Science Books, 2009. ISBN: 9781891389573 (cit. on p. 198).
- [42] H. Haken and H. C. Wolf. *Atom- und Quantenphysik*. Springer-Lehrbuch. Berlin, Heidelberg: Springer Berlin Heidelberg, 2004. ISBN: 978-3-642-62142-0. DOI: 10.1007/978-3-642-18519-9 (cit. on p. 198).
- [43] M. Szakáll et al. "On the temperature dependent characteristics of a photoacoustic water vapor detector for airborne application". In: *Infrared Physics and Technology* 51.2 (2007), pp. 113–121. ISSN: 13504495. DOI: 10.1016/j.infrared.2007.04.001 (cit. on p. 201).
- [44] L. A. Ishaku et al. "Temperature effects on photoacoustic carbon dioxide sensor developed using mid-IR LED". In: *I2MTC 2018 - 2018 IEEE International Instrumentation and Measurement Technology Conference: Discovering New Horizons in Instrumentation and Measurement, Proceedings* (2018), pp. 1–6. DOI: 10.1109/I2MTC.2018.8409855 (cit. on p. 201).
- [45] M. A. Blitz et al. "Pressure and temperature-dependent quantum yields for the photodissociation of acetone between 279 and 327.5 nm". In: *Geophysical Research Letters* 31.6 (Mar. 2004), n/a–n/a. ISSN: 00948276. DOI: 10.1029/2003GL018793 (cit. on p. 204).
- [46] J. Burkholder et al. "Tables of rate constants extracted from chemical kinetics and photochemical data for use in stratospheric modeling. Evaluation number 18". In: *International Journal of Chemical Kinetics* (Oct. 2015). ISSN: 0538-8066. DOI: 10.13140/RG.2.1.2504.2806 (cit. on p. 204).

- [47] C. Wang and A. Mbi. “A new acetone detection device using cavity ringdown spectroscopy at 266 nm: Evaluation of the instrument performance using acetone sample solutions”. In: *Measurement Science and Technology* 18.8 (2007), pp. 2731–2741. ISSN: 13616501. DOI: 10.1088/0957-0233/18/8/051 (cit. on p. 206).
- [48] H. G. Moon et al. “Hollow Pt-Functionalized SnO₂ Hemipill Network Formation Using a Bacterial Skeleton for the Noninvasive Diagnosis of Diabetes”. In: *ACS Sensors* 3.3 (2018), pp. 661–669. ISSN: 23793694. DOI: 10.1021/acssensors.7b00955 (cit. on p. 206).
- [49] X. Guan et al. “Incorporating N atoms into SnO₂ nanostructure as an approach to enhance gas sensing property for acetone”. In: *Nanomaterials* 9.3 (2019), pp. 1–18. ISSN: 20794991. DOI: 10.3390/nano9030445 (cit. on p. 206).
- [50] F. Liu et al. “Highly sensitive gas sensor based on stabilized zirconia and Cd-MoO₄ sensing electrode for detection of acetone”. In: *Sensors and Actuators B: Chemical* 248 (Sept. 2017), pp. 9–18. ISSN: 09254005. DOI: 10.1016/j.snb.2017.03.133 (cit. on p. 206).
- [51] C. Liu et al. “Facile synthesis and the enhanced sensing properties of Pt-loaded α -Fe₂O₃ porous nanospheres”. In: *Sensors and Actuators B: Chemical* 252 (Nov. 2017), pp. 1153–1162. ISSN: 09254005. DOI: 10.1016/j.snb.2017.06.012 (cit. on p. 206).
- [52] D. Zhang et al. “Metal-organic frameworks-derived zinc oxide nanopolyhedra/S, N: graphene quantum dots/polyaniline ternary nanohybrid for high-performance acetone sensing”. In: *Sensors and Actuators, B: Chemical* 288.Feb. (2019), pp. 232–242. ISSN: 09254005. DOI: 10.1016/j.snb.2019.02.093 (cit. on p. 206).
- [53] M. Y. Chuang et al. “Room-temperature-operated organic-based acetone gas sensor for breath analysis”. In: *Sensors and Actuators, B: Chemical* 260 (2018), pp. 593–600. ISSN: 09254005. DOI: 10.1016/j.snb.2017.12.168 (cit. on pp. 206, 207).
- [54] M. Masikini et al. “Review—Metal Oxides: Application in Exhaled Breath Acetone Chemiresistive Sensors”. In: *Journal of The Electrochemical Society* 167.3 (2020), p. 037537. ISSN: 1945-7111. DOI: 10.1149/1945-7111/ab64bc (cit. on pp. 206, 207).

5.2 Effects of ambient parameters and cross-sensitivities from O₂, CO₂ and H₂O on the photoacoustic detection of acetone in the UV region

5.2.1 Introduction

In the past, photoacoustic spectroscopy has proven to be a highly sensitive detection method for gas analysis. In example, Weigl et al. [1] demonstrated that their photoacoustic sensor, employing a 3D printed photoacoustic cell and a UV LED, has a high sensitivity regarding acetone detection. However, the sensor performance was studied using acetone being diluted in pure N₂ or in synthetic air. For applications in complex gas mixtures like human breath exhale, selectivity and cross-sensitivities play a very important role.

Spectroscopic approaches in general, including PAS, claim high selectivity in terms of spectral distinctiveness. However, there are some publications studying the effects of different buffer gases or components with high abundance in the measured gas matrix on the analytes relaxation times. A complete relaxation with conversion of the absorbed photon energy into heat during the off-period of the light source's duty cycle, is mandatory for a high photoacoustic signal. In general, the stored energy of an excited analyte molecule is transferred into heat by collision induced VT relaxation. This relaxation process can be preceded by a collision induced VV transfer process, too. A VV energy transfer process causes the initially absorbed photon energy to be transferred onto the collision partner, whose vibrational and rotational energy level is promoted. If the relaxation of a thus excited buffer gas molecule takes longer than the off-period of the light source's duty cycle, less heat is released contributing to the generation of a pressure fluctuation, causing the photoacoustic amplitude to diminish. However, it is also possible, that the excited buffer gas molecule shows faster relaxation than the analyte molecule. This means, if not all excited analyte molecules relax in time, the opposite effect of a higher photoacoustic signal can be observed due to VV energy transfer, too. Kalkmann and Kesteren [2] and later Rück et al. [3] observed that using a blue laser for NO₂ detection, the photoacoustic signal significantly decreased when the buffer gas contained oxygen instead of pure nitrogen only. The drop was attributed to delayed relaxation of the excited O₂ molecules. The excitation of higher internal energy levels of the O₂ molecules originated from VV energy transfer of excited NO₂ with O₂. However, Oka et al. [4] demonstrated, that adding O₂ to a mixture of acetone diluted in argon accelerated heat release after excitation and hence, caused the photoacoustic signal to increase. Besides, in photoacoustic spectroscopy H₂O is a well-known promoter in terms of faster relaxation times [5]. Examples are the enhanced relaxation times for CO diluted in N₂ [6] and for methane diluted in N₂ [7], due to the addition of water vapour. Rück et al. [8] demonstrated that for NO₂ diluted in N₂, adding H₂O does not result in an increase of the PA signal since the relaxation is already fast enough, but adding 4%V of CO₂ caused a signal attenuation, which was at-

tributed to acoustic attenuation. These examples demonstrate the importance of detailed investigations regarding the influence of high abundant gas components on the photoacoustic amplitude.

Due to that, investigations regarding cross-sensitivities in terms of spectral interference and effects on the relaxation time induced by different O_2 , CO_2 and H_2O concentrations are covered within this paper. Moreover, the impact of various parameters like temperature, pressure or flow on the photoacoustic signal were studied. Since the duty cycle of the applied LED varies depending on the applied resonance frequency, the parameters optical power, frequency and duty cycle and their effects on the photoacoustic signal are discussed, too. Furthermore, all measurements were considered to create a dataset, which was analysed using different data scientific methods to gain additional insights into the correlations between parameters and their contribution to the acquired photoacoustic signal.

Finally, low concentrations of acetone between 100 ppbV and 1 ppmV were diluted in mixtures similar to human breath exhale and the sensor's behaviour under typical conditions was investigated.

Summarizing, this work is intended to gain a better understanding of how the sensor performs under various conditions as they can occur in human breath analysis.

5.2.2 Experimental

The experimental setup used within this thesis has been described elaborately in section 4.1, hence only the employed gases and the creation of the dataset will be described within this subsection. All test gases were provided by Westfalen AG (Münster, Germany). Their purity is specified by nitrogen (6.0) and synthetic air with less than 0.1 ppmV of carbohydrates, respectively.

The test gases containing acetone or CO_2 are summarised in table 5.4. In terms of humidification, N_2 or synthetic air passed the humidifier prior to analyte dilution. The gas stream system was flushed before setting an analyte concentration in order to fasten the settling time.

All measurements that were performed between 27th of November 2019 and 27th of April 2020 were used for data scientific analysis. Those 219 measurements include mostly frequency sweeps and single point measurements. Each of the 4280 data points contains 40 different features, e.g. ambient gas concentration, mass flow, temperature, pressure and humidity of the test gas, respectively, the duty cycle and the optical power of the emitter, as well as standard deviations of 100 readings of some measured quantities, e.g. the PA signal. The dataset is cleaned by discarding implausible or missing values and uninformative features. The resulting dataset (short: SPM) serves as the basis for the resonance dataset (short: RES). Reducing this dataset to those modulation frequencies of maximum resonance amplification

Tab. 5.4. All gas mixtures used during the experiments excluding pure N₂ and pure synthetic air. Westfalen provided the analyte concentrations and accuracies.

Analyte gas	Buffer gas	Concentration of analyte in ppmV	Specified accuracy in %
Acetone	N ₂	102	±5
Acetone	Synthetic air	101	±5
Acetone	Synthetic air	9.8	±5
Acetone	Synthetic air	1.2	±10
CO ₂	Synthetic air	200 000	±2

yielded 297 data points only. Additional information on the variables in the dataset and their distribution can be found in the appendix B.

5.2.3 Measurement settings

Within this work, we investigated the performance of the UV LED photoacoustic setup at low acetone concentrations. Besides, the effects of parameters like temperature, pressure, flow, optical power and duty cycle on the photoacoustic signal are discussed. Furthermore, the influences of different O₂, CO₂ and H₂O concentrations were studied. Moreover, the sensor's performance regarding the detection of small acetone concentrations in typical breath exhale gas matrixes were investigated. Finally, different concepts of data science applied on the results of the measurements are presented, demonstrating its benefit in modern trace gas spectroscopy.

If not mentioned otherwise, the PAC* is temperature-controlled at 45 °C and the mass flow is set to 500 mL/min. The time constant and the roll-off of the lock-in amplifier were set to $\tau_{LIA} = 2$ s and 12 dB/octave, respectively. Each measurement point is averaged over 100 raw data readings with a sampling rate of 5 Hz. Error bars in figures always represent six times the standard deviation ($\pm 3\sigma$) of the acquired measurement point.

5.2.4 Calibration curves at small acetone concentrations

Since the PAC is designed to allow resonance enhanced PAS, the mathematical representation of a first longitudinal mode[†] of the acoustic resonator can be applied. Hence, the photoacoustic signal can be written as [9–12][‡]

$$p_a(\vec{r}, t) = (\gamma - 1)\rho\sigma_A(\tilde{\nu})P_0\frac{Q}{\omega}I_1p_1(\vec{r})\frac{L_{\text{res}}}{V_{\text{res}}} \quad (5.9)$$

*The PAC referred to within this section always refers to PAC1.

[†]Note that the index 1 in equation 5.9 represents the first longitudinal mode.

[‡]A detailed derivation of this equation is provided in section 2.4.1.

Tab. 5.5. Summary of the different calibration measurement series. Bottle 1 contains 1.2 ppmV of acetone in synthetic air, bottle 2 contains 9.8 ppmV and bottle 3 contains 101 ppmV acetone.

	Bottle 1	Bottle 2	Bottle 3
Slope in $\mu\text{V}/\text{ppmV}$	2.62	2.82	2.67
R^2	0.9997	0.9999	0.9999

where ρ is the analyte particle density, $\sigma_A(\tilde{\nu})$ is the absorption cross section at the wavenumber $\tilde{\nu}$ and P_0 is the optical power of the light source. γ represent the heat capacity ratio, i.e. the ratio of specific isobar and isochore heat capacities. Q is the quality factor of the acoustic resonator, ω the angular modulation frequency of the light, I_1 is the normalised overlap integral describing the normalised efficiency of energy transfer from light to heat, the distribution function of the resonant acoustic oscillation is $p_1(\vec{r})$, L_{res} is the length and V_{res} the volume of the acoustic resonator.

Equation 5.9 demonstrates the photoacoustic signal to be directly proportional to the analyte concentration. Three calibration measurements were performed using different gas bottles. In view of photoacoustic background signal measurements, τ_{LIA} was set to 10 s. Note that the concentration ranges from 0.1 to 1.1 ppmV, 0.8 – 9.8 ppmV and 8.0 – 101 ppmV of acetone in synthetic air were covered with the different pre-diluted gas mixtures of bottle 1, bottle 2 and bottle 3, respectively. The results have been summarised in table 5.5. While the coefficients of determination verify the linear dependency of PA signal and analyte concentration, the small differences in the slopes are likely due to errors of the calibration gas specification. With a noise level of $0.030 \mu\text{V}$ (3σ), which is the average of three measurement points acquired when only 500 mL/min of synthetic air was flowing through the PAC, and using the slope measured with bottle 1 $m_1 = 2.62 \mu\text{V ppmV}^{-1}$, the limit of detection was calculated to 11.4 ppbV. This LOD confirms our results from [1]. The lower noise level compared to [1] is likely due to the higher roll-off of the lock-in amplifier.

5.2.5 Influence of environmental parameters

By integrating a TpH sensor (BME280) into the measurement cell, the effects of different environmental parameters, i.e. temperature and pressure could be investigated. Besides, the flow rate has been varied to study its influence especially on the noise and the background signal, respectively. Moreover, the effect of the optical power on the background signal as well as the PA signal's dependency on the duty cycle have been investigated.

5.2.5.1 Influence of temperature

The temperature is known to be a parameter effecting many physical quantities. As described in [1], the PAC is temperature-controlled by a peltier element, while an NTC temperature sensor is used as feedback. A spiral gas stream was 3D printed into the PAC in order to ensure reproducible pre-heating of the gas sample in terms of varying mass flow. While the temperature of the cell was changed from 25 °C to 50 °C in 5 °C steps, the NTC and BME280 values showed a constant offset of 0.7 °C. In [1], we already identified the frequency to blue-shift by 7.8 Hz per °C. In addition to this frequency shift, sweeps with 10 ppmV of acetone diluted in synthetic air at the different temperatures indicated a signal loss, which can be considered linear ($R^2 = 0.95$) within this temperature range. The results are displayed in figure 5.8. Besides frequency blue-shift and signal deterioration, the heating of the cell causes the Q factor to decrease as well. While the drop in sensitivity was calculated to 0.8 $\mu\text{V}/^\circ\text{C}$, which corresponds to a relative signal loss of 0.7 % per degree Celsius, the Q-factor deteriorated by 4.9 % over 25 °C. The influence of the temperature on the background signal was studied, too. In absence of analyte molecules, this temperature induced signal drop was identified to 0.45 $\mu\text{V}/^\circ\text{C}$ in absolute and 0.5 %/ $^\circ\text{C}$ in relative terms, respectively.

The results demonstrate, that temperature changes affect those measurements containing analyte stronger than the background signal. The drop is mainly attributed

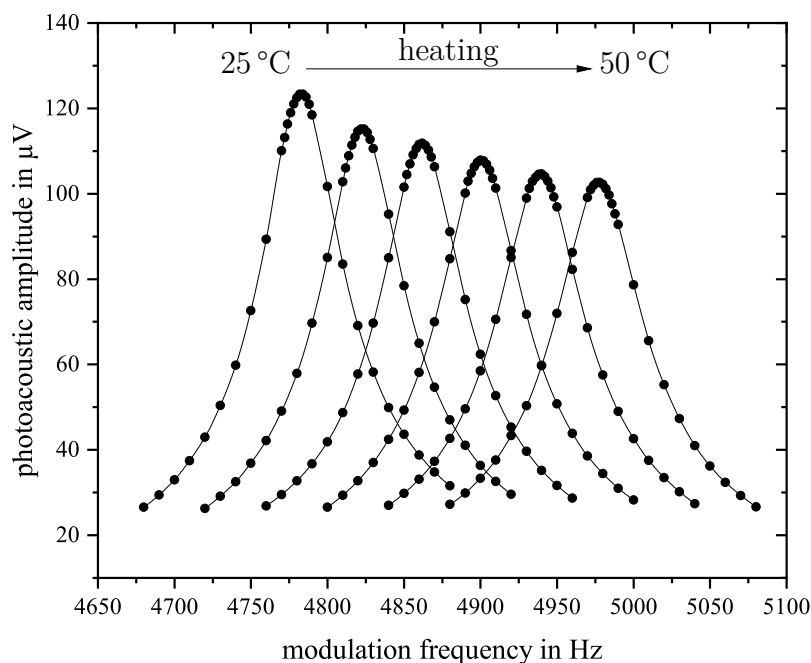


Fig. 5.8. Frequency sweeps at different temperatures. From left to right starting with 25 °C and ending with 50 °C in 5 °C steps. The gas mixture contained 10 ppmV acetone diluted in synthetic air. An Akima spline was used to connect the data points.

to (i) frequency shift towards higher frequencies $p_a(\vec{r}, t) \propto \frac{1}{\omega}$, (ii) the decrease of the Q-factor and (iii) the loss in microphone sensitivity. The dependencies (ii) and (iii) have been identified in other studies before [13, 14]. Two opposing effects are a slightly increasing absorption coefficient of acetone with higher temperatures [15] and an increasing normalised microphone amplitude at higher frequencies [16].

Finally, the noise level was identified to not depend on the temperature.

5.2.5.2 Influence of pressure

To evaluate the photoacoustic signal's dependency on the pressure of the gas sample, a vacuum pump and a pre-pressure controller were integrated into the test bench. The PPC can be set to any value between 1200 mbar and 200 mbar. Since the functioning of the test bench requires a pressure gradient from the bottles towards the exhaust, the TpH sensor usually indicated an absolute pressure of around 1030 mbar at 500 mL/min flow rate, which was always above the ambient pressure. The results are interesting and quite the same for different mixtures including pure synthetic air, pure N₂ or a mixture of 50 ppmV acetone diluted in a mixture of 16 %V O₂ and 84 %V N₂. As illustrated in figure 5.9(a) the resonance curves flatten with decreasing pressure, indicating a significant decline of the Q-factor of the cell. The signal drops linearly in the higher pressure region between 1034 mbar and 746 mbar. For pure synthetic air the drop is 0.06 μ V/mbar, which is 0.09 %/mbar relatively spoken. Towards low pressures, the drop seems to get a little bit steeper deviating from a clear linear decrease. Extrapolating the graph using an exponential fitting model $y = y_0 + A \cdot \exp(R_0 p)$ and setting the pressure $p = 0$ gives an intersection of the extrapolated graph close to 1.8 μ V giving rise to the assumption, that the background signal is almost completely dependent on the gas pressure. We assume that most of the background signal originates from the interaction of light with the windows of the measurement cell and the interaction with the walls of the acoustic resonator. For the wave to be transmitted towards the acoustic detector molecules are necessary. The sound intensity is given by

$$I_s(\vec{r}, t) = v_p(\vec{r}, t)p_a(\vec{r}, t) = \zeta_p^2(\vec{r}, t)\omega_s^2 c_s \tilde{\rho} \quad (5.10)$$

with $\zeta_p^2(\vec{r}, t)$ being the particle displacement, c_s the speed of sound and $\tilde{\rho}_e$ is the particle density. Hence, the intensity of the sound wave decreases linearly with the particle density, which is linearly related to the pressure.

In contrast, for the measurement with 50 ppmV of acetone present in the mixture the amplitude drop is 0.16 μ V/mbar (= 0.16 %/mbar) demonstrating that the effect of the pressure on the photoacoustic signal is stronger in terms of higher acetone concentration. Obviously, reducing the pressure within an analyte containing gas sample not only attenuates the propagation of sound, but also decreases the absolute number of analyte molecules contributing to photoacoustic signal generation.

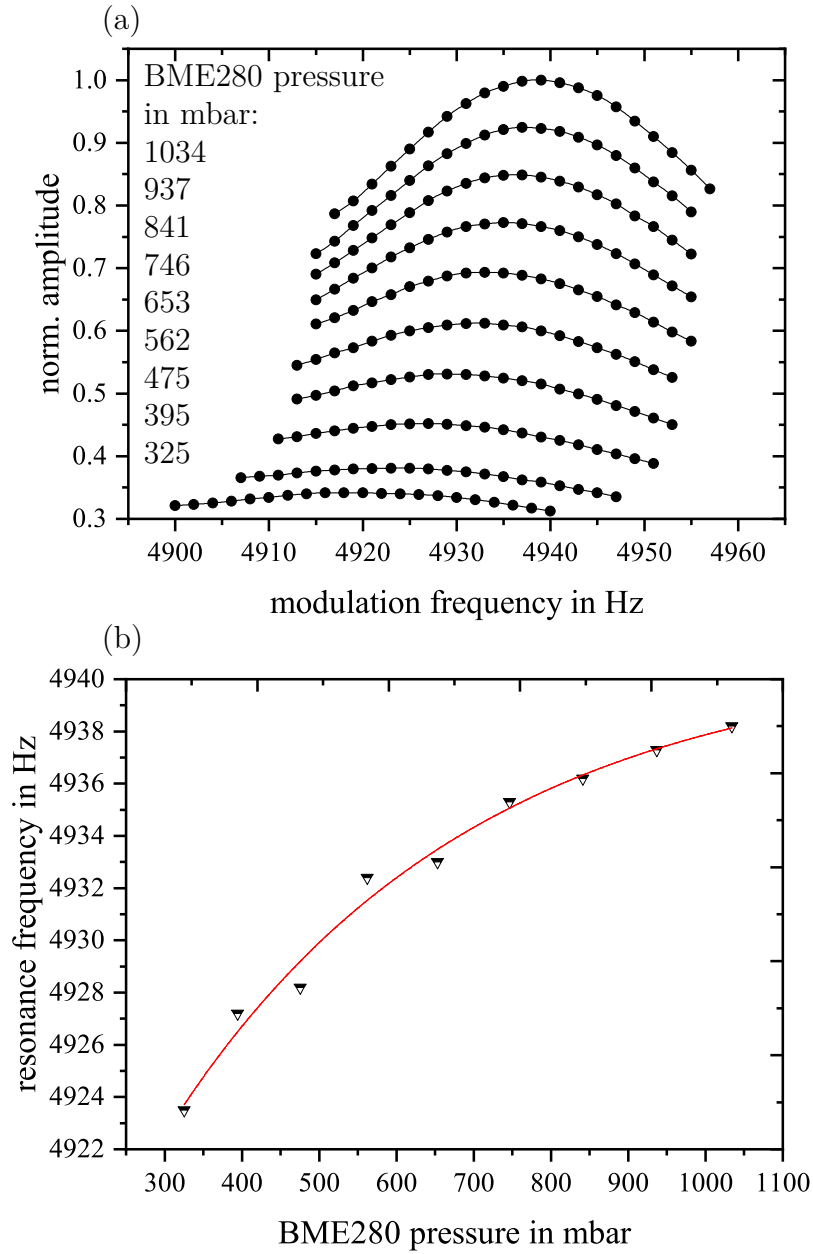


Fig. 5.9. (a) Frequency sweeps with pure synthetic air at different pressures. Points are connected using an Akima spline. (b) Shift of the resonance frequency due to pressure variations.

In figure 5.9(b) the frequency shift induced by pressure variations is presented. This behaviour seems surprising at first, since the resonance frequency is given by

$$f_{\text{res}} = \frac{c_s}{2L_{\text{eff}}} \quad (5.11)$$

where L_{eff} is the effective length of the acoustic resonator of the PAC and the speed of sound c_s is not altering as long as the gas can be considered an ideal gas.

$$c_s = \sqrt{\frac{\gamma RT}{M}} \quad (5.12)$$

In figure 5.9(a) it can be seen, that the acoustic resonator loses its amplifying property since the Q-factor decreases rapidly. We assume that reducing the pressure of the gas sample, causes a resonance frequency shift due to the node shifting of the acoustic wave into the buffer volumes at lower pressures. Besides, the PA signal decrease by Q-factor deterioration may result from the lower number of molecules present in the PAC. Since future applications are rather accompanied by overpressure, further detailed investigations of this effect were dispensed.

5.2.5.3 Influence of flow

During this work, we used 500 mL/min as flow rate to be able to create complex gas mixtures. Note, that all the measurements were performed with 10 s of LIA integration time.

Using pure synthetic air and a solution of 50 ppmV of acetone diluted in synthetic air the flow rate was varied from 100 to 500 mL/min in 100 mL/min steps in order to investigate the mass flow dependency on the PA signal. The results demonstrated a linear increase of the photoacoustic signal for both mixtures. According to the T_pH sensor, increasing the flow caused a linear pressure rise, too, which is approximately 12.7 mbar per 100 mL/min. The relative increase of the signal is 0.7 % per 100 mL/min in terms of pure synthetic air and 1 % per 100 mL/min for a 50 ppmV acetone mixture in synthetic air, respectively. The increase of the photoacoustic signal is entirely attributed to the rise in pressure with a higher mass flow rate. The noise showed no significant correlation towards the flow rate in this setup.

To further investigate the influence of the flow onto the background signal and noise, the LED was switched off and the PA signal was monitored. As expected, the background signal dropped below 1 μ V and showed no variation with varying flow rates. Again, flow rate and noise showed no significant correlation. The results demonstrate that the background signal solely depends on the optical power. This confirms our assumption from section 5.2.5.2, that the background signal is generated by the interaction of modulated light with parts of the PAC.

5.2.5.4 Influence of optical power and duty cycle

The photoacoustic signal itself linearly depends on the intensity of the light source, which is valid for the background signal, too. By varying the LED current and hence the optical output power of the LED, the noise level remains constant though. For all measurements with a duty cycle of approximately 50 %, the monitored optical power of the LED after passing the PAC was about 14.8 mW, which equals an average intensity of about 131 W m⁻² since the powermeter's sensor area is 0.000113 m².

Depending on the used modulation frequency, the duty cycle of the light source slightly varies in the 5 kHz region. This is due to the fact, that the LED driver can be triggered by a rising edge and the pulse length is set within a resolution of 1 μ s.

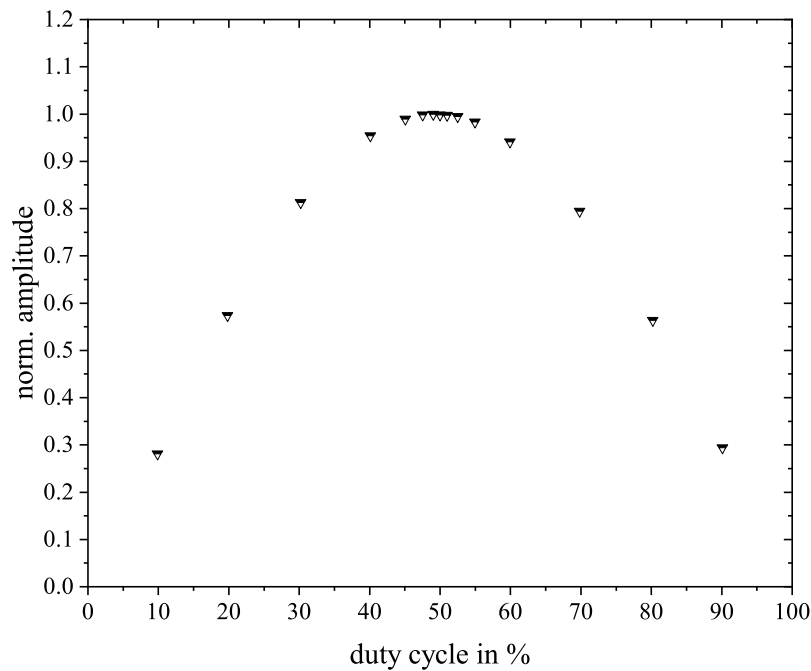


Fig. 5.10. Different duty cycles applied to the UV LED. The gas mixture was 30 ppmV of acetone diluted in buffer gas consisting of 16 %V O₂ and 84 %V N₂. The amplitude was normalised to 1.

To study the influence of the duty cycle on the photoacoustic signal, different duty cycles were set between 10 % to 90 %. The measurements were performed for pure N₂, pure synthetic air, 30 ppmV acetone diluted in N₂ and 30 ppmV diluted in a mixture consisting of different oxygen and nitrogen mixtures, respectively. All of these measurements show the same result. Figure 5.10 demonstrates a Gaussian shaped graph, with a maximum close to 49 % duty cycle. The maximum photoacoustic amplitude is expected at 50 % duty cycle. For other duty cycles, the spectral composition of the acquired acoustic signal deviates and other frequencies, mainly harmonics of the modulation frequency, are amplified, while the signal at the modulation frequency attenuates. In our setup, the maximum is at 49 %, because the LED driver generates imperfect square waves with a finite slew rate of the current at the edges of the square wave. Since the powermeter applied in the measurements to monitor the optical power of the LED is slow, only the average power is detected. This means, that the measured signal of the powermeter increases with the duty cycle, but for the photoacoustic signal only the intensity of the light during the on-phase is of interest. Due to that, it is not possible to simply normalise the acquired signal to the optical power measured with the powermeter, but the duty cycle must be considered, too. Since LEDs or other light sources degrade over time, which causes a decrease in output power and intensity, self-calibration should be performed on a regular basis. Setting a 100 % (cw-mode) duty cycle and a default LED current, optical power degradation over time can be tracked easily, e.g. by means of a photodiode. However, self-calibration is only applicable for the LED's optical power and care should be taken to use a stable photodiode as the monitor-

ing system can degrade over time as well. Wavelength shifts of the emitted LED spectrum might occur over time as well. This would have an influence on the ACS and the photodissociation rate of acetone, hence, regular recalibration of the system will be necessary. For example, the ACS of acetone at 285 nm is deteriorated by approximately 10 % compared to the ACS at 278 nm, which would cause a 10 % drop in the photoacoustic signal. Moreover, further studies would be necessary, to evaluate the influence of a changing photodissociation rate in detail. Besides, long-term investigations regarding additional LED aging processes in general are of interest, too, and thus are subject to further research.

To significantly simplify matters, a driver with a constant duty cycle of 50 % at all frequencies should be applied in a later application.

5.2.6 Cross-sensitivities towards O₂, CO₂ and H₂O

In this section, we describe the influence of different concentrations of high abundant human breath exhale components like oxygen, carbon dioxide and water. The test bench was modified to allow measurements with typical concentrations of these interferences, as they are present in human breath exhale. The peak wavelength of the UV LED is around 278 nm and thus coincides with the absorption band peak of the carbonyl group's $n_S \rightarrow \pi_S^*$ energy transition. A visualisation of the different absorption

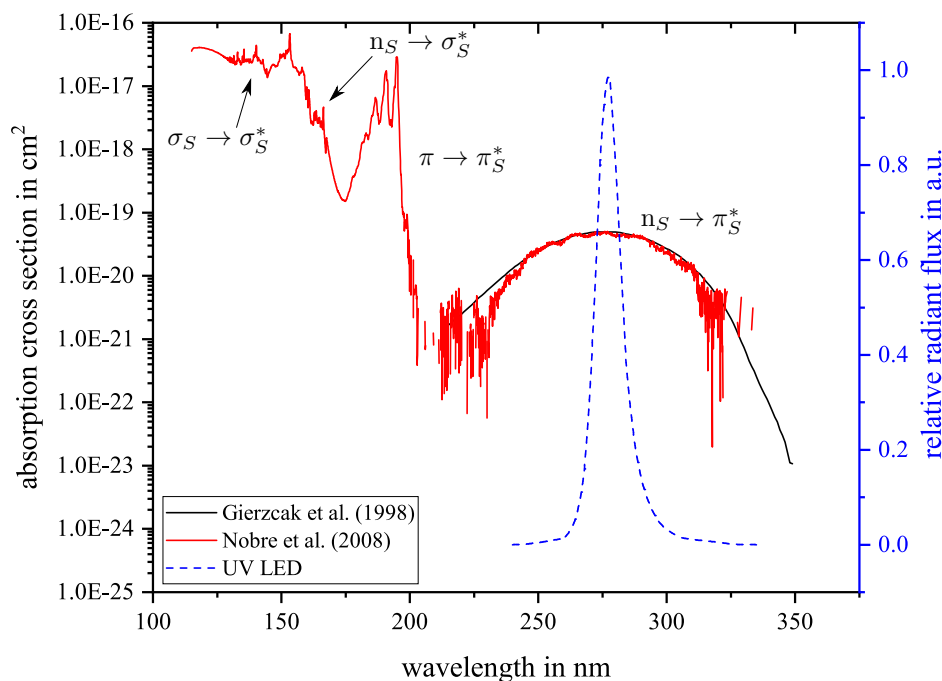


Fig. 5.11. UV absorption cross section by Gierczak et al. [17] (black) and Nobre et al. [18] (red) of acetone and the corresponding electronic energy transitions [19, p. 13]. The blue dotted line is the emission spectrum of the UV LED provided by the manufacturer.

bands of acetone in the UV region and the associated electronic energy transitions are illustrated in figure 5.11*. Since none of the high abundant interferents has such a carbonyl group[†], low spectral interferences are expected. Nevertheless, a literature research regarding the spectral interference of the gas species was performed consulting the UV/VIS spectral atlas of the MPI Mainz [20]. For O₂ Bogumil et al. [21] measured an ACS of below $1.0 \times 10^{-24} \text{ cm}^2$ from 260 to 300 nm though Fally et al. [22] measured only around $1.0 \times 10^{-26} \text{ cm}^2$. The absorption cross section of CO₂ was measured by Shemansky (1972) [23] and the intensity of the cross section was found to be below $2.0 \times 10^{-25} \text{ cm}^2$ between 250 nm and 300 nm. The results have been verified by Ityaksov et al. [24] in 2008. However, Ityaksov assigned the measured absorption in the region from approximately 200 nm onwards to higher wavelengths almost completely to Rayleigh scattering. For H₂O not much data is present for the wavelength region of interest. Nevertheless, Du et al. [25] measured a fine structure with peaks at 330 nm and 315 nm and a rising absorption coefficient at 290 nm, all in the range of $2.0 \times 10^{-24} \text{ cm}^2$ to $3.0 \times 10^{-24} \text{ cm}^2$. However, Wilson et al. [26] contradicts these values publishing a curve with another profile and absorption cross sections more than an order of magnitude lower. Furthermore, Lampel et al. [27] used calculated data simulating absorption cross sections in the order of $1.0 \times 10^{-27} \text{ cm}^2$ per molecule between 330 nm and 370 nm. Due to the lack of reliable data, no statement regarding the absorption coefficient of water in the region between 270 – 280 nm is possible.

5.2.6.1 Oxygen

In [1] we demonstrated that the photoacoustic signal was promoted when synthetic air was employed as a buffer gas for acetone measurements instead of pure nitrogen. Therefore, we started a measurement with 30 ppmV of acetone diluted in N₂ and gradually added oxygen. Already at 1 %V oxygen, the signal reached the same level as with 30 ppmV diluted in synthetic air. As discussed by Oka et al. [4] oxygen is a strong promoter regarding the relaxation of excited acetone. O₂ increases both, the heat producing nonradiative relaxation rate of acetone and the recombination rate of fragments originating from acetone photodissociation within the UV region, which also contributes to the photoacoustic signal. We assume that since only small concentrations of acetone are present, 1 %V of O₂ is sufficient to promote the heat release of all excited acetone molecules.

However, with oxygen, the molar mass of the gas and hence, the speed of sound and the resonance frequency changes, too. The shift was investigated by means of a series of frequency sweep measurements and calculated to 3.44 Hz/%V-O₂, which

*For more details on the transitions refer to figure 2.12.

[†]CO₂ actually has two carbonyl groups but does not show a transition around 278 nm.

is 0.07 %/%V-O₂ in relative terms. The speed of sound is calculated by means of equation 5.12, though care was taken at the correct derivation of γ .

$$c_s = \sqrt{RT \frac{\sum_i N_i \gamma_i}{\sum_i N_i M_i}} \quad (5.13)$$

Therein i represents each gas species present in the mixture, although only the high abundant molecules change the speed of sound significantly and N_i is the molecular volume ratio of each component. Since γ is the ratio of $\frac{C_p}{C_v}$ and C_v can be replaced by $C_p - R$ only C_p must be considered. Since γ depends on the temperature itself, an approximation provided by “Extended Third Millennium Thermodynamic Database for Combustion and Air-Pollution Use with updates from Active Thermochemical Tables” [28] was used for calculations. The general approximation is given by

$$C_p = R(y_1 + y_2 T + y_3 T^2 + y_4 T^3 + y_5 T^4) \quad (5.14)$$

with y_1 to y_5 being the first five fixed polynomials unique for each gas species from the thermodynamic database. Applying equation 5.13 it was verified, that the measured shift equals the theoretical shift.

With the changing resonance frequency, the LED duty cycle varies, too, since with a finite resolution of the pulse length being 1 μ s not every frequency can be represented with a 50 % duty cycle. Hence, slight fluctuations of the photoacoustic signal occur with different oxygen concentrations. Within the interesting range from 14.5 %V to 19.7 %V of oxygen, the variation of the signal is less than 1 %. Thus in a later application a light source driver with a constant duty cycle will be employed to avoid the duty cycle induced signal fluctuations.

5.2.6.2 Carbon dioxide

In the human body carbon dioxide is produced by metabolic processes that consume O₂. Thus, if 20 %V of oxygen are inhaled and 4 %V of carbon dioxide are exhaled, then only 16 %V of oxygen will be exhaled, too. Inhaled CO₂ can be neglected. This means, if the CO₂ level is monitored, valuable feedback regarding the metabolism rate and breath composition can be provided. Besides, carbon dioxide is known for its signal diminishing property in PAS. Since CO₂ can have a concentration of up to 5 %V in breath, its influence on the photoacoustic signal was studied [29]. In a measurement series, the CO₂ level was increased in 1 %V steps starting from zero CO₂ and ending at 8 %V of CO₂. Since CO₂ exhibits a strong influence on the speed of sound, each measurement point was acquired performing a frequency sweep measurement. The CO₂, which itself was diluted in synthetic air, was added to a mixture of 30 ppmV of acetone diluted in synthetic air and to pure synthetic air, respectively. Figure 5.12 indicates a strong decrease of the photoacoustic signal with rising CO₂ concentration. The slope is 3.9 μ V/%V-CO₂, which is 2.7 %/%V-CO₂ in relative terms. The same effect occurs in terms of pure synthetic air, but

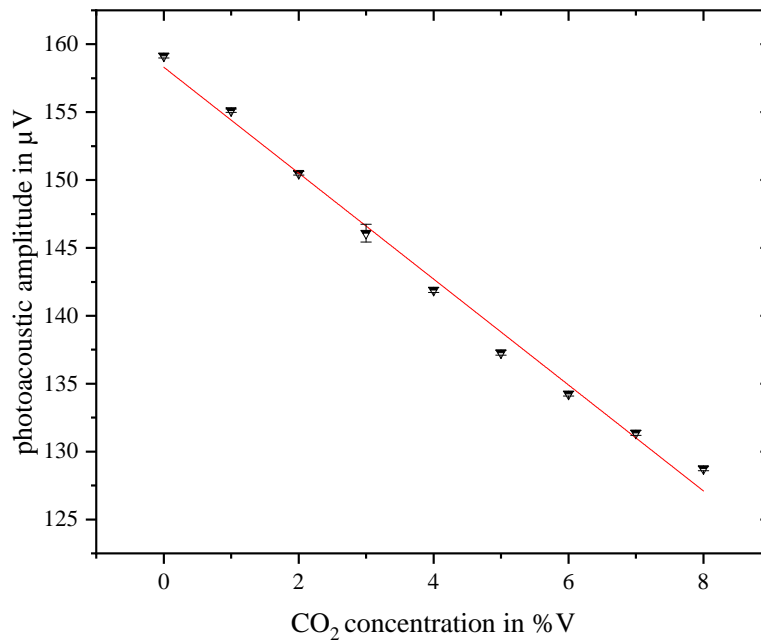


Fig. 5.12. Influence of CO₂ added to 30 ppmV of acetone diluted in synthetic air. Error bars indicate $\pm 3\sigma$ of the standard deviation of the measurement points.

with a linear slope of $2.0 \mu\text{V}/\%V\text{-CO}_2$, which is $2.9 \%/ \%V\text{-CO}_2$. The result indicates that CO₂ does not affect the relaxation rate of acetone. No changes in view of the photoacoustic phase reinforce this assumption. In the work of Lang et al. [30] the phase shift is used to calculate the relaxation time of the analyte.

We assume the signal decrease to result from deviations of the sound absorption coefficient α_a due to the changing gas composition. To calculate the loss in pressure of an acoustic wave, the following equation can be applied.

$$p_x = p_0 e^{-\alpha_a(\omega_s)x} \quad (5.15)$$

Therein p_x is the sound pressure of the acoustic wave after travelling a distance x , p_0 is the initial sound pressure of the acoustic wave and $\alpha_a(\omega_s)$ represents the acoustic attenuation of a sound wave with an angular frequency ω_s . The overall acoustic attenuation considers classical and molecular sound absorption. Classical attenuation consists of losses from thermal and viscous boundary layer formation [31], whereas molecular sound absorption is induced by the excitation of vibrational modes of the molecules taking part in the sound wave transmission process. As a consequence of molecular absorption, acoustic dispersion might occur. A characteristic of sound dispersion is an increase of the speed of sound at higher frequencies [32]. Further details can be found in [33].

The data from Ejakov et al. [34] indicates, that at 8 %V of CO₂ a slight acoustic dispersion could be present at a modulation frequency of 5 kHz, although the buffer gas in their study was N₂. However, in our experiments, the measured shift of the resonance frequency was 14.9 Hz/%V-CO₂ (= 0.31 %/%V-CO₂), which agrees well with the theoretical shift. Hence, we assume that none or only weak acoustic dispersion is present at 5 kHz. Nevertheless, we assume that the CO₂ induced loss in signal is mainly caused by an increase of the acoustical attenuation.

The results indicate that the CO₂ level must be monitored in a later application in breath analysis to get valuable feedback regarding metabolism and to allow reliable photoacoustic measurements at the resonance frequency.

5.2.6.3 Water

In general, it is assumed, that exhaled breath contains close to 100 % of relative humidity, while its temperature is slightly lower than the body temperature. In 2020, however, Mansour et al. [34] demonstrated, that neither the temperature nor the humidity was constant for different participants of their study and that the relative humidity was well below 100 %. According to them, the temperature varied between 31.4 °C – 35.4 °C and the relative humidity was between 65 % – 91 %, which equals a range of water being present in breath from approximately 2.9 %V – 5.0 %V. In our studies, a humidity generator was used to humidify the buffer gas used for dilution of the acetone mixtures as well as for background measurements. Humidified synthetic air with water concentrations between 0.9 %V to 5.6 %V as well as 30 ppmV of acetone diluted in N₂ and synthetic air with water concentrations between 1.2 %V to 5.2 %V have been studied, respectively. Similar water concentrations were used for the measurements with N₂ as buffer gas. Since solely dilution gas was lead through the humidity generator, the maximum setting of H₂O is about 5.2 %V for mixtures containing more than solely buffer gas. All measurements are based on frequency sweeps to ensure maximum resonance amplification. Each point of a sweep consists of 300 measurement points being acquired at 5 Hz with $\tau_{LIA} = 10$ s. Figure 5.13(a) visualises the measurements performed in synthetic air. With rising water concentration, the curve shows an exponential increase. Figure 5.13(b) in contrast shows no H₂O dependency of the PA signal in the presence of acetone. With regard to the measurements containing N₂ as dilution gas, i.e. no oxygen is present, the PA signal decreases by adding water. For acetone diluted in N₂ adding water causes the signal to linearly decrease with 0.38 % per %-H₂O. Besides, no promotion of the acetone relaxation similar to O₂ was found. The shift of the resonance frequency induced by water is approximately 7.7 Hz/%V-H₂O (= 0.15 %/%V-H₂O) in synthetic air and 7.4 Hz/%V-H₂O (= 0.15 %/%V-H₂O) in N₂. The shifts fit well with theoretical shifts, minor deviations are due to measurement errors. The results are difficult to interpret. The measurements with acetone diluted in N₂ demonstrate, that water does not have a promotion effect as O₂ does. Moreover, the photoacoustic signal rather decreases with higher water content for mixtures employing N₂ as buffer gas. The reason for the exponential signal increase in pure synthetic air but not with

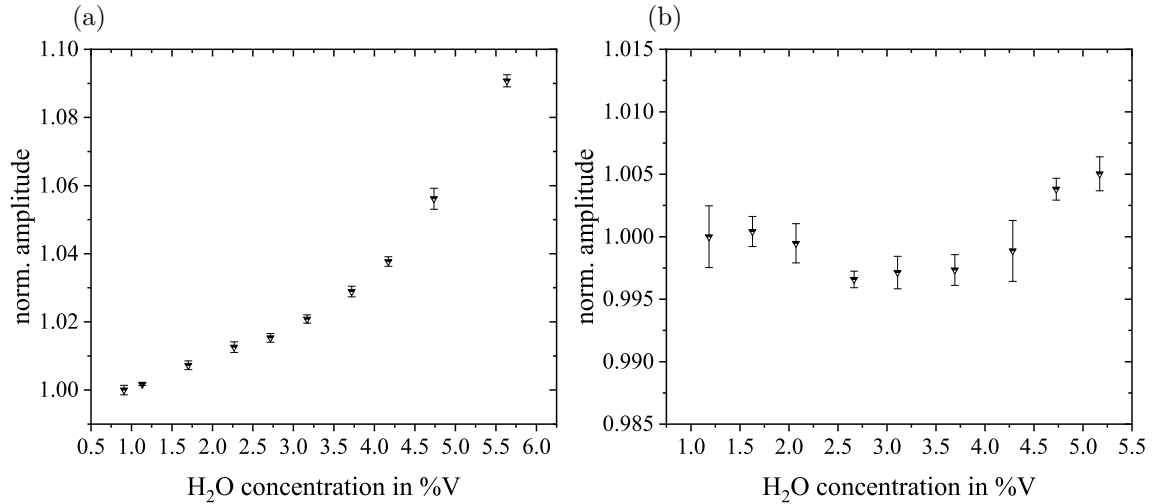


Fig. 5.13. (a) Signal increase with rising H₂O concentration in pure synthetic air and (b) stable signal with 30 ppmV of acetone diluted in synthetic air with rising H₂O concentration. Error bars indicate $\pm 3\sigma$ of the standard deviation of the measurement points.

30 ppmV of acetone present in the gas mixture remains unclear, too. Employing different photoacoustic setups and different analytes, our group has found various complex and partly counteracting effects on the photoacoustic signal when H₂O was added. Hence, at this point the explanations for some of the experimental results cannot be conclusively clarified but are subject to further studies.

5.2.6.4 Measurements in typical gas mixtures

In this section, we used gas mixtures consisting of typical human breath exhaled components and altered the concentration of one of the high abundant gas species. Again, each point of a sweep consists of 300 measurement points being acquired at 5 Hz with $\tau_{LIA} = 10$ s. Therefore, we changed the H₂O, CO₂ and acetone concentrations successively. The H₂O concentration was varied between 1.1 %V to 5.4 %V, while CO₂ was kept at 3.0 %V and acetone was set to 0.5 ppmV, while synthetic air was used for dilution. Figure 5.14(a) indicates the same course of the graph as in figure 5.13(a). Figure 5.14(b) shows that gradually adding CO₂ to a 3.7 %V of H₂O containing mixture causes the signal to decrease for 1.5 %, but to remain constant in view of further adding CO₂. It looks like H₂O counteracts the signal attenuation effect of CO₂ illustrated in figure 5.12. In section 5.2.6.2, we assumed the signal drop by adding CO₂ not to result from delayed relaxation. Therefore, we tried to find hints in literature considering classical or molecular acoustic absorption. Like before, literature, which studies similar complex mixtures, is scarce or even non-existent. However, Knudsen et al. [35] discusses the influence of H₂O being added to pure CO₂. According to their interpretation, adding H₂O to CO₂ causes the sound dissipation induced by molecular absorption, i.e. sound dispersion, to blue shift. Hence, we assume that this blue shift of molecular absorption causes the signal

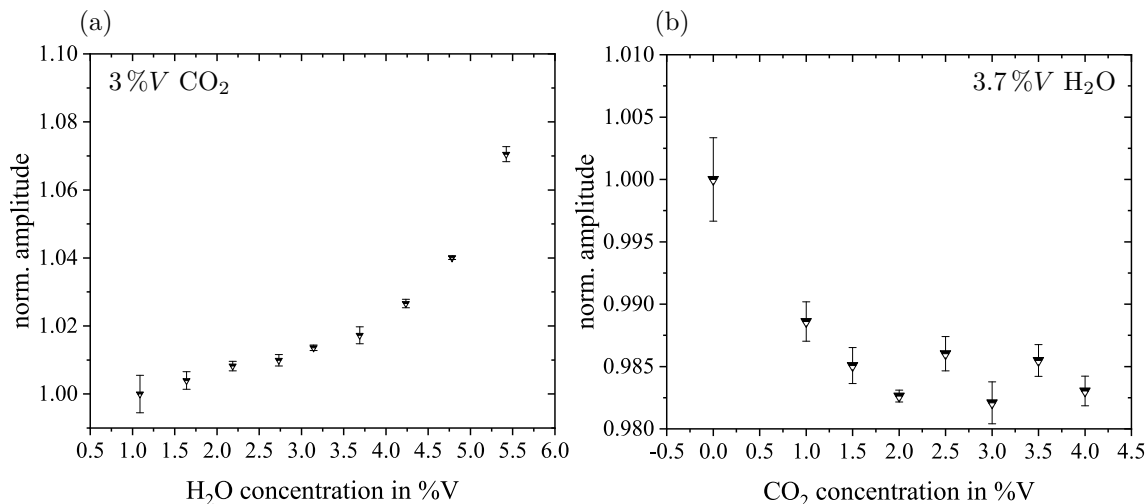


Fig. 5.14. (a) The influence of H₂O on the photoacoustic signal with 3.0 %V CO₂ and 0.5 ppmV of acetone diluted in synthetic air and (b) the influence of CO₂ on the photoacoustic signal with 3.7 %V H₂O and 0.5 ppmV of acetone diluted in synthetic air. Error bars indicate $\pm 3\sigma$ of the standard deviation of the measurement points.

to remain constant after adding H₂O. Fortunately, in breath exhale H₂O is always present, and varying CO₂ concentrations within typical breath concentrations will not affect the photoacoustic amplitude. Further tests studying these effects introduced by H₂O and CO₂ would be interesting since they are likely to occur in other photoacoustic applications, too, but are out of the scope of this work.

Finally, to investigate the acetone sensing performance under typical conditions, H₂O was kept at 3.3 %V, CO₂ was set to 2.8 %V and acetone was altered from 1 to 0 ppmV. Bottle 1 and bottle 2 were used to be able to set the different acetone concentrations. As described in section 5.2.4, bottle 2 demonstrated a slightly steeper linear calibration curve slope, however, for the calculation of the LOD in a typical breath mixture we employed only the slope from bottle 1, which was 2.65 $\mu\text{V/ppmV}$ in this measurement series. The sensitivity and noise ($3\sigma = 0.033 \mu\text{V}$ for $\tau_{\text{LIA}} = 10 \text{ s}$) are comparably to the measurements from section 5.2.4, hence, the LOD was determined to 12.5 ppbV (3σ).

5.2.7 Analysis of the prepared dataset

5.2.7.1 Correlation of the measured variables

From the two datasets that are discussed in section 5.2.2 of this work, 18 variables were considered for further linear correlation analysis. Using the Pearson correlation coefficient with a two tailed p-value of 0.01 as a minimal requirement for consideration many bivariate linear correlations were found. The full correlation matrices can be found in appendix B.

Those correlations can be divided into three different categories: causal influence on the measurement, experiment setup artefacts and redundant information. Whilst causal influences are essential for accurate prediction and compensation, redundant features might still lead to an increased accuracy if they hold some additional information.

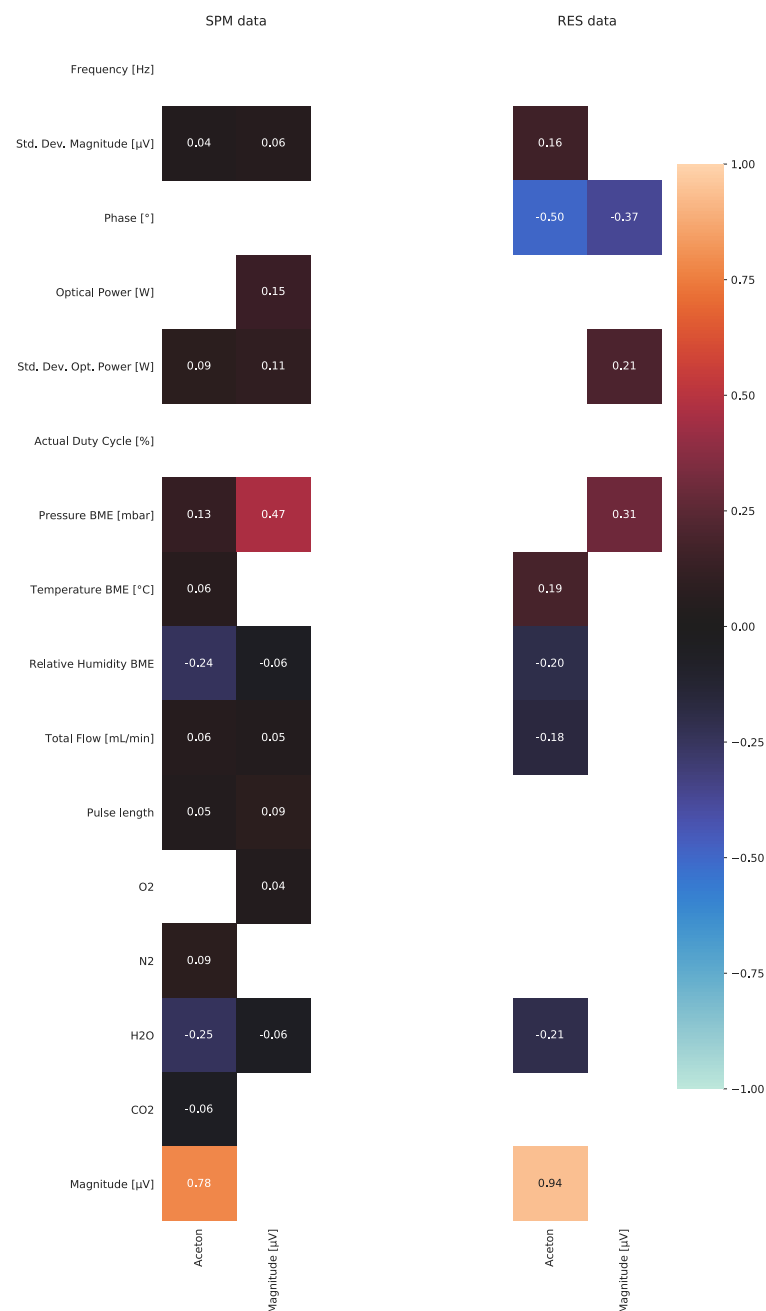


Fig. 5.15. Pearson correlation values of acetone and the measured magnitude to the other features.

Experiment setup artefacts deteriorate the performance of the prediction and need to be excluded from the final model to avoid overfitting. Those artefacts include a non-causal correlation of acetone concentration to N_2 concentration in the full dataset, for example ($p = 0.086$, $r = 1.4 \times 10^{-8}$). This correlation stems from an uneven distribution of the measurements. Additionally, strong correlations between N_2 and O_2 setpoints have been identified. Since direct comparison measurements did not show any influence on the signal, they can be discarded. Decisions on the nature of correlations have to be drawn from physics and knowledge about the experimental setup and cannot be derived exclusively from data.

Comparing the overall dataset to the resonance dataset important changes in some correlations are visible. Most obviously, the photoacoustic phase linearly correlates with the acetone concentration and the magnitude, which only appears in the resonance dataset. It is evident, that the phase suffers from nonlinear effects if not measured at the resonance frequency. The pearson correlation coefficients for the signal magnitude and the acetone concentration for both datasets can be found in figure 5.15. A pearson coefficient of 0.8 between two features implies, that if the first feature increases by one, the other increases by 0.8.

5.2.7.2 Feature importance and linear influence on the signal

In order to provide additional insights for the further development of a PAS based sensor for acetone detection in human breath the different measurement features are ranked on their importance for a linear model. From the ranked list of external influences on the prediction quality the importance of compensation for different parameters becomes evident. This method extends the measurement series' presented within this work as it includes additional data points and therefore can catch additional subtle dependencies and interdependencies and put those in perspective. The ranking was performed using decreasing valued Lasso regularisation during the linear model creation. This corresponds to an intrinsic feature ranking method [36]. It performs linear regression including all parameters but adds the absolute parameter values into the optimisation term, thus forcing them towards zero. Prior of ranking, all features and the target variable were scaled to zero mean and a variance of one to account for numerical differences, which would bias feature selection.

The seven most important features are presented in table 5.6 since all additional features only lead to very small improvements. The train R^2 score results from a single Ridge regularised regression model on all data using all features selected up to now, the validation R^2 score is the mean R^2 score of a ten-fold cross validation of a Ridge regularised regression model. Both cross validation and Ridge regularised regression models are explained in more detail in [37] and [38]. The most informative feature for both datasets is the measurement signal magnitude as expected. The great difference in R^2 scores from SPM to RES models can be explained by the nonlinear influence of the resonance factor of the cell when a frequency different from the resonance frequency is used.

Tab. 5.6. Seven most important features from Lasso ranking in decreasing order and their corresponding R^2 scores including only the mentioned features.

#	SPM Parameter	Train R^2 SPM	Val R^2 SPM	RES Parameter	Train R^2 RES	Val R^2 RES
1	Magnitude in μV	0.614	0.566	Magnitude in μV	0.885	0.629
2	H ₂ O	0.654	0.614	Phase in $^\circ$	0.910	0.742
3	Current in mA	0.681	0.636	Pressure BME in mbar	0.961	0.861
4	Pressure BME in mbar	0.731	0.667	Std. dev. opt. power in W	0.969	0.879
5	N ₂	0.740	0.685	CO ₂	0.973	0.892
6	Optical power in W	0.744	0.687	O ₂	0.973	0.893
7	Phase in $^\circ$	0.748	0.690	Act. duty cy- cle in %	0.973	0.890

The strong influence of the H₂O setpoint in the full dataset can be attributed to the experiment setup since most H₂O measurements have been performed without added acetone and thereby bias the dataset. This bias is less prominent in the resonance dataset but still prevails as can be seen from the correlation analysis. The other two strong influences on the performance of linear models stem from pressure in the cell and the optical power. In the resonance dataset, the optical power is strongly correlated with its standard deviation, therefore only the standard deviation of the optical power is taken into account in the model. Ambient gas as well as the duty cycle only provide small improvements in R^2 score. Therefore, the most important features to deduce the correct acetone concentration from the measurement must include the primary measurement variables magnitude and phase. Compensation of the incident optical power and pressure is vital. In addition, knowledge about the actual duty cycle can enhance the measurement but with less influence on prediction capabilities. Improvements from knowledge of the ambient gas in this case most likely stem from experiment setup artefacts. The final application should take care, to only measure at the resonance frequency since this improves linearity and qualifies linear prediction models. Additionally, if measurements are performed at the resonance frequency, the phase holds additional information, which can be used to increase prediction capabilities.

It is important to note, that this ranking only took linear correlations into account. Nonlinear influences and therefore compensations were not considered.

5.2.7.3 Bayesian linear regression

Bayesian linear regression [37] was used to get an estimate of the trustworthiness of the linear model on the given data. With the Bayesian treatment of the linear modelling process each parameter of the linear model is interpreted as a distribution of itself and this prior distribution is fitted with the given data. Afterwards a posterior distribution is obtained, whose standard deviation holds information on the certainty of the parameter given by the data.

The linear models were initialised with Gaussian priors of zero mean and one variance for all parameters. The input features as well as the targets were also normalised to zero mean and one variance. The resulting model using the mean value of each parameter is given in appendix B. The standard deviation for the data likelihood is 0.5 for the full model, which corresponds to ± 10 ppmV and 0.17 for the resonance model, which corresponds to ± 3.5 ppmV, respectively. All parameter distributions can be found in the traceplots within appendix B. This is clearly not enough for direct application but given the wide feature range and low number of samples especially for the resonance set, it can serve as a trustworthy estimate of the feature influences and a prior for models with a more constrained feature space.

The influence of the acetone concentration on the magnitude is similar for both models; it increases about $2.62 \mu\text{V/ppmV}$ acetone, which is close to the slope measured in single experiments ranging from $2.6 \mu\text{V/ppmV}$ to $2.8 \mu\text{V/ppmV}$. For the resonance model, the influence of pressure is assumed to reduce the predicted acetone value by -0.347 ppmV/mbar , which corresponds to counteracting an increase in measured magnitude of $0.91 \mu\text{V/mbar}$. From direct measurements, only an increase of $0.17 \mu\text{V/mbar}$ on a signal containing 30 ppmV acetone was found. This leads to the conclusion, that some other effect plays a major role in terms of signal deterioration by reducing the pressure of the gas sample.

This shows that while insights from data analysis help to understand the physical dependencies of PA signal generation, caution has to be taken to continuously check for experiment setup artefacts. Data analysis in return can point towards correlations and influences that could be missed otherwise.

5.2.8 Conclusion

We reported a photoacoustic system, which is highly sensitive with an LOD of about 12.5 ppbV (3σ) of acetone in typical breath exhale mixtures, which satisfies human breath exhale analysis. Besides, we investigated the effects of ambient parameters such as temperature or pressure as well as cross-sensitivities towards O_2 , CO_2 and H_2O . Finally, we presented our first approach of how data sciences can be useful for photoacoustic sensors being applied in a complex field like breath analysis.

Regarding the influences of ambient parameters, we provided suggestions on how to improve our system to facilitate an application in breath analysis and for other applications. Pressure should be monitored and depending on the application included into signal correction if high variations occur. If low pressures are applied an adaption of the resonance frequency might be necessary due to node shifting. Temperature should be maintained at a constant level as the signal and the resonance frequency are varying significantly with temperature. Since measurements demonstrated, that a non-constant duty cycle may affect the photoacoustic signal, it is recommended to use a light-source driver with a constant duty cycle for different frequencies. Besides, different duty cycles have an influence on the detected optical power if the optical detector is not fast enough. If applicable, a fast optical detector, e.g. a photodiode, is recommended. If normalisation of the photoacoustic signal considering the optical power is necessary, e.g. due to degradation of the light source, only the detected signal at the on-phase should be consulted, which is equal to the cw power. If no such detector is available, the optical power should be checked in cw-mode occasionally to detect deteriorations in the output power. Note that the degradation of the photodiode itself must be considered as well. This method, however, can only be applied for optical power recalibration but not for an emission wavelength shift compensation of the LED, which can also occur due to degradation. Therefore, regular recalibration of the whole system will be necessary. Long-term investigations regarding additional LED aging processes in general as well as the influence of the photodissociation rate on the photoacoustic signal are of interest and have to be investigated in further studies. Since all effects discussed within section 5.2.5 do also apply for the background signal, a background check before each measurement should be performed to correctly identify the background level of the sensor. The results from this work highlight that minimizing the background signal is useful to facilitate a reliable application in a complex gas matrix like in terms of breath analysis. Approaches for background signal reduction are a better collimation of the LED light, optimisation of the PAC design or the application of a modulation cancellation method (MOCAM) [39]. The latter approach will be investigated in the future.

Optical sensor techniques generally claim high sensitivity and selectivity. The results show, that PAS is a highly sensitive measurement technique. The spectral selectivity of PAS in the UV region is good and superior to classic absorption spectroscopy since effects like Rayleigh scattering do not influence the signal. However, altering the concentrations of O_2 , H_2O and CO_2 within the measurement matrix cause different effects to occur. All of them cause a change in the speed of sound and thus alter the resonance frequency. It is therefore important to know the correct speed of sound of the gas matrix at all times. This can be achieved by implementing an ultrasound sensor, for example, which measures the speed of sound at a certain frequency. Note, that the temperature of the gas stream at the point of measurement should be known and that sound dispersion could be an issue if the applied ultrasound frequency is too high. Another approach is to measure the CO_2 and H_2O content of the gas because the O_2 and N_2 concentration can be calculated based on this information. If the composition of the gas and the temperature is known, the speed of sound

can be easily calculated using equation 5.13. The variation of oxygen above 1 %V showed no significant influence on the signal and if H₂O is present neither does CO₂ in the range between 2 – 4 %V. Only the H₂O concentration has a significant effect on the photoacoustic signal and must be monitored.

The data analysis performed on the dataset created during these experiments confirms many of the findings from single experiments. It highlights the importance of measuring exactly at the resonance frequency to obtain mostly linear effects not only on the magnitude reading but also on the phase. External linear influences were ranked on their importance for prediction. The compensation for pressure changes as well as changes in the optical power are vital whilst changes in humidity, the actual duty cycle and the ambient gas mixture only become important in terms of trace concentrations of acetone. For future models to be trained on PAS measurements, special care must be taken to ensure causality and avoid experiment setup artefacts. The fitting of a predefined model, which corresponds to the known physical model of absorption, could lead to better understanding the actual model parameters. Additionally, models that provide a trust region in feature space like Gaussian Mixture Models would increase prediction accuracy and certainty in regions with high data coverage as well as a criterion for dataset augmentation and active learning approaches, respectively.

The investigation of small concentrations of acetone in dry synthetic air and typical breath exhale mixtures demonstrated the potential of the UV LED based photoacoustic sensor system for different applications. Towards reliable breath analysis, a better understanding of the occurring effects and a lower background signal are necessary. Our further research will address approaches to reduce the background signal as well as the development of an interface to allow sampling and analysis of real breath exhale.

References

- [1] S. Weigl et al. “Photoacoustic detection of acetone in N₂ and synthetic air using a high power UV LED”. In: *Sensors and Actuators B: Chemical* 316.August 2020 (Aug. 2020), p. 128109. ISSN: 09254005. DOI: 10.1016/j.snb.2020.128109 (cit. on pp. 213, 216, 217, 223).
- [2] J. Kalkman and H. W. Van Kesteren. “Relaxation effects and high sensitivity photoacoustic detection of NO₂ with a blue laser diode”. In: *Applied Physics B: Lasers and Optics* 90.2 (2008), pp. 197–200. ISSN: 09462171. DOI: 10.1007/s00340-007-2895-0 (cit. on p. 213).
- [3] T. Rück et al. “NO₂ trace gas monitoring in air using off-beam quartz enhanced photoacoustic spectroscopy (QEPAS) and interference studies towards CO₂, H₂O and acoustic noise”. In: *Sensors and Actuators, B: Chemical* 255.2 (2018), pp. 2462–2471. ISSN: 09254005. DOI: 10.1016/j.snb.2017.09.039 (cit. on p. 213).

- [4] T. Oka et al. “Photoacoustic Study of 280 nm Band of Acetone Vapor”. In: *Bulletin of the Chemical Society of Japan* 61.1 (1988), p. 199. DOI: <https://doi.org/10.1246/bcsj.61.199> (cit. on p. 213).
- [5] Z. Bozókai et al. “Photoacoustic instruments for practical applications: Present, potentials, and future challenges”. In: *Applied Spectroscopy Reviews* 46.1 (2011), pp. 1–37. ISSN: 05704928. DOI: 10.1080/05704928.2010.520178 (cit. on p. 213).
- [6] X. Yin et al. “Impact of humidity on quartz-enhanced photoacoustic spectroscopy based CO detection using a near-IR telecommunication diode laser”. In: *Sensors (Switzerland)* 16.2 (2016). ISSN: 14248220. DOI: 10.3390/s16020162 (cit. on p. 213).
- [7] A. A. Kosterev et al. “QEPAS methane sensor performance for humidified gases”. In: *Applied Physics B: Lasers and Optics* 92.1 (2008), pp. 103–109. ISSN: 09462171. DOI: 10.1007/s00340-008-3056-9 (cit. on p. 213).
- [8] T. Rück et al. “Low-cost photoacoustic NO₂ trace gas monitoring at the pptV-level”. In: *Sensors and Actuators A: Physical* 263.2 (2017), pp. 501–509. ISSN: 09244247. DOI: 10.1016/j.sna.2017.06.036 (cit. on p. 213).
- [9] P. Claspy et al. *Optoacoustic spectroscopy and detection*. Academic Press, 1977. ISBN: 0-12-544150-9 (cit. on p. 215).
- [10] A. Rosencwaig. *Photoacoustics and Photoacoustic Spectroscopy*. John Wiley & Sons, 1980, pp. 17–30. ISBN: 0471044954 (cit. on p. 215).
- [11] T. Rück. “Development, characterization and miniaturization of a trace gas detection system for NO₂ in air based on photoacoustic spectroscopy”. Ph. D. thesis. University of Regensburg, 2017 (cit. on p. 215).
- [12] A. Miklós et al. “Application of acoustic resonators in photoacoustic trace gas analysis and metrology”. In: *Review of Scientific Instruments* 72.4 (2001), pp. 1937–1955. ISSN: 00346748. DOI: 10.1063/1.1353198 (cit. on p. 215).
- [13] L. A. Ishaku et al. “Temperature effects on photoacoustic carbon dioxide sensor developed using mid-IR LED”. In: *I2MTC 2018 - 2018 IEEE International Instrumentation and Measurement Technology Conference: Discovering New Horizons in Instrumentation and Measurement, Proceedings* (2018), pp. 1–6. DOI: 10.1109/I2MTC.2018.8409855 (cit. on p. 218).
- [14] M. Szakáll et al. “On the temperature dependent characteristics of a photoacoustic water vapor detector for airborne application”. In: *Infrared Physics and Technology* 51.2 (2007), pp. 113–121. ISSN: 13504495. DOI: 10.1016/j.infrared.2007.04.001 (cit. on p. 218).
- [15] J. D. Koch et al. “Measurements of near-UV absorption spectra of acetone and 3-pentanone at high temperatures”. In: *Journal of Quantitative Spectroscopy and Radiative Transfer* 109.11 (July 2008), pp. 2037–2044. ISSN: 00224073. DOI: 10.1016/j.jqsrt.2008.02.010 (cit. on p. 218).
- [16] InvenSense. *ICS-40720 Ultra-Low Noise Microphone with Differential Output*. Tech. rep. 2016 (cit. on p. 218).

- [17] T. Gierczak et al. “Photochemistry of acetone under tropospheric conditions”. In: *Chemical Physics* 231.2-3 (June 1998), pp. 229–244. ISSN: 03010104. DOI: 10.1016/S0301-0104(98)00006-8 (cit. on p. 222).
- [18] M. Nobre et al. “The VUV electronic spectroscopy of acetone studied by synchrotron radiation”. In: *Phys. Chem. Chem. Phys.* 10.4 (2008), pp. 550–560. ISSN: 1463-9076. DOI: 10.1039/B708580J (cit. on p. 222).
- [19] M. Hesse et al. *Spektroskopische Methoden in der organischen Chemie*. Ed. by M. Hesse et al. 8th ed. Stuttgart: Georg Thieme Verlag, 2012. ISBN: 9783135761084. DOI: 10.1055/b-002-46984 (cit. on p. 222).
- [20] H. Keller-Rudek et al. “The MPI-Mainz UV/VIS Spectral Atlas of Gaseous Molecules of Atmospheric Interest”. In: *Earth System Science Data* 5.2 (Dec. 2013), pp. 365–373. ISSN: 1866-3516. DOI: 10.5194/essd-5-365-2013 (cit. on p. 223).
- [21] K. Bogumil et al. “Measurements of molecular absorption spectra with the SCIAMACHY pre-flight model: instrument characterization and reference data for atmospheric remote-sensing in the 230–2380 nm region”. In: *Journal of Photochemistry and Photobiology A: Chemistry* 157.2-3 (May 2003), pp. 167–184. ISSN: 10106030. DOI: 10.1016/S1010-6030(03)00062-5 (cit. on p. 223).
- [22] S. Fally et al. “Fourier Transform Spectroscopy of the O₂ Herzberg Bands. III. Absorption Cross Sections of the Collision-Induced Bands and of the Herzberg Continuum”. In: *Journal of Molecular Spectroscopy* 204.1 (Nov. 2000), pp. 10–20. ISSN: 00222852. DOI: 10.1006/jmsp.2000.8204 (cit. on p. 223).
- [23] D. E. Shemansky. “CO₂ Extinction Coefficient 1700–3000 Å”. In: *The Journal of Chemical Physics* 56.4 (Feb. 1972), pp. 1582–1587. ISSN: 0021-9606. DOI: 10.1063/1.1677408 (cit. on p. 223).
- [24] D. Ityaksov et al. “Deep-UV absorption and Rayleigh scattering of carbon dioxide”. In: *Chemical Physics Letters* 462.1-3 (Sept. 2008), pp. 31–34. ISSN: 00092614. DOI: 10.1016/j.cplett.2008.07.049 (cit. on p. 223).
- [25] J. Du et al. “The influence of water vapor absorption in the 290–350 nm region on solar radiance: Laboratory studies and model simulation”. In: *Geophysical Research Letters* 40.17 (Sept. 2013), pp. 4788–4792. ISSN: 00948276. DOI: 10.1002/grl.50935 (cit. on p. 223).
- [26] E. M. Wilson et al. “Upper limits for absorption by water vapor in the near-UV”. In: *Journal of Quantitative Spectroscopy and Radiative Transfer* 170 (Feb. 2016), pp. 194–199. ISSN: 00224073. DOI: 10.1016/j.jqsrt.2015.11.015 (cit. on p. 223).
- [27] J. Lampel et al. “On the relative absorption strengths of water vapour in the blue wavelength range”. In: *Atmospheric Measurement Techniques* 8.10 (Oct. 2015), pp. 4329–4346. ISSN: 1867-8548. DOI: 10.5194/amt-8-4329-2015 (cit. on p. 223).

- [28] A. Burcat and B. Ruscic. *Third millenium ideal gas and condensed phase thermochemical database for combustion with update from active thermochemical tables*. Tech. rep. Argonne, IL: Argonne National Laboratory (ANL), Sept. 2005. DOI: 10.2172/925269 (cit. on p. 224).
- [29] D. Zhao et al. “A novel real-time carbon dioxide analyzer for health and environmental applications”. In: *Sensors and Actuators B: Chemical* 195 (May 2014), pp. 171–176. ISSN: 09254005. DOI: 10.1016/j.snb.2013.12.110 (cit. on p. 224).
- [30] B. Lang et al. “Molecular relaxation effects on vibrational water vapor photoacoustic spectroscopy in air”. In: *Applied Physics B: Lasers and Optics* 126.4 (2020), pp. 1–18. ISSN: 09462171. DOI: 10.1007/s00340-020-7409-3 (cit. on p. 225).
- [31] R. H. Johnson et al. “Loss mechanisms in resonant spectrophones”. In: *Applied Optics* 21.1 (Jan. 1982), p. 81. ISSN: 0003-6935. DOI: 10.1364/AO.21.000081 (cit. on p. 225).
- [32] H. O. Kneser and J. Zühlke. “Einstelldauer der Schwingungsenergien bei CO₂ und N₂O”. In: *Zeitschrift für Physik* 77.9-10 (Sept. 1932), pp. 649–652. ISSN: 1434-6001. DOI: 10.1007/BF01330888 (cit. on p. 225).
- [33] T. Rück et al. “NO₂ trace gas monitoring in air using off-beam quartz enhanced photoacoustic spectroscopy (QEPAS) and interference studies towards CO₂, H₂O and acoustic noise”. In: *Sensors and Actuators B: Chemical* 255 (Feb. 2017), pp. 2462–2471. ISSN: 09254005. DOI: 10.1016/j.snb.2017.09.039 (cit. on p. 225).
- [34] S. G. Ejakov et al. “Acoustic attenuation in gas mixtures with nitrogen: Experimental data and calculations”. In: *The Journal of the Acoustical Society of America* 113.4 (2003), pp. 1871–1879. ISSN: 0001-4966. DOI: 10.1121/1.1559177 (cit. on p. 226).
- [35] V. O. Knudsen and E. Fricke. “The Absorption of Sound in Impurities , Containing Added The Absorption of Sound in CO₂, N₂O, COS , and in CS₂, Containing Added Impurities”. In: *The Journal of the Acoustical Society of America* 12 (1940), pp. 255–259 (cit. on p. 227).
- [36] V. Fonti. “Feature Selection using LASSO”. In: *VU Amsterdam* (2017), pp. 1–26. ISSN: 2169-3536. DOI: 10.1109/ACCESS.2017.2696365 (cit. on p. 230).
- [37] C. M. Bishop. *Pattern Recognition and Machine Learning*. 1st ed. Springer New York, 2006, p. 152. ISBN: 978-0-387-31073-2 (cit. on pp. 230, 232).
- [38] M. Kubat. *An Introduction to Machine Learning*. 2nd ed. Springer International Publishing, 2017, pp. 244–500. ISBN: 978-3-319-63912-3. DOI: 10.1007/978-3-319-63913-0 (cit. on p. 230).
- [39] H. Zheng et al. “Scattered light modulation cancellation method for sub-ppb-level NO₂ detection in a LD-excited QEPAS system”. In: *Optics Express* 24.10 (May 2016), A752. ISSN: 1094-4087. DOI: 10.1364/OE.24.00A752 (cit. on p. 233).

5.3 Further UV LED measurements

This section covers the measurements comparing the performance of further PAC designs. Besides, the different PAC designs and optical setups are described. Since the UV LED from Innotech LG (LED1) has been declared obsolete, a UV LED from Bulb (LED2) has been employed for photoacoustic measurements, too. During the experiments, a second Bulb UV LED (LED2*) with a bit more optical output power, was used since the first was not operating properly anymore.

5.3.1 Experimental

PAC2 is similar to PAC1 (see figure 5.1). However, the PAC's resonator has a diameter of 13 mm instead of 10 mm in order to be able to place a fused silica tube (FST) into the original PAC resonator. The tube has an inner diameter of approximately 10 mm and a wall thickness of 1 mm. The length is about 33 mm to facilitate alignment of the 1 mm inner diameter outcoupling hole (a) of the tube with the PACs outcoupling hole. The FST was mounted within the resonator using a two-component epoxy-based adhesive of the Type EP 601 from Polytech Pt (Karlsbad, Germany). The adhesive was chosen, since according to the vendor the outgassing rate is very low. Besides, neither the emitted gases nor the adhesive itself are assumed to cause absorption of the UV light. However, mounting the FST is considered an irreversible step.

Section 5.1.2 already discussed the collimation optics for LED1. The collimation optics for LED2, however, have been adopted. Instead of the expensive aspheric lens, a small and cheap half ball lens (#67397, Edmund Optics Ltd, Nether Poppleton, UK), with a diameter of 5 mm, was used instead. This was possible, as the light emitting surface area of LED2 is smaller than the one of LED1. The biconvex lens applied in the collimation setup of LED1 was replaced by a smaller biconvex lens having only a diameter of 18 mm (#46290, Edmund Optics Ltd.). This setup reduced the costs for the optical system by a factor of four and increased the compactness. The optical power has been monitored by means of a PM100D with the S302C sensor head.

PAC5 is a totally new approach, which will be only addressed briefly within this thesis. The concept of this design allows for high compactness and simplicity, since neither windows nor lenses are employed. The only optical component is a biconvex shaped reflector consisting of two concave highly polished aluminum parts (refer to figure 5.16 item (d)). The resonator diameter has been reduced to 6 mm in order to integrate an FST with a 4 mm inner diameter. The thickness is 1 mm and the length of the FST is about 33 mm. In addition, one half of the outer surface of the tube was coated with aluminium. In detail, the side of the LED, which was coated with aluminium, is opposite to the LED mounting in order to ensure illumination of the tube. The coating was meant to reflect the light, thus,

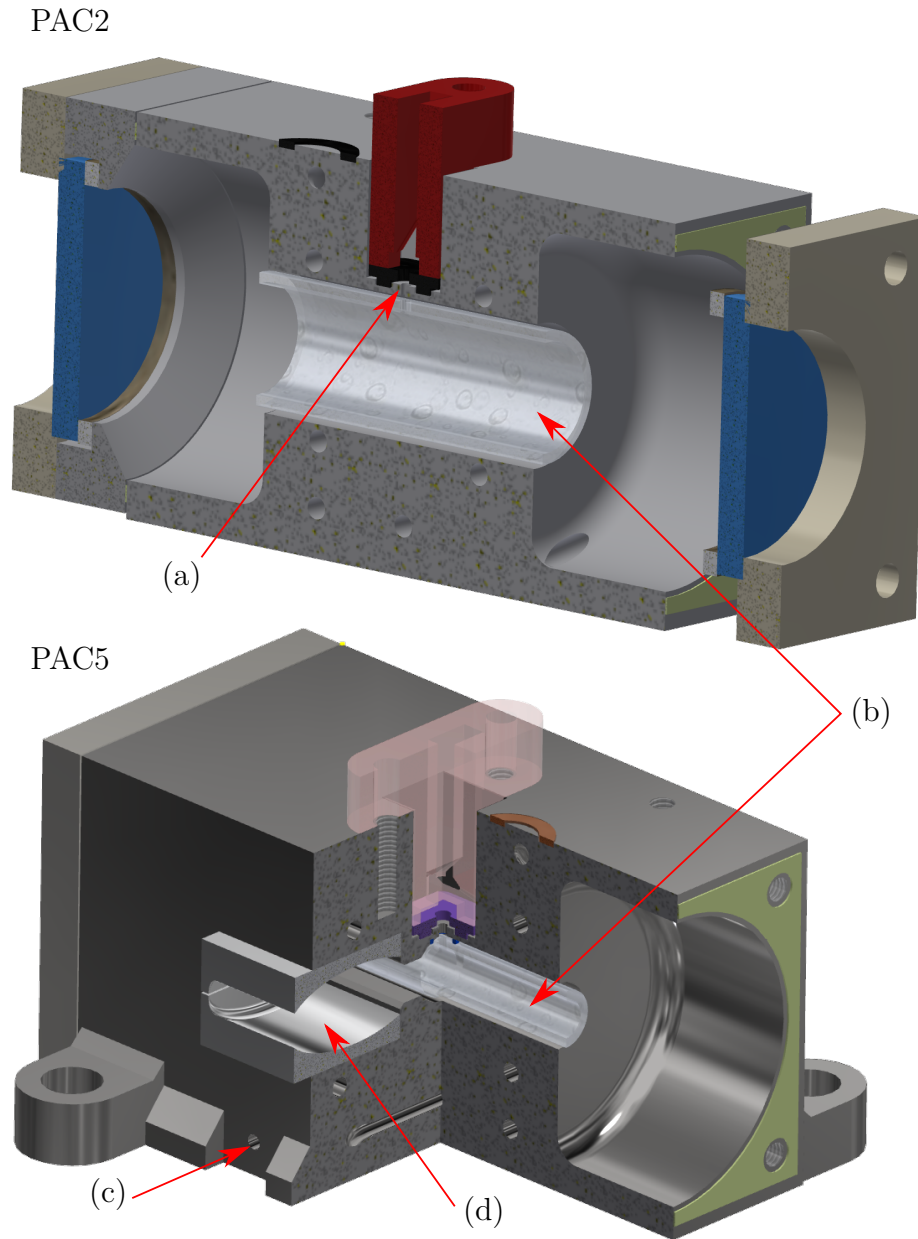


Fig. 5.16. Image of a half section of PAC2 and a three-quarter cut of PAC5, visualising the integration of a short, thin-walled fused silica tube (b) into the respective resonator. PAC5 further contains a convex aluminium reflector (d) and a hole (c) in order to fixate the PCB of the UV LED. (a) points to the acoustic outcoupling channel of PAC2.

increasing the overall optical power within the resonator. The mounting of the LED, was achieved by means of a thin 3D printed adapter plate, which allowed for attachment of the LED to the cell using the hole (c) indicated in figure 5.16. Note that in terms of this PAC, no photodiode was implemented for monitoring the optical power. However, the integration of a monitoring photodiode into one of the buffer

closing caps should provide essential information in more detailed future studies. To achieve gas tightness, the edges of the resonator openings were clogged with the PAC's resonator walls using another, removable adhesive from a hot glue dispenser. However, the vendor was not able to provide details regarding the composition of the adhesive. LED2* was used for illuminating the PAC.

5.3.2 Results and discussion

If not mentioned otherwise, the measurements have been performed at 500 mL/min flow rate, while τ_{LIA} was set to 2 s for sweep measurements and 10 s for calibration measurements, respectively. The LIA filter slope was set to 12 dB/octave, the LED current was set to 298 mA and the data acquisition rate was 5 Hz. Every measurement point plotted within this work was recorded with 20 s averaging time, i.e. 100 measurement points. The temperature of the PAC was set to 45 °C except for PAC5, which was set to 25 °C to avoid LED overheating. All sweep measurements were performed at an acetone concentration of 10 ppmV in synthetic air.

It has to be mentioned, that during the experiments described hereinafter, realignment of the LEDs had to be performed several times. Therefore, the presented results might suffer from alignment errors, which might cause misinterpretations at some point.

5.3.3 Comparison of different photoacoustic cells and LEDs

PAC2 was first characterised without the FST using LED2. The results were then compared with PAC2 including the FST in order to investigate the influence of

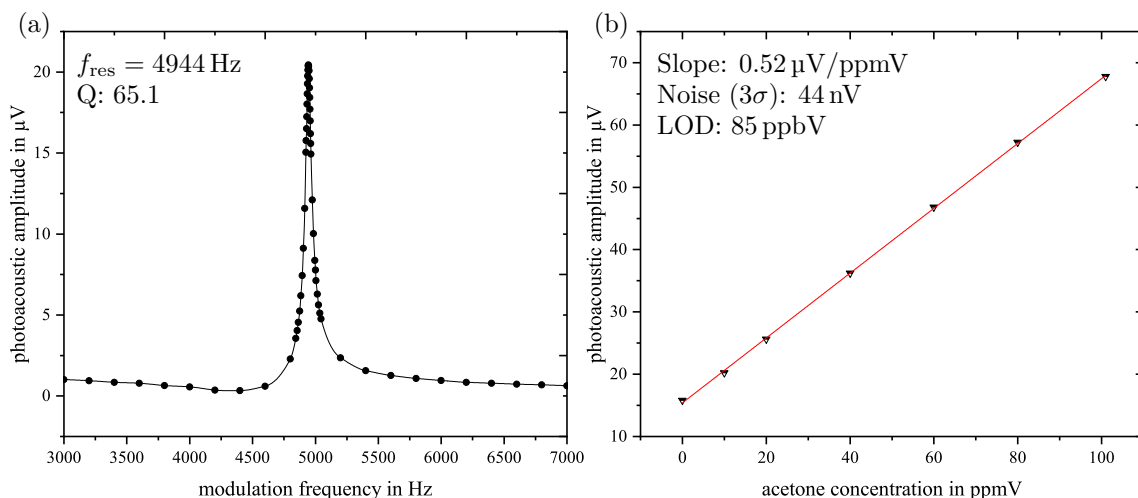


Fig. 5.17. Frequency sweep (a) and calibration curve results (b), measured using LED2 and PAC2. The slope represents the sensitivity of the system.

the resonator's surface smoothness on the background signal. PAC2* refers to the setup of PAC2 including the FST. In addition, PAC2* was combined with LED1 to directly compare the performance of both LED types and the results between the measurements combining PAC1 with LED1 and PAC2* with LED1.

Figure 5.17 visualises a frequency sweep (a) and a calibration curve (b) using PAC2 with LED2. Table 5.7 lists the different characterisation parameter acquired during the measurements of the different combinations of light source and PACs.

Tab. 5.7. Summary of the key parameters of the different UV LED measurement setups. PAC/LED represents the employed system components, e.g. 2/2 refers to PAC2 and LED2. f_{res} is the resonance frequency of the PAC and Q the quality factor of the cell. The sensitivity of a photoacoustic system is represented by the slope of the calibration curve. For better comparability, the monitored optical power P_0 of each setup is listed as well. Only measurements in synthetic air are compared.

PAC/ LED	f_{res} in Hz	Q	Noise (3σ) in nV	Sensitivity in $\mu\text{V}/\text{ppmV}$	LOD (3σ) in ppbV	P_0 in mW
2/2	4944	65.1	44	0.52	85	7.1
2*/2	4812	53.5	30	0.62	48	7.7
2*/2*	4812	51	40	0.78	51	10.4
2*/1	4813	52.6	55	1.97	27.9	11.9
1/1	4938	51.4	53	2.71	19.6	15.0

The resonance frequency of PAC2 without the tube was 4944 Hz and mounting the FST caused a red-shift of 132 Hz to 4812 Hz. This equals a relative shift of 2.7 %. However, the relative change of the effective length L_{eff} , calculated after equation 5.6, is only 1.3 %. Besides, although the effective length of PAC1 and PAC2 differs 4 % according to equation 5.6, they have almost identical resonance frequencies. This confirms the assumption, that there is no simple, universal equation applying for different setups. Hence, determining the resonance frequency of a system manually is mandatory.

The Q-factor of PAC2 is higher than that of PAC2* or PAC1, whereas the two different light sources LED2 and LED2* did not have an influence on the Q-factor as expected. The volumetric dissipation effects are described by $Q_{k,V}^{-1}$ (refer to equation 2.151). Since $Q_{k,V} \propto \frac{c_s^2}{\omega_s} = \omega_s \lambda_s^2$ applies, and assuming, that the other terms describing $Q_{k,V}$ are constant, $Q_{k,V}$ increases with decreasing frequency. For the surface losses $Q_{k,s}^{-1}$, the situation is different. Referring to equation 2.152, $Q_{k,s} \propto \sqrt{\omega_s}$ applies and $Q_{k,s}$ increases with an increasing resonator radius r_{res} . According to the

results from table 5.7, the effect of a decreasing $Q_{k,s}$, due to a lower resonance frequency and a smaller resonator radius, exceeds the growth of $Q_{k,v}$, leading to a smaller Q-factor* for PAC2* and PAC1.

According to the results presented in section 5.2.5.4, the noise is hardly dependent on the background signal or optical power. Therefore, the different noise levels listed in table 5.7 rather originate from small fluctuations in the gas mixture or the flow rate.

Comparing the background signal from the measurements performed in the 2/2 and 2*/2 setup, the former one was determined to 15.8 μV and the latter one to 41.0 μV , respectively. The results demonstrate, that the system employing an FST had a significantly higher background signal. However, the background signal of the 2*/2* setup was only 23.0 μV although the optical power was significantly higher. The origin of the higher background signal from setup 2*/2 remains unclear but could be due to worse optical alignment. Light hitting the microphone membrane can be excluded since the resulting background signal would be frequency independent resulting in a higher background signal at frequencies far from the resonance frequency, which was not the case.

Comparing the sensitivity of the 2/2 and 2*/2 setup, the latter setup has a 19 % better performance although the Q-factor is smaller. This can be explained by referring to equation 2.134, which indicates that $p_a \propto Q$ and $p_a \propto r_{\text{res}}^{-2}$ apply. Since the Q-factor decreases by 18 % and the resonator radius decreases by 23 % an overall increase of about 40 % is calculated, if all other parameters remain constant[†]. The detected increase, however, is only 23 %. The main reason for less amplification is probably due to the greater length of the outcoupling channel, which describes the path from the inner wall of the resonator to the microphone membrane. Due to the thickness of the FST, the path is about 1/3 longer, probably causing the pressure wave to further diminish before reaching the microphone. This assumption is supported by comparing the results from 1/1 with 2*/1, since in both setups the diameter of the resonator is equal, the same LED is applied and the resonator length of PAC2* is larger, which should cause a higher sensitivity (refer to equation 2.134) in the 2*/1 configuration. However, the sensitivity of the 1/1 setup is 35 % higher, which is mainly attributed to the losses due to a longer outcoupling channel.

The sensitivity of the setup 2*/2 is 21 % lower than the sensitivity of the 2*/2* setup. This difference can be explained by the different optical output power of the two LEDs detected after the PAC, which is about 26 %.

The high sensitivity of the 2*/1 setup, however, is striking. Although, the optical power was only 14.4 % higher compared to the 2*/2* setup, its sensitivity is more than two times higher. There is only one explanation for that observation. The light of the 2*/1 setup is less collimated and a significantly lower share of the inci-

*Refer to section 2.5.1 for further information on the calculation and composition of the Q-factor.

[†]Since also $p_a \propto \omega^{-1}$ is valid and the frequency decreased by 2.7 %, the frequency drop would actually cause an even higher amplification.

dent light, illuminating the resonator, is expected to reach the sensor head of the powermeter due to scattering inside the resonator. According to section 5.1.2 the optical power detected before the measurement was almost six times higher than after PAC1 for LED1. The optical power of LED2* detected before the PAC was about two times higher compared to the optical power detected after the PAC2*, verifying this assumption and demonstrating, that the optical power detected at the end of a PAC is sometimes misleading. This further explains the comparably high background signal of 136 μV of system 2*/1, which is about six times higher than that of setup 2*/2*.

Summarizing the results, all approaches presented provide an LOD well below 100 ppbV and thus are sufficiently sensitive for breath acetone detection. Besides, the results show, that the implementation of a smooth surface resonator by means of an FST is certainly not worth the expenses. Based on the results, a measurement cell with a small resonator cross section and a short outcoupling channel is recommended for high sensitivity.

Concluding this subsection, a measurement series was performed employing the side illumination concept visualised in 5.16. Performing a frequency sweep and a calibration curve lead to quite unsatisfactory results, which are difficult to interpret. Several frequency sweeps and a calibration measurement demonstrated a signal decrease over time. No resonance frequency and no sensitivity could be derived from the resulting graphs. In addition, the noise was more than one order of magnitude higher compared to the other UV measurements and no reproducibility was given. A satisfying explanation for the results cannot be provided at this point. However, some error sources can be excluded. Gas was certainly flowing through the PAC and the microphone as well as the lock-in amplifier were operating properly, when the microphone was stimulated by means of an acoustic signal generator from a cell phone. The employed adhesive within this setup might provide an explanation for the drift due to interaction of the light with the glue itself or its outgassing components. Most likely, interaction between scattered light with the microphone and the FST cause this behavior. Re-thinking the design, a beam-dump behind the resonator instead of a reflective coating of the rear side of the tube could be one measure to significantly improve the system for further studies.

5.4 IR measurements

This section describes the photoacoustic acetone detection using IR light sources. It covers the first proof of concept measurements using an OPO (section 5.4.2) and addresses the high performance using ICL (section 5.4.4) and especially QCL (section 5.4.3) light sources. Finally, a calibration measurement for a gas mixture containing two analytes, namely acetone and methane, is presented and discussed considering the multicomponent analysis approach mentioned in section 3.2.7.

5.4.1 Experimental

The photoacoustic cells employed within this section have the same geometry like PAC1 presented in section 5.1.1, except for the resonator diameter, which is 4 mm. The 3D printed plastic material PAC employed during the OPO measurements will be referred to as PAC6 and has been described in [1] elaborately. The PAC applied within the measurements using the QCL is referred to as PAC3 using wedged ZnSe windows (WW80530-E3, Thorlabs GmbH, Munich, Germany) and PAC4 represents the measurement cell combined with the ICL light source containing sapphire windows (WG30530-E1, Thorlabs GmbH). The temperature of PAC3 and PAC4 were set to 45 °C and 25 °C, respectively. PAC6 could not be temperature controlled since it was made out of 3D plastic material and not aluminum, hence its temperature can be considered equal to room temperature, which was around 21 °C.

Each single point measurement contains 100 values and the acquisition rate of the LIA was 5 Hz. The roll-off of the LIA was 12 dB/octave for the OPO measurements and 18 dB/octave for the ICL and QCL measurements.

5.4.2 OPO measurements

In order to perform a frequency sweep to detect the resonance frequency of PAC6, the cell was filled with 50 ppmV of NO₂ diluted in N₂ and synthetic air, respectively. The flow rate was set to 500 mL/min and a blue laser diode for NO₂ detection was employed to perform the sweep measurement. Using this laser diode facilitated the frequency sweep measurement significantly, since the modulation frequency of the laser was more stable and easier to sweep compared to chopper modulation of the OPO emission. More information regarding the laser setup can be found elsewhere [1]. The frequency sweeps resulted in resonance frequencies of about 4155 Hz and 4090 Hz for NO₂ diluted in N₂ and synthetic air, respectively. Since only a trace gas amount of 50 ppmV of NO₂ was present in the cell, no shift of the resonance frequency is expected for similar trace gas amounts of acetone diluted in the same buffer media. If not mentioned otherwise, the LIA time constant was set to 2 s.

The OPO was used for calibration measurements, which were performed at a flow rate of 300 mL/min. In terms of these measurements, seven different acetone concentrations between 100 ppmV and 0 ppmV were set. The OPO emission wavelength was monitored by the spectrum analyzer and was constantly emitting at a wavenumber of $2972.6 \text{ cm}^{-1}\text{-vac}$. The attribute "vac" indicates that this is the wavenumber $\tilde{\nu}_{\text{vac}}$ propagating in vacuum. For the respective wavenumber in air $\tilde{\nu}_{\text{air}}$, the wavenumber has to be divided by the refractive index of dry air $n_{\text{r,air}}$.

$$\tilde{\nu}_{\text{air}} = \frac{\tilde{\nu}_{\text{vac}}}{n_{\text{r,air}}} \quad (5.16)$$

With $n_{\text{r,air}}$ being about 1.00028, the emitted wavenumber in air is 2971.8 cm^{-1} . The absorption cross section of acetone at this wavenumber is about $7.8 \times 10^{-20} \text{ cm}^2$. The calibration measurements are summarised in table 5.8. The normalised sensitivity describes the slope of the calibration curve for each measurement point being divided by its corresponding optical power value.

Tab. 5.8. Summary of the OPO measurements. Further information is provided in the text.

Buffer gas	Sensitivity in $\mu\text{V/ppmV}$	Noise (3σ) in μV	Norm. sens. in $\frac{\mu\text{V}}{\text{ppmV mW}}$	LOD (3σ) in ppmV
N_2	14.0	11.0	0.222	0.78
Synthetic air	24.2	35.0	0.220	1.45

The results of table 5.8 demonstrate, that the high fluctuations in the output power of the OPO cause different sensitivities and normalisation of the acquired signal regarding the optical power is mandatory for comparison. In addition, the noise is about three orders of magnitude higher compared to the results employing a UV LED. The next paragraph addresses this issue. The normalised sensitivity presented in table 5.8, however, shows that the sensitivity of the sensor is not influenced by the buffer gas, which was the case in the UV measurements. Besides, the normalised sensitivity indicates, how much optical power is necessary to reach a certain LOD, if the noise level is known. For an ACS of about $7.8 \times 10^{-20} \text{ cm}^2$ the corresponding normalised sensitivity in synthetic air was determined to $0.220 \frac{\mu\text{V}}{\text{ppmV mW}}$. For a noise level of $0.1 \mu\text{V}$ (3σ) and an LOD of 0.1 ppmV a necessary optical power of 4.55 mW is obtained. In analogy, for an ACS of about $5.2 \times 10^{-20} \text{ cm}^2$ around 3024 cm^{-1} requires an average optical power of 6.8 mW , if all other parameters remain constant.

In order to determine the source of the high noise level, further tests were performed. After an optimisation of the beam alignment, the noise could be reduced significantly to $1.91 \mu\text{V}$ (3σ). Using the OPO, the noise due to interactions between laser light and walls was stronger compared to stable light sources, since the high fluctuations

of the laser power caused the background signal to oscillate, too. Furthermore, the contribution of the chopper to the noise signal was significant. Even when the OPO light was switched off, the noise introduced by the chopper was up to several microvolts and was varying strongly over time. After switching off the chopper, too, the noise dropped to 240 nV (3σ). The remaining noise probably originated from the intrinsic noise of the microphone and noise introduced by the flowing gas within the cell.

Summarizing, the OPO provides a viable tool for proof of concept measurements. Based on these results, an estimation regarding the necessary optical power for a target LOD was possible. In addition, the results demonstrate no difference in the sensitivity between acetone measurements with N_2 or synthetic air as dilution medium. This gives rise to the assumption, that VT-relaxation lifetimes of vibrational excited acetone molecules are less dependent on the buffer gas and no VV energy transfer towards N_2 and O_2 occur at the employed wavenumber. Based on the high normalised sensitivity of the system, it can be assumed, that the nonradiative lifetime of excited acetone fulfils the requirement of equation 2.77 with a modulation frequency of 5 kHz at around 2971.8 cm^{-1} .

5.4.3 QCL measurements

The measurements presented within this section have been performed by Florian Feldmeier. However, each measurement as well as the evaluation and interpretation of the measurement results have been realised in close consultation with the author.

As a first step, the laser emission was characterised by means of the spectrum analyzer. Figure 5.18 visualises the calibration curves indicating the tuneability of the laser by the current. The tuneability by means of the input current depends on the temperature and is about 0.049 nm mA^{-1} at 22°C and increases steadily towards 0.063 nm mA^{-1} at 50°C with an overall average of 0.058 nm mA^{-1} . The tuneability by means of the temperature is specified to 0.78 nm K^{-1} at 350 mA and increases steadily towards 0.85 nm K^{-1} at 530 mA. The average tuneability by temperature is 0.82 nm K^{-1} . Combining the temperature and current tuning capability results in an emission range of about 35.8 nm from 8266.8 nm to 8302.6 nm, which corresponds to the wavenumber range from 1204.4 cm^{-1} to 1209.7 cm^{-1} , covering the whole region of interest defined in section 3.2.6. τ_{LIA} was set to 2 s during the sweeps and to 10 s during the calibration measurements.

Table 5.9 provides the results of the frequency sweep and calibration curves from the QCL measurements. In terms of the sweep measurements, the laser was set to 25°C and 420 mA at the high phase of the duty cycle and to 300 mA at the low phase of the duty cycle. The 300 mA laser current represents the threshold current of the QCL at 25°C . The flow rate was set to 500 mL/min and the acetone concentration was 10 ppmV.

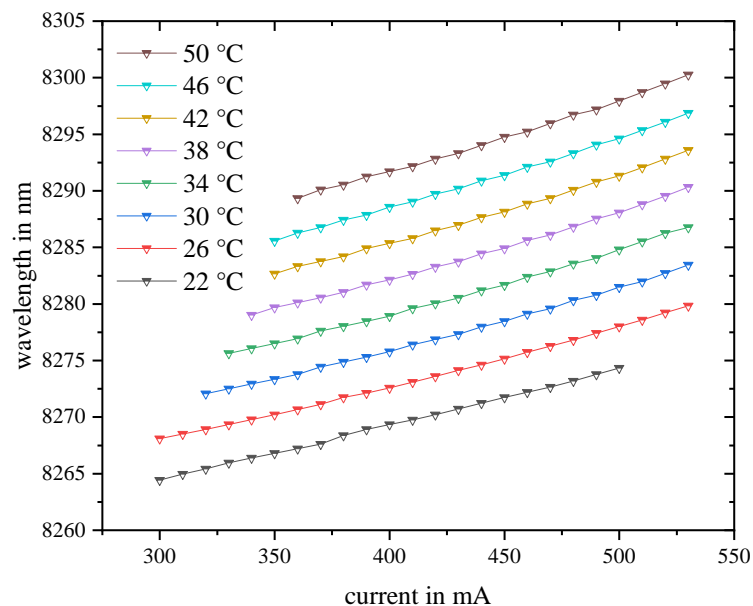


Fig. 5.18. Characterisation of the QCL emission tuneability in cw-mode.

The sensitivity of both systems is quite similar demonstrating again, that the O₂ and N₂ content within the buffer gas has less influence on the photoacoustic signal in the IR compared to the UV region. The Q-factor for the sweeps in N₂ and synthetic air are equal as well, which was expected. The high sensitivity and the resulting LOD is remarkable. This is mainly due to a higher optical power and a higher ACS. The exact ACS could not be determined, since the emission wavelength at 50 % duty cycle is probably lower compared to 100 % duty cycle (cw-mode), as the average temperature within the QCL chip is lower.

Tab. 5.9. Summary of the QCL measurement results at a laser temperature of 25 °C and at a laser current of 420 mA and 520 mA for the sweep and the calibration measurement, respectively.

Buffer gas	f_{res} in Hz	Q	Noise (3σ) in nV	Sensitivity in $\mu\text{V/ppmV}$	LOD (3σ) in ppbV	P_0 in mW
N ₂	5200	20.3	65	82.9	0.79	98.8
Syn. air	5129	20.1	76	83.2	0.92	97.5

However, the ACS is expected to be around $2.4 \times 10^{-19} \text{ cm}^2$ and is thus five times higher than the ACS at 278 nm or at 3024 cm^{-1} , which is about $5.0 \times 10^{-20} \text{ cm}^2$. Furthermore, the small resonator cross section leads to a higher acoustical amplification as well. The higher noise compared to the UV LED measurements is attributed to the insufficient flushing duration prior to the detection of the noise level in pure buffer medium. Since the sensitivity of the QCL setup is extremely high, even minor fluctuations of the acetone concentration within the PAC due to residing acetone molecules, contribute to a higher noise level. Hence, a significant improvement of the noise level is expected if a longer flushing period is applied.

Unfortunately, the QCL stopped working after the calibration measurements due to internal chip damage, preventing further studies regarding multicomponent analysis. However, the results from the QCL demonstrate once more the excellent sensitivity provided by photoacoustic spectroscopy. Moreover, the results presented within this subsection provide a good basis for further studies towards acetone detection in human breath.

5.4.4 ICL measurements

The ICL wavelength characterisation presented in this section has been performed by Viktor Weingardt in close consultation with the author. All further measurement results presented within this section have been acquired by the author.

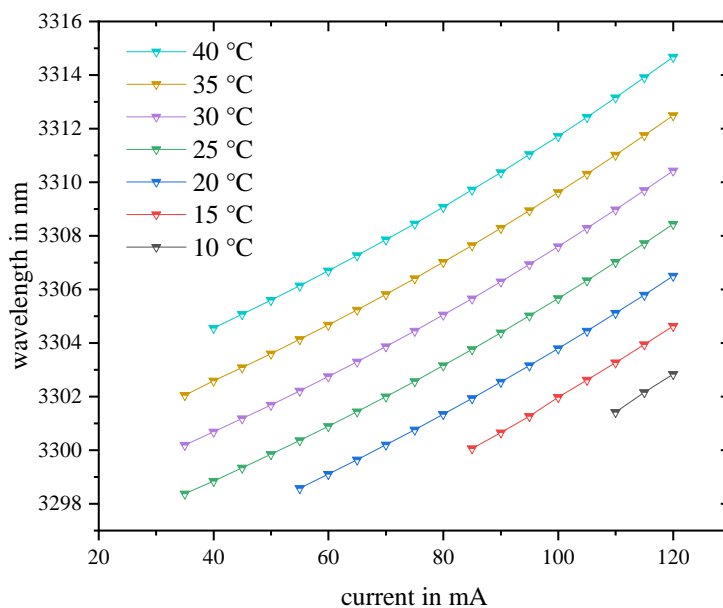


Fig. 5.19. Characterisation of the ICL emission tuneability in cw-mode.

Tab. 5.10. Summary of the ICL measurement results with an optical output power of about 6.2 mW.

Buffer gas	f_{res} in Hz	Q	Noise (3σ) in nV	Sensitivity in $\mu\text{V/ppmV}$	LOD (3σ) in ppbV	P_0 in mW
N ₂	5089	22.2	17	1.2	14.2	6.2

Figure 5.19 presents the characterisation of the ICL in cw-mode. Exploiting both, its tuneability by temperature and current, results in an overall tuning range of 16.3 nm between 3298.4 nm – 3314.7 nm. The corresponding wavenumber range is thus from 3016.9 cm⁻¹ – 3031.8 cm⁻¹ covering the wavenumber region around 3024 cm⁻¹, where low spectral interference is expected according to section 3.2.6.

Since no difference of the sensitivity of the photoacoustic system regarding the buffer gas was detected in section 5.4.2, the frequency sweep and calibration measurements were performed in N₂. The flow rate was set to 300 mL/min for both, the calibration and the frequency sweep measurement. 10 ppmV of acetone diluted in N₂ were set in terms of the frequency sweep measurement. τ_{LIA} was set to 2 s and 10 s for the frequency sweep and the calibration curve measurements, respectively. The laser was temperature controlled at 25 °C and supplied with 108 mA at the high level of the duty cycle and with 28 mA at the low level of the duty cycle since the threshold current of the ICL is stated to be approximately 31 mA according to the datasheet (refer to C.3). The key performance parameters of the photoacoustic ICL characterisation results are presented in table 5.10.

Comparing the ICL results with the QCL measurements, the ICL setup shows a higher Q-factor, which is likely due to the lower PAC temperature and the concomitant lower resonance frequency. The relation between Q-factor and PAC temperature was already addressed in section 5.2.5.1. Although the optical power and the sensitivity of the system are quite low, the LOD is excellent due to the extremely low noise. Since the maximum laser current is specified to 120 mA, LODs below 10 ppbV are accessible using this setup. Moreover, since ICLs for this wavelength region are still in the early development stage, light sources with higher output power will be available in the near future, further increasing the performance of photoacoustic systems employing such emitters.

Concluding this section, figure 5.20 visualises a typical photoacoustically detected spectrum. Since the optical output power of the laser varies during current tuning, the acquired photoacoustic signal has to be normalised. This is achieved by dividing one measurement point with its corresponding optical power and multiplying the result by the average optical output power of the laser within one current sweep.

Three measurements have been performed. One containing only 10 ppmV of acetone (red) and one with 10 ppmV methane (blue), both analytes were diluted in N₂. The

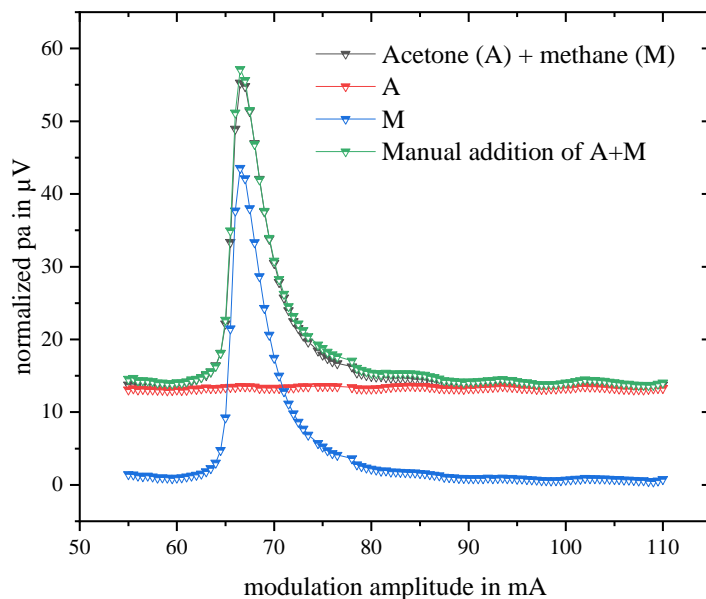


Fig. 5.20. Photoacoustic spectrum 10ppmV of acetone (A) and methane (M) diluted in N_2 . The green line represents the manually added single component measurements.

gas mixture of the third measurement contained 10ppmV of both analytes (black). The green curve represents the manual addition of the red and blue curve. The curves represent the response R_{ni} discussed in section 3.2.7. These responses have to be collected for all molecules causing spectral interference.

The green and the black curve show a quite good agreement demonstrating the potential of tuneable photoacoustic spectroscopy regarding multicomponent analysis. Considering a later application, a complete current sweep as indicated in figure 5.20 is rather not applicable due to the high duration. Applying a LIA time constant of 2s and a current increment of 0.5mA, one sweep lasted two and a half hours. Therefore, a simulation similar to the one discussed in 3.2.7, but based on the collected photoacoustic spectra, is necessary in order to identify suitable wavelengths for multicomponent analysis, reducing the overall amount of measurement points significantly.

Although the first measurements provide promising results, further studies will be necessary to determine the applicability of this approach regarding multicomponent analysis of exhaled breath, in order to determine breath acetone or further components of interest. Especially recalibration of the system might be quite elaborate, thus a high reproducibility and long term stability of the system is required, in particular, if applied in clinical environment.

References

- [1] T. Rück et al. “Low-cost photoacoustic NO₂ trace gas monitoring at the pptV-level”. In: *Sensors and Actuators A: Physical* 263.2 (2017), pp. 501–509. ISSN: 09244247. DOI: 10.1016/j.sna.2017.06.036 (cit. on p. 244).

5.5 Comparison of the photoacoustic systems

Concluding the results chapter, a comparison of most of the systems presented within this thesis have been summarised in table 5.11 based on their LODs and NNEA coefficients. As mentioned in the introduction of this thesis, the NNEA coefficient is a good measure for comparing the performance of different photoacoustic sensor systems.

The NNEA coefficients are calculated after equation 5.8. Determining the optical power within the PAC and its resonator during a measurement correctly is quite difficult, especially for the LEDs. For the ICL and QCL, the overall loss of optical power due to traveling through the PAC, was determined to about 55 % and 20 %, respectively. The dissipation of the QCL beam intensity can be attributed to losses at the windows. Thus the optical power within the PAC is estimated to be 111.2 mW. The losses of the ICL, however, are too high to be completely assigned to absorptions or reflections at the windows. According to the manufacturer, approximately 95 % of the light is transmitted per window. Thus, the optical power within PAC3 is estimated to be 13.1 mW. Contrary to the approach used in section 5.1.4.5 to calculate the NNEA coefficient, the optical power within the LED setup 1/1 is estimated to be 60 mW, accounting for light intensity losses at the first window and within the first buffer volume of PAC1. For the combination 2*/1 an optical power of 54 mW is assumed, since a degradation of the LED of about 10 % was detected. For the setup employing LED2*, the average optical power within the PAC is estimated to 20 mW.

The ACS for the UV and ICL measurements is $5 \times 10^{-20} \text{ cm}^2$, while for the QCL measurement it is specified to $2.4 \times 10^{-19} \text{ cm}^2$. The molar volume is $26\,094 \text{ cm}^3 \text{ mol}^{-1}$ (1 atm and 318 K) for all measurements except for the ICL measurement, where the PAC was at 25 °C resulting in a molar volume of $24\,453 \text{ cm}^3 \text{ mol}^{-1}$. To distinguish between the different setups, the same approach from table 5.7 was applied. Thus, the setup 1/1 describes PAC1 combined with LED1 and so on.

The ENBW for the QCL and ICL are $0.01375 \sqrt{\text{Hz}}$ and for the two UV LED setups applying PAC2* the ENBW is $0.017 \sqrt{\text{Hz}}$. The ENBW values for 1/1 in N₂ and synthetic air are $0.025 \sqrt{\text{Hz}}$ and for the measurements in typical breath mixtures, it was $0.017 \sqrt{\text{Hz}}$. Further ENBW values for different LIA settings can be found in the appendix A.5.

All presented NNEA coefficients from table 5.11 indicate a quite good performance compared to other optical sensor systems described in literature (refer to the references provided in the introduction of this thesis). The performance of the ICL is superior to the others, which is mainly attributed to the extremely low noise level present during the measurements. The lower noise level is likely due to the new microphone of the type ICS-40730, being specified with a lower noise floor (refer to section 4.1.2) and a higher LIA roll-off. The comparably high noise level of the QCL, employing the same ICS-40730 microphone, was discussed before. Therefore, a bet-

ter LOD and as a consequence, a better NNEA coefficient is expected to be achieved using the QCL setup and flushing the PAC properly prior to the blank value detection. The NNEA coefficients of the UV system are about two times worse than the coefficient of the ICL setup. However, the estimation of the optical power used for the NNEA coefficient calculation might have been disfavoured for the LEDs.

Tab. 5.11. Comparison of the normalised noise equivalent absorption coefficients of the employed PAC systems. The different systems are titled using the PAC/LED notation.

	1/1	1/1	1/1	2*/1	2*/2*	3/QCL	4/ICL
Buffer gas	N ₂	syn. air	breath*	syn. air	syn. air	N ₂	N ₂
LOD (3σ) in ppbV	80.9	19.6	12.5	27.9	51	0.79	14.2
NNEA in $\frac{W}{cm\sqrt{Hz}} \times 10^{-8}$	7.47	1.81	1.70	3.41	2.39	1.18	0.56

A final conclusion, specifying if the UV LED or tuneable laser approach is more promising cannot be made at this point since it depends on the later application. In view of the system's sensitivity, especially the high power QCL provides an LOD, superior to the one of LED2. Using UV LEDs, however, decreases the susceptibility towards spectral interferences within breath acetone detection significantly. Furthermore, on the one hand, the cost of the UV LED is expected to be about one order of magnitude lower than the cost of the ICL or QCL system. On the other hand, according to the manufacturers, the lifetime is about 2000 h and 20 000 h for the Bolb LEDs and ICL, respectively[†]. Since the UV LEDs have only recently appeared on the market, significantly performance increase regarding lifetime and output power can be expected in the next years. Due to their ability to be tuned over a wide wavenumber range, ICLs and QCLs provide the opportunity of multicomponent analysis, which can legitimate a higher price and opens up new possibilities. Summarizing, the results of this work present a good basis for further research, which is necessary in order to provide a reliable tool for breath acetone detection in the clinical environment. If a low cost sensor with less sensitivity is sufficient, the approach using the UV LED is more suitable, but for a sensor, which has to be able to measure several components in breath with high precision, an ICL or a QCL should be used.

*In mixtures typical for breath. For a detailed description of the composition of gas refer to section 5.2.6.4.

[†]For the QCL, no lifetime was provided by the manufacturer, but it is estimated to be similar to the ICLs lifetime according to nanoplus.

Chapter 6

Summary

The breath analysis section of this thesis outlines the potentials but also emphasises the concomitant challenges of human breath analysis. The section further describes the usefulness of a point-of-care (POC) device for breath acetone detection. In addition, it covers various breath analysis related subjects, which can be useful considering further developments of breath analysers. This includes an extensive summary involving the high abundant endogenous as well as the exogenous breath species present in a clinical environment.

Subsequently, a detailed discussion about the theoretical aspects of absorption spectra is provided, forming the basis for the spectral interference chapter. Classical absorption spectroscopy (AS) is compared with photoacoustic spectroscopy (PAS) in view of trace gas analysis. Different modulation schemes for signal generation, i.e. amplitude modulation (AM) and wavelength modulation (WM) are part of the comparison, while the advantages and disadvantages of each technique are highlighted. As a result, PAS is considered superior to AS and hence is selected as the method of choice regarding the development of a sensor for breath acetone detection.

A detailed mathematical derivation of the photoacoustic signal generation as well as the signal enhancement by means of acoustic resonance amplification is provided. Moreover, several phenomena causing signal attenuation are outlined, including vibrational-translational (VT) relaxation, vibrational-vibrational (VV) energy transfer mechanism, acoustic detuning and photodissociation.

Various simulations regarding spectral interferences in the infra-red (IR) and ultra-violet (UV) region are presented, demonstrating the susceptibility towards spectral cross-sensitivities in the IR region, hence, rather suggesting the UV region for acetone detection. However, this simulation can be easily adopted to other target analytes and serves as a basis for multicomponent analysis approaches in the IR region using tuneable light sources.

Ultra sensitive acetone detection employing a high power UV LED is presented and a detailed analysis considering the effects of environmental parameters onto the pho-

toacoustic signal, including temperature, pressure, LED duty cycle and flow rate, is provided. In addition, general cross-sensitivities of the photoacoustic signal towards the high abundant species O_2 , CO_2 and H_2O have been investigated and discussed. Moreover, several LED and photoacoustic cell (PAC) combinations have been compared in order to evaluate improvement approaches regarding an enhancement of the system's sensitivity.

Finally, photoacoustic sensor setups employing an interband cascade laser (ICL) or a quantum cascade laser (QCL) have been studied and compared to various UV setups in view of different key performance parameters, including the limits of detection (LOD) and the normalised noise equivalent absorption (NNEA) coefficients. The juxtaposition of the different approaches once more emphasises the extraordinary sensitivity of photoacoustic spectroscopy. To the best of the author's knowledge, the LODs (3σ) of the UV LED based photoacoustic measurement in typical breath conditions (12.5 ppbV) and the LOD of the QCL measurement (0.79 ppbV) provide two world records. First, regarding photoacoustic acetone detection using an UV LED and second, in view of other published results for photoacoustic acetone detection in general.

Chapter 7

Zusammenfassung in deutscher Sprache

Zu Beginn der Arbeit werden zum einen die Potentiale der Analyse des menschlichen Ausatemgases aufgezeigt und zum anderen die damit verbundenen Herausforderungen beschrieben. Dabei wird auch die Nützlichkeit eines Point-of-Care (POC) Gerätes zur Bestimmung des Acetongehalts im Ausatemgas hervorgehoben. Darüber hinaus werden verschiedene mit der Atemgasanalyse zusammenhängende Themen behandelt, die hinsichtlich weiterer Entwicklungen von Atemgasanalysegeräten sehr hilfreich sein können. Dazu gehört u. a. eine ausführliche Analyse der Zusammensetzung des menschlichen Ausatemgases, die sowohl die hauptsächlichen endogenen als auch die im klinischen Umfeld verstärkt vorkommenden, exogenen Bestandteile, auflistet.

Anschließend werden die theoretischen Grundlagen von Absorptionsspektren detailliert behandelt, da sie die Grundlage für das Kapitel über die spektralen Interferenzen bilden. Des Weiteren werden die klassische Absorptionsspektroskopie (AS), als auch die photoakustische Spektroskopie (PAS), hinsichtlich ihrer Eignung für die Spurengasanalytik verglichen. Verschiedene Modulationsschemata für die Signalerzeugung, d. h. Amplitudenmodulation (AM) und Wellenlängenmodulation (WM), sind Teil des Vergleichs, wobei die Vor- und Nachteile jeder Technik hervorgehoben werden. Als Ergebnis wurde die PAS gegenüber der AS als überlegen angesehen und daher als Methode der Wahl bei der Entwicklung eines Sensors zur Bestimmung des Acetongehalts in der Ausatemluft ausgewählt.

Eine detaillierte mathematische Herleitung der photoakustischen Signalerzeugung sowie der Signalverstärkung mittels akustischer Resonanzverstärkung ist ebenso in der Arbeit enthalten. Darüber hinaus werden mehrere Phänomene der Signaldämpfung skizziert, dazu zählen u. a. die Schwingungs-Translation Relaxation, der Schwingungs-Schwingungs Energieübertragungsmechanismus, die Photodissoziation und die akustische Resonanzverschiebung.

Es werden verschiedene Simulationen bezüglich spektraler Interferenzen im infraroten (IR) und ultravioletten (UV) Wellenlängenbereich vorgestellt, die die Anfälligkeit gegenüber spektralen Querempfindlichkeiten im IR-Bereich demonstrieren und somit eher den UV-Bereich für die Acetonbestimmung nahelegen. Die Simulationsergebnisse können leicht auf weitere Zielanalyten übertragen werden und dienen somit als Grundlage für Multikomponenten-Analyseansätze im IR-Bereich mittels durchstimmbarer Lichtquellen.

Im Ergebnisteil wird u. a. ein hochempfindliches System zur Acetondetektion unter Verwendung einer Hochleistungs-UV LED vorgestellt. Dieses System wurde außerdem einer detaillierten Analyse unter Berücksichtigung der Auswirkungen von Umgebungsparametern auf das photoakustische Signal, einschließlich Temperatur, Druck, LED-Tastverhältnis und Durchflussrate, unterzogen. Zusätzlich wurden Querempfindlichkeiten des photoakustischen Systems gegenüber den im Ausatemgas hochkonzentrierten Stoffen O_2 , CO_2 und H_2O untersucht und die Ergebnisse diskutiert. Darüber hinaus wurden verschiedene Kombinationen von LEDs und photoakustischen Zellen verglichen, um Verbesserungsansätze hinsichtlich der Empfindlichkeit des Systems zu untersuchen.

Abschließend wurden photoakustische Sensorsysteme, die einen Interbandkaskadenlaser (ICL) oder einen Quantenkaskadenlaser (QCL) verwenden, untersucht und mit verschiedenen UV LED Systemen im Hinblick auf unterschiedliche Leistungsparameter, einschließlich der Nachweisgrenzen (NWG) und den normierten, rauschäquivalenten Absorptionskoeffizienten, verglichen. Die Gegenüberstellung der verschiedenen Ansätze unterstreicht einmal mehr die außerordentliche Empfindlichkeit der photoakustischen Spektroskopie. Nach bestem Wissen des Autors stellen die NWGs (3σ) der photoakustischen Messung mit einer UV LED in typischer Atemgaszusammensetzung (12.5 ppbV) und die NWG der QCL-Messungen (0.79 ppbV) zwei Weltrekorde dar. Zum einen gibt es keine Veröffentlichung hinsichtlich einer besseren, photoakustisch ermittelten NWG für Aceton mittels einer UV LED und zum anderen stellt die mit dem QCL photoakustisch gemessene NWG im Allgemeinen die beste, je veröffentlichte photoakustische NWG für Aceton dar.

Appendices

A Miscellaneous

A.1 Acoustic modes and Bessel function

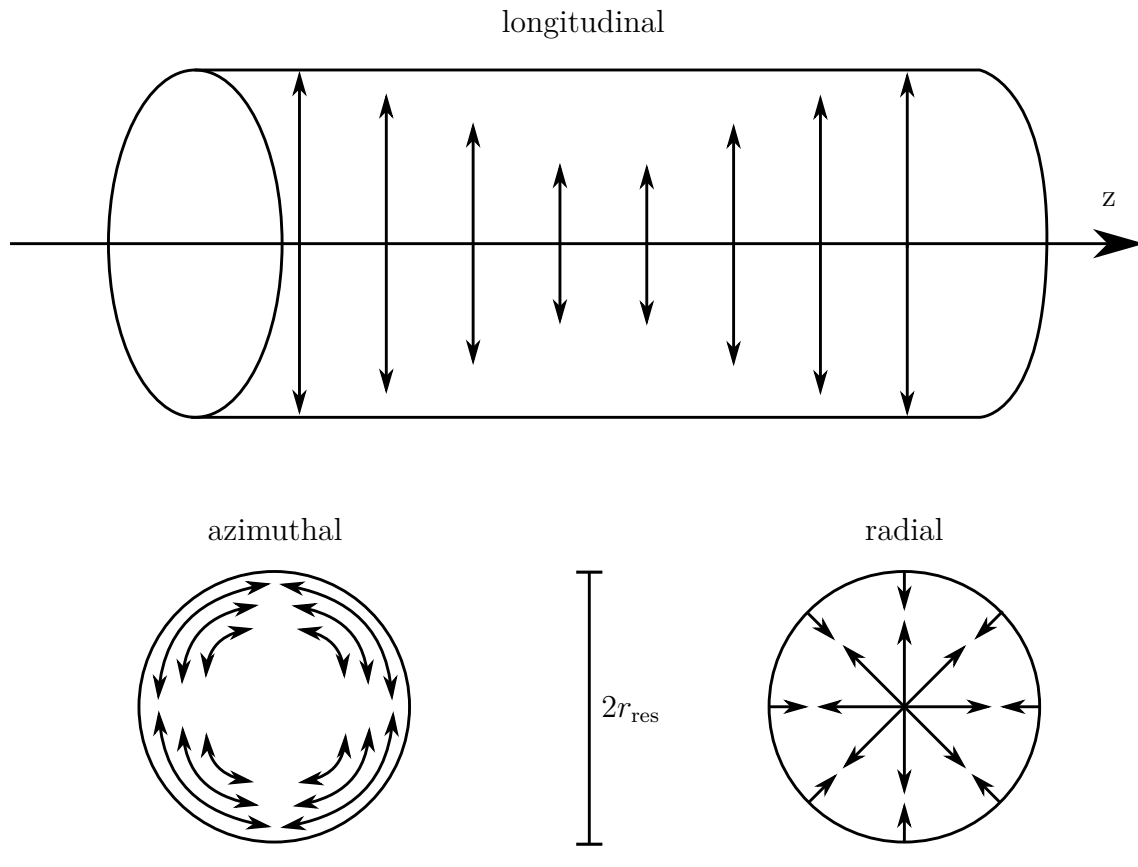


Fig. A1. Schematic of the longitudinal, radial and azimuthal acoustic modes in a cylindrical acoustic resonator. Arrows represent the particle displacement.

Tab. A1. Values of $\pi\alpha_{\hat{u}\hat{v}}$ for some of the first radial (index \hat{u}) and azimuthal (index \hat{v}) modes of a cylindrical acoustic resonator.

$\pi\alpha_{\hat{u}\hat{v}}$	$\hat{v} = 0$	$\hat{v} = 1$	$\hat{v} = 2$	$\hat{v} = 3$
$\hat{u} = 0$	0	3.832	7.016	10.173
$\hat{u} = 1$	1.841	5.331	8.526	11.706
$\hat{u} = 2$	3.054	6.706	9.969	13.170
$\hat{u} = 3$	4.201	8.015	11.346	14.586

A.2 Relations between different types of viscosities

Since in literature different symbols and terms are presented to described the different types of viscosities, the following equations shall shed some light onto these ambiguities.

The general relation between dynamic viscosity η_d , sometimes referred to as absolute viscosity, to the kinematic viscosity μ_k is

$$\eta_d = \mu_k \tilde{\rho}_e$$

Furthermore, it applies that

$$\mu_k = \frac{4\eta_s}{3\tilde{\rho}_e} + \frac{\eta_b}{\tilde{\rho}_e}$$

where η_s is the shear viscosity and η_b the bulk viscosity, sometimes also referred to as effective viscosity, respectively. The latter equation therefore proofs, that

$$\eta_d = \frac{4}{3}\eta_s + \eta_b$$

is valid.

A.3 Photodissociation quantum yield parameter

Parameter 0:

$$A_0 = \left[\frac{a_0}{1 - a_0} \right] \exp [b_0 (\lambda_{ph} - 248)]$$

$$a_0 = (0.350 \pm 0.003) \left(\frac{T}{295} \right)^{-1.28 \pm 0.03}$$

$$b_0 = (0.068 \pm 0.002) \left(\frac{T}{295} \right)^{-2.65 \pm 0.20}$$

Parameter 1:

$$A_1 = a_1 \cdot \exp \left[-b_1 \left(\frac{10^7}{\lambda_{ph}} - 33113 \right) \right]$$

$$a_1 = (1.600 \pm 0.032) \times 10^{-19} \left(\frac{T}{295} \right)^{-2.38 \pm 0.08}$$

$$b_1 = (0.55 \pm 0.02) \times 10^{-3} \left(\frac{T}{295} \right)^{-3.19 \pm 0.13}$$

Parameter 2:

$$A_2 = a_2 \cdot \exp \left[-b_2 \left(\frac{10^7}{\lambda_{ph}} - 30488 \right) \right]$$

$$a_2 = (1.62 \pm 0.06) \times 10^{-17} \left(\frac{T}{295} \right)^{-10.03 \pm 0.20}$$

$$b_2 = (1.79 \pm 0.02) \times 10^{-3} \left(\frac{T}{295} \right)^{-1.364 \pm 0.036}$$

Parameter 3:

$$A_3 = a_3 \cdot \exp \left[-b_3 \left(\frac{10^7}{\lambda_{\text{ph}}} - c_3 \right) \right]$$

$$a_3 = (26.29 \pm 0.88) \left(\frac{T}{295} \right)^{-6.59 \pm 0.23}$$

$$b_3 = (5.72 \pm 0.20) \times 10^{-7} \left(\frac{T}{295} \right)^{-2.93 \pm 0.09}$$

$$c_3 = (30006 \pm 41) \left(\frac{T}{295} \right)^{-0.064 \pm 0.004}$$

Parameter 4:

$$A_4 = a_4 \cdot \exp \left[-b_4 \left(\frac{10^7}{\lambda_{\text{ph}}} - 30488 \right) \right]$$

$$a_4 = (1.67 \pm 0.14) \times 10^{-15} \left(\frac{T}{295} \right)^{-7.25 \pm 0.54}$$

$$b_4 = (2.08 \pm 0.02) \times 10^{-3} \left(\frac{T}{295} \right)^{-1.16 \pm 0.15}$$

A.4 Simulation parameter

Tab. A2. Simulation parameter for the *MolExplorer* and *HITRAN on the Web* simulations. H₂O was simulated using *MolExplorer* and CO₂ was simulated exploiting *HITRAN on the Web*.

Parameter	Molecule	
	H ₂ O	CO ₂
Wavenumber	500 – 5700 cm ⁻¹	500 – 5000 cm ⁻¹
Temperature	296 K	296 K
Total pressure	1013 mbar	1013 mbar
Partial pressure analyte	0.000 101 3 mbar	1013 mbar
Partial pressure N ₂	1013 mbar	-
Profile	Lorentz	Voigt

A.5 Equivalent noise bandwidth (ENBW)

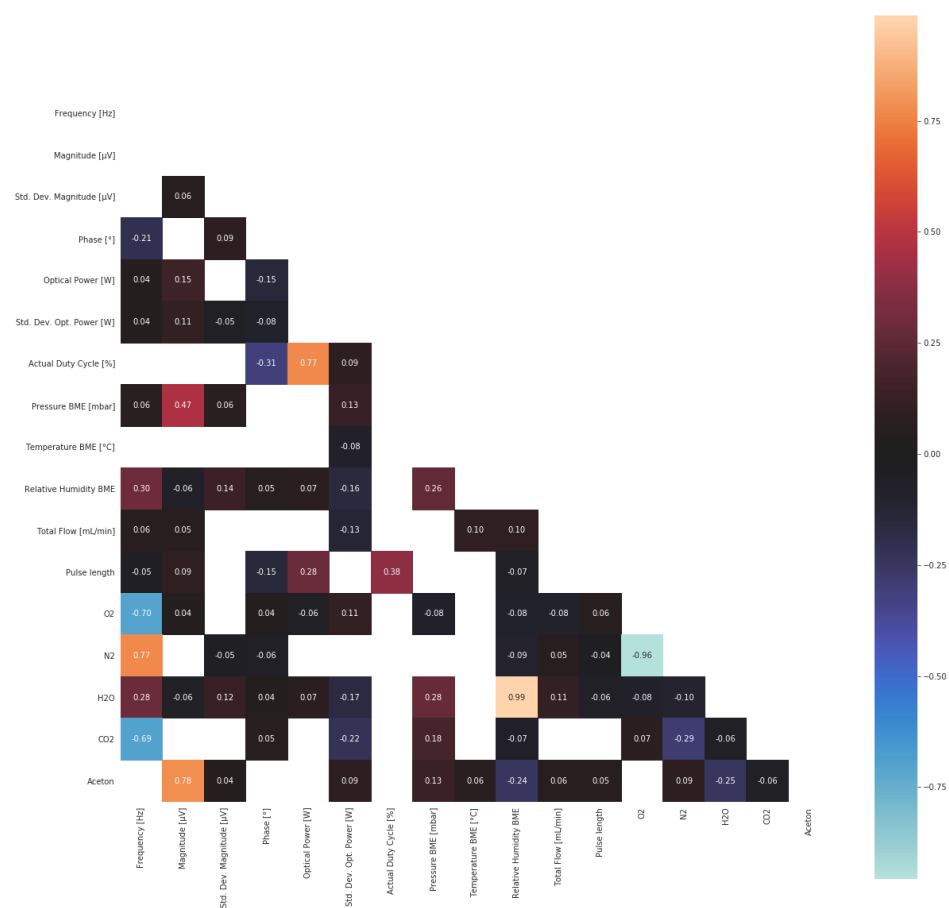
Tab. A3. Equivalent noise bandwidth for different time constants and filter slopes provided by the manufacturer of the lock-in amplifier.

τ_{LIA}	ENBW for different filter slopes in $\sqrt{\text{Hz}}$			
	6 dB/octave	12 dB/octave	18 dB/octave	24 dB/octave
5 ms	50	37.5	31.25	27.35
10 ms	25	17.2	14.15	12.35
20 ms	12.5	8.3375	6.875	5.9875
50 ms	5	3.335	2.75	2.395
100 ms	2.5	1.6675	1.375	1.1975
200 ms	1.25	0.83375	0.6875	0.5978
500 ms	0.5	0.3335	0.275	0.2395
1 s	0.25	0.16675	0.1375	0.11975
2 s	0.125	0.083375	0.06875	0.059875
5 s	0.05	0.0335	0.0275	0.02395
10 s	0.025	0.016675	0.01375	0.011975

B Supplement to the datasets

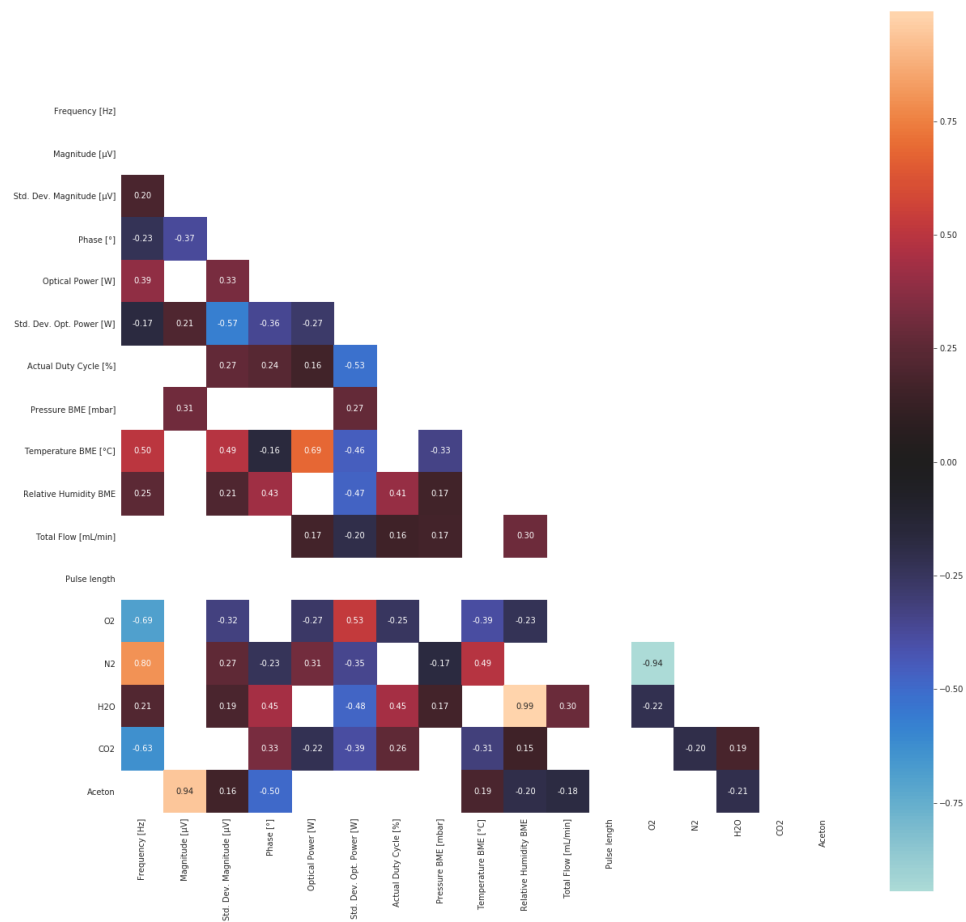
Full correlation matrix (SPM dataset)

The full pearson correlation matrix of the SPM dataset. Only correlations with a two tailed t-value below 0.01 are shown.



Full correlation matrix (RES dataset)

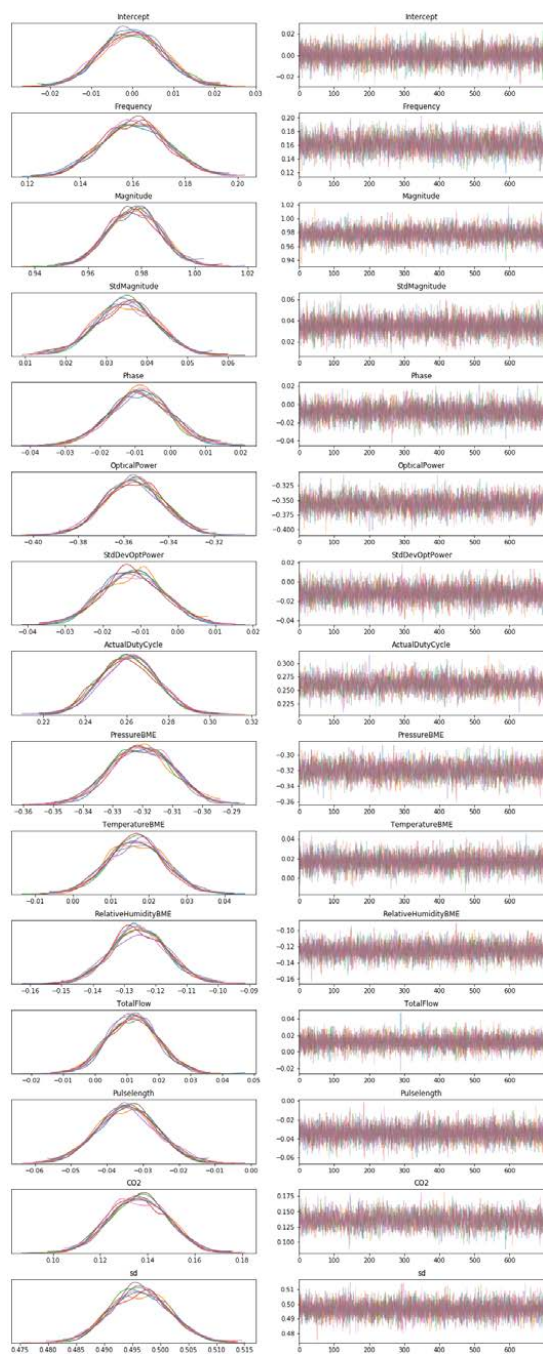
The full pearson correlation matrix of the RES dataset. Only correlations with a two tailed t-value below 0.01 are shown.



Traceplot (SPM dataset)

The traceplot of the Monte Carlo Sampling Routine after fitting the linear model on the SPM dataset.

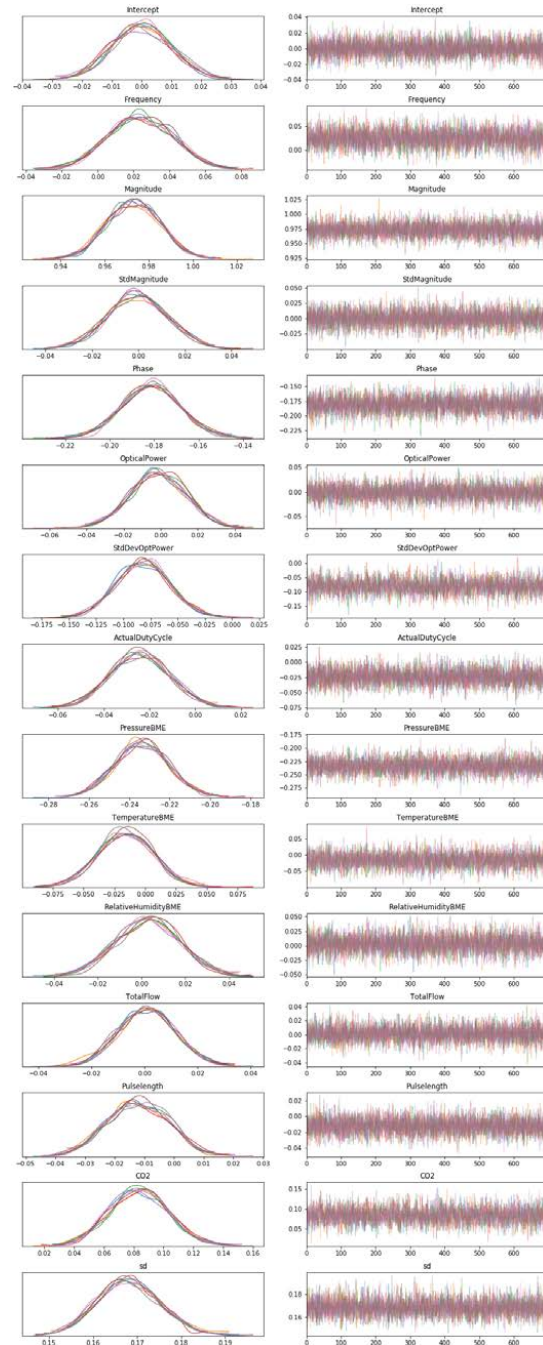
The first field indicates the distribution obtained during 8 runs using 700 samples each. The width of the distribution corresponds to the certainty associated with this parameters influence. The second field shows all samples in temporal order. Here a uniform distribution can be observed which shows, that all runs converged.



Traceplot (RES dataset)

The traceplot of the Monte Carlo Sampling Routine after fitting the linear model on the RES dataset.

The first field indicates the distribution obtained during 8 runs using 700 samples each. The width of the distribution corresponds to the certainty associated with this parameters influence. The second field shows all samples in temporal order. Here a uniform distribution can be observed which shows, that all runs converged.



Resulting bayesian linear model on all datapoints (SPM)

The feature coefficients correspond to the mean of the Gaussian distributions which can be found in the traceplots.

$$\begin{aligned} \text{Aceton} \sim & 0.16 \text{ Frequency} + 0.98 \text{ Magnitude} + 0.03 \text{ Std. Magnitude} - 0.01 \text{ Phase} - 0.36 \text{ Optical Power} - 0.01 \text{ Std. Dev. Opt. Power} \\ & + 0.26 \text{ Actual Duty Cycle} - 0.32 \text{ Pressure BME} + 0.02 \text{ Temperature BME} - 0.13 \text{ Relative Humidity BME} + 0.01 \text{ Total Flow} \\ & - 0.03 \text{ Pulse Length} + 0.14 \text{ CO}_2 \end{aligned}$$

Resulting Bayesian linear model on resonance data only (RES)

The feature coefficients correspond to the mean of the Gaussian distributions which can be found in the traceplots.

$$\begin{aligned} \text{Aceton} \sim & 0.02 \text{ Frequency} + 0.97 \text{ Magnitude} - 0.18 \text{ Phase} - 0.08 \text{ Std. Dev. Opt. Power} - 0.02 \text{ Actual Duty Cycle} - 0.23 \text{ Pressure BME} \\ & - 0.02 \text{ Temperature BME} - 0.01 \text{ Pulse length} + 0.08 \text{ CO}_2 \end{aligned}$$


	RES data description							
	count	mean	std	min	25%	50%	75%	max
Frequency [Hz]	2.97E+03	4.95E+15	4.01E+16	4.82E+04	4.94E+04	4.94E+15	4.95E+04	5.05E+04
Magnitude [μV]	2.97E+03	1.07E+16	5.71E+15	2.55E+05	7.94E+05	8.29E+05	1.14E+16	3.53E+16
Std. Dev. Magnitude [μV]	2.97E+03	4.08E+16	3.64E+16	0.00E+00	1.44E+16	3.30E+15	5.82E+15	2.51E+14
Phase [°]	2.97E+03	1.03E+16	2.37E+15	9.28E+05	1.02E+16	1.03E+16	1.05E+06	1.09E+16
Optical Power [W]	2.97E+03	1.47E+16	1.93E+16	1.33E+10	1.46E+16	1.46E+16	1.48E+16	1.50E+10
Std. Dev. Opt. Power [W]	2.97E+03	3.01E+14	3.71E+14	5.94E+08	7.50E+09	8.58E+09	7.21E+15	1.08E+16
Actual Duty Cycle [%]	2.97E+03	5.00E+15	1.29E+16	4.98E+05	4.99E+05	4.99E+05	5.01E+05	5.03E+15
Pressure BME [mbar]	2.97E+03	9.95E+15	1.58E+16	2.86E+09	1.03E+10	1.05E+11	1.05E+11	1.05E+11
Temperature BME [°C]	2.97E+03	4.56E+16	1.23E+15	4.54E+15	4.55E+05	4.55E+05	4.57E+05	4.59E+15
Relative Humidity BME	2.97E+03	1.09E+16	1.87E+15	0.00E+00	0.00E+00	0.00E+00	1.85E+10	7.34E+10
NO2	2.97E+03	1.73E+08	8.83E+06	0.00E+00	1.41E+08	2.25E+07	2.30E+07	2.32E+08
O2	2.97E+03	1.54E+16	7.87E+15	0.00E+00	1.25E+15	2.01E+16	2.05E+15	2.07E+15
N2	2.97E+03	8.29E+15	7.84E+15	7.31E+15	7.95E+15	7.95E+15	8.36E+15	1.00E+01
H2O	2.97E+03	9.28E+15	1.56E+16	0.00E+00	0.00E+00	0.00E+00	1.57E+16	5.25E+14
CO2	2.97E+03	8.37E+15	1.76E+15	0.00E+00	0.00E+00	0.00E+00	8.00E+00	8.00E+15
Aceton	2.97E+03	1.31E+11	2.07E+11	0.00E+00	0.00E+00	6.93E+07	3.03E+10	1.01E+02
Total Flow [mL/min]	2.97E+03	4.97E+16	3.88E+15	4.82E+16	4.95E+15	4.99E+04	5.00E+16	5.02E+04
Current [mA]	2.97E+03	2.96E+03	0.00E+00	2.96E+03	2.96E+03	2.96E+03	2.96E+03	2.96E+03


	SPM data description							
	count	mean	std	min	25%	50%	75%	max
Frequency [Hz]	4.28E+04	4.96E+15	4.95E+16	4.89E+04	4.93E+04	4.95E+08	5.00E+04	5.07E+04
Magnitude [μV]	4.28E+04	9.41E+15	4.19E+15	2.79E+03	6.70E+15	8.06E+15	1.30E+08	3.53E+16
Std. Dev. Magnitude [μV]	4.28E+04	7.32E+15	1.33E+16	0.00E+00	4.07E+15	5.71E+15	8.01E+15	5.60E+15
Phase [°]	4.28E+04	1.04E+16	2.50E+15	-1.75E+16	8.96E+15	1.04E+06	1.19E+08	1.78E+06
Optical Power [W]	4.28E+04	1.46E+16	2.02E+16	-4.51E+02	1.46E+16	1.48E+10	1.49E+16	2.55E+10
Std. Dev. Opt. Power [W]	4.28E+04	1.87E+16	3.65E+16	5.65E+09	7.34E+09	8.08E+09	1.74E+11	4.95E+15
Actual Duty Cycle [%]	4.28E+04	4.99E+15	6.21E+15	4.95E+15	4.99E+05	5.00E+05	5.01E+05	9.02E+03
Pressure BME [mbar]	4.28E+04	9.60E+15	1.94E+15	2.86E+10	1.03E+16	1.04E+16	1.04E+16	1.05E+16
Temperature BME [°C]	4.28E+04	4.56E+15	1.14E+16	2.42E+15	4.56E+16	4.57E+15	4.57E+15	4.59E+05
Relative Humidity BME	4.28E+04	1.37E+16	2.06E+16	0.00E+00	0.00E+00	0.00E+00	2.76E+10	9.10E+10
NO2	4.28E+04	1.35E+08	9.75E+06	0.00E+00	9.20E+05	1.84E+08	2.25E+08	2.32E+08
O2	4.28E+04	1.20E+16	8.69E+15	0.00E+00	8.20E+15	1.64E+16	2.00E+16	2.07E+16
N2	4.28E+04	8.60E+15	9.01E+15	7.31E+15	7.87E+15	8.36E+15	9.61E+14	1.00E+01
H2O	4.28E+04	1.13E+16	1.64E+15	0.00E+00	0.00E+00	0.00E+00	2.29E+15	6.82E+15
CO2	4.28E+04	9.45E+14	1.95E+16	0.00E+00	0.00E+00	0.00E+00	0.00E+00	8.00E+15
Aceton	4.28E+04	1.32E+11	1.55E+11	0.00E+00	0.00E+00	4.98E+08	3.05E+10	1.01E+02
Total Flow [mL/min]	4.28E+04	4.96E+15	2.27E+15	5.00E+15	4.96E+16	4.99E+15	5.00E+16	5.03E+14
Current [mA]	4.28E+04	2.93E+16	2.26E+16	4.00E+02	2.96E+03	2.96E+03	2.96E+03	3.52E+03

C Datasheets

C.1 LG Innotek UV LED

Laser
Diodes

 **LG Innotek**



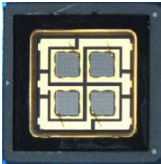
CUSTOMER : _____

DATE : _____

REV : Rev. 0.0 _____

preliminary

SPECIFICATIONS FOR APPROVAL





278nm 300mW 6868 4in1 Flat LED PKG

MODEL NAME : LEUVA77M00HU00

RoHS
Compliant

Halogen
Compliant

APPROVAL	REMARK	APPENDIX

DESIGNED	CHECKED	APPROVED
2017.06.20 H.S.Kang	2017.06.20 M.J.Jin	2017.06.20 J.J.Yoon
		

11/17 / V01 / IF / lg/leuva77m00hu00_278nm_high-power_4in1

1

LGIT Confidential and Proprietary

3. Applications

- Disinfection, Phototherapy, Fluorescent Spectroscopy, Sensor Light,
Bio-Analysis / Detection, Counterfeit Detectors, etc.

4. Absolute Maximum Ratings

(Ta= 25°C)

Items	Symbols	Ratings	Unit
Forward Current	If	TBD	A
Power Dissipation	Pd	TBD	W
Operating Temperature	Topr	-10 ~ +85	°C
Storage Temperature	Tstg	-40 ~ +100	°C
Junction Temperature	Tj	125	°C
Soldering Temperature		JEDEC-J-STD-020D	
ESD Classification		Class 2 (ANSI/ESDA/JEDEC JS-001)	

- ※ Operating the LED beyond the listed maximum ratings may affect device reliability and cause permanent damage.
These or any other conditions beyond those indicated under recommended operating conditions are not implied.
The exposure to the absolute maximum rated conditions may affect device reliability.
- ※ The LEDs are not designed to be driven in reverse bias.

5. Electro-Optical Characteristics

(Ta=25°C)

Items	Symbol	Condition	Target Spec.			Unit
			Min.	Typ.	Max.	
Forward Voltage	Vf	If = 0.35 A	-	-	34	V
Radiant Flux	Φe		-	300	-	mW
Peak Wavelength	λp		270	278	285	nm
Spectrum Half Width	Δλ		-	10.0	-	nm
Viewing Angle	2Θ1/2		-	125	-	deg
Thermal Resistance *1)	Rth j-c		-	4.3	-	°C/W

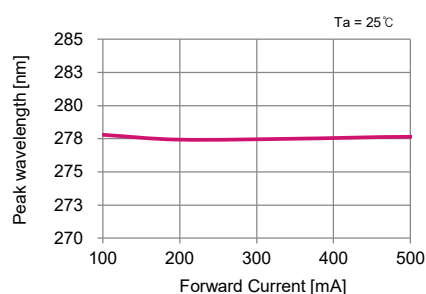
*1) Rthj-c = Thermal Resistance (Junction – Case)

- ※ These values are measured by the LG Innotek optical spectrum analyzer within the following tolerances.
- Forward Voltage(Vf) : ±0.1V
 - Peak Wavelength(λp) : ±3.0nm
 - Radiant Flux(Φv) : ±10%
- ※ Although all LEDs are tested by LG Innotek equipment, some values may vary slightly depending on the conditions of the test equipment.

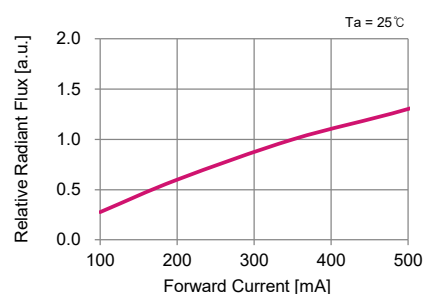
LGIT Confidential and Proprietary

7. Typical Characteristic Curves

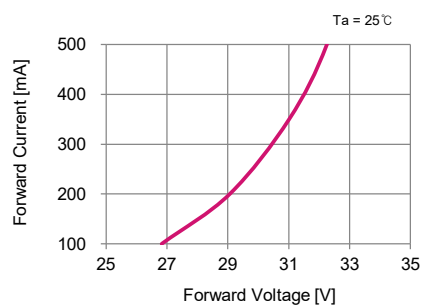
▪ Forward Current vs. Peak Wavelength



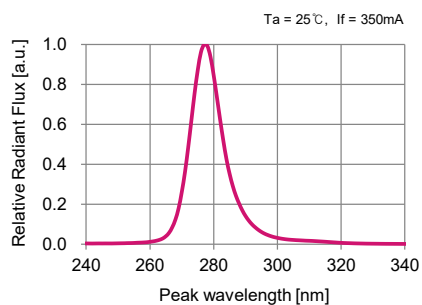
▪ Forward Current vs. Relative Radiant Flux



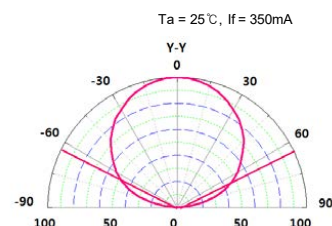
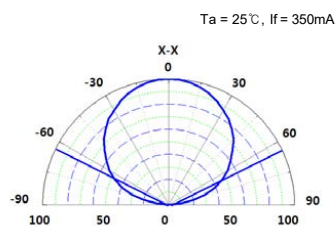
▪ Forward Current vs. Forward Voltage



▪ Spectrum



▪ Radiation Characteristics (Angle of Beam Spread, Directivity)



C.2 Bolb UV LED



High Power UV-C LED Product Specifications 6060 SMD Packaged LED

V1.6.2GHSP April 2020

05/20 / V07 / OSIF / BOLB / smd6060uv-led-high-power

1

Germany & Other Countries
Laser Components GmbH
Tel: +49 8142 2864 - 0
Fax: +49 8142 2864 - 11
info@lasercomponents.com
www.lasercomponents.com

France
Laser Components S.A.S.
Tel: +33 1 39 59 52 25
Fax: +33 1 39 59 53 50
info@lasercomponents.fr
www.lasercomponents.fr

United Kingdom
Laser Components (UK) Ltd.
Tel: +44 1245 491 499
Fax: +44 1245 491 801
info@lasercomponents.co.uk
www.lasercomponents.co.uk

Nordic Countries
Laser Components Nordic AB
Tel: +46 31 703 71 73
Fax: +46 31 703 71 01
info@lasercomponents.se
www.lasercomponents.se

USA
Laser Components USA, Inc.
Tel: +1 603 821 - 7040
Fax: +1 603 821 - 7041
info@lasercomponents.com
www.lasercomponents.com

UVC LED: Electro-optical parameters

TABLE 1. Performance @ 250 mA forward current (25°C ambient, packaged)

Parameter	Symbol	Unit	Min.	Typ.	Max
Peak Wavelength	λ_p	nm	265	272	278
Radiant Flux	ϕ_e	mW	90	100	110
Forward Voltage	V _F	V	6.0	6.5	7.0
Spectrum Half Width	$\Delta\lambda$	nm		10	
View Angle	2 $\theta_{1/2}$	°		150	
Thermal Resistance	R _{J-b}	°C/W		<10 (TBD)	

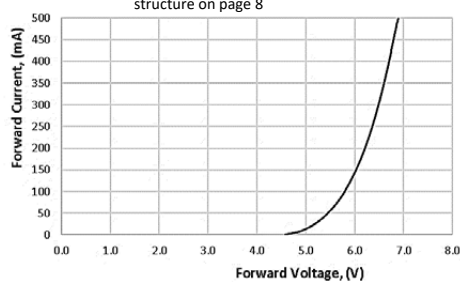
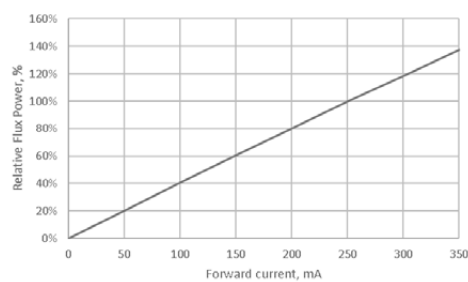
FIG 1. Forward Current vs. Forward Voltage
Please also check typical value and BIN structure on page 8

FIG 2. Relative Radiant Flux vs. Forward Current



Specifications may subject to change without notice

UVC LED: Electro-optical parameters (continued)

FIG 3. Peak Wavelength vs. Forward Current

[Ta=25°C]

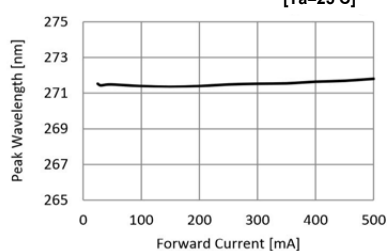


FIG 4. Spectrum

[Ta=25°C, IF=250mA]

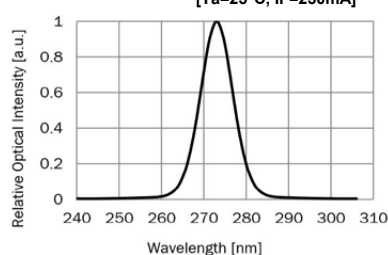


Fig 5. Forward Voltage vs. Ambient Temperature

[IF=250mA]

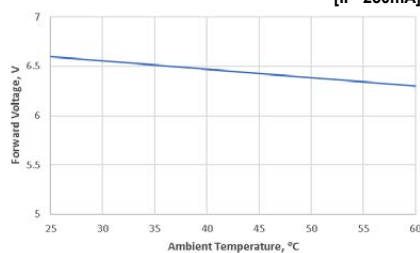


Fig 6. P-IF data vs SMD Temperature

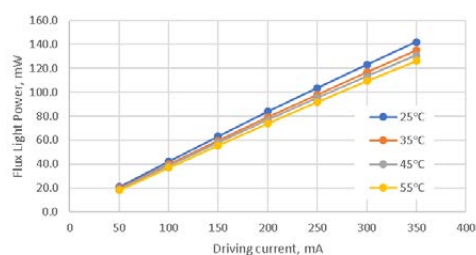
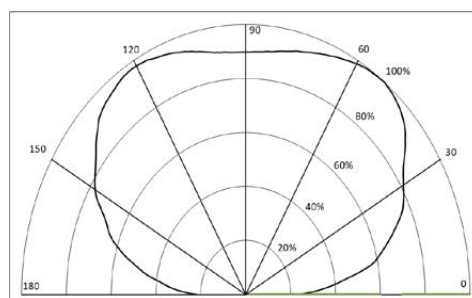


Fig 7. Far-field Emission Pattern (Relative Intensity vs. Emission Angle)

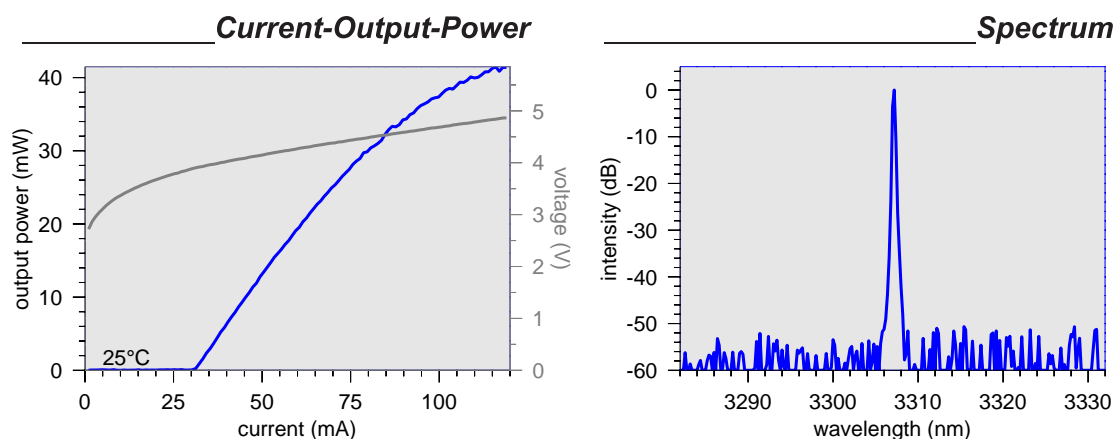


C.3 nanoplus ICL

S/N: 3159/22-16

Nanosystems and
Technologies
GmbH

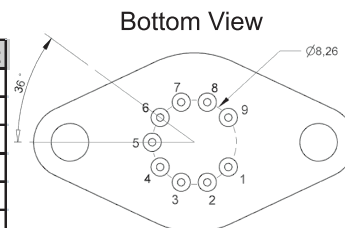

Datasheet for 3307nm DFB Laser



The laser is mounted on: TO66 with TEC and cap. Electrical connection as shown:

Pin	Function
1	Peltier (+)
2	Thermistor
3	Thermistor
4	N/C
5	N/C
6	N/C
7	LD (+)
8	LD (-)
9	Peltier (-)

Parameter	Symbol	Value	Unit
Max. temperature diff.	ΔT_{max}	67	K
Max. current	I_{max}	1.4	A
Max. voltage	U_{max}	3.8	V
Max. power	Q_{max}	3.0	W
Thermistor R_0 @ 25°C	R_0	10000	Ω
Thermistor b	b	3930	



Caution: Before operating the cooler: TO66 has to be connected to a heat sink. **Characteristics**

Parameter	Symbol	Unit	min	typical	max
Operation voltage	U	V			6
Max. Current	I_{max}	mA			120
Threshold current	I_{th}	mA		31	
Slope efficiency	e	mW/mA		0.69	

Operation conditions

Parameter	Symbol	Unit	min	typical	max
Operation temperature	T	°C	10	20	45
Wavelength	λ	nm		3307.2	
Operation current	I	mA		100	120
Output power	P_{opt}	mW		40	

Device protected by US patent no. 6,671,306; 6,846,689



Caution:

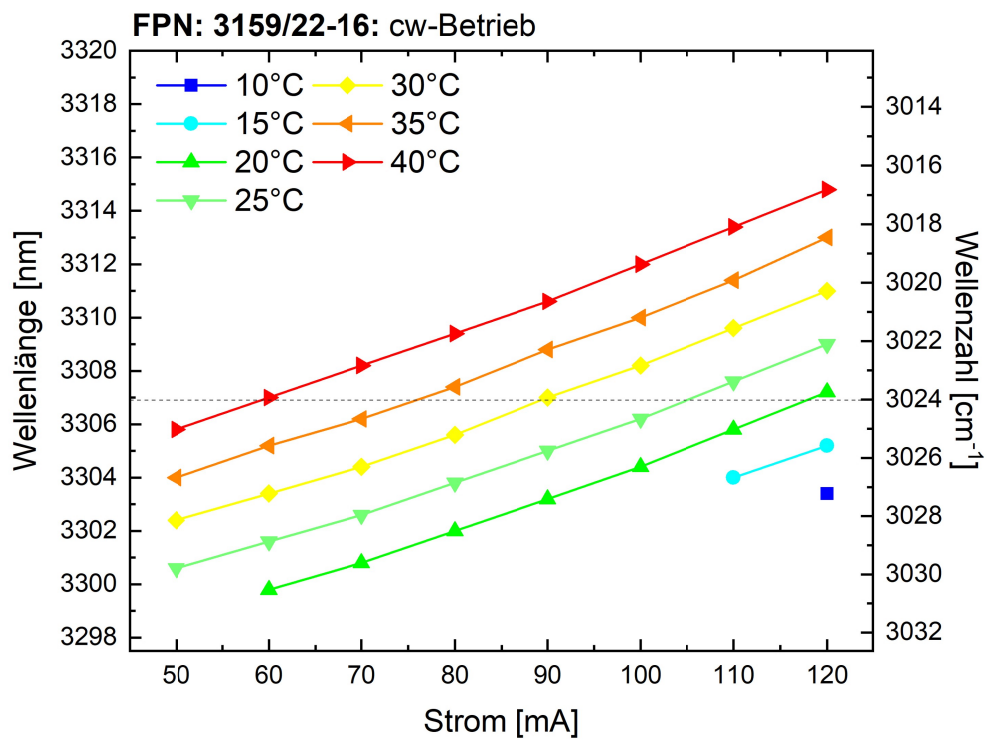
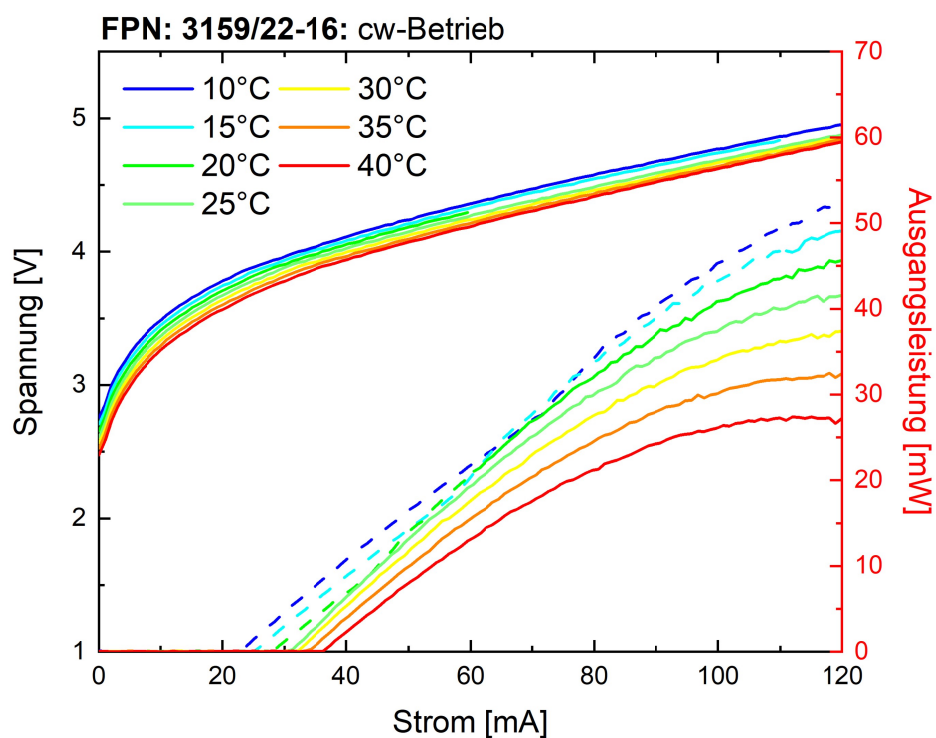
High voltage, high temperature, and mechanical forces may cause irreversible damage to the laser. When handling the laser diode proper ESD (electrostatic discharge) precautions are recommended to avoid performance degradation or loss of functionality.



nanoplus GmbH
Oberer Kirschberg 4
97218 Gerbrunn

Tel: +49 (0)931 90827-0
Fax: +49 (0)931 90827-19

<http://www.nanoplus.com>
email: sales@nanoplus.com



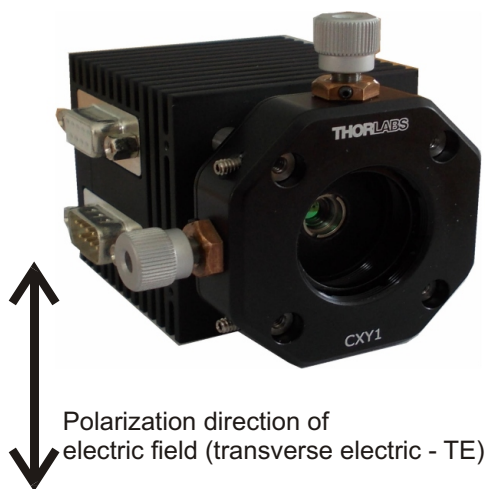
S/N: 3159/22-16

Nanosystems and
Technologies
GmbH**nanoplus**

Package option: TO66 with collimating lens

handling instructions

Nanoplus cube with X-Y collimator

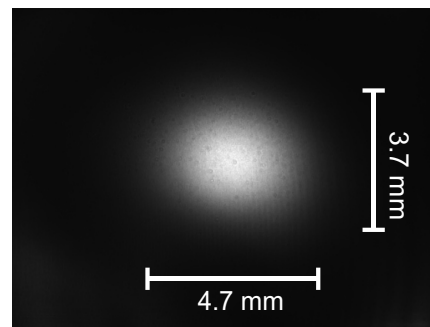


Do not touch the screws! Turning or touching of the screws will harm the beam collimation.

Apply protective cap when laser is not in use to avoid dust deposition on lens.

beam profile

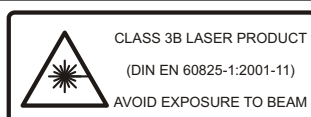
Thermal image of the collimated laser beam at 3.0 m distance from the laser facet.



Laser temperature: 20°C
Laser current: 120 mA

LOCKED: DO NOT TURN SCREWS!
Turned screws will void warranty.

Note: The collimation may reduce the laser output power by up to 20%.



Caution:

High voltage, high temperature, and mechanical forces may cause irreversible damage to the laser. When handling the laser diode proper ESD (electrostatic discharge) precautions are recommended to avoid performance degradation or loss of functionality.



nanoplus GmbH
Gleimershäuser Str. 10
98617 Meiningen

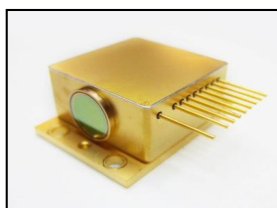
Tel: +49 (0)3693 505000-0
Fax: +49 (0)3693 505000-19

<http://www.nanoplus.com>
email: sales@nanoplus.com

C.4 AdTech QCL



8.3 μm DISTRIBUTED FEEDBACK (DFB) QCL PART NO: HHL-19-26



HIGH HEAT LOAD (HHL) PACKAGE

OVERVIEW

- Pulse or CW operated lasers
- Thermo-electrically cooled. External heat sink still required.
- Sensitive to electrostatic discharge, must have standard ESD precautions during handling
- Package dimensions: 1.75 x 1.25 x 0.72 in (excluding pins).

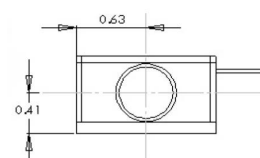
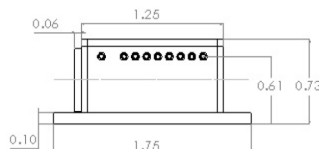
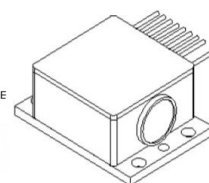
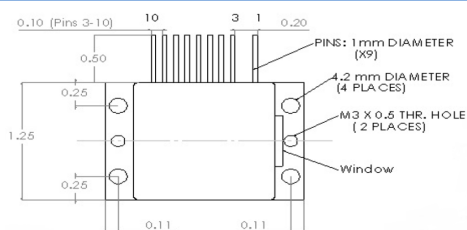
HHL SPECIFICATIONS

Model No		HHL – xx – xx	HHL –xx – xxLP	HHL –xx – xxHP	Units
TEC Parameters (25 °C)	I _{max}	7.9	----	----	A
	V _{max}	14.4	----	----	V
	Max. Heat Capacity	65.0	----	----	W
	Module Resistance	1.678	----	----	Ω
Temperature Sensor	Type	10.0 k Ω Thermistor			----
	Thermistor Constant	$A = 1.129 \text{ e}^{-3}$, $B = 2.341 \text{ e}^{-4}$, $C = 0.878 \text{ e}^{-7}$			----
Window	Material	ZnSe			----
	Thickness	0.04			in
	Diameter	0.5			in
	Transmission	> 95			%
Lens	Type	Aspheric			----
	Spectral Range	MWIR			----
Weight (approx.)		110.0			g

HHL DIMENSIONS

- Dimension: in

Pin 1 - TEC (-)
Pin 2 - Not Installed
Pin 3 - No connection
Pin 4 - Laser (+)
Pin 5 - Thermistor (+)
Pin 6 - Thermistor (-)
Pin 7 - Laser (-)
Pin 8 - No connection
Pin 9 - No connection
Pin 10 - TEC (+)



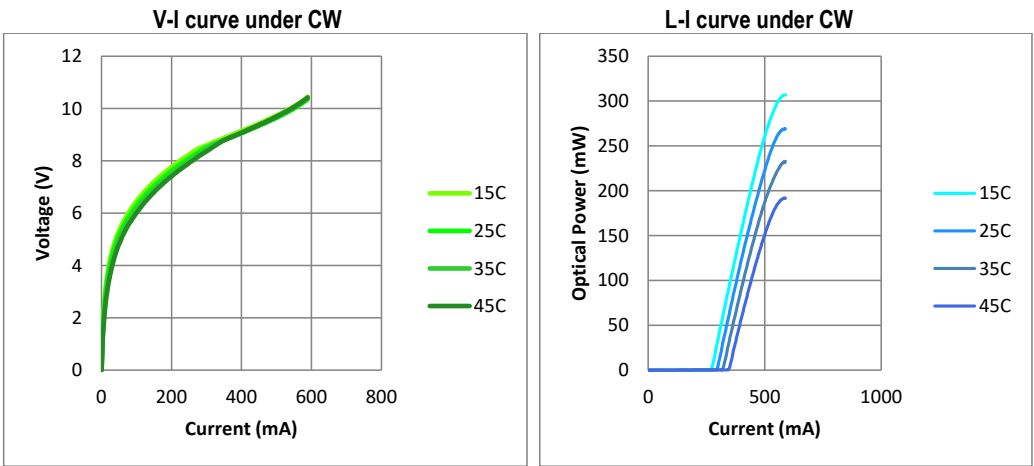


8.3 μm DISTRIBUTED FEEDBACK (DFB) QCL
PART NO: HHL-19-26

LASER SPECIFICATIONS

		Measurement Conditions	Specs	Units
Electrical	Operation Mode	-----	CW	-----
	Device Type	-----	DFB	-----
	Oper. Temperature Limits	-----		°C
	Max Oper. Currents	@ 15°C	530	mA
		@ 45°C	525	mA
	Max Oper. Voltage	-----	10.5	V
Optical	Thresh. Current	@25°C	300	mA
	Thresh. Voltage	@25°C	8.6	V
	Max. Power Output	@25°C, 420mA	144	mW
	Center Wavelength	@25°C, 420mA	8.276	μm
	Laser Efficiency (WPE)	@25°C	4.6	%
	Wavelength Tuning	Temperature	-----	nm/°C
		Current	-----	nm/mA

DEVICE OPERATIONAL CHARACTERIZATION



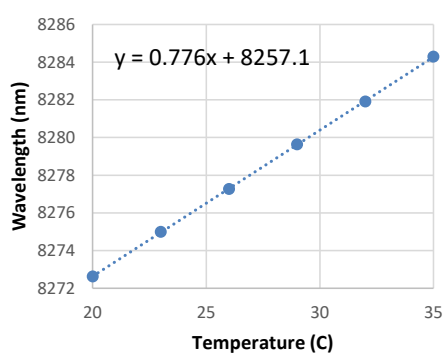


8.3 μm DISTRIBUTED FEEDBACK (DFB) QCL

PART NO: HHL-19-26

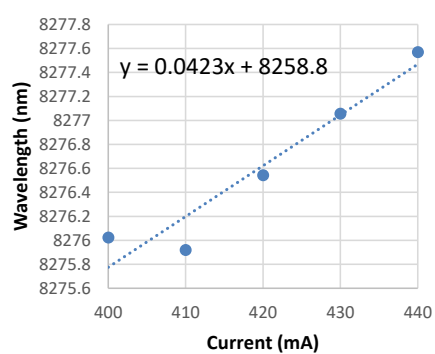
Wavelength Tuning by Temperature

Wavelength Tuning at 420mA



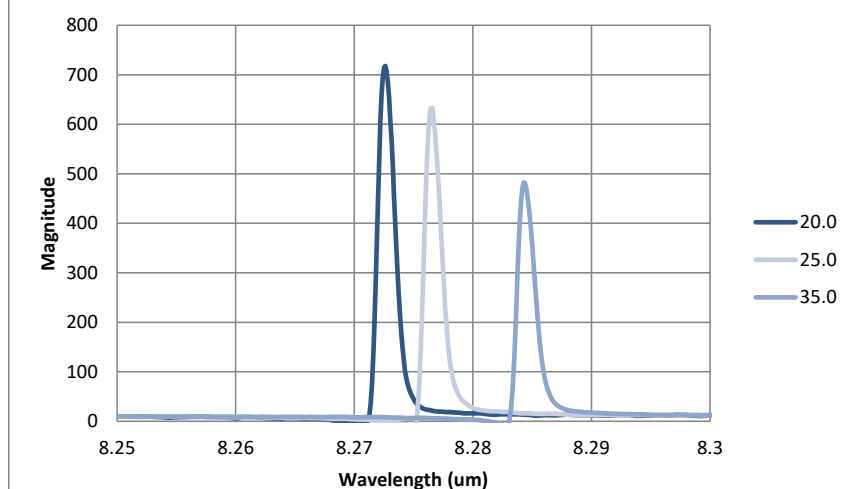
Wavelength Tuning by Current

Wavelength Tuning at 25C



Spectral Characterization:

Spectrums at 420mA



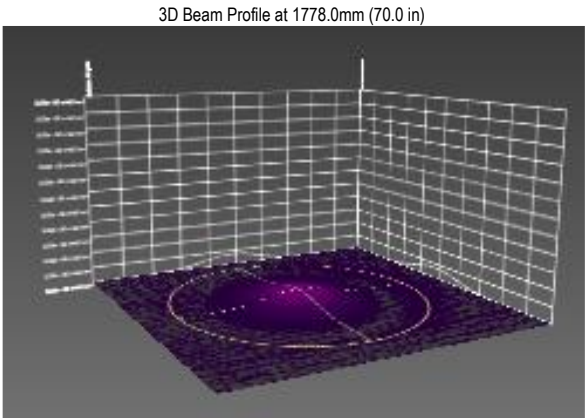
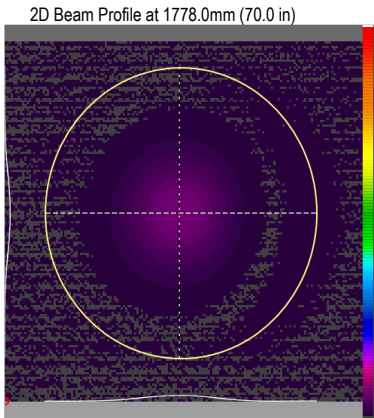


8.3 μm DISTRIBUTED FEEDBACK (DFB) QCL
PART NO: HHL-19-26

BEAM PROFILE CHARACTERIZATION⁽³⁾ UNDER CW OPERATION

	Slow – Axis (Horizontal)	Fast – Axis (Vertical)	Units
Full Beam Diameter	3.44	3.77	mm
Beam Waist Location	773.6	980.7	mm
Divergence Angle	1.53	1.39	mrاد
M ²	1.11	1.25	---

(3) I = 0.32 A, V = 8.7 V, T = 15 °C, Measured at 1/e²



Erklärung

Ich erkläre hiermit an Eides statt, dass ich die vorliegende Arbeit ohne unzulässige Hilfe Dritter und ohne Benutzung anderer als der angegebenen Hilfsmittel angefertigt habe; die aus anderen Quellen direkt oder indirekt übernommenen Daten und Konzepte sind unter Angabe des Literaturzitats gekennzeichnet.

Andere Personen waren an der inhaltlich-materiellen Herstellung der vorliegenden Arbeit nicht beteiligt. Insbesondere habe ich hierfür nicht die entgeltliche Hilfe eines Promotionsberaters oder anderer Personen in Anspruch genommen. Niemand hat von mir weder unmittelbar noch mittelbar geldwerte Leistungen für Arbeiten erhalten, die im Zusammenhang mit dem Inhalt der vorgelegten Dissertation stehen.

Die Arbeit wurde bisher weder im Inland noch im Ausland in gleicher oder ähnlicher Form einer anderen Prüfungsbehörde vorgelegt.

Regensburg, 18.11.2020

Stefan Weigl